

Antonio Giulietti *Editor*

Laser-Driven Particle Acceleration Towards Radiobiology and Medicine

Laser-Driven Particle Acceleration Towards Radiobiology and Medicine

BIOLOGICAL AND MEDICAL PHYSICS, BIOMEDICAL ENGINEERING

The fields of biological and medical physics and biomedical engineering are broad, multidisciplinary and dynamic. They lie at the crossroads of frontier research in physics, biology, chemistry, and medicine. The Biological and Medical Physics, Biomedical Engineering Series is intended to be comprehensive, covering a broad range of topics important to the study of the physical, chemical and biological sciences. Its goal is to provide scientists and engineers with textbooks, monographs, and reference works to address the growing need for information.

Books in the series emphasize established and emergent areas of science including molecular, membrane, and mathematical biophysics; photosynthetic energy harvesting and conversion; information processing; physical principles of genetics; sensory communications; automata networks, neural networks, and cellular automata. Equally important will be coverage of applied aspects of biological and medical physics and biomedical engineering such as molecular electronic components and devices, biosensors, medicine, imaging, physical principles of renewable energy production, advanced prostheses, and environmental control and engineering.

Editor-in-Chief:

Elias Greenbaum, Oak Ridge National Laboratory, Oak Ridge, Tennessee, USA

Editorial Board:

Masuo Aizawa, Department of Bioengineering,
Tokyo Institute of Technology, Yokohama, Japan

Olaf S. Andersen, Department of Physiology,
Biophysics and Molecular Medicine,
Cornell University, New York, USA

Robert H. Austin, Department of Physics,
Princeton University, Princeton, New Jersey, USA

James Barber, Department of Biochemistry,
Imperial College of Science, Technology
and Medicine, London, England

Howard C. Berg, Department of Molecular
and Cellular Biology, Harvard University,
Cambridge, Massachusetts, USA

Victor Bloomfield, Department of Biochemistry,
University of Minnesota, St. Paul, Minnesota, USA

Robert Callender, Department of Biochemistry,
Albert Einstein College of Medicine,
Bronx, New York, USA

Britton Chance, University of Pennsylvania
Department of Biochemistry/Biophysics
Philadelphia, USA

Steven Chu, Lawrence Berkeley National
Laboratory, Berkeley, California, USA

Louis J. DeFelice, Department of Pharmacology,
Vanderbilt University, Nashville, Tennessee, USA

Johann Deisenhofer, Howard Hughes Medical
Institute, The University of Texas, Dallas,
Texas, USA

George Feher, Department of Physics,
University of California, San Diego, La Jolla,
California, USA

Hans Frauenfelder,
Los Alamos National Laboratory,
Los Alamos, New Mexico, USA

Ivar Giaever, Rensselaer Polytechnic Institute,
Troy, New York, USA

Sol M. Gruner, Cornell University,
Ithaca, New York, USA

Judith Herzfeld, Department of Chemistry,
Brandeis University, Waltham, Massachusetts, USA

Mark S. Humayun, Doheny Eye Institute,
Los Angeles, California, USA

Pierre Joliot, Institute de Biologie
Physico-Chimique, Fondation Edmond
de Rothschild, Paris, France

Lajos Keszthelyi, Institute of Biophysics, Hungarian
Academy of Sciences, Szeged, Hungary

Robert S. Knox, Department of Physics
and Astronomy, University of Rochester, Rochester,
New York, USA

Aaron Lewis, Department of Applied Physics,
Hebrew University, Jerusalem, Israel

Stuart M. Lindsay, Department of Physics
and Astronomy, Arizona State University,
Tempe, Arizona, USA

David Mauzerall, Rockefeller University,
New York, New York, USA

Eugenie V. Mielczarek, Department of Physics
and Astronomy, George Mason University, Fairfax,
Virginia, USA

Markolf Niemz, Medical Faculty Mannheim,
University of Heidelberg, Mannheim, Germany

V. Adrian Parsegian, Physical Science Laboratory,
National Institutes of Health, Bethesda,
Maryland, USA

Linda S. Powers, University of Arizona,
Tucson, Arizona, USA

Earl W. Prohofsky, Department of Physics,
Purdue University, West Lafayette, Indiana, USA

Andrew Rubin, Department of Biophysics, Moscow
State University, Moscow, Russia

Michael Seibert, National Renewable Energy
Laboratory, Golden, Colorado, USA

David Thomas, Department of Biochemistry,
University of Minnesota Medical School,
Minneapolis, Minnesota, USA

Antonio Giulietti
Editor

Laser-Driven Particle Acceleration Towards Radiobiology and Medicine



Springer

Editor

Antonio Giulietti
Sezione “Adriano Gozzini”
Istituto Nazionale di Ottica
Pisa
Italy

ISSN 1618-7210 ISSN 2197-5647 (electronic)
Biological and Medical Physics, Biomedical Engineering
ISBN 978-3-319-31561-4 ISBN 978-3-319-31563-8 (eBook)
DOI 10.1007/978-3-319-31563-8

Library of Congress Control Number: 2016935958

© Springer International Publishing Switzerland 2016

This work is subject to copyright. All rights are reserved by the Publisher, whether the whole or part of the material is concerned, specifically the rights of translation, reprinting, reuse of illustrations, recitation, broadcasting, reproduction on microfilms or in any other physical way, and transmission or information storage and retrieval, electronic adaptation, computer software, or by similar or dissimilar methodology now known or hereafter developed.

The use of general descriptive names, registered names, trademarks, service marks, etc. in this publication does not imply, even in the absence of a specific statement, that such names are exempt from the relevant protective laws and regulations and therefore free for general use.

The publisher, the authors and the editors are safe to assume that the advice and information in this book are believed to be true and accurate at the date of publication. Neither the publisher nor the authors or the editors give a warranty, express or implied, with respect to the material contained herein or for any errors or omissions that may have been made.

Printed on acid-free paper

This Springer imprint is published by Springer Nature
The registered company is Springer International Publishing AG Switzerland



Professor Wolfgang Sandner (1949–2015). Courtesy Max-Born Institut Berlin © Ralf Günther/MBI

This volume is dedicated to Wolfgang Sandner who left us suddenly in December 2015. His memory will remain with us as an active and productive scientist, as a lab leader, as a science and culture organizer, as a manager of scientific organizations.

Many of the authors of this book could appreciate Wolfgang's authority together with his friendship as Coordinator of the Laserlab-Europe network.

His contribution to the topics of this volume was enormous, both directly with his outstanding scientific works and through Laserlab, making possible for many young scientists to perform their researches inside the major European laser facilities.

The Editor

Preface

The idea of this volume was originally to provide a state-of-the-art review and perspective of laser technologies addressed at implementing compact particle accelerators for biological researches and clinical uses. As long as the editorial work was progressing, it was more and more clear that the expectation level for this novel technology is quite high in a broad community of scientists, including laser, plasma and nuclear physicists, medical physicists, radiation biologists, radiologists. Contributions from each one of these classes of expertise became highly desirable and luckily they were offered by some of the leading experts and groups presently operating in these fields.

So, the original scheme expanded its branches like a fruitful tree. Physicists involved in the particle acceleration with laser techniques, provided not only the state of the art of laser-driven electron, proton and ion accelerators most suitable for biological studies and future clinical therapies, but also a deep insight of the most advanced experiments and novel ideas. It comes out that laser-produced particles beams have been already used in a variety of physical processes to generate secondary sources of high-energy photons, another kind of ionizing radiation. In turn, photons of tens of MeV have been used to produce, via photonuclear reactions, radionuclides of interest for the nuclear medicine. The reader will also discover how high-resolution ultrafast radiography can be easily performed with particles accelerated by laser.

On the other hand, radiotherapists describe some of the most advanced RF-based devices and protocols, extremely effective, they actually use in a hospital. The novel practice in radiotherapy of tumors is the benchmark (continuously moving forward) for the laser-driven technologies. While a number of biologists are systematically investigating the response of living matter to the particle bunches produced by lasers, some others are already speculating on how this new opportunity can extend and empower the most recent concepts of radiobiology.

A major point to be addressed by the research is the extremely shorter duration of bunches produced by laser with respect to bunches produced by conventional accelerators. A factor exceeding 1,000,000 is involved, from μ s to sub-ps timescale.

The ultrashort duration of laser-produced particle bunches may involve unexpected consequences for cancer therapy. In fact, it is not known if delivering the same dose with particles of the same kinetic energy but at much higher instantaneous dose-rate may lead to a different tissutal effects with possible consequences on therapeutic strategies.

From the physical point of view, we can expect that the extreme particle density we can reach in a bunch with laser acceleration could produce some nonlinear or “collective” effects which cannot be described by the usual single-particle Monte Carlo simulation. In other words, it is possible that each ultradense bunch of electrons could produce not only the statistic sum of the effects of each low-LET particle but also some high-LET effect due to the total charge involved. If this would be true, the biological action could not only concern DNA but also some structural cellular feature, like membrane.

This major issue, in turn, calls for a dedicated research on radiobiological effects to be performed with the ultrashort particle bunches produced by laser technology. It is evident that such a research also has a high conceptual value since it enables, for the first time, the investigation of very early processes occurring in the time-scales of physical, chemical, biological responses of the living matter to ionizing radiation. The action of such kind of radiation can be followed for the first time on femtosecond time scale and nanometric spatial scale.

The novel acceleration technologies, based on the interaction of ultrashort intense laser pulses with matter, delivering sub-picosecond pulses of ionizing radiation, also demand a general renewing of dosimetry and safety protocols. Both absolute and relative dosimetry are reconsidered, in the framework of international protocols. While suitable existing devices are examined, including radiochromic foils, ionization chambers, and Faraday cups, novel concepts for ad hoc detectors are introduced and need to be carefully investigated. Dosimetric simulations with Monte Carlo methods, in particular with the GEANT4 toolkit, provide a precious support to this effort.

Also radiological safety has to be reconsidered while thinking to transfer technologies based on high-power lasers in a clinical context. It is not exactly the same issue as with conventional accelerators delivering a well defined type of particle with an almost monoenergetic spectrum. We are dealing now with a mix of radiological products delivered by laser–matter interaction, at a given but changeable intensity, with a variety of materials acting as accelerating media. Of course this kind of problems have already been faced in high-power laser facilities devoted to studies on laser–matter interactions and in particular to particle acceleration, but for a medical facility the safety of patients and personnel is paramount, then also doses from any secondary radiation and any kind of other hazards have to be carefully minimized.

This volume tries to introduce the reader to the complex conceptual system growing very quickly from the advent of laser-driven particle acceleration and leading to a concrete expectation of benefits for basic knowledge and health care. The multidisciplinary contribution of several experts and research groups has been organized in 12 chapters, which in turn have been grouped into three parts, each one

including four chapters organized by major issues rather than by disciplines. A general introduction precedes the 12 chapters, while the volume is opened with a dedication to Prof. Wolfgang Sandner, whose memory is strongly linked to all the scientific efforts and successes in this field.

The editorial effort, hard as usual, was largely compensated by the enthusiastic support and friendly attitude of all the authors as well as of a few colleagues from the ILIL group of National Institute of Optics in Pisa.

The editor cannot personally forget the continuous lovely encouragement of his wife Angelica.

Pisa, Italy

Antonio Giulietti

Contents

1	Lasers Offer New Tools to Radiobiology and Radiotherapy	1
	Antonio Giulietti and Toshiki Tajima	
1.1	Introduction	1
1.2	Dealing with Protons and Ions	6
1.3	Dealing with Electrons and Photons	9
1.4	Dosimetry and Safety	12
1.5	How Far We Are	13
	References.	14

Part I Updating Radiobiology, Radiotherapy and Radiation Safety

2	Laser-Plasma Accelerators Based Ultrafast Radiation Biophysics.	19
	Yann A. Gauduel	
2.1	General Introduction	19
2.2	Ultrafast Laser Science and Real-Time Radiation Processes: the Synergy Between LERF and HERF Domains	20
2.2.1	Low Energy Radiation Femtochemistry of the Life Solvent	21
2.2.2	Multiparametric Approach of High Energy Radiation Femtochemistry	23
2.3	High Energy Electron Bunches and Ultrafast Radiation Chemistry	25
2.3.1	Laser-Accelerated High Energy Electron Beams	25
2.3.2	High Energy Radiation Femtochemistry	27
2.3.3	Towards a Real-Time Probing of Prethermal Events in the Ionization Tracks.	31
2.4	Spatio-Temporal Radiation Biomedicine	33
2.4.1	Ultrashort Pulsed Irradiation Effects at Sub-cellular Level.	35
2.4.2	Potential Applications for Pulsed Cancer Therapies	39

2.5	Concluding Remarks on Future Challenges	41
	References	43
3	Cyberknife, Dose Fractioning for Clinical Protocols	51
	Raphaëlle Mouttet-Audouard, Thomas Lacornerie and Eric Lartigau	
3.1	Stereotactic Body Radiotherapy (SBRT)	
	Using the Cyberknife®	51
3.2	The CyberKnife® and Brain Lesions	53
3.3	The CyberKnife® and Spine Lesions	54
3.4	The CyberKnife® and Lung Lesions	56
3.5	The CyberKnife® and Liver Lesions	57
3.6	The CyberKnife® and Prostate Lesions	60
3.7	The CyberKnife® and Reirradiation	60
3.8	Conclusion	62
	References	62
4	Radiation Therapy Towards Laser-Driven Particle Beams: An “OMICS” Approach in Radiobiology	67
	Luigi Minafra, Valentina Bravatà, Francesco Paolo Cammarata and Giusi Irma Forte	
4.1	Introduction	68
4.2	DNA Repair Mechanisms IR-Induced	71
4.3	Cell Death Mechanisms	72
4.4	Epigenetic Changes and Bystander Post-irradiation Effects	77
4.5	Gene Expression Profiling Induced by IR	78
4.6	Genetic Background Influences Radiation Response	83
4.7	Proteomic Profiles Activated by IR	85
4.8	Inflammatory Response to IR	87
4.9	Conclusion	90
	References	91
5	Radiological Safety in Laser Facilities	99
	Andrew Simons	
5.1	Introduction	99
5.2	Management Strategies for Radiological Facilities	101
5.2.1	Risk Mitigation Strategies	103
5.2.2	ERICPD	104
5.2.3	Essential Messages	105
5.3	Assessment Methods for Activity and Doses	106
5.3.1	First Principle Calculations	106
5.3.2	Transport	112
5.3.3	Proton and Ion Producing Laser-Targets	116
5.3.4	Photon Producing Targets	117
5.3.5	Neutron Targets	118
5.3.6	1D Simulator	118

5.3.7	Dose Calculations	120
5.3.8	Full Simulation Schemes	125
5.4	Activating the Fluid Environment	127
5.4.1	Target Hall Air Discharge	128
5.4.2	Managing the Discharge of Activated Gases.	128
5.4.3	The Management Solution	129
5.5	Overview of Calculation Methodology.	129
5.6	Summary	130
	References.	131

Part II Updating Laser-driven Electron Acceleration and Dosimetry

6	Generation of Multi-GeV Electron Beams and Bio-medical Applications	135
	Tae Moon Jeong and Jongmin Lee	
6.1	Introduction	135
6.2	Electron Acceleration in Linear and Non-linear Regimes	137
6.2.1	Formation of Laser Wake-Field	137
6.2.2	Formation of Plasma Bubble	140
6.2.3	Diffraction, Dephasing, and Depletion	141
6.2.4	Self-trapping in the Wake-Field	143
6.3	Self-guided and Channel-guided Electron Acceleration	144
6.3.1	Self-guiding in Gas Jets and Gas Cells	146
6.3.2	Gas-filled Hollow Capillary	148
6.4	Multiple Stage Acceleration	149
6.5	Applications of High Energy Electrons in Bio-medical Fields	152
6.5.1	Electron Radiation Therapy	152
6.5.2	Electron Radiography	153
6.5.3	Secondary Sources of High Energy Photons	154
6.6	Conclusion.	158
	References.	159
7	Ionization Induced Electron Injection in Laser Wakefield Acceleration	163
	Min Chen and Zheng-Ming Sheng	
7.1	Principle of Ionization Injection	164
7.2	Using Ionization Injection to Get Low Energy Spread Electron Beams	167
7.2.1	Self-truncated Ionization Injection.	168
7.2.2	Two-Color Ionization Injection.	170
7.3	Using Ionization Injection to Get Low Transverse Emittance Electron Beams	173
7.3.1	Two-Color Ionization Injection.	173
7.3.2	Ionization Injection Assisted by Transverse Colliding Pulses	175

7.4	Ionization Injection Demonstration Experiments	177
7.5	Further Development of Ionization Induced Electron Injection	178
7.6	Conclusion	180
	References	181
8	All-Optical X-Ray and γ-Ray Sources from Ultraintense Laser-Matter Interactions	183
	Leonida A. Gizzi	
8.1	Introduction	183
8.2	Basic Physical Processes	184
8.2.1	Laser-Plasma Acceleration	184
8.2.2	Laser-Solid Interactions	187
8.3	Bremsstrahlung from Laser-Driven Electrons	190
8.4	Betatron in Laser-Wakefield Acceleration	191
8.5	Thomson Scattering	192
8.5.1	Scattering Parameters	194
8.5.2	Thomson Scattering in the Laboratory	197
	References	200
9	Dosimetry of Laser-Driven Electron Beams for Radiobiology and Medicine	203
	Luca Labate, Debora Lamia and Giorgio Russo	
9.1	Introduction	203
9.2	Absolute and Relative Dosimetry of Laser-Driven Beams	205
9.2.1	Radiochromic Films	207
9.2.2	Ionization Chambers	209
9.2.3	Faraday Cups	212
9.2.4	Development of Dedicated Detectors: An Example	213
9.3	Dosimetric Simulations with Monte Carlo Methods	214
9.4	Summary and Conclusions	217
	References	218
Part III Updating Laser-driven Ion Acceleration for Biomedical Applications		
10	Laser-Driven Ion Accelerators: State of the Art and Applications	221
	Marco Borghesi and Andrea Macchi	
10.1	Introduction	221
10.2	Acceleration Mechanisms	222
10.2.1	Target Normal Sheath Acceleration	223
10.2.2	Radiation Pressure Acceleration	226
10.2.3	Collisionless Shock Acceleration	230
10.2.4	Acceleration in Underdense and Relativistically Transparent Plasmas	232

10.3	Perspectives for Biomedical Applications	233
10.3.1	Oncological Ion Beam Therapy	233
10.3.2	Radiobiology Studies	235
10.3.3	Production of Short-Lived Isotopes and Neutrons	236
10.4	Concluding Remarks	237
	References	238
11	Biological Responses Triggered by Laser-Driven Ion Beams	249
	Akifumi Yogo	
11.1	Introduction	249
11.2	Overview of IBT from a Perspective of Physics	251
11.3	Experimental Investigations	252
11.4	Discussion: Dose Rate that Can Induce Nonlinear Effect on the Biological Response	264
11.5	Conclusion and Future Prospect	265
	References	266
12	High Resolution Ion and Electron Beam Radiography with Laser-Driven Clustered Sources	271
	Anatoly Faenov, Tatiana Pikuz and Ryosuke Kodama	
12.1	Introduction	271
12.2	Laser-Accelerated Proton/Ion Beams Applied to Radiography of Solids and Plasmas	272
12.3	Features of Laser-Cluster Compared with Laser-Solid and Laser-Gas Interactions	274
12.4	High-Resolution Radiography Using a Femtosecond Laser-Driven-Cluster Based Source of Multicharged Ions	276
12.5	Using Laser-Accelerated Electron Beams for High Resolution Radiography	283
12.6	High Resolution Electron Radiography Using a Laser-Driven-Cluster-Based Source	285
12.7	Conclusions and Perspectives	289
	References	290
13	Recent Progress in Laser Ion Acceleration	295
	Toshiki Tajima	
13.1	Introduction	295
13.2	Self-consistent Electrostatic Sheath Dynamics	301
13.3	Self-similar Evolution of Ion Dynamics	304
13.4	Single-Cycled Pulse Acceleration (SCPA)	306
13.5	Conclusions	310
	References	312
Index		315

Contributors

Marco Borghesi Queen's University of Belfast, Belfast, UK

Valentina Bravata Consiglio Nazionale delle Ricerche, Istituto di Bioimmagini e Fisiologia Molecolare, Cefalù, Italy

Francesco Paolo Cammarata Consiglio Nazionale delle Ricerche, Istituto di Bioimmagini e Fisiologia Molecolare, Cefalù, Italy

Min Chen Key Laboratory for Laser Plasmas (Ministry of Education) and Department of Physics, Shanghai Jiao Tong University, Shanghai, China

Anatoly Faenov Institute for Academic Initiatives, Osaka University, Suita, Osaka, Japan; Joint Institute for High Temperatures, RAS, Moscow, Russia

Giusi Irma Forte Consiglio Nazionale delle Ricerche, Istituto di Bioimmagini e Fisiologia Molecolare, Cefalù, Italy

Yann A. Gauduel LOA, ENSTA ParisTech, CNRS, Ecole Polytechnique, University Paris-Saclay, Palaiseau, France

Antonio Giulietti Consiglio Nazionale delle Ricerche, Istituto Nazionale di Ottica, Pisa, Italy

Leonida A. Gizzi Consiglio Nazionale delle Ricerche, Istituto Nazionale di Ottica, Pisa, Italy

Tae Moon Jeong Advanced Photonics Research Institute, GIST, Gwangju, Korea

Ryosuke Kodama Institute for Academic Initiatives, Osaka University, Suita, Osaka, Japan; PPC and GSE Osaka University, Suita, Osaka, Japan

Luca Labate Consiglio Nazionale delle Ricerche, Istituto Nazionale di Ottica, Pisa, Italy

Thomas Lacornerie Academic Radiation Oncology Department, Centre Oscar Lambret and University, Lille, France

Debora Lamia Consiglio Nazionale Delle Ricerche, Istituto di Bioimmagini e Fisiologia Molecolare, Cefalù, Italy

Eric Lartigau Academic Radiation Oncology Department, Centre Oscar Lambret and University, Lille, France

Jongmin Lee Advanced Photonics Research Institute, GIST, Gwangju, Korea; Global Institute of Laser Technology, HGU, Pohang, Gyung-buk, Korea

Andrea Macchi Consiglio Nazionale Delle Ricerche (CNR/INO), Istituto Nazionale di Ottica, Pisa, Italy

Luigi Minafra Consiglio Nazionale delle Ricerche, Istituto di Bioimmagini e Fisiologia Molecolare, Cefalù, Italy

Raphaëlle Mouttet-Audouard Academic Radiation Oncology Department, Centre Oscar Lambret and University, Lille, France

Tatiana Pikuz Joint Institute for High Temperatures, RAS, Moscow, Russia; Graduate School of Engineering, Osaka University, Suita, Osaka, Japan

Giorgio Russo Consiglio Nazionale Delle Ricerche, Istituto di Bioimmagini e Fisiologia Molecolare, Cefalù, Italy

Zheng-Ming Sheng Key Laboratory for Laser Plasmas (Ministry of Education) and Department of Physics, Shanghai Jiao Tong University, Shanghai, China; SUPA, Department of Physics, University of Strathclyde, Glasgow, UK

Andrew Simons Atomic Weapons Establishment, Aldermaston, Reading, UK

Toshiki Tajima Department of Physics and Astronomy, University of California at Irvine, Irvine, CA, USA

Akifumi Yogo Institute of Laser Engineering, Osaka University, Suita, Osaka, Japan

Chapter 1

Lasers Offer New Tools to Radiobiology and Radiotherapy

Antonio Giulietti and Toshiki Tajima

Abstract Multidisciplinary contributions of scientists actively operating in frontier laser science, radiation biology, tumor therapy, dosimetry and radiation safety provide a wide description of the status and perspectives of a primary field for human health care, in view of the emerging novel technology providing laser-driven sources of ionizing radiation.

1.1 Introduction

Though the rate of survivals increases regularly year by year, cancer is still the first cause of death everywhere. The number of *new* cases of cancer in the world is estimated to have been about 14 millions in the year 2012, with an expectation of more than 20 millions in 2020 [1]. About 50 % of cases are treated with radiation therapies, possibly in combination with surgery and/or chemotherapy, with an emerging problem for the access of low- and middle-income countries (LMIC) to radiation therapy [2].

Among these treatments, more than 90 % use RF-driven linear accelerators of electrons (RF-Linac). Other techniques include internal radiation (brachytherapy) and proton-ion beams (hadrotherapy). In most cases electrons delivered by a RF-linac are not used directly on the tumor but converted into photons (hard X-rays) by bremsstrahlung through a suitable target. In some case electrons are used directly, either to cure superficial tumors or in the Intra-Operative Radiation Therapy (IORT) which can be applied during surgical operation of a tumor [3, 4].

A. Giulietti (✉)

Istituto Nazionale di Ottica, Consiglio Nazionale delle Ricerche, Pisa, Italy
e-mail: antonio.giulietti@ino.it

T. Tajima

Department of Physics and Astronomy, University of California at Irvine,
Irvine, CA, USA
e-mail: ttajima@uci.edu

Radiation therapy techniques evolve and progress continuously and so do accelerators and dose delivering devices, which share a global market of about \$ 4 billions, growing at an annual rate exceeding 5 % [5]. Most of the progress involves precision in tumor targeting, multi-beam irradiation, reduction of damage on healthy tissues and critical organs, fractionation of dose delivering for a more effective cure [6]. Among these novel techniques and protocols of treatment, particularly effective appears the so-called Cyberknife. This technique uses a multitude of small beams which creates a large dose gradient resulting in the delivery of high dose to the tumor while minimizing the dose to adjacent healthy tissues [7]. This fast evolving scenario is the moving benchmark for the progress of the laser-based accelerators in order to become appealing towards clinical uses.

Basically, requested electron kinetic energy ranges from 4 to 25 MeV, but rarely energy above 15 MeV is used. Required dose/rate usually ranges from 1 to 10 Gy/min. These two ranges of performances are presently well fulfilled by plasma accelerators driven by ultrashort laser pulses of “moderate” peak power, i.e. tens of TW, operating within high efficiency laser-plasma interaction regimes at a pulse repetition rate of the order of tens of Hz [8]. However further work has to be done on laser acceleration in order to reach the clinical standard in terms of the electron output stability and reproducibility.

Several tasks have to be afforded before proceeding to a technical design of a laser-driven linac prototype for clinical tests. A first task is the optimization of both laser and gas-jet (or other possible targets) as well as their coupling (involving mechanical stability and optical design). Another task is the energy control of the electron bunch to provide different electron energies on clinical demand. These goals would require a complex scientific and technological investigation addressed to both the laser system, in order to make it as stable, simple and easy to use as possible and to the physics of the acceleration process, in order to get the highest possible efficiency, stability and output control [9].

We may nevertheless try and list some of the expected advantages of future Laser-linac’s for clinical uses. Laser technology strongly reduces size and complexity of the acceleration section (Mini-linac) of the device; it also totally decouples the “driver” from the acceleration section: we can imagine a single high power laser plant in a dedicated hospital room (with no need for radioprotection) which delivers pulses to a number of accelerators located in several treatment or operating rooms, suitably radioprotected. Laser managing and maintenance can proceed independently from the managing and maintenance of the Mini-linac’s. Each Mini-linac could be easily translated and rotated according to the given radiotherapy plan. Current studies could prove that the extreme dose-rate per pulse delivered by the Laser-linac would reduce the total dose for a therapeutical effect. This latter of course would be a major advantage of laser-driven radiotherapy.

The original idea of Laser Wake-Field Acceleration [10] and the advent of the decisive CPA laser technology [11] originated one of the most appealing scientific case of the last decades. Since then, a number of schemes for laser driven acceleration of electrons in plasmas have been proposed and studied, some of which were successfully tested. New experimental records have been reported in the

recent literature, in terms of the maximum electron energy achieved, the minimum energy spread, as well as maximum collimation, stability, and so on. These records are in general obtained with lasers of outstanding performances and/or with very sophisticated methods hardly applicable for practical uses. On the other hand, many labs are intensively working on scientific and technological innovations aimed at demonstrating that reliable laser-based devices can be built which are able to produce electron beams fulfilling requirements of specific applications. A major task is addressed to the possible clinical use of electron Laser linacs and their potential advantages with respect to the existing RF-linacs operating today for millions of daily hospital treatments in the world.

This is the context in which the exciting progress of laser-driven electron acceleration try to make this technique competitive with existing RF-based devices involved in 90 % of tumor treatments with radiation therapy. It has to be said however that Hadrotherapy, presently limited to a few percent of global treatments, is by far the most desirable way for the future to treat tumors with ionizing radiation. This is due to the peculiar character of energy deposition of hadrons in a medium. Figure 1.1 clearly shows that, treating a tumor at 15 cm depth, monoenergetic protons and Carbon ions of suitable kinetic energy deliver most of the dose in a thin layer (Bragg peak) around the tumor site, while monochromatic gamma rays (usually generated by bremsstrahlung of electrons) leave a lot of energy inside healthy tissues, before and after the tumor, with possible damages on these latter tissues.

It has to be said, this drawback for electron-based clinical devices has been strongly reduced with modern configurations allowing multi-beam irradiations at different angles [6, 7]. Nevertheless, hadrotherapy still remains the primary option for the future of radiotherapy, 70 years after its first conceptual proposition [12] followed by pioneering experimental tests [13]. Since then, hadron therapy was

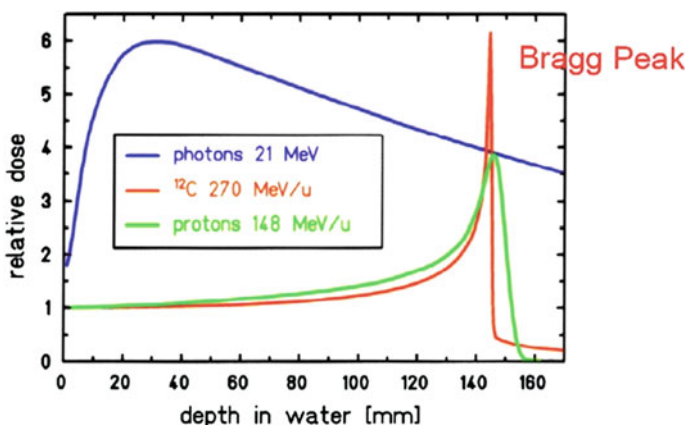


Fig. 1.1 Relative dose deposition versus depth in water for three kinds of ionizing agents, each one with a specific energy

occasionally performed inside accelerator facilities devoted to high energy physics, until the opening (1990) of a first clinical center equipped with a proton accelerator facility at Loma Linda Hospital in California (USA). In the last decades both the number of centers and the number of treated patients grew almost exponentially worldwide as shown in Fig. 1.2 [14]. More than 137,000 patients were treated with this therapy worldwide from beginning up to 2014, including 15,000 in 2014, 86 % of which were treated with protons and 14 % with carbon ions and with other particles.

Though the total number of treatments is still a small fraction of the total number of radiation treatments, this impressive growth demanded a huge capital investment which could be afforded only by the most rich countries. In fact, size and cost (both for construction and maintenance) of such facilities are presently major drawbacks for a wider diffusion of hadrotherapy. RF-based ion accelerators have faced an impressive progress, mostly in the synchrotron configuration [15] but typical acceleration gradients still remain of the order of 1 MeV/m, so that the typical diameter of an accelerator ring is several tens of meters for energies of clinical interest, namely $E \approx 100\text{--}400 \text{ MeV/u}$, with severe costs involved [16]. Additional high costs and large spaces are requested by the very heavy gantry systems necessary to guide the particle beam onto the patient body from the right direction(s) and focus it with a millimeter precision [17].

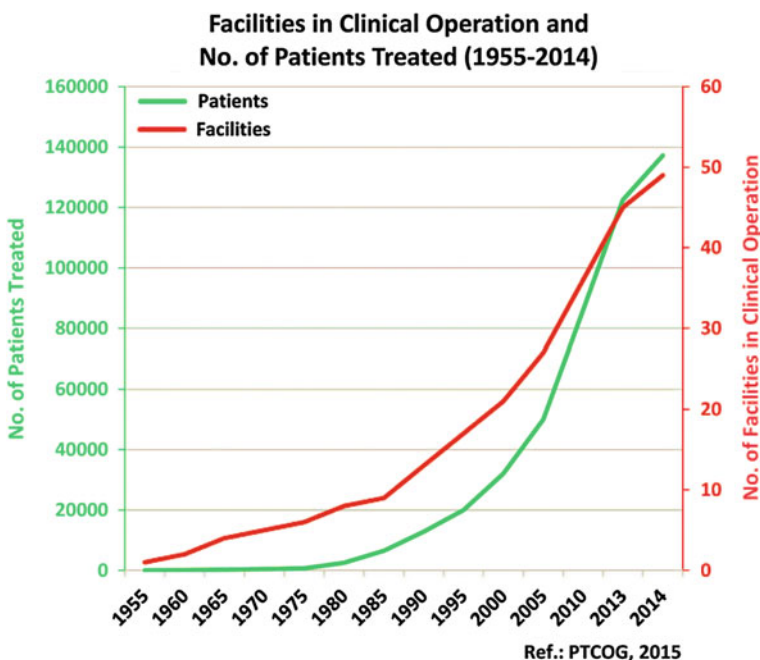


Fig. 1.2 Growth of hadrotherapy in treatment centers and treated patients worldwide (from [14])

With such a strong motivation, research on laser-based proton acceleration has been considerably supported in the last decade, mostly in the direction of achieving the challenging performances requested by the clinical standards. A usable device for cancer therapy needs to produce 200–250 MeV protons and/or 400–450 MeV/u carbon ions. In order to really profit of the Bragg peak, no more than 1 % energy bandwidth is requested. Further, to release a dose of therapeutic interest in a reasonable time, more than 10^{10} particle/s have to reach the tissue under treatment. None of these performances has been achieved so far with laser techniques. Some of them seem still hard to achieve with existing lasers or even with the next generation lasers, at least in a configuration practically usable in a hospital context. Nevertheless, the impressive crop of knowledge [18], the preliminary successful biological tests already performed [19] and some exciting new ideas [20] strongly encourage laser community in carrying on towards this challenging task.

Laser driven electron acceleration via excitation of plasma waves acts on free electrons already available in a plasma. In general the primary interaction of the laser field is with electrons (either bound or free), while action on massive particles (protons and ions) needs the intermediate role of electrons. For this reason, though evidence of the effect of the laser field on the ion velocity was found as early as high power lasers entered the laboratory, the first relevant effects on ion acceleration were observed, in the fusion research context, with powerful CO₂ lasers [21, 22]. These latter in fact, due to their large wavelength (10-μm) can induce huge electron quiver velocities on plasma electrons.

Historically, ion acceleration in plasmas was proposed before the invention of optical lasers, as early as 1956 [23] and initially tested with electrons propagating in plasmas. Apart from initial observations related to fusion studies with infrared CO₂ lasers cited above, the laser driven ion acceleration studies with optical lasers could really start only after some decisive breakthrough towards high peak power lasers, like mode-locking (ML) for picosecond pulses and chirped pulse amplification (CPA) for femtosecond pulses [11]. About 1-MeV ions were produced in the early Nineties with picosecond laser pulses [24]. Since then, an impressive progress towards higher kinetic energies was continuously driven by both innovation in laser technology and better comprehension of the complex physics involved in the ion acceleration processes. Several proposals raised for a variety of schemes of laser-matter interaction at ultra-high (ultra-relativistic) intensities able to drive protons and light ions to near-relativistic energies. Most of them can be attributed either to *target normal sheath acceleration* (TNSA) or *radiation pressure dominated acceleration* (RPDA). This matter is deeply discussed by Borghesi and Macchi in the Chap. 10.

In a general view, considering the present state of the art, we can say that laser-driven acceleration to kinetic energies suitable for radiotherapy of cancer is well consolidated in the case of electrons and bremsstrahlung photons (with bunches delivering the requested dose). Effort is being invested towards achievement of corresponding energies for protons and light ions. Time for technological and commercial alternative with existing Hospital electron-Linac's as well as with huge plants already operating hadron therapy, may not be so far. In the case of electrons

most of the work to be still done, in order to achieve clinical standards, has to address the control of the electron energy, as well as stability and reliability of the laser-linac. In the case of protons and light ions the work to be done still includes the identification of an acceleration scheme able to produce particles of suitable energy (and energy spread) in bunches delivering the right dose.

However, there is a major scientific issue which has to be addressed from now, concerning potential radiobiological effects of the extremely different duration of bunches produced by laser with respect to bunches produced by conventional accelerators. A factor exceeding 1,000,000 is involved, from μs to sub-ps timescale. The ultrashort duration of laser-produced particle bunches may involve unexpected consequences for cancer therapy. In fact, it is not known if delivering the same dose with particles of the same kinetic energy but at much higher instantaneous dose-rate may lead to a different tissutal effects with possible consequences on therapeutic strategy and protocols [25]. From the physical point of view we can expect that the extreme particle density we can produce in a bunch with laser acceleration could behave “collectively” and/or lead to non-linear effects (see Sect. 11.4 of Chap. 11) which cannot be described by the usual single-particle Monte Carlo simulation. In other words it is possible that each ultradense bunch of electrons could produce not only the statistic sum of the effects of each low-LET particle but also some high-LET effect due to the total charge involved. If this would be true, the biological action could not only concern DNA but also some structural cellular feature, like membrane. This major issue, in turn, calls for a dedicated research on radiobiological effects to be performed with the ultrashort particle bunches produced by laser technology. It is evident that such a research also has a high conceptual value since it enables, for the first time, the investigation of very early processes occurring in the timescales of physical, chemical, biological responses of the living matter to ionizing radiation [26]. Investigation of very early effects arising from ultrashort ionizing pulses at nanometric scale become possible in a framework of advanced *femtochemistry*. This opportunity move also the interest of biologists, aimed at improving the “OMIC” approach to radiation therapy [27]. It should be pointed out that the use of laser in combination of an electron beam is capable of creating collimated energy-specific (and energy-tunable) X-rays and γ -rays via the laser Compton scattering process. Such photons can be a valuable source for radiation oncology. For example, this can yield valuable radioisotopes useful for specific purposes in radiobiology and oncology [28].

1.2 Dealing with Protons and Ions

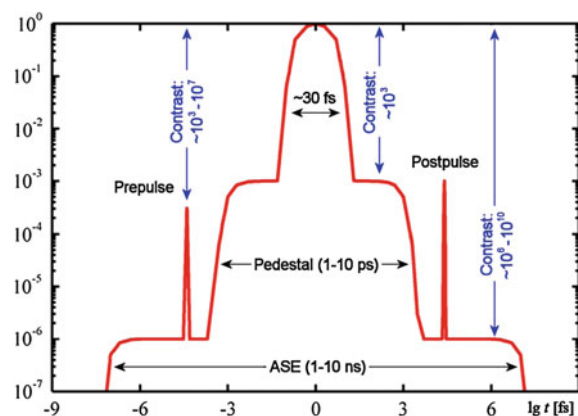
A high power laser primarily acts with its e.m. field on electrons (first bound, then free after ionization), while action on massive particles (protons and ions) needs the intermediate role of these electrons. This scenario has been described in many works after the advent of powerful laser systems and has been recently reviewed within the correct theoretical background by Mulser and Bauer [29]. More recent

review papers specifically devoted to laser-driven ion acceleration includes [30] and [31], this latter more addressed to applications. The reader can find an updated discussion of the main acceleration mechanisms, including *Target Normal Sheath Acceleration*, *Radiation pressure acceleration* and *Collisionless shock acceleration*, in the Sect. 10.2 of Chap. 10.

Apart for some “exotic” targets or sophisticated configurations reviewed in [30, 31], proton spectra produced by TNSA show a broad, thermal-like energy spectrum. This feature risks to vanish the advantages of the Bragg peak in deep energy deposition, which is the strongest motivation for hadron therapy. Most of the energy broadening in the TNSA acceleration is due to the initial distribution of protons in a wide region where the accelerating field varies considerably. An effort at designing special targets (e.g. with small dots of proton-rich material on surface or “grating targets” [32]) is currently in progress with a partial but encouraging success. At the same time several kind of passive filters able to reduce the outgoing proton spectrum are tested. It has to be considered, however, that any kind of passive particle filtering will introduce an additive radioactivation trouble in a clinical context. Novel simulations of acceleration with single-cycle laser pulses, based on a very recent idea of realizing single-cycle laser emission at high power [33], are discussed in Sect. 13.4 of Chap. 13.

In most of the laser-based ion acceleration schemes a crucial role is played by the *laser pulse contrast*, more exactly by the ratio between the main pulse peak *power* and the power associated with the light emitted by the laser chain *before* the main pulse itself. In Fig. 1.3 the emitted power versus time is sketched in a log-log diagram. Though all the early emission is often indicated as *prepulse*, the actual prepulse (left hand peak in Fig. 1.3) is an ultrashort pulse, similar to the main pulse but much weaker, leaking from the electro-optical shutter out of the oscillator. This prepulse usually carries a negligible amount of energy (and power). More dangerous is the *amplified spontaneous emission* (ASE), which lasts typically a few nanosecond and then carries a considerable amount of energy, comparable with the main pulse energy if the contrast is worse than 10^6 . In most of the previous

Fig. 1.3 Time evolution of parasitic laser emission before and after the main pulse (image from [35])



experiments on laser-driven proton acceleration this *ns-contrast* had to be increased above 10^9 , with several means, including the “plasma mirror” technique [34].

Early emission a few picosecond before the main pulse (*ps-pedestal*) involves the *ps-contrast* which is usually 3–4 orders of magnitude worse than the ASE-contrast, but carries much less energy. It can be nevertheless dangerous as well. It can be reduced only assuring high quality and accuracy in the optical compression of the stretched amplified pulse at the end of the laser chain. A critical feature of the pre-pulse problem is that most of the undesired effects depend on the absolute value of the pre-pulse energy and power and not from the value of the contrast. In other words, increasing the laser power, as requested by most of the advanced schemes of acceleration, the contrast has to be increased correspondingly. This technical point deserves a special attention for the future of laser-driven ion accelerators.

It has been clear for a long time that, differently from electrons, proton sources driven by laser need not only high pulse peak intensity but also high energy per pulse. A pioneering experiment from Lawrence Livermore National Laboratory, demonstrated high current proton beams of several tens of MeV’s [36] with PW laser pulses whose high contrast was assured by a plasma-mirror technique [34]. Preliminary investigations were performed in many laboratories with femtosecond and picosecond pulses of different power. These investigations were quite useful to assess the validity of various schemes achievable at the available laser fluence but they also evidenced that for getting kinetic energy and mean proton current suitable for clinical application, a general laser upgrading was necessary. Further, a decisive progress of laser technology towards higher peak power, higher contrast (see above), higher repetition rate has to be faced.

Though protons produced with laser-plasma techniques are still far from clinical requirements, they are currently used for preliminary tests on biological samples in order to assess their capability as ionizing agent, also considering the ultra-short duration of the laser-produced particle bunches, compared with the ones delivered by RF-based machines. Relatively low kinetic energy, broad energy spectrum and large divergence of the beams do not prevent possibility of such investigations.

Taking into account their high-LET (linear energy transfer), a few MeV protons have been compared, in terms of relative biological effectiveness (RBE), with both RF-accelerated protons and standard X-ray sources. Yogo et al. have first demonstrated breaking of DNA in human cancerous cells with laser-accelerated protons [37], then measured their RBE [38]. A relevant feature of laser-produced proton bunches lies on their outstanding instantaneous dose rate, due to their duration of about 1 picosecond, more than one million times shorter than RF-produced pulses. Dose rate as high as 10^9 Gy/s have been obtained and tested on biological samples [39]. A more extended overview on this kind of experimental investigations can be found in Sect. 11.3 of Chap. 11.

Another interesting biological application of energetic protons and ions produced with laser techniques is radiography [40]. In fact, the unique properties of protons, multicharged ions and electron beams generated by high-intensity laser-matter interactions, particularly in terms of spatial quality and temporal

duration, have opened up a totally new area of high-resolution radiography. Laser-driven radiographic sources obtained by irradiation of clustered gases were proved to be particularly effective, leading to large-field high-contrast images with 1 μm spatial resolution [41].

1.3 Dealing with Electrons and Photons

If we limit our consideration to radiotherapy, present table-top laser driven electron accelerators can be already considered as candidate. In fact, for this medical application, most of the requirements usually asked to electron bunches are practically achieved. Small divergence, monochromaticity, pointing stability, etc. are requested at a moderate level, while the main effort has to be devoted to efficiency, stability and reliability of the process in order to provide clinically acceptable devices.

As far as the efficiency is concerned, in an experiment performed at CEA-Saclay (France) a regime of electron acceleration at high efficiency was found, using a 10 TW laser and a supersonic jet of Helium [8]. This *table-top* accelerator delivered high-charge (nC), reproducible, fairly collimated, and quasimonochromatic electron bunches, with peak energy in the range 10–45 MeV. In Fig. 1.4 a typical cross section of the relativistic electron beam at 25 MeV is shown, after de-convolution of experimental data from the SHEeba radiochromic film stack device [42].

3D particle-in-cell simulation performed with the numerical code CALDER [43] reveals that the unprecedented efficiency of this accelerator was due to the achievement of a physical regime in which multiple electron bunches are accelerated in the gas-jet plasma during the action of each laser shot.

With this experiment, laser driven electron acceleration approached the stage of suitability for medical uses, in particular for Intra-Operative Radiation Therapy (IORT) of tumors [3, 4]. Comparison of the main parameters of electron bunches

Fig. 1.4 25-MeV electron beam cross section (Giulietti et al. [8])

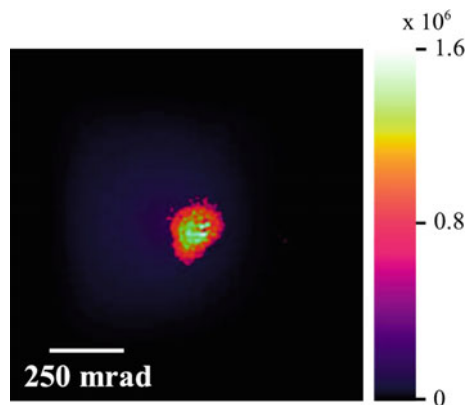


Table 1.1 Comparison between commercial RF-linac's and experimental laser-linac pulse (table from [34])

Linac	IORT-NOVAC7	LIAC	Laser-linac (experimental)
Company	(SORDINA SpA)	(Info & Tech Srl)	(CEA-Saclay)
Max electron energy (MeV)	10	12	45
Available energies (MeV)	3, 5, 7, 9	4, 6, 9, 12	5–45
Peak current	1.5 mA	1.5 mA	>1.6 KA
Bunch duration	4	1.2 μ s	<1 ps
Bunch charge (nC)	6	1.8	1.6
Repetition rate (Hz)	5	5–20	10
Mean current	30 nA @ 5 Hz	18 nA @ 10 Hz	16 nA @ 10 Hz
Released en. in 1 min.	18 J @ 9 MeV	14 J @ 12 MeV	21 J @ 20 MeV

produced by a commercial RF Hospital accelerator for IORT treatment and those of the present laser driven accelerator is shown in the Table 1.1.

In the same experiment electron bunches of \approx 40 MeV were converted, via bremsstrahlung in a tantalum foil, into gamma rays with a strong component in the range 10–20 MeV, which matches the Giant Dipole Resonance of nuclei. This gamma rays could in turn activate a foil of gold according to the nuclear reaction $^{197}\text{Au}(\gamma, n)^{196}\text{Au}$. The number of radioactive gold atoms produced in this way was measured [8]. This achievement opens the way to table-top laser-driven nuclear physics and production of radio-isotopes for medical uses. It is also noted that the laser Compton X-rays (and γ -rays) may be generated off an electron beam, whose applications have been mentioned in [28].

As already said in the Introduction, in most cases electrons delivered by a RF-linac currently used in Hospitals, are not sent directly on the tumor but previously converted into photons (hard X-rays) by bremsstrahlung through a suitable target. Of course this is possible also for electrons of comparable energy currently produced in high-power laser labs. Laser-driven electron accelerators would be then ready for clinical uses provided a suitable stability, uniformity and reproducibility of the electron bunches will be reached [9].

Interestingly, such level of performances have been recently approached with sub-MeV electron bunches produced by a laser-plasma device [44]. This source delivers ultrashort bunches of electrons with kinetic energy around 300 keV, uniformly over a large solid angle. The device is presently setup for radiobiological tests covering a previously untested energy range. Each bunch combines high charge with short duration and sub-millimeter range into a record instantaneous dose rate, as high as 10^9 Gy/s. Both such a high dose rate and high level of Relative Biological Effectiveness, attached to sub-MeV electrons, make this source very attractive for radiobiological tests on thin samples of living cells.

Secondary sources of high-energy photons are another exciting by-product of laser-driven electron acceleration. They include the above mentioned bremsstrahlung sources and betatron sources originated during the laser wakefield process itself by the strong restoring forces moving electron bunches towards the laser propagation axis. Further, the electron beam produced by laser-driven acceleration can be sent to collide with another powerful laser pulse and produce energetic photons by Compton scattering [45, 46].

Generation of radiation via Thomson (Compton) scattering of a laser pulse by energetic counter-propagating electrons was initially proposed in 1963 [47, 48] as a quasi monochromatic and polarized photons source. With the development of ultra intense lasers the interest on this process has grown and the process is now being exploited as a bright source of energetic photons from UV to gamma-rays and atto-second sources in the full nonlinear regime. In view of medical application, tuneability of the X-ray photon energy may be an important option of an *all-optical* laser-based Thomson source. Recent experiments performed by Sarri et al. [49] and Liu et al. [50] obtained photons of several tens of MeV and opened a new phase of these studies.

We mentioned in the previous Section radiography performed with protons and ions. A similar technique can be used also with electron beams produced by laser-driven accelerators. This topics is treated in Sects. 13.5 and 13.6 of Chap. 13 where several preliminary results are discussed, leading to high resolution imaging of material and biological samples. The laser-driven electron sources included interaction with both ordinary and clustered gas jets [51, 52].

As we saw so far, the present status of laser-driven electron acceleration already allow to (i) consider the feasibility of clinical devices; (ii) to perform outstanding experiments in order to assess further, more advanced applications. Nevertheless, we can't ignore the continuous progress of the acceleration methods and techniques that could lead in short period of time to unexpected opportunities also of biomedical interest. The possible biomedical impact of laser-generated multi-GeV electron beams is deeply discussed in the Chap. 6 of this Volume [53] together with a wide overview of the basic concept [54] and emerging results making possible to design and test novel configurations including multi-stage accelerators [55].

In this context of advanced researches, an increasing interest has been raised by the *ionization induced* electron *injection* in laser wakefield acceleration [56]. Compared with other electron injection schemes [57] for laser wakefield acceleration, this scheme shows the merits of relatively simple operation and controllable final beam quality. In the *single-color* laser ionization injection scheme, quasi-monoenergetic electron acceleration is possible through the control of laser self-focusing. In this way the effective injection length can be controlled within a hundred micrometers range and the absolute energy spread of the beam can be controlled within tens of MeV. In the *two-color* laser ionization injection scheme, the effective injection length can be further reduced to tens of micrometers length, and the absolute energy spread of the electrons can be reduced to a few MeV, i.e. the relative energy spread can be less than 0.5 %. A further interesting result is the

generation of multi-color electron bunches by use of two-color lasers [58]. These electrons can be used for multi-color X-ray generation through laser beam Thomson scattering.

1.4 Dosimetry and Safety

Several primary issues have to be addressed before transferring laser-driven particle beams from laboratory to clinic, including suitable and reliable dosimetric methods and ad hoc protocols for radiation safety. Chapter 9 is actually devoted to dosimetry of laser-driven electron beams for radiobiology and medicine [59]. Both absolute and relative dosimetry are considered, in the framework of international protocols [60]. Several existing devices are considered and discussed, including radiochromic foils, ionization chambers and Faraday cups. Novel concepts for ad hoc detectors are presented, including a recently published, innovative Faraday cup [61]. The response of each device to the very high dose rates delivered by laser-driven accelerators needs to be carefully investigated.

Section 9.3 of Chap. 9 is devoted to dosimetric simulations with Monte Carlo methods, in particular with the GEANT4 toolkit, widely used for medical physics. Simulations have been adapted to the peculiar geometry of laser-driven acceleration and can produce realistic evaluations of dose distribution, as well as duration and spectrum, of the particle bunch at the source, at the vacuum/air interface, and finally on the biological specimen.

Dosimetric issues concerning protons and ions accelerated with laser techniques are also treated in Chaps. 10 and 11 [18, 19]. In particular, in Sect. 10.3 of Chap. 10 reports dose measurements performed with devoted dosimetric techniques [62]. In Sect. 11.3 of Chap. 11 the proton dose is estimated from the measured proton number and energy spectrum per bunch using a Monte-Carlo simulation with the TRIM code. TRIM is a group of programs which calculate the stopping power and range of ions (10 eV–2 GeV/u) in matter using a quantum mechanical treatment of ion-atom collisions. Note that the TRIM code accurately calculates the range and energy loss of ions having energies below the region where Bethe-Bloch equation is adopted. The stopping power table used in this work was SRIM2008 [63].

One of the primary issues to be considered, while thinking to transfer laser-driven acceleration technology in a clinical context, is radiological safety. This would be not exactly the same set of problems and protocols as for conventional accelerators delivering a well defined type of particle with an almost monoenergetic spectrum. We are dealing with a complex of radiological products delivered by laser interaction, at a given but changeable intensity, with a variety of materials acting as accelerating media. Of course this kind of problems have already considered and studied by managing high-power laser facilities devoted to laser-matter interactions and more specifically to particle acceleration. Activation of experimental targets is often an experimental goal but activation of diagnostics, vacuum

chambers and the facility beyond needs to be considered. Experimenters, technicians and other facility personnel will come into contact with this equipment often within minutes of a shot or short series and their safety is the central concern to any facility or program manager. For a medical facility the safety of the patient is paramount, i.e. ensuring the radiation interacts as intended whilst minimizing doses from any secondary radiations and considering all other hazards [64]. To this fundamental and somehow challenging topic is deeply analyzed in Chap. 5.

1.5 How Far We Are

A complex culture made by many multidisciplinary contributions is growing up from the original scientific case of laser-driven particle acceleration in order to make it useful and usable for biology and medicine. This volume may provide a partial but significant insight on this new, fast progressing scientific and technological reality.

How far we are from prototyping novel classes of laser-based accelerators able to get the huge market of radiotherapy is difficult to understand. For sure a new class of radiobiological investigations is running. Some of them are mostly tests on the RBE of the laser-produced particle bunches and are very important to asses the validity of the laser technologies. Some others try to explore the very early effects of the ionizing radiation on temporal and spatial scale not attainable before. These latter can improve significantly the basic knowledge to be transferred into future, less aggressive models of radiotherapy.

For laser-driven electron acceleration, many scientific issues of the physics of laser electron acceleration have been already addressed [65], while the technology of intense laser needs to be improved in such elements as in the repetition rate and efficiency. The recently invented fiber laser technology [33] specifically targeted and proposed remedies on these issues in a novel fashion. As to laser ion acceleration, as mentioned in some of the chapters of this volume, it is important to make the bucket that traps ions move in a fashion of the adiabatic acceleration [20] to be more efficacious and of higher quality for the ion beam. There are multiple of directions to improve on this point. Some of these need to be further developed to see their full potential, consequences, and impacts in the future. The breadth of spectrum of these attempts is encouraging.

Acknowledgments We are delighted by and appreciative of all the authors who contributed to this volume. These efforts make our paper writing so much easier. This work was in part supported by the Norman Rostoker Fund.

References

1. IARC, Cancer fact sheets. Globocan, <http://globocan.iarc.fr/>
2. D. Rodin et al., Lancet Oncol. **15**, 378 (2014)
3. U. Veronesi et al., Ann. Oncol. **12**, 997 (2001)
4. A.S. Beddar et al., Med. Phys. **33**, 1476 (2006)
5. <http://www.businesswire.com/news/home/20140313005577/en/Research-Markets-External-Beam-Radiation-Therapy-Devices>
6. R. Baskar et al., Int. J. Med. Sci. **9**, 193 (2012)
7. R. Mouttet-Audouard, T. Lacornerie, and E. Lartigau, Chapter 3 of this volume (2016)
8. A. Giulietti et al., Phys. Rev. Lett. **101**, 105002 (2008)
9. F. Baffigi et al., The LEARC concept: laser-driven electron accelerator for radiotherapy of cancer, INO-CNR internal report (2014). Available at: www.ilil.ino.it
10. T. Tajima, J. Dawson, Phys. Rev. Lett. **43**, 267 (1979)
11. D. Strickland, G. Mourou, Opt. Commun. **56**, 219 (1985)
12. R.R. Wilson, Radiology **47**, 487 (1946)
13. J. Lawrence, Cancer **10**, 795 (1957)
14. M. Jermann, Int. J. Particle Ther. **2**, 50 (2015)
15. S. Sawada, Nucl. Phys. A **834**, 701 (2010)
16. M. Goitein, A.J. Lomax, E.S. Pedroni, Phys. Today **55**, 45 (2012)
17. M. Schippers, Beam delivery system for particle therapy, in *Proton and Ion Carbon Therapy*, ed. by C.-M. Charlie Ma, Tony Lomax (CRC Press, Boca Raton, FL, 2013), p 43
18. M. Borghesi, A. Macchi, Chapter 10 of this volume (2016)
19. A. Yogo, Chapter 11 of this volume (2016)
20. T. Tajima, Chapter 13 of this volume (2016)
21. W. Priedhorsky, D. Lier, R. Day, D. Gerke, Phys. Rev. Lett. **47**, 1661 (1981)
22. D.M. Villeneuve, G.D. Enright, M.C. Richardson, Phys. Rev. A **27**, 2656 (1983)
23. V. I. Veksler, *Proceedings CERN Symposium on High Energy Accelerators and Pion Physics*, vol. 1 (Geneva, Switzerland, 1956), p 80
24. A.P. Fews, P.A. Norreys, F.N. Beg, A.R. Bell, A.R. Dangor, C.N. Danson, P. Lee, S.J. Rose, Phys. Rev. Lett. **73**, 1801 (1994)
25. S.S. Bulanov et al., Med. Phys. **35**, 1770 (2008)
26. Y.A. Gauduel, Chapter 2 of this volume (2016)
27. L. Minafra, V. Bravatà, F. P. Cammarata, G. I. Forte, Chapter 4 of this volume (2016)
28. D. Habs, T. Tajima, U. Koester, Laser-driven radiation therapy, in *Current Cancer Treatment: Novel Beyond Conventional Approaches*, Chap. 10, ed. by O. Ozdemir (Intech, Rijeka, 2011), p. 199. ISBN 978-953-307-397-2. doi:[10.5772/24190](https://doi.org/10.5772/24190). <http://www.intechopen.com/books/show/title/current-cancer-treatment-novel-beyond-conventional-approaches>
29. P. Mulser, D. Bauer, *High Power Laser-Matter Interaction*. Springer Tracts in Modern Physics, vol. 238 (Springer, New York, 2010)
30. A. Macchi, M. Borghesi, M. Passoni, Rev. Mod. Phys. **85**, 751 (2013)
31. H. Daido, M. Nishiuchi, A.S. Pirozhkov, Rep. Prog. Phys. **75**, 056401 (2012)
32. T. Ceccotti et al., Phys. Rev. Lett. **111**, 18501 (2013)
33. G. Mourou, B. Brocklesby, T. Tajima, J. Limpert, Nat. Photonics **7**, 258 (2013)
34. M.D. Perry et al., Opt. Lett. **24**, 160 (1999)
35. A. Giulietti et al., Laser-plasma particle sources for biology and medicine, in *Progress in Ultrafast Intense Laser Science XII*, ed. by K. Yamanouchi et al., Springer Series in Chemical Physics, vol. 112 (Springer International Publication, Switzerland, 2015). doi [10.1007/978-3-319-23657-5_8](https://doi.org/10.1007/978-3-319-23657-5_8)
36. R.A. Snavely et al., Phys. Rev. Lett. **85**, 2945 (2000)
37. A. Yogo et al., Appl. Phys. Lett. **94**, 181502 (2009)
38. A. Yogo et al., Appl. Phys. Lett. **98**, 053701 (2011)
39. D. Doria et al., AIP Advances **2**, 011209 (2012)
40. A.Ya. Faenov, T.A. Pikuz, R. Kodama, Chapter 12 of this volume (2016)

41. A.Ya. Faenov, T.A. Pikuz, Y. Fukuda et al., *Appl. Phys. Lett.* **95**, 101107 (2009)
42. M. Galimberti et al., *Rev. Sci. Instrum.* **76**, 053303 (2005)
43. E. Lefebvre et al., *Nucl. Fusion* **43**, 629 (2003)
44. L. Labate et al., LESM: a laser-driven sub-MeV electron source delivering ultra-high dose rate on thin biological samples. *J. Phys. D Appl. Phys.* (2016)
45. L.A. Gizzi, Chapter 8 of this volume (2016)
46. L.A. Gizzi et al., *IEEE Trans. Plasma Sci.* **39**, 2954 (2011)
47. R.H. Milburn, *Phys. Rev. Lett.* **10**, 75 (1963)
48. C. Bemporad, R.H. Milburn, N. Tanaka, M. Fotino, *Phys. Rev.* **138**, B1546 (1965)
49. G. Sarri et al., *Phys. Rev. Lett.* **113**, 224801 (2014)
50. C. Liu et al., *Opt. Lett.* **39**, 4132 (2014)
51. G.C. Bussolino et al., *J. Phys. D Appl. Phys.* **46**, 245501 (2013)
52. P. Koester et al., *Laser and particles beams* **33**, 331 (2015)
53. T.M. Jeong, J. Lee, Chapter 6 of this volume (2016)
54. W. Leemans, E. Esarey, *Phys. Today* **62**, 44 (2009)
55. H.T. Kim et al., *Phys. Rev. Lett.* **111**, 165002 (2013)
56. M. Chen, Z.-M. Shen, Chapter 7 of this volume (2016)
57. E. Esarey et al., *Phys. Rev. Lett.* **79**, 2682 (1997)
58. M. Zeng et al., *Phys. Rev. Lett.* **114**, 084801 (2015)
59. L. Labate, D. Lamia, G. Russo, Chapter 9 of this volume (2016)
60. International Atomic Energy Agency, *Absorbed Dose Determination in External Beam Radiotherapy: An International Code of Practice for Dosimetry Based on Standards of Absorbed Dose to Water*, IAEA Technical Reports Series no. 398—IAEA, Vienna (2000)
61. G.A. Cirrone et al., *Nucl. Instrum. Meth. Phys. Res. A* **796**, 99 (2015)
62. F. Fiorini et al., *Phys. Med. Biol.* **56**, 6969 (2011)
63. J.F. Ziegler, J.P. Biersack, M.D. Ziegler, *SRIM, the Stopping and Range of Ions in Matter*. SRIM Company (2008)
64. A. Simons, Chapter 5 of this volume (2016)
65. W. Leemans, W. Chou, M. Uesaka (eds.), *Beam Dynamics Newsletter*, vol. 56, (ICFA, Fermilab, 2011), p. 7

Part I

Updating Radiobiology, Radiotherapy and Radiation Safety

Chapter 2

Laser-Plasma Accelerators Based Ultrafast Radiation Biophysics

Yann A. Gauduel

Abstract The innovating advent of TeraWatt lasers able to drive laser-plasma accelerators and produce ultra-short relativistic electron beams in the MeV range, combined with ultrafast spectroscopy methods, opens exciting opportunities for the emerging domain of high energy radiation femtochemistry (HERF). In synergy with low energy radiation femtochemistry (LERF), HERF favours the development of new conceptual approaches for pulsed radiation biology and medicine. The unprecedented high dose rate delivered by ultrashort relativistic electron beams (10^{12} – 10^{13} Gy s $^{-1}$) with laser techniques can be used to investigate the spatio-temporal approach of early radiation processes. The chapter focuses on early physico-chemical phenomena which occur in the prethermal regime of secondary electrons, considering the sub-structures of tracks and very short-lived quantum probes. This interdisciplinary breakthrough would provide guidance for the real-time nanodosimetry of molecular targets in integrated biologically relevant environments and would open new perspectives for the conceptualisation of time-dependent molecular RBE (Relative Biological Effectiveness), in synergy with particle based anticancer radiotherapies.

2.1 General Introduction

The innovating advent of powerful TW laser sources ($\sim 10^{19}$ W cm $^{-2}$ on target) and laser-plasma interactions provide ultra-short relativistic particle beams (electron, proton) in the MeV domain [1–5]. These advances open exciting opportunities for the simultaneous development of high energy radiation femtochemistry (HERF) and ultrafast radiation biology [6–10]. The complex links that exist between the physical aspects of early radiation events and the delayed evolution of biological endpoints, carcinogenesis or cell survivals need the development of an advanced

Y.A. Gauduel (✉)

LOA, ENSTA ParisTech, CNRS, Ecole Polytechnique, University Paris-Saclay,
Palaiseau, France

e-mail: yann.gauduel@ensta-paristech.fr

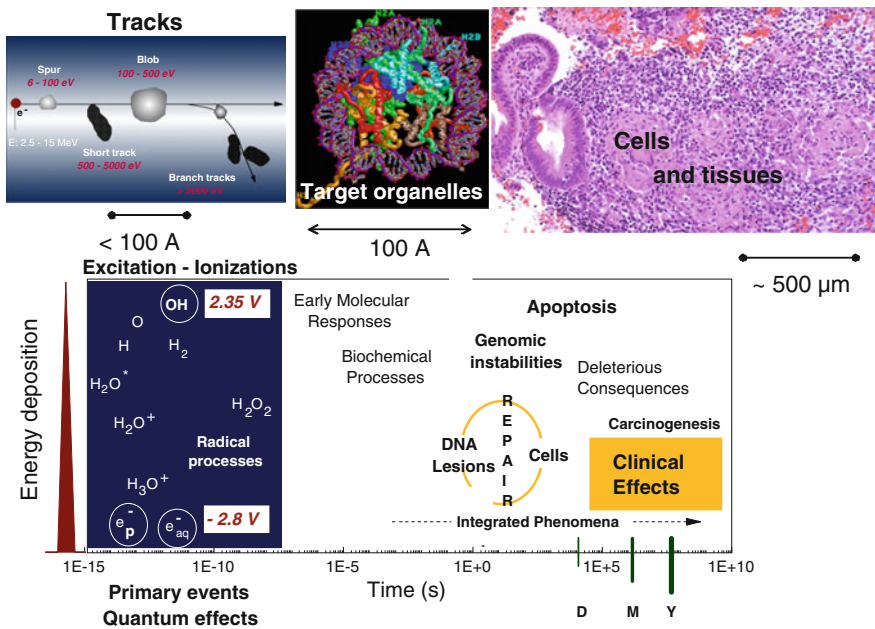


Fig. 2.1 Synthetic representation of spatio-temporal radiation effects that take place over several orders of magnitude, from an initial energy deposition in molecular targets (quantum events) to more delayed consequences at the biological and clinical levels (*D* Day, *M* Month, *Y* Year)

spatio-temporal radiation biomedicine [11]. A very important challenge of this emerging domain concerns the thorough understanding of multiple events that are triggered by an initial energy deposition inside confined clusters of ionization. These multiple electronic and molecular events evolve over several orders of magnitude, typically from femtosecond and sub-micrometric scales (Fig. 2.1).

Nanoscale insight into early physico-chemical processes and native ionisation tracks represents a prerequisite for the complete knowledge of radiation-induced bio-effects in the confined environments of integrated biomolecular targets. Some innovative aspects of spatio-temporal radiation biomedicine are growing rapidly as a result of advanced technical solutions enabling improved pulsed radiation sources and selective protocols for anticancer radiotherapies.

2.2 Ultrafast Laser Science and Real-Time Radiation Processes: the Synergy Between LERF and HERF Domains

The real-time investigation of elementary physico-chemical processes in condensed phase of biological interest can be carried out in synergy with the most recent developments of ultra-short laser sources, combining the complementary concepts

of low and high energy radiation femtochemistry (LERF and HERF respectively) [6–8, 10, 12–15]. The course of ultrafast elementary events occurring in nascent ionization tracks (see Fig. 2.1) are largely unknown because up to now the pulse widths of contemporary radiations sources like LINAC accelerators are technically limited to several picoseconds. The magnitude of these primary radiation events remains uncertain, depending on indirect approaches such as stochastic modeling of non-homogeneous processes with different simulations: Monte Carlo calculations of particle pathway during the energy scattering, semi-quantum simulations of ultrafast electronic trajectories taking into account the local structure of reactive environment [15–21].

With the intensive development of ultra-short laser technologies leading to the generation of ultrafast photon or particles sources and advanced high-time resolved spectroscopic methods, the courses of short lived non-equilibrium trajectories are more and more observable on the molecular motion scale [12–15]. The most fundamental aspects of radiation damage in condensed molecular environments concerns the dissociative electron attachment processes that take place in confined ionization spaces. Such processes involve a hierarchy of electronic states of delocalized electrons whose energy varies from the thermal value ($kT \sim 0.025$ eV) to the sub-excitation and relativistic levels i.e. a few eV and MeV respectively. These primary phenomena are crucial for the solvent of life, i.e. water molecules. The microscopic understanding of primary physico-chemical processes triggered by ionizing radiation requires the real-time probing of multiple non-equilibrium states whose lifetimes are mostly in the sub-picosecond regime.

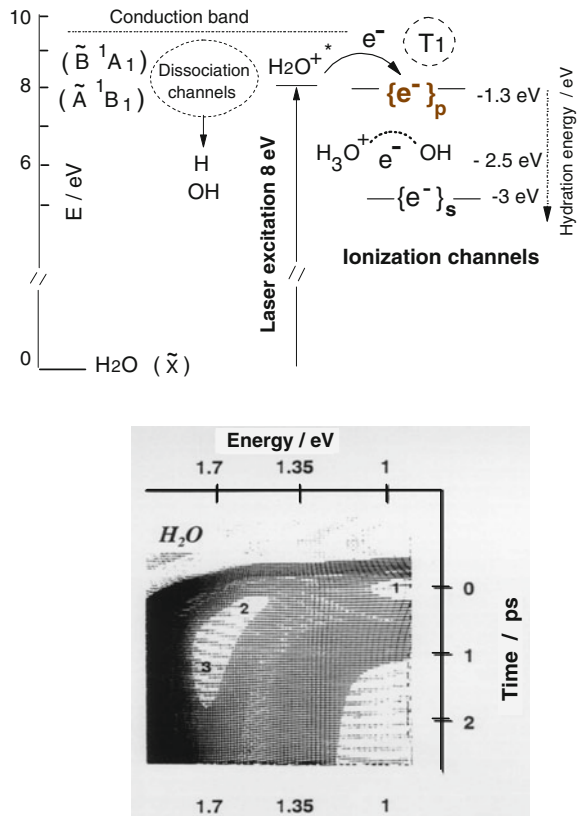
2.2.1 Low Energy Radiation Femtochemistry of the Life Solvent

In the framework of non-linear interactions of neat water molecules in liquid phase with femtosecond UV laser pulses whose peak power density is around 10^{10} W cm⁻², a direct excitation can be triggered by a two-photon process [15, 22]. For a wave plane propagation through an aqueous sample, this phenomenon is expressed by the (2.1), for which I represents the radiation intensity, B the two photon absorption coefficient and v the light velocity in the medium.

$$\frac{\partial I}{\partial x} + \left(\frac{1}{v} \right) \frac{\partial I}{\partial t} = -BI^2 \quad (2.1)$$

Considering an excited A[~] state of water molecules (1b1 → 3a1 for instance), a nonlinear two-photon UV excitation process ($E_{Excit} = 2 \times 4$ eV) can be considered to investigate the LERF signals dynamics of early water molecules radical processes. Femtosecond UV-IR absorption spectroscopic investigations in the energy range 3–1 eV allow to discriminate the sequential events of ionization channels (Fig. 2.2). The non-linear two-photon energy deposition of 8 eV in a water bulk

Fig. 2.2 LERF of neat liquid water at 294 K. *Upper part:* Energy diagram levels of transient electronic configurations induced by two-photon excitation with of femtosecond UV pulses (2×4 eV). *Lower part:* 2D spectral signatures of transient electronic states due to ionization channels. 1: p state of excited electron, 2: electron radical pairs, 3: s-state of fully relaxed electron. Adapted from Gauduel et al. [23–27]



triggers early water defects including the hydronium ion (H_3O^+) and hydroxyl radical (OH) via an ultrafast positive hole $\text{H}_2\text{O}^{*+}-\text{H}_2\text{O}$ reaction in less than 100 fs, the generation of multiple non-equilibrium delocalized electron configurations such as quasi-free delocalized electron $\{\text{e}_q^-\}$, p-like excited prehydrated electrons $\{\text{e}_p^-\}$, electron-radical pairs and hydrated electron ground state $\{\text{e}_s^-\}$. All these ultrafast physico-chemical channels mostly occur in less than 5×10^{-13} s [23–27].

During the last two decades, LERF researches have permitted to clearly establish that a nonlinear femtosecond excitation of neat liquid water leads to an electron hydration process via a nonadiabatic relaxation of an infrared 2p-like excited prehydrated electron; this $2p(\text{e}_{\text{prehyd}}^-) \rightarrow 1s(\text{e}_{\text{hyd}}^-)$ transition occurs in the range 250–500 fs at 294 K [24, 27–29]. Additional ultrafast pathway contributes to the formation of transient solvent bridged three-bodies complex $[\text{OH}^* \dots \text{e}^- \dots \text{H}_3\text{O}^+]_{n\text{H}_2\text{O}}$ in less than 500 fs. The deactivation frequency of these transient solvent bridged pairs ($0.29 \times 10^{13} \text{ s}^{-1}$) remains comparable to the estimate of a vibrationally excited water molecules relaxation frequency ($V_{\text{H}_2\text{O}}^* \sim 0.33 \times 10^{13} \text{ s}^{-1}$) [26]. Indeed, LERF of neat

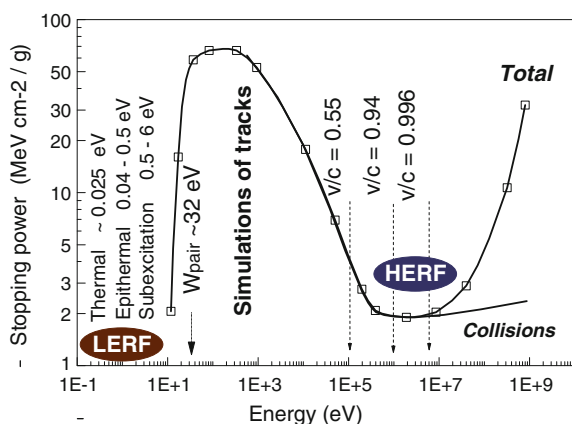
liquid water contributes to deeply understand (i) the nature of complex branching between ultrafast radical pathways, (ii) the contribution of ultrashort-lived solvent configurations within multiple potential energy surface crossing zones.

2.2.2 Multiparametric Approach of High Energy Radiation Femtochemistry

The advanced TW laser plasma accelerators delivering ultrashort high energy electron bunches [1–5, 30–37] foreshadow the development of innovative researches in the field of radiation physical-chemistry, on the time scale of molecular motions, i.e. angstrom or sub-angstrom displacements [6, 38–42]. Laser-plasma accelerators based High Energy Radiation Femtochemistry (HERF) represents a newly emerging interdisciplinary field which can be driven in strong synergy with the generation of ultrashort particle beams in the MeV energy domain. In the framework of multiparametric approaches that include energy, time and space, innovating developments of HERF would favour, in synergy with LERF data, the investigation of prethermal radiation processes in aqueous and biochemically relevant environments [43].

Considering the energy dependence of the electron stopping power in liquid water for instance (Fig. 2.3) and [44], the real-time investigation of early radiation events in native tracks becomes accessible. This approach requires also the contribution of LERF which is generally devoted to the ultrafast spectroscopy of low energy radiation processes, typically for $E < 6$ eV. The interactions of relativistic MeV electrons with water molecules induce ultrafast energy scattering processes and the formation of fractionated ionization clusters (Fig. 2.4). These ionization processes involve a hierarchy of electron populations for which the energy varies from relativistic levels to the thermal value kT .

Fig. 2.3 Energy dependence of the electron stopping power in liquid water. The specific domains of energy covered by low and high energy radiation femtochemistry (LERF and HERF respectively) are indicated on the figure



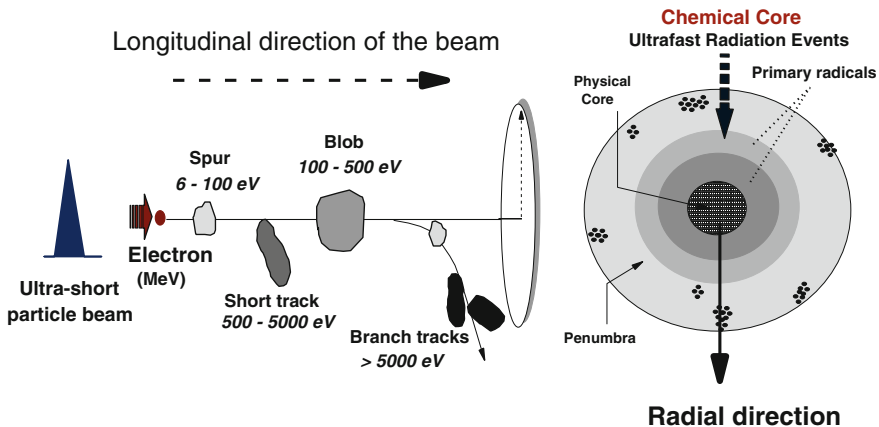


Fig. 2.4 Simplified representation of a spatial distribution of inhomogeneous ionisation tracks following the interaction of relativistic MeV particles with an aqueous environment. In the radial direction of the radiation beam, early radiation events take place within the chemical core i.e. at the interface of the physical core and penumbra zone. Adapted from Gauduel and Malka [76]

Typically, in less than 10^{-16} s, different energy quanta of 20–200 eV are delivered in nanometric tracks and spurs [17, 45]. Due to the uncertainty relation for time and energy, the fastest ionising events occurring in confined clusters take place in less than 0.33×10^{-16} s (2.2).

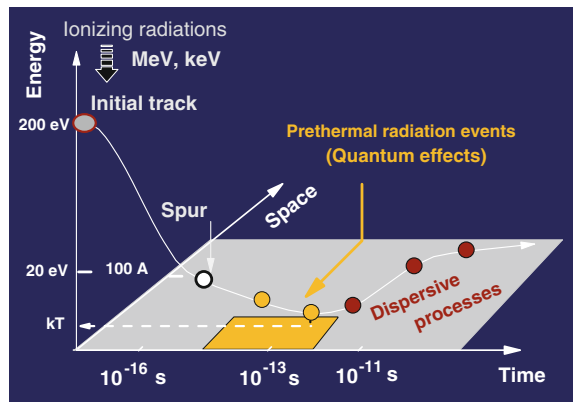
$$\Delta t \cdot \Delta E = \hbar = 6.6 \times 10^{-16} \text{ eV s} \quad (2.2)$$

A second uncertainty principle for the position and momentum of relativistic particle must also be considered: $\Delta p \cdot \Delta x = \hbar$ with p the momentum of the particle and $\Delta p = \Delta E/u$ if u represents the particle velocity ($\sim 3 \times 10^{10} \text{ cm s}^{-1}$). From these two incertitude principles, an expression of Δx can be extracted (2.3).

$$\Delta x = \hbar \cdot u / \Delta E \quad (2.3)$$

In this condition, an energy of 20 eV deposited by relativistic particles would occur on 10^{-6} cm ($\sim 100 \text{ \AA}$) and involve a nanometric distribution of ionization clusters (Fig. 2.5). As early radiation damages can be highly dependent on the survival probability of low-energy secondary electrons and of the spatial distribution of primary radicals produced from water molecules, a thorough knowledge of native tracks requires the real-time probing of radiation events in the 10^{-15} – 10^{-11} s range. For aqueous environment, this temporal domain concerns mainly prethermal events for which quantum states of very low excited electrons involve ultrafast nonadiabatic transitions. These ultrafast events lead to the sub-picosecond localization of secondary electrons in water bath. Beyond 10^{-11} s, fully relaxed electrons contribute to sub-micrometric dispersive diffusion processes which can be carefully described by more classical approaches such as the master diffusion equation [16, 45–49].

Fig. 2.5 Synthetic representation of a time-space-energy relationship for primary events triggered by the MeV-keV ionising radiation of a water environment. In nanometric ionisation tracks, the prethermal regime of very low energy secondary electrons corresponds to the specific temporal window $10^{-14}\text{--}10^{-12}$ s for which quantum effects predominate



The ionisation densities being a major factor of biological radiation efficiencies, the spatio-temporal radiation physico-chemistry and biomedicine beneficite of recent advances of ultrashort particle bunches delivered by TW laser-plasma accelerators. In the MeV domain, the most promising aspects concern the real-time investigation of early radical events in the radial direction of a particle beam, using molecular sensors at the interface of a physical core and a penumbra zone (Fig. 2.4).

2.3 High Energy Electron Bunches and Ultrafast Radiation Chemistry

2.3.1 *Laser-Accelerated High Energy Electron Beams*

The injection of femtosecond electron bunches into plasma wakefields has been one of the greatest experimental challenge in the field of laser plasma accelerators. Inspired by the pioneering work of Tajima and Dawson [1], the development of laser–plasma accelerators began in the early 1980s. Plasma can support immense electric fields of 100 GV/m and greater [2]. This value is 3–4 orders of magnitude higher than the 10–100 MV/m achieved in radiofrequency cavities of conventional accelerators. Such large electric fields generation can be achieved by focusing an ultra-short and powerful TW laser onto the edge of a supersonic helium gas jet. Rapidly ionized by the intense laser pulse, the helium gas provides a plasma medium in which the laser is then able to generate the wakefield. Large electric field is obtained by separating ions from electrons. This charge separation can be achieved using a high-intensity and ultra-short laser: the ponderomotive force, a force related to the laser intensity gradient, is able to push electrons away from regions of high laser intensity, while the ions stay immobile because of their higher mass. The passage of an intense laser pulse into a underdense plasma generates an electron density perturbation in the wake of the laser pulse. This travelling density

perturbation is referred to as an electron plasma wave and is the source of an accelerating longitudinal electric field, the wakefield. In low density underdense plasma, the laser propagates at a velocity close to c the velocity of light in vacuum, so that the phase velocity of the wakefield is also close to the light velocity. By surfing on this travelling wave, the electrons are boosted to high energies, typically 100 MeV, over a millimetric distance. For getting an efficient excitation, the laser pulse has to be “resonant” with the plasma wave, which occurs when the laser pulse duration is on the order of half the plasma period: $\tau_{\text{laser}} \approx \lambda_p/(2c)$. Consequently, the pulse duration needs to be ultra-short, typically around 30 fs. Two injection techniques have recently lead to the generation of ultrashort electron bunches, with high quality parameters for experimental and medical applications [36].

Previously, a first injection procedure has favored the successful generation of quasi-monoenergetic electrons beams and is wave breaking (Fig. 2.6, upper part). In this regime, a very intense TW-laser focused pulse is used to drive a nonlinear wakefield: plasma bubbles filled with ions and surrounded by a wall of electrons. Electrons are expelled by the laser and circulate around this plasma bubble. At the back of the plasma bubble, electrons accumulate and form an electron density spike. Above a certain threshold value, this density spike collapses by injecting some of its electrons into the plasma bubble, where they are subsequently accelerated. This bubble regime had been initially predicted by Pukhov and Meyer-ter-Vehn [31] which showed that the injection is sufficiently local and short to produce high quality mono-energetic electron beams. The breakthrough experiments, performed in 2004 by different groups from Imperial College, Lawrence Berkeley National Laboratory (USA) and Laboratoire d’Optique Appliquée (France), were the first demonstration of such regime [32, 33, 50]. The electron energy distribution is “quasi-monoenergetic” and generally consists of a single narrow spike which could have a small energy bandwidth of about few percents. The electron beams are extremely collimated, the full width half maximum (FWHM) divergence is smaller than 10 milliradians.

A second configuration provides enhanced control over the injection of electrons and requires two counterpropagating femtosecond laser pulses at the same wavelength (Fig. 2.6, lower part). A first laser beam called “pump” creates a strong wakefield which can be nonlinear but does not lead to wave breaking as in the previous case. In consequence, no electron beam is produced when using this laser pulse alone. A second laser pulse called “the injection pulse” counter propagates to the first laser and injects electrons. When the two pulses collide, the laser beams interfere and generate an electromagnetic beatwave pattern. In this beatwave, the plasma electrons are heated and can gain sufficient kinetic energy to be injected in the wakefield. Electron injection occurs during the laser pulse collision which only lasts about 30 fs, so that the injected electron bunch is ultrashort. Once injected, electrons are accelerated in the wakefield to relativistic energies. The first laser-plasma accelerator using injection by colliding pulse was demonstrated by Faure et al. [34]. Experimental developments emphasize that the electron beams showed enhanced stability when compared to the previous self-injection regime. Although, the stability is not perfect, the peak energy only varies by about 5 %.

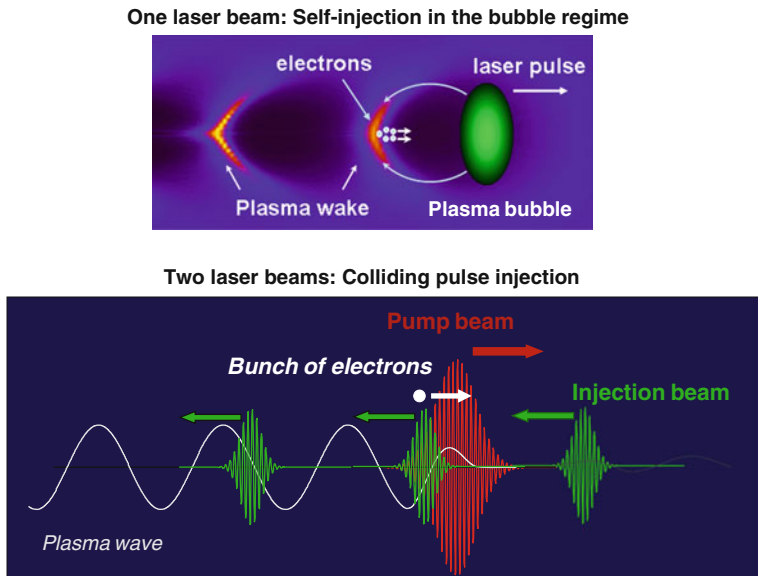


Fig. 2.6 Principles of two laser-plasma accelerator configurations used for HERF experiments and spatio-temporal radiation biology in the MeV energy domain. *Upper part:* self-injection in the plasma bubble regime. The electronic density configuration is greatly non-linear. The with arrows show the electron motions in the reference frame of the pulsed laser. *Lower part:* configuration of colliding pulse injection. The laser pump propagates from the left to right and the injection pulse propagates in the opposite direction. During the collision, the laser pulses interfere and induce a beat pattern. The electrons are injected by the second laser pulse and then accelerated by the wakefield of the pump beam [5, 7, 34]. Adapted from [10]

Energy spreads of a few percent have already been observed [35]. With this colliding pulse configuration, the beam parameters can be adjusted: (i) the beam energy can be tuned by choosing the location of the collision in the plasma, (ii) the beam charge and energy spread can be tuned by changing the parameters of the electron beam. Indeed, femtosecond electron bunch energy can be continuously tuned from 10 to 250 MeV by adjusting the position of the collision in the supersonic gas jet. This is realized by changing the injection distance Z_{inj} via the delay between the two counter propagating laser pulses [35]. The charge can be adjusted in the 0–100 pC range, with a relative energy spread in the 1–20 % range. Experimental developments demonstrate that relativistic electron bunches have a duration shorter than 100 fs.

2.3.2 High Energy Radiation Femtochemistry

In the framework of innovative developments of pulsed radiation sources such as LINACs, synchrotrons, table-top laser system, proton and ion accelerators, it appears that new physical concepts on radiation-matter interactions would include

time-dependent energetic fluence profile, peak dose delivery energy radial distribution functions and spatio-temporal dose rate profiles. Recently, TW laser plasma accelerators that provide ultrashort high and very high energy electron bunches (HEE: 50 MeV, VHEE: 150–200 MeV respectively) open several exciting opportunities for a careful investigation of ultrafast radiation events in native ionization tracks. The specific qualities and properties of these ultrashort relativistic particle bunches foreshadow the development of advanced researches to deepen the understanding of primary molecular damage triggered by physical radiation processes. In this way, the powerful laser techniques (table-top terawatt Ti:Sa laser oscillators followed by amplifier systems) combined to laser plasma interactions provide femtosecond high-energy electrons beams in the MeV energy domain. These new accelerators foreshadow the development of innovative researches in the field of high energy radiation physical-chemistry [6, 39, 41] and might conjecture the direct observation of primary radiation events in heterogeneous spur and track distributions (Fig. 2.4).

Regarding the temporal range 10^{-15} – 10^{-10} s, an emerging research field concerns the High-Energy Radiation Femtochemistry (HERF) of prethermal radiation events (Fig. 2.5). One major challenge concerns the real-time investigation of radiation processes triggered by an initial energy deposition in confined ionization tracks, using the high potentialities of femtosecond laser-plasma accelerators in the MeV domain [3, 4, 51]. Based on advanced TW laser accelerator previously developed by Malka et al. [7], recent investigations concern the implementation of a pump-probe configuration mixing: (i) the generation of laser-plasma accelerator that delivers femtosecond electron bunches in the MeV energy domain, with an initial duration of the order of 50–100 fs, a total charge of the collimated electron beam around 150 pC and characterized by a very high dose rate of 10^{13} Gys⁻¹ per pulse; (ii) a femtosecond optical beam operating in the visible or near-infrared spectral range for real-time probing of early radiation processes.

During the last decade, pioneered femtolysis experiments (Femto_{second} radio)lysis) of aqueous targets performed with femtosecond electron bunches in the energy domain 2.5–15 MeV have provided new insights onto the early behaviour of secondary electrons in native ionisation clusters.

These researches have emphasized the pre-eminent role of non-independent radiations events during ultrafast electronic relaxation processes [41]. For instance, a 820 nm TW titanium-doped sapphire laser beam with an on-target energy of 960 mJ in 30 fs FWHM pulses can be focused onto the sharp edge of a 2 mm diameter supersonic helium gas jet. With intensities on the order of 2.7×10^{19} W/cm² in vacuum, the femtosecond laser pulse ionises the gas and excites relativistic plasma waves within the underdense plasma. A total charge of the electron beam determined by an integrating current transformer equals 2.5 ± 0.2 nC and corresponds to a mean number of $(1.55 \pm 0.15) \times 10^{10}$ electrons. For an effective temperature of the femtosecond electron beam of about 4.5 MeV, the integrated energy flux in aqueous samples equals 5.8×10^{10} MeV cm⁻². The specific qualities and properties of ultra-short relativistic particle bunches foreshadow the development of high energy radiation femtochemistry. Using a

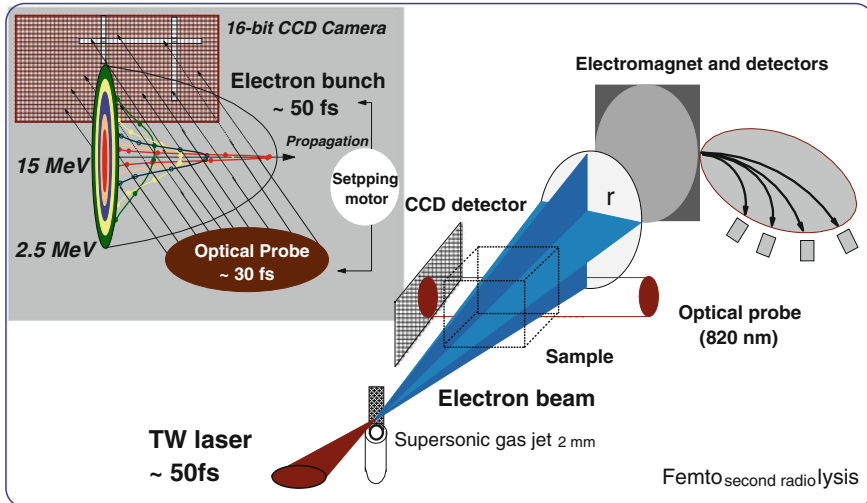


Fig. 2.7 Experimental set-up used for the development of HERF in aqueous liquid phase [9, 55]. The energy of the femtosecond relativistic electron bunches is in the range 2.5–15 MeV. The electron beam radius is “ r ”. The typical Femtolysis set-up is defined with a perpendicular pump (electron bunch)—probe (optical pulse) configuration

highly-time-resolved pump (femtosecond electron bunch)—optical probe (femtosecond photon pulse) orthogonal configuration (Fig. 2.7) and a detection system based on cooled 16-bit CCD camera (Andor Technology), the real-time investigation of primary radiation processes is performed in the radial direction of femtosecond electron bunches (Fig. 2.4). Concerning recent water femtolysis studies, laser-plasma accelerator based high energy radiation femtochemistry gives new insights into the time dependence of early events occurring in native ionisation clusters (Fig. 2.8).

Different transient HERF absorption signals can be analysed in the framework of non-homogeneous ionising events that lead to the formation of fully hydrated electrons (steps A and B in Fig. 2.8): a first dynamics (t_1) characterizes the trapping process of secondary electrons in water bath (prehydration of delocalised electrons) and the second one (t_2) corresponds to a nonradiative relaxation of trapped electron (p-like state of prehydrated electron) towards a 1s-like electron ground state (complete hydration process). A prehydration time t_1 of 150 ± 30 fs has been determined from computed analysis. The best fit of the overall near-infrared HERF signal risetime is obtained with a t_2 value of 850 ± 50 fs. Femtolysis experiments emphasize the electron hydration process within nascent tracks is slightly slower than low-energy electron localization dynamics in water bath [24, 25, 27]. Femtolysis studies suggest also that local anisotropic configurations due to electric field effects of charged prototropic entities slacken the relaxation dynamics of infrared p-like excited electron towards a 1s-like ground state (e_{aq}^-).

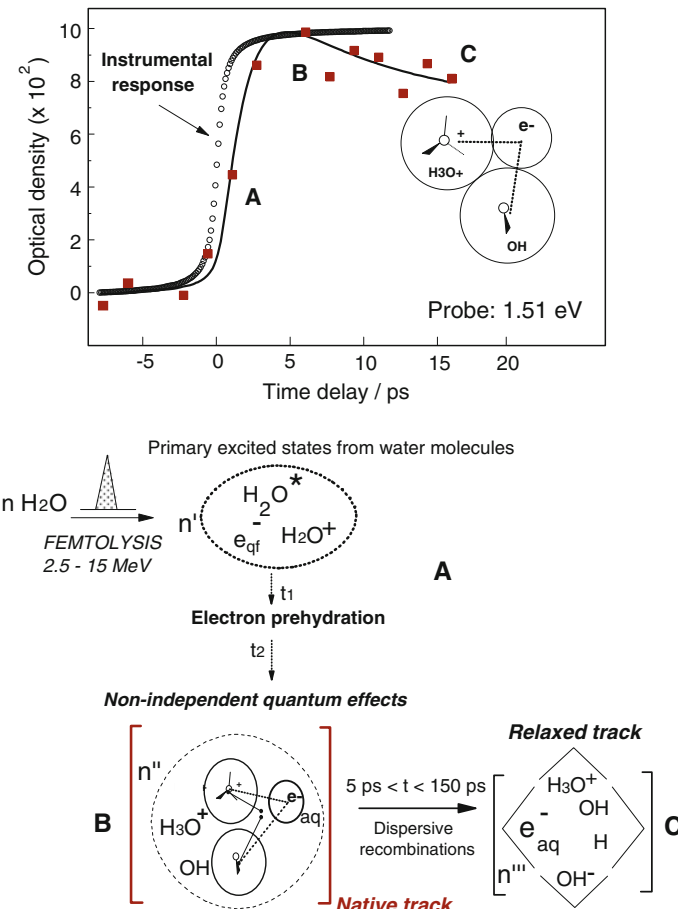


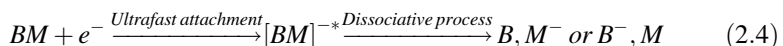
Fig. 2.8 Femtolysis of neat liquid water at 294 K. *Upper part:* the steps A, B, C of a time-resolved absorption curve correspond respectively to an electron ejection from water molecule, a sub-picosecond electron relaxation (prehydration) in the vicinity of water radicals and an early recombination processes leading to fully relaxed radicals having. A typical instrumental response obtained with orthogonal pump-probe configurations is also reported. *Lower part:* synthetic representation of main events occurring in native ionization tracks following the interaction of ultra-short relativistic electron bunches (2.5–15 MeV) with water molecules. Adapted from Gauduel et al. [41]

Femtolysis of neat water has also revealed that in native ionisation tracks, the short-time behavior of the ubiquitous e_{aq}^- radical (1s ground state) is mainly governed by ultrafast geminate recombination processes (steps B and C in Fig. 2.8). These phenomena are highly dependent on the transient distribution of electron-hole pairs and the short-time spatial configurations of electron-prototropic entities (hydronium ion H_3O^+ and radical hydroxyl OH). Indeed, when an electron ejected from a water molecule is directly trapped by the structured hydration shell

of hydronium ion (H_3O^+) or hydroxyl radical (OH^\bullet), the initial separation distances are shorter than the Onsager radius ($R_c \sim 7 \text{ \AA}$ in water) [52]. A limit case corresponds to very short-range electron-proton couplings for which hydronium ion (H_3O^+) undergoes one jump (1D motion by a finite process). Considering a diffusion coefficient of H_3O^+ expressed as $D \sim \lambda d^2/6$ [17, 53] and an experimental jump frequency $\lambda = 1/T_j = 0.5 \times 10^{12} \text{ s}^{-1}$, the initial proton jump distance would be around 2.8 \AA . The favorable configurations of three-bodies radical complexes [$\text{OH}^\bullet \dots \text{e}^- \dots \text{H}_3\text{O}^+$], also named non-independent radical pairs, recombine fastly or execute a 1D random walk within a fluctuating hydrogen bonds network. The early quantum yield of hydrated electron measured at $t \sim 5 \text{ ps}$ is higher than the predictions of classical stochastic modeling of irradiated water [46, 47, 54–58]. This important result of high energy radical femtochemistry of water molecules strongly argues for the pre-eminence of a quantum character of ultrafast water radiation damage in native tracks. Laser-plasma accelerators based HERF may contribute to a better knowledge of tracks sub-structure and allow the direct observation of primary radiation events in function of local environments induced by the presence of short-lived prototropic entities.

2.3.3 Towards a Real-Time Probing of Prethermal Events in the Ionization Tracks

The advent of powerful laser techniques (table-top terawatt Ti:Sa laser amplified systems) and laser-plasma interactions providing bright and ultra-short high-energy particle sources of several MeV, typically in the 5–250 MeV range, open also promising opportunities for the real time investigation of high energy radiation effects in the prethermal regime of secondary electrons. In this regime, the energy of partially localized electrons is higher than the thermal energy kT ($\sim 0.025 \text{ eV}$) [45]. Ultrafast radiation events occurring in less than 1 ps (10^{-12} s) after an energy deposition induced by a ionizing radiation represent a specific domain for which the quantum character of short-lived events becomes preeminent. This is particularly important when biomolecular damages take place during the prethermal regime of secondary electrons (Fig. 2.5). One of the most fundamental aspects of a biomolecule (BM) damage induced by ionising radiations concerns the dissociative electron attachment processes occurring in confined ionization spaces (2.4). An important challenge concerns the spatio-temporal understanding of events induced by the initial energy deposition of an electromagnetic ray or energetic particle in the medium and their subsequent effects on solvated biomolecules (Fig. 2.9).



These molecular damages involve generally a hierarchy of secondary electron populations for which the energy varies from the thermal value ($\sim 0.025 \text{ eV}$) to the

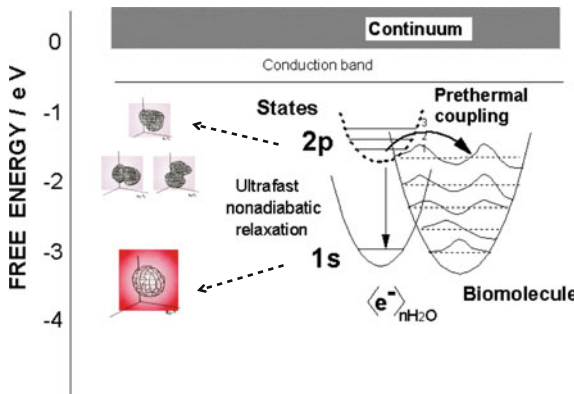


Fig. 2.9 Energy diagram of an ultrafast coupling between the quantum state of a localized electron (p-state of an excited electron) and a disulfide biomolecule. In aqueous environment, this coupling competes with an ultrafast nonadiabatic p-s transition that leads to the formation of a fully relaxed electron (1s-state hydrated electron) [24]. The representations of 2p and 1s state wave-functions calculated by semi-quantum molecular dynamic simulations [70] are reported on the left part of the figure

sub-excitation and relativistic levels i.e. few eV and MeV respectively. The prethermal processes and early spatial distributions of transient couplings between secondary low energy electron and biomolecules may play an important role during the early steps of radiation damage [59–62]. Previous Gauduel's researches devoted to low and high energy radiation effects on water molecules have suggested the crucial role of ultra-fast quantum effects for which short-lived configuration of very low energy quasi-delocalized secondary electrons would be involved [63–65]. For instance, in the framework of a nonlinear two-photon excitation process of water molecules by femtosecond UV pulses, multiple non-equilibrium configurations of delocalized electron are generated in less than 5×10^{-13} s at 294 K. One of these short-lived configurations (p like state excited electron) has been analyzed in term of quantum eigenstates [66–70]. In a water environment, these transient delocalized electron configurations can be considered as specific probes for investigating ultrafast prethermal reactions linked to biomolecular damage induced by the interaction of ionizing radiations (photons or accelerated particles) [6, 61, 64, 71–75].

The spatio-temporal coherences which are required to get an efficient coupling between a very short-lived quantum probe (p-state electron) and a biomolecule need additional investigations of ultrafast phenomena by infrared spectroscopy techniques. Indeed, the nano-scale insight of primary radical processes triggered by ionizing radiation requires the real-time probing of non-equilibrium states for which the lifetimes are typically in the sub-picosecond regime. Advanced laser-plasma accelerator based femtolysis experiments permit to extend our understanding of

very short-time radical events in the prethermal regime of nascent ionization tracks, typically in the 10^{-14} – 10^{-12} s window. Following a dose delivery of 15 Gy in less than 500 fs, it has been shown that an ultrafast collapse takes place between a low energy electron (precursor of fully hydrated electrons) and biomolecules localized in the chemical core of the tracks i.e. at the interface between the physical core and penumbra zone. In presence of biomolecules, a decrease of the early signal amplitude assigned to the hydrated electron population in native ionization tracks has been observed [38, 42, 43]. This early effect argues for a prethermal attachment of a p-state excited electron on biomolecules in less than 0.85×10^{-12} s. Consequently, in sub-nanometric ionization tracks, a biomolecular radical formation ($\text{BM}^\cdot_{\text{aq}}$) would occur faster than the nonadiabatic radiationless relaxation of excited prehydrated electrons ($p \rightarrow s$ transition). A major stride of a short-range biomolecular alteration triggered by an ultrafast electron attachment in the prethermal regime of ionization clusters will be the quantitative characterization of two parameters at very short time ($t \ll 1$ ps): the effective reaction radius and interaction cross section of the fleeting quantum probe(2p state electron) with a biomolecule. Real-time infrared spectroscopic measurements in the spectral range 1.1–1.6 μm , based on laser-plasma accelerator technologies and HERF considerations, are still in progress.

In the framework of an energy/time/space approach of the prethermal regime of very low energy secondary electron ($E \ll 1$ eV), sub-picosecond IR spectroscopy of short-lived eigenstates of p-like excited prehydrated electron in the radial directions of ultrashort electron bunches would be used as quantum probe for the sub-nanometric investigation of radiation-induced biomolecular damage at early time. The ubiquitous character of this short-lived electronic probe will be essential to (i) explore the dynamics of prethermal radical processes and the early sub-structure of ionization tracks, (ii) define short-time interaction cross section and characterize pertinent bio-effect parameters in function of a pulsed radiation quality. In a near future, new physical concepts on biodosimetry at nanometer scale would provide guidance to estimate radiation-induced molecular alterations in environments of biological interest [76].

2.4 Spatio-Temporal Radiation Biomedicine

The innovative aspects of radiation therapy in cancer domain are growing rapidly as a result of new technical solutions enabling improved radiation sources, diagnostics and precision treatments [8, 10, 77–84]. The exposure of living systems to different types of ionizing radiations (X- and γ -rays, electrons, protons or ions) induces a broad range of complex physical responses and signalling processes that cells and tissues integrate or remove to maintain their functional integrity and prevent tumor formation [85–90]. It is commonly admitted that the early spatial distribution of energy deposition events triggered by ionizing radiation interacting with simple or complex biomolecular architectures is decisive for the control of damages at

cellular or tissue levels and for the prediction of delayed responses in radiation medicine and cancer therapy [86, 91–93]. Cancer radiotherapy based on X-ray photons and high energy electron, proton or ions represents about 45 % of curative and palliative treatments. Clinical accelerators currently delivering electron beams of 5–50 MeV are used for conventional surface therapy of shallow tumors but the innovative developments of radiation sources (LINACs, synchrotrons, ultrashort table-top laser systems, proton and ion accelerators) with specific dose distribution profiles make them suitable for treating deep tumors.

The potential interest of ultra-short particle bunches for clinical applications such as protontherapy is totally dependent on the development of compact laser-plasma accelerator providing quasi monoenergetic particle with an energy spread of 10 % and having lower cost investment than conventional radiotherapy machines [83, 93]. However, compared to classical dose rate used in conventional radiotherapy ($\sim 1 \text{ Gy min}^{-1}$ or 2 Gy per session, with a total integrated dose delivery of $\sim 60 \text{ Gy}$ for 6 treatment weeks), the very high dose rate delivered by laser plasma accelerators $\sim 10^{13} \text{ Gy s}^{-1}$ may challenge new concepts for interactive radiotherapy planning, taking into account multicriteria optimization of fractionated doses and personalized clinical treatments.

Deeply understanding the multi-scale mechanism of radiation damage in living matter, starting from the early radical and molecular processes to mutagenic DNA lesions, cell signalling, genomic instability, apoptosis, microenvironment and bystander effects, would have many practical consequences like the customization of more predictive and selective radiotherapy protocols. The complex links that exist between the physical aspects of early radiation events and the delayed evolution of biological endpoints such as those involved in double strand break (DSB) repair pathways of DNA (pH2AX, pATM, MRE11...), during carcinogenesis or cell survivals need the development of advanced spatio-temporal radiation biomedicine [92, 95]. For this transdisciplinary and interfacial domain, new physical concepts on radiation-matter interactions are more and more considered, taking into account several important parameters of pulsed radiation sources such as the time-dependent energetic fluence profile, peak dose delivery, energy radial distribution functions or spatial dose rate [7–10, 82, 92–99].

Reducing the dose deposition before the tumor would limit some deleterious radiation effects on health tissue while the presence of a significant dose deposition after tens of centimeters could be beneficial to cure deep cancer tumors of obese patients. Some undeniable prerequisites such as a well-defined dosimetric characterization have to be realized in tissue-like medium. From the theoretical point of view, the isodose distributions of very high-energy electron and accelerated proton or ion beams are generally investigated with semi-classical Monte Carlo methods performed with the code GEANT 4 [8, 82, 100, 101]. These approaches take into account various parameters of the electron beam such as the fact that electrons are accelerated in a very limited region of a few microns, the divergence, energy spectrum of relativistic electrons and particle cross section at the phantom entrance (aqueous-like phantom). Indeed, a detailed investigation of the dosimetric properties of very high monoenergetic electrons beams (VHEE) in the range of

150–250 MeV have demonstrated that for parallel and opposed beams, the sharpness of the lateral penumbra is of comparable quality to characteristic values of clinical photon beams.

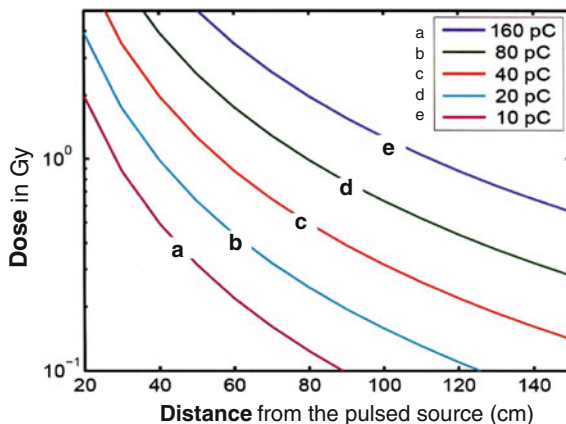
Regarding the physical aspects of particle-target interactions, Monte Carlo simulations include electromagnetic, electron and photonuclear processes. Most of these semi-classical simulations address the fundamental question of dose deposition at macro or microscopic levels [20, 88]. These approaches, whose TRAX simulation code, are quite suitable to define the physical dose delivered in living cells and tissues during cancer radiotherapy planning [86, 102] but do permit to estimate the biological dose profile at the local order i.e. at the scale of biomolecular architectures. This fundamental point seems also particularly important for radiotherapy protocols with targeted radiosensitizers such as nanoparticles [103–107]. An accurate description of the initial processes at extremely short space (nanometer scale) and time scale (sub-picosecond level) is mandatory.

Spatio-temporal radiation biomedicine is expected to provide new insights into yet unknown domains such as cell and tissue responses to pulsed high dose rate or determine the fate of confined cluster of ionization in the nanometric environment of biological target [92, 108–110]. Whatever the ionizing radiation is (electromagnetic radiation, accelerated particles or ions), the deposition of energy takes place in confined ionization spaces (tracks) for which the nanoscopic dimensions correspond to those of biomolecular entities in living matter (DNA and nucleosomes, proteins pockets, enzymatic machinery). Despite a considerable body of knowledge on nucleic lesions formation and repair, identification of protein damage and signalling pathways in normal and cancer cells [89, 92, 111], little is known on biological alterations in native tracks. Indeed, correlations between early radiation effects and cell surviving fraction cannot be defined from a macroscopic dose profile and require the innovating concept of radiation biomedicine at the nanometer scale. This newly emerging interdisciplinary field can be driven in strong synergy with the development of innovating ultrashort radiation sources and the most recent progresses of semi-quantum simulations, optical methods for sub-cellular imaging, molecular biology, genomics and proteomics, biomarkers detection, vectorized nanoparticles and radionuclides.

2.4.1 Ultrashort Pulsed Irradiation Effects at Sub-cellular Level

During the last decade several attempts were focused on nanosecond or picosecond irradiations of living cells [112–115] and the deleterious consequence of pulsed radiations on cell populations were analyzed in the framework of classical dose-survival curves and 2D imaging of foci [82, 97, 116]. When multi-shot irradiations of several Grays are performed, the integrated irradiation time greatly interferes with the multi-scale dynamics of biomolecular damage-repair sequences

Fig. 2.10 Calculated influence of the irradiation distance from the laser-plasma source on the dose delivered by monochromatic electron bunches (150 MeV) in a biological sample (water phantom). A typical divergence is 5 mrad FWHM and dispersive effects can be investigated for different charges of the high-energy electron beam



and cell signalling steps. Ultra-short radiation accelerators offer interesting perspectives for exploring the complex biological effects of single shot irradiation, considering that the irradiation time (~ 100 fs) is the same order of magnitude than early molecular damage such as bond breaking [117]. The energy and charge of ultrashort electron beam can be modulated, considering colliding beam geometry of laser-plasma source. In the energy range 90–200 MeV, as the electron beam area varies with the distance between the accelerator source and the sample, the dose delivered in living matter can be properly adjusted (Fig. 2.10). For that, the physical dose delivered in a cell pellet is determined from Monte Carlo calculations, taking into account the exact number of electrons determined from scintillator measurements. Mylar window of 300 μm can be used to extract the electron beam form the vacuum and different mini-tubes containing the biological sample are positioned in air.

Experimental conditions with an electron beam diameter of 9.2 mm permit an optimized overlap between a 2D dose deposited by a femtosecond quasi-monoenergetic electron bunch at a mean energy of 95 MeV (Fig. 2.11) and a semi-ellipse pellet profile of 1.5–2 mm containing about 5×10^5 human skin carcinoma cells (A431 carcinoma cell line).

Two different approaches can be considered: either an *ultrafast single irradiation shot* for which the dose delivered in the tumor cell pellet is 1.02 ± 0.13 Gy and the dose rate $10^{13} \text{ Gy s}^{-1}$ or *multiple high dose rate irradiation shots* permitting higher dose deposited in the biological sample (Figs. 2.11 and 2.12). In this later case, the integrated irradiation time remains long compared to the 100 fs pulse duration of a quasi-monoenergetic electron bunch [117].

One of the most promising aspect of a single shot irradiation of living material damage within a very short temporal window would be the real-time investigation of early high dose rate radiation-induced molecular damage in the confined spaces of cell compartments (nucleus, cytoplasm or membranes for instance). Considering that DNA represents an important molecular target for radiation biology, a first decisive step has been obtained by the investigation of the impact of a 100 fs single

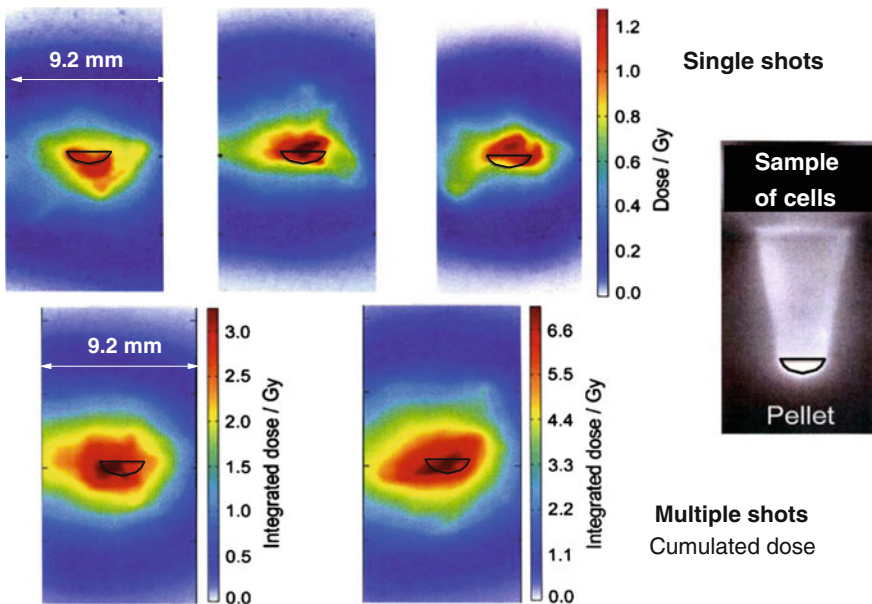
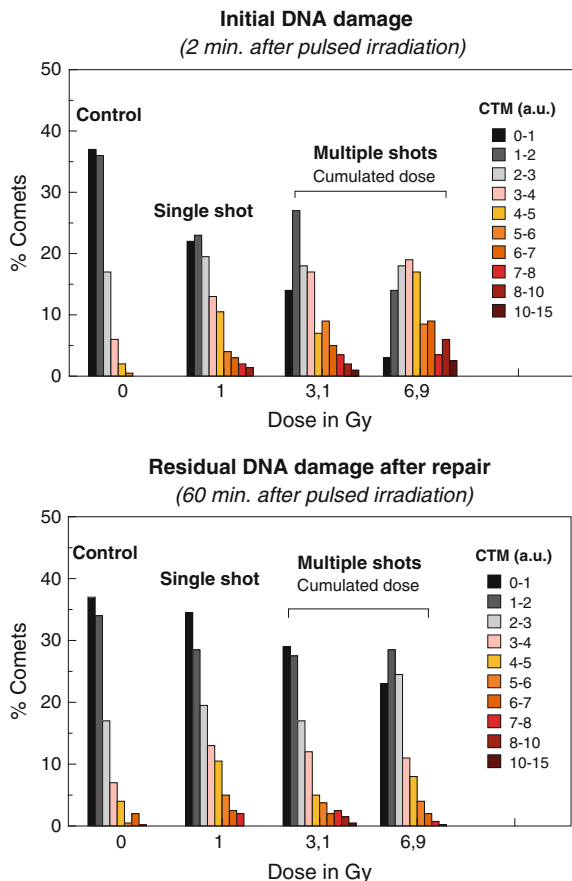


Fig. 2.11 Ultrashort irradiation of skin carcinoma cells (A431 carcinoma cell line) with femtosecond high energy electron bunches (95 MeV). *Upper part:* set of images showing the overlap between the pellet containing human skin carcinoma cells and the 2D single shot dose profile. The dose (~ 1 Gy) delivered in the semi-ellipse of the cell pellet by ultrafast single shot is determined by Monte Carlo calculations. *Lower part:* cumulated 2D dose profile showing multiple shots irradiation: 5 shots (left) and 10 shots (right) respectively. Adapted from [10]

shot with 1 Gy exposure on the level of DNA damage, using a well-established alkaline comet assay [116]. This procedure quantifies global radiation DNA damage (single and/or double-strand breaks) in individual cells. From a statistical distribution of comet tail moment with a 300 cells population, an initial distribution of single shot irradiated cells exhibits a shift towards a population of more damaged cells as compared to non-irradiated cells (Fig. 2.12). The fraction of cells with damage above a control tail moment value of 4 exhibited an 8-fold increase over that of the control cells. The recovery of a near homogeneous distribution of low comet tail moments, one hour after the ultrafast irradiation, argues for an efficient repair of the global DNA lesions. The complete reparability of DNA damage triggered by a single femtosecond irradiation shot at 1 Gy is not entirely observed when the same comet assays are performed on carcinoma cell populations submitted to multiple shots irradiations (Fig. 2.12). The initial nuclear DNA damages can be amplified by increasing the dose level delivered by femtosecond electron bunches. Two minutes after a multiple shot irradiation, a significant shift towards high comet tail moments can be progressively observed with the dose level. Compared to control sample (0 Gy) and single shot data at 1 Gy, the distribution of low comet tail moments is not entirely recovered, one hour after the end of multiple

Fig. 2.12 Distribution of DNA damage induced by an Irradiation of human carcinoma cells (A431 carcinoma cell line) with ultrashort electron bunches (95 MeV). For single or multiple shots configurations, the statistical distribution of DNA damage in function of time delay after an irradiation (2 or 60 min) is expressed from the determination of comet tail moments [116, 117]. Adapted from [10]



shot irradiations at 3.1 and 6.9 Gy for instance. These single and multiple shots studies suggest that repair process of DNA damage in tumor cells are dose dependent and become less efficient when multiple irradiation exposures are performed with ultrafast electron bunches.

In the framework of innovative applications of pulsed radiation sources for medical physics and cancer radiotherapy, ultrafast *in vivo* irradiation in the MeV domain can be achieved by single and multiple shot strategies. Recent investigations performed by different research groups are mainly focalised on integrated cellular responses, using cumulative effects of multiple radiation shots. In this approach, the integrated irradiation time (few minutes) remains very long compare to ultrafast molecular responses such as DNA single-double strand breaks (SSB and DSB respectively) or more generally molecular bond breakings (few hundred femtoseconds) [113–115]. The spatio-temporal radiation processes must be underpinned by advanced biophysical concepts on the impact of native tracks in biologically relevant environments. Some fundamental aspects of spatio-temporal

radiation biomedicine concern the adaptative responses of cells and tissues to clustered DNA damage-repair processes that may take place on the time scale of molecular motion.

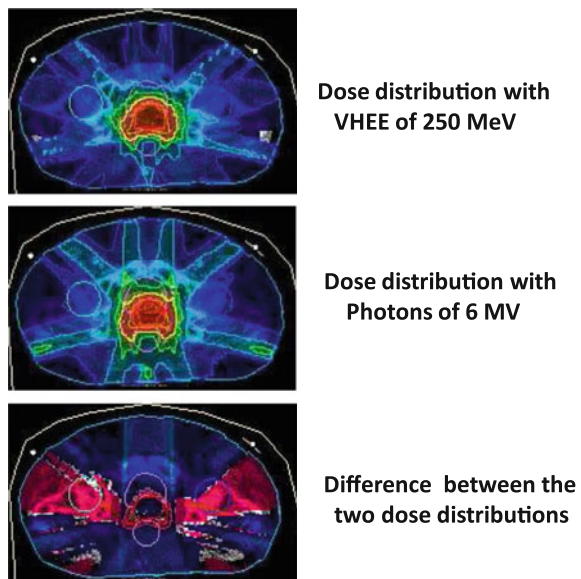
2.4.2 Potential Applications for Pulsed Cancer Therapies

From a strict biomedical point of view, the progresses of conventional and conformational radiotherapies are highly dependent on innovative developments of radiation source quality. Up to now, X rays and accelerated electron beams in the energy range of 4–25 MeV represent the essential of ionizing radiations currently used for cancer radiotherapy of several millions of patients all over the world. Proton and hadron therapies are still at their emerging stage but they represent very promising methods for the specific treatment of deep tumors and radio-resistant solid cancers [118, 119]. Concerning relativistic particle accelerated by laser-plasma interaction, very high energy electron (VHEE) in the range 150–250 MeV correspond to very penetrating radiation. They would be of interest for new radio-therapeutic approaches, considering the dose deposition profiles and high dose rate delivery. Compared to low energy electron curves ($E < 20$ MeV) currently used in classical therapy protocols whose penetration depth is below 5 cm, the deposited dose profile of 170 MeV electron is very broad with a maximum around 20 cm of depth path. The potential interest of VHEE for clinical applications is totally dependent on the development of compact laser-plasma accelerators which provide quasi-monoenergetic electron spectrums with high quality and stability of particle beams [120] and an energy spread of 10 % [50, 101]. However, compared to classical dose rate delivery in conventional radiotherapy i.e. 1 Gy/min, 2 Gy per session, the very high dose rate delivered with laser plasma accelerators $\sim 10^{13}$ Gy s⁻¹ may challenge new concepts for interactive radiotherapy planning, in the framework of multicriteria optimization of fractioned doses and personalized clinical treatments. Up to now, the isodose distributions of very high energy electron beams are investigated, from the spatial point of view, with Monte Carlo calculations (GEANT 4), including electromagnetic, electron and photonuclear processes but also specific parameters of the electron beam: electron beam divergence, energy spectrum of relativistic electrons, cross section of the particle beam at the phantom entrance (aqueous like phantom). The shape of isodose curves is strongly dependent on the initial distribution of electron and multiple scattering collisions in depth. For medical application of pulsed electron bunches in cancer therapy, the control of the integrated dose curve with the depth of the tumor remains essential. The difference between VHEE beams and X-rays or low energy electrons of a few MeV indicates that the dose deposited by VHEE in the tissue depth is higher and remains still efficient after a few tens of centimeters. Reducing the dose deposition before the tumor environment would limit some deleterious radiation effects on health tissue while the presence of a significant dose deposition after tens of centimeters could be beneficial to cure deep cancer tumors of obese patients. Some undeniable

prerequisites such as a well-defined dosimetric characterization have to be realized in tissue-like medium. For instance, some detailed investigation of the macro-dosimetric properties (physical dose) of very high monoenergetic electrons beams (VHEE) in the range of 150–250 MeV have predicted that for parallel and opposed beams, the sharpness of the lateral penumbra is of comparable quality to characteristic values of clinical photon beams [80]. Radially, the dose deposition profile is narrow and longitudinally, the penetration distance of these energetic electrons is higher than for 20 MeV conventional accelerators. The high laser energy conversion into accelerated electrons (10 %) and the control of the interaction parameters may allow, in the future, the optimisation of a tunable electron source adapted for new developments in pulsed radiotherapy, considering specific aspects such as a high dose rate delivery or a short-time control of fractionating protocol. Some predictive comparisons between classical radiation sources and new laser-driven particle accelerators based protocols would be of significant interest before developing preclinical trials. Indeed, in the framework of an approved treatment planning of prostate cancer in with 6 MV photons, detailed comparisons between classical X ray source and 250 MeV electron beam have been performed [121]. Compared to classical irradiation with X-ray photons, the target coverage is the same or even slightly better for VHEE sources (Fig. 2.13). Except for an over-irradiation of the femora, the dose sparing of sensitive structures and organs at risk is improved (up to 19 %) with high energy electron beams. A difference of the two dose distributions shows this more clearly on the lower part of the figure.

Predictive dose simulations permit reasonably to emphasize that electron beams produced with laser plasma accelerators would be well suited for delivering a high dose peaked on the propagation axis, a sharp and narrow transverse penumbra,

Fig. 2.13 *Upper part:* calculated transversal dose distributions in human pelvis for laser-accelerated VHEE of 250 MeV, in the framework of a treatment planning. The physical dose distribution shows the same target coverage as 6 MV photons (*middle part*). But the dose sparing of sensitive structures (except for the femurs) is improved with VHEE of 250 MeV, as shown in the difference of the two dose distributions (*lower part*). Adapted from Fuchs et al. [121]



combined with a deep penetration in the human body. However, VHEE produce energetic bremsstrahlung photons around 50 MeV which can, in return, activate the medium. In particular, photons of a few tens of MeV can induce efficiently photo-nuclear reactions, with neutron generation, via Giant Dipole Resonance of nuclei [120]. Additional effects inherent to VHEE, such as neutron contamination, would be also investigated in order to clarify the exact conditions for using ultra-short particle beams during anticancer pulsed radiotherapy protocols.

The Gaussian shape of the radial dose profile being dependent on Coulomb scattering effects, the importance of penumbra width during a single shot dose delivery seems crucial to establish a link between the concept of very high dose rate delivery in the range 10^{12} – 10^{13} Gy s $^{-1}$ and the biomolecular consequence of a local dose fractioning at very short time. They concerns the adaptative responses of cells and tissues to clustered DNA damages-repairs processes, following ultrafast radiation perturbations triggered on the time scale of molecular motion. For a relativistic particle beam, the spatial distribution of primary radical events being dependant on the sub-structure of ionization tracks at the physical core-penumbra interface (Fig. 2.4), well collimated femtosecond electron beams should be useful for the development of spatio-temporal radiation biology and medicine. Significant advances would concern the quantification of an effective biological dose in the prethermal regime of secondary electrons. An extension of these innovating concepts to other pulsed sources such as pulsed X ray and relativistic particles beams (proton and heavy ions for instance) would be of a significant interest for conceiving selective medical treatment plannings [9, 77, 81–83, 93, 102, 122].

2.5 Concluding Remarks on Future Challenges

The physics of advanced TW laser plasma accelerators delivering ultrashort high and very high energy electron bunches (50 and 150–200 MeV respectively) open promising perspectives for ultrafast radiation physico-chemistry and biomedicine [9, 19, 38, 41–43, 81, 83, 92, 123, 124]. The specific qualities and properties of short relativistic particle bunches foreshadow the development of advanced researches to deepen our biophysical understanding of early radiation events in native ionization tracks close to complex biomolecular architectures (membranes, nuclear and cytoplasmic environments, intercellular junctions).

Deeply understand the multi-scale mechanism of radiation damage in living matter, starting from the early radical and molecular processes to mutagenic DNA and protein lesions, cell signalling, genomic instability, apoptosis, and microenvironment effects [59, 60, 85, 87, 92, 95, 125, 126], would have, in a near future, many practical consequences like the customization of more predictive and selective radiotherapy protocols. The complex links that exist between the physical aspects of early radiation events and the delayed evolution of biological endpoints,

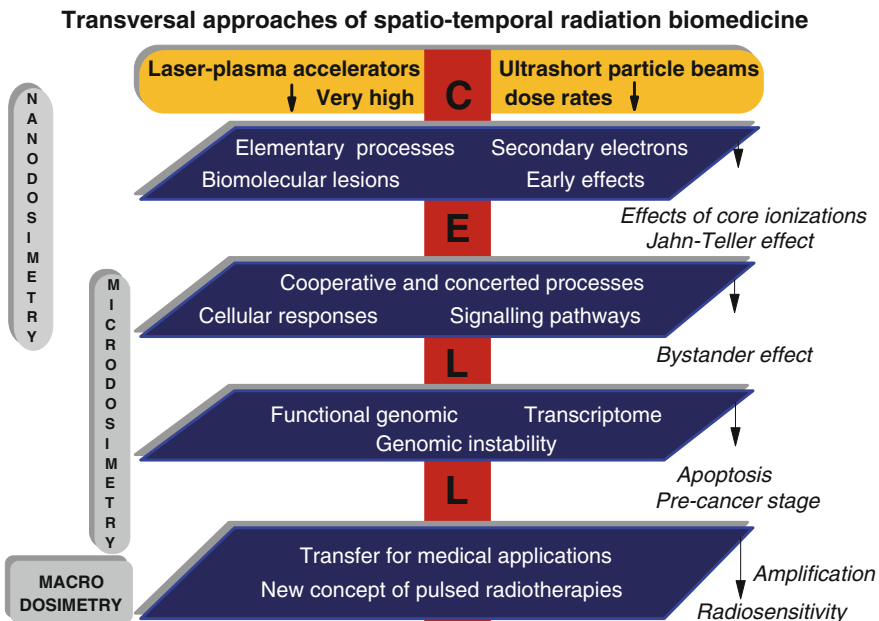


Fig. 2.14 Importance of laser-plasma accelerators and ultrashort particle beams for getting significant advances in transversal approaches of spatio-temporal radiation biomedicine. One of the main domains concerns the emerging concept of real-time nanodosimetry. (The Jahn-Teller effect corresponds to a geometrical distortion of non-linear molecules in specific conditions, including vibronic interactions [127]; in a cell, the transcriptome represents the set of different RNA molecules [128])

carcinogenesis or cell survivals need the reinforcement of interdisciplinary researches of advanced spatio-temporal radiation biomedicine (Fig. 2.14).

This interdisciplinary domain would provide guidance for the future development of physical and theoretical researches devoted to nanobiodosimetry for radiation cancer therapy and concerns main topics such as: the spatio-temporal description of processes cascade leading to cell DNA damage response (foci formation) and multiple gene amplification following an initial and local energy deposition by radiation; 3D identification of specific biomolecular markers of DNA damages and cell signalling in function of radiation quality (electromagnetic, particle or ion beams, energy and temporal characteristics); biophysical effects of secondary low-energy electrons in the prethermal regime of radiation interactions with living matter; semi-quantum simulations of biomolecular clustered damages in native ionization tracks, taking into account the time-dependent track sub-structure, within the temporal window 10^{-14} – 10^{-11} s; the conceptualisation of time-dependent molecular RBE (Relative Biological Effectiveness) for normal and cancerous tissues [86]. These major issues are ubiquitous and concern the different types of radiation characterized either by low (X and γ rays, electron, proton) or high density of ionisation (ions). All the innovating aspects of protontherapy and

hadrontherapy require also a strong synergy between experimental developments performed with ultrashort particle beams and advanced numerical quantum simulations of ultrafast radiation phenomena [72, 129, 130].

One of the most promising developments of future laser-accelerator based HERF researches will concern the real-time investigation of ultrafast nanometric and sub-nanometric biomolecular damages in the prethermal regime of native ionization tracks, considering the presence of short-lived low energy secondary electrons at the frontier of physical core and penumbra zone. The quantum character of very-short lived p-like configuration of excited electron provides a sub-nanometric probe to explore their short-time interactions with bio-molecules and offers the opportunity to characterize the pertinent bio-effect parameters in native ionization tracks. This approach opens the new concept of real-time nanobiodosimetry as a function of the pulsed radiation quality factors [9, 81–84, 91, 100, 102, 130–132], considering the transient sub-structures of ionization tracks. For biomolecular targets whose the size is less than 20 Å at a density of 1.0 g cm^{-3} , the corresponding target areal mass will be less than $1 \times 10^{-6} \text{ g cm}^{-2}$ [133, 134]. The femtosecond electron bunches are more adapted than picosecond proton beams for this new challenge, owing to the fact that these primary bio-effects take place mainly in less than 10^{-12} s . Establishing an innovating approach of nanobiodosimetry on the temporal and spatial scales of biomolecular architectures, the laser-plasma accelerators based spatio-temporal radiation biomedicine represents a prerequisite for the control of pulsed radiotherapy of cancerous cells and tissues at very high dose rates.

The modulated response of non-irradiated cell localized in the vicinity of irradiated cells (Bystander effect [126]) represents also a real challenge (see Fig. 2.14) for getting (i) the predictive molecular response to dose delivery profile (biological dose) in normal tissue/cancerous tumor, (ii) the optimized control of ultra-high dose-rate effects in order to reduce the deleterious complications of radiation cancer therapy. The high laser energy conversion into accelerated electrons and the control of the interaction parameters may allow the optimization of a tunable electron source adapted for new developments of pulsed radio-chemotherapy of cancers, considering the specific aspects of a high dose rate delivery, the advanced prodrug and radiosensitizer strategies [106, 107, 134–138] and the complex control of short-time fractionating treatments. These future developments are crucial to fully understand the early biomolecular consequences of ultra-short pulsed radiations performed with laser-driven particle sources and to predict and estimate, at cell and tissue levels, the time-dependence of radiation risks linked to pulsed radiotherapy protocols.

References

1. T. Tajima, J.M. Dawson, Laser electron accelerator. Phys. Rev. Lett. **43**, 267–270 (1979)
2. V. Malka, S. Fritzler, E. Lefebvre, M.M. Aleonard, F. Burgy, J.P. Chambaret, J.F. Chemin, K. Krushelnick, G. Malka, S.P.D. Mangles, Z. Najmudin, M. Pittman, J.P. Rousseau, J.N. Scheurer, B. Walton, A.E. Dangor, Electron acceleration by a wake field forced by an intense ultrashort laser pulse. Science **298**, 1596–1600 (2002)

3. E. Erasey, C.B. Schroeder, W.P. Leemans, Physics of laser-driven plasma-based electron accelerators. *Rev. Mod. Phys.* **81**, 1229–1285 (2009)
4. T. Tajima, Laser acceleration and its future. *Proc. Jpn. Acad. Ser.* **86**, 147–157 (2010)
5. Malka, V., Laser plasma accelerators, in *Laser-Plasma Interactions and Applications*, eds. by P. McKenna, D. Neely, R. Bingham, D. Jaroszynski (Springer International Publishing, Switzerland, 231–301, 2013)
6. Y. Gauduel, S. Fritzler, A. Hallou, Y. Glinec, V. Malka, Femtosecond relativistic electron beam triggered early bioradical events, in *Femtosecond Laser Applications in Biology*, SPIE, vol. 5463 (2004), pp. 86–96
7. V. Malka, J. Faure, Y. Gauduel, E. Lefebvre, A. Rousse, K. Ta Phuoc, Principles and applications of compact laser-plasma accelerators. *Nat. Phys.* **4**, 447–453 (2008)
8. V. Malka, J. Faure, Y.A. Gauduel, Ultra-short electron beams based spatio-temporal radiation biology and radiotherapy. *Mut. Res. Rev.* **704**, 142–151 (2010)
9. A. Giulietti, M.G. Andreassi, C. Greco, Pulse radiobiology with laser-driven plasma accelerators, in *SPIE Proceedings*, vol. 8079 (2011), p. 80791J
10. Y.A. Gauduel, O. Lundh, M.T. Martin, V. Malka, Laser-plasma accelerators-based high-energy radiation femtochemistry and spatio-temporal radiation biomedicine, in *SPIE Optics and Optoelectronics Laser sources and applications*, vol. 8433 (2012), p. 843313
11. Y.A. Gauduel, Spatio-temporal radiation biology: an emerging transdisciplinary domain. *Mut. Res. Rev.* **704**, 1 (2010)
12. J.C. Diels, W. Rudolph (eds.), *Ultrashort laser pulse phenomena* (Academic Press, New York, 1996)
13. H.A. Zewail (ed.), *Femtochemistry: ultrafast dynamics of the chemical bond* (World Scientific, Singapore, 1994)
14. W. Castelman (ed.), *Femtochemistry VII Fundamental Ultrafast Processes in Chemistry, Physics and Biology* (Elsevier, Amsterdam, 2006)
15. Y.A. Gauduel, *Femtochemistry: Lasers to Investigate Ultrafast Reactions Lasers in Chemistry*, ed. by M. Lackner, vol. 2 (Wiley-VCH, 2008), pp. 861–898
16. J.H. Baxendale, F. Busi (eds.), *The Study of Fast Processes and Transient Species by Electron Pulse Radiolysis* (Reidel Publishing Company, Dordrecht, 1982)
17. J.E. Turner, J.L. Magee, A. Wright, A. Chatterjee, R.N. Hamm, R.H. Ritchie, Physical and chemical development of electron tracks in liquid water. *Rad. Res.* **96**, 437–449 (1983)
18. Y. Gauduel, P.J. Rossky (eds.), *Ultrafast Reaction Dynamics and Solvent Effects* (AIP Press, New York, 1994)
19. M.P. Allen, D.J. Tildesley (eds.), *Computer Simulation of Liquids* (Oxford Science Publications, 1987)
20. M.N. Varma, A. Chatterjee (eds.), *Computational Approaches in Molecular Radiation Biology—Monte Carlo Methods* (Plenum Press, New York, 1993)
21. J.R. Sabin, E. Brandas (eds.), *Advances in Quantum Chemistry: Theory of the Interaction of Radiation with Biomolecules* (Elsevier, Amsterdam, 2007)
22. D.N. Nikogosyan, A.A. Oraevsky, V.I. Rupasov, Two-photon ionization and dissociation of liquid water by powerful laser UV irradiation. *Chem. Phys.* **77**, 131–143 (1983)
23. Y. Gauduel, S. Pommeret, A. Migus, A. Antonetti, Some evidence of ultrafast H_2O^+ -water molecule reaction in femtosecond photoionization of pure liquid water: influence on geminate pair recombination dynamics. *Chem. Phys.* **149**, 1–10 (1990)
24. A. Migus, Y. Gauduel, J.L. Martin, A. Antonetti, Excess electrons in liquid water: first evidence of a prehydrated state with femtosecond lifetime. *Phys. Rev. Lett.* **58**, 1159–1162 (1987)
25. S. Pommeret, A. Antonetti, Y. Gauduel, Electron hydration in pure liquid water. Existence of two nonequilibrium configurations in the near-infrared region. *J. Am. Chem. Soc.* **113**, 9105–9111 (1991)
26. Y. Gauduel, Ultrafast electron-proton reactivity in molecular liquids, in *Ultrafast Dynamics of Chemical Systems*, ed. by J.D. Simon (Kluwer Publisher, 1994), pp. 81–136

27. Y. Gauduel, Ultrafast concerted electron-proton transfers in a protic molecular liquid, in *Ultrafast Reaction Dynamics and Solvent Effects*, eds. by Y. Gauduel, P.J. Rossky (AIP Press, New York, 1994), pp. 191–204
28. Y. Kimura, J.C. Alfano, P.K. Walhout, P.F. Barbara, Ultrafast transient absorption-spectroscopy of the solvated electron in water. *J. Phys. Chem.* **98**, 3450–3458 (1994)
29. R. Laenen, T. Roth, Generation of solvated electrons in neat water: new results from femtosecond spectroscopy. *J. Mol. Struct.* **598**, 37–43 (2001)
30. E. Esarey, R.F. Hubbard, W.P. Leemans, A. Ting, P. Sprangle, Electron injection into plasma wakefields by colliding laser pulses. *Phys. Rev. Lett.* **79**, 2682–2685 (1997)
31. A. Pukhov, J. Meyer-ter-Vehn, Laser wake field acceleration: the highly non-linear broken-wave regime. *Appl. Phys. B* **74**, 355–361 (2002)
32. C.G.R. Geddes, C.S. Toth, J. van Tilborg, E. Esarey, C.B. Schroeder, D. Bruhwiler, C. Nieter, J. Cary, W.P. Leemans, High-quality electron beams from a laser wakefield accelerator using plasma-channel guiding. *Nature* **431**, 538–541 (2004)
33. S.P.D. Mangles, C.D. Murphy, Z. Najmudin, A.G.R. Thomas, J.L. Collier, A.E. Dangor, E. J. Divall, P.S. Foster, J.G. Gallacher, C.J. Hooker, D.A. Jaroszynski, A.J. Langley, W.B. Mori, P.A. Norreys, F.S. Tsung, R. Viskup, B.R. Walton, K. Krushelnick, Monoenergetic beams of relativistic electrons from intense laser-plasma interactions. *Nature* **431**, 535–538 (2004)
34. J. Faure, C. Rechatin, A. Norlin, A. Lifschitz, Y. Glinec, V. Malka, Controlled injection and acceleration of electrons in plasma wakefields by colliding laser pulses. *Nature* **444**, 737–739 (2006)
35. C. Rechatin, J. Faure, A. Ben-Ismail, J. Lim, R. Fitour, A. Specka, H. Videau, A. Tafzi, F. Burgy, V. Malka, Controlling the phase-space volume of injected electrons in a laser-plasma accelerator. *Phys. Rev. Lett.* **102**, 164801 (2009)
36. V. Malka, Laser plasma accelerators: towards high quality electron beam, in *Laser pulse phenomena and applications*. ed. by F.J. Duarte (Intechweg. Org, 2010)
37. C. Thaury, E. Guillaume, A. Doepp, R. Lehe et al., Demonstration of relativistic electron beam focusing by a laser-plasma lens. *Nature Comm.* **6**, 6860 (2015)
38. Y.A. Gauduel, J. Faure, V. Malka, Ultrashort relativistic electron bunches and spatio-temporal radiation biology, in *Proceedings of SPIE*, vol. 7080 (2008), pp. 708002–1
39. D.A. Oulianov, R.A. Crowell, D.J. Gosztola, I.A. Shkrob, O.J. Korovyanko, R.C., Rey-de-Castro, Ultrafast pulse radiolysis using a terawatt laser wakefield accelerator. *J. Appl. Phys.* **101**, 053102-1-9 (2007)
40. B. Brozek-Pluska, D. Gliger, A. Hallou, V. Malka, Y. Gauduel, Direct observation of elementary radical events: low and high-energy radiation femtochemistry in solution. *Rad. Phys. Chem.* **72**, 149–157 (2005)
41. Y.A. Gauduel, Y. Glinec, J.P. Rousseau, F. Burgy, V. Malka, High energy radiation femtochemistry of water molecules: early electron-radical pairs processes. *Eur. Phys. J. D* **60**, 121–135 (2010)
42. Y.A. Gauduel, Laser-plasma accelerator based femtosecond high energy radiation chemistry and biology. *J. Phys. CS* **373**, 012012 (2012)
43. Y.A. Gauduel, Synergy between low and high energy radical femtochemistry. *J. Phys Ser.* **261**, 012006 (2011)
44. T. Kai, A. Yokoya, M. Ukai, R. Watanabe, Cross sections, stopping powers, and energy loss rates for rotational and phonon excitation processes in liquid water by electron impact *Rad. Phys. Chem.* **108**, 13–17 (2015)
45. Farhataziz, M.A.J. Rodgers (eds.), *Radiation Chemistry* (VCH Publishers, 1987)
46. G.R. Freeman (ed.), *Kinetics of Nonhomogeneous Processes* (Wiley, New York, 1987), pp. 377–403
47. N.J.B. Green, M.J. Pilling, S. Pimblott, P. Clifford, Stochastic modeling of fast kinetics in radiation tracks. *J. Phys. Chem.* **94**, 251–258 (1990)

48. D.M. Bartels, A.R. Cook, M. Mudaliar, C.D. Jonah, Spur decay of the solvated electron in picosecond radiolysis measured with time-correlated absorption spectroscopy. *J. Phys. Chem. A* **104**, 1686–1691 (2000)
49. S.A. Isaacson, The reaction-diffusion master equation as an asymptotic approximation of diffusion at a small target. *J. Appl. Math.* **70**, 77–111 (2009)
50. J. Faure, Y. Glinec, A. Pukhov, S. Kiselev, S. Gordienko, E. Lefebvre, J.P. Rousseau, F. Burgý, V. Malka, A laser-plasma accelerator producing monoenergetic electron beams. *Nature* **431**, 541–544 (2004)
51. S.M. Hooker, Developments in laser-driven plasma accelerators. *Nat. Photonics* **7**, 775–782 (2013)
52. L. Onsager, Electric moments of molecules in liquids. *J. Am. Chem. Soc.* **58**, 1486 (1936)
53. A.C. Chernovitz, C.D. Jonah, Isotopic dependence of recombination kinetics in water. *J. Phys. Chem.* **92**, 5946–5950 (1988)
54. H.G. Paretzke, Radiation track structure theory, in *Kinetics of nonhomogeneous processes*, ed. by G.R. Freeman (Wiley, New York, 1987), pp. 89–170
55. K.Y. Lam, J.W. Hunt, Picosecond pulsed-radiolysis 6. Fast electron reactions in concentrated solutions of scavengers in water and alcohols. *Int. J. Radiat. Phys. Chem.* **7**, 317–338 (1975)
56. S.M. Pimblott, J.A. La Verne, D.M. Bartels, C.D. Jonah, Reconciliation of transient absorption and chemically scavenged yields of the hydrated electron in radiolysis. *J. Phys. Chem.* **100**, 9412–9415 (1996)
57. C.D. Jonah, D.M. Bartels, A.C. Chernovitz, Primary processes in the radiation chemistry of water. *Radiat. Phys. Chem.* **34**, 145–156 (1989)
58. P. Han, D.M. Bartels, H/D isotope effects in water radiolysis 2. Dissociation of electronically excited water. *J. Phys. Chem.* **94**, 5824–5833 (1990)
59. Y. Gauduel, S. Berrod, A. Migus, N. Yamada, A. Antonetti, Femtosecond charge separation in organized assemblies: free-radical reactions with pyridine nucleotides in micelles. *Biochemistry* **27**, 2509–2518 (1988)
60. J. Nguyen, Y. Ma, T. Luo, R.G. Bristow, D.A. Jaffray, Q.B. Lu, Direct ultrafast-electron-transfer reaction unravels high effectiveness of reductive DNA damage. *Proc. Nat. Acad. Sci.*, **108**, AA778–11783 (2011)
61. L. Sanche, Beyond radical thinking. *Nature* **461**, 358–359 (2009)
62. E. Alizadeh, L. Sanche, Precursors of solvated electrons in radiological physics and chemistry. *Chem. Rev.* **112**, 5578–5602 (2012)
63. Y. Gauduel, M. Sander, H. Gelabert, Ultrafast reactivity of IR-excited electron in aqueous ionic solutions. *J. Phys. Chem. A* **102**, 7795–7803 (1998)
64. Y. Gauduel, H. Gelabert, F. Guilloud, Real-time probing of a three-electron bonded radical: Ultrafast one-electron reduction of a disulfide biomolecule. *J. Am. Chem. Soc.* **122**, 5082–5091 (2000)
65. Y. Gauduel, A. Hallou, B. Charles, Short-time water caging and elementary prehydration redox reactions in ionic environments. *J. Phys. Chem. A* **107**, 2011–2024 (2003)
66. E.R. Bittner, P.J. Rossky, Quantum decoherence in mixed quantum-classical systems nonadiabatic processes. *J. Phys. Chem.* **103**, 8130–8143 (1995)
67. T.H. Murphrey, P.J. Rossky, Quantum dynamics simulation with approximate eigenstates. *J. Chem. Phys.* **103**, 6665 (1995)
68. B.J. Schwartz, P.J. Rossky, Aqueous solvation dynamics with a quantum mechanical solute: computer simulation studies of the photoexcited hydrated electron. *J. Chem. Phys.* **101**, 6902–6916 (1994)
69. O.V. Prezhdo, P.J. Rossky, Solvent mode participation in the nonradiative relaxation of the hydrated electron. *J. Phys. Chem.* **100**, 17094 (1996)
70. L. Turi, P.J. Rossky, Theoretical studies of spectroscopy and dynamics of hydrated electrons. *Chem. Rev.* **112**, 5641–5674 (2012)
71. Q.B. Lu, Effects and applications of ultrashort-lived prehydrated electrons in radiation biology and radiotherapy of cancer. *Mut. Res. Rev.* **704**, 190–199 (2010)

72. P. Lopez-Tarifa, M.P. Gaigeot, R. Vuilleumier, I. Tavernelli, M. Alcami, F. Martin, M.A.H. du Penhoat, M.F. Politis, Ultrafast damage following radiation-induced oxidation of uracil in aqueous solution. *Angew. Chem. Int. Ed.* **52**, 3160–3163 (2013)
73. S. Minardi, C. Milián, D. Majus, A. Gopal, G. Tamošauskas, A. Couairon, T. Pertsch, A. Dubietis, Energy deposition dynamics of femtosecond pulses in water. *Appl. Phys. Lett.* **105**, 224104 (2014)
74. M.H. Elkins, H.L. Williams, A.T. Shreve, D.M. Neumark, Relaxation mechanism of the hydrated electron. *Science* **342**, 1496–1499 (2013)
75. J. Savolainen, F. Uhlig, S. Ahmed, P. Hamm, P. Jungwirth, Direct observation of the collapse of the delocalized excess electron in water. *Nat. Chem.* **6**, 687–701 (2014)
76. Y.A. Gauduel, V. Malka, Ultrafast sub-nanometric spatial accuracy of a fleeting quantum probe interaction with a biomolecule: innovating concept for spatio-temporal radiation biomedicine, in *SPIE Proceedings*, vol. 8954, 89540A1–12 (2014)
77. H. Blattmann, J.O. Gebbers, E. Brauer-Krisch, A. Bravin, G. Le Duc, W. Burkard, M. Di Michiel, V. Djonov, D.N. Slatkin, J. Stepanek, J. Laissue, Applications of synchrotron X-rays to radiotherapy. *Nucl. Instrum. Methods Phys. Res. Sect. A* **548**, 17–22 (2005)
78. K.M. Prise, New advances in radiation biology. *Occup. Med.* **56**, 156–161 (2006)
79. A.V. Solov'yov, E. Surdutovich, E. Scifoni, I. Mishustin, W. Greiner, Physics of ion beam cancer therapy: a multiscale approach. *Phys. Rev. E*, **79**, 011909 (2009)
80. C. DesRosiers, V. Moskin, C. Minsong, Laser-plasma generated very high energy electrons in radiation therapy of the prostate, in *SPIE Proceedings*, vol. 6881 (2008), pp. 688109–1
81. J. Tajima, D. Habs, X. Yan, Laser acceleration of ions for radiation therapy. *Rev. Acc. Sci. Tech.* **2**, 201–228 (2009)
82. S.D. Kraft, C. Richter, K. Zeil, M. Baumann, E. Beyreuther, S. Bock, M. Bussmann, T.E. Cowan, Y. Dammene, W. Enghardt, U. Helbig, L. Karsch, T. Kluge, L. Laschinsky, E. Lessmann, J. Metzkes, D. Naumburger, R. Sauerbrey, M. Schürer, M. Sobiella, J. Woithe, U. Schramm, J. Pawelke, Dose-dependent biological damage of tumour cells by laser-accelerated proton beams. *New J. Phys.* **12**, 085003 (2010)
83. K.W.D. Ledingham, P.R. Bolton, N. Shikazono, C.M.C. Ma, Towards laser driven hadron cancer radiotherapy: a review of progress. *Appl. Sci. Basel* **4**, 402–443 (2014)
84. U. Masood, M. Bussmann, T. Cowan, W. Engardt, L. Karsch, F. Kroll, U. Schramm, J. Pawelke, A compact solution for ion beam therapy with laser accelerated proton. *Appl. Phys. B., Lasers and Optics*, **117**, 41–52 (2014)
85. Y.E. Dubrova, M. Plumb, B. Gutierrez, E. Boulton, A.J. Jeffreys, Transgenerational mutation by radiation. *Nature* **405**, 37 (2000)
86. W.R. Hendee, G.S. Ibbott, E.G. Hendee, Radiation therapy physics (Wiley-Liss Ed., 2005)
87. C. Von Sonntag (ed.), *Free-radical-Induced DNA Damage and its Repair* (Springer, Heidelberg, 2006)
88. Y. Horowitz (ed.), *Microdosimetric Response of Physical and Biological Systems to Low and High Let Radiations: Theory and Application to Dosimetry* (Elsevier, Amsterdam, 2006)
89. M. Shukla, J. Leszczynski, *Radiation Induced Molecular Phenomena in Nucleic Acids: A Comprehensive Theoretical and Experimental Analysis* (Springer Ed., 2008)
90. I. Baccarelli, I. Bald, F.A. Gianturco, E. Illenberger, J. Kopyra, Electron-induced damage of DNA and its components: experiments and theoretical models. *Phys. Rep.* **508**, 1 (2011)
91. D. Verellen, G. Soete, N. Linthout, S. Van Acker, P. De Roover, V. Vinh-Hung, J. Van de Steen, G. Storme, Quality assurance of a system for improved target localization and patient set-up. *Rad. Oncol.* **67**, 129–141 (2003)
92. Y.A. Gauduel (ed.), Spatio-temporal radiation biology: transdisciplinary advances for medical applications. *Mut. Res. Rev.* **704**, 214 (2010)
93. M. Orth, K. Lauber, M. Miyazi, A.A. Fried, M.L. Li, C. Maihafer, L. Schuttrumpf, A. Ernst, O.M.M. Niemoller, C. Belka, Current concepts in clinical radiation oncology. *Rad. Env. Biophys.* **53**, 1–29 (2014)
94. S. Feuerhahn, J.M. Egly, Tool to study DNA repair: what's in the box? *Trends Genet.* **24**, 467–474 (2008)

95. M. Shukla, J. Leszczynski, *Radiation Induced Molecular Phenomena in Nucleic Acids: A Comprehensive Theoretical and Experimental Analysis* (Springer Ed., 2008)
96. X. Kong, S.K. Mohanty, J. Stephene, J.T. Feale, V. Gomez-Godinez, L.Z. Shi et al., Comparative analysis of different laser systems to study cellular responses to DNA damage in mammalian cells. *Nucleic Acids Res.* **37**, 2–14 (2009)
97. E. Beyreuther, W. Enghardt, M. Kaluza, L. Karsch, L. Laschinsky, E. Lessmann, M. Nicolai, J. Pawelke, C. Richter, R. Sauerbrey, H.P. Schlenvoigt, M. Baumann, Establisment of technical prerequisites for cell irradiation experiments with laser-accelerated electrons. *Med. Phys.* **37**, 1393–1400 (2010)
98. C. Richter, I. Karsch, Y. Dammene, S.D. Kraft, J. Metzkes, U. Schramm, M. Schürer, M. Sobella, A. Weber, K. Zeil, Pawelke, J.A dosimetric system for quantitative cell irradiation experiments with laser-accelerated protons. *Phys. Med. Biol.* **56**, 1529–1543 (2011)
99. S. Auer, V. Hable, C. Greubel, G.A. Drexler, T.E. Schmid, C. Belka, G. Dollinger, A.A. Friedl, Survival of tumor cells after proton irradiation with ultra-high dose rates. *Rad. Oncol.* **6**, 139 (2011)
100. V. Malka, in *Laser Plasma Accelerators, Laser-Plasma Interactions and Applications*, eds. by P. McKenna, D. Neely, R. Bingham and D. Jaroszynski (Springer International Publishing, Switzerland, 2013), pp. 231–301
101. Y. Glinec, J. Faure, V. Malka, T. Fuchs, H. Szymanski, U. Oelke, Radiotherapy with laser-plasma accelerators: Monte-Carlo simulation of dose deposited by an experimental quasimonoenergetic electron beam. *Med. Phys.* **33**, 155–162 (2006)
102. M. Kramer, M. Durante, Ion beam transport calculations and treatment plans in particle therapy. *Eur. Phys. J. D* **60**, 195–202 (2010)
103. J.F. Hainfeld, F.A. Dimanian, D.N. Slatkin, H.M. Smilowitz, Radiotherapy enhancement with gold nanoparticles. *J. Pharm. Pharmacol.* **60**, 977–985 (2008)
104. S.X. Zhang, J. Gao, T.A. Buchholtz, Z. Wang, M.R. Salehpour, R.A. Drezek, T. Yu, Quantifying tumor-selective radiation dose enhancements using gold nanoparticles: a Monte Carlo simulation study. *Biomed. Microdevices* **11**, 925–933 (2009)
105. W.N. Rahman, N. Bishara, T. Ackerly, C.F. He, P. Jackson, C. Wong, R. Davidson, M. Geso, Nanomed. Nanotech. Biol Med. **5**, 136–142 (2009)
106. S.J. McMahon, W.B. Hyland, M.F. Muir, J.A. Coulter, S. Jain, K.T. Butterworth, G. Schettino, G.R. Dickson, A.R. Hounsell, J.M. O'Sullivan, K.M. Prise, D.G. Hirst, F. J. Currell, Biological consequences of nanoscale energy deposition near irradiated heavy atom nanoparticles. *Sci. Reports* **1**, 18 (2011)
107. E. Porcel, O. Tillement, F. Lux, P. Mowat, N. Usami, K. Kobayashi, Y. Furusawa, C. LeSech, S. Li, S. Lacombe, Gadolinium-based nanoparticles ti improve the hadrontherapy performances. *Nanomed. Nanothec. Biophys. Med.* **10**, 1601–1608 (2014)
108. N. Gault, O. Rigaud, J.L. Poncy, J.L. Lefaix, Biochemical alterations in human cells irradiated with alpha particles delivered by macro- or microbeams. *Radiat. Res.* **167**, 551–562 (2007)
109. G. Schettino, M. Ghita, K.M. Prise, Spatio-temporal analysis of DNA damage repair using the X-ray microbeam. *Eur. Phys. J. D* **60**, 157–161 (2010)
110. H. Kempf, M. Bleicher, M. Meyer-Hermann, Spatio-temporal cell dynamics in tumour speroid irradiation. *Eur. Phys. J., D* **60**, 177–193 (2010)
111. A.L. Hein, M.M. Ouellette, Y. Yan, Radiation-induced signaling pathways that promote cancer cell survival. *Int. J. Oncol.* **45**, 1813–1819 (2014)
112. C. Tillman, G. Grafström, A.C. Jonsson, I. Mercer, S. Mattsson, S.E. Stand, S. Svanberg, Survival of mammalian cells exposed to ultrahigh dose rates from a laser-produced plasma X-ray source. *Radiobiol.* **213**, 860–865 (1999)
113. K. Shinohara, H. Nakano, N. Miyazaki, M. Tago, T. Kodama, Effects of single-pulse (≤ 1 ps) X-rays from laser-produced plasmas on mammalian cells. *J. Radiat. Res.* **45**, 509–514 (2004)
114. A. Yogo, K. Sato, M. Nishikino, M. Mori, T. Teshima, K. Numasaki, M. Murakami, Application of laser-accelerated protons to the demonstration of DNA double-strand breaks in human cancer cells. *Appl. Phys. Lett.* **94**, 181502 (2009)

115. K. Sato, M. Nishikino, Y. Okano, S. Ohshima, N. Hasegawa, M. Ishino, T. Kawachi, H. Numasaki, T. Teshima, H. Nishimura, γ -H2AX and phosphorylated ATM focus formation in cancer cells after laser plasma X irradiation. *Rad. Res.*, **174**, 436–445 (2010)
116. P.L. Olive, J.P. Banath, The comet assay: a method to measure DNA damage in individual cells. *Nat. Protocols* **1**, 23–26 (2006)
117. O. Rigaud, N.O. Fortunel, P. Vaigot, E. Cadio, M.T. Martin, O. Lundh, J. Faure, C. Rechatin, V. Malka, Y.A. Gauduel, Exploring ultrashort high-energy electron-induced damage in human carcinoma cells. *Cell Death Dis.* **1**, e73 (2010)
118. S.S. Lo, B.S. Teh, J.J. Lu, T.E. Shefter (eds.), *Stereotactic Body Radiation Therapy* (Springer, 2012)
119. S.M. Huber, L. Butz, B. Stegen, D. Klumpp, N. Braun, P. Ruth, F. Eckert, Ionizing radiation, ion transports and radioresistance of cancer cells. *Front. Physiol.* **14**, 212 (2013)
120. A. Giulietti, N. Bourgeois, T. Ceciotti, X. Davoine, S. Dobosz, P. D’Oliveira, M. Galimberti, J. Galy, A. Gamucci, D. Giulietti, L.A. Gizzi, D. Hamilton, E. Lefebvre, L. Labata, J.R. Marques, P. Monot, A. Popescu, F. Reau, G. Sarri, P. Tomassini, P. Martin, Intense gamma-ray source in the giant dipole resonance range driven by 10-TW laser pulses *Phys. Rev. Lett.* **101**, 105002 (2008)
121. T. Fuchs, H. Szymanowski, U. Oelfke, Y. Glinec, C. Rechatin, J. Faure, V. Malka, Treatment planning for laser-accelerated very-high energy electrons. *Phys. Med. Biol.* **54**, 3315–3328 (2009)
122. T. Elsässer, R. Cunrath, M. Krämer, M. Scholz, Impact of track structure calculations on biological treatment planning in ion radiotherapy. *New J. Phys.*, **10**, 07005.1–07005.17 (2008)
123. E. Guillaume, A. Döpp, C. Thaury, A. Lifschitz, J.P. Goddet, A. Tafzi, F. Sylla, G. Iaquanello, T. Lefrou, P. Rousseau, K. Ta Phuoc , V. Malka, Physics of fully-loaded laser-plasma accelerators. *Phys. Rev. ST Accel. Beams*, **18**, 061301 (2015)
124. E. Beyreuther, L. Karsch, L. Laschinsky, E. Lebmann, D. Namburger, M. Oppelt, C. Richter, M. Schürer, J. Woithe, J. Pawelke, Radiobiological response to ultra-short pulsed megavoltage electron beams of ultra-high pulse dose rate. *Int. J. Rad. Biol.* **91**, 643–652 (2015)
125. M. Weik, R.B. Ravelli, G. Kryger, S. Mc Sweeney, M.L. Raves, M. Harel, P. Gros, I. Silman, J. Kroon, J.L. Sussman, Specific chemical and structural damage to proteins produced by synchrotron radiation. *Proc. Nat. Acad. Sci. USA*, **97**, 623–628 (2000)
126. P.J. Coastes, S.A. Lorimore, E.G. Wright, Damaging and prospective cell signalling in the untargeted effects of ionizing radiation. *Mut. Res.* **568**, 5–20 (2004)
127. I.B. Bersuker, *The Jahn-Teller Effects and Vibronic Interactions in Modern Chemistry* (Plenum Press Ed., New York, 1984)
128. L.M. Mendes Soares, J. Valcarcel, The expanding transcriptome: the genome as the “Book of Sand”. *EMBO J.* **25**, 923–931 (2006)
129. M.P. Gaigeot, R. Vuilleumier, C. Stia, M.E. Galassi, R. Rivarola, B. Gervais, M.F. Politis, A multi-scale ab initio theoretical study of the production of free radicals in swift ion tracks in liquid water. *J. Phys. B* **40**, 1–12 (2007)
130. I. Tavernelli, M.P. Gaigeot, R. Vuilleumier, C. Stia, M.A. Hervé du Penhoat, M.F. Politis, Time dependent density functional theory molecular dynamics simulations of liquid water radiolysis. *ChemPhysChem* **9**, 2099–2103 (2008)
131. A. Ogata, T. Kondoh, J. Yang, A. Yoshida, Y. Yoshida, LWFA of atto-second and femtosecond bunches for pulse radiolysis. *Int. J. Mod. Phys.* **21**, 447–459 (2007)
132. H.P. Schenvoigt, K. Haupt, A. Debus, F. Budde, O. Jäckel, S. Pfotenhauer, H. Schwoerer, E. Rohwer, J.G. Gallacher, E. Brunetti, R.P. Shanks, S.M. Wiggins, D.A. Jaroszynski, A compact synchrotron radiation source driven by a laser-plasma wakefield accelerator. *Nat. Phys.* **4**, 130–133 (2008)
133. B. Grosswendt, Nanodosimetry, from radiation physics to radiation biology. *Rad. Protec. Dos.* **115**, 1–9 (2005)

134. V. Conte, P. Colautti, B. Grosswendt, D. Moro, L. De Nardo, Track structure of light ions: experiments and simulations. *New J. Phys.* **14**, 093010 (2012)
135. X. Guano, H. Mcleod, Strategies for enzyme/prodrug cancer therapy. *Clin. Canc. Res.* **7**, 3314–3324 (2001)
136. F. Kratz, I.A. Müller, C. Ryppa, A. Warnecke, Prodrug strategies in anticancer chemotherapy. *ChemMedChem* **3**, 20–53 (2008)
137. Y. Zheng, D.J. Hunting, P. Ayotte, L. Sanche, Role of secondary low-energy electrons in the concomitant chemoradiation therapy of cancer. *Phys. Rev. Lett.* **100**, 198101 (2008)
138. J. Biau, F. Devun, W. Jdey, E. Kotula, M. Quanz, E. Chautard, M. Sayarath, S.S. Sun, P. Verrelle, M. Dutreix, A Preclinical study combining the DNA Repair Inhibitor Dbait with radiotherapy for the treatment of melanoma. *Neoplasia* **16**, 835–844 (2014)

Chapter 3

Cyberknife, Dose Fractioning for Clinical Protocols

**Raphaëlle Mouttet-Audouard, Thomas Lacornerie
and Eric Lartigau**

Abstract Stereotactic radiotherapy (SRT) is a radiation technique initially designed for intracranial tumors which allows the delivery of hypofractionated treatment with high precision. This technique uses a multitude of small beams which creates a large dose gradient resulting in the delivery of high dose to the tumor while minimizing the dose to adjacent normal structures. As a result, stereotactic radiotherapy was more recently developed for extracranial tumors allowing a new method for delivering high doses in a single or limited number of sessions. The Cyberknife® is a noninvasive robotic image-guided system which delivers SRT with high level of accuracy due to its intrafraction motion detection and correction. Nowadays, SRT has become a standard of care for certain indications such as inoperable patients suffering from lung cancer for instance. Moreover, this technique seems promising for other indications such as liver lesions or reirradiation. Nevertheless, studies are needed to define the optimal fractionated scheme for each tumor location.

3.1 Stereotactic Body Radiotherapy (SBRT) Using the Cyberknife®

Stereotactic radiotherapy (SRT) was initiated by neurosurgeons and radiation oncologists in the 1970s and used exclusively in the brain. It was used for static targets which could be located precisely with imaging techniques such as Computed Tomography (CT) or Magnetic Resonance Imaging (MRI), and the treatment required a small number of sessions using an invasive stereotactic frame. Most of the time, a single session called a fraction was necessary, thus defining radiosurgery.

R. Mouttet-Audouard · T. Lacornerie · E. Lartigau (✉)
Academic Radiation Oncology Department, Centre Oscar Lambret & University,
Lille II 3 rue Frédéric Combemale, 59000 Lille, France
e-mail: e-lartigau@o-lambret.fr

T. Lacornerie
e-mail: t-lacornerie@o-lambret.fr

Intracranial radiosurgery is practical because the lesions are fixed with respect to the cranium, which can be immobilized rigidly in a stereotactic frame. In recent decades, important progress was made in the field of robotics and image guided radiotherapy which allowed the development of stereotactic body radiotherapy (SBRT) to treat mobile extracranial tumors and intracranial tumor without the need of a frame.

Stereotactic radiotherapy offers a method for delivering high doses of radiation in a single or limited number of fractions to a small volume encompassing the tumor while minimizing the dose to adjacent normal structures due to a large dose gradient and therefore reducing the risk of sequelae. Unlike conformational 3D radiotherapy, SBRT is a radiation technique which uses a multitude of small beams requiring extremely precise control of position and movement of the linear accelerator. Moreover, SBRT needs a real-time image-guided technique that tracks the target during treatment allowing an automatic reset based on the image acquired pretreatment. SBRT enables hypo-fractionated treatments, i.e. strong doses delivered in a small number of fractions, due to its high level of accuracy. SBRT can be delivered with different systems including the Cyberknife® (Accuray Incorporated, Sunnyvale, CA, USA).

The CyberKnife® is a dedicated noninvasive robotic image-guided system which delivers radiosurgery and hypofractionated SBRT with intrafraction motion detection and correction [1]. The robot has a 6 MV accelerator, and the orthogonal X-ray system (amorphous silicon detectors) enables real-time tracking during treatment, with the use of implanted markers or bone correlations. The treatment table has 6 degrees of freedom for automatic re-positioning and the robot's arm also has 6 degrees of freedom, providing up to 1200 treatment positions with 5–60 mm collimators. The arm can position the linear accelerator at a source-to-axis distance ranging from 100 to 65 cm with a targeting accuracy of around 0.2 mm [2]. For treatment planning, the arm passes automatically through certain points in space, called nodes, following a pre-defined pathway that is followed systematically. There are 23–133 nodes with 12 possible angles per node for the robot head, hence a total of up to 1600 potential beams. Several collimators may be used to give optimal diameters to the beams. The new CyberKnife® M6 series is built with a multileaf collimator designed to allow faster treatments giving the ability to treat larger tumors more efficiently. For inverse treatment planning, the algorithm will first calculate, for each node, the orientation of the angle of the robot so that the central axis of the beam crosses the target volume. Afterwards, the algorithm calculates the weight of each beam so that the dose delivered by all the beams takes into account the constraints of all the volumes to be treated (target and organs at risk), while limiting the number of monitor units.

A localization system made up of two X-ray tubes and two perpendicular detectors is used for initial positioning and target tracking. After checking the target position, this system transfers the information required to control algorithms for dynamic re-positioning of the treatment table and/or the robotic arm (real-time comparison of orthogonal X-ray with digitally reconstructed radiographs). The overall precision of treatment delivery (CT scan, treatment planning, image guidance, robot and linear accelerator) is 0.5 mm for skull lesions and 0.9 mm for

moving targets (SynchronyTM) module with a mean error of 0.7 ± 0.3 mm and treatment precision of 0.3 ± 0.1 mm.

The CyberKnife[®] can track the tumor during the treatment using fiducials inserted close to the tumor, or using a fiducial-free tracking system called Xsight[®] Lung Tracking System (XLTS) for lung tumors.

With the Synchrony system, internal fiducial markers are detected during treatment (X-ray) and external, electro-luminescent diodes are detected in real time (32 images per second) by three LED cameras fixed to the ceiling. A model correlating the movements of the implanted internal markers and those of the external markers is acquired. This model correlates internal and external markers throughout treatment and compares estimated movements with the real positions of markers. Any deviation in positioning exceeding a set value triggers system discontinuation. Treatment duration depends on the dose delivered and the real-time controls performed (30–120 min).

3.2 The CyberKnife[®] and Brain Lesions

Even though the most recent and significant developments with the CyberKnife[®] were made in the field of extracranial stereotactic radiotherapy, this technique can be used for intracranial lesions with single dose radiosurgery. For example, the CyberKnife[®] can be used to treat meningioma, acoustic neuromas, pituitary adenoma, metastases, arteriovenous malformations, refractory pain such as trigeminal neuralgia and brain metastases without the need of an invasive stereotactic frame [3, 4].

Concerning brain metastases, Shaw et al. defined, in the RTOG 90-05 study, the maximum tolerable doses to be delivered to the periphery of the lesion for a minimum complication rate: 24 Gy for lesions with diameter less than or equal to 20 mm, 18 Gy for lesions with diameter between 21 and 30 mm and 15 Gy for those with diameter between 31 and 40 mm [5]. The authors showed that unacceptable nervous toxicity was more likely to appear in patients with larger tumors, whereas local tumor control was most dependent on the type of recurrent tumor. The actuarial incidence of radionecrosis in this study was 5, 8, 9 and 11 % at 6, 12, 18 and 24 months following radiosurgery, respectively. Using those maximum dose recommendations, Vogelbaum et al. evaluated the local control in 202 patients treated with single dose radiosurgery [6]. The 1-year local control rate was 85 % (95 % CI 78–92 %) in tumors treated with 24 Gy, 49 % (95 % CI 30–68 %) in tumors treated with 18 Gy and 45 % (95 % CI 23–67 %) in tumors treated with 15 Gy. The authors concluded that tumors larger than 2 cm were less effectively controlled than smaller lesions with radiosurgery.

Therefore, large tumors are not considered suitable for stereotactic radiosurgery because size correlates with decreased response rate to radiation and increased risk

of neurotoxicity [7, 8]. Furthermore, when the target is located near or within critical brain structures such as the brainstem, optic pathway, or motor cortex, the toxicity risk with single dose radiosurgery is higher and the use of fractionated stereotactic radiotherapy becomes necessary to avoid serious toxicity [9].

Many studies have used fractionated stereotactic radiotherapy for brain metastases but total doses and fractionation schemes differ from one study to another [8, 10–12]. For instance in 2011, Kim et al. reported on their experience in 98 patients with brain metastases, 58 treated with a single dose of 20 Gy in radiosurgery and 40 patients treated with fractionated stereotactic radiotherapy, 36 Gy in 6 fractions due to large lesions or lesions located near critical structures [13]. The 1-year local control rate was similar in the 2 groups (71 vs. 69 %, $p = 0.31$) and the toxicity rate was higher in patients treated with radiosurgery than in those treated with fractionated stereotactic radiotherapy (17 vs. 5 %, $p = 0.05$). Other studies have been published with different fractionation schemes (35 Gy in 4 fractions, 30 Gy in 5 fractions, 35 Gy in 7 fractions, 40 Gy in 10 fractions) and further investigation is warranted to determine the optimal dose per fraction. Moreover, stereotactic radiotherapy can also be used to treat resection cavity after initial surgery using either one fraction or a fractionated scheme according to the initial tumor size and localization [14, 15].

3.3 The CyberKnife® and Spine Lesions

In the case of spinal tumors, surgery is usually reserved to patient with spinal instability or neurologic deficits whereas radiation is used to obtain a palliation of pain and to prevent pathologic fractures. Conventional radiotherapy has proven to be an efficient technique to reduce the pain due to bone metastases. However, this technique only enables to deliver a dose below the optimal therapeutic dose, due to the spinal cord low tolerance to radiation [16]. Therefore, in order to increase the dose to the treatment volume while minimizing the spinal cord injury risk, stereotactic radiotherapy has been evaluated in this case.

In 2007, Gerszten et al. reported on their clinical experience of stereotactic radiotherapy using the Cyberknife® on 500 cases of spinal metastases, 86 % of which were treated with fiducial tracking [17]. 344 lesions had previously been treated with external radiotherapy and the authors used a mean dose of 20 Gy (12.5–25 Gy) of stereotactic radiosurgery. With a median follow up of 21 months, they showed a long-term pain improvement in 86 % and a long-term tumor control in 90 % of lesions treated with radiosurgery as a primary treatment and in 88 % of lesions treated for progression. Moreover, a clinical improvement was found in 84 % of cases with a progressive neurologic deficit prior to the radiosurgery.

Wowra et al. reported on their experience of 134 cases treated with the Cyberknife® with a fiducial-free tracking system using the Xsight skeletal structure

tracking system [18]. A median dose of 19.4 Gy (15–24 Gy) of stereotactic surgery was delivered to the 70 % isodose. With a median follow-up of 15 months, the local tumor control rate was 98 and 2 % of patients had late complication after radiosurgery (segmental neuropathy and vertebral instability). The authors concluded that stereotactic surgery using the Cyberknife® is a safe, non invasive, single session treatment that can improve the quality of life of patients with advanced diseases.

Studies have also been published with different fractionated schemes. In 2007, Gibbs et al. reported on their results of 102 lesions treated with the Cyberknife® in 1 to 5 fractions [19]. 74 % of the lesions had had prior radiation treatment [19]. A dose of 16–25 Gy was delivered in 1–5 fractions (with a dose per fraction ranging from 7 to 20 Gy), 10 Gy being the greatest permissible spinal cord dose delivered in a single fraction. With a mean follow-up of 9 months, 84 % of the symptomatic patients reported improvement or resolution of symptoms and three patients developed treatment-related severe myelopathy.

Various studies have reported a range of prescribed doses and currently the main fractionation schemes include single fraction ranging from 8 to 24 Gy, or hypofractionated regimens consisting mainly of 20 Gy in five fractions, 30 Gy in five fractions, 24 Gy in three fractions, and 27 Gy in three fractions [20–22]. However, none of the studies describing mixed populations of unirradiated and previously irradiated tumors specified different prescriptions for the two populations [23]. Moreover, this technique can also be used for lesions close to the spine (Fig. 3.1).

As of today, there is no evidence to support one fractionated scheme over another and studies are needed to define optimal radiation doses and fractionations.

In a retrospective study, Heron et al. compared the effectiveness of radiosurgery and fractionated schemes of SBRT using the CyberKnife® in 348 spine lesions [24]. The authors concluded that while both regimens were effective, radiosurgery provided greater early pain control and the fractionated scheme achieved greater tumor control and less need for retreatment in long-term survivors.

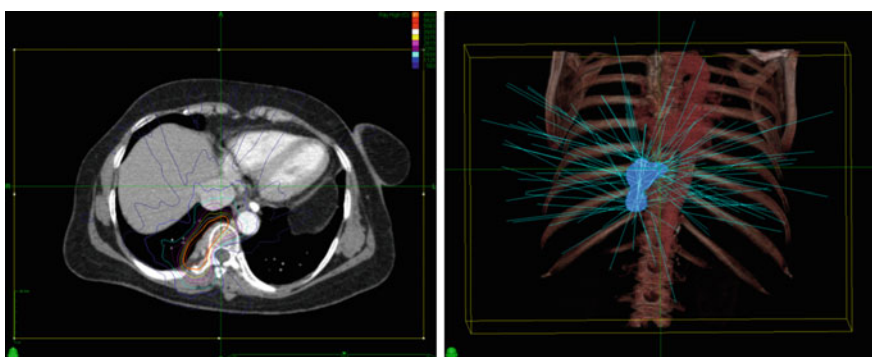


Fig. 3.1 Example of a paravertebral lesion treated with the Cyberknife®

3.4 The CyberKnife® and Lung Lesions

In the case of lung cancer, the use of SBRT is rapidly increasing among patients with early-stage non small cell lung cancer (NSCLC) who are not candidate for surgery on the basis of age or medical comorbidities. Indeed, this technique offers a new treatment option with minimal risk of toxicity to these often fragile patients and the French National Authority for Health published a report in 2006 stating that the benefits expected from extracranial stereotactic radiation treatment for primary bronchopulmonary tumors and slow-growing pulmonary metastases with a controlled primary tumor were considered sufficient [25].

Since then, many studies have been published initially with tumor tracking done with fiducials [26]. For instance in 2006, Nuyttens et al. reported on their initial experience of 20 patients treated for 22 lung tumors [27]. With a median follow-up of 4 months, the authors reported a local control rate of 100 %. In 2007, Collins et al. reported on their results of 24 patients and, with a median follow-up of 12 months, found a crude survival rate of 83 % [28]. However, seven of patients presented with pneumothorax. Indeed, fiducial implantation is a procedure that can cause pneumothorax in up to 13–23 % of the patients, according to different studies [29].

Therefore, a fiducial-free tracking system, the Xsight® Lung Tracking System (XLTS), was designed to correlate intensity similarities in the digitally reconstructed radiographs (DRRs) to the position of the tumor and allow a non-invasive treatment method for these patients. Moreover, in order to use the latter, the target must be larger than 15 mm and visible in the orthogonal X-ray images. Bibault et al. reported on their experience of 51 patients treated with the XLTS and the median dose delivered was 60 Gy (45–60 Gy) in 3 fractions [30]. With a median follow-up of 15 months, the 1-year local control rate was 92 % (95 % CI 84–99 %) and the 2-year local control rate at 86 % (95 % CI 75–97 %). No pneumothorax was observed since the tumor tracking was fiducial-free and no severe toxicity was described. Those results, which are comparable to other studies, indicate that this technique can be safely used.

Considering the dose delivered with SBRT in lung lesions, the majority of studies were done using multiple fractions. Both Nuyttens and Collins used a hypofractionated scheme to deliver a median dose of 45 Gy (30–60 Gy) in 3 fractions [27, 28]. Brown et al. delivered a dose ranging from 15 to 67.5 Gy in 1 to 5 fractions to 59 patients with lung lesions [31]. With a median follow-up of 33 months, the overall survival rate was 86 %. In 2008, Castelli et al. published a study about 34 patients, 30 with lung cancers and 4 with lung metastases due to colorectal cancer, who received a median dose of 60 Gy (30–75) in 2 to 5 fractions [32]. At 3 months, the local control rate was 96 %.

Some studies have also been published using a single fraction of SBRT with the Cyberknife® for lung lesions. In 2003, Whyte et al. reported on their preliminary phase I experience of single fraction in 23 patients, 15 of whom had primary NSCLC [29]. Treatment dose consisted of 15 Gy in 1 fraction. With a median

follow-up of 7 months, there were no grade 3 or higher toxicities and radiographic response was scored as complete in 2 patients, partial in 15 and stable in 4. In 2006, the same others reported on a dose escalation using a single fraction on 32 patients (21 NSCLC and 11 metastatic tumors) [33]. Nine to 20 patients were treated per dose cohort starting at 15 Gy per fraction followed by dose escalation of 5–10 Gy to a maximal dose of 30 Gy per fraction. The authors found that at 25 Gy, pulmonary toxicity was noted in patients with prior pulmonary irradiation and in those with treatment volumes greater than 50 cc; therefore, dose escalation to 30 Gy was applied only to unirradiated patients and treatment volume less than 50 cc. Treatment-related complications were noted for doses greater than 25 Gy and included four cases of grade 2–3 pneumonitis, 1 pleural effusion, and 3 possible treatment-related deaths. The one-year freedom from local progression was 91 % for doses greater than 20 Gy and 54 % for doses less than 20 Gy in NSCLC ($p = 0.03$). The authors concluded that a single dose of 25 Gy may be too toxic for patients with prior thoracic irradiation and that higher dose was associated with improved local control in selected patients with lung tumors.

Regardless of the dose scheme, single fraction or hypofractionated regimens, these excellent results in inoperable patients raise the question of the use of SBRT in operable patients as an alternative to surgical treatment. However, two prospective phase III studies (ROSEL and STARS) randomizing surgery with SBRT in operable stage IA NSCLC were terminated due to lack of enrollment [34].

3.5 The CyberKnife® and Liver Lesions

Concerning hepatocellular carcinoma (HCC) and liver metastases, SBRT studies have shown encouraging local control rates with low toxicity for patients who are not candidate for curative treatments such as surgery or liver transplantation. Indeed, the Synchrony™ system allows respiratory motion tracking during irradiation. It requires the positioning of fiducial inside or near the treatment target. Motion tracking is performed by means of correlation with external optical markers that can be tracked in real time.

In 2008, Choi et al. reported on their experience in 32 HCC lesions treated with the Cyberknife® delivering a median dose of 36 Gy (30–39 Gy), in 3 fractions over 3 consecutive days [35]. With a median follow-up of 10.5 months, the local control was 71.9 % and no patient experienced grade 4 toxicity.

Ambrosino et al. reported in 2009 on their 27 patients with unresectable liver metastases treated with 25–60 Gy in 3 fractions [36]. With a median follow-up of 13 months (6–16 months), the overall control rate was 85.2 % and no major toxicity was described.

In 2012, Dewas et al. described their experience of 153 stereotactic liver treatments (99 liver metastases, 48 HCC and 6 cholangiocarcinoma) treated with 27–45 Gy in 3 to 4 fractions over 12 days [37]. With a median follow-up of 15 months, local control rates at one and 2 years were 89 and 81 % for HCC. Concerning

cholangiocarcinoma, overall survival and local control rate were 100 % at one year. Reported toxicity, which consisted mainly of nausea, abdominal pain and asthenia, was correlated with the duration of treatment ($p < 0.04$). 12 patients experienced grade 3 or 4 gastro-intestinal toxicity, half of them having lesions which were close to digestive structures. In this study, prognostic factors associated with better local control were lesion size < 50 mm ($p = 0.019$), PTV volume < 200 cc ($p = 0.014$) and a delivered dose ≥ 45 Gy.

In 2011, a dose-response relationship for liver metastases was evaluated by Vautravers-Dewas et al. [38]. In this study, 42 patients with 62 liver metastases were treated with two dose levels of 40 Gy in four fractions and 45 Gy in 3 fractions. With a median follow-up of 14.3 months, the one-year and 2-year local control rates were 90 and 86 %, respectively. In this study, the dose level did not significantly contribute to the outcome, toxicity or survival.

In 2014, Yuan et al. reported on 57 patients with 80 liver metastases treated with a median dose of 42 Gy (39–54 Gy) in 3 fractions [39]. With a median follow-up of 20.5 months, the one-year and 2-year local control rates were 94.4 and 89.7 %, respectively and no grade 3 or higher side effect was observed.

Concerning single fraction SBRT, Goodman et al. performed in 2010, a dose-escalation study in 19 patients (19 liver metastases, 5 intrahepatic cholangiocarcinomas and 2 HCC) [40]. The prescribed dose was escalated from 18 to 30 Gy at

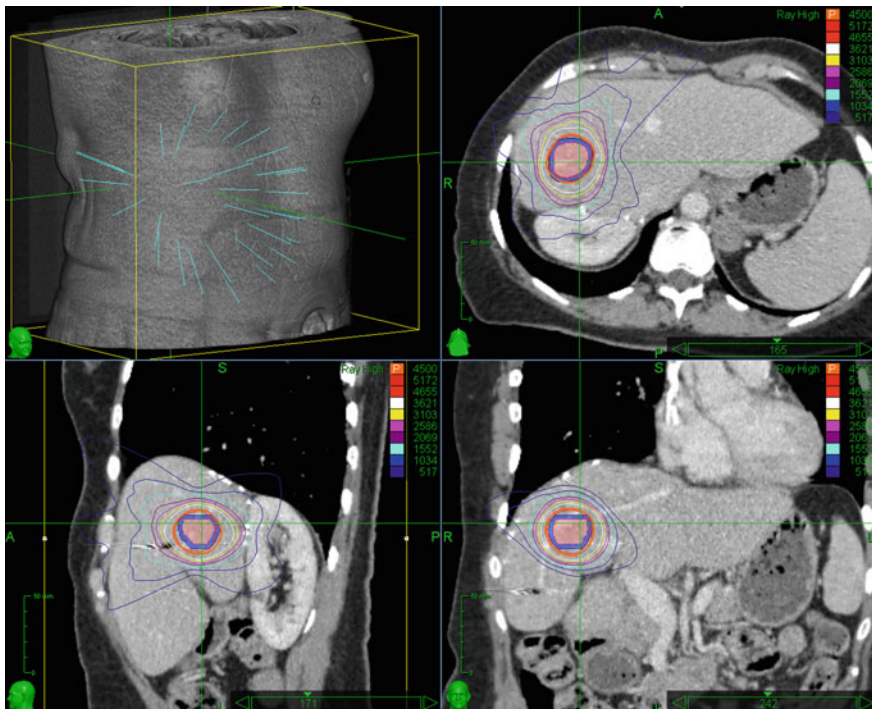


Fig. 3.2 Example of liver lesion treated with the Cyberknife®

4 Gy increments with a planned maximum dose of 30 Gy. With a median follow-up of 17.3 months, the one-year local control rate was 77 % and no dose-limiting toxicity was described. The authors showed a trend toward a dose-effect difference in local control with 25 Gy being the cut-off, but due to the small number of cases, it did not reach statistical significance (Fig. 3.2; Tables 3.1, 3.2).

In the literature, the treatment dose and fractionation used to treat liver lesions vary from one study to the other. Nonetheless, SBRT offers a safe and effective treatment option for patients not suitable for surgery. Randomized studies are warranted to compare the efficacy of SBRT with other possible treatments.

Table 3.1 Selected studies results of SBRT with the Cyberknife® for early stage lung cancers

Author	Patients	Doses	Median follow up	Control rates	Toxicity grade ≥ 3
Nuyttens [27]	20	30–60 Gy/3fx	4 months	4 months LC* 100 %	5 %
Collins [28]	24	45–60 Gy/3fx	12 months	12 months LC 92 % OS** 83 %	8 %
Brown [31]	59	15–67.5 Gy/15fx	33 months	33 months OS 86 %	0
Castelli [32]	30	30–75 Gy/2-5fx	74 days	3 months LC 95 %	0
Bibault [30]	51	36–60 Gy/3fx	15 months	2 years LC 86 % OS 79.4 %	0

*LC Local Control

**OS Overall Survival

Table 3.2 Selected studies results of SBRT with the Cyberknife® for liver lesions

Author	Patients	Doses	Median follow up (months)	Control rates	Toxicity grade ≥ 3
Choi [35]	31 (32 HCC*)	30–39 Gy/3fx	10.5	10.5 months LC 71.9 %	3.2 %
Ambrosino [36]	27 (LM**)	25–60 Gy/3fx	13	13 months LC 85.2 %	0
Goodman [40]	26 (19 LM 2 HCC 5 CC***)	18–30 Gy/1fx	17	12 months LC 71 %	0
Dewas [37]	120 (99 LM 48 HCC 6 CC)	27–45 Gy/3–4fx	15	12 months LC 80.4 %	7.8 %
Yuan [39]	57 80 LM	39–54 Gy/3fx	20.5	12 months LC 94.4 %	0

*HCC Hepato Cellular Carcinoma

**LM Liver Metastases

***CC Cholangiocarcinoma

3.6 The CyberKnife® and Prostate Lesions

Concerning prostate lesions, most SBRT studies report data from patients with low or intermediate risk prostate cancers. Prostate cancer is characterized by a lower α/β ratio than that of the normal tissues around the tumor. Therefore, hypofractionation in that case is very appropriate to increase the biological effect while protecting the normal organ at risk. Several fractionated schemes have been reported in the literature, such as 34 Gy in four fractions of 8.5 or 39 Gy in four fractions of 9.5 Gy, but most studies use a total dose of 35–36.25 Gy with a five fractions protocol of 7–7.25 Gy [41–43].

In 2009, King et al. reported their experience of 41 low risk patients treated with 36.25 Gy in 5 fractions of 7.25 Gy [44]. With a median follow-up of 33 months, no patient presented a biological failure and 2 patients experienced grade 3 late urinary toxicity. The authors also showed that a reduced rate of severe rectal toxicities was observed with every-other-day versus 5 consecutive days treatment regimen (0 vs. 38 %, $p = 0.0035$). The same team published in 2012 their long-term outcomes in 67 patients with low risk prostate cancer [45]. With a median follow-up of 2.7 years, no grade 4 toxicity was reported and the 4-year PSA relapse free survival was 94 %.

In 2011, Katz et al. published their results of 82 patients with low and intermediate risk prostate cancers treated with 35 or 36.25 Gy in 5 fractions [46]. With a median follow-up of 51 months, the biological progression free survival was 97.6 % and no grade 3 or higher toxicity was observed.

Lartigau et al. coordinated a multi-center Phase II study evaluating the feasibility of delivering a boost of 18 Gy in 3 fractions after the delivery of 46 Gy with 3D conformal radiotherapy or IMRT for intermediate risk tumors. 72 patients were included and no acute toxicity was described (personal communication).

Those preliminary results show that SBRT with the Cyberknife® seems to be a safe and effective treatment option for low and intermediate risk prostate cancers. However, longer follow-up and control randomized phase III trials are necessary to compare this technique to standard treatment options. In that effect, the PACE phase III trial (Prostate Advances in Comparative Evidence) will randomize laparoscopic prostatectomy vs stereotactic body radiotherapy (SBRT) and conventionally fractionated radiotherapy vs SBRT for early stage prostate cancer.

3.7 The CyberKnife® and Reirradiation

One of the major achievements with the development of SBRT is the possibility of reirradiation. Indeed, for recurrent or second primary head and neck cancers, surgery is the standard treatment but can only be performed in 25 % of the patients. In this case, SBRT offers a new treatment option which is better tolerated by patients with poor overall prognosis in view of the limited irradiation of healthy tissues and the short duration of the treatment.

In 2006, Voynov et al. reported on a series of 22 patients treated with a dose of 20 Gy in four fractions or 30 Gy in six fractions [47]. The median survival was 12 months, 2-year locoregional control and overall survival rates were 26 and 22 %, respectively. Grade 3 acute toxicities were described in 4.5 % of patients but no late toxicity was reported. Then in a phase I trial, the same team evaluated the safety of stereotactic radiotherapy with dose escalation in 25 patients using five dose levels up to a dose of 44 Gy in five fractions delivered over two weeks [48]. The overall response rate was 28 % and no grade 3 or higher toxicity was noted. The median overall survival was six months and the median progression-free survival four months.

In 2009, Roh et al. described their experience of 36 patients treated with 4 different dose schemes: three fractions of 10 Gy, three fractions of 13 Gy, five fractions of 5 Gy or five fractions of 8 Gy [49]. The median survival was 16.2 months, and the two-year survival rate was 30.9 %. Complete response, partial and progress response rates were 42.9, 37.1 and 11.4 %, respectively. Grade 3 acute complication rate was 30 % and grade 3 late complication rate was 8 %.

In 2010, Unger et al. reported on their experience of 65 patients, 36 of whom received concomitant chemotherapy, treated with a dose of 30 Gy in two to five fractions [50]. The median overall survival was 12 months and the two-year locoregional control and overall survival rates were 30 and 41 %, respectively. The complete response, partial and progression rates were 54, 27 and 20 %. Severe complications were observed in 11 % of patients with one treatment-related death described.

In 2011, Kodani et al. reported the results on 34 patients treated with a median dose of 30 Gy (19.5–42 Gy) in three to eight fractions [51]. The complete response and partial response rates were 32 and 38 %. The median overall survival was 28 months and the two-year overall survival rate was 58.3 %. Six patients had severe late complications including two treatment related deaths due to massive hemorrhages.

In 2012, Comet et al. published a series of 40 patients treated with stereotactic re-irradiation using the CyberKnife® with a dose of 36 Gy delivered in 6 fractions over 11–12 days [52]. Constraints to organs at risk were dependent on the dose previously received. For patients with squamous cell carcinoma, treatment with cetuximab with a 400 mg/m^2 loading dose was delivered the week before irradiation and then a dose of 250 mg/m^2 was administered during the two weeks of treatment and during the two following weeks. Fifty percent of the tumors were squamous cell carcinoma and the recurrence sites were oropharynx (15 %), neck nodes (12.5 %), paranasal sinuses (15 %), hypopharynx (10 %) and oral cavity (7.5 %). With a median follow-up of 25.6 months, four patients experienced grade 3 toxicities and 34 patients were evaluable for tumor response. Median overall survival was 13.6 months and response rate was 79.4 % (15 complete and 12 partial responses). The one and two-year overall survival rates were 58 and 24 %. This excellent local control in this poor prognosis population was confirmed in a prospective multicentric study [53].

Concerning reirradiation with the CyberKnife[®], Dewas et al. published a series of 16 patients reirradiated for non-operable pelvic lesions with a dose of 36 Gy in 6 fractions delivered over 3 weeks [54]. With a median follow-up of 10.6 months, the one-year local control rate was 51.4 % and no acute grade 3 toxicity was observed.

SBRT strategies with the CyberKnife[®] offer new short and well-tolerated treatment possibilities for patients with poor overall prognosis. Further studies are needed to evaluate the late toxicity for this treatment.

3.8 Conclusion

SBRT with the CyberKnife[®] represent a recent well-tolerated radiation technique with good locoregional control rates. New developments in lesion tracking have allowed the delivery of less invasive treatments while preserving precision. Although some indications, such as lung lesions, have become standard of care, long term efficacy and toxicity studies are still needed to validate others. Moreover, studies are necessary to evaluate the different fractionated schemes used and to define guidelines for each tumor location.

References

1. S.D. Chang, W. Main, D.P. Martin, I.C. Gibbs, M.P. Heilbrun, An analysis of the accuracy of the CyberKnife: a robotic frameless stereotactic radiosurgical system. *Neurosurgery* **52**, 140–146 (2003). discussion 146–147
2. E. Coste-Maniere, R. Simmons (2000) Architecture, the backbone of robotic systems. In: Proceedings of ICRA 00 IEEE International Conference Robotics and Automation 2000, vol 1, pp 67–72. doi:[10.1109/ROBOT.2000.844041](https://doi.org/10.1109/ROBOT.2000.844041)
3. T. Gevaert, M. Levivier, T. Lacornerie, D. Verellen, B. Engels, N. Reynaert et al., Dosimetric comparison of different treatment modalities for stereotactic radiosurgery of arteriovenous malformations and acoustic neuromas. *Radiother. Oncol. J. Eur. Soc. Ther. Radiol. Oncol.* **106**, 192–197 (2013). doi:[10.1016/j.radonc.2012.07.002](https://doi.org/10.1016/j.radonc.2012.07.002)
4. D. Greto, L. Livi, P. Bonomo, L. Masi, B. Detti, I. Meattini et al., Cyberknife stereotactic radiosurgery for the re-irradiation of brain lesions: a single-centre experience. *Radiol. Med. (Torino)* **119**, 721–726 (2014). doi:[10.1007/s11547-014-0383-2](https://doi.org/10.1007/s11547-014-0383-2)
5. E. Shaw, C. Scott, L. Souhami, R. Dinapoli, R. Kline, J. Loeffler et al., Single dose radiosurgical treatment of recurrent previously irradiated primary brain tumors and brain metastases: final report of RTOG protocol 90-05. *Int. J. Radiat. Oncol. Biol. Phys.* **47**, 291–298 (2000)
6. M.A. Vogelbaum, L. Angelov, S.-Y. Lee, L. Li, G.H. Barnett, J.H. Suh, Local control of brain metastases by stereotactic radiosurgery in relation to dose to the tumor margin. *J. Neurosurg.* **104**, 907–912 (2006). doi:[10.3171/jns.2006.104.6.907](https://doi.org/10.3171/jns.2006.104.6.907)
7. M. Scorselli, A. Facoetti, P. Navarria, M. Bignardi, M. De Santis, S.A. Ninone et al., Hypofractionated stereotactic radiotherapy and radiosurgery for the treatment of patients with radioresistant brain metastases. *Anticancer Res.* **29**, 4259–4263 (2009)

8. M.A. Manning, R.M. Cardinale, S.H. Benedict, B.D. Kavanagh, R.D. Zwicker, C. Amir et al., Hypofractionated stereotactic radiotherapy as an alternative to radiosurgery for the treatment of patients with brain metastases. *Int. J. Radiat. Oncol. Biol. Phys.* **47**, 603–608 (2000)
9. E.J. Hall, D.J. Brenner, The radiobiology of radiosurgery: rationale for different treatment regimes for AVMs and malignancies. *Int. J. Radiat. Oncol. Biol. Phys.* **25**, 381–385 (1993)
10. H. Aoyama, H. Shirato, R. Onimaru, K. Kagei, J. Ikeda, N. Ishii et al., Hypofractionated stereotactic radiotherapy alone without whole-brain irradiation for patients with solitary and oligo brain metastasis using noninvasive fixation of the skull. *Int. J. Radiat. Oncol. Biol. Phys.* **56**, 793–800 (2003)
11. A. Ernst-Stecken, O. Ganslandt, U. Lambrecht, R. Sauer, G. Grabenbauer, Phase II trial of hypofractionated stereotactic radiotherapy for brain metastases: results and toxicity. *Radiother. Oncol. J. Eur. Soc. Ther. Radiol. Oncol.* **81**, 18–24 (2006). doi:[10.1016/j.radonc.2006.08.024](https://doi.org/10.1016/j.radonc.2006.08.024)
12. A. Fahrig, O. Ganslandt, U. Lambrecht, G. Grabenbauer, G. Kleinert, R. Sauer et al., Hypofractionated stereotactic radiotherapy for brain metastases—results from three different dose concepts. *Strahlenther. Onkol. Organ Dtsch. Röntgenges. Al.* **183**, 625–630 (2007). doi:[10.1007/s00066-007-1714-1](https://doi.org/10.1007/s00066-007-1714-1)
13. Y.-J. Kim, K.H. Cho, J.-Y. Kim, Y.K. Lim, H.S. Min, S.H. Lee et al., Single-dose versus fractionated stereotactic radiotherapy for brain metastases. *Int. J. Radiat. Oncol. Biol. Phys.* **81**, 483–489 (2011). doi:[10.1016/j.ijrobp.2010.05.033](https://doi.org/10.1016/j.ijrobp.2010.05.033)
14. A.C. Hartford, A.J. Paravati, W.J. Spire, Z. Li, L.A. Jarvis, C.E. Fadul et al., Postoperative stereotactic radiosurgery without whole-brain radiation therapy for brain metastases: potential role of preoperative tumor size. *Int. J. Radiat. Oncol. Biol. Phys.* **85**, 650–655 (2013). doi:[10.1016/j.ijrobp.2012.05.027](https://doi.org/10.1016/j.ijrobp.2012.05.027)
15. G. Minniti, V. Esposito, E. Clarke, C. Scaringi, G. Lanzetta, M. Salvati et al., Multidose stereotactic radiosurgery (9 Gy × 3) of the postoperative resection cavity for treatment of large brain metastases. *Int. J. Radiat. Oncol. Biol. Phys.* **86**, 623–629 (2013). doi:[10.1016/j.ijrobp.2013.03.037](https://doi.org/10.1016/j.ijrobp.2013.03.037)
16. J.S.-Y. Wu, R. Wong, M. Johnston, A. Bezjak, T. Whelan, Cancer care ontario practice guidelines initiative supportive care group, meta-analysis of dose-fractionation radiotherapy trials for the palliation of painful bone metastases. *Int. J. Radiat. Oncol. Biol. Phys.* **55**, 594–605 (2003)
17. P.C. Gerszten, S.A. Burton, C. Ozhasoglu, W.C. Welch, Radiosurgery for spinal metastases: clinical experience in 500 cases from a single institution. *Spine* **32**, 193–199 (2007). doi:[10.1097/BRS.0b013e31818c76595.a2](https://doi.org/10.1097/BRS.0b013e31818c76595.a2)
18. B. Wowra, S. Zausinger, C. Drexler, M. Kufeld, A. Muacevic, M. Staehler et al., CyberKnife radiosurgery for malignant spinal tumors: characterization of well-suited patients. *Spine* **33**, 2929–2934 (2008). doi:[10.1097/BRS.0b013e31818c680a](https://doi.org/10.1097/BRS.0b013e31818c680a)
19. I.C. Gibbs, P. Kamnerdsupaphon, M.-R. Ryu, R. Dodd, M. Kiernan, S.D. Chang et al., Image-guided robotic radiosurgery for spinal metastases. *Radiother. Oncol. J. Eur. Soc. Ther. Radiol. Oncol.* **82**, 185–190 (2007). doi:[10.1016/j.radonc.2006.11.023](https://doi.org/10.1016/j.radonc.2006.11.023)
20. J.-T. Tsai, J.-W. Lin, W.-T. Chiu, W.-C. Chu, Assessment of image-guided CyberKnife radiosurgery for metastatic spine tumors. *J. Neurooncol.* **94**, 119–127 (2009). doi:[10.1007/s11060-009-9814-7](https://doi.org/10.1007/s11060-009-9814-7)
21. A.M. Levine, C. Coleman, S. Horasek, Stereotactic radiosurgery for the treatment of primary sarcomas and sarcoma metastases of the spine. *Neurosurgery* **64**, A54–A59 (2009). doi:[10.1227/01.NEU.0000339131.28485.4A](https://doi.org/10.1227/01.NEU.0000339131.28485.4A)
22. A. Sahgal, C. Ames, D. Chou, L. Ma, K. Huang, W. Xu et al., Stereotactic body radiotherapy is effective salvage therapy for patients with prior radiation of spinal metastases. *Int. J. Radiat. Oncol. Biol. Phys.* **74**, 723–731 (2009). doi:[10.1016/j.ijrobp.2008.09.020](https://doi.org/10.1016/j.ijrobp.2008.09.020)
23. A. Sahgal, D.A. Larson, E.L. Chang, Stereotactic body radiosurgery for spinal metastases: a critical review. *Int. J. Radiat. Oncol. Biol. Phys.* **71**, 652–665 (2008). doi:[10.1016/j.ijrobp.2008.02.060](https://doi.org/10.1016/j.ijrobp.2008.02.060)
24. D.E. Heron, M.S. Rajagopalan, B. Stone, S. Burton, P.C. Gerszten, X. Dong et al., Single-session and multisession CyberKnife radiosurgery for spine metastases—University of

- Pittsburgh and Georgetown University experience. *J. Neurosurg. Spine.* **17**, 11–18 (2012). doi:[10.3171/2012.4.SPINE11902](https://doi.org/10.3171/2012.4.SPINE11902)
25. Haute Autorité de Santé - Radiothérapie extracrânienne en conditions stéréotaxiques, (n.d.). http://www.has-sante.fr/portail/jcms/r_1498752/fr/radiotherapie-extracranienne-en-conditions-stereotaxiques Accessed 8 Sept 2014)
26. A. Muacevic, C. Drexler, B. Wowra, A. Schweikard, A. Schlaefer, R.T. Hoffmann et al., Technical description, phantom accuracy, and clinical feasibility for single-session lung radiosurgery using robotic image-guided real-time respiratory tumor tracking. *Technol. Cancer Res. Treat.* **6**, 321–328 (2007)
27. J.J. Nuyttens, J.-B. Prévost, J. Praag, M. Hoogeman, R.J. Van Klaveren, P.C. Levendag et al., Lung tumor tracking during stereotactic radiotherapy treatment with the CyberKnife: Marker placement and early results. *Acta Oncol. Stockh. Swed.* **45**, 961–965 (2006). doi:[10.1080/02841860600902205](https://doi.org/10.1080/02841860600902205)
28. B.T. Collins, K. Erickson, C.A. Reichner, S.P. Collins, G.J. Gagnon, S. Dieterich et al., Radical stereotactic radiosurgery with real-time tumor motion tracking in the treatment of small peripheral lung tumors. *Radiat. Oncol. Lond. Engl.* **2**, 39 (2007). doi:[10.1186/1748-717X-2-39](https://doi.org/10.1186/1748-717X-2-39)
29. R.I. Whyte, R. Crownover, M.J. Murphy, D.P. Martin, T.W. Rice, M.M. DeCamp et al., Stereotactic radiosurgery for lung tumors: preliminary report of a phase I trial. *Ann. Thorac. Surg.* **75**, 1097–1101 (2003)
30. J.-E. Bibault, B. Prevost, E. Dansin, X. Mirabel, T. Lacornerie, E. Lartigau, Image-guided robotic stereotactic radiation therapy with fiducial-free tumor tracking for lung cancer. *Radiat. Oncol. Lond. Engl.* **7**, 102 (2012). doi:[10.1186/1748-717X-7-102](https://doi.org/10.1186/1748-717X-7-102)
31. W.T. Brown, X. Wu, F. Fayad, J.F. Fowler, B.E. Amendola, S. García et al., CyberKnife radiosurgery for stage I lung cancer: results at 36 months. *Clin. Lung Cancer.* **8**, 488–492 (2007). doi:[10.3816/CLC.2007.n.033](https://doi.org/10.3816/CLC.2007.n.033)
32. J. Castelli, J. Thariat, K. Benezery, B. Padovani, D. Ducreux, N. Venissac et al., Feasibility and efficacy of cyberknife radiotherapy for lung cancer: early results]. *Cancer Radiothérapie J. Société Fr. Radiothérapie Oncol.* **12**, 793–799 (2008). doi:[10.1016/j.canrad.2008.06.002](https://doi.org/10.1016/j.canrad.2008.06.002)
33. Q.-T. Le, B.W. Loo, A. Ho, C. Cotrutz, A.C. Koong, H. Wakelee et al., Results of a phase I dose-escalation study using single-fraction stereotactic radiotherapy for lung tumors. *J. Thorac. Oncol. Off. Publ. Int. Assoc. Study Lung Cancer* **1**, 802–809 (2006)
34. C.W. Hurkmans, J.P. Cuijpers, F.J. Lagerwaard, J. Widder, U.A. van der Heide, D. Schuring et al., Recommendations for implementing stereotactic radiotherapy in peripheral stage IA non-small cell lung cancer: report from the Quality Assurance Working Party of the randomised phase III ROSEL study. *Radiat. Oncol. Lond. Engl.* **4**, 1 (2009). doi:[10.1186/1748-717X-4-1](https://doi.org/10.1186/1748-717X-4-1)
35. B.O. Choi, I.B. Choi, H.S. Jang, Y.N. Kang, J.S. Jang, S.H. Bae et al., Stereotactic body radiation therapy with or without transarterial chemoembolization for patients with primary hepatocellular carcinoma: preliminary analysis. *BMC Cancer* **8**, 351 (2008). doi:[10.1186/1471-2407-8-351](https://doi.org/10.1186/1471-2407-8-351)
36. G. Ambrosino, F. Polistina, G. Costantin, P. Francescon, R. Guglielmi, P. Zanco et al., Image-guided robotic stereotactic radiosurgery for unresectable liver metastases: preliminary results. *Anticancer Res.* **29**, 3381–3384 (2009)
37. S. Dewas, J.-E. Bibault, X. Mirabel, I. Fumagalli, A. Kramar, H. Jarraya et al., Prognostic factors affecting local control of hepatic tumors treated by Stereotactic Body Radiation Therapy. *Radiat. Oncol. Lond. Engl.* **7**, 166 (2012). doi:[10.1186/1748-717X-7-166](https://doi.org/10.1186/1748-717X-7-166)
38. C. Vautravers-Dewas, S. Dewas, F. Bonodeau, A. Adenis, T. Lacornerie, N. Penel et al., Image-guided robotic stereotactic body radiation therapy for liver metastases: is there a dose response relationship? *Int. J. Radiat. Oncol. Biol. Phys.* **81**, e39–e47 (2011). doi:[10.1016/j.ijrobp.2010.12.047](https://doi.org/10.1016/j.ijrobp.2010.12.047)
39. Z.-Y. Yuan, M.-B. Meng, C.-L. Liu, H.-H. Wang, C. Jiang, Y.-C. Song et al., Stereotactic body radiation therapy using the CyberKnife® system for patients with liver metastases. *OncoTargets Ther.* **7**, 915–923 (2014). doi:[10.2147/OTT.S58409](https://doi.org/10.2147/OTT.S58409)

40. K.A. Goodman, E.A. Wiegner, K.E. Maturen, Z. Zhang, Q. Mo, G. Yang et al., Dose-escalation study of single-fraction stereotactic body radiotherapy for liver malignancies. *Int. J. Radiat. Oncol. Biol. Phys.* **78**, 486–493 (2010). doi:[10.1016/j.ijrobp.2009.08.020](https://doi.org/10.1016/j.ijrobp.2009.08.020)
41. J.-K. Kang, C.K. Cho, C.W. Choi, S. Yoo, M.-S. Kim, K. Yang et al., Image-guided stereotactic body radiation therapy for localized prostate cancer. *Tumori* **97**, 43–48 (2011)
42. S. Aluwini, P. van Rooij, M. Hoogeman, C. Bangma, W.J. Kirkels, L. Incrocci et al., CyberKnife stereotactic radiotherapy as monotherapy for low- to intermediate-stage prostate cancer: early experience, feasibility, and tolerance. *J. Endourol. Endourol. Soc.* **24**, 865–869 (2010). doi:[10.1089/end.2009.0438](https://doi.org/10.1089/end.2009.0438)
43. C. Choi, C. Cho, G. Kim, K. Park, M. Jo, C. Lee et al., Stereotactic radiation therapy of localized prostate cancer using cyberknife. *Int. J. Radiat. Oncol. Biol. Phys.* **69**, S375 (2007)
44. C.R. King, J.D. Brooks, H. Gill, T. Pawlicki, C. Cotrutz, J.C. Presti, Stereotactic body radiotherapy for localized prostate cancer: interim results of a prospective phase II clinical trial. *Int. J. Radiat. Oncol. Biol. Phys.* **73**, 1043–1048 (2009). doi:[10.1016/j.ijrobp.2008.05.059](https://doi.org/10.1016/j.ijrobp.2008.05.059)
45. C.R. King, J.D. Brooks, H. Gill, J.C. Presti, Long-term outcomes from a prospective trial of stereotactic body radiotherapy for low-risk prostate cancer. *Int. J. Radiat. Oncol. Biol. Phys.* **82**, 877–882 (2012). doi:[10.1016/j.ijrobp.2010.11.054](https://doi.org/10.1016/j.ijrobp.2010.11.054)
46. A.J. Katz, M. Santoro, R. Ashley, F. Diblasio, Stereotactic Body Radiation Therapy for Low-and Low-Intermediate-Risk Prostate Cancer: Is there a Dose Effect? *Front. Oncol.* **1**, 49 (2011). doi:[10.3389/fonc.2011.00049](https://doi.org/10.3389/fonc.2011.00049)
47. G. Voynov, D.E. Heron, S. Burton, J. Grandis, A. Quinn, R. Ferris et al., Frameless stereotactic radiosurgery for recurrent head and neck carcinoma. *Technol. Cancer Res. Treat.* **5**, 529–535 (2006)
48. D.E. Heron, R.L. Ferris, M. Karamouzis, R.S. Andrade, E.L. Deeb, S. Burton et al., Stereotactic body radiotherapy for recurrent squamous cell carcinoma of the head and neck: results of a phase I dose-escalation trial. *Int. J. Radiat. Oncol. Biol. Phys.* **75**, 1493–1500 (2009). doi:[10.1016/j.ijrobp.2008.12.075](https://doi.org/10.1016/j.ijrobp.2008.12.075)
49. K.-W. Roh, J.-S. Jang, M.-S. Kim, D.-I. Sun, B.-S. Kim, S.-L. Jung et al., Fractionated stereotactic radiotherapy as reirradiation for locally recurrent head and neck cancer. *Int. J. Radiat. Oncol. Biol. Phys.* **74**, 1348–1355 (2009). doi:[10.1016/j.ijrobp.2008.10.013](https://doi.org/10.1016/j.ijrobp.2008.10.013)
50. K.R. Unger, C.E. Lominska, J.F. Deeken, B.J. Davidson, K.A. Newkirk, G.J. Gagnon et al., Fractionated stereotactic radiosurgery for reirradiation of head-and-neck cancer. *Int. J. Radiat. Oncol. Biol. Phys.* **77**, 1411–1419 (2010). doi:[10.1016/j.ijrobp.2009.06.070](https://doi.org/10.1016/j.ijrobp.2009.06.070)
51. N. Kodani, H. Yamazaki, T. Tsubokura, H. Shiomi, K. Kobayashi, T. Nishimura et al., Stereotactic body radiation therapy for head and neck tumor: disease control and morbidity outcomes. *J. Radiat. Res. (Tokyo)* **52**, 24–31 (2011)
52. B. Comet, A. Kramar, M. Faivre-Pierret, S. Dewas, B. Coche-Dequeant, M. Degardin et al., Salvage stereotactic reirradiation with or without cetuximab for locally recurrent head-and-neck cancer: a feasibility study. *Int. J. Radiat. Oncol. Biol. Phys.* **84**, 203–209 (2012). doi:[10.1016/j.ijrobp.2011.11.054](https://doi.org/10.1016/j.ijrobp.2011.11.054)
53. E.F. Lartigau, E. Tresch, J. Thariat, P. Graff, B. Coche-Dequeant, K. Benezcery et al., Multi institutional phase II study of concomitant stereotactic reirradiation and cetuximab for recurrent head and neck cancer. *Radiother. Oncol. J. Eur. Soc. Ther. Radiol. Oncol.* **109**, 281–285 (2013). doi:[10.1016/j.radonc.2013.08.012](https://doi.org/10.1016/j.radonc.2013.08.012)
54. S. Dewas, J.E. Bibault, X. Mirabel, P. Nickers, B. Castelain, T. Lacornerie et al., Robotic image-guided reirradiation of lateral pelvic recurrences: preliminary results. *Radiat. Oncol. Lond. Engl.* **6**, 77 (2011). doi:[10.1186/1748-717X-6-77](https://doi.org/10.1186/1748-717X-6-77)

Chapter 4

Radiation Therapy Towards Laser-Driven Particle Beams: An “OMICs” Approach in Radiobiology

Luigi Minafra, Valentina Bravatà, Francesco Paolo Cammarata and Giusi Irma Forte

Abstract The main goal of radiation therapy (RT) treatments is to achieve local tumor control, to selectively kill cancer cells without causing significant damage to the surrounding normal tissues. RT uses ionizing radiation (IR) generated with conventional accelerators, such as X-rays, γ -rays, electrons, protons and ions. It is now well recognized by the entire scientific community that to evaluate the biological effects of IR it is essential an “OMIC” approach to take into account both the different cell types involved and the different IR’s used. The latest advances on cell and molecular response to IR, the most relevant data emerging from recent studies (genomics, epigenetics, proteomics and immunology) about different cell types, will be reported. We will discuss mainly biological effects of IR generated by conventional accelerators but we will also consider the few and preliminary radiobiological studies performed so far with laser-driven electron and proton beams. This will allow us in particular to speculate on cell and molecular effects of the laser-driven electron beams, a topic that can be now carefully investigated thanks to the impressive progress of “table-top” laser-driven accelerators.

L. Minafra (✉) · V. Bravatà · F.P. Cammarata · G.I. Forte
Istituto di Bioimmagini e Fisiologia Molecolare, Consiglio Nazionale delle Ricerche,
Cefalù, Italy
e-mail: luigi.minafra@ibfm.cnr.it

V. Bravatà
e-mail: valentina.bravata@ibfm.cnr.it

F.P. Cammarata
e-mail: francesco.cammarata@ibfm.cnr.it

G.I. Forte
e-mail: giusi.forte@ibfm.cnr.it

4.1 Introduction

Radiation therapy (RT) is a treatment modality used for many types of cancer: more than 50 % of cancer patients receive RT. The main goal of RT treatments is to achieve local tumor control, to kill selectively cancer cells without causing significant damage to the surrounding normal tissues. RT uses high energy ionizing radiation (IR) generated with conventional accelerators, such as X-rays, γ -rays, charged particles, e.g. electrons with high dose rate, protons and heavy ions [1, 2].

Hadrontherapy represents a form of advanced RT providing superior dose distribution compared with photon and electron therapy for the treatment of cancer [3]. In fact, the use of particle ion beams in cancer RT has the physical advantage of delivering dose in a sharp layer corresponding to the well known Bragg peak. Further benefit of the ion beam therapy was found on the increased relative biological effectiveness (RBE) within the Bragg peak region [2, 4].

The type of charged particles and the means by which radiation is administered in RT has continually evolved so as to improve overall outcomes and minimize side effects in normal cells. More recently, intensifying efforts have been invested in devising improved and novel radiation therapy treatments based on innovative technologies and devices.

Particle acceleration driven by high-intensity laser systems is widely attracting interest as a potential competitor of conventional, Radio Frequency based. Potential advantages include reduced size and cost of the designed treatment units. Further impressive features are the ultra-short duration of particle bunches, of picoseconds, and the extremely high dose-rate, which can exceed 10^9 Gy/s, delivered by laser-based devices [5–7].

In conventional electron or proton accelerators the dose rate is 10 Gy/s and duration of particle bunches is microseconds. These data reveal differences in the peak dose rate of 6–9 orders of magnitude. Thus, before utilization of a laser-driven electron or proton therapy in a clinical setting, it is crucial to understand whether an ultra-high dose rate alters any relevant biological endpoints [8]. The radiobiology at ultra-high dose rates is almost completely unknown, in particular for laser-driven particle beams, therefore it is crucial to investigate the biological effect of these ultrashort pulses at the cellular and molecular level in order to highlight the processes underlying the response of cells to this type of ion irradiation [9]. The few radiobiological studies available in literature are often preliminary and include mainly laser protons. Yogo et al. [10] described the irradiation effects of laser-accelerated protons on human lung cancer A549 cells treated with a proton dose of 20 Gy, resulting in a distinct formation of γ -H2AX foci as an indicator of DNA double-strand breaks. Unfortunately, in some of these studies an uncertainty in dose, mainly due to the finite size (2.5 mm) of the cell dots, estimated about 20 % was reported [11]. Doria et al. [11] report on results of experiments conducted on the radiosensitive Chinese hamster fibroblasts, V79 cell line, in the ultra-high dose-rate regime ($>10^9$ Gy/s), with the dose (up to 5 Gy) delivered in a single exposure. The survival curves, obtained after proton irradiation, showed the

expected higher biological efficiency of protons with respect to X-rays. From the comparison between proton and X-ray data, a RBE of 1.4 ± 0.2 can be calculated at 10 % SF (surviving fraction). The authors suggested that at the dose levels investigated, the ultrahigh dose rate employed had no significant effect on cell survival [11]. In line with these results, Bin et al. [12] reported that the preliminary RBE obtained in their study performed on the human cervical cancer cells (HeLa cell line) delivering single shot doses up to 7 Gy was in agreement with proton RBE values in conventional beams at comparable proton energies. The authors believe that for future applications in RT, where bunches of at least nanoseconds length (due to the propagation along an inevitable beamline of at least one meter between target and patient) and a maximum dose of a few Gy per shot will be applied, the same RBE as for conventional sources can be assumed [12].

As regard the biological effects induced by laser-driven electron beams, the first and preliminary data of the Laschinsky L. et al. study show no significant differences in radiobiological response of in vitro cell experiments between laser accelerated pulsed and clinical used electron beams. In particular, human squamous carcinoma cell line FaDu and normal mammary gland epithelium cell line 184A1, were treated with doses in the range of 0.4–10.2 Gy delivering radiation beams or in a laser-driven modality by 125–4900 electron pulses with a repetition rate of 2.5 Hz, or using a clinical electron linear accelerator LINAC with a dose rate of 3 Gy/min and the energy of 6 MeV [13]. According to the authors, these experimental data, as well as previous studies on conventional radiation beams, demonstrated that there was no systematic difference between ultra short pulsed laser electrons and clinical used LINAC electrons, suggesting also that the next step before the therapeutic applications may include in vivo responses to laser accelerated electron beams [13].

Rapid advances in our understanding of radiation responses, at the subcellular, cellular, tissue and whole body levels have been driven by the advent of new technological approaches for radiation delivery. In general IR, both electromagnetic and corpuscular, causes direct or indirect damage to principal biological molecules according to the LET of the particular kind of radiation. Cell damages are mainly induced by direct ionization of macromolecules including DNA, RNA, lipids and proteins. Indirect damage to macromolecules may be due to the generation of reactive oxygen species (ROS) from the radiolysis of intracellular H₂O and reactive nitric oxide species (RNOS). Finally, IR activate both pro- and anti-proliferative signal pathways producing an imbalance in cell fate decision regulated by several genes and factors involved in cell cycle progression, survival and/or cell death, DNA repair and inflammation [2, 14]. Radiation responses are not only dedicated to safe-guarding genomic integrity, but regard also the activation of molecular key factors able to regulate gene expression and proteomic profiles, giving us the opportunity to understand the complex cell networks activated by using high throughput approaches [15–17].

The Human Genome Project has given to scientific community a considerable amount of information on DNA and gene structure [18]. In addition to genomic data, transcriptomic has progressively evolved from the simple analysis of

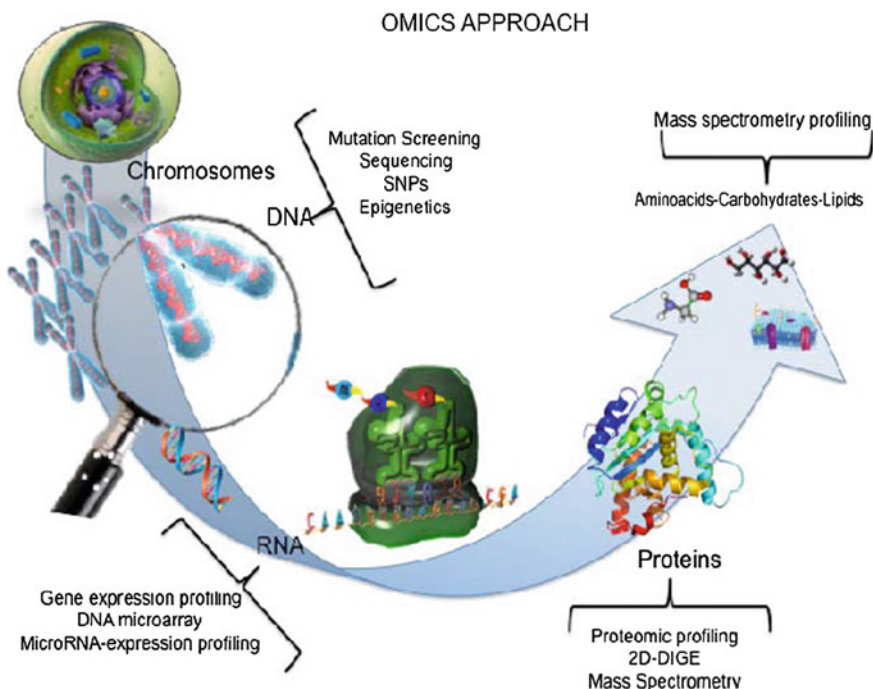


Fig. 4.1 The proteogenomic ways: an integrated “OMICS” approach, including analyses at the DNA (genomics), RNA (transcriptomics) and protein (proteomics) levels, allows to detect the molecular steps driving cellular functions and to identify new biomarkers

individual transcript levels to the simultaneous sequencing of all RNAs expressed within individual cells. The “functional genomics”, born from the integration of genomics and transcriptomics, has opened a new window for a better understanding of the relationship between genotypes and phenotypes, thus significantly impacting the fields of biology and medicine. Moreover, the last step for understanding gene functions and associated phenotypes are represented by proteins, the functional effectors of gene function. Thus, the necessity of a better integration of functional genomics with analysis at the protein level, i.e. proteomics, has progressively emerged [19].

“OMICS” approach (see Fig. 4.1) represents, therefore, the best way to analyze biological effects induced by IR, direct or indirect damage to principal biological molecules, allowing also to find new prognostic and predictive biomarkers of the cell sensibility to IR [19, 20].

Experimental data from proteomics, genomics and transcriptomics, termed all together “Proteogenomics”, are emerging as a fundamental step to analyze globally and simultaneously DNA, RNA, protein expression, and epigenetic modifications in order to understand molecular mechanisms underlying cellular processes and biological events induced by several type of stress stimuli such as IR [21].

It is now well recognized by the entire scientific community that to evaluate the biological effects of IR is essential an OMIC approach to take into account both the complexity of the different cell types involved and several types of particles and doses delivered [22].

While considering the few and preliminary rabiobiological studies on laser-driven electron and proton beams, we will principally discuss as necessary benchmark, the biological effects of IR mainly used in RT and generated with conventional accelerators, such as X-rays, γ -rays, electrons with high dose rate and other charged particles, i.e. hadrons. The latest advances on cell and molecular response to IR, the most relevant data emerging from “OMICS” recent studies (genomics, transcriptomics, epigenetics, proteomis and immunology) about different cell types, will be reported. This will allow us to speculate on the possible cell and molecular effects of the laser-driven electron beams, a topic that needs to be carefully investigated. The possibility to clarify cell molecular strategies to choose between death and survival, after a particle beam-induced damage, opens new avenues for the selection of a proper therapy schedule, to counteract cancer growth and preserve healthy surrounding tissue from radiation effects. In this context the innovative laser-driven acceleration technologies, rapidly progressing, could provide an unprecedented tool for advanced studies clinical perspectives.

4.2 DNA Repair Mechanisms IR-Induced

Among the direct radiation effects, the DNA repair mechanisms are crucial in the cell fate decision. Cells have evolved mechanisms, collectively termed the DNA-damage response (DDR), to detect DNA lesions, signal their presence and promote their repair [15, 16]. Generally, proliferating cells are more sensitive than quiescent cells to IR-induced cell death, due to their shorter cell cycle and reduced time to repair DNA damage [2, 23, 24]. However, even if cancer cells proliferate more quickly, these cells often carry multiple mutations causing constitutive activation of DNA repair mechanisms, allowing them to survive after damage [25–27].

Cells have evolved a variety of mechanisms to overcome different types of DNA damages. IR mainly produces Single Strand Breaks (SSBs) and Double Strand Breaks (DSBs) [28]. It has been calculated that approximately 40 DSB/cell are induced for each dose delivered (1–2 Gy for most cells) and that non-transformed or non-immortalized cells, i.e., normal cells, are able to repair about 70 DSB/cell within 24 h following the radiation exposure [29, 30]. Two main complementary pathways are involved in the DSBs repair: the non homologous end joining (NHEJ) and the homologous recombination (HR) which can be differentially activated, according to the cell cycle phase [15, 23, 31]. Following DNA injury, a rapid phosphorylation of the H2AX histone on chromatin alongside DSBs, over some megabase of DNA regions flanking the breaks, occurs. The resulting phosphorylated H2AX (γ H2AX) sites can be detected during the interphase, preferentially in euchromatic regions, by using immunofluorescence microscopy, already 3 min after

IR exposure, giving us the possibility to quantify cell damage post IR administration. These sites are named γ H2AX foci, also known as Ionizing Radiation Induced Foci (IRIF) [32–34].

In a recent study, we evaluated the time course of γ -H2AX foci appearance in two human breast epithelial cell lines, the non-tumorigenic MCF10A and the tumorigenic MCF7, which have been subjected to intraoperative electron radiation therapy (IOERT) treatment with high-energy electrons using 9 and 23 Gy doses [35, 36]. In particular, the γ -H2AX assays were conducted 0.5, 1, 3, 6 and 24 h after IR exposure. In both the two cell lines, it has been observed that the γ -H2AX foci formation was rapid, occurring within 15 or 30 min after irradiation at 9 and 23 Gy, for MCF7 and MCF10A respectively. Moreover, a dose-dependent increase of γ -H2AX foci can be observed following exposure to IOERT treatments. Their number gradually reduced in 6 and 24 h after 9 Gy exposure, whereas they remained increased respect to untreated cells within 24 h after irradiation with 23 Gy in both the two cell lines [35, 36].

As far as laser-accelerated proton pulses are concerned, similar results are reported in a study conducted after irradiation of squamous cell carcinoma (SCC) cell-line SKX. In particular, delivering low, medium and high doses by applying 12, 20 and 29 Gy of laser-accelerated protons, an increase in the number of DNA DSBs can be observed with the dose increasing, indicating the dose-effect of the biological damages occurring in tumor cells. However, the uncertainty in the dose delivered can be estimated to be about 20 % with this technique [37].

Yogo A. et al. also described the irradiation effects of laser-accelerated protons on human lung cancer A549 cells treated with a dose of 20 Gy, resulting in a distinct formation of γ -H2AX foci as an indicator of DNA double-strand breaks. γ -H2AX focus formation was detected in the nuclei only post 20-Gy irradiation [10].

In conclusion, the effect of laser-driven IR seems to produce DNA damages similarly to what described in literature for conventionally accelerated particles. However, a direct comparison between the two modality of irradiation is necessary on the same cell lines. Further, most of the experimental methods employed so far are not suitable at accounting for the early time effects, on the sub-nanosecond time-scale, which are expected to arise with laser-produced ultra-short particle bunches.

4.3 Cell Death Mechanisms

It is well known that IR are both carcinogens and a therapeutic agents. Even exposure at low doses, for example, can increase an individual risk of developing cancer, while sufficient high doses can slow down or stop tumor growth [1, 2, 4]. The biological effects of irradiation, including cell death, are highly dependent by several pathways controlling response to DNA damage, such as the DNA damage response (DDR). The DDR is able not only to determine the cell probability to die following irradiation but also the type of cell death that arises and the cell death

timing. As the DDR may differ among different type of normal and tumor cells, and also within different tumor cells population, cell death mechanism can also differ among different cell types [15, 16]. Nowadays, accumulating evidence reveals that induction of cell death is a very complex mechanism to account for the different therapeutic effects of IR. Several pathways are today known that can affect cell death after irradiation, so cell death remains very difficult to be tested. Quantification is complicated by the fact that cells do not die immediately after treatment with IR, but at various times after irradiation. In general, it is possible to classify cell death mechanisms into two big categories: (1) those that occur soon after irradiation and before cell division, generally in a small minority of cell type, such as thymocytes, lymphocytes, and others cells in rapidly proliferating tissues. Early cell death is also observed in some types of hematological tumors derived from these cell types, such as lymphomas but rarely in solid tumors; (2) those that occur after cell division or later on. For the vast majority of proliferating normal and tumor cells, death post irradiation arise after replications, frequently after 3–4 cell divisions and among surviving cells that continue to proliferate [2, 15, 38]. Therefore, radiobiologist focused on assessing clonogenic survival, which is defined as the cell ability to proliferate indefinitely after irradiation [39]. For this reason, this aspect represents a very important parameter to test radiation effect since any cell that maintains proliferative capacity can account failure of local tumor control resulting tumor radioresistance. Accordingly, in radiobiology cell death represents a process that causes a permanent loss of clonogenic capacity. Indeed, it is becoming clearer that the inhibition of neoplastic cells proliferative capacity following irradiation, in particular for solid tumors, can occur through different types of cell death such as: apoptosis, necrosis, mitotic catastrophe (MC), autophagy and senescence [40, 41]. Many factors, including radiation type and dose intensity, cell type, cell cycle phase, oxygen tension, DNA repair ability, genetic variations such as SNPs (Single Nucleotide Polymorphisms) sited on genes involved in radiosensitivity and/or radiotherapy toxicity, can define the type of cell death after irradiation with IR, briefly summarized below and in Fig. 4.2 [41–43].

Apoptosis. Apoptosis or programmed cell death, is a highly regulated mechanism. Typical cytoplasmic and nuclear morphologic changes are recognizable in apoptotic cells, such as cell shrinkage, contraction and membrane blebbing, nuclear condensation, DNA fragmentation and cell destruction into membrane-bound particles [44]. The apoptotic mechanism involves a complex network of factors according to the origin of death signal. Two principal apoptotic pathways are the so-called intrinsic and extrinsic pathways [38, 45]. In IR exposed cancer cells, both intrinsic and extrinsic apoptotic pathways may occur, according to delivered doses and cell type. DNA IR-induced SSBs and DSBs primarily trigger apoptosis by intrinsic pathway, when DNA lesions are unrepairable. Apoptotic pathways can be dependent by p53 factor, “the genome guardian”, which exerts a crucial role following IR-induced DNA damage [34, 43, 45].

The p53 expression level and mutational status affect cell decision to undergo death through apoptosis after irradiation. It has been observed that the tissues more sensitive to radiation-induced apoptosis, such as the spleen, the thymus and the

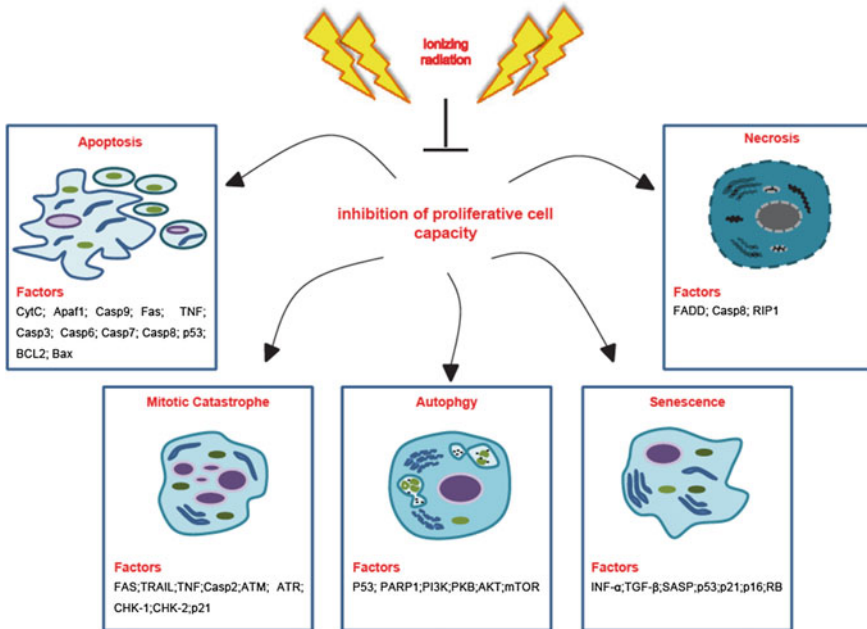


Fig. 4.2 Different radiation-induced cell death mechanisms and their principal factors

testis, show higher levels of p53 in respect of the liver and the kidney radioresistant tissues. Tumors that result responsive to p53-dependent apoptosis are generally radiosensitive, whereas tumors that overexpress antiapoptotic proteins such as BCL2, Bcl-XL and Survivin, or do not express pro-apoptotic crucial proteins, including p53, are more radioresistant [34, 46, 47]. In general, many types of cancer cells, such as lung, prostate, colon cancer and immortalized keratinocytes, undergo apoptosis upon IR exposure from 1 to 20 Gy of X-rays. Some non-immortalized cells exhibit apoptotic responses only when treated with higher doses of IR (>20 Gy) [40, 43, 48].

Necrosis. Necrosis has generally been accounted as a tumor cell death mechanism that predominates after a high IR dose treatment, while at a lower dose it has been indicated as a unregulated event. High radiation exposures, ranging from 32 to 50 Gy, for example, were able to induce necrosis in *in vitro* cultured neurons and in p53-deficient human leukemia cells. In contrast, lower IR doses, in particular 0.5 Gy of γ -rays, induced necrosis in the immortalized human keratinocyte cell line HaCaT [40, 49]. Recent studies show that IR can induce regulated cell death by necrosis in some types of tumor such as endocrine cancers, a mechanism defined as programed necrosis or necroptosis [50, 51]. It may be induced by apoptotic signals, particularly when the apoptotic machinery results either inefficient or blocked. Necrotic cells display some typical morphological characteristics, such as plasma membranes permeabilization with consequent loss of intracellular contents,

organelle swelling, mitochondrial dysfunction, but unlike apoptotic, necrotic cells generally do not show any signs of DNA fragmentation. In contrast to apoptosis, radiation-induced necrosis is often associated with increased inflammation of the surrounding normal tissue [48].

Senescence. In normal epithelial cells, senescence is a known strategy during aging and an increase of senescent cells in older tissues or in IR-treated tissues may be the cause of the onset of some pathology. Several stress stimuli, in addition to IR-induced DNA damage, can trigger senescence, such as oxidative stress, chemotherapeutic agents and extended signalling by some cytokines, including interferon- α (INF- α) and transforming growth factor- β (TGF- β) [52, 53]. Different gene expression alterations, such as deregulated expression of cell cycle regulatory proteins, which induce cell cycle arrest, upregulation of anti-apoptotic factors, high expression levels of inflammatory cytokines, growth factors and proteases, have been observed in senescent cells. These characteristics are defined as senescence associated secretory phenotype (SASP) [52–54].

When grown in culture, senescent cells display a specific and typical morphology with plasma membrane and nucleus macroscopic alterations, cytoskeletal organization, changes in cell-cell interactions showing the well-known “fried egg” like appearance. A well recognized senescence marker is the senescence-associated β -galactosidase (SA- β -gal), whose increased expression has been correlated with senescence in many cell types. The DNA damage-induced signalling pathways which trigger senescence associated cell cycle arrest are mainly regulated by p53/p21 (waf1, CDKN1A), by p16 (INK4a, CDKN2A) and Rb (retinoblastoma) factors [53, 54].

IR may induce accelerated cellular senescence, a state of irreversible growth arrest in which the damaged cells show altered functions and, despite being vital, are no longer competent for proliferation. It has been demonstrated that senescence is the principal response of some cell types at IR lower doses, whereas higher doses are required for the induction of apoptosis or necrosis in the same cells. In particular, a study conducted in pulmonary artery endothelial cells, irradiated with X-rays, using doses ranging from 2 to 50 Gy, has shown that increasing IR dosages induce a cell response which can change from senescence to apoptosis and/or autophagy, until necrosis at higher doses [48]. Actually, most radiobiologic studies demonstrate that there is not a unique and absolute kind of response for all cell types to a certain IR dose. For example, primary human hematopoietic cells (CD34+) undergo apoptosis, whereas pulmonary artery endothelial cells become senescent when treated with the same dose of radiation [55, 56]. Today the aspects establishing the specific cellular fate after IR exposure have not been clearly defined, but increasing evidence suggests that the type and radiation doses are primarily important, as well as different cell features [57].

In order to evaluate cell and molecular effects induced by IR during IOERT with high-energy electrons and to select potential new biomarkers of radiosensitivity or radioresistance, our research group performed a molecular study in BC cell lines irradiated with 9 and 23 Gy doses [15, 35]. Cell and molecular traits observed in MCF7 cells revealed a typical senescent morphology associated with cell

proliferation arrest after both treatments with 9 and 23 Gy, confirmed by SA- β -Gal activity which increased in a dose- and time-dependent manner [35]. On the contrary, the non-tumorigenic MCF10A cell line, used as a model of normal breast epithelial cells, did not reveal any cellular senescence activation in response to IOERT treatments. In particular, while the 23 Gy irradiation inhibited the growth and proliferation of MCF10A cells, after 9 Gy of exposure, the selection of a radioresistant cell fraction was observed, in both cases without any senescent traits [36].

Autophagy. Autophagy is a basic catabolic mechanism that involves cell degradation of unnecessary or dysfunctional cell components, such as damaged ER (endoplasmic reticulum) and other cytoplasmic constituents through lysosomes action. In the context of a disease, autophagy has been described as an adaptive response to survival, whereas in other cases it appears to promote programmed cell death. However, several evidences reveal a cross-talk between autophagy and apoptosis [40, 58, 59]. In tumor cells undergoing chronic hypoxia and nutrient depletion, autophagy is a strategy to maintain metabolic homeostasis. After stress stimuli, such as nutrient starvation, organelle damage, protein aggregation, oxidative or genotoxic stress, including IR, the autophagy activation promotes cell death and this is also the case of macroautophagy [60]. Autophagic pathways can induce survival or cell death following IR treatment, processes that might be cell and tissue specific and dependent on the expression of genes and proteins controlling apoptosis [61, 62]. In several types of cancer cells, such as breast, prostate, colon, lung, esophageal and glioma, IR-induced microautophagy or macroautophagy has been showed [48, 63].

It has been observed that following 6 Gy X-ray irradiation, some autophagy regulatory factors significantly decreased in lung tissue, indicating a specific and strong dysregulation of IR-induced autophagy, effect not observed in liver or kidney tissues subjected to the same radiation conditions [48, 64]. In the literature there are controversial data with respect to the IR-triggered autophagic effect, resulting in survival or cell death promotion. Some studies show that, the autophagy inhibition is radiosensitive, while the autophagy promoting is radioprotective, suggesting that IR-induced autophagy may represent an adaptive response to maintain tumor growth and survival. For example, in radioresistant BC cells a strong post-irradiation autophagy induction has been observed as a protective and pro-survival mechanism of radioresistance after exposure to X-rays of 4–5 Gy [65]. In contrast with these data, other studies show that induced autophagy in some radioresistant cancer cells, including glioblastoma and lung cells, sensitizes to IR increasing cell death [64–67]. The molecular machinery involved in IR-induced autophagy is not entirely known. IR-induced DNA damage represents the initiating event that causes autophagy.

Mitotic catastrophe. Mitotic catastrophe (MC) has initially been described as a cell death mechanism, occurring during or after aberrant mitosis, associated with various morphological and biochemical changes following radiation-induced incomplete DNA synthesis. Several evidence has revealed that it can also be caused by chemical or physical stresses and represents an oncosuppressive mechanism to avoid genomic instability. MC has been defined as a special example of

apoptosis because it shows several biochemical apoptosis features, including mitochondrial membrane permeabilization and caspase activation. However, it has been observed that MC may result in death that requires both caspase-dependent or caspase-independent mechanisms. Tumor cells, harboring checkpoint deficiencies that cause incomplete DNA repair, replicative infidelity or aberrant chromosome segregation, may undergo to MC. Thus, the IR-induced loss of checkpoint control in treated cancer cells may lead to the generation of aneuploid progeny and MC associated cell death. Cells display an increased frequency of multiple nuclei and micronuclei. In IR-treated tumor cells, MC is often associated with delayed apoptosis following increased expression of some receptors and their ligands. Identifying the different radiation-induced cell deaths, their induction mechanisms, and their putatively synergistic effects for the therapeutic outcome has potential and practical implications for improving RT in cancer treatment [40, 68, 69].

In this context it is very important to evaluate if IR pulses extremely shorter and higher dose-rate laser generated by laser accelerators are able to change this scenario and the factors regulating cell death mechanisms. So, further studies are necessary in order to test this ipotesis.

4.4 Epigenetic Changes and Bystander Post-irradiation Effects

Epigenetic changes are heritable structural and functional genome modifications occurring without changes in DNA sequence, directly influencing gene expression by mechanisms including histone modifications, DNA methylation and the annealing of non-coding antisense RNAs. Aberrant epigenetic events cause global changes in chromatin packaging and in specific gene promoters, affecting the gene transcription and function [70, 71]. For examples, two principal types of changes in the DNA methylation pattern occur in cancer cells: hypo- and hyper-methylation of specific genes [72, 73].

A number of reports suggest that radiation exposure leads to changes in DNA methylation [74]. Some of radiation-induced epigenetic changes have been found associated with loss of methylation and decrease in expression levels of some methyltransferases and the methyl CpG binding proteins (MeCP2) [75]. In a recent study conducted on the MDA-MB-231 human BC cell line following irradiation with 2 and 6 Gy of X-rays, global DNA methylation changes (at > 450,000 loci) have been analyzed to determine potential epigenetic response to IR. The study has revealed significant differentially methylated genes related to cell cycle, DNA repair and apoptosis pathways. The degree of methylation variance of these pathways changes with radiation dose and time post-irradiation, suggesting that DNA methylation variations exert an important epigenetic role in cell response to radiation [76]. In the MCF7 BC cells treated with different fractionated X-ray doses (until 20 Gy), several locus-specific DNA methylation alterations have been observed, which predominantly were loss of methylation of TRAPP9, FOXC1 and LINE1

loci [77]. Recently, it has been reported that radiosensitive and radioresistant cancer cells may acquire epigenetic changes at different genomic regions, in dependence of time after irradiation and cell genetic background. In addition, several data suggest that the defining of specific factors regulating gene expression by DNA epigenetic changes may be a useful target for tumor radiosensitization [78].

Responses to IR were also observed in cells that were in contact with directly irradiated cells or have received signals from them. These responses represent the “non-targeted” or IR “bystander effects” [79, 80]. In this respect, a much less understood type of cell death that has been described following irradiation is the so-called bystander-induced death, a phenomenon in which death occur in cells owing to irradiation of neighbouring cells. Evidences of this effect come from some studies using high LET α -particles and also with microbeam irradiation in which selected cells or nuclei were irradiated with particles both α -particles and protons or X-rays. In these experiments irradiation of a group of cells can lead to increased cell death in unirradiated cells [81, 82]. In addition to cell death, bystander effect has also been observed for other known biological irradiation effects, such as DNA damage, mutations, chromosomal aberrations, transformation and gene expression changes [83]. Indeed, the bystander effect is increasingly considered as a long-term side effect of IR exposure. Recent studies indicate that this effect can be positive or negative and it is dependent on the radiation LET, total dose, dose rate and radiosensitivity of treated cells, similarly to the IR direct effects. The negative effects comprise apoptosis, necrosis, accelerated senescence, contributing to decreasing cell survival [84]. In contrast, in some conditions, a positive radiation effect on bystander cells is an increased tumor cell proliferation. For example, increased cell proliferation has been observed in normal liver epithelial cells and in non-transformed fibroblasts, as well as in several transformed cells [85, 86]. In vitro evidence suggests that the bystander effects are communicated between cells through either the gap junction connections or by the transmission of soluble factors between irradiated cell and non-irradiated cells through the cell culture medium. Several soluble factors are involved in the bystander effect, such as reactive oxygen species, nitric oxide, cyclooxygenase-2 and cytokines including TNF- α and TGF- β 1 [84, 87]. Nevertheless, some unanswered questions remain unclear such as the signals transmitted from irradiated to bystander cells and the relationship between the bystander response and other non-targeted effects of irradiation. To date, no data are available about epigenetic and bystander effects generated by laser beams, therefore it is necessary to study this important radiobiological issue in vitro and in vivo.

4.5 Gene Expression Profiling Induced by IR

Gene expression profile (GEP) experiments by microarrays are able to highlight the whole cell response in term of gene expression changes after a specific stress or treatment and represent an useful OMIC approach to understand complex heterogeneous diseases [88, 89]. The fate of a cancer cell after RT is known to be

controlled by a network of signalling pathways that lead to different modes of cell death or survival. Even if DNA represents the critical target of the biological effects of IR, the responses generated are not solely dedicated to safe-guarding genomic integrity, but regard also the activation of GEP able to generate specific radiation cell responses and signal pathways [15, 90]. Nevertheless, the contribution of these genes and the signalling pathways involved in cellular response to high radiation doses is not entirely known.

Regarding laser-driven electron beams treatments, no information are available on cell network activated after the ultrashort pulses generated. Therefore it is crucial to investigate their biological effects at the cellular and molecular level in order to highlight the ultrafast processes underlying the biological response of cells to this type of irradiation [11]. More precisely, no data regarding gene expression changes are available in literature but we trust that GEP analyses could give in this sense a powerful contribution. Thus, we will principally discuss on GEP profiles induced by IR mainly used in RT and generated with conventional accelerators, speculating on the possible cell and molecular effects of the laser-driven electron beams.

DNA represents the critical target for the IR but not the only one. In mammalian cells, IR can induce a multi-layered signalling response by activating many pro-survival pathways that converge to transiently activate key transcription factors (TFs). These include the Nuclear Factor kappa B (NF- κ B), Activator Protein 1 (AP-1) signal transducers and activators of transcription members (STATs) and hypoxia-inducible factor 1 α (HIF-1 α) [91–95] as displayed in Fig. 4.3.

Together, these TFs regulate a wide spectrum of genes involved in cell cycle checkpoint regulation, inflammation, apoptosis, invasion and angiogenesis processes, contributing to confer tumor cell radioresistance [96, 97]. Moreover, NF- κ B is a well-defined radiation-responsive transcription factor: after exposure to IR, NF- κ B activation is initially triggered by ATM which is activated by DNA DSBs [98]. Its activity increases cell sensitivity in several tumor cell lines and also, NF- κ B down-regulation is probably required for TP53-dependent apoptosis. NF- κ B is able to influence cell cycle regulation after irradiation and is supposed to be able to induce radioresistance by cell cycle regulation, alteration in apoptosis and changes in the ability to repair DNA damage. Aberrant survival signalling after disruption of NF- κ B has recently become an important issue to study therapy of several chemoresistant/radioresistant cancers [99–101]. Recently, we have confirmed this assumption because both NF- κ B and TNF α genes were up-regulated in MCF7 BC cell line after 9 Gy of electron beam exposure [35].

The exposure of mammalian cells to extracellular stress such as IR also induces the expression of immediate early genes, such as FOS and JUN and activates AP-1, a heterodimeric TF composed of FOS- and JUN-related proteins [102–104]. AP-1 proteins and c-FOS play an important role in the induction and development of radiation late effects in normal tissues. In particular, we have recently showed that after 9 Gy of electron beam irradiation, MCF7 BC cells up regulate JUN, JUNB, FOS and FOSB genes. Our data confirm previous studies indicating that JUNB gene is responsive to IR and is immediately induced after stimulation, revealing its important role in the early cell response process following irradiation [35, 104].

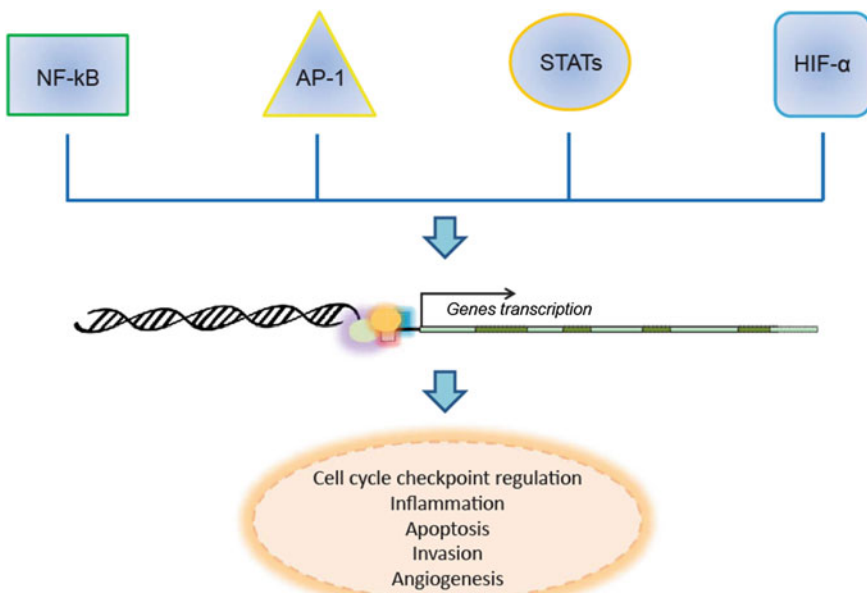


Fig. 4.3 Key transcription factors IR activated and relative processes modulated

AP-1 proteins play an important role in the induction and development of late radiation effects in normal tissues, regulating the expression of several genes involved in oncogenic transformation and cellular proliferation such as those coding for MMPs, and TGF β [103, 104].

Another pathway that plays a key role in regulating the IR cell response is driven by JAK-STAT signalling. It has been shown that STAT TF proteins can have a significant role in tumor development and they are included among potential oncogenes [90]. The two members of this family STAT1 and STAT3 are very similar proteins (40 % identity) that can often be activated by the same extracellular ligand (such as EGF, PDGF or IL-6). They appear to play opposite roles in tumorigenesis: STAT3 is considered an oncogene because it promotes cell survival/proliferation, while STAT1 enhances inflammation and immunity, triggering anti-proliferative and pro-apoptotic responses in tumor cells [105, 106]. STAT-3 activation has also been associated with both chemoresistance and radioresistance processes. STAT-3 mediates these effects through its collaboration with various other TF, including NF-κB, hypoxia-inducible factor-1 (HIF1), and peroxisome proliferator activated receptor-gamma (PPARG). Also STAT1 can induce a radiation resistant phenotype and can also favour carcinogenesis and tumor survival. Moreover, this gene also interacts with ATM protein following DNA damage and participates in the repair of DNA damage IR-induced [107]. Otherwise, its down-regulation could significantly increase the radiosensitivity of renal carcinoma cell lines.

Another TF involved in cell radiation response and probably able to regulate radioresistance controlling the gene expression after IR exposure, is HIF-1 α . Under hypoxia condition the HIF-1 α TF is activated and confers protection against cell death, playing an adaptive role. Of importance, radiation-activated p38 MAPK mediates the stabilization of HIF-1 α . As known, the radioresistance of tumor cells is closely related to the hypoxia status and is considered to be a major obstacle in RT [108–110]. Elevated HIF-1 α expression is associated with tumor metastasis, resistance to therapy and poor survival [93]. Radiation-induced HIF-1 α expression has been shown to be highly relevant to the malignancy of cancer cells [93, 111].

IR exposure of tumor cells induces the simultaneous compensatory activation of multiple mitogen-activated protein kinase (MAPK). Their pathways transduce signals from the cell membrane to the nucleus in response to a variety of different stimuli and participate in various intracellular signalling pathways that control a wide spectrum of cellular processes including growth, differentiation, stress responses, and it is known to have a key role in cancer progression. Multiple signal transduction pathways stimulated by IR are mediated by the MAPK superfamily including the extracellular signal-regulated kinase (ERK), c-Jun N-terminal kinase (JNK), and p38 MAPK. IR has been shown to activate all three MAPKs, although with different intensities and in a cell type-dependent context [91, 112]. It has been demonstrated that MAPK signalling is involved in cell cycle progression through the G2-M checkpoint after irradiation. Pro-survival ERK pathway is known to be activated following irradiation in dependence on the expression of multiple growth factor receptors and autocrine factors. Ras MAPK signalling is able to influence tumor cell radiosensitivity because of their activity associated with radiation-induced DNA damage response [15, 113].

In addition, many authors have showed distinct differences in molecular response, in particular gene expression changes, between a single dose (SD) versus multi-fraction doses (MFD) of IR and also that cellular and molecular responses, comprising the GEP induction after IR, could be regulated in a time-, dose- and cell line-dependent manners [5, 35, 36, 107, 114–116]. For example, Tsai M.H. et al. have showed distinct differences in molecular response between a single dose of 10 Gy of X-ray irradiation versus multi-fractions of 5 \times 2 Gy dose in breast (MCF7), prostate (DU145) and glioma (SF539) cell lines. These cells were characterized by a large comparable number of differentially expressed genes with a 1.5 or 2 fold change threshold, within a 24 h time course. Their GEP comparison by multidimensional scaling analysis revealed differences rather than similarities among the IR-treated cell lines, as well as between the SD and MF dose regimens. More precisely, the number of genes up-regulated by at least 2-fold, after either SD or MF protocols, common to all three cell lines, was found to be small and composed by only 13 interferon (IFN)-related genes. This group of genes are also known to be transcriptionally activated STAT1, underling once again, its key role in transcription regulation during cell IR response. The results of this study clearly show distinct differences in the molecular response of cells between SD and MF radiation exposures and show that the tumor microenvironment can significantly influence the pattern of gene expression after radiation exposures [107]. In addition, although p53

is one radiation-responsive gene, other genes may also contribute to the radiation response. For example, has been reported that only MCF7 cells show a cluster of p53-related genes, regulated by both single and multi-fraction schedules, while no p53-related genes were detected in either prostate and glioma cell lines [15, 107]. As described by several authors, many IR induced genes are p53 regulated but there is also a substantial IR transcriptional response p53-independent, with NF-κB that plays a contributing role to radioresistance. As p53, NF-κB activates a varied set of genes ranging from cyclins to those involved in lipid signalling and translation. Considering that half of human cancers have a mutated p53 gene, these pathways should be further targeted to improve cancer cells radiosensitizing [15].

In addition, gene profiles after IR exposure, can vary extensively depending on the dose delivered [35, 36]. More precisely, we have recently investigated the GEPs induced by 9 and 23 Gy of electron beam irradiation delivered by IOERT in the MCF7 BC cells and MCF10A breast non tumorigenic cells. We have reported a dose-dependent transcriptome able to regulates cell fate decisions in different ways, according to the doses delivered. Therefore, we have also designed two models of genes and networks activated by 9 and 23 Gy doses, using the selected and validated genes according to the two cell lines analyzed. We hypothesized that exposure to these high doses of electrons could differentially regulate, at transcription level, some cellular processes such as gene transcription, DNA repair, inflammation, cell death and cell cycle. Some positive regulators of cell cycle could be up- or down-expressed according to the two doses used. Among genes involved in the above mentioned processes, and in line with other literature data we suggested to investigate the role of some validated genes in order to clarify the networks activated by radiation exposure and able to regulate cell fate and survival/death balance [35, 36].

In addition to DNA damage and inhibition of DNA synthesis, IR could induce the down regulation of histone mRNA levels in mammalian cells through the G1 checkpoint pathway. IR-induced inhibition of histone gene transcription depends on the p21 protein, which we found up regulated in MCF7 cells treated with 23 Gy. It has been reported that exposure to high and low LET radiation negatively regulates histone gene expression in human lymphoblastoid and colon cancer cell lines regardless of p53 status, finding also confirmed by our group [35, 36, 117].

GEP induced by IR also may vary widely in cell lines derived by different tissues of origin and with different genetic background, highlighting the importance of cellular microenvironment to genotoxic stress responses [15, 35, 36, 118]. In line with these observations, Amundson SA et al., by applying fluorescent cDNA microarray hybridization on human myeloid cell line (ML-1) 4 h after 20 Gy γ -rays exposure, selected 48 transcripts significantly changed by radiation treatment and known to be radiation inducible, as well as many genes not previously reported as IR regulated. Some of these coded for proteins involved in cell cycle, cell fate, transcriptional regulation and generally in intracellular signalling cascades that could play an important role in the induction and development of cell radiation effects. Interestingly, the majority of the IR-responsive genes showed a p53-independent regulation. The induction of these selected stress-response genes

was next measured by the authors in a panel of 12 cancer cell lines of lung, breast and colon, derived from myeloid-lymphoid lineage, in order to determine their role in IR-response. Only the SSAT, MBP-1, c-IAP1, RELB and BCL3 genes were primarily IR induced in all the 12 examined cell lines [114, 118].

As previously reported, many differences exist in GEP IR-induced, according principally to type of radiation treatment used. Suetens A. et al. performed a GEP study by microarray in human prostate cancer cell line PC3 exposed to different doses of carbon ions and X-rays (0.0, 0.5 and 2.0 Gy) and founded that 2 Gy carbon ion irradiation induced more pronounced changes in gene expression compared to similar doses of X-rays both in terms of number of genes and magnitude of changes. A down regulation of many genes involved in cell cycle regulation, invasion and angiogenesis, which may be responsible for the aggressive phenotype of cancer cells, was also observed. In particular, the down regulation of genes involved in cell motility was generally more pronounced after carbon ion irradiation compared to X-rays. Dysregulation of signalling pathways in surviving cells after RT, such as those associated with cell migration and motility, can determine the fate of the tumor and consequently the fate of the patient [119].

The high variability of transcriptional responses described in different cell types, using different types of radiation and different doses emphasizes that a single cell line or a specific radiation treatment cannot provide a general model of response to stress IR-induced [120]. Moreover, as technology increases in complexity, the correlations between the proteomic and transcriptional profiles of IR treated cells will yield a more cohesive picture of cell responses to RT.

4.6 Genetic Background Influences Radiation Response

The individual response to RT is well established and can be modified by extrinsic factors, including dose, age, additional treatment and co-morbidities [121–124]. Nevertheless, about the 80 % of individual responses to RT remain unexplained, raising the possibility of underlying genetic variability as a cause of those responses [125].

Radiogenomic is the whole genome application of radiogenetics, which focuses on uncovering the genetic causes of individual variation in sensitivity to radiation. There is a growing consensus that radiosensitivity is a complex response, inherited on polygenic traits and dependent on the interaction of many genes involved in multiple cell processes [17, 125].

Many studies address the hypothesis that normal genetic alterations, such as single-nucleotide polymorphisms (SNPs, i.e. natural variations in a DNA sequence occurring commonly with fairly high frequency within a population), rather than rare mutations, are responsible for most of the variation in toxicity between patients receiving the same dose of RT [126–128]. Successful identification of this genetic determinants will allow predictive tests for tissue radiosensitivity, contributing to better outcomes through biological individualization of RT.

In radiogenomic research two commonly methodologies are used to discover new genes involved in the radioresistant/radiosensitive phenotype: a candidate gene approach and genome-wide analysis study (GWAS). Candidate gene study has the advantage of a relatively low cost, and it uses a priori knowledge about the biological functions involved in radiation response, but it limits the aim to a manageable number of investigated genes. The recent development of GWAS has provided a radical alternative to the candidate gene approach. This technology offers the opportunity to conduct a hypothesis-free survey for SNP associations without any need of a prior understanding of the biology underlying the phenotype of interest [129, 130].

With recent developments in high-throughput genotyping, it is now possible to genotype up to 1×10^6 SNPs that together represent all the common variations across the genome in a single large experiment. Apart from germline mutations in specific known genes such as ATM, NBS1, MRE11, and Ligase IV, genetic polymorphic variations in a number of nuclear genes have been associated with radiosensitivity [130]. Interestingly, Guo et al. [129] have recently published a comprehensive review in which they explain how radiogenomics could help to achieve personalized therapy by evaluating patient responses to radiation treatment. Radiogenomic studies published to date have adopted the candidate gene approach to look for variations in DNA damage repair genes, oxidative stress response genes, apoptosis-related genes and fibroblast proliferation gene. Guo Z. et al. also described how cell line-based GWASs were useful to identify genes associated with radiation sensitivity also yielding certain novel biomarkers. Through the initial screening in 227 human lymphoblastoid cell lines and further functional validations using small interfering RNA knockdown in multiple tumor cell lines, it has been demonstrated that a set of lesser known genes, were all significantly linked with radiosensitivity [131]. More recently, Barnett et al. [132] have performed a phase-designed GWAS in three independent cohorts RT-treated for prostate cancer or BC in order to provide evidence that common SNPs are associated with risk of toxicity 2 years after RT.

Another list of genetic alterations involved in radiation response was reviewed by Barnett GC and colleagues. They summarized a list of genes in which, specific genetic alterations were analyzed in radiogenomic studies conducted on many kind of tumors (breast, head and neck, prostate etc.), with controversial results [121].

At present it is not yet clear what extent genetic variation links to an overall measure of toxicity rather than tissue-specific toxicity. The former would be better and an element of generalized sensitivity is plausible. However, tissue-specific factors are also involved and indicate the need to collect samples from multiple tumor types, also related to multiple normal tissues. Evidence is emerging, at least for some toxicity end points, that SNP profiles are tissue specific. Therefore, there may not be a single SNP profile that can be used as predictive indicator for any RT side-effect [125]. The ultimate goal of radiogenomics is to add an additional element in personalised medicine to plan RT and to improve the patient outcome. Such individualization, combined with the very efficient RT treatment planning and delivery techniques, will also allow the best combination with pharmaceutical

agents obtaining both lower toxicity and higher cure rates. Concluding, personalized radiogenomic is useful for the translational study of individual genetic variations that may be associated with the tissue response to RT treatments used for all types of cancer. In this sense, the aim of personalized radiogenomic research are: (1) to reveal the related genes, proteins, and biological pathways responsible for non-tumor or tumor tissue toxicity following RT that could be targeted with radio-sensitizing and/or radio-protective agents; (2) on the other hand, to identify specific genetic markers that can be used in risk prediction and evaluation models before and after clinical cancer surgery.

4.7 Proteomic Profiles Activated by IR

Proteomic science represents one of the latest technological developments, allowing scientists to complement genomic information and increase levels of knowledge about the destiny of codified sequences from DNA to one or more proteins due to different stimuli. Proteomic comparison of healthy and physio/pathological samples, using experimental approaches normally sorted in “non mass spectrometry (MS)-based and MS-based” studies, strongly improves the potential discovery of new diagnostic and prognostic biomarkers, as well as novel targets of new therapeutic treatments. Gel-based proteomic, i.e. two-dimensional polyacrylamide gel electrophoresis (2D-PAGE) and Sodium Dodecyl Sulphate (SDS)-PAGE, is the most popular method of global protein separation and quantification [18–20].

The emergence of novel biomarkers to predict cancer cell insensitivity to IR could help to improve therapy results in cancer patients receiving RT. The proteomic approach could be effectively used to identify proteins associated with cancer radiation resistance and sensitivity [133, 134].

Several studies described the biological effectiveness of IR using a proteomic approach. In the study of Jung S et al., a global analysis of the protein expression pattern was performed using 2D-PAGE and MS to identify radiation-responsive proteins in MCF7 BC cell line irradiated with different doses of γ -rays of 1, 5, 10, or 20 Gy, in which the cell growth was repressed after exposure to 20 Gy of radiation [135]. The IR treatment of the MCF7 cells did not affect cell viability, but the cell growth was repressed due to cell cycle arrest at the G2 phase, suggesting that IR-irradiated MCF7 cells undergo cell cycle arrest rather than apoptosis. In order to establish the factors responsible for this phenotype the authors identified the radiation-responsive proteins in γ -irradiated MCF7 cells. In particular, one set of proteins was up-regulated and another set of proteins was down-regulated after exposure to γ -rays. These proteins are known to be related to cell cycle control, apoptosis, DNA repair, cell proliferation and other signalling pathways, defining a molecular signature, at protein level, of MCF7 response to this type of treatment with γ -rays [135].

The proteomic study of Liao E.C. et al. performed in MDA-MB-231 BC cell line irradiated with 6 Gy of X-rays reports the metabolic alterations induced by this radiation treatment. The authors found that X-rays irradiation induced senescence of MDA-MB-231 cells and the activation of glyceraldehyde-3-phosphate dehydrogenase and lactate dehydrogenase, involved in glycolysis and in the conversion of pyruvate to lactate, allowing the lactate release and the acidification of the extracellular environment. In addition, 6 Gy X-ray irradiation induced activation of the 50'-adenosine monophosphate-activated protein kinase (AMPK) and nuclear factor kappa B (NF- κ B), senescence-promoting factors. Interestingly, these metabolic alterations were also detected in non-irradiated, surrounding cells and promoted their invasiveness. Therefore, changes in metabolism are crucial for both radiation-induced senescence and the bystander effect [136].

As regard molecular studies about proton beam irradiation effects, even though this clinical treatment has been developing for several decades, the proton radiobiology critical to the optimization of proton RT is far from being understood. Proteomic changes were analyzed in human melanoma BLM cell line treated with a sublethal dose (3 Gy of a 60 keV) of proton beam irradiation [137]. The authors reported that the 3 Gy of proton beam irradiation slowed down cell growth in culture and starting from fourth day the number of viable cells in culture decreased, result in agreement with the increase in DNA damage shortly after the treatment. By proteomic analysis of melanoma cells after proton beam irradiation they found 17 protein expression levels significantly changed: 4 down-regulated and 13 up-regulated. The differentially changed proteins, up- or down-regulated after proton beam irradiation, were classified according to protein function, into four groups: (1) DNA repair and stress, (2) proliferation, survival and apoptosis, (3) metabolic pathways, and (4) cytoskeleton. In this classification some proteins have multiple functions and can play a role in different group. Relatively few protein levels were changed after proton irradiation in comparison with other type of IR, such as X-and γ -rays [138, 139]. Moreover, relatively few proteins engaged in DNA repair were up-regulated and these unexpected results for the authors may arise from the long period given for recuperation after the irradiation insult (4–5 weeks post treatment). Allowing cells to undergo several passages in culture to repair proton irradiation damage before carrying out the proteomic analysis ensures that the effects shown were long-term [137]. In addition in this study, of particular interest was the substantial deregulation of vimentin, a marker of epithelial-mesenchymal transition (EMT) and of the metastatic properties of melanoma.

With regard to the heavy ions, the study of Li H et al., describe the use of a proteomic approach based on the 2D-PAGE and MS to determine alterations in protein expression in the testes of pubertal mice subjected to whole-body carbon ion radiation (CIR) with 1 and 4 Gy doses. Eight differentially expressed proteins were identified. These proteins were mainly involved in energy supply, endoplasmic reticulum function, cell proliferation, cell cycle, antioxidant capacity and mitochondrial respiration, which play important roles in the inhibition of testicular function in response to CIR. In addition, the authors confirmed the relationship between transcription of mRNA and the protein abundance. Their data indicated

that these proteins may lead to new insights into the molecular mechanism of CIR toxicity, and suggested that the gene expression response to CIR involves diverse regulatory mechanisms from transcription of mRNA to the formation of functional proteins [140].

Further *in vitro* and *in vivo* studies are needed in order to obtain specific proteomic profiles of differentially irradiated cells and to identify new biomarkers, that may be used to understand cell and tissue responses to a different RT cancer treatments. In this perspective laser techniques of IR production could greatly help the experimental research.

4.8 Inflammatory Response to IR

Immune system plays a crucial role in the cancer development and progression, as well as in radioresistance mechanisms. The effectors can be subpopulations of different immunological cells as well as a great variety of molecules (cytokines, chemokines, grow factors etc.), which orchestrate the systemic and local response to such a type of stress, like IR [90].

However, a primary concept is that tumor cells themselves are able to produce immunological molecules, releasing them in the tumor microenvironment, strongly conditioning tumor radiosensitivity/radioresistance [141]. On one hand, immunological factors can suppress tumor development by killing cancer cells or inhibiting their growth. On the other hand, they can contribute to promote tumor progression, through inflammatory molecules and proteases, which affect cell invasion, bystander effect and radiation tissue complications such as fibrosis [142–144] (Fig. 4.4).

Overall, upon IR administration, pleiotropic effects produced by immunological molecules sustain a pro-survival/cell death pathways balance, through transient activation of key transcription factors (TFs), including the NF- κ B, as previously described. Together, these TFs regulate a wide spectrum of genes involved in inflammation, apoptosis, invasion and angiogenesis processes, contributing to confer tumor cell radioresistance [96, 97]. NF- κ B regulates the expression of different pro- and anti-inflammatory molecules (such as TNF- α , IL1, IL2, IL6, IL-10 and MCP-1), and like p53, it activates a variety of genes ranging from cyclins to those involved in lipid signalling. This fact justifies the observation that NF- κ B inhibition increased sensitivity of cancer cells to the apoptotic action of different chemo-radiotherapies [145, 146].

Among the IR induced complications, the gain in cell metastatic ability and tissue fibrosis are certainly mediated by inflammatory signalling. Particularly, IL-8, IL-6 and TGF- β signalling are involved in cancer cell invasiveness. IL-6 has been reported to be increased in a variety of tumors, contributing to aggressive tumor growth and resistance to treatment [147–150].

Some preclinical models suggest that radiation activated TGF- β could contribute to metastasis inducing with the appearance of EMT [151–153], which is an

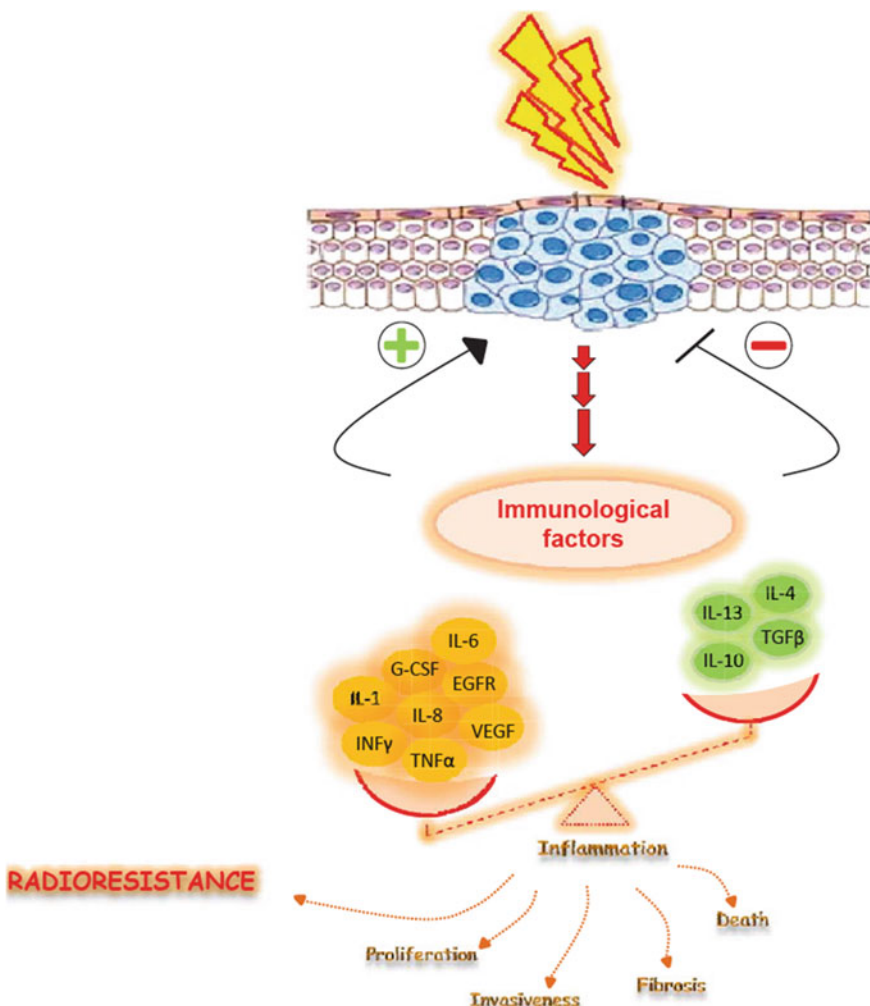


Fig. 4.4 The figure displays how IR could stimulate cancer cells to produce immunological factor able to regulate, in an opposite way, cell fate

important step in cancer invasion and metastasis [154–156]. In this perspective, Zhou et al. [157] related the IR induced enhancing of invasive capabilities with the TGF- β mediated EMT in cancer cells.

Furthermore, the TGF- β family proteins are even primarily involved in the initiation, development, and persistence of radiation induced fibrosis [158]. TGF- β 1 induces the extracellular proteolytic cleavage in response to the ROS production generated by IR [159]. Moreover, fibroblasts activation into myofibroblasts is another key step in radiation fibrosis [160].

Different in vitro and in vivo studies report that cells or tissues exposed to IR secrete many cytokines, chemokines and growth factors [161–163]. Cytokine production is time-dependent, peaking usually at 4–24 h after irradiation with subsequent decrease to baseline levels within 24 h to a few days [164]. However, their release is also qualitatively cell-type dependent and quantitative dose-dependent. An informative study has been conducted by the group of Desai [165], which compared the cytokines secretion profile of five human tumor cell lines. HT1080 (fibrosarcoma), U373MG (glioblastoma), HT29 (colon carcinoma), A549 (lung adenocarcinoma) and MCF-7 BC, either before (basal) or after acute (6 Gy) and fractionated doses (3×2 Gy) of gamma radiations. The authors observed that the secretion of certain cytokines was cell line-specific and that pro-inflammatory cytokines (TNF- α , IL-1 β , IL-6), growth factors (PDGF-AA, TGF- α , TGF- β 1) and chemokines (fractalkine, IL-8, MCP-1, and IP-10) were highly represented in irradiated conditioned medium (ICM), rather than immunomodulatory cytokines (IFN- γ , IL-2, IL-3, and IL-10). In addition, cytokine release increased markedly in a dose-dependent manner and that the magnitude of such increase was lower in ICM of tumor cells collected after fractionated IR doses compared to those collected after an acute dose [165].

Our group has also extensively evaluated the cytokine signatures released in the conditioned media by MCF10A epithelial cells, MCF7 and MDA-MB-231 BC cells after single high electron dose of 9 and 23 Gy delivered by IOERT, in order to evaluate differences in the immune signature profiles in terms of dose-effects [141]. Respect to the work of Desai et al. [165], our study has demonstrated that cell type differences are strongly observable among cell lines belonging to the same tissue type. Moreover, we also have explored, for the first time, an early and a late cytokine production profile to IR, analysing the time windows from 30 min to 24 h and from 24 to 72 h post IOERT treatments. The most relevant results were obtained from analysing the late time points, because the expression profiles observed within 24 h were characterized by low release of molecules in comparison to the late time points investigated. Concerning the cell line differences observed, three different cytokines signatures can be described for the three cell lines analyzed [141]. Particularly, respect to the non-tumorigenic MCF10A cells, MCF7 BC cells showed strongly reduced inflammatory signals in agreement with the study of Desai et al. [165], both in terms of systemic and local inflammation. On the other hand, the metastatic MDA-MB-231 BC cell line was characterized by an exacerbated inflammation signature, as these cells produced much higher levels of several cytokines and factors able to mediate stronger systemic and local cell responses. In our work, the MCF10A cell line, routinely used as a model of normal breast epithelial cells [36], could represent how normal breast tissue cells react to high doses of radiation. Their inflammatory profile was quite moderate and featured by signals related to a local inflammation and cell mediated response. Interestingly, overall the cell line signatures studied revealed that the cytokine secretion by epithelial mammary cell lines after high IR doses was featured by an unbalanced inflammation. Another remarkable consideration on our results concerns the observation that, at high doses delivered such as 9 and 23 Gy, the dose-effect affects

more the cell killing efficiency rather than the cytokines signature. In fact, the 9 Gy treatment induced the selection of radioresistant cell fractions (RCF) in MCF10A and MDA-MB-231 cells, which were analyzed in a very late time window (from 7 to 28 days after IR treatment). RCFs showed an increased and persistent production of pro-inflammatory cytokines, effect particularly exacerbated in MDA-MB-231 cell line [141]. Thus, our data suggest that an IOERT exclusive treatment using 23 Gy, could kill cells in a unique session freeing the tumor microenvironment of immune molecules able to affect the cell survival/cell death balance, metastasis and/or fibrosis induction and thus affecting the tumor outcome. In our study, some of the molecules characterized by a significant secretion increase after IR treatment participate to the senescence process induction and are listed among the senescence-associated secretory phenotype (SASP) [52, 54, 161, 166]. However, our results showed that the cell-senescence phenomenon did not correlate with the amount of SASP molecules released in media. Indeed, despite the low levels of some of these factors released, the MCF7 cells displayed a senescent phenotype. In contrast, MCF10A able to secrete significantly higher levels of these cytokines, did not become senescent. In addition, despite the high levels of SASP molecules produced by MCF10A and MDA-MB-231 RCF cells, we did not observe senescence traits from 7 to 28 days post irradiation. These observations suggest that additional mechanisms are probably needed to induce the senescent process. We also speculated that when cells resist to high IR dose are less prone to develop a senescent phenotype [141].

As it has described by this dissertation, the cell-type specific inflammatory local and systemic status, induced by IR treatment, generate a long list of direct and indirect consequences, which need to be more investigated for a better comprehension of detrimental or beneficial modification in peritumoral microenvironment, induced by different modalities of IR treatments.

It is hoped that these results could be translated soon in clinical practice, in order to improve personalized IR treatments, through the cytokine signature analysis of IR treated cancer cells from biopsy of candidate patients.

4.9 Conclusion

The main goal of Radiation Therapy is to deprive cancer cells of their reproductive potential, inducing neoplastic cell death. Radiation response is very complex because of the different cell types involved and several types of particles and doses delivered. In this context, particle acceleration driven by high-intensity laser systems is widely attracting interest as a potential alternative to conventional ion acceleration in order to improve tumor RT, mainly due to its flexibility and the unprecedented high dose-rate that can be delivered. In fact, the notable progress in laser particle acceleration technology promises potential medical application in cancer therapy and care.

In this chapter we tried to give the reader an idea of how powerful is the “OMICS” approach to this matter, in terms of both conceptual modeling and experimental researches. These latter have been performed so far mostly with Ionizing Radiation provided by conventional devices. Nevertheless, we showed that, in spite of the few and preliminary results already obtained with laser-driven sources of IR, this novel technique could provide a unique tool for radiobiological experiments addressed in the line of the OMICS approach to the field.

“OMICS” approach represents the best way to analyze biological effects induced by IR, i.e. direct or indirect damage to principal biological molecules, allowing also to find new biomarkers prognostic and predictive of the cell sensibility to IR [167]. The possibility to clarify cell molecular strategies to choose between death and survival, after an particle beam-induced damage, opens new avenues for the selection of a proper therapy schedule, to counteract cancer growth and preserve healthy surrounding tissue from radiation effects. “OMICS” research strategy combined with the availability of the emerging new class of laser-driven IR sources (featured by ultra-short IR pulses delivering ultra-high dose rate) could provide a novel powerful mean to progress in radiobiology and radiotherapy.

References

1. J. Bernier, E.J. Hall, A. Giaccia, Radiation oncology: a century of achievements. *Nat. Rev. Cancer* **4**, 737–747 (2004)
2. E.J. Hall, A.J. Giaccia, Radiobiology for the Radiologist. 6th edn. (Lippincott Williams & Wilkins, Philadelphia, 2006), pp. 16–180
3. G. Schettino, S.T. Al Rashid, K.M. Prise, Radiation microbeams as spatial and temporal probes of subcellular and tissue response. *Mutat. Res.* **704**(1–3), 68–77 (2010)
4. G. Kraft, M. Scholz, U. Bechthold, Tumor therapy and track structure. *Radiat. Environ. Biophys.* **38**(4), 229–237 (1999)
5. U. Linz, J. Alonso, What will it take for laser driven proton accelerators to be applied to tumor therapy? *Phys. Rev. St. Accel. Beams* **10**, 1–8 (2007)
6. A. Giulietti et al., Intense gamma-ray source in the Giant Dipole Resonance range driven by 10-TW laser pulses. *Phys. Rev. Lett.* **101**, 105002 (2008)
7. A. Giulietti, M.G. Andreassi, C. Greco, Pulsed radiobiology with laser-driven plasma accelerators, in *SPIE Proceedings*, vol. 8079, 80791J (2011)
8. O. Zlobinskaya, C. Siebenwirth, C. Greubel, V. Hable, R. Hertenberger, N. Humble, S. Reinhardt, D. Michalski, B. Röper, G. Multhoff, G. Dollinger, J.J. Wilkens, T.E. Schmid, The effects of ultra-high dose rate proton irradiation on growth delay in the treatment of human tumor xenografts in nude mice. *Radiat. Res.* **181**(2), 177–183 (2014)
9. D. Doria, K.F. Kakolee, S. Kar et al., Biological effectiveness on live cells of laser driven protons at dose rates exceeding 10^9 Gy/s. *AIP Adv.* **2**, 011209 (2012)
10. A. Yogo, K. Satoa, M. Nishikinoa, M. Moria, Radiobiological study by using laser-driven proton beams, in *AIP Conference Proceedings*, vol. 1153 (2009), p. 438
11. D. Doria, K.F. Kakolee, S. Kar, K.S. Litt, Biological cell irradiation at ultrahigh dose rate employing laser driven protons, in *AIP Conference Proceedings*, vol. 1462 (2012), p. 135
12. J. Bin, K. Allinger, W. Assmann, G. Dollinger, G.A. Drexler et al., A laser-driven nanosecond proton source for radiobiological studies. *Appl. Phys. Lett.* **101**, 243701 (2012)

13. L. Laschinsky, M. Baumann, E. Beyreuther, W. Enghardt, M. Kaluza, L. Karsch, E. Lessmann, D. Naumburger, M. Nicolai, C. Richter, R. Sauerbrey, H.P. Schlenvoigt, J. Pawelke, Radiobiological effectiveness of laser accelerated electrons in comparison to electron beams from a conventional linear accelerator. *J. Radiat. Res.* **53**(3), 395–403 (2012)
14. A.J. Giaccia, Molecular radiobiology: the state of the art. *J. Clin. Oncol.* **32**(26), 2871–2878 (2014)
15. L. Minafra, V. Bravatà, Cell and molecular response to IORT treatment. *Transl. Cancer Res.* **3**, 32–47 (2014)
16. S.P. Jackson, J. Bartek, The DNA-damage response in human biology and disease. *Nature* **461**(7267), 1071–1078 (2009)
17. C.M. West, G.C. Barnett, Genetics and genomics of radiotherapy toxicity: towards prediction. *Genome Med.* **3**, 52 (2011)
18. S. Renuse, R. Chaerkady, A. Pandey, Proteogenomics. *Proteomics* **11**(4), 620–630 (2011)
19. S. Faulkner, M.D. Dun, H. Hondermarck, Proteogenomics: emergence and promise. *Cell Mol. Life Sci.* **72**, 953–957 (2015)
20. V. Bravatà, F.P. Cammarata, G.I. Forte, L. Minafra, “OMICS” of HER2-positive breast cancer. *OMICS* **17**(3), 119–129 (2013)
21. J.D. Jaffe, H.C. Berg, G.M. Church, Proteogenomic mapping as a complementary method to perform genome annotation. *Proteomics* **4**, 59–77 (2004)
22. A.I. Nesvizhskii, Proteogenomics: concepts, applications and computational strategies. *Nat. Methods* **11**(11), 1114–1125 (2014)
23. P. Tamulevicius, M. Wang, G. Iliakis, Homology-directed repair is required for the development of radioresistance during S phase: interplay between double-strand break repair and checkpoint response. *Radiat. Res.* **167**, 1–11 (2007)
24. A.M. Güerci, F.N. Dulout, C.A. Grillo et al., Differential response of two cell lines sequentially irradiated with low X-ray doses. *Int. J. Radiat. Biol.* **81**, 367–372 (2005)
25. M. Ghardi, M. Moreels, B. Chatelain et al., Radiation induced double strand breaks and subsequent apoptotic DNA fragmentation in human peripheral blood mononuclear cells. *Int. J. Mol. Med.* **29**, 769–780 (2012)
26. E. Mladenov, S. Magin, A. Soni et al., DNA double-strand break repair as determinant of cellular radiosensitivity to killing and target in radiation therapy. *Front. Oncol.* **3**, 113 (2013)
27. B.J. Moeller, R.A. Richardson, M.W. Dewhirst, Hypoxia and radiotherapy: opportunities for improved outcomes in cancer treatment. *Cancer Metastasis Rev.* **26**, 241–248 (2007)
28. A. Kakarougkas, P. Jeggo, DNA DSB repair pathway choice: an orchestrated handover mechanism. *Br. J. Radiol.* **87**(1035), 20130685 (2014)
29. K. Rothkamm, M. Löbrich, Evidence for a lack of DNA double-strand break repair in human cells exposed to very low x-ray doses. *Proc. Natl. Acad. Sci. USA* **100**, 5057–5062 (2003)
30. L.M. Martin, B. Marples, M. Coffey et al., DNA mismatch repair and the DNA damage response to ionizing: making sense of apparently conflicting data. *Cancer Treat. Rev.* **36**, 518–527 (2010)
31. C. Escribano-Díaz, A. Orthwein, A. Fradet-Turcotte et al., A cell cycle-dependent regulatory circuit composed of 53BP1-RIF1 and BRCA1-CtIP controls DNA repair pathway choice. *Mol. Cell* **49**, 872–883 (2013)
32. J.H. Lee, T.T. Paull, Activation and regulation of ATM kinase activity in response to DNA double-strand breaks. *Oncogene* **26**, 7741–7748 (2007)
33. I.G. Cowell, N.J. Sunter, P.B. Singh et al., gammaH2AX foci form preferentially in euchromatin after ionising-radiation. *PLoS ONE* **2**(10), e1057 (2007)
34. J. Pflaum, S. Schlosser, M. Müller, p53 Family and cellular stress responses in cancer. *Front. Oncol.* **4**, 285 (2014)
35. V. Bravatà, L. Minafra, G. Russo, G.I. Forte, F.P. Cammarata, M. Ripamonti, C. Casarino, G. Augello, F. Costantini, G. Barbieri, C. Messa, M.C. Gilardi, High dose ionizing radiation regulates gene expression changes in MCF7 breast cancer cell line. *Anticancer Res.* **35**, 5 (2015)

36. L. Minafra, V. Bravatà, G. Russo, G.I. Forte, F.P. Cammarata, M. Ripamonti, G. Candiano, M. Cervello, A. Giallongo, G. Perconti, C. Messa, M.C. Gilardi, Gene expression profiling of MCF10A breast epithelial cells exposed to IOERT. *Anticancer Res.* **35**, 6 (2015)
37. S.D. Kraft, C. Richter, K. Zeil et al., Dose-dependent biological damage of tumor cells by laser-accelerated proton beams. *New J. Phys.* **12**, 085003 (2010)
38. R.A. Panganiban, A.L. Snow, R.M. Day, Mechanisms of radiation toxicity in transformed and non-transformed cells. *Int. J. Mol. Sci.* **14**, 15931–15958 (2013)
39. N.A.P. Franken, H.M. Rodermond, J. Stap, J. Haveman, C. van Bree, Clonogenic assay of cells in vitro. *Nat. Protoc.* **1**, 2315–2319 (2006)
40. O. Surova, B. Zhivotovsky, Various modes of cell death induced by DNA damage. *Oncogene* **32**(33), 3789–3797 (2013)
41. D. Eriksson, T. Stigbrand, Radiation-induced cell death mechanisms. *Tumor Biol.* **31**(4), 363–372 (2010)
42. R.D. Stewart, V.K. Yu, A.G. Georgakilas, C. Koumenis, J.H. Park, D.J. Carlson, Effects of radiation quality and oxygen on clustered DNA lesions and cell death. *Radiat. Res.* **176**(5), 587–602 (2011)
43. E.B. Golden, I. Pellicciotta, S. Demaria, M.H. Barcellos-Hoff, S.C. Formenti, The convergence of radiation and immunogenic cell death signalling pathways. *Front. Oncol.* **7**(2), 88 (2012)
44. Y. Fuchs, H. Steller, Programmed cell death in animal development and disease. *Cell* **147**(4), 742–758 (2011)
45. K. Kuribayashi, N. Finnberg, J.R. Jeffers, G.P. Zambetti, W.S. El-Deiry, The relative contribution of pro-apoptotic p53-target genes in the triggering of apoptosis following DNA damage in vitro and in vivo. *Cell Cycle* **10**(14), 2380–2389 (2011)
46. A.R. Cuddihy, R.G. Bristow, The p53 protein family and radiation sensitivity: yes or no? *Cancer Metastasis Rev.* **23**, 237–257 (2004)
47. D.J. Grdina, J.S. Murley, R.C. Miller, H.J. Mauceri, H.G. Sutton, J.J. Li, G.E. Woloschak, R.R. Weichselbaum, A survivin-associated adaptive response in radiation therapy. *Cancer Res.* **73**(14), 4418–4428 (2013)
48. R.A. Panganiban, O. Mungunsukh, R.M. Day, X-irradiation induces ER stress, apoptosis, and senescence in pulmonary artery endothelial cells. *Int. J. Radiat. Biol.* **89**(8), 656–667 (2013)
49. R.S. Hotchkiss, A. Strasser, J.E. McDunn, P.E. Swanson, Cell death. *N. Engl. J. Med.* **361** (16), 1570–1583 (2009)
50. L. Galluzzi, G. Kroemer, Necroptosis: a specialized pathway of programmed necrosis. *Cell* **135**(7), 1161–1163 (2008)
51. M.A. Nehs, C.I. Lin, D.E. Kozono, E.E. Whang, N.L. Cho, K. Zhu, J. Moalem, F.D. Moore Jr, D.T. Ruan, Necroptosis is a novel mechanism of radiation-induced cell death in anaplastic thyroid and adrenocortical cancers. *Surgery* **150**(6), 1032–1039 (2011)
52. F. Rodier, J. Campisi, Four faces of cellular senescence. *J. Cell Biol.* **192**(4), 547–556 (2011)
53. J. Campisi, Aging, cellular senescence and cancer. *Annu. Rev. Physiol.* **75**, 685–705 (2013)
54. T. Tchkonia, Y. Zhu, J. van Deursen, J. Campisi, J.L. Kirkland, Cellular senescence and the senescent secretory phenotype: therapeutic opportunities. *J. Clin. Invest.* **123**(3), 966–972 (2013)
55. M. Xiao, C.E. Inal, V.I. Parekh, C.M. Chang, M.H. Whitnall, 5-Androstenediol promotes survival of gamma-irradiated human hematopoietic progenitors through induction of nuclear factor-kappaB activation and granulocyte colony-stimulating factor expression. *Mol. Pharmacol.* **72**(2), 370–379 (2007)
56. M.S. Mendonca, H. Chin-Sinex, R. Dhaemers, L.E. Mead, M.C. Yoder, D.A. Ingram, Differential mechanisms of x-ray-induced cell death in human endothelial progenitor cells isolated from cord blood and adults. *Radiat. Res.* **176**(2), 208–216 (2011)
57. K.J. Lindsay, P.J. Coates, S.A. Lorimore, E.G. Wright, The genetic basis of tissue responses to ionizing radiation. *Br. J. Radiol.* **80**(Spec No 1), S2–S6 (2007)

58. M. Dodson, V. Darley-Usmar, J. Zhang, Cellular metabolic and autophagic pathways: traffic control by redox signalling. *Free Radic. Biol. Med.* **63**, 207–221 (2013)
59. D. Denton, S. Nicolson, S. Kumar, Cell death by autophagy: facts and apparent artefacts. *Cell Death Differ.* **19**(1), 87–95 (2012)
60. W.K. Wu, S.B. Coffelt, C.H. Cho, X.J. Wang, C.W. Lee, F.K. Chan, J. Yu, J.J. Sung, The autophagic paradox in cancer therapy. *Oncogene* **31**(8), 939–953 (2012)
61. H. Rodriguez-Rocha, A. Garcia-Garcia, M.I. Panayiotidis, R. Franco, DNA damage and autophagy. *Mutat. Res.* **711**(1–2), 158–166 (2011)
62. S. Palumbo, S. Comincini, Autophagy and ionizing radiation in tumors: the “survive or not survive” dilemma. *J. Cell. Physiol.* **228**(1), 1–8 (2013)
63. W. Zhuang, Z. Qin, Z. Liang, The role of autophagy in sensitizing malignant glioma cells to radiation therapy. *Acta Biochim. Biophys. Sin. (Shanghai)* **41**(5), 341–351 (2009)
64. S.H. Chang, A. Minai-Tehrani, J.Y. Shin, S. Park, J.E. Kim, K.N. Yu, S.H. Hong, C.M. Hong, K.H. Lee, G.R. Beck Jr, M.H. Cho, Beclin1-induced autophagy abrogates radioresistance of lung cancer cells by suppressing osteopontin. *J. Radiat. Res.* **53**(3), 422–432 (2012)
65. H. Chaachouay, P. Ohneseit, M. Toulany, R. Kehlbach, G. Multhoff, H.P. Rodemann, Autophagy contributes to resistance of tumor cells to ionizing radiation. *Radiother. Oncol.* **99**(3), 287–292 (2011)
66. Y. Kuwahara, T. Oikawa, Y. Ochiai, M.H. Roudkenar, M. Fukumoto, T. Shimura, Y. Ohtake, Y. Ohkubo, S. Mori, Y. Uchiyama, M. Fukumoto, Enhancement of autophagy is a potential modality for tumors refractory to radiotherapy. *Cell Death Dis.* **2**, e177 (2011)
67. D.A. Gewirtz, Autophagy and senescence in cancer therapy. *J. Cell. Physiol.* **229**(1), 6–9 (2014)
68. S. Mansilla, W. Priebe, J. Portugal, Mitotic catastrophe results in cell death by caspase-dependent and caspase-independent mechanisms. *Cell Cycle* **5**(1), 53–60 (2006)
69. I. Vitale, L. Galluzzi, M. Castedo, G. Kroemer, Mitotic catastrophe: a mechanism for avoiding genomic instability. *Nat. Rev. Mol. Cell Biol.* **12**(6), 385–392 (2011)
70. M.A. Surani, K. Hayashi, P. Hajkova, Genetic and epigenetic regulators of pluripotency. *Cell* **128**(4), 747–762 (2007)
71. T. Kouzarides, Chromatin modifications and their function. *Cell* **128**(4), 693–705 (2007)
72. P.A. Jones, S.B. Baylin, The epigenomics of cancer. *Cell* **128**(4), 683–692 (2007)
73. Y. Ilnytskyy, O. Kovalchuk, Non-targeted radiation effects—an epigenetic connection. *Mutat. Res.* **714**, 113–125 (2011)
74. I. Pogribny, J. Raiche, M. Slovack, O. Kovalchuk, Dose-dependence, sex- and tissue-specificity, and persistence of radiation-induced genomic DNA methylation changes. *Biochem. Biophys. Res. Commun.* **320**(4), 1253–1261 (2004)
75. D.A. Antwihi, K.M. Gabbara, W.D. Lancaster, D.M. Ruden, S.P. Zielske, Radiation-induced epigenetic DNA methylation modification of radiation-response pathways. *Epigenetics* **8**, 839–848 (2013)
76. C. Kuhmann, D. Weichenhan, M. Rehli, C. Plass, P. Schmezer, O. Popanda, DNA methylation changes in cells regrowing after fractionated ionizing radiation. *Radiother. Oncol.* **101**(1), 116–121 (2011)
77. M.A. Chaudhry, R.A. Omaruddin, Differential DNA methylation alterations in radiation sensitive and -resistant cells. *DNA Cell Biol.* **31**(6), 908–916 (2012)
78. W.F. Morgan, M.B. Sowa, Effects of ionizing radiation in non irradiated cells. *Proc. Natl. Acad. Sci. USA* **102**, 14127–14128 (2005)
79. W.F. Morgan, M.B. Sowa, Non-targeted bystander effects induced by ionizing radiation. *Mutat. Res.* **616**, 159–164 (2007)
80. K.K. Jella, A. Garcia, B. McClean, H.J. Byrne, F.M. Lyng, Cell death pathways in directly irradiated cells and cells exposed to medium from irradiated cells. *Int. J. Radiat. Biol.* **89**, 182–190 (2012)

81. A. Luce, A. Courtin, C. Levalois, S. Altmeyer-Morel, P.H. Romeo, S. Chevillard, J. Lebeau, Death receptor pathways mediate targeted and non-targeted effects of ionizing radiations in breast cancer cells. *Carcinogenesis* **30**(3), 432–439 (2009)
82. O. Kovalchuk, J.E. Baulch, Epigenetic changes and nontargeted radiation effects—is there a link? *Environ. Mol. Mutagen.* **49**, 16–25 (2008)
83. J.B. Little, Cellular radiation effects and the bystander response. *Mutat. Res.* **597**(1–2), 113–118 (2006)
84. W. Han, S. Chen, K.N. Yu, L. Wu, Nitric oxide mediated DNA double strand breaks induced in proliferating bystander cells after alpha-particle irradiation. *Mutat. Res.* **684**, 81–89 (2010)
85. O.A. Sedelnikova, A. Nakamura, O. Kovalchuk, I. Koturbash, S.A. Mitchell, S.A. Marino, D.J. Brenner, W.M. Bonner, DNA double-strand breaks form in bystander cells after microbeam irradiation of three-dimensional human tissue models. *Cancer Res.* **67**, 4295–4302 (2007)
86. R. Baskar, A.S. Balajee, C.R. Geard, Effects of low and high let radiations on bystander human lung fibroblast cell survival. *Int. J. Radiat. Biol.* **83**, 551–559 (2007)
87. J.G. Kim, M.T. Park, K. Heo, K.M. Yang, J.M. Yi, Epigenetics meets radiation biology as a new approach in cancer treatment. *Int. J. Mol. Sci.* **14**(7), 15059–15073 (2013)
88. L. Chin, J.W. Gray, Translating insights from the cancer genome into clinical practice. *Nature* **452**(7187), 553–563 (2008)
89. J.A. Sparano, H. Ostrer, P.A. Kenny, Translating genomic research into clinical practice: promise and pitfalls. *Am. Soc. Clin. Oncol. Educ. Book*, 15–23 (2013)
90. F.M. Di Maggio, L. Minafra, G.I. Forte et al., Portrait of inflammatory response to ionizing radiation treatment. *J. Inflamm. (Lond.)* **12**, 14 (2015)
91. P. Dent, A. Yacoub, P.B. Fisher et al., MAPK pathways in radiation responses. *Oncogene* **22**, 5885–5896 (2003)
92. W.H. McBride, K.S. Iwamoto, R. Syljuasen et al., The role of the ubiquitin/proteasome system in cellular responses to radiation. *Oncogene* **22**, 5755–5773 (2003)
93. Q. Gu, Y. He, J. Ji et al., Hypoxia-inducible factor 1 α (HIF-1 α) and reactive oxygen species (ROS) mediates radiation-induced invasiveness through the SDF-1 α /CXCR4 pathway in non-small cell lung carcinoma cells. *Oncotarget* **6**(13), 10893–10907 (2015)
94. P. Dent, A. Yacoub, J. Contessa, R. Caron, G. Amorino, K. Valerie et al., Stress and radiation-induced activation of multiple intracellular signalling pathways. *Radiat. Res.* **159**, 283–300 (2003)
95. T. Criswell, K. Leskov, S. Miyamoto, G. Luo, D.A. Boothman, Transcription factors activated in mammalian cells after clinically relevant doses of ionizing radiation. *Oncogene* **22**, 5813–5827 (2003)
96. B.B. Aggarwal, G. Sethi, K.S. Ahn, S.K. Sandur, M.K. Pandey, A.B. Kunnumakkara et al., Targeting signal-transducer-and-activator-of-transcription-3 for prevention and therapy of cancer: modern target but ancient solution. *Ann. N. Y. Acad. Sci.* **1091**, 151–169 (2006)
97. H. Shimamura, Y. Terada, T. Okado, H. Tanaka, S. Inoshita, S. Sasaki, The PI3-kinase-Akt pathway promotes mesangial cell survival and inhibits apoptosis in vitro via NF-kappa B and Bad. *J. Am. Soc. Nephrol.* **14**, 1427–1434 (2003)
98. C.E. Hellweg, The Nuclear Factor κ B pathway: A link to the immune system in the radiation response. *Cancer Lett.* **15**, 00122–00126 (2015). (pii S0304-3835)
99. X. Chen, B. Shen, L. Xia et al., Activation of nuclear factor kappaB in radioresistance of TP53-inactive human keratinocytes. *Cancer Res.* **62**, 1213–1221 (2002)
100. J. Veeraraghavan, M. Natarajan, S. Aravindan, T.S. Herman, N. Aravindan, Radiation-triggered tumor necrosis factor (TNF)- α -NF κ B cross-signalling favors survival advantage in human neuroblastoma cells. *J. Biol. Chem.* **286**, 21588–21600 (2011)
101. S. Aravindan, M. Natarajan, V. Awasthi, T.S. Herman, N. Aravindan, Novel synthetic monoketone transmute radiation triggered NF κ B-dependent TNF α cross-signalling feedback maintained NF κ B and favors neuroblastoma regression. *PLoS ONE* **8**(8), e72464 (2013)
102. H. Zhou, J. Gao, Z.Y. Lu, L. Lu, W. Dai, M. Xu, Role of c-Fos/JunD in protecting stress-induced cell death. *Cell Prolif.* **40**, 431–444 (2007)

103. M. Benkoussa, C. Brand, M.H. Delmotte, P. Formstecher, P. Lefebvre, Retinoic acid receptors inhibit AP1 activation by regulating extracellular signal-regulated kinase and CBP recruitment to an AP1-responsive promoter. *Mol. Cell. Biol.* **22**, 4522–4534 (2002)
104. R. Kajanne, P. Miettinen, M. Tenhunen et al., Transcription factor AP-1 promotes growth and radioresistance in prostate cancer cells. *Int. J. Oncol.* **35**, 1175–1182 (2009)
105. V. Calò, M. Migliavacca, V. Bazan, M. Macaluso, M. Buscemi, N. Gebbia et al., STAT proteins: from normal control of cellular events to tumorigenesis. *J. Cell. Physiol.* **197**, 157–168 (2003)
106. Y. Shen, G. Devgan, J.E. Darnell Jr, J.F. Bromberg, Constitutively activated Stat3 protects fibroblasts from serum withdrawal and UV-induced apoptosis and antagonizes the proapoptotic effects of activated Stat1. *Proc. Natl. Acad. Sci. USA* **98**, 1543–1548 (2001)
107. M.H. Tsai, J.A. Cook, G.V. Chandramouli et al., Gene expression profiling of breast, prostate, and glioma cells following single versus fractionated doses of radiation. *Cancer Res.* **67**, 3845–3852 (2007)
108. P. Vaupel, The role of hypoxia-induced factors in tumor progression. *Oncologist* **9**(Suppl 5), 10–17 (2004)
109. K.L. Bennewith, S. Dedhar, Targeting hypoxic tumor cells to overcome metastasis. *BMC Cancer* **11**, 504 (2011)
110. M. Yoshimura, S. Itasaka, H. Harada, M. Hiraoka, Microenvironment and radiation therapy. *Biomed. Res. Int.* **2013**, 685308 (2013)
111. N. Burrows, B. Telfer, G. Brabant, K.J. Williams, Inhibiting the phosphatidylinositide 3-kinase pathway blocks radiation-induced metastasis associated with Rho-GTPase and hypoxia-inducible factor-1 activity. *Radiother. Oncol.* **108**(3), 548–553 (2013)
112. R.K. Schmidt-Ullrich, P. Dent, S. Grant, R.B. Mikkelson, K. Valerie, Signal transduction and cellular radiation responses. *Radiat. Res.* **153**, 245–257 (2000)
113. A. Munshi, R. Ramesh, Mitogen-activated protein kinases and their role in radiation response. *Genes Cancer* **4**(9–10), 401–408 (2013)
114. S.A. Amundson, M. Bittner, Y. Chen et al., Fluorescent cDNA microarray hybridization reveals complexity and heterogeneity of cellular genotoxic stress responses. *Oncogene* **18**, 3666–3672 (1999)
115. K.Y. Jen, V.G. Cheung, Transcriptional response of lymphoblastoid cells to ionizing radiation. *Genome Res.* **13**, 2092–2100 (2003)
116. N.F. Marko, P.B. Dieffenbach, G. Yan et al., Does metabolic radiolabeling stimulate the stress response? Gene expression profiling reveals differential cellular responses to internal beta vs. external gamma radiation. *FASEB J* **17**, 1470–1486 (2003)
117. C. Su, G. Gao, S. Schneider, C. Helt, C. Weiss, M.A. O'Reilly, D. Bohmann, J. Zhao, DNA damage induces down regulation of histone gene expression through the G1 checkpoint pathway. *EMBO J.* **23**, 1133–1143 (2004)
118. S.A. Amundson, K.T. Do, S. Shahab et al., Identification of potential mRNA biomarkers in peripheral blood lymphocytes for human exposure to ionizing radiation. *Radiat. Res.* **154**, 342–346 (2000)
119. A. Suetens, M. Moreels, R. Quintens, S. Chirietti, K. Tabury, A. Michaux, V. Grégoire, S. Baatout, Carbon ion irradiation of the human prostate cancer cell line PC3: a whole genome microarray study. *Int. J. Oncol.* **44**(4), 1056–1072 (2014)
120. A.R. Snyder, W.F. Morgan, Gene expression profiling after irradiation: clues to understanding acute and persistent responses? *Cancer Metastasis Rev.* **23**, 259–268 (2004)
121. G.C. Barnett, C.M. West, A.M. Dunning et al., Normal tissue reactions to radiotherapy: towards tailoring treatment dose by genotype. *Nat. Rev. Cancer* **9**, 134–142 (2009)
122. N.G. Burnet, J. Johansen, I. Turesson, J. Nyman, J.H. Peacock, Describing patients' normal tissue reactions: concerning the possibility of individualising radiotherapy dose prescriptions based on potential predictive assays of normal tissue radiosensitivity. Steering Committee of the BioMed2 European Union Concerted Action Programme on the Development of Predictive Tests of Normal Tissue Response to Radiation Therapy. *Int. J. Cancer* **79**, 606–613 (1998)

123. T. Holscher, S.M. Bentzen, M. Baumann, Influence of connective tissue diseases on the expression of radiation side effects: a systematic review. *Radiother. Oncol.* **78**, 123–130 (2006)
124. G.C. Barnett, G. De Meerleer, S.L. Gulliford, M.R. Sydes, R.M. Elliott, D.P. Dearnaley, The impact of clinical factors on the development of late radiation toxicity: results from the Medical Research Council RT01 trial (ISRCTN47772397). *Clin. Oncol. (R. Coll. Radiol.)* **23**(9), 613–624 (2011)
125. N.G. Burnet, G.C. Barnett, R.M. Elliott, D.P. Dearnaley, P.D. Pharoah, A.M. Dunning, C.M. West, RAPPER investigators: RAPPER: the radiogenomics of radiation toxicity. *Clin. Oncol. (R. Coll. Radiol.)* **25**(7), 431–434 (2013)
126. D.B. Goldstein, Common genetic variation and human traits. *N. Engl. J. Med.* **360**, 1696–1698 (2009)
127. K. Offit, Genomic profiles for disease risk: predictive or premature? *JAMA* **299**, 1353–1355 (2008)
128. K. Offit, Breast cancer single-nucleotide polymorphisms: statistical significance and clinical utility. *J. Natl. Cancer Inst.* **101**, 973–975 (2009)
129. Z. Guo, Y. Shu, H. Zhou, W. Zhang, H. Wang, Radiogenomics helps to achieve personalized therapy by evaluating patient responses to radiation treatment. *Carcinogenesis* **36**(3), 307–317 (2015)
130. J.C. Liu, W.C. Shen, T.C. Shih, C.W. Tsai, W.S. Chang, Y. Cho, C.H. Tsai, D.T. Bau, The current progress and future prospects of personalized radiogenomic cancer study. *Biomedicine (Taipei)* **5**(1), 2 (2015)
131. N. Niu, Y. Qin, B.L. Fridley, J. Hou, K.R. Kalari, M. Zhu, T.Y. Wu, G.D. Jenkins, A. Batzler, L. Wang, Radiation pharmacogenomics: a genome-wide association approach to identify radiation response biomarkers using human lymphoblastoid cell lines. *Genome Res.* **20**, 1482–1492 (2010)
132. G.C. Barnett, D. Thompson, L. Fachal et al., A genome wide association study (GWAS) providing evidence of an association between common genetic variants and late radiotherapy toxicity. *Radiother. Oncol.* **111**, 178–185 (2014)
133. F. Chevalier, Highlights on the capacities of “Gel-based” proteomics. *Proteome Sci.* **8**, 23 (2010, Apr 28)
134. S. Skvortsov, P. Debbage, W.C. Cho et al., Putative biomarkers and therapeutic targets associated with radiation resistance. *Expert Rev. Proteomics* **11**(2), 207–214 (2014)
135. S. Jung, S. Lee, J. Lee et al., Protein expression pattern in response to ionizing radiation in MCF-7 human breast cancer cells. *Oncol. Lett.* **3**(1), 147–154 (2012)
136. E.C. Liao, Y.T. Hsu, Q.Y. Chuah et al., Radiation induces senescence and a bystander effect through metabolic alterations. *Cell Death Dis.* **5**, e1255 (2014)
137. S. Kedracka-Krok, U. Jankowska, M. Elas et al., Proteomic analysis of proton beam irradiated human melanoma cells. *PLoS ONE* **9**(1), e84621 (2014)
138. E.I. Azzam, J.P. Jay-Gerin, D. Pain, Ionizing radiation-induced metabolic oxidative stress and prolonged cell injury. *Cancer Lett.* **327**(1–2), 48–60 (2012)
139. F. Marchetti, M.A. Coleman, I.M. Jones et al., Candidate protein biodosimeters of human exposure to ionizing radiation. *Int. J. Radiat. Biol.* **82**(9), 605–639 (2006)
140. H. Li, Y. He, H. Zhang et al., Differential proteome and gene expression reveal response to carbon ion irradiation in pubertal mice testes. *Toxicol. Lett.* **225**(3), 433–444 (2014)
141. V. Bravatà, L. Minafra, G.I. Forte et al., Cytokine profile of conditioned medium from MCF10A mammary epithelial cell line and MCF7 and MDA-MB-231 breast cancer cell lines after high radiation doses. (Paper submitted) (2016)
142. S.I. Grivennikov, F.R. Greten, M. Karin, Immunity, inflammation, and cancer. *Cell* **140**, 883–899 (2010)
143. G. Multhoff, J. Radons, Radiation, inflammation, and immune responses in cancer. *Front. Oncol.* **2**, 58 (2012)
144. A. Deorukhkar, S. Krishnan, Targeting inflammatory pathways for tumor radiosensitization. *Biochem. Pharmacol.* **80**, 1904–1914 (2010)

145. D. Starenki, H. Namba, V. Saenko et al., Inhibition of nuclear factor-kappaB cascade potentiates the effect of a combination treatment of anaplastic thyroid cancer cells. *J. Clin. Endocrinol. Metab.* **89**, 410–418 (2004)
146. Y. Yamamoto, R.B. Gaynor, Therapeutic potential of inhibition of the NF-kappaB pathway in the treatment of inflammation and cancer. *J. Clin. Invest.* **107**, 135–142 (2001)
147. Z. Yang, L. Guo, D. Liu et al., Acquisition of resistance to trastuzumab in gastric cancer cells is associated with activation of IL-6/STAT3/Jagged-1/Notch positive feedback loop. *Oncotarget* **10**, 5072–5087 (2015)
148. Z.T. Schafer, J.S. Brugge, IL-6 involvement in epithelial cancers. *J. Clin. Invest.* **117**, 3660–3663 (2007)
149. Z. Culig, M. Puhr, Interleukin-6: a multifunctional targetable cytokine in human prostate cancer. *Mol. Cell. Endocrinol.* **360**, 52–58 (2012)
150. Y. Guo, F. Xu, T. Lu et al., Interleukin-6 signalling pathway intarted therapy for cancer. *Cancer Treat. Rev.* **38**, 904–910 (2012)
151. Y. Katsuno, S. Lamouille, R. Deryck, TGF- β signalling and epithelial mesenchymal transition in cancer progression. *Curr. Opin. Oncol.* **25**, 76–84 (2013)
152. K.L. Andarawewa, A.C. Erickson, W.S. Chou et al., Ionizing radiation predisposes nonmalignant human mammary epithelial cells to undergo transforming growth factor beta induced epithelial to mesenchymal transition. *Cancer Res.* **67**, 8662–8670 (2007)
153. M. Wang, M. Hada, J. Huff et al., Heavy ions can enhance TGF β mediated epithelial to mesenchymal transition. *J. Radiat. Res.* **53**, 51–57 (2012)
154. E. Buck, A. Eyzaguirre, S. Barr et al., Loss of homotypic cell adhesion by epithelial-mesenchymal transition or mutation limits sensitivity to epidermal growth factor receptor inhibition. *Mol. Cancer Ther.* **6**, 532–541 (2007)
155. L. Minafra, V. Bravatà, G.I. Forte et al., Gene expression profiling of epithelial-mesenchymal transition in primary breast cancer cell culture. *Anticancer Res.* **34**, 2173–2183 (2014)
156. L. Minafra, R. Norata, V. Bravatà et al., Unmasking epithelial-mesenchymal transition in a breast cancer primary culture: a study report. *BMC Res. Notes* **5**, 343 (2012)
157. Y.C. Zhou, J.Y. Liu, J. Li et al., Ionizing radiation promotes migration and invasion of cancer cells through transforming growth factor-beta-mediated epithelial-mesenchymal transition. *Int. J. Radiat. Oncol. Biol. Phys.* **81**, 1530–1537 (2011)
158. J. Yarnold, M.C. Brotons, Pathogenetic mechanisms in radiation fibrosis. *Radiother. Oncol.* **97**, 149–161 (2010)
159. M.F. Jobling, J.D. Mott, M.T. Finnegan et al., Isoform-specific activation of latent transforming growth factor beta (LTGF-beta) by reactive oxygen species. *Radiat. Res.* **166**, 839–848 (2006)
160. D. Sheppard, Transforming growth factor beta: a central modulator of pulmonary and airway inflammation and fibrosis. *Proc. Am. Thorac. Soc.* **3**, 413–417 (2006)
161. A.R. Young, M. Narita et al., SASP reflects senescence. *EMBO Rep.* **10**, 228–230 (2009)
162. J.P. Coppé, P.Y. Desprez, A. Krtolica et al., The senescence-associated secretory phenotype: the dark side of tumor suppression. *Annu. Rev. Pathol.* **5**, 99–118 (2010)
163. G.V. Raghuram, P.K. Mishra, Stress induced premature senescence: a new culprit in ovarian tumorigenesis? *Indian J. Med. Res.* **140**, S120–S129 (2014)
164. J. Brieger, P. Schroeder, J. Gosepath et al., Vascular endothelial growth factor and basic fibroblast growth factor are released by squamous cell carcinoma cell lines after irradiation and increase resistance to subsequent irradiation. *Int. J. Mol. Med.* **16**, 159–164 (2005)
165. S. Desai, A. Kumar, S. Laskar, B.N. Pandey, Cytokine profile of conditioned medium from human tumor cell lines after acute and fractionated doses of gamma radiation and its effect on survival of bystander tumor cells. *Cytokine* **61**, 54–62 (2013)
166. B. Frey, Y. Rubner, R. Wunderlich et al., Induction of abscopal anti-tumor immunity and immunogenic tumor cell death by ionizing irradiation—implications for cancer therapies. *Curr. Med. Chem.* **19**, 1751–1764 (2012)
167. M. Pucci, V. Bravatà, G.I. Forte et al., Caveolin-1, breast cancer and ionizing radiation. *Cancer Genomics Proteomics* **12**(3), 143–152 (2015)

Chapter 5

Radiological Safety in Laser Facilities

Andrew Simons

Abstract High intensity lasers have the capability of producing large numbers of electrons, ions, neutrons and photons which have sufficient energy, to create measurable levels of residual activity within the host facility. Activation of experimental targets is often an experimental goal but activation of diagnostics, vacuum chambers and the facility beyond needs to be considered. Experimenters, technicians and other facility personnel will come into contact with this equipment often within minutes of a shot or short series and their safety is the central concern to any facility or programme manager. For a medical facility the safety of the patient is paramount, i.e. ensuring the radiation interacts as intended whilst minimising doses from any secondary radiations and considering all other hazards. This is often managed in two ways: Pre-experiment or treatment assessment of the likely levels of activity and subsequent dose to personnel and patients; post-experiment monitoring through remote or portable diagnostics and personal dosimeters.

5.1 Introduction

The safety of personnel and visitors to a laser facility, either experimental or medical, is paramount. Before any work can or should commence with a new laser the risks must be fully assessed and properly mitigated. At the same time one must be practical. Money, time and knowledge are finite and ultimately an assessment that is suitable and sufficient for purpose should be sought. The sections of this chapter should be seen as a guide born of the practical experience gained from creating a safe operational envelope for the Orion facility [1] at AWE. This envelope seeks to maximise the use of the facility's lasers, minimise disruption to laser operations, minimise procedures for the facility users and ensure that the best techniques and practices are used to minimise the radiation dose to personnel.

A. Simons (✉)

Atomic Weapons Establishment, Aldermaston, Reading, UK
e-mail: Andrew.Simons@awe.co.uk

During the course of assessing the Orion laser facility two philosophies were used. The first had strict limits for the dose personnel could receive and that could be discharged from the facility. From an assessment point of view this system is relatively simple—assess likely doses and discharges and refuse any shots that will exceed them. The simplicity of this approach is appealing but it raises further issues. Discharge and dose limits are often given in terms of rates (sV/month or Bq/year). The simplest way is to limit the number of shots per year and set targets per shot. This can lead to inefficient use of the facility. Tracking the emissions and doses of every shot carries an overhead but does allow some flexibility in facility operation. When limits are not prescribed then estimates can be made of likely emissions, which can become a self imposed impediment to efficient operations. But overall what should be done if emissions are too low to measure and doses are statistically indistinguishable from the background. At this point a second philosophy utilised the Best Available Technique (BAT) approach. This is a much more subjective approach requiring the likely issues to be listed and a process of considering possible solutions before deciding which most suitably mitigates the issues identified. Thus there are no discharge or dose limits as such and this philosophy suggests that each experiment should consider, on a shot by shot basis, the likely dose and discharges to be created. This becomes impractical placing a lot of work on the facility users and the review process. Instead an operational envelope that overestimated the dose and discharge for any given shot was created. The mitigation strategy is guided by this overarching assessment of likely doses and discharge levels and rates that the facility could produce. Individual experiments are then assessed as to if they fall in or out of the scope of this envelope. If they fall outside then further work is required by the user to show that their unique application of the facility is safe. Determining the scope of the envelope is key, a well defined envelope will allow nearly all operations to proceed without over predicting the dose people could receive (increasing costs, unnecessarily inconveniencing staff and possibly curtailing the facility's capabilities) and discharges from the facility (again increasing costs and potentially altering a facilities design needlessly).

The remainder of this chapter is split into three sections:

1. Management strategies for radiological facilities—this discusses what should be considered before any simulation work or calculations are undertaken. It is too easy to undertake nugatory work because the correct questions have not been identified to begin with.
2. Assessment methods for activity and doses which describe the basics of these calculations, the tools developed at AWE to accomplish this and a brief discussion of more complex simulation tools.
3. Activation of the fluid environment—describing the activation of air and the creation and discharge of radioactive gaseous material.

There is then a summary section to draw the chapter together.

Terminology

There are several terms that are not common across all research disciplines to aid understanding and provide clarification several terms are defined below:

Field—A field is a convenient way of describing radiation. It is an ensemble concept with average properties of many radiation quanta (protons, neutrons, X-rays γ rays etc.) akin to temperature. Thus a field may have an average energy of the field quanta within it and a distribution of energies. The field's properties may vary with time. For some concepts it is easier to discuss the effects on a field rather than on the individual field quanta.

X-rays and gamma rays—Some disciplines use these labels differently. In nuclear physics the labels are applied according to the provenance of the photon. X-rays come from re-arrangements of the atomic electrons and γ rays come from the rearrangement of nucleons in the nucleus. In plasma physics X-rays have lower energies (<100 keV) while gamma rays have higher energies. Both schemes have merit with the nuclear physics definition being more appropriate for considering decays and the plasma physics scheme being more apt for spectroscopy.

Source term—A description of the radiation field(s) in a simulation. For deterministic codes this will be in functional form giving intensity information as a function of space, time and energy. For Monte-Carlo codes this description would be in the form of probability distributions allowing the energy and momentum of the fields to be sampled and input into simulated environments one quantum at a time.

5.2 Management Strategies for Radiological Facilities

Before any calculations are undertaken the first assessment should always be—what questions am I trying to answer. Some of these questions may be legislated for in the country of operation giving clarity as to what is and is not legal for example: What is the maximum permissible dose to the public or classified and monitored radiation workers or to patients? What is the maximum permissible level of radioactivity that may be discharged to the atmosphere? From where in a facility are radiological discharges permitted (activated material if uncontrolled can exit a facility through doors, windows or ventilation systems—is this wanted and permitted)?

The most basic questions to ask are:

Who am I protecting?

What am I protecting them from?

What equipment may be affected?

What constitutes a problem?

What constitutes protection?

Taking each question in turn:

Who am I protecting?

The intention is to protect everyone; the facility staff, visitors, service personnel, contractors and the public. Anyone who is going to come into contact with the hazards during the facilities entire lifecycle from commissioning, through normal use, facility and equipment upgrades and eventually disposal and decommissioning. Will there be any legacy issues and thus risk to people after the facility has closed? It is important to recognise at an early stage not to design and build a facility or machine that may operate for a few years and slowly create an environmental hazard or risk to personnel. Be sure to know where you have hazards for example gaseous activated products may occupy the entire volume within a vacuum envelope from the radiations origin to the eventual discharge point. Personnel may come into contact with this hazard anywhere along such a path.

What am I protecting them from?

Radiation and electromagnetic pulses are the two main radiological risks associated with laser operations. But from a management perspective ignorance and not respecting the hazards are the biggest issues. Ignorance of radiation dose levels and their effects can lead to staff ignorance or complacency or over complex mitigation strategies. One axiom to adopt is: Respect radiological hazards but only mitigate for the credible. That is to say promote awareness, assess the risks—based on likelihood of occurrence and severity of consequence—and mitigate proportionately to those assessments.

What equipment may be affected?

In the first instance any equipment near the radiation source may become activated. That is unstable nuclei may be created through one or more nuclear reactions. Target materials can become activated and then be dispersed all over the interaction chamber and vacuum pipe work and equipment located within these. Also consider gaseous products may be transported all the way through a facility either through a vacuum system or by activation of the air.

What constitutes a problem?

Largely this is down to the legislation of the host country for acceptable dose and discharge limits, however, there may be limits agreed by a company or institution with regulating authorities that supersede these limits. But one must also be aware of acceptable doses for visiting personnel e.g. a maintenance contract involving foreign nationals may only permit them to have a lower exposure.

What constitutes protection?

Managerially a good knowledge of and respect for radiation are the first forms of protection, everything flows from the head of a facility desiring to inspire the correct safety culture, minimising radiological hazards and informing and inspiring staff and

visitors to follow their lead. With informed staff, that are unafraid to challenge operational processes to check safety, the creation of hazards can be minimised. Practically reducing exposure times and levels are the obvious steps for mitigation. But protection from risks should begin well before these measures are considered at the concept phase of a project attempting to design out as many foreseeable issues as possible. The choice of facility layout, construction materials and methods for production of radiation all play a part in the creation of a radiological hazard. Following this process and procedures can be tailored to mitigate radiological risk.

5.2.1 Risk Mitigation Strategies

There is a wide choice of radiological mitigation strategies that can be tailored to suit the specific needs of a laser acceleration facility. If the facility has a specific purpose such as a medical treatment facility then the range of hazards can be assessed and appropriate designs tailored to mitigate those hazards adopted at an early stage. If a facility is to house an experimental facility then the mitigation strategy becomes more complex. It is impossible to foresee every possible experiment that may be fielded on a facility and thus the approach commonly adopted is to mitigate for a worse case. The issues are identifying what constitutes that worse case and the usually elevated cost implication. Flexibility is expensive—more concrete for greater shielding, more robust and complex control systems may be required and an increase in staff. This is particularly important for laser driven acceleration facilities that commonly have the issues of a laser laboratory combined with those of an accelerator facility.

From a radiological standpoint the Orion facility has adopted a three tier strategy: First a worse case operational envelope has been developed that defines an upper bound on the activity that may be produced on a shot by shot basis and an upper bound on the gaseous discharge—the bulk of operations work is anticipated to fall within this envelope. Secondly the proposer of a experiment (termed PI—principle investigator) is responsible for assessing if the likely radiological impact of the experiment falls outside the operational envelope and if it does then tailored calculations and/or simulations are required to satisfy the scheduling and facility committees that Orion will not put the public, staff or visitors at risk nor will discharge limits be broken. At this stage the PI should identify any likely activation hot spots (diagnostic snouts, laser-target mounts etc.) that are likely to become activated. Thirdly after a shot and before access is granted to the experimental teams, trained facility staff monitor the dose to ensure there is no risk to personnel in either the target hall or target chamber.

Any laser shot that produces more activity than expected is flagged and investigated—in practice this is extremely rare because of the overestimates in the operational envelope originally developed. The investigation's findings are then fed back to the facility's management team and a review learn and improve exercise is

undertaken which may recommend a change in practise, operational process or an amendment to the current levels of mitigation.

5.2.2 ERICPD

The full risk mitigation strategy employed at the Orion facility is a stepped process termed ERICPD: Elimination, Reduction, Isolation, Control, Protection and Discipline

Elimination of risks—i.e. design out risk. What are the options to reach the desired goal? Are any of these options practical? Should any facility be built at all? For an experimental or medical facility this is usually done as part of the bid to build in the first place. For a research facility where the advancement of science is the main focus then the elimination of risk is often fundamentally antagonistic to the evolving requirements of the scientific method. However, the elimination of risk should be considered as part of the scheduling process, i.e. refusing to field an experiment because the overall risk is too high—there are just too many unknowns. From a science perspective the prime question asked is often “Can I do this?” and from a facility perspective the prime question is “Should this be done?” This should also influence the types of radiation a facility can produce—handling neutrons can be particularly problematic—eliminating this as an option will save considerable time, money and resources.

For a treatment facility the elimination of risk is primarily a medical decision—should this treatment be offered? From a treatment facility perspective, through its design and operations phases, the onus is to ensure that the facility only exposes patients to exactly the doses from the radiation fields intended.

Reduction of risks—Consider all options for an operating process from a risk perspective. A prime example of this is material selection when building a facility, especially the laser interaction chamber and the equipment in the immediate vicinity. Some materials activate less and for shorter periods than others. To assess this fully the activity level and the half lives need to be considered: higher numbers of nuclei that are longer lived may pose a lower risk than shorter lived ones that are less numerous. A further example is the choice of laser-target interaction. A particular laser-target combination may give the highest number of field quanta with the optimal characteristics, but consider the effects of all the field quanta generated with the technique and does this introduce more overall risk, i.e. more overall activation or generate unwanted secondary radiation fields. For example it may be better to create a sub-optimal ion field to reduce the risks from protons or X-rays created at the same time.

Isolation of risks—Physically separate people from the radiological hazard through distance, shielding or time. For an experimental facility like Orion this entails removing personnel from the target hall and laser hall until post shot checks have been completed and the radiation dose levels have been checked. Isolation may then be ensured by engineering controls such as the use of interlock systems. For a medical

facility this may be done by generating the laser accelerated ions in one part of the facility and transporting them to the patient in another part. Also consider how, once a piece of equipment is activated, it will be stored and who will have access to it.

Control of risks—These are in the first instance engineering or else procedural methods for reducing risk. Engineering controls such as remote detection devices can serve to mitigate by providing feedback remotely from potentially hazardous areas. Control of risk through process is itself a risk. A process defines what the correct steps are but its weakness is with human error incorrectly interpreting or understanding the correct steps. Furthermore, a process can only cover so many scenarios before it is too unwieldy. Thus the process has a defined scope and any activities that fall outside this scope should not proceed without further review.

With activated materials or radiation sources if exposure cannot be avoided then control of the hazard is principally established by maximising distance and minimising time of exposure. This also means reducing the number of people exposed at any given time to a minimum, i.e. a single member of staff conducting a dose check before opening an area for generally use. Furthermore, controlling risks covers facility wide monitoring, i.e. the use of personal thermo-luminescent detectors to track personnel dose—ensuring no-one gets a high cumulative dose through daily operations—and facility radiation alarms if required.

Protection of personnel—if a risk cannot be eliminated or isolated and has been reduced as far as practical through design, engineering control and processes then the final steps involve direct mitigation strategies such as personal protective equipment (PPE). This is most likely to be in the form of gloves (rather than lead aprons) but a full assessment of the residual risk allows the correct PPE to be identified. With the correct culture, respect for and knowledge of the residual risks personnel are more likely to ensure PPE is used as required.

Discipline of personnel—This is paramount. Knowledge and respect of radiation is the first line of defence. Staff without suitable knowledge may accidentally overcome procedural controls or not understand when PPE is required. Everyone within a facility needs a basic knowledge, understanding and respect for the facility's risks including radiological hazards.

There is a large degree of defence in depth with the ERICPD strategy. No one element should be used in isolation (unless unavoidable). For example not all people in a facility may have knowledge of radiation—consider emergency workers. In this event the radiological risks will be mitigated by other factors such as the engineering controls failing safe or procedures being followed to secure hazardous items in suitable storage vessels.

5.2.3 Essential Messages

Developing the correct facility culture is essential. Staff and visitors need to develop a healthy respect for radiation being neither to afraid to work with it or too casual in the handling or assessment of it. For a medical facility patients should be made

aware of, and given the opportunity to understand, the rudimentary science behind their treatment. Staff training is essential. Knowledge of radiation, its affects and its likely forms with in a facility need to be shared with all facility personnel not just those likely to come into day to day contact with activated material. Anyone, a facility director, a member of cleaning staff, a laser technician even a visitor should be able to spot hazards and obey facility warnings and instructions. The discipline of staff and visitors need to be monitored and a vigilant mentality for safety works well for finding and correcting aberrant behaviour. The AWE Orion and the Rutherford Appleton Laboratory's Vulcan [2, 3] and Astra-Gemini [2, 4] facilities are examples of good safety practice for laser and radiological assessment and safety.

5.3 Assessment Methods for Activity and Doses

How should one approach the problem of assessing a radiological hazard—what level of effort and resource is appropriate? This depends on the type of facility the likely levels of radiation field production and the frequency of its generation. One of the current favoured methods is to adopt a full Monte-Carlo simulation strategy. This does provide a snap-shot of how a known radiation field will interact with the local environment and the simulation can be made as large and complex as is required (limited only by the computational resources available). This can become impractical for a research facility with many configurations and source terms to simulate. But this is not the only method and a lower level, first principles, approach may be sufficient especially if combined with a worse case methodology. Indeed a hybrid approach can be employed using a series of worse case scenarios, which define an operational envelope, which are then modelled in detail.

The following sections discuss the basics of first principle calculations for assessing activation in a number of simple scenarios. Then transport effects are introduced. Next a discussion of the likely radiation fields to be generated by lasers and the envelope fields developed for assessing the Orion facilities doses and discharges. There follows a description of the 1D solver codes devised to assess these simple activation scenarios and then a description of how these activities can be used to assess the doses staff may experience. Finally full simulation schemes are briefly discussed.

5.3.1 First Principle Calculations

A simple one dimensional scheme can often be adopted to give an estimate of the likely levels of activation. The scheme can accrue complexity as approximations are discarded but the basics of the scheme are introduced here.

The instantaneous population of a specific unstable nucleus (N) created within a target while exposed to a radiation field is given by:

$$N(t) = \sum_C \int_{t1}^{t2} \left(\int_{E1}^{E2} (S(E, t) \cdot \sigma_c(E) \cdot \rho_N \cdot x) \cdot \partial E - \lambda \cdot \bar{N} \right) \cdot \partial T \quad (5.1)$$

Note: Integral limits ($t1$, $t2$, $E1$ and $E2$) are defined by the times the radiation source is active and energy range of the spectrum and the threshold of the cross section being considered and the sum is over the reaction channels.

$S(E, t)$ —spectral flux function for the radiation field

$\sigma_c(E)$ —the specific cross section for the reaction channel

ρ_N —The number density of the target

x —The target thickness

ΔE —the width of the energy bin (may not be constant)

ΔT —the width of the temporal bin (may not be constant)

λ —is the half life of the reaction product being considered

\bar{N} —is the instantaneous average population of the reaction product given by

Other terms defined below

$$\bar{N} = \frac{\int_{t1}^{t1 + \partial t} N(t) \cdot \partial t}{\int_{t1}^{t1 + \partial t} \partial t} \quad (5.2)$$

This can be determined numerically by using the approximate relationship given in (5.3).

$$N(t) = \left[\sum_C \sum_t \sum_E S(E, t) \cdot \sigma_c(E) \cdot \rho_N \cdot x \cdot \Delta E - \lambda \cdot \bar{N} \right] \cdot \Delta T \quad (5.3)$$

The three summations are:

- Summing over all competing reaction channels creating the population
- Summing over the time the field interacts
- Summing over all energies
- $S(E, t)$ —spectral flux function for the radiation field (binned in steps of ΔE and ΔT)
- $\sigma_c(E)$ —the specific cross section for the reaction channel (described in steps of ΔE)
- \bar{N} —is the average population of the reaction product over the time interval ΔT

Caveats

The change in population over ΔT is small

The thickness of the sample (x) is short compared with the mean free path of all the radiation field quanta that contribute to the overlap integral between $S(E)$ and $\sigma_c(E)$.

A number of basic concepts have been introduced here:

- (a) The target property ρ_N requires a brief discussion. The number density is the number of target atoms for the specific channel being calculated. Thus what must be ascertained are the elemental and isotopic abundances of the specific isotope being considered. Then ρ_N may simply be obtained:

$$\rho_N = \frac{I_c \cdot m_c \cdot M}{V \cdot m_{isotope}} \quad (5.4)$$

I_c is the isotopic abundance (the decimal fraction of the abundance of the specific isotope in the element)

m_c is the mass fraction of the channel element of interest in the material

M is the mass of the material

V the volume of the material

$m_{isotope}$ is the mass of an atom of the channel material

Care must be taken to ensure that the isotopic and elemental fractions of materials are quoted by number fraction of atoms and not by mass fraction of atoms. Furthermore, this simple approach assumes a homogeneous mixture of the elements in the material of interest.

- (b) The spectral function $S(E,t)$ is the energy-time matrix of the radiation field with each element being the energy bin ΔE intensity averaged over the surface of the target per time interval ΔT . This matrix can be simplified to a spectrum provided it is temporally invariant. If only the amplitude of the spectrum changes rather than the spectral shape then this can be considered as two functions: $S(E)$ the energy spectrum of the field and $\xi(t)$ a function describing the intensity profile.

For laser-driven fields the non-zero intensity of the field is usually short on the natural timescale of the activation problem and thus the temporal function $\xi(t)$ can be considered δ -like. A major exception to this is high-repetition rate systems such as Astra-Gemini [2, 4] or the proposed ELI-NP systems [5, 6]. In these circumstances a function such as a Dirac comb would be most appropriate.

For many short-pulse systems including ORION [2, 3] and Vulcan [2, 4] a single pulse is considered and the temporal integral is not required. Thus the problem may now be modelled as an instantaneous creation and a simple decay from this point forward and (5.3) is simplified to:

$$N_0 = \sum_C \sum_E S(E) \cdot \sigma_C(E) \cdot \rho_N \cdot x \cdot \Delta E \quad (5.5)$$

where:

N_0 —is the population created in the interaction of the field with the target
 $S(E)$ is the spectral function of the field integrated over the full interaction
 $\sigma_c(E)$, ρ_N , x and ΔE are as defined before

The decay of this population is simply described by (5.6).

$$N(t) = N_0 e^{-\lambda t} \quad (5.6)$$

- (c) The cross section $\sigma_c(E)$ is uniquely defined per channel. A channel is defined by two parameters—the entry channel and the exit channel. The entry channel is defined by the target atoms being considered (X) and the radiation field quanta (a), the minor reaction product or products (b) and the main residual nucleus. This is usually written as:

$$X(a, b)Y \quad (5.7)$$

Usually a calculation is undertaken to find the number of atoms created (Y) given a known target of atoms (X) being impinged on by known field quanta of type (a). Care must be taken that all channels that fulfil these requirements are summed in a calculation. For example consider $^{27}\text{Al}(p, d)^{26}\text{Al}$ —that is a proton (p) reacts with an ^{27}Al nucleus creating a deuterium nucleus (d) and a ^{26}Al residual nucleus—the nomenclature used is n—neutron, p—proton, d—deuteron (^2H), t—triton (^3H) and α —alpha particle (^4He) as these are the most likely particles to be liberated/created during a reaction.

A cross section for this reaction can be found and the calculation performed to find the number of ^{26}Al atoms created. But the reaction $^{27}\text{Al}(p, p+n)^{26}\text{Al}$ will also contribute to the final population of ^{26}Al atoms created and thus must be calculated and summed with the previous answer.

This example may seem trivial but consider a material like steel. It will be composed of numerous elements and some like iron, manganese and chromium can interact to create the same final isotope. Consider ^{54}Mn production from a proton field interacting with stainless steel material as shown in Fig. 5.1

The channels $^{53}\text{Cr}(p, \gamma)^{54}\text{Mn}$, $^{54}\text{Cr}(p, n)^{54}\text{Mn}$, $^{55}\text{Mn}(p, d)^{54}\text{Mn}$, $^{55}\text{Mn}(p, p+n)^{54}\text{Mn}$, $^{56}\text{Fe}(p, ^3\text{He})^{54}\text{Mn}$, $^{56}\text{Fe}(p, 2p+n)^{54}\text{Mn}$, $^{56}\text{Fe}(p, d+p)^{54}\text{Mn}$, $^{57}\text{Fe}(p, ^4\text{He})^{54}\text{Mn}$, $^{57}\text{Fe}(p, 2d)^{54}\text{Mn}$, $^{57}\text{Fe}(p, ^3\text{He}+n)^{54}\text{Mn}$, $^{57}\text{Fe}(p, t+p)^{54}\text{Mn}$, $^{58}\text{Fe}(p, ^4\text{He}+n)^{54}\text{Mn}$, $^{58}\text{Fe}(p, 2d+n)^{54}\text{Mn}$, $^{58}\text{Fe}(p, ^3\text{H}+d)^{54}\text{Mn}$ and $^{58}\text{Fe}(p, ^3\text{He}+2n)^{54}\text{Mn}$ are all possible and all create the same isotope. Thus to calculate the correct production of ^{54}Mn all channels must be considered. This situation becomes further complicated if the radiation field contains a number of field quanta types, protons, deuterons, alphas and X-rays for example. In this scenario each type of field quanta should be considered separately to avoid confusion.

Co55	Co56	Co57	Co58	Co59
Fe54	Fe55	Fe56	Fe57	Fe58
Mn53	Mn54	Mn55	Mn56	Mn57
Cr52	Cr53	Cr54	Cr55	Cr56

Fig. 5.1 A portion of the Segre chart depicting the elements that may be found in steel. There are multiple ways to create the same activated isotope ^{54}Mn from the isotopes in some types of steel

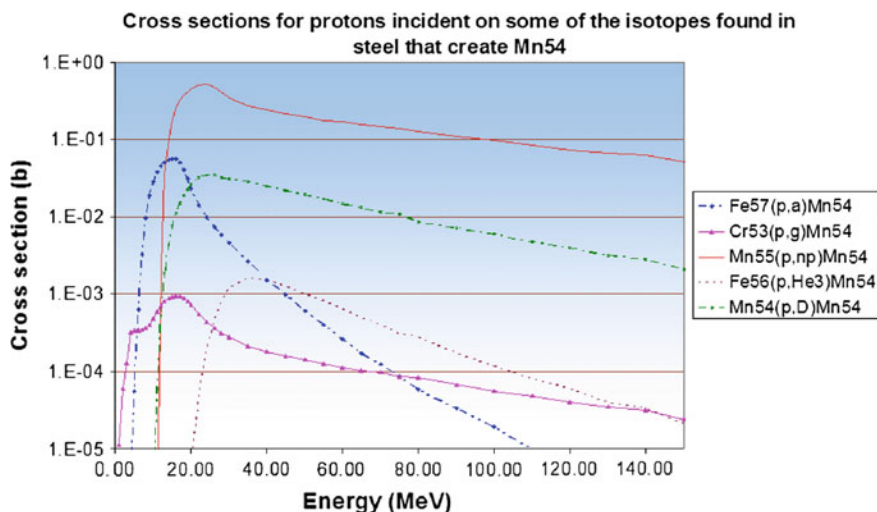


Fig. 5.2 A plot of the cross sections from Cr, Mn and Fe isotopes that may lead to the creation of ^{54}Mn . Not all of the reactions listed have cross section data available created with Janis [7]

It is possible to truncate the list of possible reactions by considering likely reactions. Consider Fig. 5.2

An assumption often made is that the reason for data being missing is due to the channel being small—else it would be easy to measure—this is often likely true but isn't strictly robust. However, there is nothing that can be done if there is no nuclear data in any of the nuclear data libraries save calculating a likely cross section with a code such as Taly [8–10] or GNASH [11]. One tool for checking multiple libraries and evaluation databases is Janis [7]. Note: always check the Exfor database, (now re-named Csisrs) [12, 13], for experimental data in the absence of, or as a check of, evaluated and calculated data.

As a general rule of thumb the more particles liberated the less likely the specific channel is to occur and the more energy will be required to access the channel. Discounting some channels can be done using Qtool [14] simply input the highest energy expected of the relevant field quanta and it will calculate the feasible channels. This can still be misleading as it does not give probabilities (relative or actual) but in general emission of an alpha particle is far more likely than the emission of 2d or t+p or ${}^3\text{He}+\text{n}$. Care should be taken with the emission of a deuterons as this is often smaller but not negligible when compared to the emission of n+p.

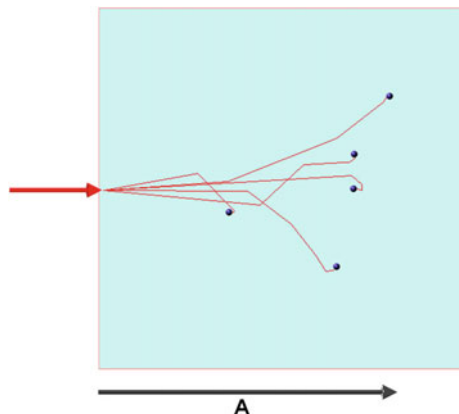
A comparison of the reaction cross sections is only part of the full analysis. The elemental and isotopic abundances (in terms of relative number of atoms not by weight) must also be considered. For the steel elements example this may be 50 % iron, 3 % chromium and 5 % manganese by element with ${}^{53}\text{Cr}$ being 9.5 % abundant in chromium and ${}^{54}\text{Cr}$ being 2.4 % abundant. In manganese ${}^{55}\text{Mn}$ is the only stable isotope and thus is 100 % abundant and for iron ${}^{56}\text{Fe}$ is 91.2 % abundant, ${}^{57}\text{Fe}$ is 2.1 % and ${}^{58}\text{Fe}$ is 0.3 %. Thus each cross section should be scaled by a factor of the elemental abundance multiplied by the isotopic abundance. So for reactions on ${}^{57}\text{Fe}$ a factor of 0.0105 should be applied. A comparison can now be made of these relative “cross sections” scaled specifically to the material being analysed. Often a visual inspection is all that is required to see that some cross sections will not contribute significantly (less than a percent) to the final answer and can be discarded.

- (d) There are several approaches for the target thickness x that can be used. The simplest is to use the longest vector through the material seen by the radiation field. This neglects any scattering of the field. The worst case is to use largest dimension of the object and perform a calculation—this can obviously lead to huge overestimations but if the result is still so low as to not be of concern then there is no need to refine any further.

If refinement is needed then the range of an ion in a given material can be used—this can be calculated simply using SRIM [15]. The SRIM program can also be used to gauge the likely level of scattering in a 2D calculation. This will give an indication as to the appropriateness of making a simple 1D calculation. An even simpler worse case approach can be taken—consider Fig. 5.3. A SRIM calculation will give an average range of a particle to be worst case one may wish to consider the longest path that could be travelled. Simply taking the maximum 1D distance (labelled A) traversed in the simulation and multiplying by a factor of 1.5 or 2 will give an overestimate. For many calculations this figure is sufficient. Note that TRIM will calculate a range should this be desired.

Thus it is visually simple to check the maximum range or an ion with a given energy. The x value could be made energy dependent but for a simple calculation use SRIM to calculate the maximum range of the highest energy particle to be considered. If further refinements are needed then transport issues must be considered (see next section).

Fig. 5.3 Appropriateness of x for simple calculations. Ions are tracked through a SRIM simulation as they enter a medium. The initial energy is specified and a number of potential histories are generated. SRIM will calculate the range and generate a plot similar to the image above complete with axes. For a simple overestimation of x take the distance A and multiply by a factor of 1.5 to 2



- (e) There is one point to note for ΔT and ΔE and that is they do not need to be constant. A group structure can be implemented in both the energy and time domains of the problem but care must be taken that appropriate averaging is done especially for the channel cross sections. For example if the channel cross section is unvarying over the range ΔE then the choice of value to represent the cross section over this bin is simple. If it is rapidly varying then this presents an issue especially if in the same bin the spectral function is also rapidly varying.

In (5.1) the decrease in population in time ΔT is taken as the average activity of the time step multiplied by the time step. For ΔT that is too large this may provide an erroneous answer depending on the averaging scheme. Care must be taken to ensure the binning scheme is appropriate as large inaccuracies can be obtained simply through inappropriate binning choices.

5.3.2 Transport

For interactions of fields with objects with dimensions larger than a few percent of any field quanta's mean free path then transport effects must be included in the calculation. In essence these effects modify the original field function $S(E,t)$ as the field quanta are scattered, absorbed or created through interactions. The inclusion of transport effects significantly increases the complexity as the problem must now be broken down into path lengths (ΔX) short enough that transport effects with the step are small. For each path step the population is calculated and then separately a new

field function $S(E,t)$ ' is calculated. The most appropriate scheme depends upon both the scale of the problem and the field type being considered.

Proton/Ion transport

The most important effect to consider is stopping. For a 1D calculation the energy of each field quanta needs to be re-assessed. The basic method for calculating energy loss is the Bethe-Bloch formula [17, 18] see (5.8).

$$\frac{dE}{dx} = \frac{4\pi Z^2 e^4 Z_t N L_0}{m_e v^2} \quad \text{where } L_0 = \ln\left(\frac{2mc^2\beta^2\gamma^2}{I}\right) - \beta^2 \quad (5.8)$$

Here:

- dE/dx is typically calculated in units MeV per cm
- N is the number density of the target atoms in cm^{-3}
- β B is simply $\frac{v}{c}$
- γ is the standard relativistic factor $\left[1 - \frac{v^2}{c^2}\right]^{-1/2}$
- Z_t is the target atoms atomic number
- Z is the projectiles atomic number
- m_e is the electron mass (with $m_e c^2 = 0.511 \text{ MeV}$)
- L_0 is termed the stopping number
- I is the average excitation energy of all electrons in the target atoms and a value of $11.4Z_t$ (in eV) can be used for work at this level [19].

There are several points to note regarding the Bethe formula:

It is independent of the mass of the stopping particle because the interaction imparts momentum primarily to the electrons rather than to the ions. Furthermore, the key component suggested by Bohr, is the relative velocity of the ion to the velocity of the outer electrons orbiting atoms in the stopping materials—the electrons orbit at the Bohr velocity or 13.6 eV for electrons. 25 keV protons have a similar velocity to these electrons and thus there is optimal chance for energy exchange between the stopping ion and the electrons. At lower velocities the electron orbit becomes perturbed and less energy is transferred while at higher velocities the impulse transfer is reduced due to the interaction lasting for a shorter time.

The formula was derived for interactions with free atoms i.e. the stopping material is treated as a series of non-interacting atoms with no binding to nearest neighbours.

There are two further terms that are now usually added to L_0 in Bethe's original equation:

The $-C/Zt$ term is a correction term accounting for different contributions from different electron shells—the different shells having considerably different orbital velocities so for a given ion velocity they will contribute at different levels. Calculations of this term are beyond the scope of this brief discussion. It is worth noting that for light ions with less complex electronic configurations this term produces an overall change around the 5 % level.

The $-\delta/2$ term accounts for the density effect, that is, the field of an ion is reduced by a materials dielectric constant, reducing the field felt by atomic electrons and hence reducing stopping at high energies. This term has little affect except for high energies (100 s MeV/amu).

A typical value for the stopping power in air for a 10 MeV proton is ~ 0.045 MeV/mm for an MeV proton this reduces to ~ 0.002 MeV/mm.

The field of ion stopping is much larger than this chapter can do justice to and (5.8) gives only the basic introduction to stopping. For further summaries see references [15, 19, 20] with fuller descriptions given in [21, 22].

For a simple calculation scheme a library of stopping powers is required. For protons or helium ions NIST's Pstar and Astar libraries [23] can be used. For a full library of interactions TRIM calculations (within SRIM [15, 16]) will give a list of stopping powers. Here again binning can be an issue if the ΔE of the $S(E,t)$ function is large compared to the change in the stopping function over that bin.

Assuming that $S(E,t)$ can be broken into spectral pulses $S(E)$ at the source and transport of each pulse can be calculated separately then $S(E)$ will describe a number of field quanta (N) per energy bin (ΔE). The field quanta in each bin are associated with the average energy of that bin. As they traverse ΔX they will lose energy ΔE and populate a lower energy bin. Doing this for all energy bins will transform $S(E,t)$ to $S(E,t)'$ for the next step.

5.3.2.1 Photon Transport

Photon fields interact with matter by five main processes: Elastic scattering (Rayleigh or coherent scattering; indexed cs), Inelastic scattering (Compton or incoherent scattering; indexed ics), photoelectric absorption (indexed pa), pair production (indexed pp) and to a much reduced extent photo-nuclear reactions (indexed pn). And the cross sections for each of these processes sum to give the total cross section for photon interaction:

$$\sigma_{tot} = \sigma_{cs} + \sigma_{ics} + \sigma_{pa} + \sigma_{pp} + \sigma_{pn} \quad (5.9)$$

The total cross section is related to the mass absorption coefficient (μ/ρ) by:

$$\left(\frac{\mu}{\rho}\right) = \frac{\sigma_{tot}}{uA} \quad (5.10)$$

where:

U is the atomic mass unit ($1.6605E-27$ kg)

A is the atomic mass of the atoms in the material

For the purposes of modelling the transport of the photon field through matter inelastic scattering and pair production are of principle importance at the energies required for nuclear activation, i.e. a few MeV and above. These mechanisms will

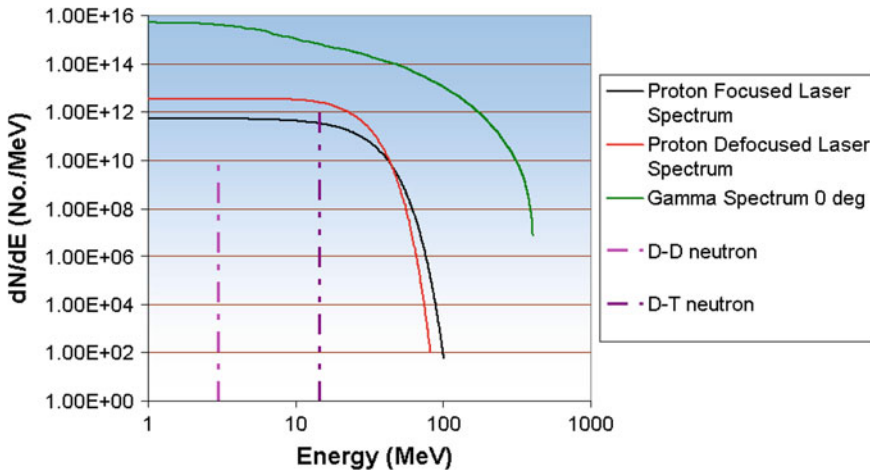


Fig. 5.4 Envelope spectra developed for use assessing doses on the Orion facility. Note double log scale

reduce the intensity of the initial radiation field at higher energies and produce a secondary scattered field component consisting of lower energy photons. Next an approximation is made that this secondary field need not be considered because of its reduced intensity and lower energy quanta.

The primary radiation field spectrum is reduced at each energy by a mass attenuation coefficient according to (5.9).

$$I = I_0 \exp(-(\mu/\rho) \cdot \rho \cdot x) \quad (5.11)$$

Tables of mass attenuation coefficients can be found at reference [24]. While this approach is not strictly rigorous it does preserve the maximum number of the initial radiation field quanta for a 1D simulation and thus maximise the number of photons above any threshold for nuclear reactions. It may not give the correct number of photons in the region of a cross section resonance as it is assumed here that the depletion from the relevant bins due to these processes is greater than the additional population from higher energy bins down-scattering.

In general this has been shown to be a good approximation for the hard X-ray spectra sources considered for Orion as the number of photons per bin decreases exponentially with energy (see Fig. 5.4) and the total attenuation curves for all materials slowly rise by a factor of a few from ~ 10 to ~ 100 MeV to a near constant value at higher energies.

5.3.2.2 Neutron Transport

Neutron transport is harder to simplify than the transport of ions or photons largely because they have longer mean free paths and when neutrons down scatter the

chance of undergoing a nuclear reaction increases. In all cases if neutron field transport is needed then much more rigorous treatments are needed such as Monte Carlo simulations.

For completeness the following case for a simple calculation can be made. The mean free path of a neutron (Λ) is given by:

$$\Lambda = (\sigma \cdot \rho_N)^{-1} \quad (5.12)$$

where:

ρ_N is the number density of the material being considered

σ is the total reaction cross section for neutrons within that material

If the activity is being assessed in a material with dimensions far smaller than Λ and the space around it is devoid of scattering centres then a simplified scheme with no transport is applicable.

5.3.2.3 Field Types

To this point the discussion of fields has been generic with the field being discussed in general terms as a function of energy and possibly time $S(E,t)$. The first assessment to be made is the likely form of $S(E)$ —which quanta will be produced in what number with which energies.

The discussion that follows largely concentrates on the fields assessed for the Orion laser at AWE. There are an inexhaustible number of scenarios for laser-target interactions with multiple lasers, complex target geometries and layering. What was done was to simplify the assessment by not attempting to quantify the exact nature of any field that could be generated but rather to establish credible bounding cases for each distinct field type. If an experiment were to produce a mixed field then the appropriate bounding cases would be summed and a single figure for a worse-case activity generated.

5.3.3 Proton and Ion Producing Laser-Targets

These are typically flat foils of a few to a few hundred microns thickness. Following the laser interaction a dense plasma forms which is opaque to the incident laser. The laser interacts with this plasma and electrons are accelerated via the two dominant mechanisms of resonance absorption [25] and ponderomotive acceleration [26]. A portion of this electron population is accelerated through the target creating a space charge electrostatic field near the rear of the target (of the order of Teravolts per metre). This space charge field is the mechanism by which the ion are accelerated termed TNSA target normal sheath acceleration. Typically hydrocarbon and water contaminants adsorbed onto the surface of these foils experience the

electrostatic force generated by the space charge fields and the protons, having the highest charge to mass are accelerated preferentially. Gold (20 µm) and aluminium (100 µm) foils are broadly considered to give the ‘best’ proton acceleration for Petawatt class lasers—though this is highly subjective.

In order to accelerate ions with a high degree of efficiency the laser targets must have the hydrocarbon layer cleaned off. The bulk ions then see the full electrostatic field. A more complete and detailed description of the possible ion acceleration scheme with lasers can be read in other chapters of this book. From radiation safety point of view the consideration below can be basically applied to all of these schemes.

The exact shape of the spectrum obtained varies from shot to shot with many parameters including, laser energy, laser focus, laser contrast prior to main pulse, target thickness, target morphology and topography, target composition, and target surface contamination. The approach taken to assess Orion was to utilise data taken at the Vulcan [2, 3] laser (rather than create a best fit or average fit to the data sets) to create an envelope encompassed all the spectra that had been observed. This envelope was to be sufficient to account for future “hot shots” producing unexpectedly energetic spectra either through the number of proton or ion field quanta generated or by an increase in the end point energy of the spectrum. The requirement does not need to be anymore rigorously defined than this. A more generous spectral envelope will give more activity but a greater degree of experimental flexibility.

Both the RAL Vulcan Petawatt’s [3] and 100 Terawatt system’s [2] spectra were considered in an attempt to capture the effects of changing the laser intensity on target. The assumptions were that a tightly focused Orion short-pulse laser spot will give a spectrum similar to the Vulcan Petawatt system. Defocusing the laser to reduce the intensity delivered to target by a factor of 10 it is assumed would give a spectrum similar to the 100 terawatt system (as the intensities delivered to target are the same), however, the magnitude of the spectrum is increased by the factor of 10. Thus a “best-focused” proton spectral envelope is a worse case in terms of more highly energetic protons and the defocused proton spectral envelope is a worse-case for more protons with lower energies. This is shown in Fig. 5.4.

5.3.4 *Photon Producing Targets*

The worse-case photon production targets are generally thicker (in the range 1–5 mm) and made of heavy materials such as tungsten. Electrons are accelerated during the laser interaction and travel through the target scattering and stopping, thus creating a Bremsstrahlung source. Since the electrons are relativistic the photons emitted will be forward peaked.

A photon spectrum has been devised from experimentally measured differential photon spectra—a worse-case methodology was again employed in the fitting of

this spectrum and the maximum credible energy that can be present in the spectrum given pessimistic conversion factors. The spectrum created was differentiated by twenty degree cone angles, however the forward cone angle (0°) was used as this contained the greatest number of, and the most energetic, field quanta.

5.3.5 Neutron Targets

The targets considered are small spheres, typically made from glass, containing a mix of deuterium and tritium gas. Long pulse lasers compress the DT gas mixture and initiate fusion reactions. Deuterium and tritium nuclei fuse creating an alpha particle and a neutron with a kinetic energy of 14.5 MeV. Two deuterium nuclei may also fuse releasing a 2.45 MeV neutron. This type of target is expected to produce an isotropic neutron emission spectrum with two peaks. Utilising the Orion facility's 10 long pulse lasers the predicted best case output was expected to be of $\sim 10^{13}$ neutrons at ~ 14.5 MeV and $\sim 10^{11}$ neutrons at ~ 2.45 MeV. This neutron spectrum has been assessed to be an overestimate in terms of yield (by \sim an order of magnitude) thus it represents a worse-case for activation. No attempt was made to assess activation or dose from back-scattered neutrons; only the initial spectrum is considered to interact, on a single pass, with the targets considered. Such an assessment requires a more sophisticated treatment than a 1D approach can provide.

Other schemes for neutron production have been demonstrated such as the laser break-out afterburner (or BOA) [27]. In this technique the intense laser field is impinged upon thin <0.5 μm targets. The laser field accelerates electrons through the target and penetrates through the target's bulk continuously accelerating electrons and thus increasing the length of the space charge separation region at the rear of the target. This in turn allows for greater numbers of ions to be accelerated to higher energies. This mechanism has been demonstrated [28] and used to accelerate deuterons to energies up to ~ 150 MeV. The deuterons will break up and create a forward peaked neutron field or will undergo nuclear reactions which in turn produce neutrons. This scheme was not included in the Orion safety case but has been subsequently assessed using MCNP. This is one of the first experimental proposals that has fallen outside of the originally assessed envelope.

5.3.6 1D Simulator

A code has been developed at AWE which calculates the populations of activated nuclei with the assumptions and limits of applicability detailed in the previous sections. As the scope of the activation problems for the Orion Facility increased it became increasingly difficult to justify which reactions to include or exclude. This was resolved by linking the existing 1D solver to nuclear data libraries and the Talys 1.0 codes. Talys in particular calculated the energetically possible reactions

and the cross sections for each one-one calculation for each cross section at the mid point of each bin in the group structure specified. The output of the code gives the number of activated nuclei sorted and listed by the creating reaction.

A flow diagram of the logic of this simple 1D solver is shown in Fig. 5.5.

This code (once combined with Talys 1.0) was used as the workhorse for the Orion safety case assessing both potential activation issues and discharge issues—creating the library of results that have been interpolated with appropriate functional forms and that can now be accessed through a simple spread sheet interface.

This library of results is unique to the Orion facility largely because of the approximations made and their validity to the facilities current radiation sources and

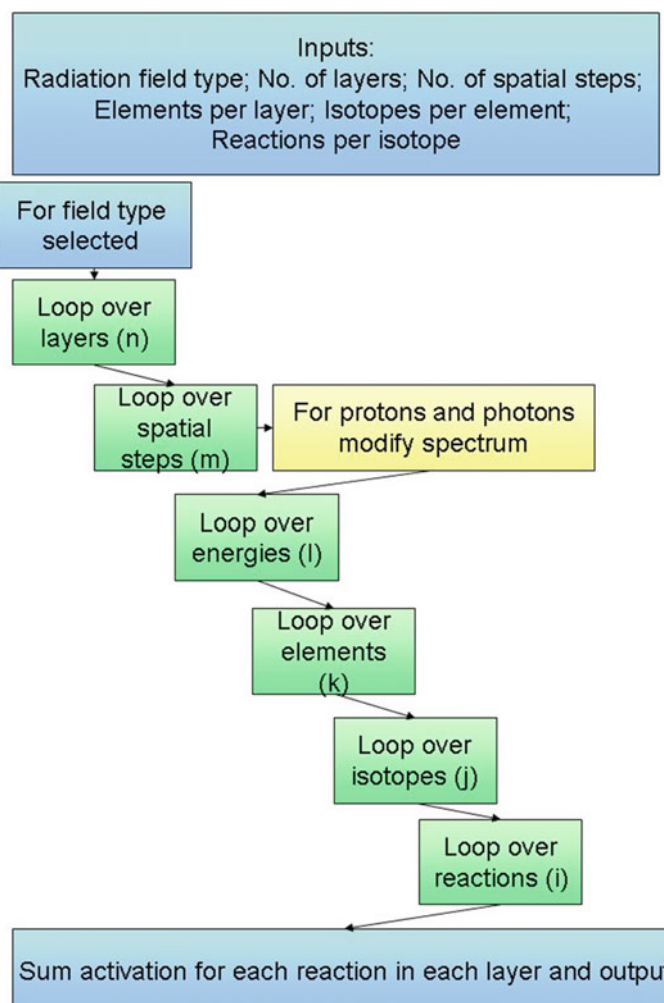


Fig. 5.5 Flow diagram of the 1D solver code

the materials selected (partially driven by these assessments) in its construction. The 1D solver is not computationally expensive and has run on a standard PC with a number of Linux operating systems. The recommendation is that with the physics outlined in this chapter the reader can relatively simply and cheaply develop their own 1D simulation package suitable to the facility being considered and generate worse case activation levels. The next sections discuss how to consider calculating the likely doses from activated materials.

5.3.7 Dose Calculations

The amount of dose received by personnel depends on how quickly they come into contact with the activated materials, how long the contact lasts, what types of field quanta are emitted and in what numbers, what mitigation there is in place, and the type of contact e.g. a surface contact, a point source exposure or a submersion dose there could be.

The starting point for a worse case assessment is to find a minimum credible time for personnel to come into contact with activated material after its creation. Is this seconds or minutes etc. For the Orion facility a time of 5 min was adopted as a realistic fastest post-shot access time to the target hall and potentially to material activated within the target chamber.

The next question to answer is: Are there any tasks that will take place in proximity to the potential hazard that will take a foreseen amount of time? For the assessments conducted for the Orion facility a time of 1 h was adopted as the worst-case time for personnel to be in the target hall post shot. In the case of Orion each shot is a creation event. The worst case was considered to be when staff access times were limited to an hour but that then the laser fires again, increasing the level of activity and the potential dose received by personnel.

Firstly dose is defined as the energy deposited by a radiation field per unit mass and is measured in Greys where 1 Grey is 1 J per kg and has the symbol D. A second unit, the Sievert has the same units but defines the effective dose or “dose equivalent” to tissue—this has the symbol H. The Sievert is broadly a Grey multiplied by a factor (Q), often termed the radiation quality factor, which accounts for the effectiveness of radiation damage to the tissue being considered. This is dependent on the type radiation quanta and their energy. For the assessments considered here for beta and gamma radiations Q = 1 and thus D and H are broadly interchangeable. For ease D will be the symbol used and the units will be Greys.

The type and energy of the radiation also have a significant bearing on the dose received. Three types of radiation are considered: gamma radiation, beta plus and beta minus. Neutron and alpha emitters were not considered for standard operations. The beta plus radiation is modelled as X-rays radiation because typically positrons have a limited range ($\sim 2\text{--}3$ cm in air) before annihilating with an electron and emitting two 511 keV X-rays which have a much longer range.

Furthermore, all personnel would be wearing PPE and clean room clothes. This would make direct contact of the skin with beta plus irradiation unlikely.

The dose received from radiations is calculated using the methods described in the following sections. These methods are taken from reference [29].

5.3.7.1 Beta Minus Radiation Absorption Coefficient

Beta decay is a three body process resulting in the emitted beta particles having a range of kinetic energies from ~ 0 MeV to a maximum beta-particle energy E_m MeV. To observe the rate at which betas particles lose energy a beta source of known energy and intensity (ψ_0) is transmitted through a material of known thickness (x) and density (ρ) and the subsequent beta intensity (ψ_x) is measured. By varying the thickness of the material the transmitted intensity as a function of absorber thickness can be obtained and fitted. From this data a near exponential decay trend is observed and a coefficient in the exponent can be obtained. This coefficient is the absorption coefficient. It can be expressed as either a mass coefficient (with dimensions of $\text{cm}^2 \text{ g}^{-1}$) or as a linear coefficient (with dimensions of cm^{-1}).

The absorption coefficients for air and tissue (in $\text{cm}^2 \text{ g}^{-1}$) are defined relative to the maximum energy (in MeV) of a beta's emission and are quoted for tissue and air by reference [29] to be:

$$\mu_B(\text{tissue}) = 18.6(E_{\max} - 0.036)^{-1.37} \quad (5.13)$$

$$\mu_B(\text{air}) = 16(E_{\max} - 0.036)^{-1.4} \quad (5.14)$$

These are mass absorption coefficients (μ_m) and they are derived empirically by fitting the absorption curves discussed. It is useful to define coefficients in terms of areal density to account for variations in density of the absorber.

They are related to the linear absorption coefficient (μ_l) and the material density (ρ) by:

$$\mu_l = \mu_m \cdot \rho \quad (5.15)$$

The densities of tissue and air are 1 g/cm^3 and $1.2E-03 \text{ g/cm}^3$. For 1 MeV particles the mass absorption coefficients as calculated with (5.13) and (5.14) for tissue and air are 19.6 and 16.8 cm^2/g respectively. Thus the linear coefficients are 19.6 and 0.02 cm^{-1} respectively.

If the intensity of a beam of beta particles is modelled as only an exponential decay then the energy of the betas will asymptote to 0 but never reach it. Thus a separate means is required to define the range of a beta. A sufficient definition is to

use the distance over which the beam has dropped in intensity by three orders of magnitude. Then $\Psi_x/\Psi_0 = 0.001$ and thus:

$$R = \frac{-\ln 0.001}{\mu_l} \quad (5.16)$$

Thus R for a 1 MeV beta in tissue is: 0.35 cm and in air is 345 cm.

These quantities give the ranges of interest for consideration i.e. what is the physical extent of a beta radiation field in air and would the beta field penetrate through the skin.

5.3.7.2 Beta Minus Radiation from a Surface

This methodology calculates the total dose delivered to a body, NOT just the dose delivered to the basal skin cells.

Consider a plane beta emitting surface with surface concentration C_a Bq/cm² of a long half life radioactive substance spread over the top of the surface in a very thin layer. Assuming isotropic emission then 50 % of the betas move away from the surface and 50 % move into it. Some of the betas moving into the surface are backscattered by the material encountered—this can be crudely estimated to be ~25 % of the flux moving into the surface [29] thus the fraction (f_b) of betas moving upward from the surface is roughly 0.625. The energy flux at the contaminated surface $\phi(E)$ (in MeV cm⁻² s⁻¹) is given by:

$$\phi(E) = C_a \cdot BR \cdot f_b \cdot \bar{E} \quad (5.17)$$

Here BR (Branching ratio) is the number of radiation quanta, i.e. beta particles emitted per disintegration (typically but not always this is 1). Furthermore, in these worst case calculations the average energy of the emitted quanta \bar{E} (in MeV) is replaced with the energy point energy which is roughly 3 times the average energy thus, this will result in a higher dose estimate. Multiplying the result from (5.18) by a factor of 5.76E-10 converts the units to J cm⁻² h⁻¹.

Dose is measured in Grays (Gy) and is defined as the energy deposited per unit mass (1 Gy is 1 J kg⁻¹)

From here one can account for the absorption of energy in any intervening layers between the basal skin cells and the surface such as any air gap and the layers of non viable surface skin. For a worse case this can be omitted in the first instance. Thus the contact surface dose rate (\dot{D} in Gy h⁻¹) is given by:

$$\dot{D}_{\beta,surface} = 1E3 \cdot \phi(E) \cdot \mu_B \quad (5.18)$$

With $\phi(E)$ in units of J cm⁻² h⁻¹, μ_B in cm² g⁻¹ (as defined in (5.13))

It is trivial now to multiply the hourly dose rate by the exposure time (in hours) and calculate the dose. But for the activation cases being considered it is not always

appropriate to make the approximation that the half life of the surface contaminant is long compared with the typical figure of an hour's exposure time. What is required is to calculate the number of decays per unit area in the exposure time from five minutes (300 s) post shot to 65 min (3900 s) post shot. For a varying population of nuclei integrating the activity per unit area ($p.u.A$) yields the correct number of decays for the period. Activity is given by:

$$A_{p.u.A} = dN_{p.u.A}/dt = \lambda N_{p.u.A}(t) = \lambda N_{0,p.u.A} e^{-\lambda t} \quad (5.19)$$

And thus the number of decays over the period being considered is given by:

$$NoD_{p.u.A} = \int_{300}^{3900} \frac{dN_{p.u.A}}{dt} \cdot dt = N_{0,p.u.A} (e^{-\lambda \times 300} - e^{-\lambda \times 3900}) \quad (5.20)$$

where:

λ is the constant of disintegration for the activated nuclei given by $\ln(2)/t_{1/2}$ (and $t_{1/2}$ is the half-life of the nuclei being considered)

Replacing C_a in (5.18) with the number of decays (NoD) in (5.22) yields the total energy fluence Φ (in MeV cm^{-2}) for the whole exposure time rather than the energy flux. This can be trivially converted to J cm^{-2} by multiplying by a factor of $1.6E-13$. The total dose received from the hour's exposure (in Gy) is thus given by:

$$D_{\beta,surface} = 1E3 \cdot \Phi(E) \cdot \mu_B \quad (5.21)$$

With $\Phi(E)$ in units of J cm^{-2} and μ_B in $\text{cm}^2 \text{ g}^{-1}$ similar to (5.20).

5.3.7.3 Submersion Dose

The derivation here uses similar concepts as to the surface dose considered in the last section. Consider an infinite cloud of activated air with a concentration of $C \text{ Bq/m}^3$. In any volume within such a cloud the rate of energy emission equals the rate of energy absorption. The dose rate \dot{D} (in Gy/h) to the air within the cloud given by [31]:

$$\dot{D}_{\text{inf}} = \frac{C \cdot BR \cdot \bar{E}}{\rho(\text{air})} \text{ or } \dot{D}_{\text{inf}} = 4.45E - 10 \times C \times \bar{E} \quad (5.22)$$

where:

\bar{E} is the average energy per quanta in MeV (again for a worst case the end point energy can be used) and the simple conversion of $1.6E-13 \text{ J} = 1 \text{ MeV}$.

BR is the branching ratio (number of quanta per decay)

$\rho(\text{air})$ is 1.293 kg m^{-3}

Again C is assumed to be long lived over the duration of the exposure and thus once again calculating the actual number of decays per unit volume (p.u.V) over the time interval of interest would yield a dose D_{air} (in Gy).

$$D_{air} = \frac{NoD_{p.u.V} \cdot BR \cdot \bar{E}}{\rho(\text{air})} \quad (5.23)$$

The skin of a test person is only irradiated from one side and absorbs $\sim 10\%$ more energy per kilogram than air [REF]. Thus the dose rate to the basal cells of the skin (at 0.007 g/cm^2 areal density or $\sim 1.8 \text{ mm}$ deep) is given by:

$$D_b = 0.55 \cdot D_{air} \cdot e^{-\mu_b(tissue) \times 0.007} \quad (5.24)$$

Thus the dose to the basal skin cells is given by combining (5.23) and (5.24):

$$D_b = \frac{0.55 \cdot NoD_{p.u.V} \cdot BR \cdot \bar{E} \cdot e^{-\mu_b(tissue) \times 0.007}}{\rho(\text{air})} \quad (5.25)$$

For the Orion facility the assumption was made that all the activated isotopes generated post shot would become evenly mixed throughout the target hall during the five minutes of air circulation prior to the entry of facility personnel. Thus the number of activated nuclei calculated using the 1D code were evenly distributed through the $11,000 \text{ m}^3$ of air in the target hall.

5.3.7.4 Gamma Dose

One of the most important gamma doses to consider in many scenarios is that from 511 keV X-rays created during beta decay. The simplest scheme is to utilise the mass absorption coefficient for X-rays. Again a mono energetic beam of photons of intensity (ϕ_0) and energy (E) is passed through an absorber and an intensity of the same energy photons is measured on the other side (ϕ_x). Thus $\phi_0 - \phi_x$ gives the number of quanta lost. So if the assumption is made that scattering of photons and secondary field generation is negligible and that the energy is simply absorbed then this represents a worse case for the material. Denoting ϕ_A as the absorbed flux then:

$$\phi_A = \phi_0 - \phi_x = \phi_0(1 - e^{-\mu_l x}) \quad (5.26)$$

where:

- μ_l is the linear attenuation coefficient; this is the attenuation coefficient per unit distance
- x distance travelled through the body

Providing the product μt is small then $(1 - e^{\mu m t}) \rightarrow \mu_m t$ hence:

$$\phi_A = \phi_0 \mu_l x \quad (5.27)$$

As previously discussed the mass attenuation coefficient (the attenuation coefficient per unit mass) is related to the linear attenuation coefficient thus:

$$\mu_l = \mu_m \cdot \rho \quad (5.28)$$

μ_m is the energy absorption coefficient; typically taken as 0.0312 cm^{-1} for tissue. From here:

$$\phi = \phi_0 \mu_m \rho x \quad (5.29)$$

Total dose delivered to a body exposed to the fluence is given by:

$$D = \phi_A \cdot E \cdot \mu_m \cdot \rho \cdot x \quad (5.30)$$

If ϕ_A is temporally dependent, such as the field produced from the decaying of activated nuclei then the integral of the rate of decay will yield the total dose.

$$D = \int \frac{d\phi_A(t)}{dt} \cdot E \cdot \mu_m \cdot \rho \cdot x \cdot dt \quad (5.31)$$

For simplicity (5.31) may be used provided the initial value of ϕ_A for the period is utilised. This can result in an overestimation of the dose but again if this overestimation is sufficiently low then no further refinement to the calculation is needed.

Once the induced radioactivity has been assessed for an object there is then a separate geometric question: For a person in the vicinity of the activated object what portion of the emitted field quanta will interact with that person? In the first instance the assumption can be made that all of the field quanta generated from the decay of the activated materials are incident upon a test person's body. The area of the body is taken to be 1 m^2 or 10^4 cm^2 . This is correct to within a factor of 2 for an average person. At large distances from an activated object the number of photons can be evenly distributed over the whole body and a whole body dose calculated. At closer distances it would be more appropriate to distribute the photons over say 0.02 m^2 to represent a hand. This really depends on the specifics of the scenario being considered.

5.3.8 Full Simulation Schemes

If a simple simulation, such as the one outlined in the previous sections, proves to be inappropriate then there is a selection of much more advanced tools available.

These tools are much more powerful but consequently require much more time to learn and utilise. For an experimental facility this is likely to be a full time job for an employee, for a medical facility undertaking the same work in the same configuration it is possible that a single series of calculations in the design phase would be sufficient—but any change of the facility or the operations will require these calculations to be revisited to ensure the results are still valid. It should be noted that there are many full simulation schemes available and the most ubiquitously utilised are discussed. This is by no means an exhaustive list and for specific problems there may be tools that have been developed that are more appropriate.

FISPACT

The FISPACT 2007 [30] and 2010 [31] codes are inventory codes designed for modelling neutron, proton and deuteron fields interacting with fusion devices. The FISPACT code does not undertake neutron transport but does keep a dynamic inventory of the activation products i.e. creates and decays them with time. Nuclear data is taken from the European Activation File (EAF). It is available through the NEA databank [32] and written and maintained primarily at the CCFE in the UK.

FISPACT II [33] is a re-written version of the code with many extensions including the ability to use alpha and gamma fields. It can also utilise the ENDFB-VII [34], JENDL 4.0 [35] and JEFF 3.2 [36] libraries as well as the original EAF library. There are also many other new features.

MCNP

MCNP (now at version 5 [37]) is a general Monte Carlo code for simulating neutron, photon and electron field interactions with a user created simulated environment. The code provides full transport and reaction physics and is regarded as an (if not the) industry standard for full radiation simulations. It has been widely adopted and developed with many user forums, workshops and training courses. There is a critical mass of knowledge required to run even basic simulations, but once the user is suitably familiar it is a very flexible platform. The program is written in Fortran 90 and can be utilised on Linux, Mac OS X and Windows based operating systems.

MCNP6 [38] is a merger of MCNP5 and MCNPX and has the capability to model photon, electron, positron, muon, neutron, proton, light ion and heavy ion fields over different energy ranges see reference [38] for details. The code has many additions and advantages over the previous versions; far too many to detail here. The reader is simply directed to the MCNP homepage [39] to review the available releases and ascertain if a version of MCNP would be suitable for their application.

The use of MCNP is controlled and is disseminated by the Radiation Safety Information Computational Centre (RISCC), Oak Ridge Laboratory, Tennessee. Two versions are available, the full version and an executable only version. The latter is easier to obtain, however, permission for distribution to non-US citizens must be obtained from the United States Department of Energy (DoE) and can take several months to accomplish.

5.3.8.1 GEANT4

Geant4 [40] is a tool kit for simulating the interaction of radiation fields with matter. Its flexibility generally exceeds that of MCNP as does its complexity. The tool kit is based in the object orientated language of C++ and offers the ability to simulate the interaction of many hadrons including mesons, protons, neutrons and ions as well as electrons and photons. The philosophy is modular allowing the user to select the models and physics lists to include in their simulation; which is powerful for the experienced user but a potential pit fall for the inexperienced. A wealth of information is available for GEANT4 with the main references being [40, 41]. Again the reader is advised to decide if the problem to be simulated requires the time and effort required to learn to use and run GEANT4. GEANT4 is publically available and can be down loaded from [42].

5.3.8.2 TART2012

Is a neutron and gamma transport and reaction code with a 3D geometry capability. It is available from [43] and is developed at LLNL. TARTs main advantage is speed but it is not as complete as either MCNP or GEANT.

5.3.8.3 Electron/Photon Codes

The Integrated Tiger Series (ITS), Penelope, EGS, MC-SET and CASINO perform simulations of electron photon interactions in arbitrary materials. ITS and Penelope are available through the NEA databank [44].

EGS is a photon transport tool developed by Canada's National Research Council (NRC) primarily for medical physics simulations. It is available from [45].

CASINO and MC-SET are tools developed for scanning tunnelling microscopy. CASINO can be obtained from [46] while MC-SET is available from [47].

5.4 Activating the Fluid Environment

In any facility there is the potential to activate or create activated gaseous material. This creates further issues, largely from a containment-of-hazard perspective, but also for a facility's emissions into the environment. For the Orion facility several aspects were considered. The dose to personnel from activated target hall air was found to be extremely low, however, the total emissions from the facility also needed to be estimated. The following sections describe the methods used to calculate worse case discharges from the facility.

5.4.1 Target Hall Air Discharge

The Orion target hall is essentially a concrete cube with an air conditioning system used to circulate the air. The pumping system expels at a rate of one cubic metre of air per second. The target hall is a cuboid with dimensions $21 \times 24 \times 22$ m giving a total volume of $\sim 11,000$ m³. It thus takes 11,000 s to cycle all the air once assuming no mixing with the post shot air. This is a worse case assumption—discharging the activated air as quickly as possible. During the two and three quarter hours between the shot and the last volume of unmixed air to be expelled the activity will drop as nuclei decay. Thus summing the remaining activity discharged per unit time gives the total discharged activity per shot (A_{tot}).

$$A_{tot} = \int_{20}^{10020} \frac{A_0}{11000} \cdot \left[-\frac{1}{\lambda} e^{-\lambda t} \right] dt \quad (5.32)$$

where:

$A_0/11000$ is the activity per unit volume

20 and 10,020 are the initial and final times respectively as the discharged gas takes 20 s to travel from the target hall to the discharge point.

So having ascertained the likely level of activation in the target hall (A_0) it becomes a trivial matter to calculate the worse case total discharged activity assuming no mixing of activated and fresh air. Any such mixing would only serve to dilute the instantaneous emissions and so the approximation can be made.

5.4.2 Managing the Discharge of Activated Gases

In many laser-target interactions the target will be plasmafied and activated. Most of this activated material will remain inside the target chamber, ‘plating out’, i.e. chemically bonding to, the interior surfaces of the chamber, the vacuum pumping system pipe-work, the ten-inch manipulators and diagnostics therein and the CPA pressure vessels. However, some materials will more readily form gases and these will eventually be discharged from the facility primarily through the vacuum system. These discharges must be managed and thus within the procedure to field an experiment at the facility the principle investigator (PI) is required to assess the discharge from their proposed experiment. The following section details the process developed at Orion to manage this.

5.4.3 *The Management Solution*

The expected level of activation per shot will vary significantly with many experimental parameters; far more than can be reasonably modelled in an n-dimensional space. Furthermore, the activity at any instant passing through the facility's vacuum system exhaust is likely to be far too small to measure. Thus a full parameter scan of a simulated space is intractable and direct measurement techniques will be insensitive and inaccurate.

Adopting a calculational methodology the discharges to the environment are to be calculated using the a spreadsheet. This spreadsheet gives an interface to a library of results generated by the 1D code. The library is indexed by just three parameters—the Z of the target, the thickness (x) of the target and the field number which will access calculations for one of focused lasers generating protons, defocused lasers generating protons, neutron field or γ /X-ray fields. A further field option calculates a worst case and calculated the focused and defocused laser generated proton fieldsFocused laser generated proton fields and adds the largest to the γ /X-ray field.

In order to simplify to just these three parameters some assumptions had to be made to create the spreadsheet:

1. The radiation source terms are the same (worse case) for each shot.
2. The radiation source will be at the point of the laser-target interaction or for neutrons at the centre of a spherical target.
3. Only gaseous materials will be discharged the rest will condense in the vacuum system.
4. Only radioactive materials with a half-life in excess of one hundred seconds are included.
5. Only a certain range (microns to several centimetres) of target thicknesses have been modelled.
6. Only solid density targets have been modelled.

5.5 Overview of Calculation Methodology

The central methodology remains to adopt a worst case approach. For certain quantities this has been tempered with reasonable estimates taken from modelling and practical experience. This ensures when discharges are calculated the maximum reasonable activity is estimated.

The list of potential target materials included the bulk of the periodic table. When considering gaseous discharges four pertinent facts reduce this enormously:

1. Following the interaction with the radiation field(s) the products must be gaseous or form gaseous compounds.

2. Only products with half-lives greater than one hundred seconds are included in the site discharges—shorter lived products do not need to be considered.
3. Only stable nuclei need be considered for targets
4. Only the primary decay needs to be considered—when considering isotopes decaying through a sequence of nuclei, e.g. a decay chain, one need only count the original decay

The periodic table was reduced to just a few elements that were potentially problematic if created and discharged (see Fig. 5.1). The method was to consider what gaseous isotopes would be an issue and work back to how they could be created from stable targets. There were a couple of exceptions: tritium production from hydrogen was discounted because of the low probability of a double capture event; Production of radon gas was omitted because the facility has no plans to use actinium, francium, radium or astatine and there are no stable isotopes of any of these elements to create into targets.

For each reaction a calculation was undertaken for a range of target thicknesses and a modified error function was fitted to the results obtained. The error function provided the correct form asymptoting between two levels—the lower of which represents the limit in the confidence of the activity calculation and the higher level is the maximum amount of activity that can be created for a specific field function $S(E,t)$ impinging on a material at solid density (increasing thickness beyond this point produces no more activity as the field itself has been stopped). Thus the spreadsheet inputs of Z , and field number select which of these reactions could occur and the target thickness parameter is input into the modified error function to produce the final worse case figure on a reaction by reaction basis. The activities are then individually decayed until the discharge time is reached and all the remaining activity is then summed. This is possible because the worse case discharge time (actually created as a hidden forth parameter) is assumed the same for all the elements.

5.6 Summary

In summary the methods for radiological assessment are varied and will depend on exactly what questions require answering. Simple 1D schemes can become complicated especially when attempting to track all the possible reactions that could significantly contribute to the problem but this has been accomplished with the creation of the a 1D solver at AWE. Once activity has been calculated then using further assumptions about specific scenarios for staff coming into contact with the activated materials, dose assessments can be made.

There are limits to the applicability of the 1D scheme and for many scenarios (nearly all scenarios for neutron fields) more robust modelling tools like MCNP6 or GEANT4 are required—these tools can and are used to model doses, however, they require a large degree of experience to run.

However radiological hazards are assessed the most important message is to develop a respect for the radiological hazards, to understand it and mitigate it appropriately.

References

1. N.W. Hopps et al., Comprehensive description of the Orion laser facility. *Plasma Phys. Controlled Fusion* **57**, 064002 (2015)
2. STFC central laser facility—laser facilities. <http://www.clf.stfc.ac.uk/CLF/Facilities/11996.aspx>
3. C.N. Danson et al., Vulcan PetaWatt—an ultra-high-intensity interaction facility. *Nucl. Fusion* **44**, S239–S246 (2004)
4. J.L. Collier et al., The Astra Gemini project a high repetition rate dual beam petawatt laser facility, in *Quantum Electronics and Laser Science Conference*, vol. 3, 22–27 May 2005, pp. 2024–2025
5. D. Habs et al., Extreme light infrastructure—nuclear physics (ELI-NP): new horizons for photon physics in Europe. *Nuclear Physics news* **21**(1), 23–29 (2011)
6. ELI—extreme light infrastructure: nuclear physics. <http://www.eli-np.ro/>
7. OECD nuclear energy agency: Janis, <http://www.nea.fr/janis>
8. A.J. Koning et al., Talys: comprehensive nuclear reaction modelling, in *Proceedings of International Conference on nuclear data science and technology*, vol. 769, no. ND2004 (2004)
9. TALYS: <http://www.talys.eu/>
10. A.J. Koning et al., Talys-1.0: a nuclear reactions programme: user manual, NRG Report 21297/04. 62741/P FAI/AK/AK (2004)
11. P.G. Young, E.D. Arthur, GNASH A pre-equilibrium, statistical nuclear model code for calculation of cross sections and emission spectra., Los Alamos National Laboratory Report LA-6947 (1977)
12. N. Otuka et al., Towards a more complete and accurate experimental nuclear reaction data library (EXFOR): international collaboration between nuclear reaction data centres (NRDC). *Nucl. Data Sheets* **120**, 272–276 (2014)
13. Experimental nuclear reaction data (EXFOR): <http://www.nndc.bnl.gov/exfor/exfor.htm>
14. Qtool: calculation of reaction Q-values and thresholds: www.t2.lanl.gov/nis/data/gtool.html (2009)
15. J.F. Ziegler, J.P. Biersack, U. Littmark, *The Stopping Ranges of Ions in Solids*, vol. 1 (Pergamon Press, 1985)
16. SRIM, <http://www.SRIM.org>
17. H.A. Bethe, *Ann. Physik.* **5**, 352 (1930)
18. H.A. Bethe, *Z. Phys.* **76**, 293 (1932)
19. N.J. Carron, *An Introduction to the Passage of Energetic Particles Through Matter* (CRC Press, Taylor & Francis Group). ISBN 0-7503-0935-0
20. G.F. Knoll, *Radiation Detection and Measurement*, 4th edn. (Wiley, Inc., 2010). ISBN 978-0-470-13148-0
21. J.F. Ziegler, The stopping of energetic light ions in elemental matter. *J. Appl. Phys. Rev. Appl. Phys.* **85**, 1249–1272 (1999)
22. ICRU, Stopping powers and ranges for protons and alpha particles, International Commission on Radiation Units and Measurements, Report 49, May 1993
23. M.J. Berger et al., ESTAR, PSTAR, ASTAR: computer programs for calculating stopping-power and range tables for electrons, protons and helium ions (1992) (see also <http://www.nist.gov/pml/data/star/index.cfm>)

24. NIST mass coefficients: <http://physics.nist.gov/PhysRefData/XrayMassCoef/tab3.html>
25. J.P. Friedberg et al., Resonant absorption of laser light by plasma targets. *Phys. Rev. Lett.* **28**, 795 (1972)
26. J.D. Lindl, Ponderomotive force on laser-produced plasmas. *Phys. Fluids (1958–1988)* **14**(2), 371–377 (1971)
27. L. Yin et al., GeV laser ion acceleration from ultrathin targets: the laser break-out afterburner. *Laser Part. Beams* **24**, 291 (2006)
28. L. Yin et al., Mono-energetic and GeV ion acceleration from the laser breakout afterburner using ultrathin targets. *Phys. Plasmas* **14**, 056706 (2007)
29. H. Cember, T.E. Johnson, *Introduction to Health Physics* 4th edn. (McGraw-Hill Companies Inc., 2009). ISBN: 978-0-07-142308-3
30. R.A. Forrest, J. Kopecky, EASY-2007: a new generation of activation modelling including neutron-, proton- and deuteron-induced reactions, in *ND 2007—International Conference on Nuclear data for Science and Technology 2007*, No. 196, Published online: <http://dx.doi.org/10.1051/ndata:07170> (2008)
31. The European Activation File: EAF-2010 neutron-induced cross section library CCFE-R (10) 05
32. NEA Data bank, NEA-1564 EASY-2010: <http://www.oecd-nea.org/tools/abstract/detail/nea-1564>
33. J. Soublet et al., EASY-II: a system for modelling of n, d, p, g and a activation and transmutation, Joint International Conference on Supercomputing in Nuclear Applications and Monte Carlo 2013 (2013)
34. M.B. Chadwick, ENDF/B-VII.1 nuclear data for science and technology: cross sections, covariances, fission product yields and decay data. *Nucl. Data Sheets*, **112**(12), 2887–2996 (2011)
35. K. Shibata et al., JENDL-4.0: a new library for nuclear science and engineering. *J. Nucl. Sci. Technol.* **48**(1), 1–30 (2011)
36. A.J. Koning et al., Status of the JEFF nuclear data library, in *Proceedings of the International Conference on Nuclear Data for Science and Technology* (2010)
37. MCNP-Version 5, Vol. 1: Overview and theory, X-5 Monte carlo Team, LA-UR-03-1987 (2003)
38. Initial MCNP6 Release Overview. *Nucl. Technol.* **180**, 298–315 (2012)
39. A General Monte Carlo N-Particle (MCNP) Transport Code, MCNP homepage: <https://mcnp.lanl.gov/>
40. S. Agostinelli et al., GEANT4—a simulation toolkit. *NIM A* **506**(3), 250–303 (2003)
41. J. Allison et al, GEANT4 developments and applications. *IEEE Trans. Nucl. Sci.* **53**(1) (2006)
42. GEANT4 website: <http://geant4.cern.ch>
43. TART homepage: <https://wci.llnl.gov/codes/tart/>
44. NEA Data bank CCC-0467 ITS-3.0: <http://www.oecd-nea.org/tools/abstract/detail/ccc-0467>
45. National Research Council Canada EGSnrc: software tool to model radiation transport: http://www.nrc-cnrc.gc.ca/eng/solutions/advisory/egsnrc_index.html
46. CASINO homepage: <http://www.gel.usherbrooke.ca/casino/index.htm>
47. MC-SET homepage: <http://www.mc-set.com/>

Part II

**Updating Laser-driven Electron
Acceleration and Dosimetry**

Chapter 6

Generation of Multi-GeV Electron Beams and Bio-medical Applications

Tae Moon Jeong and Jongmin Lee

Abstract Laser-driven high-energy electrons are becoming unique and important sources in various research disciplines including radiobiology and medicine as well as basic science and nuclear engineering. The primitive idea on the laser-field-assisted electron acceleration was proposed by Tajima and Dawson in 1979, and since then tremendous progress has been made to realize multi-GeV electron beams through the laser-matter interaction. Despite the marvelous success in the laser-driven high-energy electron generation, considerable improvements in terms of physical parameters such as maximum energy, stability, mono-energeticity, charge, and so on are still requested for practical engineering applications. In this chapter, the basic principle and parameters for building a laser-driven electron accelerator is briefly described and the outstanding experimental achievements carried out in the laser-driven electron acceleration are summarized in following sections. Finally, the bio-medical applications of laser-driven high-energy electron beams are introduced before concluding the chapter. The unique high-energy electron beams driven by ultrashort high-power laser pulses will be a promising source for a next-generation, compact, low-cost, high-resolution imaging machine for bio-medical engineering.

6.1 Introduction

The advance in the high-power laser technology [1–3] makes it possible to build a small-scale charged particle (electron, proton, and ions) accelerator due to the high field gradient (~ 100 GeV/m) formed by an intense laser pulse. (Instead, the accelerating field of radio-frequency- (rf-) based accelerators ranges as relatively low as 10–50 MV/m.) A small-scale laser-driven electron accelerator offers unique

T.M. Jeong · J. Lee (✉)

Advanced Photonics Research Institute, GIST, Gwangju 500-712, Korea
e-mail: leejm@gist.ac.kr

J. Lee

Global Institute of Laser Technology, HGU, Pohang, Gyung-buk 791-708, Korea

(ultrashort and tunable) high-brightness and high-energy photon (x-ray and γ -ray) sources. Those sources are now tested for imaging biological samples and will bring us a low-cost, high-resolution, high-energy photon imaging machine.

The principal idea on electron acceleration using a laser field propagating in a plasma medium was proposed by Tajima and Dawson in 1979 [4]. This idea uses a plasma wave (or more precisely the associated *wake-field*) formed behind a laser pulse to accelerate electrons trapped in a high-field gradient region, and it is now known as laser wake-field acceleration (LWFA). Instead of using the laser pulse, energetic electron bunches can be used for the formation of a plasma wave, which is known as the plasma wake-field acceleration (PWFA). Before the idea of using a wake-field, a direct electron acceleration was considered for many decades and its limitation was summarized in the Lawson-Woodward theorem [5]. The conclusion of the theorem is that a certain kind of broken symmetry in time and space is required for the electron acceleration by electromagnetic field. The LWFA provide a symmetry breaking in an indirect way. However, a direct electron acceleration scheme with a broken symmetry is still of great interest for the academic research.

Since the birth of LWFA, the electron acceleration using high power laser pulses were realized in several ways including plasma beat-wave acceleration [6, 7], self-modulated LWFA [8], plasma bubble acceleration [9–11], and plasma waveguide acceleration [12]. In particular, the plasma bubble acceleration and plasma waveguide acceleration schemes could demonstrate the production of GeV electron bunches with quasi-monoenergetic features. Recent experimental results showed the production of quasi-monoenergetic electron beams with an energy of over 4 GeV by employing petawatt (PW) laser pulses [13]. The acceleration of electrons to 10-GeV or even 100-GeV level will be the next step in near future. In early days of LWFA research, despite the great process in LWFA, the unstable electron beam characteristics, such as energy and beam pointing, were challenging issues. Now, the stability of electron energy and pointing are being improved with the help of sophisticated techniques (for example, colliding pulse and laser beam pointing stabilization techniques) developed by several groups. This improvement will be helpful in developing a practical and compact electron accelerator for various applications, in which GeV electrons with unique features are requested.

In this chapter, we summarize basic principles of the laser wakefield acceleration and progresses recently achieved in the electron acceleration. Two major acceleration mechanisms, laser wake-field and plasma bubble, are explained in detail. For these purpose, basic concepts and parameters (i.e., diffraction, dephasing, depletion, trapping, beam loading, etc.) commonly used in the electron acceleration are described in Sect. 6.2. Recent progresses on electron acceleration are summarized in Sects. 6.3 and 6.4. These sections mostly contain experimental results on the production of multi-GeV-class electron beams in the bubble and in the plasma waveguide acceleration regimes using single stage or multiple acceleration stages. Section 6.5 is dedicated to applications of energetic electron beams in bio-medical fields. The energetic electrons can be used for bio-medical applications in direct and indirect manner. Exposure of energetic electrons to cancer cells is the direct use of electron beams produced from accelerators. The energy of energetic electrons is

converted into high-energy photons through several mechanisms, such as undulator radiation, betatron radiation, and inverse Compton scattering. Those mechanisms to produce high-energy photon from energetic electrons have been also demonstrated, and applications for imaging bio-medical samples with such high-energy photon are being under way.

The electron acceleration by ultrashort high-power laser has shown a great progress in both experimental and theoretical results after its first theoretical proposal. Now, the electron acceleration by laser pulses is not only an interesting research topic in the laboratory but also becomes an important engineering tool in research and in industrial and medical applications. Many challenging issues still remain in scientific and engineering viewpoints. However, the unique high-energy electron beams driven by ultrashort high-power laser pulses will be a promising source for a next-generation, compact, low-cost, high-resolution imaging machine for bio-medical engineering.

6.2 Electron Acceleration in Linear and Non-linear Regimes

The invention of laser has made great impacts on scientific (optical, atomic, plasma, and acceleration) communities. As in other communities, the laser (in particular, high-power laser) tremendously contributed to the research and development in the accelerator community by proposing brilliant ideas for building efficient and compact (table-top scale) accelerators. Historically, the direct acceleration of electrons by a propagating electromagnetic field was considered even before the invention of laser, and it was concluded that charged particles cannot gain net energy from the plane electromagnetic wave propagating in vacuum. This is known as the Lawson-Woodward theorem. However, it has been proven that net energy gain is possible when that symmetry is broken by the propagation of a laser pulse in a plasma medium, due to the finite size of laser pulse in the spatial and temporal domains. This concept can be tested by focusing a pulsed high-power laser into a plasma. This kind of electron acceleration using a wake-field in a plasma medium is known as the Laser Wake-field Acceleration (LWFA).

6.2.1 Formation of Laser Wake-Field

According to the theory [4], an intense laser pulse passing a plasma medium pushes electrons and separates them from background ions, and forms a plasma wave. In fact, an electron under an electromagnetic (\vec{E} and \vec{B}) field is governed by the Lorentz force as follows:

$$\frac{d(\gamma m_0 \vec{v})}{dt} = -e\vec{E} - e\left(\frac{\vec{v}}{c} \times \vec{B}\right) \quad (6.1)$$

Here, m_0 is the electron rest mass and γ the Lorentz factor. When a laser pulse is not strong enough, the $\frac{\vec{v}}{c} \times \vec{B}$ term in the right hand side is usually negligible and does not affect the electron motion. However, as the intensity of a laser pulse becomes strong, the transverse electron motion (expressed in \vec{v}/c) pushes the electron along the laser pulse propagation direction. Figure 6.1 shows the transverse oscillation and longitudinal push (or separation) of a single electron under two different laser intensities. The longitudinal push by the laser field becomes apparent when a higher a_0 is applied in the calculation. The oscillation amplitude, x , and the longitudinal push (or separation), z , are given by $x = \lambda a_0 / 2\pi$ and $z = \lambda a_0^2 / 4$, respectively. Here, a_0 is the normalized vector potential defined as $a_0 = eE/m_0 c\omega$ that represents the strength of the electromagnetic field. The normalized vector potential is also the measure of momentum gained by a quivering electron in one laser wavelength in units of $m_0 c$. At a wavelength of 0.8 μm, the normalized vector potential of 1 corresponds to $\sim 2.14 \times 10^{18} \text{ W/cm}^2$.

In a plasma medium, the separation of electrons from background ions induces electric field by the space charge effect after an intense laser pulse passes through. Then the periodic motion of oscillation for electrons occurs around heavy ions. The resultant pattern of alternating positive and negative charges is known as the plasma wave or laser wake. The oscillation frequency is dependent on the electron density, $n_e(\text{cm}^{-3})$, and is defined as the plasma frequency by $\omega_{pe} = \sqrt{n_e e^2 / m_e \epsilon_0}$ (in SI units, or $\omega_{pe} = \sqrt{4\pi n_e e^2 / m_e}$ in cgs units). Thus, the wavelength of the plasma

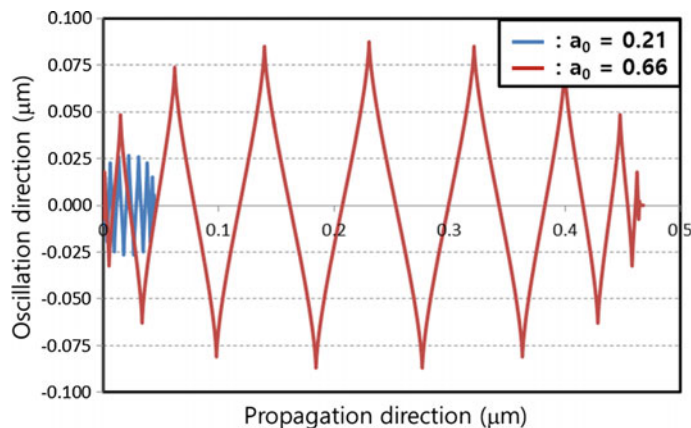


Fig. 6.1 Transverse and longitudinal motions of an electron when electromagnetic fields having two different intensities ($a_0 = eE/m_0 c\omega$) are applied to the electron. The transverse motion amplitude is $x = \lambda a_0 / 2\pi$ while the longitudinal one is $z = \lambda a_0^2 / 4$ when a linearly-polarized laser pulse is focused in the far-field limit

wave is simply given by $\lambda_p \approx 3.3 \times 10^{10} (\mu\text{m}) / \sqrt{n_e}$. It is well known that this oscillation appears behind the laser pulse and forms a plasma wave that supports a strong (up to 100 GeV/m or 1 GeV/cm) longitudinal electric field. Experimentally, the single shot image for the laser wake-field was indirectly recorded using a frequency-domain (FD) holography method by Matlis et al. [14].

Figure 6.2 shows the measured laser wake-fields in a helium gas jet. In the measurement, authors focused an intense 30-fs pump pulse into the helium gas jet with a parabolic mirror having a f-number of 13 and created a plasma and laser wake-field. Two chirped, frequency-doubled 1-ps pulses, temporally synchronized and co-propagating with the pump, were used to take holographic snapshots of the ionization front and wake. They successfully measured phase alterations imposed by these plasma disturbances at 10 and 30-TW power levels under low ($n_{e,\text{max}} = 0.95 \times 10^{18} \text{ cm}^{-3}$) and high ($n_{e,\text{max}} = 2.2 \times 10^{18} \text{ cm}^{-3}$) electron density conditions, and recovered wake structures by the Fourier transform method.

Some of electrons can be trapped in the plasma wave and accelerated by longitudinal electric field component, and thus the energy transfer from wake-field of the plasma wave to trapped electrons happens. Due to the large field gradient in the wake-field and short plasma wavelength, the laser wake-field accelerates trapped

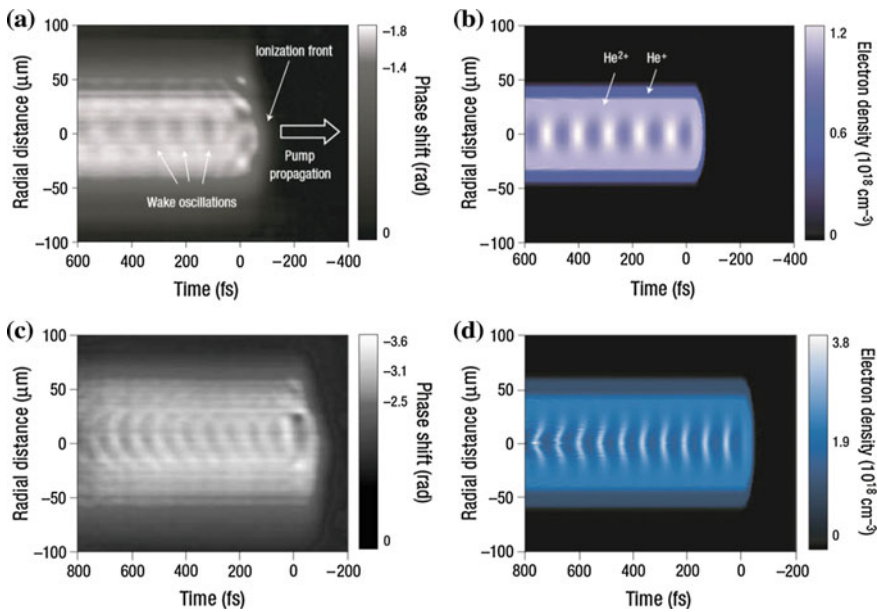


Fig. 6.2 Experimental versus simulated images of laser wake-fields. The interferometric patterns induced by electron density alteration were recorded in (a) and (c), and the electron densities were reconstructed from the patterns. At a lower intensity level, more regular density patterns are found (a). As the laser intensity grows, curved wakes are formed after several periods. The relativistic oscillation of electrons is the origin of curved wakes. b and d are simulated density profiles. (Reproduced with permission from Matlis et al. [14], Copyright (2006), Nature Publishing Group.)

electrons close to the speed of light (more than tens of MeV) within a very short range (mm to cm scale) with short electron bunch length (tens of fs to ~ 100 fs). As an example, the generation of self-trapped electrons having energies of 44 MeV was demonstrated by focusing a 1-ps, 20-TW laser pulse to an intensity of $5 \times 10^{18} \text{ W/cm}^2$ in a plasma with a density of $1.5 \times 10^{19} \text{ cm}^{-3}$ [15].

6.2.2 Formation of Plasma Bubble

Although the laser wake-field acceleration was experimentally demonstrated for electrons, their energy spectrum was very broad and peaked at a low energy. A more sophisticated electron acceleration scheme working in a highly nonlinear regime was proposed by Pukhov and Meyer-ter-Vehn [16]. This scheme uses shorter laser pulses than the plasma wavelength, λ_p , but having a higher peak power ($a_0 \gg 1$). Under such conditions, electrons are evacuated by the intense laser pulse and a region (*plasma cavity* or *bubble*), which mostly has positive ions, is formed behind the laser pulse. In this case, instead of having a periodic plasma wave, the plasma wave is broken after the first oscillation because of the electron evacuation (typically known as “blow-out”). Figure 6.3 shows the formation of a plasma cavity in the highly nonlinear regime.

Considering plasma cavity represented in Fig. 6.3, the wave breaking was invoked in order to explain trapped electrons, and an electric field strength ($E_{WB}/E_0 = \sqrt{2(\gamma_p - 1)}$ with $\gamma_p = 1/\sqrt{1 - v_g^2/c^2} = \omega_0/\omega_p$) for the wave breaking in the longitudinal direction was estimated. However, according to further simulations and experiments, it was clear that a wave breaking in the transverse direction and a trapping of returning electrons also occurs when a laser pulse propagates inside the plasma medium. Thus, it is thought that the formation of a

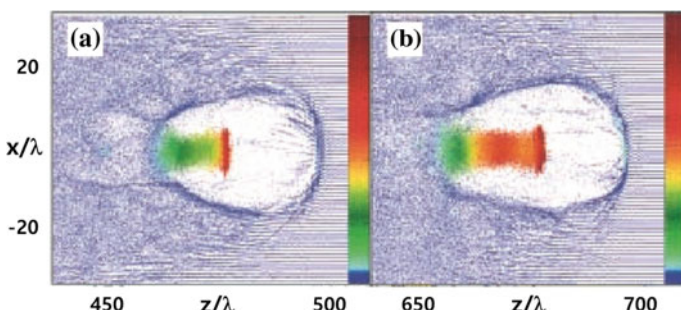


Fig. 6.3 Formation of a bubble (or plasma cavity) by an ultrashort high-intensity (33-fs, $a_0 \sim 10$) laser pulse. **a** is calculated at $ct/\lambda = 500$, and **b** at $ct/\lambda = 700$. (Reproduced with permission from Pukhov and Meyer-ter-Vehn [16]. Copyright (2002), Springer.)

plasma cavity and the acceleration of electrons in the plasma cavity are possible under a relatively smaller laser intensity ($a_0 \sim 3$). The electron acceleration using the plasma cavity significantly improved the characteristics of electron beams in terms of energy and mono-energeticity. As a result, quasi-monoenergetic electrons beams having an energy of few hundreds of MeV were produced by three different groups almost at the same time [9–11]. Since then, the production of quasi-monoenergetic electron beams became common. Moving to the nonlinear regime, a quasi-monoenergetic electron beam having a peak energy of 4.2 GeV was recently reported [13].

To date, it is thought that the LWFA is the most advanced technique because it is compact and efficient in accelerating electrons to a GeV or higher. As already mentioned, a high-field gradient of 100 GeV/m can be easily achieved in a plasma cavity and the high-field gradient can reduce the size and cost of the electron accelerators. Self-trapped electrons in a plasma cavity lead to the high conversion efficiency of laser energy into energetic electron beams. Additional benefit of electrons obtained from the LWFA technique is the synchronization of electron bunches to other probing sources (such as laser pulses). The synchronization to other sources makes it possible to apply GeV electron bunches for various application with an accurate time delay. This will allow studies of dynamics of ultrafast processes that occur in the sub-picosecond time-scale.

6.2.3 *Diffraction, Dephasing, and Depletion*

When a laser pulse propagates in a plasma medium, its propagation and consequent electron acceleration are affected by laser and plasma parameters as well as by relevant laser-plasma interactions, such as field strength, preformed density channel, depletion of pump energy, relativistic self-focusing, self-channeling, plasma wave generation, and laser-induced plasma instabilities. In this part, we will focus our attention to three basic phenomena (diffraction, dephasing, and depletion) in order to estimate how much energy can be transferred from laser pulse to electrons.

The diffraction is a fundamental effect produced a wave-like entity. The energy flow of a wave can be deviated from its original direction when the wave encounters an obstacle or an aperture. The physical origin of the diffraction is the interference of secondary waves coming from different positions within the spatial extent of the wave-front. When a laser pulse is focused to a higher intensity for the charged particle acceleration, the diffraction phenomenon occurs because of the finite spatial extent of a laser pulse, and immediately plays an important role in forming laser intensity (or electric field) distribution in the focal plane and its vicinity. Two important laser parameters, namely the spot size $\omega(z)$ and the Rayleigh range z_R , are given by the following relationship for a Gaussian beam:

$$\omega(z) = \omega_{\text{waist}} \times \sqrt{1 + z^2/z_R^2} \quad (6.2)$$

$$z_R = \pi\omega^2/\lambda \quad (6.3)$$

where ω_{waist} is the beam waist given by $\omega_{\text{waist}} = \frac{\lambda f}{\pi\omega_{in}} \frac{1}{\sqrt{1+f^2/z_{R,in}^2}}$ (λ is the wavelength of laser, f the focal length of the optics, and ω_{in} the input laser beam size).

As seen in the above relationship, the laser intensity quickly decreases as the observation position moves away from the focal plane. Thus, it becomes important to maintain a proper laser intensity over the entire acceleration range. Several ideas were proposed in order to maintain laser intensity over a long range. Firstly, according to the definition of Rayleigh range, a long-focal-length optic can provide a large Rayleigh range but with a correspondingly wide spot. This idea is simple and works in some experiments (sometimes with the self-focusing effect to form a plasma channel), but requires a high laser pulse energy to reach a suitable focal intensity. Secondly, the relativistic self-focusing effect can be used. When the laser power exceeds a critical power $(P_c \approx 17 \frac{\lambda_p^2}{\lambda^2} \text{ GW})$ and the pulse duration is long compared with the plasma wave period, it is known that a laser pulse can propagate for a long distance in a plasma channel with the help of refractive index change induced by the relativistic self-focusing. The critical power is inversely proportional to the electron density (n_e). Thus, the higher electron density, the lower critical power for relativistic self-focusing. The self-focusing of a laser pulse can be enhanced by the ponderomotive blow-out of the plasma electrons from the axis, i.e., electron cavitation. But, it is generally known that in the high electron density regime the laser pulse propagating through the plasma is inherently unstable and the acceleration scheme produces electron bunches with a large energy spread. In addition, the body of long relativistically guided pulse is subject to instabilities (Raman scattering, self-modulation, and laser hosing). Thirdly, as the light propagates in an optical fiber or a waveguide, the laser pulse can propagate in a long plasma channel. Pre-formed plasma density channels of radius r_0 and density ratio Δn are effective in the guiding of short ($L < \lambda_p$) laser pulses when $\Delta n \geq \Delta n_c = \frac{1}{\pi r_0^2}$. In addition, with such ultrashort pulses the detrimental effects of various instabilities may be reduced, owing to the reduced growth of the unstable modes within the pulse.

However it has to be considered that even though a laser pulse could travel with a minimized diffraction, a phase slip between accelerated electrons and the plasma wake occurs anyway, because the speed of the plasma wake is less than the speed of light. The dephasing length, L_d , is defined as the length that an electron travels before it experiences the phase difference by one-half of a period with respect to the plasma wave. After the dephasing length, the electron overruns the wake and slows down in the decelerating phase of the wake. This limits the possible electron acceleration length. In the linear regime ($a_0^2 \ll 1$), the dephasing length is given by

$L_{dephase} \approx (\omega_0^2 / \omega_p^2)(\lambda_p/4)$. In the nonlinear regime ($a_0^2 \gg 1$) in a plasma cavity, the dephasing length is slightly modified into $L_{dephase} \approx (\omega_0^2 / \omega_p^2)(R_b/C)$ [17]. Here, C is the dimensionless parameter given by $\frac{1}{4} \left[1 + (1 + a_0^2/2) / (1 + \beta R_b^2/4)^2 \right]$ and usually ranging between 0.5 and 1.5, while R_b is the radius of cavity. According to [18], if the acceleration distance is limited by the dephasing length, $L_{dephase}$, the energy gain, ΔE , is given in this regime by

$$\Delta E(\text{MeV}) \approx \frac{630 \times I(\text{Wcm}^{-2})}{n(\text{cm}^{-3})} \times \begin{cases} 1, & a_0 \ll 1 \\ 2/\pi N_p, & a_0 \gg 1 \end{cases} \quad (6.4)$$

where N_p is the number of plasma periods behind the driving laser pulse.

As a laser pulse propagates in a plasma medium, it loses its energy in various ways, including the plasma wave excitation in the medium. The depletion length, $L_{depletion}$, is the distance after which the laser pulse energy is reduced at 1/e of the initial energy. In the linear regime, the depletion length is given by $L_{depletion} \approx (\omega_0^2 / \omega_p^2)(\lambda_p/a_0^2)$, while, in the nonlinear regime, the depletion length is modified into $L_{depletion} \approx (\omega_0^2 / \omega_p^2)(\lambda_p a_0)$. The dephasing and depletion lengths both increase as the electron density decreases in the plasma medium. For example, under a laser intensity of $a_0 = 3$ at a laser wavelength of 0.8 μm, the dephasing and depletion lengths are approximately 2.8 cm and 1.2 m, respectively, in a gas target having a density of $\sim 10^{18} \text{ cm}^{-3}$. Generally speaking, a low electron density is preferable in the viewpoints of the output electron beam energy and quality. For most cases, the Rayleigh length is much shorter than the other two characteristic lengths (dephasing and depletion lengths), then the energy gain is usually limited by the diffraction of the laser pulse. In the cases in which the acceleration distance is limited by the depletion length $L_{depletion}$, the energy gain ΔE , is given by [18]

$$\Delta E(\text{MeV}) \approx \begin{cases} 3.4 \times 10^{21} / [\lambda^2(\mu\text{m}) n(\text{cm}^{-3})], & a_0 \ll 1 \\ 400I(\text{Wcm}^{-2}) / n(\text{cm}^{-3}), & a_0 \gg 1 \end{cases} \quad (6.5)$$

6.2.4 Self-trapping in the Wake-Field

Diffraction, dephasing, and depletion are mostly related with the electron energy gain from the laser pulse. As well as the electron energy, the total number of electrons accelerated to a high energy level is also important. The total number of electrons is related with the trapping of electrons in the plasma wake or the plasma cavity. In LWFA, there is no external source for injecting electrons. The large amount of electrons in the background plasma is self-trapped and accelerated in the wake. However, the trapped electrons also significantly modify the accelerating

field that is formed in a plasma cavity. This phenomenon is known as the beam loading effect. Beam loading can be severe limitations on the beam current, the quality of the accelerated electron bunch, and the efficiency of the plasma based accelerator. The detailed discussion on the beam loading effect can be found in [18].

Self-trapping can happen in both non-wave-breaking and wave-breaking regimes. In non-wave-breaking regime, thermal distribution and laser-plasma instabilities can spread electron momentum. For a thermal plasma electron distribution, electrons on the tail of the distribution may have sufficiently high momentum. A fraction of electrons having high longitudinal momentum can catch up the laser-plasma wake and be accelerated by the wake. Several techniques including ponderomotive injection, colliding injection, density transition, etc. can be additionally used in order to increase the fraction. In wave-breaking regime, a large amount of plasma electrons (in the order of nano-Coulombs) can be self-trapped in the wake and accelerated without interacting directly with the laser field. In this case, the length of bubble or plasma cavity is approximately one plasma wavelength λ_p and a short laser pulse (i.e., the pulse duration is $\lambda_p/2c$ or less) is assumed. Otherwise, the accelerating electrons directly interact with a long laser pulse. The theory predicted that the wave breaking can occur at an intensity of $a_0 > 2(\omega_0/\omega_p)^{2/3}$ in 1D geometry for a linearly polarized laser pulse.

Figure 6.4 represents simulation results showing the bubble formation and snapshots of electron density and electron energy spectra under two different laser intensities ($a_0 = 3$ and $a_0 = 5$) [19]. At a lower laser intensity ($a_0 = 3$), a regular plasma wave is seen in the density plot. Only a relatively small number of electrons (in the order of 10^7 MeV^{-1}) is trapped in the low-density wave buckets and accelerated to energies of 40–80 MeV. As increasing a_0 to 5, the regular wave train disappears and a large number of electrons are self-trapped in the first wake bucket behind the laser pulse and accelerated to have a peak at $70 \pm 5 \text{ MeV}$ after 200 μm of propagation. A more complicated three dimensional (3D) particle-in-cell (PIC) simulation shows that the transverse wave breaking is possible at a lower intensity. The curved plasma bubble leads to transverse wave breaking at a reduced threshold value. This implies that electron motion close to the vertex is transverse rather than longitudinal. A curved feature of the plasma bubble in the wake breaking regime is very efficient for self-trapping of background electrons.

6.3 Self-guided and Channel-guided Electron Acceleration

The first quasi-monoenergetic electrons [9–11] accelerated in the bubble regime were obtained by using gas jet targets. At those experiments, femtosecond laser pulses (pulse duration of 30–50 fs, pulse energy of 0.5–1 J) were focused onto 2–3 mm-long supersonic gas jets puffing hydrogen or helium. The normalized vector potential (a_0) ranges from 1 to 2.5, and the electron density (n_e) does from

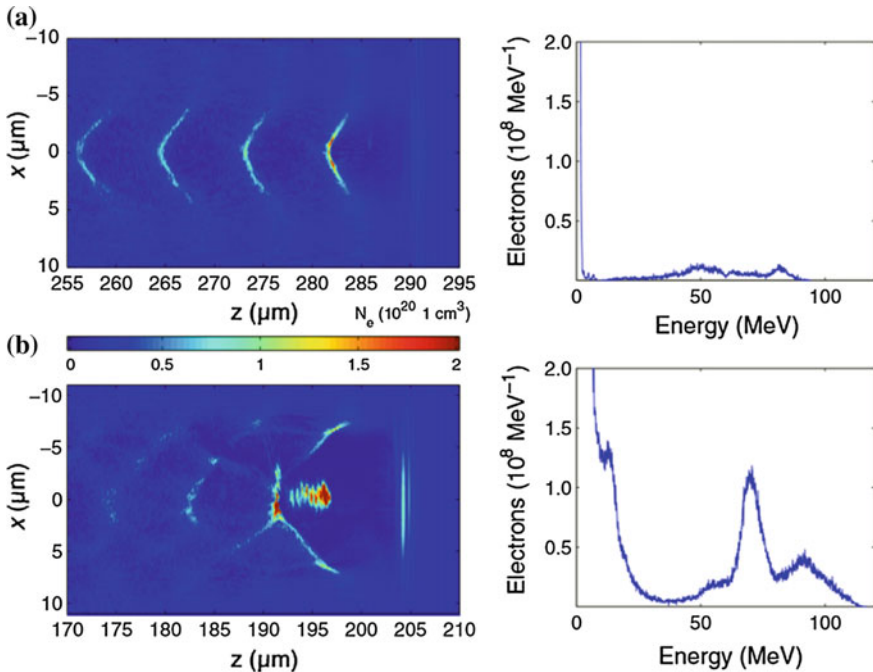


Fig. 6.4 Formation of the bubble (or plasma cavity) and self-trapping of electrons in the bubble. The laser-plasma wake and the energy spectrum of electrons in the upper row is obtained under the laser intensity of $a_0 = 3$. As increasing the laser intensity up to $a_0 = 5$, the bubble is formed and a large amount of electrons are self-trapped and accelerated, while a quasi-monoenergetic peak appears in the spectrum. (Reproduced with permission from Geissler et al. [19]. IOP Publishing. All right reserved.)

mid- 10^{18} to mid- 10^{19} cm^{-3} . The femtosecond intense laser pulse is self-guided in the gas jet target. The origin of self-guiding is the change in the refractive index. When an electromagnetic field propagates along the plasma medium, the general expression for the refractive index, n_{RI} , is given by

$$n_{RI}(r) \simeq 1 - \frac{\omega_{p0}^2}{2\omega^2} \frac{n(r)}{n_0 \gamma(r)}. \quad (6.6)$$

In the limits of $a_0^2 \ll 1$, $|\Delta n_p/n_0| \ll 1$, and $|\delta n/n_0| \ll 1$, the refractive index is

$$n_{RI}(r) \simeq 1 - \frac{\omega_{p0}^2}{2\omega^2} \left(1 - \frac{a_0^2}{2} + \frac{\Delta n_p}{n_0} + \frac{\delta n}{n_0} \right). \quad (6.7)$$

The second term in the parenthesis represents the relativistic optical guiding effect. For the Gaussian laser profile peaked on axis, the refractive index has a maximum and decreases as the radius increases. Thus, the self-focusing effect

occurs when the laser power exceeds a critical power. The third term in the parenthesis represents the pre-formed plasma density channel.

An intense laser pulse propagating in a plasma medium can create a plasma channel through ponderomotive and thermal effects. As a result, a parabolic density channel is formed. The refractive index profile for the preformed plasma channel can be $n_{RI}(r) = n_0 + \Delta n r^2 / r_0^2$, where Δn is the channel depth. This term is related with channel guiding. The last term is related with plasma wave guiding for short laser pulses ($c\tau \ll \lambda_p$) and ponderomotive self-channeling for long laser pulses ($c\tau \gg \lambda_p$). In those situations, the plasma density modulation can induce self-focusing and/or diffraction, depending on the plasma density condition.

6.3.1 Self-guiding in Gas Jets and Gas Cells

For accelerating electrons in the plasma bubble, a high-density profile with a plateau is requested for the gas jet target. A supersonic nozzle with a high Mach number ($M \gg 1$) can meet this criterion and be used for electron acceleration. The gas jet target provides the most simple LWFA-based electron accelerator. Recently, a stable GeV-class electron bunch was demonstrated by using the combination of a 10-mm-long gas jet and a spherical mirror having a focal length of 1.5 m [20]. A self-guided wakefield was supported in a stable few-millimeter-long plasma channels, and electrons were accelerated to sub-GeV level in the plasma bubble. Figure 6.5a, b show plasma channels and electron spectrum recorded for ten consecutive shots. Figures show the stable channel formation and electron energies obtained under the combination of a long gas jet and a long focal length mirror. From the figure, the average peak energy and energy fluctuation were 237 ± 12 MeV and 5 %, respectively. Although the gas jet could generate a stable and GeV-class electron bunches under specific laser and plasma conditions, the process generally suffers from a poor reproducibility and stability in peak energy and overall energy spectrum, beam pointing, charge, divergence, due to fluctuations in laser and plasma parameters as well as a number of laser-plasma instabilities. Thus, numerous efforts were undertaken in order to minimize fluctuations in laser and plasma parameters.

One of these efforts has been aimed at using gas inside a cell as laser-plasma medium. There are many possible designs for the gas cell. Let us discuss one example of gas cell designed for an electron acceleration experiment [21]. Figure 6.6 shows a 10-mm-long gas cell and the electron spectrum recorded for 40 consecutive shots from the gas cell. In the experiment, the gas cell was constructed with two sapphire plates, each with a half-cylindrical groove in its surface. The grooves were aligned to form a more than 10-mm-long, few-hundreds- μm diameter channel. Figure 6.6b shows the calculated gas pressure and implies the potential of the reduced target density fluctuation compared to supersonic gas jets. As shown in Fig. 6.6c, every shot led to electron acceleration and the peak energy was stable.

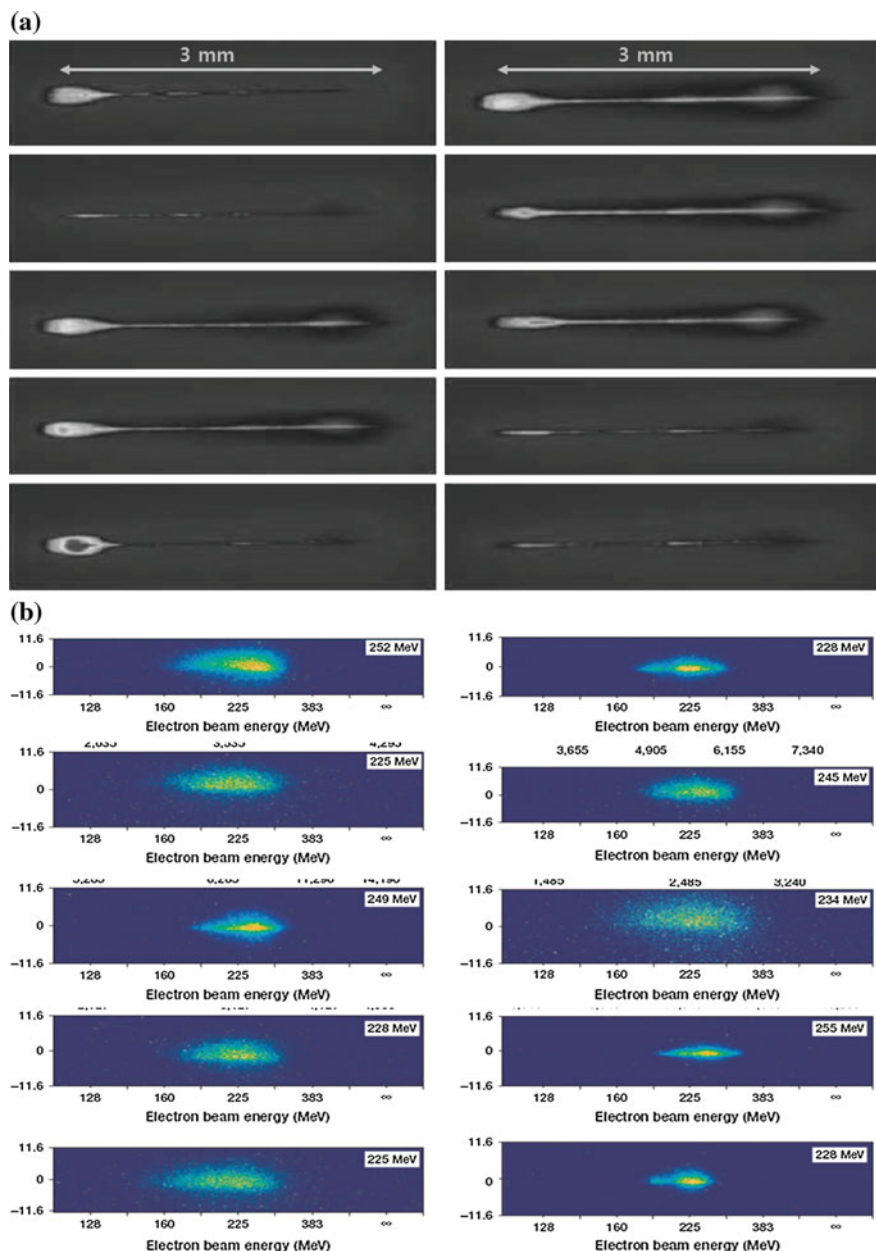


Fig. 6.5 **a** Few-mm-long plasma channels formed in the gas jet target. **b** Electron energy spectrum. In the experiment, the plasma density was $7.0 \times 10^{18} \text{ cm}^{-3}$ and the laser intensity was $6.5 \times 10^{18} \text{ Wcm}^{-2}$. **(a)** Reproduced with permission from Hafz et al. [21]. Copyright (2009), Optical Society of Korea. **(b)** Reproduced with permission from Hafz et al. [20]. Copyright (2008), Nature Publishing Group.)

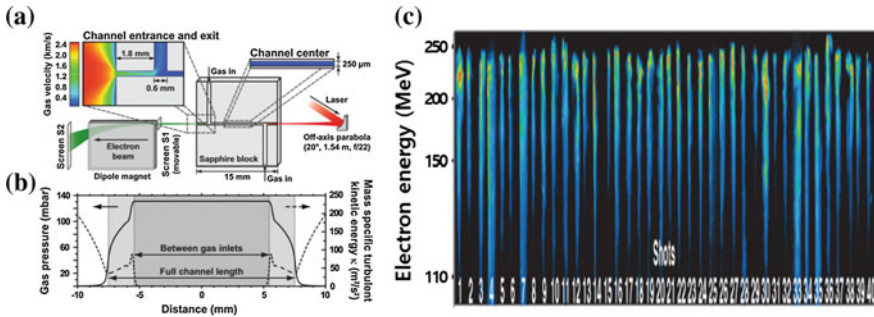


Fig. 6.6 **a** Schematics of gas cell. **b** Calculated gas pressure. **c** Electron spectrum for 40 consecutive shots. The channel was filled with hydrogen passing through a valve and two gas slots at backing pressures of up to 490 mbar and the normalized laser vector potential was 0.89 in the experiment. (Reproduced with permission from Osterhoff [22]. Copyright (2008), American Physical Society.)

The statistics shows that the standard deviations for the electron peak and for the high-energy cutoff were 6 and 3 % at 217 ± 6 MeV, respectively. And, the energy spread of the peak, $\Delta E/E$, of 8.2 % FWHM was reported with $\Delta E \approx 16.3$ MeV. As a recent result with a petawatt- class Nd:glass lasers, the production of electron beams with energy up to 2 GeV were reported when a 7-cm-long gas cell pulse-filled with He at a plasma density $4.8 \pm 0.1 \times 10^{17} \text{ cm}^{-3}$ was used [22].

6.3.2 Gas-filled Hollow Capillary

One efficient approach to produce stable energetic electrons is to use channel guiding of the intense laser pulse with a smaller spot sizes over centimeter-scale distances. This idea originated from the plasma channel created in a gas jet with the ‘ignitor-heater’ technique. In this technique, a plasma column is ionized and then heated by two pre-cursor laser pulses. A gas-filled capillary discharge waveguide was proposed to overcome the limitations imposed by a gas jet and to relativistically guide intense laser pulses in centimeter-scale, low density plasma channels (see Fig. 6.7a). Because an intense laser pulse is guided by Fresnel reflection at the inner capillary wall, this method does not rely on either laser power or plasma density. When a laser pulse couples with eigenmodes in the capillary tube, the laser energy transfers to eigenmodes and propagates through the tube. In an experiment using a 3.3-cm-long gas-filled capillary discharge waveguide, the generation of electron beam having an energy of 1.0 GeV was demonstrated with an input laser power of 40 TW [12]. Through theoretical and numerical studies, it was confirmed that such channel-guided accelerators could produce GeV electrons with laser powers as low as 40 TW [23]. In the recent experiment using a gas-filled 9-cm-long capillary discharge waveguide, the generation of electron beams with an energy of

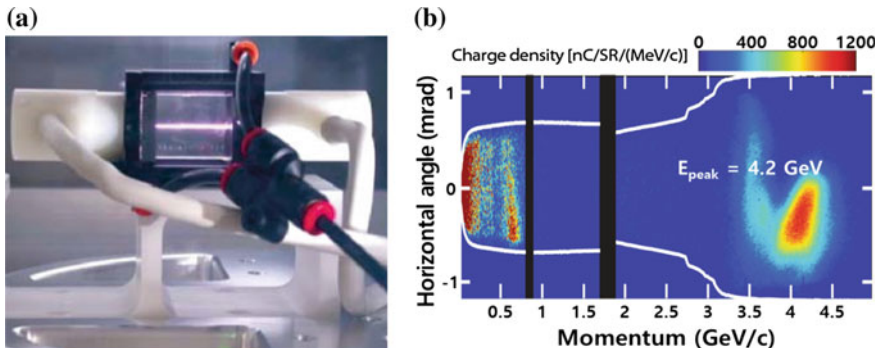


Fig. 6.7 **a** Photo of the 3-cm-long gas-filled capillary discharge waveguide. **b** Electron energy spectrum. Electron energy peaked at 4.2 GeV. In the experiment, the 9-cm-long gas-filled capillary discharge waveguide was used. (**a** Reproduced with permission from Leemans and Esarey [25]. Copyright (2009), American Institute of Physics. **b** Reproduced with permission from Leemans et al. [13]. Copyright (2014), American Physical Society.)

4.2 GeV was demonstrated with a plasma density of $\approx 7 \times 10^{17} \text{ cm}^{-3}$ [13]. For such sufficiently high intensities and an appropriate choice of density, plasma electrons were self-trapped and accelerated by the plasma wave. This is a record result: the electron beams with the highest peak energy and the lowest energy spread (6 % rms) ever produced before with laser techniques.

6.4 Multiple Stage Acceleration

The high field gradient in the plasma bubble brings up the idea on building next generation laser-plasma accelerators having an energy range of 100 GeV–1 TeV. This means that the field gradient should be maintained for a distance of over 10 m. Recent theoretical modellings and full-scale 3D particle-in-cell (PIC) simulations in a Lorentz-boosted frame show that self-injected 11-GeV and externally injected 40-GeV electron beams can be achievable provided that the pulse duration and spot size are appropriately chosen [24]. According to simulation results, the length of plasma medium should be more than 500 cm in order to obtain 40-GeV electron beams under an external guiding condition. As discussed in previous section, the maximum attainable energy is mostly determined by diffraction, dephasing, and depletion lengths. In addition, the decrease in the plasma density to 10^{16} cm^{-3} is preferable to increase the dephasing and depletion lengths to meter scales. However, the low plasma density makes it difficult for electrons to be self-trapped into the plasma bubble. An external injection scheme can be effective to accelerate electrons beyond 10 GeV. The external injection scheme can be realized also by an additional laser-plasma accelerator.

A few years ago, a TeV electron-positron collider based on multiple laser-plasma acceleration stages was discussed by Leemans [23]. In that scheme, electrons generated from the first laser-plasma accelerator (injector) are injected into a series of following laser-plasma acceleration stages (accelerators) and accelerated up to TeV level. This idea could dramatically reduce the size of a TeV electron-positron collider. In the following, we will discuss injector and accelerator schemes experimentally demonstrated in a small scale.

Quasi-monoenergetic GeV-level electron beams were experimentally produced by focusing ~ 50 TW femtosecond laser pulses into two segments of gas cells filled with He/O₂ mixture and pure He gas, respectively. This was named as the “all-optical cascaded laser wakefield accelerator” [26]. Figure 6.8 shows the setup used and the energy spectra obtained in the experiment. The first segment, 1-mm-long gas cell, had an electron density of $5.7 \times 10^{18} \text{ cm}^{-3}$, and produced electron beams with a Maxwellian spectrum tailing up to 50–80 MeV. The electrons are self-trapped through the ionization-induced injection in that first gas cell. Electrons generated from the first gas cell are seeded into the second segment, 3-mm-long gas cell having a lower electron density of $2.5 \times 10^{18} \text{ cm}^{-3}$. The electron beams are accelerated to 0.8 GeV level with a quasi-monoenergetic feature. The energy spectrum shown in Fig. 6.8b, c represents the demonstration of injector and accelerator scheme.

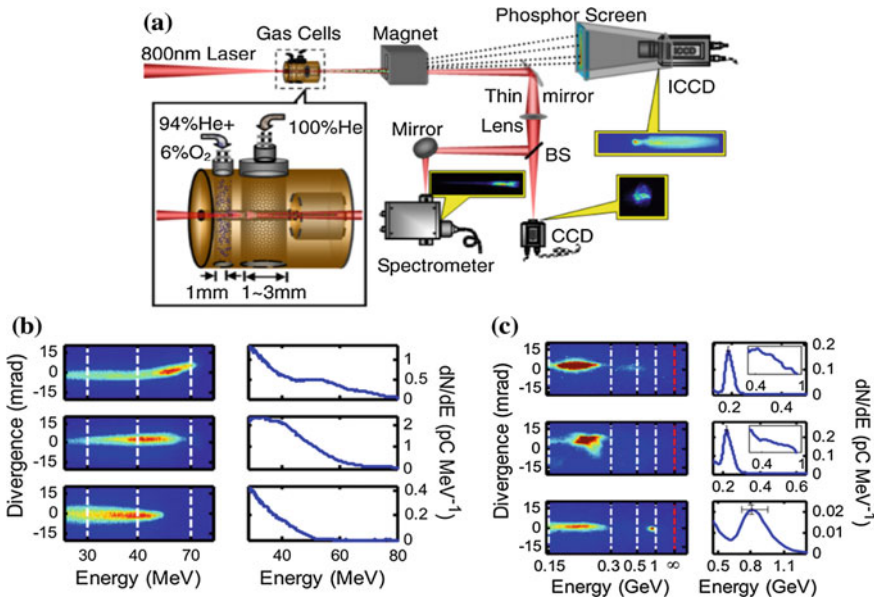


Fig. 6.8 **a** Experimental setup for the cascaded LWFA. Two-segment cylindrical gas cell is used as the laser-plasma accelerator. Electrons produced in the first gas cell are further accelerated in the second gas cell. **b** Electron energy spectrum generated from the first 1-mm-long gas cell. **c** Electron energy spectrum further accelerated from the second 3-mm-long gas cell. (Reproduced with permission from Liu et al. [27]. Copyright (2011), American Physical Society.)

The injector-accelerator scheme was further demonstrated with two independent gas jet targets [27]. Figure 6.9 shows the experimental setup for injector-accelerator scheme using two independent gas jets and relevant experimental results. In the experiment, 60-fs, 25-J laser pulses were focused into 4-mm-long and 10-mm-long gas jet targets by a spherical mirror with a focal length of 4 m. The focusing position of the laser beam was located near to the entrance of the gas jet. In the single stage acceleration, energetic electrons peaking at 400 MeV were obtained from the 4-mm-long gas jet with an electron density of $2.1 \times 10^{18} \text{ cm}^{-3}$.

Moving to the 10-mm gas jet (again in single stage operation), electron beams peaking at about 800 MeV were obtained at an electron density of $1.1 \times 10^{18} \text{ cm}^{-3}$. In the injector-accelerator scheme, the 400-MeV electron beams generated from the first gas jet (injector) were injected into the 10-mm-long jet for further acceleration. As shown in Fig. 6.9b, the highest electron energy observed exceeded 3 GeV when the electron density of the second medium was lowered down to $0.8 \times 10^{18} \text{ cm}^{-3}$. The 3D-PIC simulations support the multi-GeV electron beam generation from the injector-accelerator scheme, and provide information on the increase in both energy and energy spread in the electron spectrum. In this case, the divergence of the

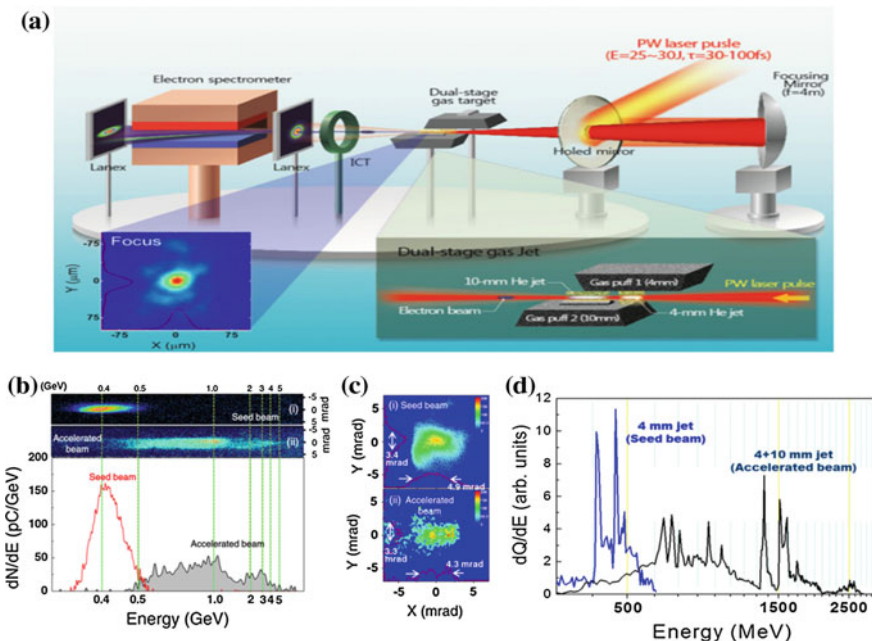


Fig. 6.9 **a** Experimental setup for the injector-accelerator scheme using two independent gas jets. **b** Electron spectrum produced from the injector and accelerated from the accelerator. Electrons peaked at 0.4 GeV were accelerated up to over 3 GeV in the accelerator. **c** Electron beam profiles. **d** 3D-PIC simulation results. Simulations supported electron energy spectra that were experimentally obtained. (Reproduced with permission from Kim et al. [28]. Copyright (2013), American Physical Society.)

electron beam was about 4 mrad, and the total charge of the beam over the whole spectrum was about 80 pC, while the total charge of the electron beam for energies over 2-GeV is estimated to be about 10 pC. The electron spectrum after the acceleration stage showed a broad energy spread over 1.5 GeV ($\Delta E/E > 50\%$) and two separate peaks were observed at 1.1 and 2.7 GeV while the maximum energy of the electron spectrum reached 4 GeV. Even though a single laser-plasma accelerator can already produce Multi-GeV electron beams, a long plasma medium length over one meter is anticipated in order to attain several tens of GeV. Considering this point, the demonstration of injector-accelerator scheme is timely and the all-laser-driven injector and accelerator scheme can be a promising candidate to accelerate electrons over several tens of GeV or 100 GeV level. The advantages of the scheme also include the flexible optimization strategy of each laser plasma accelerator and wavelength tunability in both X-ray and γ -ray ranges. In the injector-accelerator scheme, the electron acceleration can be optimized and controlled at every acceleration stage. This will provide an efficient route for accelerating electrons. For the wavelength tunability in both X-ray and γ -ray ranges, accelerated electrons can be picked up at a specific energy range from an acceleration stage, and be delivered to additional devices for generating high energy photons (X-ray or γ -ray) suitable for applications. The high energy photon generated can be used in the bio-medical, material, and industrial applications.

6.5 Applications of High Energy Electrons in Bio-medical Fields

In this section, the applications of high energy electron beams in the bio-medical field are mostly discussed. In the present day, two kinds of applications are mostly considered with high energy electron beams: one is the electron radiation therapy and the other is the bio-medical imaging.

6.5.1 *Electron Radiation Therapy*

Electron beams have been used in the radiation therapy field for over 50 years. In the direct clinical applications, electron beams having an energy range of 6–20 MeV are required for the treatment of (1) skin and lip cancers, (2) chest-wall and neck cancers, (3) respiratory and digestive-track lesions from 1 to 5 cm in depth, and (4) boost treatment to lymph nodes, operative scars and residual tumor [28]. Electrons having an energy of lower than 10-MeV have good depth-dose characteristics, which result in minimal lateral and distal damage issues. Because of the eager of evaluating the potential as a future competitor to existing technology, the feasibility study on the clinical use of laser-plasma accelerator was carried out [29].

The research concluded that the dose rate based on LWFA technology was far (1–3 %) from the clinical requirement even though laser-plasma accelerators could provide therapeutic electron beams with acceptable pulse flatness, penetration, and fall off depth dose. Clinical electron beams having energy range of tens-of-MeV are produced from betatron and linear accelerators, and other conventional rf-based accelerating devices.

Recently, because of the improved dosimetry properties, interest in the clinical use of very high energy electrons (VHEE) ranging from 100 to 250 MeV is growing [30]. The effective range of such high energy electron beams can exceed 40 cm, and lateral scattering of high-energy electrons in tissue is sufficiently small for use in intensity-modulated radiation therapy (IMRT) treatment of tumors, such as lung and prostate cancers. Advantages of VHEE beams are the possibility of irradiating the target volume from several different directions simultaneously, their small penumbra and high dose rates. Because of the size and cost of conventional LINAC-based accelerators, the laser-plasma accelerator can be a good candidate for generating low-cost VHEE beams. In addition, electron beams from laser-plasma accelerators can have unique properties such as ultra-short pulse duration, low energy spread, low transverse emittance, and high peak current. These kinds of unique features can make laser-plasma-based VHEE beams more interesting in radiation therapy.

6.5.2 *Electron Radiography*

Owing to the compact size, short bunch duration, and easy synchronization, high-power laser-driven electrons have a growing interest in electron radiography. Transmissive and contact radiographic imaging using MeV electrons was tested in a recent experiment [31]. In that experiment, 2.5-TW laser pulses (40-fs in duration and 100-mJ in energy) were focused on Ar cluster gas targets in order to produce uniform and divergent (0.4 radian) electron bunches with energy up to 2 MeV and charge of 12 ± 6 nC. The laser-plasma accelerator acted as a so-called ‘laser-electron gun’. Centimeter-scale samples including biological ones were exposed with MeV electrons for evaluating imaging performances. Direct electron radiographic images were taken using a sandwich of two radiochromic films in a contact transmission configuration. Figure 6.10 shows (a) a photo for the sample used and (b) an electron radiography obtained. Spatial resolution of the recorded images was estimated to be 60 μm for the cm-scale samples. However, the resolution can decrease to μm level with a proper detection system. Electron radiography might be a suitable imaging technique for cm-scale biological samples that requires a μm resolution.

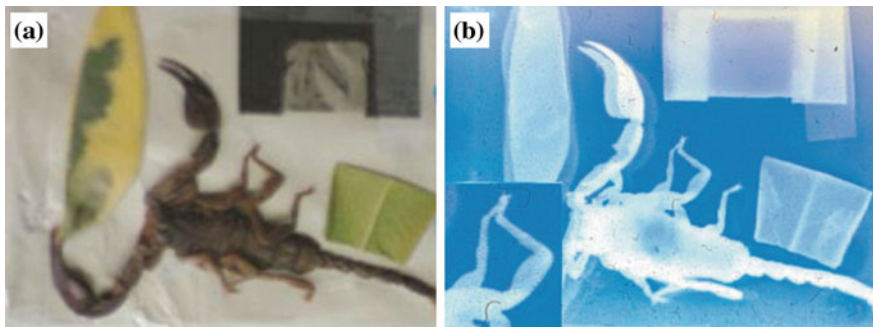


Fig. 6.10 **a** Sample for electron radiography. **b** Electron radiography of **(a)**. In the electron radiography, the spatial resolution of 60 mm was obtained with cm-scale samples. (Reproduced with permission from Bussolino et al. [32]. IOP Publishing. All right reserved.)

6.5.3 Secondary Sources of High Energy Photons

Energetic electrons are also indirectly used for bio-medical applications. Electron beam energy can be converted into high-brightness, high-energy photons (X-ray and γ -ray). For bio-medical applications, it is generally known that X-ray photon energies should range 20–100 keV to allow transmission through the human body, the bandwidth should be narrow enough to minimize the dose in order to avoid unwanted soft X-ray collateral damage, and a high degree of tunability should be required to discriminate different types of bio-sample images. Energetic electrons are suitable for generating such high energy photon sources through undulator radiation, betatron radiation, and Compton scattering processes. In the followings, recent experimental results for producing high-energy photon sources from high-energy electron beams accelerated by laser wakefields are summarized.

6.5.3.1 X-Ray Generation Through Undulator Radiation

Undulator radiation using laser-driven energetic electrons was experimentally demonstrated by Fuchs et al. [33]. Figure 6.10 shows the experimental setup for producing tunable soft X-rays from undulator radiation. In the experiment, well-collimated and stable electron beams with energies of 210 MeV were generated from a 1.5-cm-long laser-plasma accelerator and delivered into a 30-cm-long undulator to generate soft-X-ray pulses with a pulse duration of 10 fs. The spectrum of the generated undulator radiation consists of a main peak centered at a wavelength of 18 nm, a second peak near 9 nm and a high energy cutoff at 7 nm. The experiment showed that, owing to the broad range of electron energies delivered by the plasma accelerator, the generated soft X-ray can be tunable from 16 to 21 nm, depending on the position of magnetic lenses used. The peak brilliance was

estimated to be $\sim 1.3 \times 10^{17}$ photons per second per mrad² per mm² per 0.1 % bandwidth when a duration of 10 fs for the undulator radiation pulse was assumed. This laboratory-sized undulator radiation source can be used for four-dimensional imaging applications.

6.5.3.2 X-Ray Generation Through Betatron Radiation

A plasma bubble in the nonlinear regime has a confined electron density in an accelerating range formed behind the laser pulse. The relativistic electrons propagating in the plasma bubble experience a strong electrostatic field in the radial direction and oscillate with an angular frequency given by $\omega_b = \omega_p / \sqrt{2\gamma}$. The oscillation of high-energy electrons emits radiation (see Fig. 6.11). The radiation is emitted in the forward direction within a cone angle of K/γ , where K is the strength parameter of a plasma wiggler given by $K = 2\pi\gamma r_0 / \lambda_b$. This phenomenon is known as the betatron radiation in the bubble. The betatron radiation from a laser plasma bubble can be considered as a micro-undulator radiation because the wavelength (λ_b , usually micrometer-scale) of a wiggler formed in the plasma bubble is much shorter than fixed magnets in a synchrotron. The characteristics of betatron radiation depend on the oscillation amplitude, r_0 . As the oscillation amplitude becomes large (usually a few microns), high harmonics are radiated and the resulting broadband spectrum is extended up to a critical energy $\hbar\omega_c [eV] = 5 \times 10^{-21} \gamma^2 n_e [\text{cm}^{-3}] r_0 [\mu\text{m}]$ [33]. Here, ω_c is the critical frequency given by the relation $\omega_c = \frac{3}{2} \frac{\gamma^2 |F_\perp|}{mc}$. $F_\perp^2 = F_x^2 + F_y^2$ is the square of the transverse force acting on relativistic electrons.

The X-ray radiation based on betatron oscillation was observed in the experiment performed with the Vulcan Nd:glass petawatt laser [34]. The 630-fs, 280-J laser pulse was focused on the front edge of a supersonic gas jet to have a normalized vector potential of $9 < a_0 < 29$. Electrons were accelerated to have energies from 20 to 200 MeV. X-rays were measured with suitably filtered image plate detectors in the direct forward direction after the electrons had been deflected by the

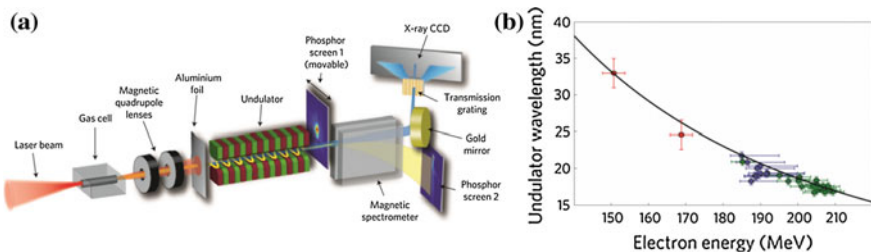


Fig. 6.11 **a** Experimental setup for generating soft-X-ray radiation from the undulator. **b** Wavelength of undulator radiation depending on electron energy. (Reproduced with permission from Fuchs et al. [33], Copyright (2009), Nature Publishing Group.)

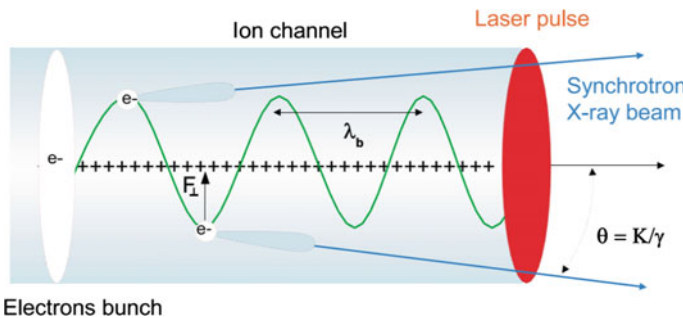


Fig. 6.12 Generation of synchrotron x-ray source based on the betatron oscillation of a relativistic electron in a laser-produced ion channel. (Reproduced with permission from Rousse et al. [34]. Copyright (2004), American Physical Society.)

magnet. A forward directed X-ray radiation extending to 50 keV was observed in the experiment. The experimental data showed that the measured X-rays were well described in the synchrotron asymptotic limit of electrons oscillating in a plasma channel. In the experiment, at low laser intensity, transverse oscillations were negligible because the electrons were predominantly accelerated axially by the laser generated wakefield. At high laser intensity, electrons were directly accelerated by the laser and entered a highly radiative regime with up to 5 % of their energy converted into X-ray radiations (Fig. 6.12).

6.5.3.3 X-Ray Generation Through Inverse Compton Scattering

Inverse Compton scattering is the elastic scattering of a photon by an energetic charged particle (usually an electron). Photons gain energy from an energetic electron through the inverse Compton scattering process while a photon loses energy to an electron through the Compton scattering process. In the femtosecond high-power laser context, the inverse Compton scattering can be accomplished by counter-propagating laser pulses to energetic electrons produced from the laser-plasma accelerator. The much higher optical frequency can be achieved through the inverse Compton scattering than the fixed-magnet arrays can provide. In 2013, quasi-monoenergetic and tunable X-ray radiations were demonstrated from a laser-driven inverse Compton scattering process [35].

Figure 6.13 shows the experimental setup for the inverse Compton scattering and experimental results for the tunability of X-ray radiation. In the experiment, a 100-TW laser beam was divided into two synchronized laser pulses. One beam line was used to produce quasi-monoenergetic electron beams with energies from 50 to 300 MeV. The other beam line acted as an undulator by scattering from the electrons. After interacting with the laser pulse, the electron beam was swept out of the X-ray path by a dipole magnet. The forward-directed X-ray radiation was recorded by a detector placed outside the vacuum system. The experiment demonstrated that

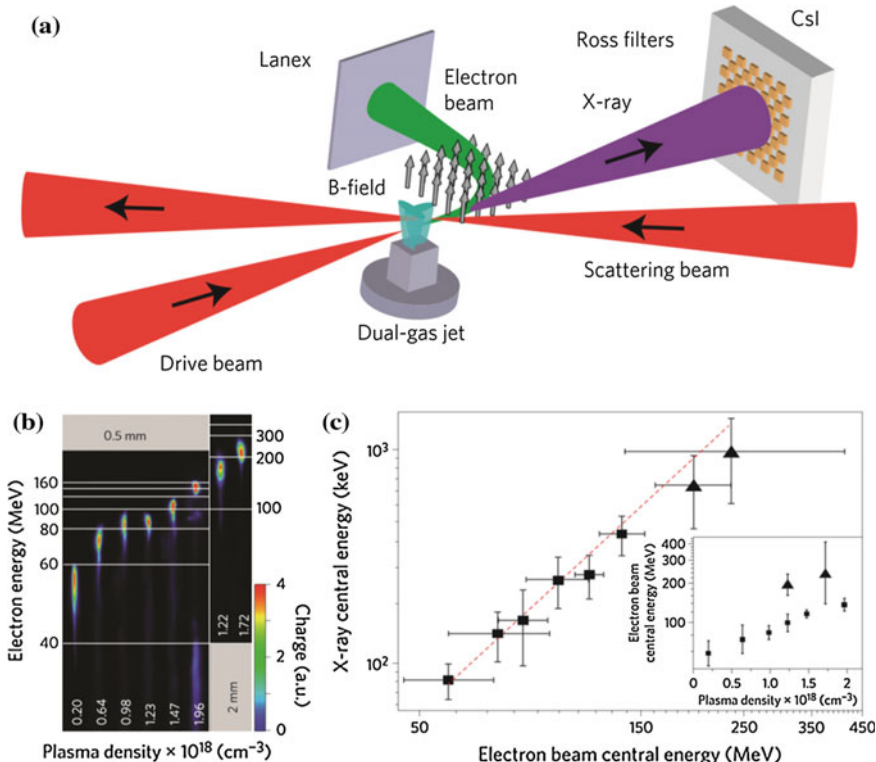


Fig. 6.13 **a** Experimental setup for producing X-ray radiation through the inverse Compton scattering. **b** Drive beam generated quasi-monoenergetic electron beams with energies from 50 to 300 MeV. **c** Measured X-ray central energy as a function of the measured electron-beam central energy. (Reproduced with permission from Powers et al. [36]. Copyright (2014), Nature Publishing Group.)

electron energy was tuned by changing the plasma density in the laser-plasma accelerator (see Fig. 6.13b) and the energy of emitted X-ray radiation was tunable from 70 keV to 1 MeV by controlling the electron energy (see Fig. 6.13c).

6.5.3.4 X-Ray Imaging of Bio-medical Sample

Ultrashort X-ray radiation can provide bio-medical imaging with a femtosecond temporal resolution. Figure 6.14 represents examples of X-ray imaging with samples [36, 37]. Either sizable or tiny bio-medical sample can be imaged with ultrashort X-ray radiation. The phase contrasting imaging technique can be applicable to image a sizable bio-medical sample in the X-ray regime. This technique is also known as X-ray Phase Contrast Imaging (XPCI). Figure 6.14a shows a single-shot X-ray image of a cricket recorded by XPCI technique. The X-ray radiation was

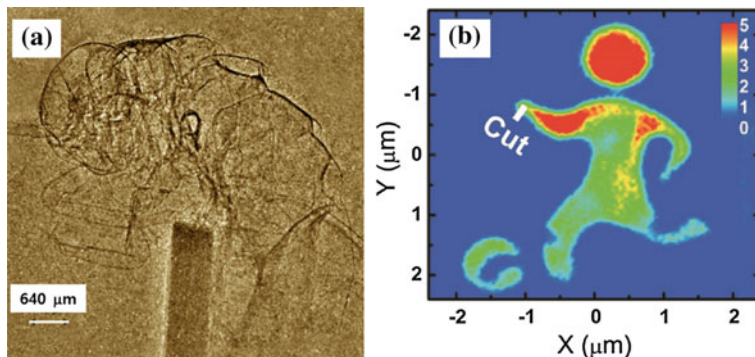


Fig. 6.14 **a** Single-shot X-ray phase contrast image of a cricket recorded with hard X-rays produced by laser-driven betatron oscillation (Image courtesy: reference #36). **b** Single-shot FT holographic image recorded with laser-driven X-ray laser. (**a** Reproduced with permission from Albert et al. [37]. IOP Publishing. All right reserved. **b** Reproduced with permission from Kim et al. [38]. Copyright (2011), American Institute of Physics.)

produced by betatron oscillation in a laser-plasma accelerator. Elastic scattering induces a phase shift when x-rays pass through a sample. The cross-section for elastic scattering of x-rays in low-Z elements is usually much greater than for absorption. It means that, for quasi transparent objects such as biological samples or tissues, this technique can be more sensitive to small density variations and offer better contrast than conventional radiography.

The ultrashort X-ray radiation is a promising source for imaging tiny nanometer scale samples with femtosecond temporal resolution. Lensless coherent diffraction imaging (CDI) and Fourier transform (FT) holographic imaging techniques can be used to study the dynamics of tiny biological samples. Figure 6.14b is an example of single-shot FT holographic image recorded with laser-driven X-ray laser. The figure shows the imaging capability of tiny samples with 100-nm spatial resolution. In conclusion, ultrafast X-ray imaging based on the laser-plasma accelerator technology will be promising imaging technology for bio-medical samples with high spatial and temporal resolution at a low cost.

6.6 Conclusion

The laser-plasma accelerator has been tremendously advanced since it has been first proposed more than 35 years ago. The laser-plasma accelerator routinely produces quasi-monoenergetic electron beams at multi-GeV energy level, and energy of electron beams is converted to high-energy photons with femtosecond pulse duration in X-ray or γ -ray range as secondary sources. Compact size and reasonable cost are primary advantages of the laser-plasma accelerator. This originates from a

high-field gradient (~ 1 GeV/cm) formed in a miro plasma bubble. The high-field gradient makes ones to consider building 100-GeV-class laser plasma accelerators.

Laser-driven energetic electrons and secondary light sources have great potential in bio-medical applications. The ultrashort pulse durations of electron and secondary radiation beams will provide opportunities to study atomic and molecular dynamics in the bio-medical samples with unprecedented temporal and spatial resolutions.

In the perspective of international activities related with the construction of femtosecond 10-PW lasers and related planned researches, much greater progresses not only in the fundamental research but also in the practical applications are expected.

References

1. D. Strickland, G. Mourou, Compression of amplified chirped optical pulses. *Opt. Commun.* **56**, 219 (1985)
2. S. Laux, F. Lureau, C. Radier, O. Chalus, F. Caradec, O. Casagrande, E. Pourtal, C. Simon-Boisson, F. Soyer, P. Lebarny, Suppression of parasitic lasing in high energy, high repetition rate Ti: sapphire laser amplifiers. *Opt. Lett.* **37**, 1913 (2012)
3. T.J. Yu, S.K. Lee, J.H. Sung, J.W. Yoon, T.M. Jeong, J. Lee, Generation of high-contrast, 30 fs, 1.5 PW laser pulses from chirped-pulse amplification Ti: sapphire laser. *Opt. Express* **20**, 10807 (2012)
4. T. Tajima, J.M. Dawson, Laser electron accelerator. *Phys. Rev. Lett.* **43**, 4428 (1979)
5. J.D. Lawson, Lasers and accelerators. *IEEE Trans. Nucl. Sci.* **NS-26**, 4217 (1979).
6. Y. Kitagawa, T. Matsumoto, T. Minamihata, K. Sawai, K. Matsuo, K. Mima, K. Nishihara, H. Azechi, K.A. Tanaka, H. Takabe, S. Nakai, Beat-wave excitation of plasma wave and observation of accelerated electrons. *Phys. Rev. Lett.* **68**, 48 (1992)
7. F. Amiranoff, D. Bernard, B. Cros, F. Jacquet, G. Matthieu, P. Miné, P. Mora, J. Morillo, F. Moulin, A.E. Specka, C. Stenz, Electron acceleration in Nd-laser plasma beat-wave experiments. *Phys. Rev. Lett.* **74**, 5220 (1995)
8. K. Nakajima, D. Fisher, T. Kawakubo, H. Nakanishi, A. Ogata, Y. Kato, Y. Kitagawa, R. Kodama, K. Mima, H. Shiraga, K. Suzuki, K. Yamakawa, T. Zhang, Y. Sakawa, T. Shoji, Y. Nishida, N. Yugami, M. Downer, T. Tajima, Observation of ultrahigh gradient electron acceleration by a self-modulated intense short laser pulse. *Phys. Rev. Lett.* **74**, 4428 (1995)
9. S.P.D. Mangles, C.D. Murphy, Z. Najmudin, A.G.R. Thomas, J.L. Collier, A.E. Dangor, E. J. Divall, P.S. Foster, J.G. Gallacher, C.J. Hooker, D.A. Jaroszynski, A.J. Langley, W.B. Mori, P.A. Norreys, F.S. Tsung, R. Viskup, B.R. Walton, K. Krushelnick, Monoenergetic beams of relativistic electrons from intense laser-plasma interactions. *Nature* **431**, 535 (2004)
10. C.G.R. Geddes, C. van Toth, J. Tilborg, E. Esarey, C.B. Schroeder, D. Bruhwiler, C. Nieter, J. Cary, W.P. Leemans, High-quality electron beams from a laser wakefield accelerator using plasma-channel guiding. *Nature* **431**, 538 (2004)
11. J. Faure, Y. Glinec, A. Pukhov, S. Kiselev, S. Gordienko, E. Lefebvre, J.-P. Rousseau, F. Burgy, V. Malka, A laser-plasma accelerator producing monoenergetic electron beams. *Nature* **431**, 541 (2004)
12. W.P. Leemans, B. Nagler, A.J. Gonsalves, C. Toth, K. Nakamura, C.G.R. Geddes, E. Esarey, C.B. Schroeder, S.M. Hooker, GeV electron beams from a centimetre-scale accelerator. *Nature Phys.* **2**, 696 (2006)

13. W.P. Leemans, A.J. Gonsalves, H.-S. Mao, K. Nakamura, C. Benedetti, C.B. Schroeder, C. Tóth, J. Daniels, D.E. Mittelberger, S.S. Bulanov, J.-L. Vay, C.G.R. Geddes, E. Esarey, Multi-GeV electron beams from capillary-discharge-guided sub petawatt Laser pulses in the self-trapping regime. *Phys. Rev. Lett.* **113**, 245002 (2014)
14. N.H. Matlis, S. Reed, S.S. Bulanov, V. Chvykov, G. Kalintchenko, T. Matsuoka, P. Rousseau, V. Yanovsky, A. Maksimchuk, S. Kalmykov, G. Shvets, M.C. Downer, Snapshots of laser wakefields. *Nature phys.* **2**, 749 (2006)
15. A. Modena, Z. Najmudin, A.E. Dangor, C.E. Clayton, K.A. Marsh, C. Joshi, V. Malka, C.B. Darrow, C. Danson, D. Neely, and F.N. Walsh, Electron acceleration from the breaking of relativistic plasma waves. *Nature* **337**, 606 (1995)
16. A. Pukhov, J. Meyer-ter-Vehn, Laser wakefield acceleration: the highly non-linear broken-waveregime. *Appl. Phys. B* **74**, 355 (2002)
17. W. Lu, C. Huang, M. Zhou, W.B. Mori, T. Katsouleas, Nonlinear theory for relativistic plasma wakefields in the blowout regime. *Phys. Rev. Lett.* **96**, 165002 (2006)
18. E. Esarey, C.B. Schroeder, W.P. Leemans, Physics of laser-driven plasma-based electron accelerators. *Rev. Mod. Phys.* **81**, 1229 (2009)
19. M. Geissler, J. Schreiber, J. Meyer-ter-Vehn, Bubble acceleration of electrons with few-cycle laser pulses. *New J. Phys.* **8**, 186 (2006)
20. N.A.M. Hafz, T.M. Jeong, I.W. Choi, S.K. Lee, K.H. Pae, V.V. Kulagin, J.H. Sung, T.J. Yu, K.-H. Hong, T. Hosokai, J.R. Cary, D.-K. Ko, J. Lee, Stable generation of GeV-class electron beams from self-guided laser—plasma channels. *Nature Photon.* **2**, 571 (2008)
21. J. Osterhoff, A. Popp, Z. Major, B. Marx, T.P. Rowlands-Rees, M. Fuchs, M. Geissler, R. Horlein, B. Hidding, S. Becker, E.A. Peralta, U. Schramm, F. Gruner, D. Habs, F. Krausz, S. M. Hooker, S. Karsch, Generation of stable, low-divergence electron beams by laser-wakefield acceleration in a steady-state-flow gas cell. *Phys. Rev. Lett.* **101**, 085002 (2008)
22. X. Wang, R. Zgadzaj, N. Fazel, Z. Li, S.A. Yi, X. Zhang, W. Henderson, Y.-Y. Chang, R. Korzekwa, H.-E. Tsai, C.-H. Pail, H. Quevedo, G. Dyer, E. Gaul, M. Martinez, A.C. Bernstein, T. Borger, M. Spinks, M. Donovan, V. Khudik, G. Shvets, T. Ditmire, M.C. Downer, Quasi-monoenergetic laser-plasma acceleration of electrons to 2GeV. *Nature Commun.* **4**, 1988 (2013)
23. W. Leemans, E. Esarey, Laser-driven plasma-wave electron accelerators. *Phys. Today* **62**, 44 (2009)
24. K. Nakamura, B. Nagler, C. Tóth, C.G.R. Geddes, C.B. Schroeder, E. Esarey, W.P. Leemans, A.J. Gonsalves, S.M. Hooker, GeV electron beams from a centimeter-scale channel guided laser wakefield accelerator. *Phys. Plasmas* **14**, 056708 (2007)
25. N.A.M. Hafz, T.M. Jeong, S.K. Lee, I.W. Choi, K.H. Pae, V.V. Kulagin, J.H. Sung, T.J. Yu, J. R. Cary, D.-K. Ko, J. Lee, Laser acceleration of electron beams to the GeV-class energies in gas jets. *J. Opt. Soc. Kor.* **13**, 8 (2009)
26. S.F. Martins, R.A. Fonseca, W. Lu, W.B. Mori, L.O. Silva, Exploring laser-wakefield-accelerator regimes for near-term lasers using particle-in-cell simulation in Lorentz-boosted frames. *Nature Phys.* **6**, 311 (2010)
27. J.S. Liu, C.Q. Xia, W.T. Wang, H.Y. Lu, C. Wang, A.H. Deng, W.T. Li, H. Zhang, X.Y. Liang, Y.X. Leng, X.M. Lu, C. Wang, J.Z. Wang, K. Nakajima, R.X. Li, Z.Z. Xu, All-optical cascaded laser wakefield accelerator using ionization-induced injection. *Phys. Rev. Lett.* **107**, 035001 (2011)
28. H.T. Kim, K.H. Pae, H.J. Cha, I.J. Kim, T.J. Yu, J.H. Sung, S.K. Lee, T.M. Jeong, J. Lee, Enhancement of electron energy to the multi-GeV regime by a dual-stage laser-wakefield accelerator pumped by petawatt laser pulses. *Phys. Rev. Lett.* **111**, 165002 (2013)
29. K.R. Hogstrom, P.R. Almond, Review of electron beam therapy physics. *Phys. Med. Biol.* **51**, R455 (2006)
30. K.K. Kainz, K.R. Hogstrom, J.A. Antolak, P.R. Almond, C.D. Bloch, C. Chiu, M. Fomytskyi, F. Raischel, M. Downer, T. Tajima, Dose properties of a laser accelerated electron beam and prospects for clinical application. *Med. Phys.* **31**, 2053 (2004)

31. A. Subiel, V. Moskvin, G.H. Welsh, S. Cipiccia, D. Reboredo, P. Evans, M. Partridge, C. DesRosiers, M.P. Anania, A. Cianchi, A. Mostacci, E. Chiadroni, D. Di Giovenale, F. Villa, R. Pomipili, M. Ferrario, M. Belleveglia, G. Di Pirro, G. Gatti, C. Vaccarezza, B. Seitz, R.C. Isaac, E. Brunetti, S.M. Wiggins, B. Ersfeld, M.R. Islam, M.S. Mendonca, A. Sorensen, M. Boyd, D.A. Jaroszynski, Dosimetry of very high energy electrons (VHEE) for radiotherapy applications: using radiochromic film measurements and Monte Carlo simulations. *Phys. Med. Biol.* **59**, 5811 (2014)
32. G.C. Bussolino, A. Faenov, A. Giulietti, D. Giulietti, P. Koester, L. Labate, T. Levato, T. Pikuz, L.A. Gizzi, Electron radiography using a table-top laser-cluster plasma accelerator. *J. Phys. D Appl. Phys.* **46**, 245501 (2013)
33. M. Fuchs, R. Weingartner, A. Popp, Z. Major, S. Becker, J. Osterhoff, I. Cortrie, B. Zeitler, R. Hörllein, G.D. Tsakiris, U. Schramm, T.P. Rowlands-Rees, S.M. Hooker, D. Habs, F. Krausz, S. Karsch, F. Grüner, Laser-driven soft-X-ray undulator source. *Nature Phys.* **5**, 826 (2009)
34. A. Rousse, K.T. Phuoc, R. Shah, A. Pukhov, E. Lefebvre, V. Malka, S. Kiselev, F. Burgy, J.-P. Rousseau, D. Umstadter, D. Hulin, Production of a keV X-ray beam from synchrotron radiation in relativistic laser-plasma interaction. *Phys. Rev. Lett.* **93**, 135005 (2004)
35. S. Kneip, S.R. Nagel, C. Bellei, N. Bourgeois, A.E. Dangor, A. Gopal, R. Heathcote, S.P.D. Mangles, J.R. Marques, A. Maksimchuk, P.M. Nilson, K.T. Phuoc, S. Reed, M. Tzoufras, F.S. Tsung, L. Willingale, W.B. Mori, A. Rousse, K. Krushelnick, Z. Najmudin, Observation of synchrotron radiation from electrons accelerated in a petawatt-laser-generated plasma cavity. *Phys. Rev. Lett.* **100**, 105006 (2008)
36. N.D. Powers, I. Ghebregziabher, G. Golovin, C. Liu, S. Chen, S. Banerjee, J. Zhang, D. P. Umstadter, Quasi-monoenergetic and tunable X-rays from a laser-driven Compton light source. *Nature Photon.* **8**, 28 (2014)
37. F. Albert, A.G.R. Thomas, S.P.D. Mangles, S. Banerjee, S. Corde, A. Flacco, M. Litos, D. Neely, J. Vieira, Z. Najmudin, R. Bingham, C. Joshi, T. Katsouleas, Laser wakefield accelerator based light sources: potential applications and requirements. *Plasma Phys. Control. Fusion* **56**, 084015 (2014)
38. H.T. Kim, I.J. Kim, C.M. Kim, T.M. Jeong, T.J. Yu, S.K. Lee, J.H. Sung, J.W. Yoon, H. Yun, S.C. Jeon, I.W. Choi, J. Lee, Single-shot nanometer-scale holographic imaging with laser-driven x-ray laser. *Appl. Phys. Lett.* **98**, 121105 (2011)

Chapter 7

Ionization Induced Electron Injection in Laser Wakefield Acceleration

Min Chen and Zheng-Ming Sheng

Abstract In this chapter we describe and discuss a special technique in laser wakefield acceleration (LWFA): electron injection by use of field ionization of atoms to high orders. Compared with other electron injection schemes in LWFA, this scheme shows the merits of relatively simple operation and controllable final beam quality. In the *single-color* laser ionization injection scheme, we show quasi-monoenergetic electron acceleration is possible through the control of laser self-focusing, which includes self-focusing accommodated ionization injection or ionization injection suppression. In these processes the effective injection length can be controlled within a hundred micrometers range and the absolute energy spread of the beam can be controlled within tens of MeV. In the *two-color* laser ionization injection scheme, we show the effective injection length can be further reduced to tens of micrometers length, and the absolute energy spread of the electrons can be reduced to a few MeV, i.e. the relative energy spread can be less than 0.5 %. A further interesting result is the generation of multi-color electron bunches by use of two-color lasers. These electrons can be used for multi-color X-ray generation through laser beam Thomson scattering. It is also found that the transverse emittance of the electron beam can be significantly reduced by a different two-color ionization injection scheme, in which the wake excitation and electron injection are made by using lasers with different wavelength, respectively. The final transverse emittance of the beam can be about 10 nm rad. Some recent progresses worldwide in experimental demonstrations of ionization injection are reviewed briefly. Some prospects of ionization injection for practical applications in laser wakefield accelerators are also discussed.

M. Chen (✉) · Z.-M. Sheng

Key Laboratory for Laser Plasmas (Ministry of Education) and Department of Physics,
Shanghai Jiao Tong University, Shanghai 200240, China
e-mail: minchen@sjtu.edu.cn

Z.-M. Sheng

SUPA, Department of Physics, University of Strathclyde, Glasgow G4 0NG, UK
e-mail: zhengming.sheng@strath.ac.uk

7.1 Principle of Ionization Injection

Laser or beam driven wakefield acceleration as demonstrated in world wide laboratories is a very promising new technology for advanced electron acceleration, radiation source, therapy, and colliders [1–4]. Currently, one of the most challenging issues to overcome the limits towards applications is to substantially improve the beam quality. For stable, high quality, high charge beam acceleration both wakefield and electron motion process should be well controlled. Wakefield control is related to the laser driver control, including guiding and mode shaping. As for the electrons, besides the beam dynamics during the acceleration, the injection stage is tremendously important, which directly affects the final beam charge, energy spread and emittance and is therefore of primary importance.

As we know, besides the high acceleration gradient, the wakefield also has a very high phase speed (closed to the speed of light) and small spatial scale (tens of micrometers). To inject an electron beam into such a high speed small structure and make it to be trapped are extremely challenging. Many kinds of injection schemes have been proposed to pursue controllable injection. By adding a plasma density downramp region along the driver propagation path, the phase speed of the wakefield can be slowed down and then some of the background thermal electrons maybe trapped by the slow wave and then be accelerated to high energy. The other way for electron injection is to boost the speed of some of the background electrons. If the pre-accelerated electrons are faster than the wave when they are located at the end of the wake bucket, the electrons can be trapped inside of the bucket and be continuously accelerated until they enter into the deceleration phase. To this purpose, a few pre-acceleration mechanisms have been already considered. Among them, colliding pulse injection is the most promising method and it has already been extensively theoretically studied and experimentally demonstrated in several labs around the world [5, 6].

Here, besides the above mentioned two injection methods, we will introduce a third, simple injection mechanism i.e. ionization injection. Before the detailed analysis of ionization injection, let us recall the injection theory for one dimensional wakefield which was firstly described by Esarey et al. [7]. In one dimensional approximation the trapping of a test electron can be well described by the Hamiltonian $H(\gamma, \psi) = \gamma - \gamma\beta\beta_p - \phi(\psi)$ or

$$H(u, \psi) = (\gamma_\perp^2 + u^2)^{1/2} - \beta_p u - \phi(\psi) \quad (7.1)$$

where β is the longitudinal velocity of the particle normalized to c , $u = \gamma\beta$ is the normalized longitudinal momentum, $\beta_p \simeq 1 - \omega_p^2/2\omega_0^2$ is the normalized phase velocity of the plasma wave, $\psi = k_p\xi = k_p(x - \beta_p t)$ is the plasma wave phase with $k_p = \sqrt{4\pi e^2 n_0/m_e c^2}$, and $\phi = e\Phi/m_e c^2$ is the electrostatic potential of the plasma wave normalized to the electronic rest energy, $\gamma_\perp = \sqrt{1 + u_\perp^2}$ is the transverse Lorentz factor and u_\perp is the normalized transverse momentum of the electron, $\gamma = \sqrt{\gamma_\perp^2 + u^2}$ is the Lorentz factor of the electron.

Usually each electron moves along a trajectory in the phase space with a constant H . Its momentum as a function of the Hamiltonian and the wake potential is

$$u = \beta_p \gamma_p^2 (H + \phi) \pm \gamma_p \left[\gamma_p^2 (H + \phi)^2 - \gamma_{\perp}^2 \right]^{1/2}. \quad (7.2)$$

The particle may move in a closed (trapped) orbit or an open (untrapped) orbit depending on its initial position in the phase space. The separatrix orbit defining these two orbit families is given by $H(\gamma_s, \psi) = H(\gamma_p, \psi_{min})$, where $\phi(\psi_{min}) = \phi_{min}$, i.e.,

$$H_s = \gamma_{\perp}(\psi_{min})/\gamma_p - \phi_{min}. \quad (7.3)$$

If one puts H_s from (7.3) into (7.2), one can see $\beta(\psi_{min}) = \beta_p$, which means that the electron in this orbit has the same velocity as the wave at $\psi = \psi_{min}$. If its velocity at this point is a little bit larger than β_p , it moves into the acceleration phase and can get energy from the wake moving forward in the wave rest frame. It will be accelerated until it goes into the dephasing region. Otherwise it slips to the deceleration phase. This is just the meaning of the separatrix orbit.

Usually an electron will be in a trapped orbit provide $H \leq H_s$. For an electron initially at rest before the laser pulse, $H = 1$. For an initially warm plasma, $H = H_t \simeq 1 - \beta_p u_t$, where $u_t \ll 1$ is the initial non-relativistic thermal momentum. If the electrons transverse momentum is 0, then trapping occurs for $\phi_{min} \leq -1 + \gamma_p^{-1} + \beta_p u_t$ which sets a minimum intensity threshold for the wake.

The wake potential is determined by the driver pulse and plasma parameters. In one dimensional geometry, the quasi-static laser driven plasma wave can be calculated according to the following equation:

$$\frac{\partial^2 \phi}{\partial \psi^2} = \gamma_p^2 \left\{ \beta_p \left[1 - \frac{1 + a^2}{\gamma_p^2 (1 + \phi)^2} \right]^{-1/2} - 1 \right\}. \quad (7.4)$$

where $a = eA/mc^2$ is the normalized vector potential of the driver laser pulse and it can be calculated from the laser intensity (I) as $a^2 = 3.6 \times 10^{-19} (\lambda [\mu\text{m}])^2 I [\text{W/cm}^2]$, assuming circular polarization, where λ is the laser wavelength. A typical wakefield and its potential are shown in Fig. 7.1a by the red and blue lines, respectively.

Equations (7.1)–(7.4) give a full description of the wake excitation and particle dynamics for one dimensional wakefield acceleration. Ionization injection in one dimensional case can also be described by this theory. The ideal of ionization injection is firstly mentioned by Umstadter et al. in 1996 at the end of his paper on ponderomotive force injection, where he said that “...Instead of using a fully ionized plasma (as above), one would use a medium with deeply bound inner shell electrons, which have an appearance intensity for tunneling ionization below that of the injection pulse but above that of the pump pulse...” [8]. The first detailed research work on ionization injection is done by Chen et al. [9], where we used a double-pulse scheme. The first

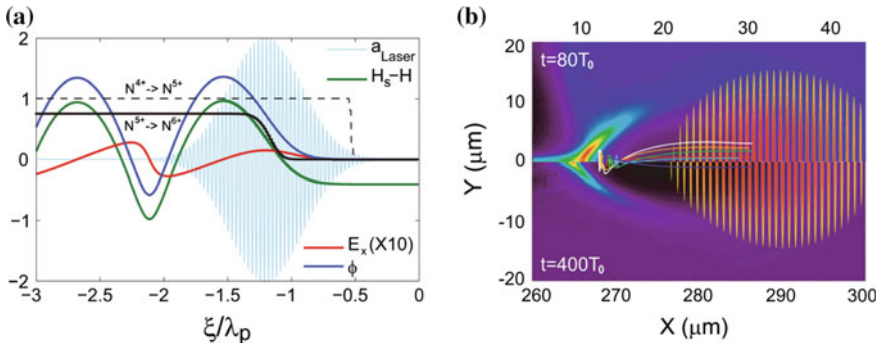


Fig. 7.1 Schematic view of ionization induced injection. **a** Analytical results for 1D ionization injection. Normalized laser vector potential (light blue/gray curve), wake potential (blue/up dark gray curve), wake electric field (red/lower gray curve), $H_s - H$ (green/middle gray curve), and degree of ionization versus ξ/λ_p . The dashed black curve shows the degree of ionization for $N^{4+} \rightarrow N^{5+}$, and the solid black curve shows $N^{5+} \rightarrow N^{6+}$. **b** 2D-PIC simulation results of ionization induced injection. Typical trajectories of trapped electrons via ionization. Laser-plasma parameters are intensity $a_0 = 2.0$, duration $L_{FWHM} = 14.89T_0$, focus spot size $W_{FWHM} = 17.66\lambda_0$, uniform plasma density with $n_e = 0.001n_c$, and mixed gas length $l = 20\lambda_0$. The Nitrogen concentration is 1 %. Top half shows $t = 80T_0$ and bottom half shows $t = 400T_0$. Reproduced with permission from Chen et al. [10]. Copyright (2012), AIP Publishing LLC

laser pulse works as a driver to excite a strong wakefield in a plasma, a second transversely propagated laser pulse ionizes the internal electrons of the high Z gas inside the wakefield at an appropriate time. In that paper, the contribution from ionization and ponderomotive force injections are compared in detail. Later on, the ionization injection scheme has been successfully generalized to a single laser pulse condition in which the wake excitation and ionization injection are performed by the same laser pulse. A lot of experimental studies have demonstrated this idea since 2010. Before that, ionization has already been used for electron injection in *beam-driven* plasma wakefield acceleration experiment.

Detailed 1D ionization injection theory for a single-pulse-driven injection scheme can be found in a paper by Chen et al. [10]. The only difference with that theory is the nonzero component of the particles' initial transverse momentum u_\perp which is usually negligible in a normal plasma wave. For an electron ionized inside the laser pulse in the 1D geometry, the transverse canonical momentum is conserved $\partial_\psi = (u_\perp - a_\perp) = 0$. So for an electron ionized at a wake phase ψ_i , $u_\perp(\psi) = a_\perp(\psi) - a_\perp(\psi_i)$, where we have assumed that the electron is born at rest, i.e. $u_\perp(\psi_i) = 0$. Once it leaves the laser field $\gamma_\perp = (1 + a_\perp^2(\psi_i))^{1/2}$. So the Hamilton of the ionized electron is $H_i = \gamma_\perp(\psi_i) - \phi(\psi_i) = 1 - \phi(\psi_i)$. The trapping condition is

$$-(\phi(\psi_i) - \phi_{\min}) \geq 1 - (1 + a_\perp^2(\psi_{\min}))^{1/2}/\gamma_p, \quad (7.5)$$

which assumes that the laser pulse has zero intensity at the trapping position i.e., $a_{\perp}(\psi_{min}) = 0$. The left side of the in-equality represents the maximum energy that the electron can get from the wakefield after its ionization. It needs to be larger than a threshold value determined by the wake properties (see γ_p). Usually the wake itself determines ϕ_{min} and γ_p . By using a mix of different gases, including high Z gas, the ionization position ψ_i can be controlled. If ionization happens at a position with large wake potential, the trapping condition can be satisfied. Common gases such as Nitrogen, Oxygen, Argon can be used in mixtures for such kind of injection. A typical process is shown in Fig. 7.1 in which the sixth and seventh electrons of Nitrogen are used for injection. The first five electrons are ionized in the early rising edge of the laser pulse where the wake potential is almost 0. The last two electrons are ionized near the pulse peak at a position where the wake potential is high. The green line shows the distribution of $H_s - H$ for the electrons ionized at different positions. Electrons ionized where $H_s - H > 0$ satisfy the injection condition. In this way only the two internal electrons of Nitrogen can be injected efficiently in the wake. Figure 7.1b shows a 2D-PIC simulation results of the injected electrons' trajectories related to the wake at two different time steps. As one can see the electrons to be injected are ionized closed to the peak of the laser pulse where the wake has a suitably high potential. Actually some of the electrons are ionized off-axis. This gives another source of transverse emittance in addition to the u_{\perp} from ionization process.

Compared with a normal injection theory, the trapping condition is modified by including the effect of the residual transverse momentum resulting from the ionization process (see $a_{\perp}(\psi_{min})$). As we will show later it is just because of this residual momentum that electrons injected by ionization may have large transverse emittance. By using two-color laser pulses to separate wake excitation and injection processes, one can overcome this problem. Since the whole process involves many nonlinear phenomena, such as laser propagation, wake excitation, ionization, electron trapping, and so on, a simple analytical theory cannot give correct and detailed information. Computational simulations and experiments are the main tools to study these processes. In the following we will discuss a variety of ionization injection schemes to obtain high quality (low energy spread, low transverse emittance) electron beams. Finally, we will show some recent experimental and theoretical progresses on this topic.

7.2 Using Ionization Injection to Get Low Energy Spread Electron Beams

From above analysis, one can see that ionization injection is a relatively easy scheme to inject electrons in a wakefield. No external laser pulse or gas jet need to be installed. Just by mixing some high Z gas in He gas may lead to ionization injection once the laser and plasma have appropriate parameters. A few earlier

experiments have already demonstrated this scheme. However, the final accelerated electron beam quality is not as good as other injection schemes [6]. The spectrum always shows a tail in the low energy part. The reason is that usually the laser path $L_{injection}$ into the mixed gas is larger than 1-mm. For electrons injected in wakefield, the distances between the initial injection positions can result in a big final energy spread $\delta\epsilon$, with a maximum energy difference of $\delta\epsilon^M = E_x \times L_{injection}$. Usually the wakefield amplitude E_x is \sim GeV/cm, so 1-mm separation in the injection distance leads to 100 MeV energy difference. To reduce the absolute energy spread, effective injection length should be controlled and kept as short as possible. In this section two schemes are aimed to decrease the effective injection length. The first one is by using the self-evolution of the wakefield due to the unmatched laser pulse: the injection is switched off by varying the wake parameters out from the injection condition range. The second is by controlling the ionization itself through laser electric field intensity modulation. Both of them can lead to mono-energetic electron spectrum. The second way is able to reduce the energy spread down to less than 1 % and can also provide multi-color electron bunches.

7.2.1 Self-truncated Ionization Injection

In the first section, we introduced the ionization injection theory in 1D geometry. In that condition, laser has no transverse evolution. However, in reality, both laser and wake experience transverse evolutions, such as laser pulse self-focusing and defocusing, accompanied by wake elongation and expansion. These phenomena have already been used for controlling self-injection in LWFA [11]. Recently this mechanism has been used in ionization injection. Zeng et al. studied the injection process with an unmatched laser [12]. There we found a simple method to cut the ionization injection length down to a few hundred micrometers in single stage with a single pulse. Finally we are able to produce an electron beam with 25.5 pC in charge and 8 % FWHM energy spread. To illustrate this mechanism a series of 2D simulation results are performed, a typical result is shown in Fig. 7.2. In the simulations a 800 nm laser pulse with vector potential of $a_0 = 2.0$, waist of $k_p W_0 = 7.594$, pulse duration of $L_{FWHM} = 33$ fs are used. The background plasma density is $1.6 \times 10^{-3} n_c$ and mixed nitrogen atom density is relatively small and varies from 5×10^{-6} to 1×10^{-4} . Snap shots of wakefield and laser pulse at two different acceleration distances are shown. At about $x = 190 \mu\text{m}$, the ionization injection condition is satisfied with $\Delta\phi = 1.179 > 1$. However at the distance $x \approx 440 \mu\text{m}$ the laser pulse is self-focused and the corresponding wake evolves significantly which makes $\Delta\phi = 0.595 < 1$ and the injection condition has been broken. Thus the injection is self-truncated by the laser and wakefield evolutions. In this way the effective injection length is not determined by the mixed gas length (usually in the scale of mm) but it is determined by the laser evolution time-scale which is in this case around $200 \mu\text{m}$.

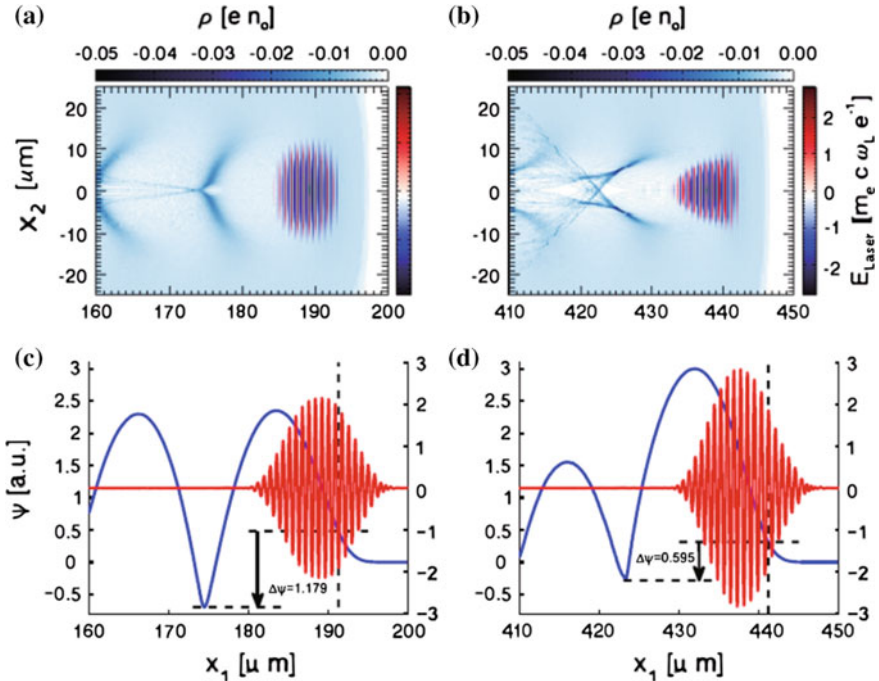


Fig. 7.2 **a** and **b** Electron density and laser electric field distribution at the laser propagation distance of 200 and 450 μm , respectively. **c** and **d** Laser (red lines) and pseudo-potential (blue lines) line-outs at these two time steps. Densities are normalized by n_c and electric fields are normalized by $E_0 = m_e c \omega_L e^{-1} = 4 \times 10^{12} \text{ V/m}$. The dashed lines show the ionization starting point of nitrogen inner shell and the fall to the bottom of the potential well ($\Delta\psi = 1.179$ and 0.595, respectively). Reproduced with permission from Zeng et al. [12]. Copyright (2014), AIP Publishing LLC

Obviously this kind of ionization injection depends on the evolution of the laser pulse. Experimentally one can vary the laser focusing spot size to control this process. Figure 7.3a shows such effects. In the 2D simulation, the laser energies are kept to be a constant by keeping $a_0^2 W_0$ unchanged. Different spot size and corresponding laser intensity are used for testing runs. As one can see in some case (the green line) the laser evolution is very mild (see Fig. 7.3b) and electrons are continuously injected into the wake (see Fig. 7.3a). In this case the final electron spectrum is a plateau structure with hundred percent of energy spread. On the contrary, if the laser is strongly evolved like the black line case in Fig. 7.3. The injection happens at the beginning, then it is self-truncated and finally a second injection happens. The final spectrum shows two peaks, each one with narrow energy spread. Combining this technique with shortening (by mechanical fabrication) of the laser path in the gas-mix, electron spectrum with a single quasi-monoenergetic peak is possible. 3D-PIC simulation done by Zeng et al.

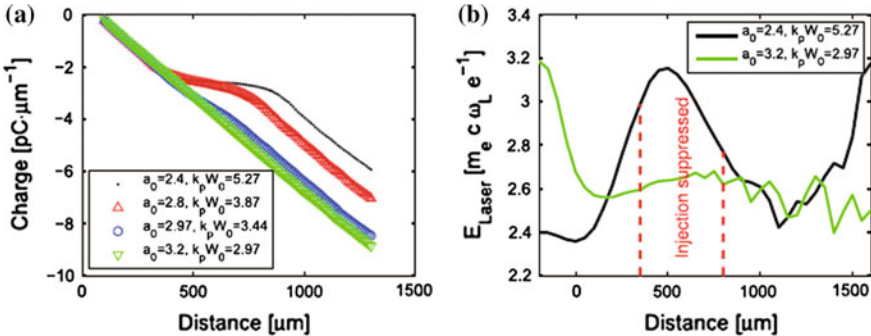


Fig. 7.3 **a** Injected charge number versus laser propagation distance from 2D PIC simulations with different normalized laser vector potential a_0 and normalized waist $k_p W_0$. The laser energies are kept the same in 2D slab geometry by keeping $a_0^2 W_0$ a constant. **b** Laser peak amplitude evolution of two cases: *black line* for $a_0 = 2.4, k_p W_0 = 5.27$ and *green line* for $a_0 = 3.2, k_p W_0 = 2.97$. The *red dashed lines* indicate the region where the injection is suppressed for the *black line* case. Reproduced with permission from Zeng et al. [12]. Copyright (2014), AIP Publishing LLC

proved how effective such a scheme can be [12]. A recent experiment done by Li et al. demonstrate this scheme. Monoenergetic electron beam with energy spread of 10 % and central energy of 400 MeV are reported [13].

7.2.2 Two-Color Ionization Injection

The above self-truncated injection scheme provides a simple way for mono-energetic electron beam acceleration. However, since basically it relies on laser self-focusing it is a not well controllable method to get stable acceleration. Further, the energy spread is still too large for many applications. Besides controlling the wake properties, the other way is to control the ionization process. Xia et al. have used this to control ionization injection [14]. However in their case, the wake evolution effect is small. The laser intensity is tuned around the ionization threshold. Only when the self-focusing happens internal electrons of the injection gas are ionized and injected. Such process can also be used for mono-energetic beam acceleration. However, it is more difficult to tune the laser energy and the energy spread is still relatively large.

A two-color ionization injection scheme is recently been proposed by our group [15]. The idea is schematically shown in Fig. 7.4. Two laser pulses with vector potential of $a_i(z, t) = a_{i0} \sin(\omega_i t - k_i z + \phi_i)$, ($i = 1, 2$) are used to excite the wake and trigger ionization injection, respectively. The injection pulse is a frequency-tripled laser. As two color pulses copropagate in the background plasma, the peak amplitude of the combined laser field is modulated in time and space

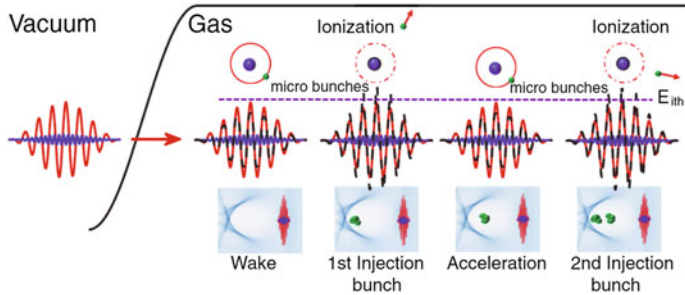


Fig. 7.4 Schematic view of dual color lasers triggered periodic injection in LWFA. A laser with base frequency ω_1 (the red curves) and its harmonic ω_2 (the blue curves) propagate in a mixed gas plasma. The dashed black curves show the superposition of the two frequency laser fields at different propagation distances. Laser parameters are chosen so that ionization-induced injection can be switched on when the beating is constructive and be switched off when the beating is destructive. In the plot, E_{ith} represents the effective threshold field for the high-Z gas inner shell ionization. Reprinted figure with permission from Zeng et al. [15]. Copyright (2015) by the American Physical Society

during the laser propagation due to the plasma dispersion ($\omega_i^2 = \omega_p^2 + c^2 k_i^2$). Ionization injection only occurs when the peak amplitude exceeds a certain threshold. The threshold is exceeded for very short duration periodically at different propagation distances, leading to multiple ionization injections and separated electron bunches.

The combined laser electric field of the two pulses can be rewritten as

$$E(\xi, s) = a_{10} \cos(\xi + \omega_p^2 s/2 + \phi_1) + a_{20} \omega_2 \cos(\omega_2 \xi + \omega_p^2 s/2\omega_2 + \phi_2), \quad (7.6)$$

where $\xi = \omega_1(t - z/c)$ and $s = \omega_1 z/c$. One can see that the electric field is a periodic function of s and ξ and the period of s is $\Delta s = 4\pi/\omega_p^2(\omega_2 - \omega_2^{-1})$. Similarly to the peak amplitude evolution of the two color pulse, the ionization injection region can be broken into small pieces. By appropriately selecting the amplitude and the frequency of the two pulses, ionization injections can be limited to a few small separated regions. Zeng et al. have shown typical simulations for this scheme [15]. In the scheme we used Nitrogen as injection gas and laser pulses with 800 nm and 266 nm wavelengths, respectively.

A typical 2D simulation is shown in Fig. 7.5, where laser parameters are: $a_{10} = 1.46$, $a_{20} = 0.162$, $L_{FWHM} = 33$ fs, $W_0 = 80$ μm , $n_e = 1.6 \times 10^{-3} n_c$, $n_N = 1.6 \times 10^{-7} n_c$. The injection stage length (the length of mixed nitrogen) is $L_{inj} = 1$ mm, which is smaller than the laser self-evolution scale length. So the laser self-focusing and wake evolution effects can be negligible. A typical distribution of the injected bunches is shown in Fig. 7.5a. The central positions of these bunches are spatially separated in this snapshot on a micrometer scale. The phase space distribution of the bunches are shown in Fig. 7.5b. It shows that within the second and the third bunches there are a few micro bunches which come from the

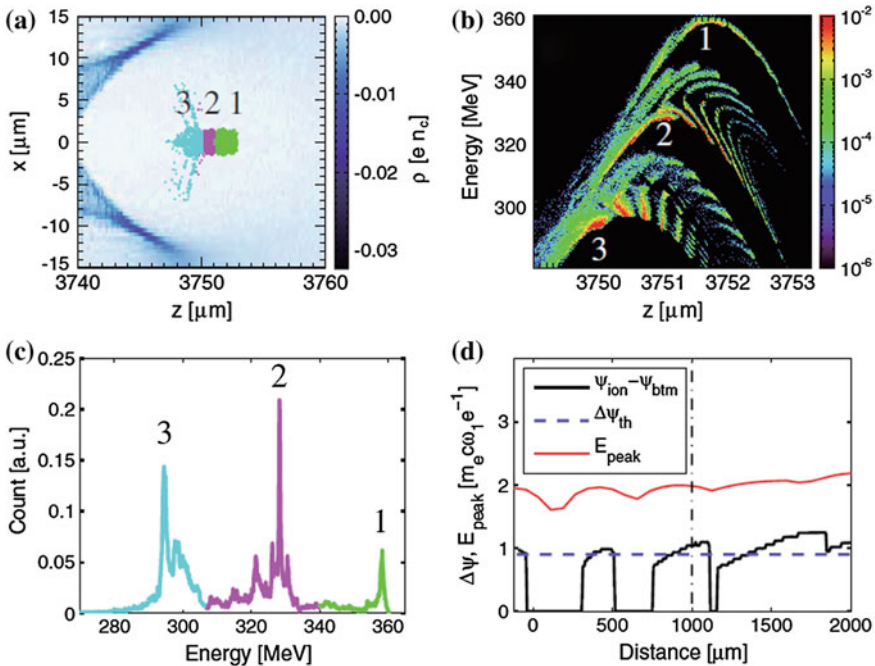


Fig. 7.5 2D PIC simulations of the two-color ionization injection scheme. **a** The density snapshot at $z = 3780 \mu\text{m}$. The colored dots show the locations of three electron bunches. **b** The energy and space distribution of the energetic electrons. **c** The spectrum of the injected electrons, showing three monoenergetic peaks. **d** The pseudopotential (ψ) difference of the wake and the laser peak field evolution. The dash-dotted line is the separation from the mixed gas region to the pure helium region. Reprinted figure with permission from Zeng et al. [15]. Copyright (2015) by the American Physical Society

overlapping of several peaks when the combined electric field is larger than the ionization threshold as schematically shown in Fig. 7.4. These bunches degrade the monochromaticity of the final beams, showing the pedestals between the peaks of the energy spectrum in Fig. 7.5c. From the simulations we found that those pedestals can be reduced by using a shorter triple frequency laser pulse, which makes the inner shell ionization occurring only in a single peak. A simulation with a 10 fs, 3ω laser gives a single injected electron bunch with final energy spread less than 0.2 % FWHM. In the simulation of Fig. 7.5, the whole spectrum is composed of three main peaks with equal separation of 30 MeV. The ionization injection analysis is shown in Fig. 7.5d. The mixed gas locates on the left side of the dashed line. The intensity of the combined laser electric field is shown by the red curve. The pseudopotential differences and the threshold for ionization injection are shown by the black solid and blue dashed lines, respectively. The former is automatically set to be zero if ionization cannot occur. As one can see, ionization injection only happens in three regions, namely around the beginning, at about $500 \mu\text{m}$, and

1000 μm . Each one occurs in a very limited region (tens of micrometers). This is consistent with the three injected electron bunches labeled by 1, 2, 3 in Fig. 7.5a–c. More 3D simulations also demonstrate the effectiveness of such scheme. More detailed information can be found in [15].

Besides the extreme low energy spread of the electrons injected and accelerated by the above two-color ionization injection method, the scheme is also unique for generating multichromatic narrow energy-spread electron bunches which can be used for multi color x-ray generation through Thomson Scattering scheme. These are interesting for medical or material imaging applications. The multichromatic beams may also be interesting for radiotherapy. From comparing the characteristics of radio physics of the multi-fields full body irradiation by mixed-energy electron beam with single-energy electron beam, results show that multi-chromatic energy electron beams can not only meet the clinical treatment requirements for treating mycosis fungoides, but also shorten the treatment time compared to the single-energy electron beam radiation treatment [16]. The current challenge is to reduce the electron energy from 100 MeV to a few MeV level [17].

7.3 Using Ionization Injection to Get Low Transverse Emittance Electron Beams

As we mentioned before, electrons ionized inside the laser pulse may carry a residual transverse momentum from ionization. These momenta increase the final beam transverse emittance ($\varepsilon_N \sim \gamma r_b p_\perp / p_{||} = r_b \hat{p}_\perp$), where r_b represents the transverse beam size. Since the residual momentum $\hat{p}_\perp \propto a$, reducing the vector potential of the ionizing laser pulse and changing its direction are possible methods to lower the final beam emittance. In the following these two schemes are introduced to get low transverse emittance within an ionization injection configuration.

7.3.1 Two-Color Ionization Injection

From (7.4) one see that a driver pulse with larger vector potential (a) can excite a stronger wakefield. This looks in contradiction with the low transverse emittance requirement (see before $u_\perp(\psi) = a_\perp(\psi) - a_\perp(\psi_i)$). However, if one uses two laser pulses to separate wake excitation from ionization injection, the contradiction no longer exists. Such scheme has recently been studied by Yu et al. [18] and Xu et al. [19]. In their scheme a low frequency (large wavelength, such as $\lambda_0 = 5 \mu\text{m}$ or CO_2 laser $\lambda_0 = 10.6 \mu\text{m}$) laser pulse, is used for wake excitation. Since the laser vector potential is $a = \sqrt{I(\text{W/cm}^2)/1.38 \times 10^{18}}\lambda (\mu\text{m})$, for a fixed linearly polarized laser pulse intensity, the longer the wavelength the larger the vector potential, which is

better for wave excitation. On the contrary, a high frequency laser pulse is used to trigger ionization injection. This is because from $E \propto \partial A / \partial t$ one gets $a \propto E / \lambda$ and for similar ionization degree (similar electric field strength E) the larger the wavelength the smaller the vector potential, which is better for keeping a small residual transverse momentum.

A typical two dimensional simulation of this scheme by Yu et al. is shown in Fig. 7.6. In the simulation Kr is used as injection gas. The electron density (after ionization by the pump laser) is fixed to $n_0 = n_e + 8n_{Kr} = 2 \times 10^{17} \text{ cm}^{-3}$, where n_e is the electron density produced by ionization of the low-Z background gas (e.g. He gas), and the pump laser ionizes the Kr gas to Kr^{8+} . The Kr gas locates from $z = -100 \mu\text{m}$ to $z = 0 \mu\text{m}$, with a plateau of $50 \mu\text{m}$ bordered by two ramp-like density profiles. The pump and injection pulses have the normalized vector potential like $a(\xi)_{0,1} = a_{0,1} \exp[-(\xi - \xi_{0,1})^2 / L_{0,1}^2]$, with amplitudes $a_0 = 1.17$ and $a_1 = 0.135$, wavelengths $\lambda_0 = 5 \mu\text{m}$ and $\lambda_1 = 0.4 \mu\text{m}$, durations (FWHM) $T_0 = 92 \text{ fs}$ and $T_1 = 16 \text{ fs}$, and spot sizes $w_0 = 36 \mu\text{m}$ and $w_1 = 5 \mu\text{m}$, respectively. Different from the two-color scheme we discussed above to get low energy spread electron beam, here the two pulses are not overlapped with each other but they are separated by an optimal delay corresponding to $|\xi_0 - \xi_1| = 106.25 \mu\text{m}$. So the

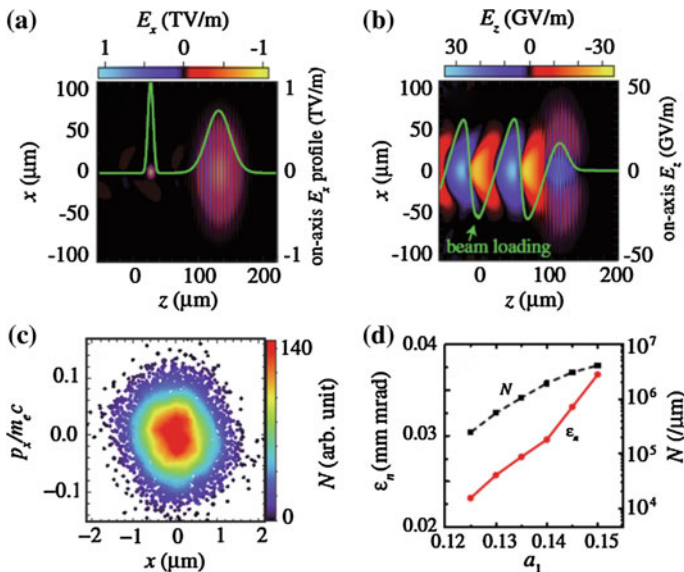


Fig. 7.6 **a** The electric field of the laser pulses (green curve is on-axis laser field profile), **b** The longitudinal wakefield (green curve is on-axis wakefield), and **c** The transverse phase space of the injected electrons, after the (mixed gas) ionization injection region. **d** The normalized transverse emittance ε_N (red solid curve) and trapped electron number N (black dashed curve) versus the injection pulse amplitude a_1 . See text for laser-plasma parameters. Reprinted figure with permission from Yu et al. [18]. Copyright (2014) by the American Physical Society

electrons ionized by the second pulse are located in the trapped orbit of the wake excited by the first pulse.

Simulation shows that all the ionized electrons (with charge of $1.05 \times 10^6/\mu\text{m}$) are trapped in the wake. So they are longitudinally accelerated by the wake (see Fig. 7.6a, b). The transverse phase-space distribution of these electrons are shown in Fig. 7.6c. As we can see most of the electrons have zero residual transverse momentum. This is because they are usually ionized at the peak of the injection laser electric field, where the laser vector potential is zero for a normal single color Gaussian pulse. Electrons ionized just off-peak of the laser electric field are trapped and produce the finite transverse momentum. The maximum momentum in Fig. 7.2c is $p_x/m_e c \simeq 0.17$, which is larger than the vector potential amplitude a_1 due to the effects of the transverse force of the wakefield and transverse ponderomotive force of the injection laser pulse. The rms beam radius and transverse momentum are $\sigma_x \simeq 0.55 \mu\text{m}$ and $\sigma_{p_x}/m_e c = 0.05$, respectively. Here σ_{p_x} is an order of magnitude smaller than that observed in simulations of single-pulse ionization injection. The final transverse emittance of the electrons is $\varepsilon_n = 0.028 \text{ mm mrad}$.

Similar idea was also studied recently by Xu et al. [19]. Instead of $5 \mu\text{m}$ driver pulse, they used CO₂ laser as a driver pulse. However, the basic idea is exactly the same. Detailed information can be found in [19].

7.3.2 *Ionization Injection Assisted by Transverse Colliding Pulses*

As we see before the ionization induced transverse emittance is due to the transverse residual from the injection pulse generated during ionization. One may think that if this momentum is not fully transverse the emittance may be reduced. A recent modified ionization injection scheme proposed by Chen et al. just uses this idea [20, 21]. The idea is schematically shown in Fig. 7.7a. A driver pulse first excite a wave in the background plasma, then two identical frequency transverse laser pulses with polarization parallel to the driver pulse propagation direction are oppositely injected and overlapped at an appropriate phase of the wake. The combined laser field of the two transverse pulses is high enough to ionize the internal electrons of the injection gas (e.g. Nitrogen). Since the vector potential of the two pulses are along the longitudinal direction of the wake, the residual momentum is along this direction and no transverse momentum is introduced.

Chen et al. have studied this scheme by using 2D particle-in-cell simulations. A driver pulse with length of $L_0 = 6.0T_0$, transverse size of $W_0 = 10\lambda_0$ and intensity of $a_0 = 1.5$ is used. The injection pulses have temporal duration of $L_1 = L_2 = 3.0T_0$ and transverse sizes of $W_1 = W_2 = 3.0\lambda_0$. They have the same wavelength as the driver pulse ($\lambda_0 = 0.8 \mu\text{m}$) and intensities $a_1 = a_2 = 0.8$. They collide with each other at the axis of the driver pulse propagation and at an optimal delay with the driver pulse which makes the electron injection possible. The background

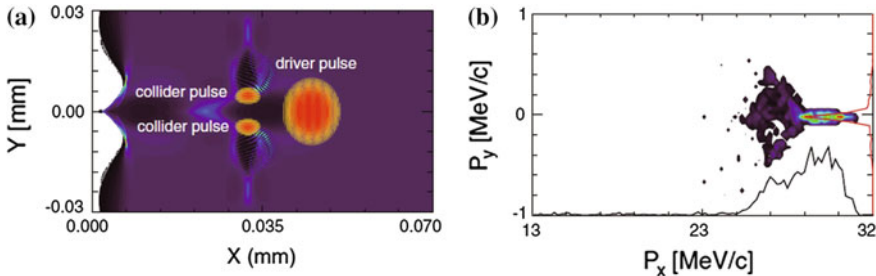


Fig. 7.7 **a** Plasma density and laser intensity distribution at $t = 200$ fs. **b** Phase space distribution ($P_x - P_y$) of trapped preionized and laser-ionized electrons after the drive pulse propagated 0.79 mm. The *right red curve* shows the transverse momentum spread after longitudinal integration. The *lower black curve* shows the beam energy spread. Reprinted figure with permission from Chen et al. [21]. Copyright (2014) by the American Physical Society

plasma has a density of $n_{pre-e} = 0.001n_c$. The density of the injection gas (Nitrogen) is $n_N = 2.0 \times 10^{-6}n_c$. Simulation results show $6.38 \times 10^6/\mu\text{m}$ electrons have been injected into the second wave bucket. The final beam transverse full-with-at-half-maximum (FWHM) momentum spread is $0.1m_ec$ as shown in Fig. 7.7b. The beam is quasi-monoenergetic with the peak energy of 29.32 MeV and FWHM energy spread $\delta E \simeq 3.84$ MeV. The transverse momentum spread is an order smaller than the one by using an usual single pulse ionization injection scheme. Further optimal simulations show the minimum transverse emittance of the electron beam injected by this method can be as small as 0.08 mm mrad which is far less than the normal value of 1 mm mrad from self-injection.

It deserves to point out that, besides ionization induced electron injection into the wakefield, the transverse ponderomotive force of the two pulses may also lead to ponderomotive injection which is similar as the scheme proposed by Umstadter in 1996 [8]. To increase ionization injection percentage one needs to use two transverse laser pulses with identical frequency, otherwise transverse beat wave will be generated which accelerates electrons transversely, resulting in a high transverse momentum of the electrons. Two pulses with different frequency may be used to increase the transverse momentum of the injected electron beam to make stronger betatron radiation.

This idea was later introduced to beam driven wakefield acceleration by Li et al. [22]. Since in a beam driven case, the field of the beam is much smaller than the driver laser's electric field, gases with very low ionization potential can also be used as injection gas such as Helium. The beam ionizes only the electrons with lower ionization potential. Two transverse pulses, with even smaller amplitudes than in the case above, can be used to ionize the internal electrons of He and induce ionization injection. This makes the final transverse electron beam emittance even smaller. In their studies ultrashort (~ 8 fs) high-current (0.4 kA) electron bunches with a normalized emittance of 8.5 and 6 nm in the two planes, respectively, and a brightness of $1.7 \times 10^{19} \text{ Arad}^{-2}\text{m}^{-2}$ can be obtained for realistic parameters [22].

7.4 Ionization Injection Demonstration Experiments

In the previous sections, we introduced ionization based electron injection from analytical and simulation points of view. Almost at the same time of the theoretical progress, ionization injection has been experimentally demonstrated and optimized both in *laser-driven* and *beam-driven* wakefield acceleration. To our knowledge the first intentioned experimental studies of ionization injection in wakefield acceleration is by Oz et al. [23], where the wakefield is driven by an electron beam of 28.5 GeV energy in a Lithium vapor column. Li plasma electrons act as the background electrons and support the wake. The doped Helium atoms are used as the ionization injection source since the higher ionization potential of He atoms makes them being ionized only inside the wakefield. As the wake amplitude is increased, the ionization induced Helium electron trapping is observed. Some electrons gain energy up to 7.6 GeV in a 30.5 cm plasma. After that the ionization injections in *laser-driven* wakefield were also reported by three groups independently in 2010 [24–26].

Pak et al. [26] observed continuous ionization injection in their experiment above an initial laser intensity threshold (e.g. $a_0 = 2.35$, still less than the laser intensity threshold for self-injection) and electrons with maximum energy up to 110 MeV were observed. The injection is due to the ionization of K-Shell of nitrogen in a He background plasma. Reducing the laser intensity to $a_0 = 1.64$ the low energy part of the spectrum disappeared and quasi-monoenergetic spectrum appeared due to the ionization stopping because of the lower laser intensity after some propagation. However, the spectrum was still very broad.

McGuffey et al. [25] used targets composed of helium and controlled amounts of various gases. In some of their experiments with laser power of 30 and 120 TW level, they found the addition of a higher Z additive (such as Ar, N₂, Ne) can increase the beam charge by as much as an order of magnitude compared to pure helium at the same electron density and decrease the beam divergence from 5.1 ± 1.0 to 2.9 ± 0.8 mrad. Their simulations for the experiments showed that electron beams with energy up to 150 MeV were generated. The spectra were basically broad (more than 20 %).

By using higher laser power (60 fs, 110 TW) and longer acceleration length (1.3 cm), Clayton et al. [24] accelerated electrons up to 1.45 GeV in a regime of matched-beam, self-guided laser propagation and ionization-induced injection. They used 3 % amounts of CO₂ gas as injection gas. The background plasma density from He is $1.3 \times 10^{18} \text{ cm}^{-3}$. At this low density and for $a_0 \leq 4$, only electrons born inside the ion bubble are expected to be trapped via ionization-induced injection. Computer simulations confirmed that it is the K-shell electrons of oxygen that are ionized and injected into the wake and accelerated to beyond 1 GeV energy. The spectrum again shows very broad character as shown in Fig. 7.3 in [24] (see beam k).

To reduce the energy spread of the electrons accelerated in LWFA by ionization injection, two groups (Liu [27] and Pollock [28]) have used a similar scheme to

separate ionization injection stage from acceleration stage and obtained quasi-monoenergetic electron acceleration. In Liu's experiment [27], electrons with a Maxwellian spectrum, generated from the first LWFA assisted by ionization-induced injection, were seeded into the second LWFA with a 3-mm-thick gas cell. The first stage was 1-mm thick and filled with 6 % oxygen gas and 94 % helium gas flow, the second stage with variable thickness from 1 to 3 mm was filled with pure He gas. The 40 ~ 60 TW laser pulses were used in the experiments. The plasma densities were $\sim 5.7 \times 10^{18} \text{ cm}^{-3}$ in the first gass cell stage and $\sim 2.5 \times 10^{18} \text{ cm}^{-3}$ in the second one, respectively. Finally a quasi-monoenergetic electron bunch peaked at an energy of 0.8 GeV was observed with 25 % energy spread, 2.6 mrad divergence, and $\sim 3.7 \text{ pC}$ charge. In Pollock's scheme [28], the gas cell is comprised of a 3 mm injection stage, filled with a mixture of 99.5 % helium and 0.5 % nitrogen gas, separated by a 1 mm diameter aperture from an immediately adjacent 5 mm acceleration stage containing pure He. Plasma density of $3 \times 10^{18} \text{ cm}^{-3}$ in each stage for a coupled laser power of 40 TW were used. Finally a $460 \pm 25 \text{ MeV}$ electron beam containing $\sim 35 \text{ pC}$ of charge was observed. PIC simulations for both these two experiments show that ionization induced injection is the main mechanism for electrons trapping in the wake in the first stage. The following acceleration stage is only used to boost the beam energy and reduce the relative energy spread. However, due to the large thickness of the first gas jet, electron beams injected by this two stage scheme are inevitably with large absolute energy spread as we mentioned before. Two-color ionization injection scheme may solve this issues. However, no experiments on this have been reported yet.

At last, we mention that recently in the laboratory for laser plasma at Shanghai Jiao Tong university, an experimental group has obtained quasi-monoenergetic electron beam with central energy of 1.14 GeV energy spread of 7 % from a single stage by using self-truncated ionization injection scheme which was discussed before in Sect. 2.2 [29]. A preliminary result from the same group was recently published in Optics Express [13]. They use a mixed gas with 0.3 % nitrogen and 99.7 % helium gas. Upon the interaction of 30-TW, 30-fs laser pulses with a gas jet of the above gas mixture, $>300 \text{ MeV}$ quasi-monoenergetic electron beams were generated at a plasma densities of $3.3 - 8.5 \times 10^{18} \text{ cm}^{-3}$.

7.5 Further Development of Ionization Induced Electron Injection

Due to the relatively simple experimental operation and flexible tunability, ionization injection is suggested as a very promising injection scheme in LWFA. Besides the above mentioned researches, it has also been modified and improved for other applications.

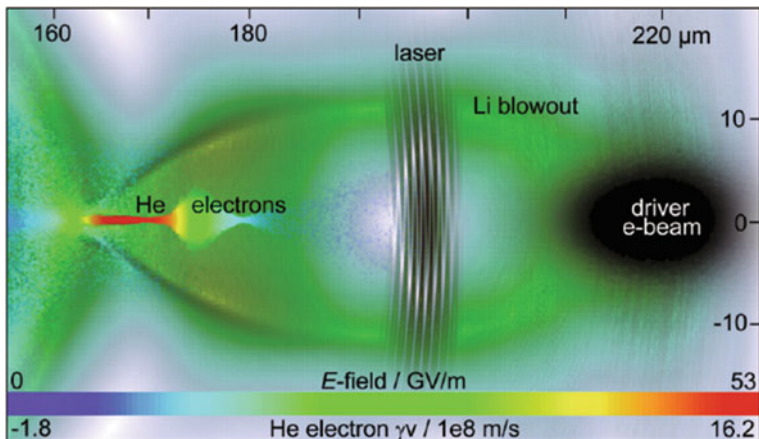


Fig. 7.8 Simulation results show how an electron driver ionizes Li gas and generates a Li blowout with an electron density of $n_e(\text{Li}) = 3.3 \times 10^{17} \text{ cm}^{-3}$. The Ti:sapphire laser pulse with a duration of 8 fs and $a_0 = 0.018$ is located at the end of the first half of the blowout at the electric fields turning point, and has already ionized some He electrons, which are then trapped and accelerated. Reprinted figure with permission from Hidding et al. [30]. Copyright (2012) by the American Physical Society

Hidding et al. recently has proposed a concept named plasma photocathode emission and used it in a beam-driven plasma blowout regime as shown in Fig. 7.8 [30, 31]. The scheme is similar as the one we mentioned before for low emittance beam generation by using two-color laser pulse. The difference is that in the current scheme the first driver laser pulse is replaced by a relativistic electron beam with charge of 300 pC and energy of 200 MeV. Same as the first ionization injection demonstrated experiment, the background is a Lithium plasma with density of $3.3 \times 10^{17} \text{ cm}^{-3}$ and the injection gas is Helium. So a very low laser intensity ($a = 0.018$) can be used to ionize He and make electron injection. In their simulation they found a beam with normalized emittance of $\varepsilon_N \simeq 4 \times 10^{-8} \text{ mrad}$ can be obtained, which opens up the possibility of its applications in future laser plasma accelerator based free electron x-ray lasers (FEL).

Another two pulse ionization injection scheme was proposed by Bourgeois et al. [32]. An important feature of their scheme is that the parameters of the injecting laser pulse are adjusted so that it diffracts faster than the driving laser pulse, meaning that the injection laser pulse intensity will remain high and hence electron trapping will occur in only a localized region. In contrast, the driving laser pulse can be guided in a plasma channel or a hollow capillary waveguide, allowing the trapped electrons to be accelerated to high energy. Particle-in-cell simulations show controlled injection and acceleration of electrons to an energy of 370 MeV, a relative energy spread of 2 %, and a normalized transverse emittance of 2.0 μm .

The final electron emittance not only depends on the initial injection process, but also on the following electrons' dynamics in phase space (mainly affected by Betatron

motion). By using theory and PIC simulations, Xu et al. have recently studied phase-space dynamics of electrons injection by ionization mechanism in plasma-based accelerators [33]. They found that the injection process involves both longitudinal and transverse phase mixing, leading initially to a rapid growth of emittance and following oscillations, decay and a slow growth up to saturation. Electrons ionized at the same time can reside over a large range of ψ of the wake, and thus feel a range of longitudinal wakefield E_x . The difference of E_x cause the longitudinal phase mixing to the ionization injected electrons because of different betatron frequency. Electrons ionized at different times (t_{ion}) can also reside within the same longitudinal beam slice. Transverse mixing can occur within a slice due to the different phase-space distributions including different initial energies of the electrons after injection. These two phase mixing processes are responsible for the complex emittance dynamics. From theory and simulations they also found an optimal acceleration distance ($x_0 = (E_x/\sigma_{E_x})\sigma_x$) to achieve minimum emittance for the trapped electrons, where $\sigma_x^2 = \langle (s_i - \langle s_i \rangle)^2 \rangle$ and $\sigma_{E_x}^2 = \langle (E_x - \langle E_x \rangle)^2 \rangle$, s_i and E_x represent the ionization position and the local wakefield intensity, respectively.

7.6 Conclusion

In this chapter, we have introduced a relatively simple electron injection method in laser wakefield acceleration, which relies on the ionization of the inner shell electrons of a high Z gas. These electrons are protected by the mother ions while passing through the deceleration phase of the wake. When they arrive at the appropriate phase of the wake they are ionized by the strong laser electric field there and then are trapped in the wake for following acceleration. Improved ionization schemes such as the two-color scheme and the transverse pulse ionization injection scheme are proposed by several groups to reduce the final energy spread and transverse emittance of the accelerated electron beams. Although such schemes can improve some aspects of the qualities of the beams, none of them can make simultaneous high quality for both longitudinal and transverse emittances. More theoretical and experimental investigations are necessary to make the LWFA beam appropriate for wide applications, such as new generation radiation source, TeV collider, and so on. Especially for external beam radiotherapy applications, the challenge is to produce high flux and high quality low energy electron beams. For this purpose, high repetition low power laser driven wakefield acceleration may be a better selection, in which ionization injection is also a good scheme since it can separate the high quality injection process from the acceleration process. At the same time, the high energy photon radio therapy such as X rays or γ rays can also benefit by the ionization injection scheme. Electrons with high quality can radiate X rays through betatron oscillation [1], plasma channel guided oscillation [34] or Bremsstrahlung radiation. For this purpose more efforts to improve the yield and quality of the radiations are still required.

Acknowledgements This work was supported by the National Basic Research Program of China (Grant No. 2013CBA01504), the National Natural Science Foundation of China (Grant Nos. 11421064, 11374209 and 11374210), the MOST international collaboration project (Grant No. 2014DFG02330). M.C. appreciates supports from National 1000 Youth Talent Project of China.

References

1. S. Corde et al., Femtosecond x rays from laser-plasma accelerators. *Rev. Mod. Phys.* **85**, 1–48 (2013)
2. E. Esarey et al., Physics of laser-driven plasma-based electron accelerators. *Rev. Mod. Phys.* **81**, 1229 (2009)
3. S.M. Hooker, Developments in laser-driven plasma accelerators. *Nature Photon.* **7**, 775–782 (2013)
4. W.P. Leemans, E. Esarey, Laser-driven plasma-wave electron accelerators. *Phys. Today* **62**, 44–49 (2009)
5. E. Esarey et al., Electron injection into plasma wake fields by colliding laser pulses. *Phys. Rev. Lett.* **79**, 2682–2685 (1997)
6. J. Faure et al., Controlled injection and acceleration of electrons in plasma wakefields by colliding laser pulses. *Nature* **444**, 737–739 (2006)
7. E. Esarey, M. Pilloff, Trapping and acceleration in nonlinear plasma waves. *Phys. Plasmas* **2**, 1432–1436 (1995)
8. D. Umstadter, J.K. Kim, E. Dodd, Laser injection of ultrashort electron pulses into wakefield plasma waves. *Phys. Rev. Lett.* **76**, 2073–2076 (1996)
9. M. Chen et al., Electron injection and trapping in a laser wakefield by field ionization to high-charge states of gases. *J. Appl. Phys.* **99**, 056109 (2006)
10. M. Chen et al., Theory of ionization-induced trapping in laser-plasma accelerators. *Phys. Plasmas* **19**, 033101 (2012)
11. S. Kalmykov, S.A. Yi, V. Khudik, G. Shvets, Electron self-injection and trapping into an evolving plasma bubble. *Phys. Rev. Lett.* **103**, 135004 (2009)
12. M. Zeng et al., Self-truncated ionization injection and consequent monoenergetic electron bunches in laser wakefield acceleration. *Phys. Plasmas* **21**, 030701 (2014)
13. S. Li et al., Enhanced single-stage laser-driven electron acceleration by self-controlled ionization injection. *Opt. Express* **22**, 29578–29586 (2014)
14. C. Xia et al., Effects of self-focusing on tunnel-ionization-induced injection in a laser wakefield accelerator. *Phys. Plasmas* **18**, 113101 (2011)
15. M. Zeng et al., Multichromatic narrow-energy-spread electron bunches from laser-wakefield acceleration with dual-color lasers. *Phys. Rev. Lett.* **114**, 084801 (2015)
16. Qian, J.S. Zhang, X.Z. and Tian, M.L.:Clinical application and characteristics of total skin electron irradiation of complex energies. *Journal of Xi'an Jiaotong University (Medical Sciences)* **1**, 122 (2013)
17. T. Shouman, Z. El-Taher, Total skin electron therapy: a modified technique for small room linear acceleration. *J Egyptian Nat. Cancer Inst.* **16**, 202–209 (2004)
18. L.L. Yu et al., Two-color laser-ionization injection. *Phys. Rev. Lett.* **112**, 125001 (2014)
19. X.L. Xu et al., Low emittance electron beam generation from a laser wakefield accelerator using two laser pulses with different wavelengths. *Phys. Rev. ST Accel. Beams* **17**, 061301 (2014)
20. M. Chen et al., Using transverse colliding-pulse injection to obtain electron beams with small emittance in a laser-plasma accelerator. *AIP Conf. Proc.* **1507**, 262 (2012)
21. M. Chen et al., Electron injection and emittance control by transverse colliding pulses in a laser-plasma accelerator. *Phys. Rev. ST Accel. Beams* **17**, 051303 (2014)

22. F. Li et al., Generating high-brightness electron beams via ionization injection by transverse colliding lasers in a plasma-wakefield accelerator. *Phys. Rev. Lett.* **111**, 015003 (2013)
23. E. Oz, S. Deng, T. Katsouleas et al., Ionization-induced electron trapping in ultrarelativistic plasma wakes. *Phys. Rev. Lett.* **98**, 084801 (2007)
24. C.E. Clayton et al., Self-guided laser wakefield acceleration beyond 1 GeV using ionization-induced injection. *Phys. Rev. Lett.* **105**, 105003 (2010)
25. C. McGuffey et al., Ionization induced trapping in a laser wakefield accelerator. *Phys. Rev. Lett.* **104**, 025004 (2010)
26. A. Pak et al., Injection and trapping of tunnel-ionized electrons into laser-produced wakes. *Phys. Rev. Lett.* **104**, 025003 (2010)
27. J.S. Liu et al., All-optical cascaded laser wakefield accelerator using ionization-induced injection. *Phys. Rev. Lett.* **107**, 035001 (2011)
28. B.B. Pollock et al., Demonstration of a narrow energy spread, 0.5 GeV electron beam from a two-stage laser wakefield accelerator. *Phys. Rev. Lett.* **107**, 045001 (2011)
29. M. Mirzaie, S. Li, M. Zeng et al., Demonstration of self-truncated ionization injection for GeV electron beams. *Sci. Rep.* **5**, 14659 (2015). doi:[10.1038/srep14659](https://doi.org/10.1038/srep14659)
30. B. Hidding et al., Ultracold electron bunch generation via plasma photocathode emission and acceleration in a beam-driven plasma blowout. *Phys. Rev. Lett.* **108**, 035001 (2012)
31. Y. Xi et al., Hybrid modeling of relativistic underdense plasma photocathode injectors. *Phys. Rev. ST Accel. Beams* **16**, 031303 (2013)
32. N. Bourgeois et al., Two-pulse ionization injection into quasilinear laser wakefields. *Phys. Rev. Lett.* **111**, 155004 (2013)
33. X.L. Xu et al., Phase-space dynamics of ionization injection in plasma-based accelerators. *Phys. Rev. Lett.* **112**, 035003 (2014)
34. M. Chen, J. Luo, F.Y. Li et al., Tunable synchrotron-like radiation from centimeter scale plasma channels. *Light: Sci. Appl.* **5**, e16015 (2016). doi:[10.1038/lsa.2016.15](https://doi.org/10.1038/lsa.2016.15)

Chapter 8

All-Optical X-Ray and γ -Ray Sources from Ultraintense Laser-Matter Interactions

Leonida A. Gizzi

Abstract With the dramatic recent development of ultraintense lasers, a new perspective for compact, all-laser driven X-ray and γ -ray sources is emerging, aiming at a brightness currently achievable only with state of the art free electron lasers and Thomson scattering Sources based on large linear accelerators. In contrast with existing sources, all-optical sources exploit laser-plasma interaction to obtain the required high energy electrons to generate radiation. Bremsstrahlung or fluorescence emission driven from fast electron generation in laser interaction with solids was demonstrated to provide effective ultrashort X-ray emission with unique properties. More recently, laser-driven electron acceleration from interaction with gas-targets is being considered in place of conventional radio-frequency electron accelerators for a variety of radiation emission mechanisms. Broadband radiation generation schemes including betatron and Bremsstrahlung are being developed while free electron laser and Thomson scattering by collision with a synchronized laser pulse are being proposed for the generation of narrow band radiation. Here we present an overview of the current developments in this field.

8.1 Introduction

The impressive progress of high power laser technology initiated by the introduction of the Chirped Pulse Amplification (CPA) concept [1] is now leading to the realization of new large laser systems within the framework of the Extreme Light Infrastructure (ELI) that, by the end of this decade, will start paving the way to the exploration of new physical domains towards the electron-positron pair creation and the possibility to reach the critical field of quantum electrodynamics [2]. At the same time, the control of ultra-high gradient plasma acceleration [3–5] is being pursued and advanced schemes are being proposed for the future TeV linear collider [6].

L.A. Gizzi (✉)

Consiglio Nazionale delle Ricerche, Istituto Nazionale di Ottica, Pisa, Italy
e-mail: la.gizzi@ino.it

Meanwhile, existing laser-plasma accelerating scheme are being considered for the development of novel radiation sources. All-optical X-ray free electron lasers (X-FEL) are already being explored [7] with encouraging chances of success in the medium term. In this context, a design for a new European Research Infrastructures of the H2020 Framework Programme named European Plasma Research Accelerator with eXcellence In Applications (EuPRAXIA) has recently been established. The programme [8] aims at developing compact and advanced X-ray sources based upon laser-plasma acceleration. Meanwhile, more affordable configurations, still based upon laser-driven high energy electrons, including Bremsstrahlung, Betatron and Thomson/Compton scattering are being explored, established and applied to different fields. Here we describe these techniques in which X-rays and γ -rays are produced using entirely optical techniques and based upon compact and scalable schemes, with a special attention to Thomson/Compton scattering. Before entering the discussion of radiation processes, an introduction to the basic ultraintense laser-plasma physics is given with attention to the conditions required for laser-plasma acceleration.

8.2 Basic Physical Processes

When an intense, short laser pulse is focused on matter, either a solid or a gas, a range of physical processes takes place which depend on the laser pulse parameters like peak intensity, overall pulse duration, wavelength, spot size, just to cite the most relevant. At the highest intensities available today, special consideration also needs to be given to the detailed temporal evolution of the laser pulse, including the so-called pre-pulses, the nanosecond-pedestal-to-short-pulse contrast and the picosecond-pedestal-to-short-pulse-contrast. Key applications of intense, short laser pulses are quite diverse and include Laser Plasma Acceleration (LPA) [9], ultrashort K- α X-ray sources [10], laser driven ion acceleration in the Target Normal Sheath Acceleration (TNSA) [11], and, going further up in intensity scale, the Fast Ignition (FI) approach [12, 13] to inertial confinement fusion (ICF). All these mechanisms have in common the ability of intense laser pulses to accelerate electrons with different basic mechanisms. A brief description of these mechanisms is given below.

8.2.1 *Laser-Plasma Acceleration*

In LPA a high intensity ultra-short pulse is focused in a gas to induce laser wakefield acceleration (LWFA) [9]. In the classical picture of LWFA, a longitudinal electron plasma wave is excited by the ponderomotive force associated to the laser pulse. The electron plasma wave exhibits a longitudinal electric field and has a

phase velocity set by the group velocity of the laser pulse, $v_g = c(1 - \omega_p^2/\omega_L^2)^{1/2}$, where $\omega_p = (n_e e^2 / \epsilon_0 m_e)^{1/2}$ is the electron plasma frequency, with n_e being the electron plasma density, e , m_e and ϵ_0 the electron charge and mass and the dielectric constant respectively and ω_L is the laser angular frequency. Electrons in phase with the wave are accelerated until, travelling faster than the electron plasma wave, overcome the accelerating field of the wave and start experiencing a decelerating field. This mechanism yields a maximum accelerating distance equal to the so-called dephasing length, given by:

$$L_d = \frac{\omega_L^2}{\omega_p^2} \lambda_p \simeq 3.2 n_{18}^{-3/2} \lambda_{\mu\text{m}}^{-2}, \quad (8.1)$$

where n_{18} is the electron density in units of 10^{18} cm^{-3} and $\lambda_{\mu\text{m}}$ is the laser wavelength in micrometers. At high laser intensity, this classical scenario is significantly modified and numerical simulations provide detailed description of plasma wave excitation and evolution as well as electron injection and acceleration. The most compact configuration to obtain GeV-range electron bunches from laser-plasma interaction is based upon a gas-jet of a few millimeters, working in the so-called blowout regime [14, 15]. As shown in Fig. 8.1 (right), a short ($c\tau < \lambda_p/2$) and intense ($a_0 > 2$) laser pulse expels the plasma electrons outward creating a bare ion column. The blown-out electrons form a narrow sheath outside the bubble and the space charge generated by the charge separation pulls the electrons back creating a bubble-like wake whose size is $\lambda_b \simeq 2\sqrt{a_0}c/\omega_p$ and the dephasing length becomes $L_d = 2/3(\omega_L^2/\omega_p^2)\lambda_b$. Here $a_0 = eA_L/mc^2$ is the normalized vector potential of the laser. For sufficiently high laser intensities ($a_0 > 3.5 \div 4$) electrons at the back of the bubble can be injected in the cavity and experience a maximum

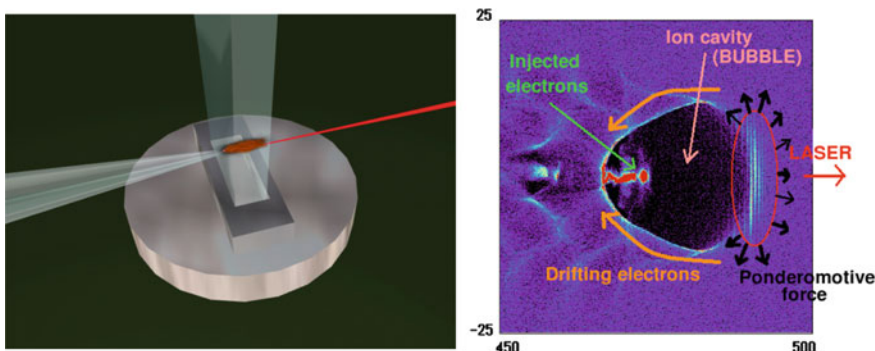


Fig. 8.1 Laser-gas interaction. *Left* Artist's view of laser interaction with a gas-jet. *Right* Plot of the electron density showing the cavity ion cavity generated by the intense laser propagating behind the laser pulse. The electron bunch injected in the bubble and accelerated by the longitudinal electric field is also visible

accelerating field of $E_{acc}[\text{GW}] \simeq 100 n_{18}^{1/2}$. Therefore, the maximum energy gain is given by [16]

$$W_{max}[\text{GeV}] = E_{acc} L_d \simeq 0.37 P_{TW}^{1/3} n_{18}^{-2/3}, \quad (8.2)$$

It can be shown that, according to this result, a matched condition (acceleration over the entire dephasing length) to achieve 1 GeV electron energy requires an electron density of $2 \times 10^{18} \text{ cm}^{-3}$. At this relatively high electron density, experiments show that laser beam quality is the key parameter to enable a satisfactory propagation, but a range of processes still play a crucial role in the propagation. Diagnostic techniques aimed at characterizing the propagation dynamics and unveiling the microscopic features of accelerating structures in the plasma are therefore needed to gain control over the acceleration process. In this context, special attention is being dedicated to the control of self-injection of electrons. Recently, several mechanisms have been identified and implemented to control injection of electrons in a well-formed wake wave. These mechanisms can be broadly divided into three categories depending on the basic physical process responsible for injection as shown in Fig. 8.2. Here the objective is to achieve a localized injection of electrons with a limited longitudinal spatial extent, to ensure reduced energy spread of accelerated electrons. Wave-breaking is certainly the most fundamental process leading to injection of electrons in a plasma wave. While transverse wave breaking [17] suffers from a delocalized injection of electrons and consequently large energy spread, longitudinal wave breaking via down-ramp [18] density-transition [19] certainly provides more localized injection and limited energy spread of electrons. Activation of such injection schemes required accurate control on shape and profile of electron distribution that can be achieved using custom gas targets and plasma tailoring. Recent successful implementations of this principle yielding very localized injection have been demonstrated which rely on plasma lensing [20] and shock-front in gas-jets [21].

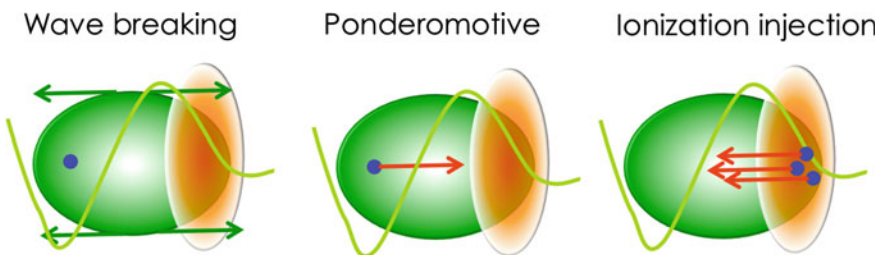


Fig. 8.2 Principal electron injection mechanisms divided schematically according to the underlying fundamental physical process currently being explored to provide localized injection and narrow electron energy spread

Ponderomotive injection [22, 23] also enables a high degree of control on the exact location of injection, but requires significantly more complex experimental configurations with additional laser pulses. In contrast, a simple technique to enhance electron injection is the so-called ionization-injection [24] in which field ionization properties of some gases are exploited to increase electron density in the bubble only at the peak of the pulse. Recent advances of this scheme also enable control of the spatial distribution of ionization injection and consequent smaller energy spread. Indeed, it is the dramatic development of these injection techniques which is currently enabling generation of narrow energy spread electrons with high energy, up to the multi GeV, uniquely by laser techniques. More effort is needed in this direction and perspectives in the near future are that injection and acceleration up to the 5 GeV energy range will be stable and accurate as required to drive a new generation of radiation sources for applications.

8.2.2 *Laser-Solid Interactions*

Interaction with a solid is fundamentally different from the interaction with a gas, mainly because the plasma produced by the interaction has a density greater than the critical density $n_c = m_e \omega_L^2 / 4\pi e^2 \simeq 1.1 \times 10^{21} \lambda_{\mu\text{m}}^{-2} \text{cm}^{-3}$. Therefore, laser light cannot propagate in the solid and is reflected at the critical density layer. At high intensity, i.e. for $a_0 > 1$, relativistic effects start to play a role due to the relativistic mass increase of the electrons oscillating in the e.m. field. Consequently, the critical density increases and laser light can propagate at higher densities than the non-relativistic case, up to densities approximately equal to $n_{cr}^* \simeq (1 + a_o^2)^{1/2} n_{cr}$. However, for a_0 values accessible today, $n_{cr}^* \ll n_{solid}$, and laser light propagation in the bulk is limited to the skin depth, typically tens of nanometers. In these circumstances, energy can penetrate deep in the target via the so-called fast electrons. These fast electrons are heated/accelerated by the laser in the interaction region at the vacuum-solid interface due to a variety of mechanisms including laser-driven plasma instabilities, resonance absorption, vacuum heating, the so-called Brunel effect [25], the $\mathbf{J} \times \mathbf{B}$ heating [26] and so on.

Both the TNSA ion acceleration, X-ray K- α sources and the Fast Ignition scenario rely on fast electron generation and propagation in dense regions of the target. In these schemes there is a great interest in understanding how fast electrons are produced, how they propagate in the target substrate, how they transfer their energy to the dense/compressed material, what is the production efficiency and what fraction of their energy can be transferred to the target. All these processes depend strongly upon the conditions that the laser pulse finds initially on the target surface and once generation of the electrons begins, their transport will be affected by several mechanisms including the electron beam parameters and the resistivity of the material. In the case of very intense laser pulses, the energy distribution of these fast electrons is found to be Maxwellian, with a characteristic parameter T_h which

increases with the laser intensity. Ponderomotive force associated with the laser pulse is expected to give rise to an efficient generation of fast electrons. However, experiments of laser interaction with solid targets show scaling with the laser intensity like the so-called Beg's law [27]:

$$T_{hot}(\text{MeV}) = 0.215 \left[I_{18} \lambda_{\mu\text{m}}^2 \right]^{1/3} \quad (8.3)$$

where I_{18} is the laser intensity in units of 10^{18} W/cm^2 and $\lambda_{\mu\text{m}}$ is the laser wavelength in μm . This law predicts a much weaker scaling than the ponderomotively driven fast electron temperature $T_{hot} \propto [(1 + cI)^{1/2} - 1]$ found in Particle-in-Cell simulations [28]. The lower scaling suggests that other mechanisms including resonance absorption could be playing a role, but a full understanding of this process is still lacking. A theoretical model has been developed [29] which shows a good agreement with Beg's law and predicts very high laser absorption at high intensities. More recently [30] a model was developed in which energy of fast electrons is found to increase with the scalelength of a preformed plasma in front of the solid target, suggesting that the counter-propagating incident and reflected light in the plasma should be taken into account. The role of counter-propagating incident and reflected light is also invoked in another recent modelling of interaction with steep density gradients [31].

Incidentally, it is worthwhile observing that fast electrons are expected to play an important role in the ICF fast ignition scheme [12] and experimental and theoretical effort world wide is aimed at studying the dynamics of fast electron generation and propagation in solids and plasmas. Scaled experiments are currently possible [32] which provide a preliminary assessment of the role of a fast ignition pulse in moderately compressed spherical pellet. At the same time several experiments use even simpler configurations in which the attention is focused on some specific processes involved in the fast ignition concept. In these experiments, laser pulses are focused to reach the highest possible intensity, typically close to 10^{20} W/cm^2 . At these intensities, a great role is played in the interaction process by the specific properties of the laser pulse including the beam quality and temporal contrast and knowledge of these features is therefore needed to model the experimental results with presently available numerical codes.

On the other hand, energetic electrons are responsible for emission of X-ray radiation characteristic of the atomic constituents of the target. In fact, while penetrating into the underlying cold target material, they knock out electrons preferentially from the inner electronic shells of the atoms or ions [33]. The radiative transitions of electrons from the outer shells finally leads to the generation of characteristic K-lines. The role of different mechanisms responsible for the generation of fast electrons is clearly visible from polarization dependent studies [34] which show strong reduction of emission for linearly S-polarized and circularly polarized radiation compared to linearly P-polarized radiation (Fig. 8.3).

This is just an example of the interplay between laser radiation properties and K- α emission which makes this type of radiation from laser-solid interaction of a

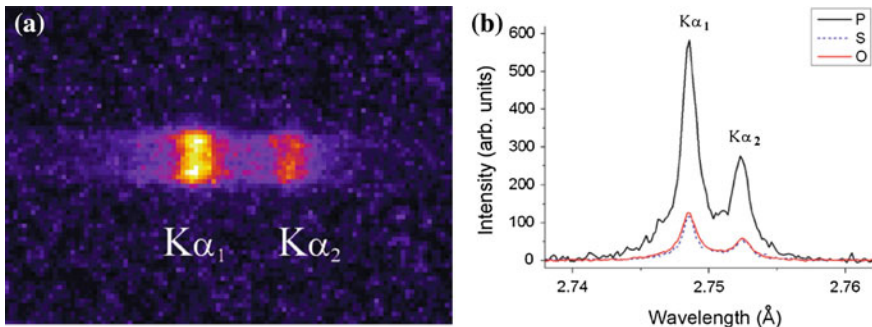


Fig. 8.3 **a** Raw spectrum of fluorescence Ti K- α emission from laser irradiation of a Ti foil at moderately relativistic intensity ($a_o \approx 1$), obtained by averaging 100 p-polarized laser pulses. **b** Ti K- α spectra obtained by different laser pulse polarizations, and obtained by averaging 100 laser shots (after [34])

great interest. In general, K- α emission spectroscopy of neutral or partially ionized atoms, possibly with spatial resolution, can be exploited for studying the fast electron transport through matter with micrometer resolution [35]. Consequently, from the point of view of applications as a radiation source, the main characteristics of K- α based ultrashort X-ray emission, such as photon yields as well as duration and size, strongly depend upon the production and transport processes of the fast electrons. The understanding of these issue plays a crucial role in laser-plasma based K- α sources and their applications and is the subject of current investigations using advanced numerical and experimental tools.

In recent years, effort in this context is directed towards the enhancement of laser-plasma coupling using micro and nano-engineered target which, in many cases, have been found to exhibit larger absorptivity of laser radiation (see [36] and references therein) or resonant excitation of surface plasma waves [37]. The specific properties of nano-structures required to influence fast electron generation are still being explored and a general understanding of governing parameters and scaling laws is still lacking. However, important milestones have been established concerning the fundamental role of laser contrast in enabling absorption and heating of dense plasma [38] by nano-structured targets. These recent observations are triggering the development of an entirely new class of radiation sources which promise to extend significantly the realm of X-ray emission from femtosecond laser solid interactions, with the possibility of activating a micro plasma waveguide capable of efficiently accelerating electrons and acting like wigglers to generate bright hard X-ray emission [39]. Although numerical and experimental investigations in this context of micro and nano plasmonics are still in their infancy, current trends promise major impact of these studies on future compact X-ray and γ -ray sources for applications.

8.3 Bremsstrahlung from Laser-Driven Electrons

If a charged particle makes a Coulomb collision with the nucleus of an atom, it undergoes acceleration and emits radiation with a continuous photon energy spectrum that extends up to approximately the electron rest energy times the γ factor of the incident electron. For value of $\gamma > 1$, the photons are emitted in the forward direction in a cone of aperture of approximately $1/\gamma$. The total radiated power scales as Z^2 and can account for a conversion of a significant fraction of the electron energy into photon energy. Practical Bremsstrahlung sources extend from the keV range, as in the X-ray tube, up to the multi MeV range. In the latter case, the high energy electron bunch, accelerated by a linac, hits a converter, typically a tungsten or a tantalum plate, and generates γ -rays with photon density as high as 1 ph/eV/sec. Alternatively, high energy electron bunches produced using compact plasma accelerators driven by lasers can be used in place of linac generated electrons. All-optical, laser-based bremsstrahlung X-ray and γ -ray sources have already been explored [40, 41] and successfully tested using self-injection electron bunches [42, 43]. Figure 8.4 shows a schematic set up of a typical laser-driven γ -ray source used in [43]. Here the source was used to activate a gold sample in the 8–17.5 MeV photon energy range of the giant dipole resonance. A total flux of 4×10^8 photons per Joule of laser energy was estimated through activation measurements which makes this class of sources the brightest Bremsstrahlung source in the considered photon energy range [44].

In this context, photon yield can be significantly enhanced if multiple bunches are generated in laser wakefield acceleration for a single laser pulse. In fact, in the experimental conditions explored in [44], the laser pulse undergoes self-phase modulation and compression that leads to the excitation of a non-linear plasma wave with multiple buckets with a similar amplitude. Injection and acceleration occurs in each bucket and consequently, multiple electron bunches of high energy electrons are generated at each laser shot as shown in Fig. 8.5.

A similar set up is being considered for other applications like imaging and non destructive testing of thick objects. In this case the source size is a very relevant parameter that must be optimized to enhance spatial resolution of the imaging technique. Recent studies [45] show that a source size as small as 30 μm can be obtained placing the Bremsstrahlung converter a few millimetres from the gas-jet downstream

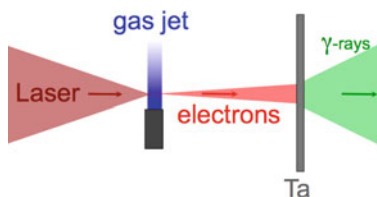


Fig. 8.4 A schematic set up of a Bremsstrahlung source based upon a laser-plasma source of high energy electrons. A Tantalum converter is placed in the proximity of the gas-jet target where the transverse size of the laser accelerated electron bunch is as small as a fraction of a millimetre

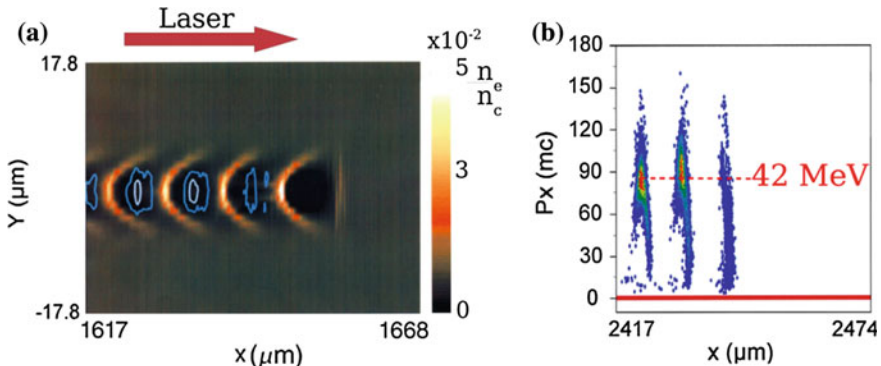


Fig. 8.5 Particle-in-cell simulation of non-linear wakefield excitation and acceleration of multiple bunches. This regime, explored in [44] provides efficient conversion of laser energy into high energy electrons and Bremsstrahlung radiation

the bunch propagation direction to perform high resolution γ -ray imaging of bulky and dense objects [46]. An additional feature of all-laser driven sources is the intrinsic ultrashort pulse duration which, combined with the potentially high degree of compactness, makes this class of sources unique and potentially advantageous for applications in a wide range of fields, both in industry and in basic research.

8.4 Betatron in Laser-Wakefield Acceleration

Another very effective mechanism of generation of X-ray radiation during laser-plasma wakefield acceleration originates from the transverse oscillation of the electron bunch in the acceleration cavity due to the strong restoring force directed towards the longitudinal laser propagation axis as shown schematically in Fig. 8.6. The typical photon energy of this emission is similar to the undulator type radiation characterised by a wavelength of the oscillation $\lambda_\beta = \sqrt{2\gamma_0} \lambda_p$, where $\lambda_p = 2\pi c/\omega_p = 3.34 \times 10^{10} n_e^{-1/2}$ μm is the electron plasma wavelength, with n_e being the electron plasma density in units of cm^{-3} . Photon energy up to the keV range can be easily achieved for electron energy up to 1 GeV.

This radiation mechanism was first observed in 2004 [47] and is currently being regarded as a very promising source for X-ray imaging up to the keV range. In fact, the effective small source size typical of this emission process makes phase contrast image possible as recently demonstrated both at 5 keV [48] and earlier at higher photon energies of 10 keV [49] and above 20 keV approximately [50]. Although betatron emission typically exhibits a broadband spectrum in the keV range, higher photon energy can be achieved in conditions of enhanced transverse electron oscillations as demonstrated in [51] where parameters of the accelerating cavity were modified in such a way to enable overlapping of the electrons with the rear of the laser pulse. In this way the betatron motion was resonantly excited and

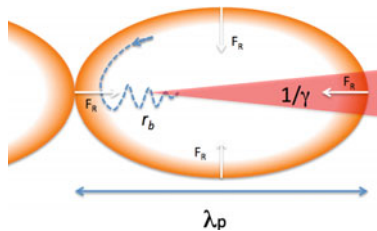


Fig. 8.6 A pictorial view of the physical principle behind the betatron radiation emission. Electrons injected in the longitudinal field of the accelerating bubble-like structure oscillate around the axis due to the restoring force and emit radiation in the forward direction

the resulting oscillation amplitude was found to increase significantly, leading to an enhanced X-ray photon energy.

8.5 Thomson Scattering

Ideally, nuclear applications require high energy and spectral density γ -rays. In this scenario, a very demanding application is the Nuclear Resonance Fluorescence (NRF) due to the small spectral width of nuclear resonance transitions (Fig. 8.7).

Once excited, the nucleus will emit characteristic fluorescence γ -rays which will depend upon the specific atomic element and isotopes [53] is. This is the principle behind the use of such a technique for safety and inspection applications. The ideal requirements for NRF applications on the gamma ray beam are bandwidths as small as possible (desired <0.1 %, present state of the art 2 %) and spectral density as high as 10^4 ph/sec/eV. These requirements are very challenging and new large installations based on state-of-the-art accelerator technology are being proposed to fulfill them. The estimated cost of such installations is currently in the 50–100 Meuro. Such new sources [54] are based upon the use of high energy Linacs and high power lasers or free electron lasers [55] to generate γ -rays via Thomson/Compton scattering. In this scenario, the use of laser-plasma accelerated electrons has also been explored [52] and is regarded as a possible way to make radiation sources far more accessible than current Linac based sources.

All-optical Thomson scattering is being considered in which a high intensity laser pulse is set to collide with a laser-accelerated electron bunch. In a pioneering experiment [56] carried out at the Jena laser Facility in 2006, all-optical Thomson scattering (TS) in the 1 keV X-ray region was first demonstrated using a compact configuration with a limited freedom for optimization and using poor quality laser-accelerated electron bunches, still affected by 100 % energy spread. Since then, laser-plasma acceleration has seen a dramatic improvement and laser accelerated electrons can now exceed 4 GeV peak energy [57] with energy spread well below 10 %, with record values close to 1 %. Moreover, new schemes are being proposed to control injection and optimize acceleration, which are now being

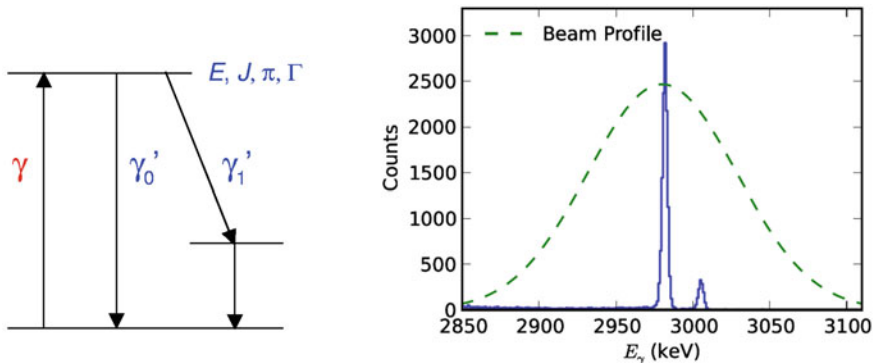


Fig. 8.7 Nuclear resonance fluorescence is based upon the detection of characteristic fluorescence emission (right) with a high intensity γ -ray beam, resulting from decay of nuclei after γ -ray excitation (left). It is used to identify isotopes and can be applied to safety and inspection. Typical excited states of nuclei lie in the MeV range and have linewidths of <1 eV (after [52] and [53] is)

implemented to further improve the quality of laser accelerated electrons. These improvements are rapidly reflecting in the development of all-optical Thomson scattering sources as described below.

Thomson scattering from free electrons is a pure electrodynamics process in which each electron radiates while accelerating under the action of an external electromagnetic wave. If the electron is at rest or is not relativistic, the magnetic field of the e.m. wave can be neglected and the motion is entirely due to the electric field. The electron oscillates along the electric field direction and emits e.m. dipole radiation. For an electron with a velocity $\beta \ll 1$ and acceleration $\dot{\beta}$, the power of the radiation emitted per unit solid angle is given by the following expression [58]:

$$\frac{dP}{d\Omega} = \frac{e^2}{4\pi c} |\mathbf{n} \times (\mathbf{n} \times \dot{\mathbf{v}})|^2 \quad (8.4)$$

which, via integration over the entire solid angle, yields the well known Larmor formula of the total radiated power for a non relativistic accelerated electron:

$$P = \frac{2e^2}{3c^3} |\dot{\mathbf{v}}|^2. \quad (8.5)$$

Radiation is emitted in directions other than that of the linearly polarized incident plane wave and the radiation frequency is the same as the incident radiation. In terms of the radiation intensity I , and the density of scattering electrons n_e , the emission coefficient is given by:

$$\varepsilon = \frac{\pi\sigma_T}{2} In_e \quad (8.6)$$

where σ_T is the so-called Thomson cross section:

$$\sigma_T = \frac{8\pi}{3} \left(\frac{e^2}{m_e c^2} \right)^2 = 6.65 \times 10^{-25} \text{ cm}^2 \quad (8.7)$$

with the quantity $r_e = e^2/m_e c^2$ being the classical electron radius. This is the situation typically used to detect propagation of laser pulse in an under dense plasma like in [59] or to measure the plasma properties [60].

If the scattering electron is moving at a relativistic velocity, the energy radiated per unit solid angle per unit frequency interval is instead given by [58]:

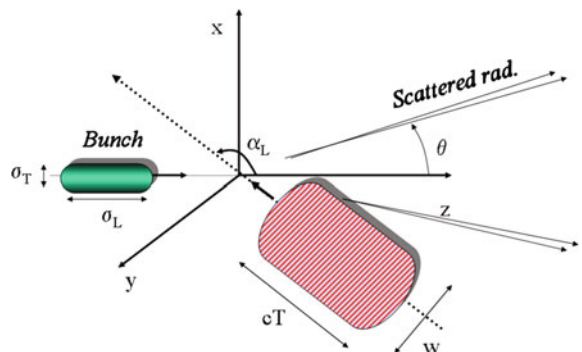
$$\frac{dI^2}{d\Omega d\omega} = \frac{e^2}{4\pi^2 c} \left| \int_{-\infty}^{+\infty} \frac{\mathbf{n} \times [(\mathbf{n} - \beta) \times \dot{\beta}]}{(1 - \beta \cdot \mathbf{n})^2} e^{i\omega(t - \mathbf{n} \cdot \mathbf{r}(t)/c)} dt \right|^2 \quad (8.8)$$

which, compared with the non-relativistic case of (8.4), increases indefinitely when $\beta \cdot \mathbf{n} \rightarrow 1$ which occurs when $\beta \simeq 1$ and β is parallel to \mathbf{n} . In this case, the scattering e.m. radiation in the particle rest frame will be Doppler shifted by a factor γ . Also, radiation emitted by the electron will be Doppler shifted in the laboratory frame resulting in a total upshift of a factor γ^2 . Also, the Lorentz transformation from the particle rest frame to the laboratory frame implies that the radiation will be emitted along the direction of the electron velocity in a small cone of aperture $d\theta \simeq 1/\gamma$ around the velocity vector direction.

8.5.1 Scattering Parameters

We consider the geometry described in Fig. 8.8. The three main parameters governing the scattering process are the electron energy $E_o = \gamma_o m_e c^2$, the laser pulse

Fig. 8.8 Thomson scattering geometry. The scattered radiation is emitted along the z axis, in a small cone of aperture $1/\gamma$. When $\alpha_L = \pi$ the backscattering geometry occurs



peak normalized amplitude $a_o = eA/(mc^2) \approx 8.5 \times 10^{-10} \sqrt{I\lambda_{\mu\text{m}}^2}$, I being the laser peak intensity in W/cm^2 , $\lambda_{\mu\text{m}}$ is the laser wavelength in μm and α_L is the angle between the propagation directions of the laser pulse and the electrons.

The pulse amplitude controls the momentum transferred from the laser pulse to the electron, i.e. the number of photons of the pulse absorbed by the electron.

8.5.1.1 Linear Regime

If $a_o \ll 1$, only one photon is absorbed and the resulting electron motion always admits a reference frame in which the quivering is non-relativistic (linear Thomson scattering) [61]. Assuming $\gamma_o \gg 1$, scattered radiation is emitted forward with respect to the electron initial motion within a cone of aperture $1/\gamma_o$. Assuming a laser pulse having a rise time much greater than the pulse period, the resulting scattered radiation ω_γ is spectrally shifted compared to the laser frequency ω_L at a peak energy given by [62]:

$$\omega_\gamma \cong 2\gamma_o^2(1 - \cos \alpha_L)\omega_L \quad (8.9)$$

Among the possible interaction geometries, the case of backscattering $\alpha_L = \pi$ is the most suitable for at least three aspects: (i) it produces photons with the highest energy

$$\omega_\gamma \cong 4\gamma_o^2\omega_L; \quad (8.10)$$

(ii) it allows the highest overlap of the electron beam and the pulse; (iii) it minimizes spurious effects induced by the transverse ponderomotive forces of the laser pulse.

The number of scattered photons and the spectral distribution of the radiation collected within a cone of aperture θ depend on the pulse parameters, the bunch quality and the product. A simplified formula, which is valid in the case of negligible beam emittance and linear scattering can be found in [61] and reads:

$$N_{TS,Linear} = \frac{1}{2} FN_e \alpha \omega_L T a_o^2 \psi^2 \frac{1 + \psi^2 + 2/3\psi^4}{(1 + \psi^2)^3} \quad (8.11)$$

where N_e is the number of electrons in the bunch, F the filling factor which depends on both the pulse and electron bunch envelopes, T is the laser pulse duration, ψ is the collection aperture angle, and $\alpha = 1/137$ the fine structure constant. Note that when $\psi \ll 1$, then $N_{Sc} \propto \psi^2$ indicating the strong dependence of the collected photons upon the collection aperture.

If we collect over the entire solid angle $\theta_{max} = 1/\gamma_o$, the formula of (8.11) simplifies to:

$$N_{TS,Linear} \cong 1.2 \times 10^{-3} FN_e \omega_L T a_o^2 \quad (8.12)$$

which clearly shows the dependence of the total scattered photons upon the main experimental parameters. Assuming a filling factor $F = 1$, a number of electrons corresponding to a total charge of 100 pC, i.e. $N_e = 6 \times 10^8$ and a laser pulse duration of $T = 100$ fs, we find:

$$N_{TS,Linear} = 1.68 \times 10^7 a_o^2. \quad (8.13)$$

According to this formula we immediately find that, for a fixed pulse duration, the scaling of $N_{TS,Linear} \propto a_o^2$ requires a relatively high intensity. The detailed description of Thomson scattering of realistic electron bunches and laser pulses, in the linear or nonlinear regime, is now made possible by using Monte Carlo codes based on the analytic description of the single particle dynamics. Some results will be shown in the description of the proposed experiment given below.

8.5.1.2 Non-linear Regime

In the nonlinear regime, $a_0 \approx 1$, the resulting strong exchange between the laser pulse and electron momentum induces a complex and relativistic electron motion, consisting of a drift and a quivering having both longitudinal and transverse components with respect to the pulse propagation. In turn, the time dependent longitudinal drifting results in a non-harmonic electron motion that produces scattered radiation with a complex spectral distribution characterised by harmonics of the fundamental frequency. If the electron interacts with a laser pulse with a constant amplitude, e.g. a flat-top laser pulse, the spectral distribution of the scattered radiation consists of equally spaced harmonics [61]. In the case of head-on collision, the peak energy of each Nth harmonics in a back-scattering configuration reads now:

$$\omega_{\gamma,N} \cong N_{th} \frac{4\gamma_o^2 \omega_L}{1 + a_o^2/2}. \quad (8.14)$$

As the intensity increases even further ($a_0 \gg 1$), radiation is emitted into many closely spaced harmonics showing a typical synchrotron radiation spectrum. When considering scattering from an electron bunch, harmonics produced by each electron will be slightly shifted due to non-ideal beam effects like energy spread and beam emittance. As a consequence, a continuous spectrum is generated which extends up to the critical frequency that scales [63] as a_o^3 .

8.5.1.3 Radiation Reaction Regime

In the classical description of Thomson scattering, the loss of energy and momentum of the particle carried away by the emitted radiation is neglected and the particle trajectory is calculated considering the external force $\mathbf{F}_{ext} = q(\mathbf{E} + \mathbf{v} \times \mathbf{B}/c)$, where q is the charge of the particle. When the laser intensity increases further, the energy and the momentum lost by the particle emitting radiation increases up to the point where the effect on the particle trajectory cannot be neglected and must be included in the calculation. Simple considerations [58] show that in the case of electrons, this so-called radiation reaction regime requires that a significant loss of energy and momentum occurs on a time scale of the order of $\tau_{RR} \approx 10^{-24}$ s and a spatial scale of the order of $l_{RR} \approx c\tau \approx r_e$. These conditions are quite extreme and in typical laboratory experiments radiation reaction effects can be neglected. However, with current development, ultraintense lasers may soon be able to enter this regime. It can be shown that the above conditions are satisfied for a laser intensity $a_o > 400$ when the equation of motion of the electron must include an additional force to describe the radiation reaction is a self consistent way [64]. A physically satisfactory description of radiation reaction is given by the Landau-Lifshitz equation [65]. Experimental validation of this theory is still lacking and the experimental configuration used for all-optical Thomson scattering is regarded as an ideal test bed to evaluate the accuracy of the theory, even at values of the laser intensity below the above threshold [66].

8.5.2 *Thomson Scattering in the Laboratory*

Generation of radiation via Thomson scattering of a laser pulse by energetic counter-propagating electrons was initially proposed in 1963 [67, 68] as a quasi monochromatic and polarized photons source. With the development of ultraintense lasers the interest on this process has grown and the process is now being exploited as a bright source of energetic photons from UV to γ -rays and attosecond sources in the full nonlinear regime. Thomson scattering in the linear regime has also been proposed to attain the angular distribution of a monochromatic electron bunch [69]. Moreover, experimental methods have been proposed to measure the length of a monochromatic electron bunch and to measure the energy spectrum of a single bunch eventually characterized by a wide energy spread or alternatively to measure the angular distribution of a single bunch with a known energy spectrum [70]. These new experimental methods are based on X-ray detectors having both a good spectral and angular resolution (cooled CCD camera used in the single photon counting regime) [71].

In the typical all-optical configuration, two laser pulses are synchronized and then focused in a counter-propagating geometry. One of the pulses propagates towards the electron bunch generated by the other pulse, producing radiation propagating along the bunch propagation direction. The counter-propagating configuration is obtained either using two separately compressed laser pulses with

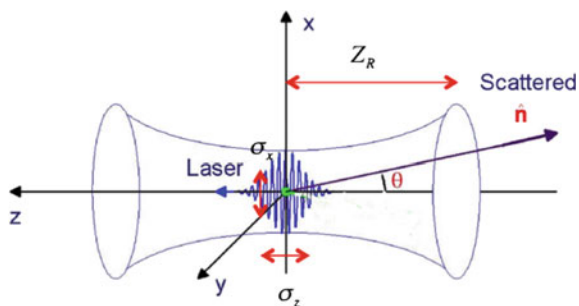
controlled energy or by splitting the main laser pulse in two pulses, with independent focusing configuration. In this case particular care must be taken in arranging the splitting configuration where one, or both laser pulses may suffer from phase front distortions introduced by the beam splitter.

According to (8.11), photon yield in the linear regime scales as a_o^2 . Therefore, for a given transverse size of the electron bunch and FWHM of the laser pulse, we obtain the laser energy required in the scattering pulse to obtain optimum photon production. If we set $a_o = 0.3$, corresponding to an intensity of $2 \times 10^{17} \text{ W/cm}^2$, we find that for realistic values of the scattering pulse focal spot diameter of 25 or 50 μm the energy required is 115 and 45 mJ respectively. This value increases up to almost 2 J for a FWHM of 100 μm . From the point of view of the accelerating laser pulse a stable self-injection with moderate energy spread requires $a_o > 1$ over a long distance in the plasma. This can be achieved with long focal length optics characterized by large diameter focal spots. Ultimately, a pulse energy exceeding 1 J for a 30 fs pulse duration is required. Both these conditions on the scattering and accelerating laser pulses suggest that the ideal laser system for the investigation of all-optical Thomson scattering is capable of delivering in excess of 2 J of energy, possibly in two independently controllable pulses.

Thomson scattering experiments require spatial and temporal overlap of the electron bunch and the scattering laser pulse at the collision point. In the case of laser-wakefield acceleration, location of the collision point relative to the acceleration region requires a careful evaluation based on the electron bunch cross section and scattering pulse focal spot and Raileigh length Z_R as shown in Fig. 8.9. Ideally, a collision point set just at the end of the accelerating region would avoid deterioration of electron bunch properties. In fact, free propagation of the accelerated bunch may result in an increase of transverse and longitudinal size, emittance and energy spread. However, at the exit of the accelerating region, electron bunches have very small transverse and longitudinal size, typically a few μm and a few fs which would set demanding conditions on the scattering laser pulse.

Current experiments typically use a collision point set a few mm downstream the accelerating region, where electron bunch transverse size is a few tens of μm , easily achievable with the scattering pulse. In the original paper by Chen et al. [72], the collision point was set 1 mm after the exit of the plasma, where the focal spot of the 800 nm scattering pulse spot size was 9 μm and the overlapping (emitting) region

Fig. 8.9 Temporal and spatial overlapping of Thomson scattering pulse and electron bunch must be controlled to optimize X-ray scattering, taking into account electron bunch evolution beyond the accelerating region and scattering pulse focal spot and Raileigh length



was estimated to be 5 μm . Scattering with a 250 MeV cut-off energy electrons enabled generation of peak photon energy of 1.2 MeV. Sarri et al. [44] used a F/2 OAP to focus the 18 J, 42 fs scattering pulse 10 mm downstream of the exit of the gas target were the electron bunch transverse size was 30 μm and the average normalized intensity was $a_o = 2$. Scattering off LWFA electrons with energy up to 600 MeV resulted in Thomson scattering photons with energy up to 18 MeV, the highest energy obtained so far with all-optical Thomson scattering.

Liu et al. [73] achieved similar photon energy with lower peak electron energy, but using frequency doubled, 400 nm optical scattering pulse. They used a separate optical compressor to control focal spot quality of the frequency doubled pulse which is more sensitive to phase front distortions. They tuned the frequency doubled scattering pulse to produce 54 mJ in a 300 fs laser pulse, focused in a 15 μm focal spot and were able to achieve >9 MeV photon energy with a broadband spectrum peaked at approximately 400 MeV.

On the other hand, depending on the perspective application, tuneability of the X-ray photon energy may be an important option of a source. According to (8.10) or (8.14), the frequency of the scattered radiation can be tuned by changing either the electron energy or the scattering photon energy. Powers et al. [74] achieved tuneability changing the electron energy in the range from 50 to 200 MeV by changing the plasma density to exploit the square root dependence of the accelerating electric field upon the electron density that occurs in LWFA. In this way they were able to achieve tuneability in the range from 70 keV to approximately 1 MeV. Tunability in the 5–42 keV was demonstrated by Khrennikov et al. [75] using a different technique to tune electron energy. They use shock-front injection [21] which exploits the properties of sharp downramps of the electron density of the plasma [70] to localize electron injection. Tunability is achieved by shifting the position of the downramp along the plasma to control acceleration length.

Finally, special attention deserves the detection of X-ray and γ -ray radiation generated by all-optical Thomson sources. Current experiments show that peak brilliance of these sources in the MeV region exceeds $10^{20} \text{ photons s}^{-1} \text{ mm}^{-2} \text{ mrad}^{-2}$ 0.1 % bandwidth. Also, as discussed above, the spectral properties of these sources is of a great interest for investigation of scattering processes at high fields. Therefore, besides calorimetric measurements aimed at measuring the total scattered energy, detectors should enable accurate spectroscopic investigation. This can be achieved using the scintillation detectors in the single photon counting regime accumulating photons over many laser shots and assuming reproducibility of the source. In general, single shot measurements are required and current detection techniques are limited. One possibility [76] is to exploit the Compton scattering effect in low Z materials to convert γ -ray photons into electrons and recover the photon spectrum from the electron spectrum. Further development of these techniques will be required to enable accurate characterization of all-optical Thomson scattering sources.

In conclusion, we have given an overview of all-laser driven techniques for generation of X-ray and γ -rays, with a detailed discussion of Thomson scattering. In the multi MeV range, state of the art technology indeed exploit this mechanism to generate bright sources based upon large conventional accelerators. The dramatic

development of laser-based electron acceleration techniques is rapidly driving the practical demonstration of a new class of all-optical, compact radiation sources. Recent experiments clearly show increasing control over source properties and promise major achievements in the near future.

References

1. D. Stickland, G. Mourou, Opt. Commun. **56**, 219 (1985)
2. J. Schwinger, Phys. Rev. **82**, 664 (1951)
3. J. Faure, Y. Glinec, A. Pukhov et al., Lett. Nat. **431**, 541 (2004)
4. W.P. Leemans et al., Nat. Phys. **2**, 696 (2006)
5. D. Giulietti et al., Phys. Plasmas **9**, 3655 (2002). (letter)
6. W.P. Leemans et al., AIP Conf. Proc. **1299**, 3 (2010)
7. J.G. Gallacher et al., Phys. Plasmas **16**, 093102 (2009)
8. <http://www.eupraxia-project.eu/home.html>
9. T. Tajima, J.M. Dawson, Phys. Rev. Lett. **43**, 267 (1979)
10. A. Rousse et al., Phys. Rev. E. Stat. Phys. Plasmas. Fluids. Relat. Interdiscip. Top. **50**, 2200 (1994)
11. R.A. Snavely et al., Phys. Rev. Lett. **85**, 2945 (2000)
12. M. Tabak et al., Phys. Plasmas **1**, 1626 (1994)
13. S. Atzeni, J.M. ter Vehn, *The Physics of Inertial Fusion* (Oxford University Press, Great Clarendon Street, Oxford ***OX2 6DP, 2004)
14. A. Pukhov, J. ter Vehn, Appl. Phys. B **74**, 355 (2002)
15. S. Gordienko, A. Pukhov, Phys. Plasmas **12**, 043109 (2005)
16. B.B. Pollock et al., Phys. Rev. Lett. **107**, 045001 (2011)
17. S.V. Bulanov, F. Pegoraro, A.M. Pukhov, A.S. Sakharov, Phys. Rev. Lett. **78**, 4205 (1997)
18. S. Bulanov, N. Naumova, F. Pegoraro, J. Sakai, Phys. Rev. E **58**, 5257 (1995)
19. P. Tomassini et al., Phys. Rev. ST Accel. Beams **6**, 121301 (2003)
20. A.J. Gonsalves et al., Nat. Phys. **7**, 862 (2011)
21. A. Buck et al., Phys. Rev. Lett. **110**, 185006 (2013)
22. D. Umstadter, J.K. Kim, E. Dodd, Phys. Rev. Lett. **76**, 2073 (1996)
23. E. Esarey et al., Phys. Rev. Lett. **79**, 2682 (1997)
24. M. Chen, Z.-M. Sheng, Y.-Y. Ma, J. Zhang, J. Appl. Phys. **99** (2006)
25. S.C. Wilks, W.L. Kruer, M. Tabak, A.B. Langdon, Phys. Rev. Lett. **69**, 1383 (1992)
26. W.L. Kruer, K. Estabrook, Phys. Fluids **28**, 430 (1985)
27. F.N. Beg et al., Phys. Plasmas **4**, 447 (1997)
28. S.C. Wilks, W.L. Kruer, M. Tabak, A.B. Langdon, Phys. Rev. Lett. **69**, 1383 (1992)
29. M.G. Haines, M.S. Wei, F.N. Beg, R.B. Stephens, Phys. Rev. Lett. **102**, 045008 (2009)
30. B.S. Paradkar et al., Phys. Rev. E **83**, 046401 (2011)
31. J. May et al., Phys. Rev. E **84**, 025401 (2011)
32. W. Theobald et al., Phys. Plasmas **18**, 056305 (2011)
33. F. Ewald, H. Schwoerer, R. Sauerbrey, Europhys. Lett. **60**, 710 (2002)
34. G. Cristoforetti et al., Phys. Rev. E **87**, 023103 (2013)
35. L.A. Gizzi et al., Plasma Phys. Control. Fusion **49**, B221 (2007)
36. G. Cristoforetti et al., Plasma Phys. Control. Fusion **56**, 095001 (2014)
37. T. Ceccotti et al., Phys. Rev. Lett. **111**, 185001 (2013)
38. M.A. Purvis et al., Nat. Photonics **7**, 796 (2013)
39. L. Yi, A. Pukhov, P.L. Thanh, B. Shen **1**, 1 (2015)
40. L.A. Gizzi et al., Phys. Rev. Lett. **76**, 2278 (1996)
41. L.A. Gizzi et al., Laser Part. Beams **19**, 181 (2001)

42. D. Giulietti et al., Phys. Rev. E **64**, 015402(R) (2001)
43. A. Giulietti et al., Phys. Rev. Lett. **101**, 105002 (2008)
44. G. Sarri et al., Phys. Rev. Lett. **113**, 224801 (2014)
45. A. Ben-Ismal, J. Faure, V. Malka, Nucl. Instrum. Methods Phys. Res. Sect. A. Accel. Spectrom. Detect. Assoc. Equip. **629**, 382 (2011)
46. A. Ben-Ismal et al., Appl. Phys. Lett. **98**, 264101 (2011)
47. S. Corde et al., Rev. Mod. Phys. **85**, 1 (2013)
48. J. Wenz et al., Nat. Commun. **6**, 7568 (2015)
49. S. Kneip et al., Appl. Phys. Lett. **99**, 093701 (2011)
50. Z. Najmudin et al., Philos. Trans. A. Math. Phys. Eng. Sci. **372**, 20130032 (2014)
51. S. Cipiccia et al., Nat. Phys. **7**, 867 (2011)
52. W. Walsh et al., in *Nuclear Science Symposium Conference Record (NSS/MIC), 2009 IEEE* (IEEE, Orlando, FL, 2009), pp. 80–85
53. C.T. Angell et al., Phys. Rev. C **90**, 054315 (2014)
54. F. Albert et al., Phys. Rev. ST Accel. Beams **13**, 070704 (2010)
55. A.M. Sandorfi et al., IEEE Trans. Nucl. Sci. **30**, 3083 (1983)
56. H. Schwoerer et al., Phys. Rev. Lett. **96**, 014802 (2006)
57. W. Leemans et al., Phys. Rev. Lett. **113**, 245002 (2014)
58. J.D. Jackson, *Classical Electrodynamics* (Wiley, New York, 1998)
59. L.A. Gizzi et al., IEEE Trans. Plasma Sci. **39**, 2954 (2011)
60. S.H. Glenzer et al., Phys. Plasmas **6**, 2117 (1999)
61. P. Tomassini, A. Giulietti, D. Giulietti, L.A. Gizzi, Appl. Phys. B **80**, 419 (2005)
62. S.K. Ride, E. Esarey, M. Baine, Phys. Rev. E **52**, 5425 (1995)
63. E. Esarey, S.K. Ride, P. Sprangle, Phys. Rev. E **48**, 3003 (1993)
64. A. Macchi, *A Superintense Laser-Plasma Interaction Theory Primer* (Springer, London, 2013)
65. L.D. Landau, E.M. Lifshitz, *The Classical Theory of Fields* (Elsevier, Oxford, 1975)
66. A. Di Piazza, K. Hatsagortsyan, C. Keitel, Phys. Rev. Lett. **102**, 254802 (2009)
67. R.H. Milburn, Phys. Rev. Lett. **10**, 75 (1963)
68. C. Bemporad, R.H. Milburn, N. Tanaka, M. Fotino, Phys. Rev. **138**, B1546 (1965)
69. W.P. Leemans, Phys. Rev. Lett. **67**, 1434 (1991)
70. P. Tomassini et al., Phys. Rev. Spec. Top. Accel. Beams **6**, 121301 (2003)
71. L. Labate et al., Nucl. Instrum. Methods Phys. Res. Sect. A. Accel. Spectrom. Detect. Assoc. Equip. **495**, 148 (2002)
72. S. Chen et al., Phys. Rev. Lett. **155**, 003, 1 (2013)
73. C. Liu et al., Opt. Lett. **39**, 4132 (2014)
74. N.D. Powers et al., Nat. Photonics **8**, 28 (2013)
75. K. Khrennikov et al., Phys. Rev. Lett. **114**, 1 (2015)
76. D.J. Corvan, G. Sarri, M. Zepf, Rev. Sci. Instrum. **85**, 1 (2014)

Chapter 9

Dosimetry of Laser-Driven Electron Beams for Radiobiology and Medicine

Luca Labate, Debora Lamia and Giorgio Russo

Abstract In this chapter, the main issues related with the usage of “standard” dosimetric methods for the characterization of laser-driven electron beams will be discussed. In particular, an overview of the main devices used for the characterization of electron beams used in medical applications will be given. The issues possibly arising in the usage of techniques established for conventional accelerators for the dosimetry of ultrashort laser-driven beams will also be given.

9.1 Introduction

In order for laser-driven electron accelerators to be used for applications in the field of radiotherapy, the capability of performing both absolute and relative dosimetry on the electron beam is an essential prerequisite. From a general point of view, a dosimetric characterization would be aimed at maximizing the dose delivered to the cancer cells while, at the same time, keeping the dose to the neighbour tissues as low as possible. This also involves a detailed characterization of the primary beam, in terms, for instance, of its energy and spatial features.

It is worth noticing, at this point, that, while already providing electron bunches with the main figures very similar to those delivered by typical LINAC-based machines employed in the radiotherapy practice [1–3], a laser-driven accelerator exhibits peculiar features as for some important parameters. As an example, Table 9.1 shows a few parameters for the electron bunches delivered by one of the

L. Labate (✉)

Istituto Nazionale Di Ottica, Consiglio Nazionale Delle Ricerche, Pisa, Italy
e-mail: luca.labate@ino.it

D. Lamia · G. Russo

Istituto Di Bioimmagini E Fisiologia Molecolare, Consiglio Nazionale Delle Ricerche,
Cefalù, Italy
e-mail: debora.lamia@ibfm.cnr.it

G. Russo

e-mail: giorgio.russo@ibfm.cnr.it

Table 9.1 Main parameters of the electron bunches delivered by an IOERT machine as compared with the ones by a possible laser-driven machine

Parameter	LIAC ®	Laser-driven
Max e^- energy	12 MeV	up to ~ 100 MeV
Charge per bunch/shot	1.8 nC	1 nC
Repetition rate	5–20 Hz	10 Hz
Average current	18 pA (@10 Hz)	10 pA
Bunch duration	~ 1 μ s	~ 1 ps
Peak current	~ 1 mA	<1 kA
Instantaneous dose rate	$\sim 10^7$ Gy/s	$\sim 10^{12}$ – 10^{13} Gy/s

The LIAC machine is produced by Sordina IORT Technologies S.p.A. (see [8])

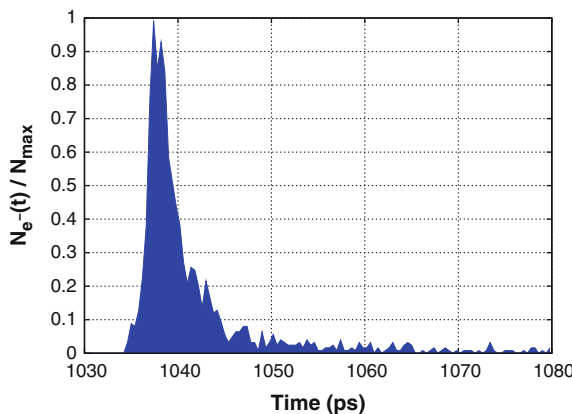


Fig. 9.1 Monte Carlo simulation (performed using the GEANT4 toolkit) of the arrival times of electrons reaching the position of an hypothetical cell sample in a typical situation encountered in a laser-driven accelerator (see text). Time $t = 0$ corresponds to the electrons leaving the acceleration region (i.e., the plasma). The width of the curve basically gives an estimate of the electron bunch lengthening due to scattering processes along the transport line

LINAC-based machines currently most employed for the so-called Intra-Operative Electron Radiation Therapy (IOERT), as compared to the same parameters of a bunch from a possible laser-driven machine. Looking at the table, it is clear that a laser-driven accelerator features an electron bunch duration much smaller than a conventional accelerator. For instance, Fig. 9.1 shows the distribution of the arrival times of the electrons on an hypothetical patient after having propagated through a collimating tube 60 cm long and having crossed a 60 μ m thick brass vacuum window. In the simulation providing the result shown in the Figure (where no account was made of Coulomb or energy dispersion bunch lengthening) all the primary electrons were considered to leave the gas-jet at the same time ($t = 0$). Thus the curve shown would actually have to be considered as a transfer curve to be convolved with the actual bunch duration in order to get the final bunch time

profile. However, since durations of a few up to a few tens of femtoseconds have been reported for the bunches on leaving the plasma [4], a bunch duration of a few picoseconds can be safely estimated/calculated at the position of the biological tissue or patient (that is, generally speaking, after a few tens of centimeters propagation and a vacuum-air interface). This figure is still about six orders of magnitude smaller than that of a typical LINAC used in radiotherapy. By taking into account the typical bunch charge in the two cases (which is more or less comparable), one can easily realize that a much higher instantaneous dose rate is actually obtained, whose biological consequences have still to be investigated in depth. Further differences of a laser-driven accelerator when compared to a conventional one rely on the broader energy spectrum (when no advanced injection schemes are implemented, such as in the typical case of a tentatively “ease-to-use” accelerator for medicine) and, in general, a higher divergence (see, for instance, [5] for a discussion of the typical spectral features encountered in an IOERT machine or [6] for a general discussion of LINAC-based accelerators for medicine).

Besides to possibly leading to new processes occurring at the biological level (see for instance [7]), the above arguments make thus clear that attention has to be paid when using standard techniques, well consolidated into the clinical practice, to carry out dosimetry of laser-driven electron bunches. In this chapter we briefly give an overview of the methods and devices currently used in medical dosimetry; the issues related with the extension of such techniques to laser-driven bunches will be highlighted.

9.2 Absolute and Relative Dosimetry of Laser-Driven Beams

As said above, many medical applications, such as radiotherapy or nuclear medicine, require a precise knowledge of the absolute dose released from ionizing radiation. In fact, the capability to carry out absolute dosimetry of a radiation treatment is a necessary prerequisite to estimate the planned dose with respect to the delivered dose.

The international dosimetry protocols recommend appropriate procedures to be followed and specific detectors to be used for high energy photon and particle beams generated by clinical accelerators [9–11]. An uncertainty higher than 5 % in the absorbed dose evaluation jeopardize the effectiveness of treatment and the patient’s health. For instance, the IAEA code of practice [9] for dosimetric measurements in radiotherapy with electron beams recommends to place the ionization chamber in water. Furthermore, the usage of a plane-parallel ionization chamber is recommended for electron beams with energy ≤ 10 MeV, whereas the usage of cylindrical chambers is required for electron beams with energy above 10 MeV. Moreover, the code of practice [9] specifies the reference conditions for determining the absorbed dose by electron beams. Any issue potentially affecting the

measurement must be taken into account, such as the geometric arrangement (distance and depth which the ionization chamber is placed at), the size of the radiation field, the material and the size of the irradiated phantom, the environment temperature and pressure. The set of values of the above quantities chosen for the ionization chamber calibration defines the reference conditions. The main parameter used as the electron beam quality index and used to obtain the reference conditions is the R_{50} . This physical quantity is the depth in water, expressed in g/cm², where the absorbed dose is 50 % of the maximum in the Percentage Depth Dose curve (PDD curve). While for any R_{50} value the reference phantom material is water, for $R_{50} < 4 \text{ g/cm}^2$ plastic phantoms can also be used. Moreover, for $R_{50} \geq 4 \text{ g/cm}^2$ the measurements can be carried out using either plane-parallel or cylindrical ionization chambers; for $R_{50} < 4 \text{ g/cm}^2$ the use of plane-parallel chambers is suggested only. The position of the reference point of the plane-parallel ionization chamber is given by $z_{ref} = 0.6 R_{50} - 0.1 \text{ g/cm}^2$. For a cylindrical chamber, the position of the reference point is $0.5r_{cyl}$ beyond z_{ref} , being r_{cyl} the internal radius of the chamber cavity. The source-surface distance (SSD), that is the distance from the source to the surface of the patient or of the phantom, is 100 cm. Finally, the field size at the phantom surface suggested by IAEA TRS-398 is at least $10 \times 10 \text{ cm}$ for $R_{50} \leq 7 \text{ g/cm}^2$ and at least $20 \times 20 \text{ cm}$ for $R_{50} > 7 \text{ g/cm}^2$. Suitable correction factors to the measured charge are also to be taken into account, should the experimental conditions differ from those of calibration of the ionization chamber. The absorbed dose in water D_w in non-reference conditions can be calculated as

$$D_w = N_D M \sum_i k_i \quad (9.1)$$

where N_D is a calibration factor depending on the dosimeter, M is the physical quantity measured by the electrometer and k_i is the i th correction factor. In particular, the correction factors to be used are:

- k_{X,X_0} : if the ionization chamber has been calibrated with a beam with quality X and the experimental measurement has been carried out with a beam with a different quality X_0 ;
- k_{Tp} : this correction factor takes into account the different values of temperature and pressure with respect to the reference conditions;
- k_S : this is a factor aimed at correcting the response of an ionization chamber for the lack of complete charge collection due to ion recombination in the sensitive volume;
- k_{pol} : this correction factor is used when a change of the sign of the polarizing voltage applied to the chamber has to be accounted for;
- k_{elec} : this is a specific calibration factor of an electrometer.

To date, no dosimetric protocols have been established for absolute dosimetry of laser-driven electron beams, due to the very high instantaneous dose rate of these beams. Indeed, as said above, a typical laser-driven accelerator delivers electron

beams with a few tens of fs up to a few ps duration; such figure is about six orders of magnitude shorter than for a typical LINAC used in radiotherapy (see [6] and references therein). In the remaining of this section we provide an overview of the different types of detectors which can be used to get either absolute or relative dosimetry of laser-driven particle beams.

9.2.1 Radiochromic Films

The radiochromic films, perhaps the most used detectors in the field of laser-driven electron acceleration, represents a class of self-developing detectors whose response is independent of the dose per pulse; as it is well known, if exposed to radiation, they blacken proportionally to the received dose. The change in the optical density is direct and does not require any chemical treatment. Radiochromic films based on polydiacetylene (PDA), a family of conductive polymers, have been introduced especially for medical applications [12], generally referred to as Gafchromic. The relationship between optical absorbance and absorbed dose by Gafchromic films can be considered semilinear [13]. Different types of Gafchromic films are available, whose usage is chosen according to the application (see for instance [14]). For instance, in the context of radiodiagnosis, Gafchromic XR-M2 films (Fig. 9.2) are used for mammography quality assurance testing; they allow the light field and the radiation field to be measured. In the same context, Gafchromic XR-CT2 films (Fig. 9.3) are designed for the measurement of radiation beam slice width on Computed Tomography (CT) scanners in real time. EBT3 Gafchromic films (Fig. 9.4) are used in radiotherapy for dosimetric measurements; the structure of these films is symmetric and they do not require post-exposure processing [15].

Gafchromic films have a fast time response, are independent on the value of dose per pulse and exhibit a low response dependence on the electron energy. For these reasons, these detectors are well suited to reveal the dose delivered by a laser-driven

Fig. 9.2 Example of an XR-M2 Gafchromic film. A single film can be used to define the relative positions of the light field and of the radiation field for quality assurance in mammography

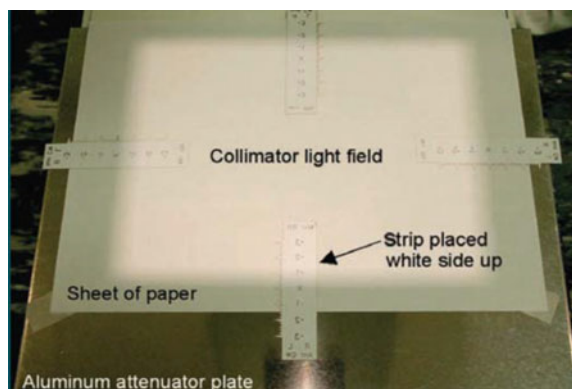
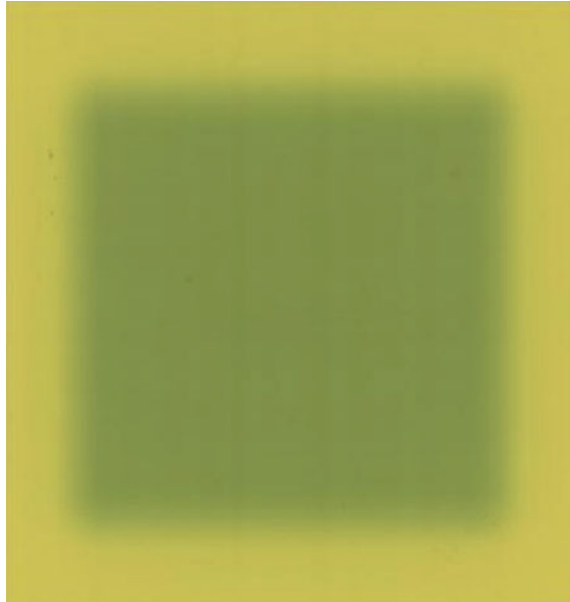




Fig. 9.3 Example of an XR-CT2 Gafchromic film. Such a film can be used to measure the beam width of a CT scanner in real time

Fig. 9.4 Example of a typical electron signal on an EBT3 type gafchromic film, used for dosimetric measurements in radiotherapy



accelerator. In particular, due to the dosimetric features similar to the accelerators used in radiotherapy, the use of the EBT3 films is mostly appropriate.

In order to account for possible slight differences in the response of each sample, the films may be calibrated with a clinical commercial accelerator. For example, if the laser-driven accelerator generates electron beams, the gafchromic films can be calibrated by an accelerator used for clinical treatment of intraoperative radiotherapy (IORT) [16]. The calibration allows a curve of dose as a function of the intensity of each pixel as gained by a film scan (see for instance Fig. 9.5).

One of the most useful features of Gafchromic films is their ability to be arranged in such a way as to obtain 3D maps of the deposited dose. For instance, suitable arrangements and subsequent analysis of gafchromic films allows the dose as a function of depth, the Percentage Depth Dose (PDD) curve, the 3D dose maps and two-dimensional dose distributions to be retrieved [16]. Moreover, the radiochromic films allow the analysis of the homogeneity and symmetry of the spatial distribution of the dose through the transverse profile of the beam [17]. It is worth reminding, at this point, that for the sake of a definition of the final expected performances of an

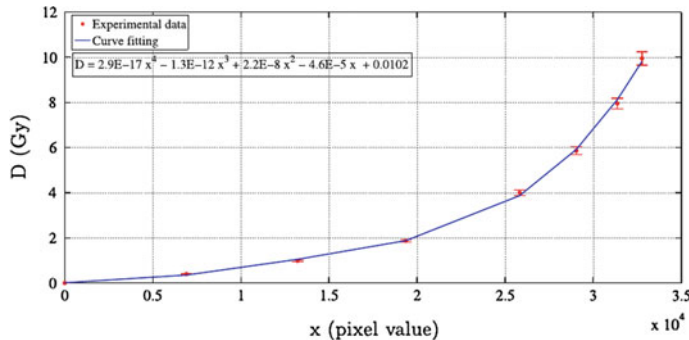


Fig. 9.5 Example of a calibration curve of EBT3 films, showing the relationship between the absorbed dose and the value of the pixel intensity as read from a film scan. Figure credit: [16]

accelerator, the code of practice for intraoperative radiation therapy using mobile electron linear accelerators [10] recommends flatness and symmetry checks monthly with a tolerance of 3 % and annually with a tolerance of 2 %.

9.2.2 Ionization Chambers

The ionization chamber is a gas-filled detector which is based on the detection of direct ionization created by the passage of the radiation. A charged particle passing through a gas, can excite or ionize the gas molecules that encounters in its path. The application of an electric field in the ionization chamber allows to collect all the charges created by the ionization of the gas. The number of ion pairs created along the track of the radiation is the measurement provided by the chamber. Because of the possible recombination processes of charged particle pairs that take place inside the cavity of the ionization chamber, it is evident that the charge separation and collection must occur in a very short time. This is the reason why the application of intense electric fields is recommended. Figure 9.6 shows the different operating regimes of a generic gas detector. The range of values of the voltage applied to the electrodes of the ionization chamber, 100–1000 V, defines the so-called saturation region in which the ionization chambers operate; in this area the number of ions collected at the electrodes per unit of time is constant.

The application of an electric field between the two electrodes ensures that positive ions have a drift velocity in the direction of the electric field, while electrons and negative ions in the opposite direction. Typical harvest times for the electrons are on the order of μ s, instead of ms as in the case of ions. The dosimetric international protocols [9, 11] states that in cases of accelerators with high dose rate ($> \text{cGy/pulse}$), the reference dosimetry using an ionization chamber cannot be

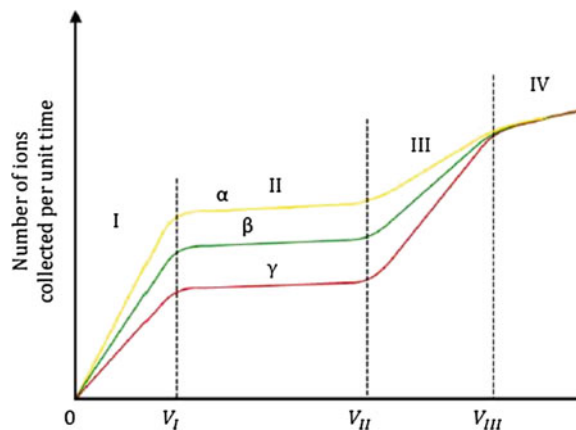


Fig. 9.6 Typical behaviour of the number of ions per unit time collected from a gas detector as a function of the applied voltage; the four regions portray different operation regimes of a gas detector. An ionization chamber operates in the region II. The constant trend indicates that all the ions produced by the passage of the radiation are collected at the electrodes (saturation). Each of the three different curves corresponds to a particular type of particle: α : heavy particles; β : light particles, including electrons and positrons; γ : photons

performed with the same accuracy typical of other clinical beams. As mentioned earlier, the laser-driven acceleration systems are characterized by a very high dose rate. The correction factor for the ion recombination could be underestimated when applying the correction methods recommended in international protocols, because of the high charge density which would be produced in the volume of the chamber for each radiation pulse [18, 19]. Therefore measurements performed with ionization chambers could include a source of error due to the ion recombination in the sensitive volume of the ionization chamber. This problem has been addressed over the years [19–21]; as for now, with an appropriate correction on the ion recombination it is possible to perform measurements of absolute dosimetry with the ionization chambers even in the case of high dose rate clinical accelerator (dose rate \sim cGy/pulse). An example of a commercial ionization chamber used for absolute dosimetry in the clinical practice is shown in Fig. 9.7.

To date, however, there are no clinical accelerators with dose rate comparable to that of a laser-driven accelerator. In this case, more detailed studies will be required regarding the coefficients of ion recombination in order to correct the measurement of the ionization chamber appropriately. However, the ionization chamber has been used for measurements of relative dosimetry, in order to control the delivered dose of biological samples irradiated with laser-driven systems [17, 22, 23]. Indeed, the ionization chamber enables to observe the accumulated dose in real time, so that the effects of the fluctuations of the electron beam can be monitored. The measurements carried out with the ionization chamber should take into account the uncertainties



Fig. 9.7 A PTW ROOS electron chamber. This is a plane parallel chamber for dosimetry of high-energy electron beams in water and solid state phantoms

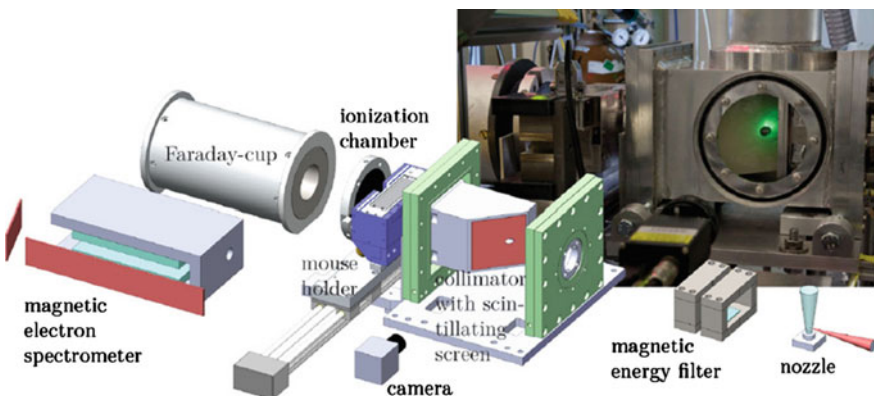


Fig. 9.8 Experimental setup used for radiobiology experiments with laser-driven electron beams in Jena. Figure credit: [17]

that arise from statistical errors, the fluctuations from shot to shot of the size of the radiation field, the beam intensity that could lead to effects of saturation. Figure 9.8 shows the experimental setup used for radiobiology experiments with laser-driven electron beams in a recent experiment carried out in Jena (Germany) and reported in [17]. In that experiment, an ionization chamber was used to measure the dose per pulse on a single-shot basis.

In case of laser-driven beams, measurements of relative dosimetry performed with the use of ionization chambers are generally supported by another detector, the Faraday cup.

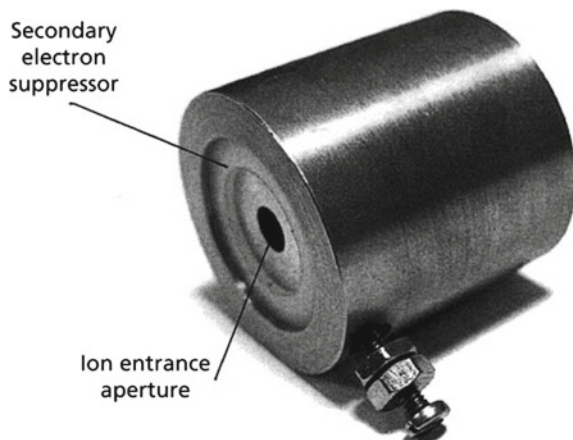
9.2.3 Faraday Cups

The Faraday cup is an instrument to measure the current generated by an accelerated particle beam that runs through the cup. This current can in turn be used to determine the number of particles N that have entered the cup per unit area in a time t , using the simple relation $N = (1/A) \int_0^t (I/q) dt$, where I is the measured current, A is the area of the beam and q is the charge carried by the particle [24]. A picture of a typical Faraday cup is shown in Fig. 9.9.

In order to retrieve the information on the absorbed dose from a Faraday cup measurement, different parameters have to be known: the beam area, the mass stopping power at a given specific energy, the energy spectrum of the particles, the total collected charge. A source of uncertainty related to measurements carried out with a Faraday Cup is the production of secondary electrons and positive ions from the interaction of the incident beam with the entrance window and with the metal surface of the cup. Indeed, the secondary particles may escape from the Faraday cup aperture. This would cause a wrong charge collection and can lead to an overestimate of the positive charge and to an underestimate of the electronic current [25, 26]. For these reasons, the use of the Faraday cup requires the knowledge of additional features of the specific accelerator used, such as the thickness of the entrance window, the guard ring, the type of vacuum, the size of the cup, the wall thickness and the material which it is made of.

A Faraday cup was also used as a detector, along with an ionization chamber and a magnetic spectrometer, in the experiment, carried out in Jena, cited above (see Fig. 9.8). Indeed, the Faraday cup provides the charge of the bunch by an average voltage per pulse multiplied by the number of pulses registered, thus obtaining a total voltage [22]. The variations in dose from shot to shot can be analyzed with the help of this detector in order to optimize, monitor and control the beam of accelerated particles. In this way the Faraday cup can be used to monitor the effective

Fig. 9.9 A Faraday cup



bunch charge delivered [23]. These online dose measurement techniques are of a fundamental importance in view of the relatively higher shot-to-shot fluctuations affecting a laser-driven accelerator as compared to a conventional one.

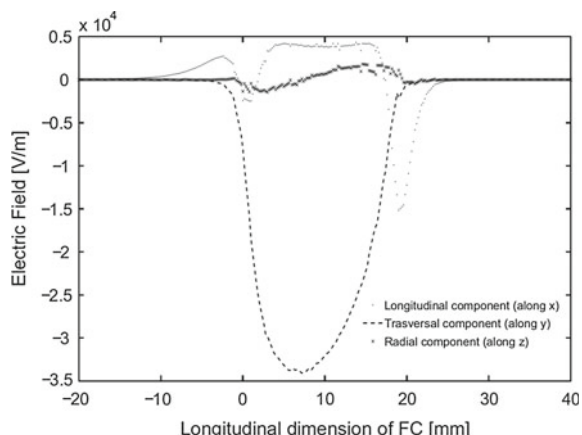
Finally, it is worth mentioning that by comparing the dose values obtained using a Faraday cup with the ones retrieved by calibrated radiochromic films, absolute dosimetry can be carried out [17].

9.2.4 Development of Dedicated Detectors: An Example

Research is ongoing worldwide in order to develop novel detectors to cope with the peculiar features of laser-driven particle beams. As an example, we just mention here an innovative Faraday Cup recently designed and developed within the ELIMED collaboration. ELIMED (ELI-beamlines MEDical applications) is a collaboration between ELI-Beamlines researchers from Prague (Czech Republic) and an INFN-LNS (Laboratori Nazionali del Sud of the Istituto Nazionale di Fisica Nucleare) research group from Catania (Italy) aiming at demonstrating clinical applications of laser-driven proton beams (see [26]).

Preliminary studies were performed in order to optimize shape, dimensions, materials and the electric field of this Faraday cup. These studies have been carried out using modeling and simulation software and, also, the Monte Carlo GEANT4 simulation toolkit. To improve the overall charge collection efficiency of the Faraday cup, maximizing the charge collection accuracy, a special-shaped electric field has been designed. An asymmetric electric field characterized by a significant transverse component was used. This field is able to maximize the deflection of the secondary electrons generated by both the entrance window and the cup, thanks to the transverse component of the electric field (Fig. 9.10). This innovative detector was realized at INFN-LNS and preliminary experimental tests were recently carried out using the device shown in Fig. 9.11.

Fig. 9.10 Transverse, longitudinal and radial components of the electric field of a Faraday cup. Figure credit: [26]



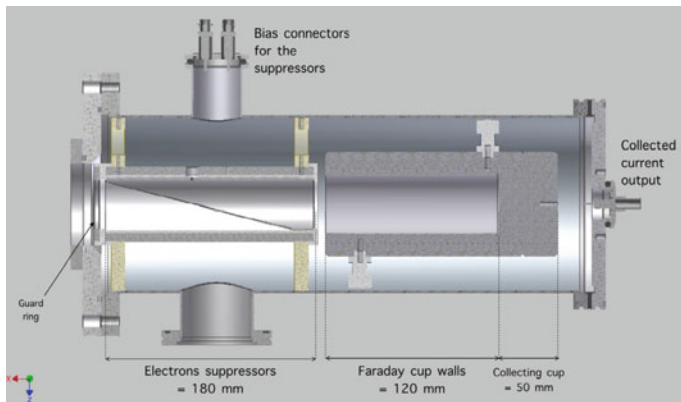


Fig. 9.11 Schematic layout of a Faraday Cup detector. The current collected in the cup is sent to an electrometer for integration. Figure credit: [26]

9.3 Dosimetric Simulations with Monte Carlo Methods

Monte Carlo simulations allow the study of new strategies and methodologies both in diagnostics and in therapy, making it possible to evaluate available techniques and to plan treatments that require mapping of appropriate dose. The Monte Carlo method is the most accurate and detailed calculation method in various fields of medical physics; for instance, it is used in the field of diagnostic imaging in radiology and nuclear medicine, in radiotherapy [for the accurate calculation of dose distributions and for the validation of the Treatment Planning System (TPS)], and for radioprotection studies. Monte Carlo applications can simulate complex models and a variety of physical processes on a wide range of energy and trace the path of each particle in volumes of different materials. The simulations can represent the geometry of the acceleration system reproducing the sizes, the shapes of the experimental set-up and the materials they are made of. For all these reasons, Monte Carlo simulations represent an important instrument to validate the dosimetric characterization of the beam.

A code that is widely used for medical physics studies is GEANT4 [27, 28]. It is a toolkit for the simulation of the interaction of radiation with matter which is able to potentially taking into account all the physical processes that involve the single particle that passes through the medium. Depending on the energy of the particles, the code can simulate, among others, the following physical processes: for photons, the production of electron/positron pairs, the Rayleigh and Compton scattering and the photoelectric effect; for electrons, energy loss due to ionization of the matter, pair production and *Bremsstrahlung* radiation; for hadrons, ionization, multiple scattering, nuclear scattering and fission.

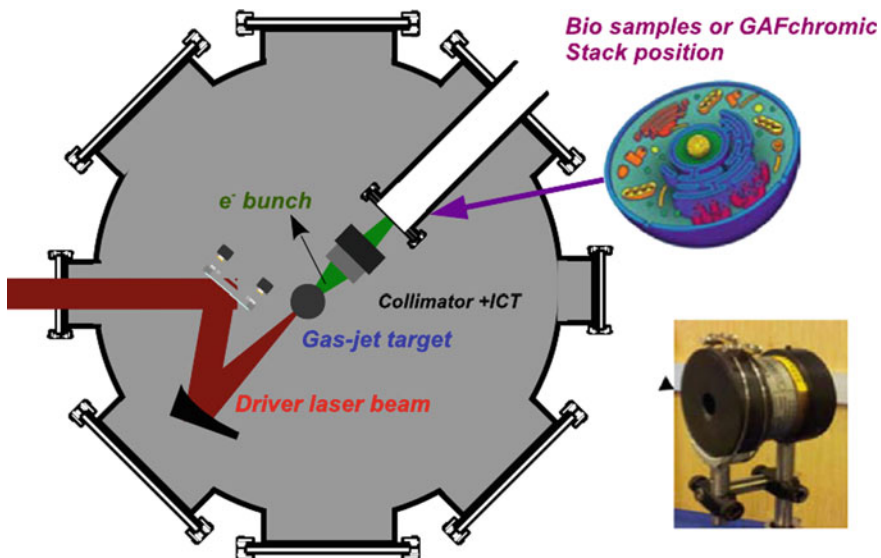


Fig. 9.12 Schematic view of the experimental setup used in the radiobiology experiments carried out at the ILIL-INO-CNR lab in Pisa, Italy

Generally speaking, Monte Carlo simulation techniques are the only method which can be applied in complex geometries for a wide range of energy and can provide a faithful simulation of the physical reality. As a general rule, the number of initial particles to be simulated depends upon the energy distribution that describes the source. Both the initial particles and the ones produced during the simulations are propagated geometrically in each volume for distances which depend upon the cross sections of the different processes the particle can undergo.

As said above, the GEANT4 toolkit is a valuable tool to study a typical laser-driven accelerator. Recently, an ad hoc tool was developed, based on it, to simulate laser-driven electron accelerators used for radiobiology experiments. In particular, it allows a full dosimetric characterization to be obtained by comparison with experimental measurements. As an example, we will be briefly describing a first application aimed at evaluating the dose distributions as obtained using a laser-driven accelerator setup at the Intense Laser Irradiation Laboratory of the Istituto Nazionale di Ottica of CNR in Pisa, Italy. A schematic view of the experimental setup is shown in Fig. 9.12. The accelerator is based upon a 10 TW laser system, delivering up to 450 mJ energy pulses with a < 40 fs pulse duration. The beam was focused, using an $f/10$ OAP mirror, onto a 1.2 mm long N_2 gas-jet at an intensity of about $3 \times 10^{18} \text{ W/cm}^2$. An acceleration regime was sought for, basically by adjusting the gas backing pressure and the focal position, mainly aiming at producing relatively low (~ 10 MeV) energy electron beams, with a total charge per bunch as high as possible. This energy range was selected as it is close to the one used in conventional IOERT (see Table 9.1). The experimental setup

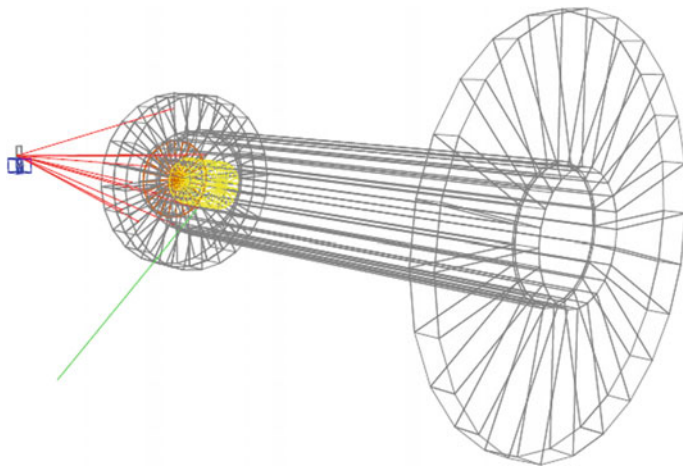


Fig. 9.13 Schematic of a typical laser-driven electron accelerator setup as simulated using GEANT4. The electron beam is generated at the gas-jet position. The sample is represented by the yellow mesh structure. Figure credit: [16]

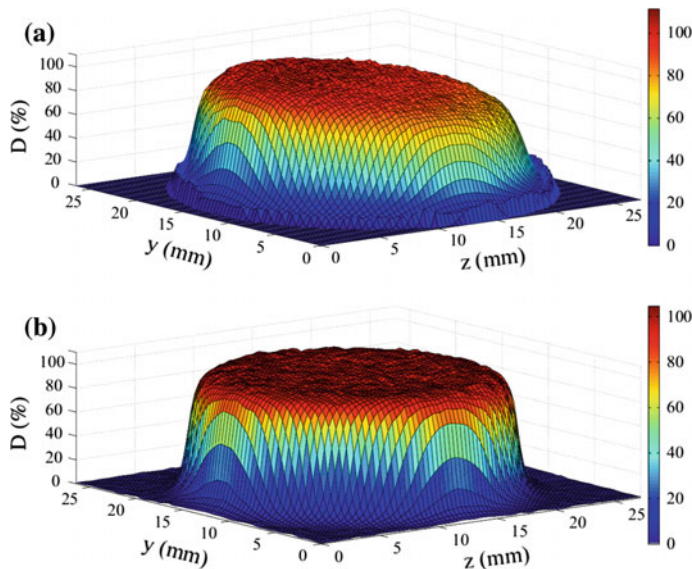


Fig. 9.14 **a** Measured dose profile measured using EBT3 gafchromic films. **b** Retrieved dose profiles of a laser-driven accelerator as provided by GEANT4 simulations. Figure credit: [16]

downstream of the “accelerator stage” (that is, the gas-jet nozzle) was optimized in order to carry out irradiation of *in vitro* samples for radiobiology studies. This involved, for instance, the usage of a cylindrical plastic tube to be used as a

collimator (as the ones used in an actual IOERT machine, see [5]) and a 100 μm thick kapton layer to act as a vacuum-air interface.

Figure 9.13 shows a sketch of the simulated setup, involving, among other elements, the electron source, an electron collimator and a vacuum-air interface. After the geometric reconstruction of the setup, the simulations can provide the energy lost at each position (identified by a voxel) by each particle created during the simulation. From such a kind of simulation, 2D and 3D distributions of the dose and PDD curves can be obtained. The data sets from simulations can also be compared with experimental measurements, carried out, for instance, using stacks of gafchromic films, to get informations on the energy and spatial distribution of the electron bunch from the source [16]. As an example, Fig. 9.14a shows the measured dose profile at the position of the biological samples to be irradiated. Figure 9.14 shows the corresponding profile as retrieved by a Monte Carlo simulation based on GEANT4.

9.4 Summary and Conclusions

In this chapter, we have briefly discussed the main issues related to the usage of “standard” dosimetric methods for the characterization of laser-driven electron beams. In particular, we have given an overview of the main devices used for the characterization of electron beams used in medical applications. From time to time, the main recommendations from international organizations supervising absolute dosimetry have also been briefly given. The issues possibly arising in the usage of techniques established for conventional accelerators for the dosimetry of ultrashort laser-driven beams have also been given whenever possible; these issues are mainly due to the very small duration of laser-driven electron beams, resulting in ultrahigh peak currents and dose rates.

As a conclusion, we stress that several issues have to be addressed before translating the usage of laser-driven beams into the clinical practice. From the point of view of the beam characterization, the possible errors due to the shot-to-shot stability, the beam homogeneity and symmetry and the dosimeter response have not to exceed standard percentage figures suggested by the recognized international dosimetry protocols. This seems currently a pretty challenging task. In general, the absolute dosimetric measurements would have to be carried out with dosimeters already in use in the clinical practice, such as ionization chambers and Fricke dosimeters (see [29] and references therein). On the other hand, the response of such devices at the very high dose rates featuring laser-driven particle beams have to be deepened as a preliminar step.

One of the key issues to be implemented in practice concerns the need of an active dose control using monitor chambers. The dose delivered by a clinical accelerator in a typical radiotherapy treatment at a specific depth with a given radiation field is expressed in monitor units. In general, two ionization chambers are used as monitor chambers in order to assess the delivered dose and to stop the beam when the prescribed monitor units have been reached.

Finally, we mention here that, unless advanced physical schemes not easily viable in a medical environment were used, current laser-driven particle beams feature a broad energy spectrum; this would possibly require an energy selection device to be used, whose insertion would in general affect the choice and/or behaviour of the device used for the dosimetric characterization.

Acknowledgements L.L. wishes to acknowledge support from the Italian Ministry of Health through the Project No. GR-2009-1608935 (Study of Radiobiological and Radiotherapeutic Effects of a Novel Laser-Driven Electron Accelerator, D.I. AgeNaS), from the CNR funded Italian research Network ELI-Italy (Attoseconds) and from the PRIN project (Contract No. PRIN2012AY5LEL). He also acknowledges contribution from the MIUR-FIRB project SPARX (Sorgente Pulsata Auto-Amplificata di Radiazione X) and the INFN Plasma-med collaboration. D.L. and G.R. acknowledge support from the project “IMINET—Italian Molecular Imaging Network”.

References

1. L. Labate et al., Proc. SPIE **8778**, 87790O (2013)
2. L.A. Gizzi et al., Appl. Sci. **3**, 559–580 (2013)
3. E. Esarey et al., Rev. Mod. Phys. **81**, 1229 (2009)
4. J. van Tilborg et al., Phys. Rev. Lett. **96**, 014801 (2006)
5. S. Righi et al., J. Appl. Clin. Med. Phys. **14**, 6–18 (2013)
6. J. M. Schippers, M. Seidel, Phys. Rev. Spec. Top. - Accel. Beams **18**, 034801 (2015)
7. V. Malka et al., Mut. Res./Rev. Mut. Res. **704**, 142–151 (2010)
8. Sordina IORT Technologies S.p.A. website: <http://soiort.com/en/>
9. International Atomic Energy Agency, *Absorbed Dose Determination in External Beam Radiotherapy: An International Code of Practice for Dosimetry Based on Standards of Absorbed Dose to Water*. IAEA Technical Reports Series no. 398 (IAEA, Vienna, 2000)
10. A.S. Beddar et al., Med. Phys. **33**, 1476–1489 (2006)
11. P.R. Almond et al., Med. Phys. **26**, 1847–1870 (1999)
12. C. Fiandra et al., Med. Phys. **35**, 5463–5470 (2008)
13. A. Niroomand-Rad et al., Med. Phys. **25**, 2093–2115 (1998)
14. <http://www.tecnologieavanzate.com/>
15. V. Casanova Borca et al., J. Appl. Clin. Med. Phys. **14**(2), 2013
16. D. Lamia et al., Nucl. Instrum. Meth. Phys. Res. A **786**, 113–119 (2015)
17. M. Nicolai et al., Appl. Phys. B **116**, 643–651 (2014)
18. A. Piermattei, Phys. Med. Biol. **45**, 1869–1883 (2000)
19. J.W. Boag, E. Hocchäuser, O.A. Balk, Phys. Med. Biol. **41**, 885–897 (1996)
20. R.F. Laitano et al., Phys. Med. Biol. **51**, 6419 (2006)
21. F. Di Martino et al., Med. Phys. **32**, 2204–2210 (2005)
22. E. Beyreuther et al., Med. Phys. **37**, 1392–1400 (2010)
23. C. Richter et al., Rad. Meas. **46**, 2006–2009 (2011)
24. B. Schmidt, K. Wetzig, *Ion Beams in Materials Processing and Analysis* (Springer, 2013)
25. C. Richter et al., Phys. Med. Biol. **56**, 1529–1543 (2011)
26. G.A. Cirrone et al., Nucl. Instrum. Meth. Phys. Res. A **796**, 99–103 (2015)
27. S. Agostinelli et al., Nucl. Instrum. Meth. Phys. Res. A **506**, 250–303 (2003)
28. J. Allison et al., IEEE Trans. Nucl. Sci **53**, 270–278 (2006)
29. L.J. Schreiner, J. Phys: Conf. Ser. **3**, 9–21 (2004)

Part III

**Updating Laser-driven Ion Acceleration
for Biomedical Applications**

Chapter 10

Laser-Driven Ion Accelerators: State of the Art and Applications

Marco Borghesi and Andrea Macchi

Abstract Laser-plasma based accelerators of protons and heavier ions are a source of potential interest for several applications, including in the biomedical area. While the potential future use in cancer hadrontherapy acts as a strong aspirational motivation for this research field, radiobiology employing laser-driven ion bursts is already an active field of research. Here we give a summary of the state of the art in laser-driven ion acceleration, of the main challenges currently faced by the research in this field and of some of the current and future strategies for overcoming them.

10.1 Introduction

Since the discovery in the year 2000 of bright, multi-MeV, charge-neutralized proton beams from high-intensity laser-solid interactions [1–3] there has been a major interest in the potential applications of such beams. Common to such proposed applications is the exploitation of highly localized energy deposition in matter (with the sharp “Bragg peak” at the end of the path) combined with the unique properties of laser-accelerated proton beams such as ultrashort duration (typically in the picosecond range at the source) and very large number of particles (ranging from $\sim 10^9$ to $\sim 10^{13}$ in the above mentioned early experiments).

Arguably, the most successful application so far has been the time-resolved probing of highly transient electric and magnetic fields in laser-plasma experiments (see [4], Sect. V.A, for a brief review). This application exploits the imaging capability of proton beams [5] related to their high luminosity and very low emittance (whose definition and measurement, however, requires special attention for

M. Borghesi
Queen’s University of Belfast, Belfast, UK
e-mail: m.borghesi@qub.ac.uk

A. Macchi (✉)
Istituto Nazionale di Ottica, Consiglio Nazionale Delle Ricerche
(CNR/INO), Pisa, Italy
e-mail: andrea.macchi@ino.it

beams with broad energy spectra [6]). Valuable results have been also obtained in the use of laser-accelerated protons for the production and study of warm dense matter (see [4], Sect. V.B) and much work has been devoted to evaluate their potential for fast ignition of inertial confinement fusion targets (see [7] for a topical review). The possibility to accelerate efficiently ions heavier than protons has been also investigated with respect to such applications.

In particular, laser-driven schemes have been foreseen as a possible compact, cost-effective alternative to traditional accelerators for applications in biology and medicine, such as oncological hadrontherapy [8–10] and radioisotope production [11–15]. This perspective has stimulated a large amount of research aimed at meeting the stringent requirements posed by such applications on particle energy, spectral width, repetition rate.

Laser-driven ion acceleration (LIA) research has focused on several different mechanisms, mostly within a general laser-plasma interaction approach based on a “coherent” or “collective” paradigm for the acceleration of large number of particles (see e.g. the Introduction to [4]), although direct laser acceleration of single ions has also been considered [16, 17]. The collective approach has unique potential in terms of acceleration gradient and efficiency, but it has to deal with typical issues of plasma physics such as highly nonlinear dynamics and instabilities. Fifteen years of experiments have yielded promising advances in the characteristics of laser-accelerated beams and progress on aspects such as cut-off energy, spectral width, beam collimation has been obtained in independent experiments and via different regimes of interaction. For instance, the highest proton energies so far were observed in experiments using solid targets and optical lasers in the framework of the sheath acceleration mechanism (Sect. 10.2.1) which typically produces quite broad spectra; at lower proton energies, narrow monoenergetic spectra were observed using gas targets and CO₂ lasers and the acceleration was related to the generation of collisionless shocks (Sect. 10.2.3).

In this contribution we give a brief overview of the state-of-the-art in laser-plasma based acceleration of ions. More details about the large amount of experimental and theoretical work carried out so far can be found in several recent reviews of the field [4, 7, 18, 19]. Here we focus in particular on preliminary work towards biomedical applications and related perspectives.

10.2 Acceleration Mechanisms

In the interaction regimes of relevance to the present context, the laser pulse is intense enough to ionize matter almost instantaneously, and couples with the freed electrons which absorb energy and momentum from the electromagnetic field. Energy absorption, i.e. electron heating, leads to electrostatic fields in the presence of density gradients, which in turn accelerate ions and drive the expansion of the plasma. Momentum absorption corresponds to a local ponderomotive force which modifies the electron density and consequently the electrostatic fields, leading as

well to ion acceleration and radiation pressure action on the plasma. Under suitable conditions, the combination of heating and radiation pressure can drive nonlinear shock waves which also lead to ion acceleration. The basic mechanisms we briefly describe below originate from the dominance of each of these effects, which however may generally coexist in experiments, leading to a complex acceleration scenario.

In the following, we also emphasize laser and target requirements and developments needed to advance each mechanism. In order to characterize the interaction regime, two dimensionless parameters are particularly useful and important. The first one is the ratio between the electron density n_e in the target and the cut-off or “critical” density n_c , i.e. the maximum value of the electron density above which the laser pulse does not propagate:

$$n_c = \frac{m_e c^2}{\pi e^2 \lambda^2} = \frac{1.1 \times 10^{21} \text{ cm}^{-3}}{(\lambda/1 \mu\text{m})^2}, \quad (10.1)$$

where λ is the laser wavelength. Plasmas with density $n_e > n_c$ ($n_e < n_c$) are called overdense (underdense) and are opaque (transparent) to the laser light. The second important parameter is the dimensionless amplitude of the laser a_0 , expressed as a function of the laser intensity I and of λ by

$$a_0 = \left(\frac{e^2 I \lambda^2}{\pi m_e^2 c^5} \right)^{1/2} = \left(\frac{I}{m_e c^3 n_c} \right)^{1/2} = 0.85 \left(\frac{I \lambda^2}{10^{18} \text{ W cm}^{-2} \mu\text{m}^2} \right)^{1/2}. \quad (10.2)$$

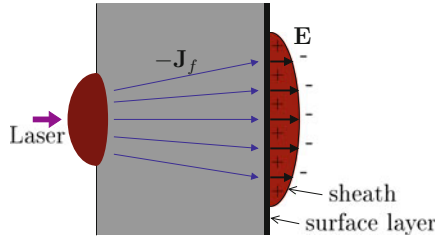
When $a_0 \gtrsim 1$, the electron dynamics in the laser field is relativistic. Most of the experiments on ion acceleration have been performed with optical or near-infrared lasers ($\lambda = 0.8 - 1 \mu\text{m}$) and in the intensity range $I = 10^{18} - 10^{21} \text{ W cm}^{-2}$, corresponding to $a_0 \simeq 0.7 - 22$ for $\lambda = 0.8 \mu\text{m}$.

The transmission of a laser pulse through a plasma is modified by relativistic effects on electron motion, which favor pulse penetration at densities higher than n_c , a phenomenon known as “relativistic transparency”. Details depend on the laser and target parameters. A simple, although far from rigorous criterion applicable to targets significantly thicker than λ raises the cut-off density from n_c to $n_c \gamma$ with $\gamma = (1 + a_0^2/2)^{1/2}$; this effect arises from assuming an effective electron mass equal to $m_e \gamma$ due to the oscillation energy of electrons in the laser field.

10.2.1 Target Normal Sheath Acceleration

Target Normal Sheath Acceleration (TNSA) is the basic mechanism leading to proton acceleration from “thick” solid targets investigated in the early experiments presented in [1–3] as well as in most experiments reported so far (see [4], Sect. III, for a detailed overview and list of references). TNSA relies on the generation of

Fig. 10.1 The basic scheme of TNSA [21, Sect. 5.2]



large numbers of energetic (“hot”) electrons during high intensity interactions with solid density targets, opaque to the laser light (see e.g. [20, 21] for tutorials). The hot electron spectrum will be typically Maxwellian with a temperature¹ T_h of the order of the so-called ponderomotive energy \mathcal{E}_p , which corresponds to the relativistic oscillation energy in the electric field of the laser:

$$T_h \simeq \mathcal{E}_p = m_e c^2 \left(\left(1 + a_0^2 / 2 \right)^{1/2} - 1 \right). \quad (10.3)$$

The ponderomotive energy is independent from parameters such as the target density or the pulse duration. In typical experiments, $a_0 = 1 - 30$ corresponding to an electron energy of several MeV. Hot electrons are produced with typical densities n_h equal to a fraction of n_c ; thus, a typical value for $\lambda \simeq 1 \mu\text{m}$ is $n_h \sim 10^{20} \text{ cm}^{-3}$. The conversion efficiency η_h of laser energy into hot electrons may reach several tens per cent, which is broadly consistent with a balance condition for the energy flux:

$$\eta_h I \simeq n_h v_h T_h, \quad (10.4)$$

where v_h is the typical velocity of hot electrons ($v_h \simeq (2T_h/m_e)^{1/2}$ and $v_h \simeq c$ in the non-relativistic and strongly relativistic cases, respectively). It should be noticed that numbers vary significantly between different experiments and there is not an unique (or universally accepted) model for hot electron generation, so even the scaling is a matter of debate and there is evidence for a more complex dependence on laser and target parameters. However, the quoted values and scalings are accurate enough for the following discussion.

Hot electron generation at very high values of $I\lambda^2$ (i.e. of a_0) leads to very intense electrical currents through the target. If the latter is relatively thin (from few tens of microns down to sub-micrometric values) the hot electrons reach the rear side of the target (opposite to the laser-plasma interaction side, see Fig. 10.1) producing a sheath region with an electric potential drop $\Delta\Phi \simeq T_h/e$. A test ion of charge Z crossing the sheath region will acquire an energy $\mathcal{E}_i = Ze\Delta\Phi \simeq ZT_i$ which

¹Here we use “temperature” to indicate the parameter T of a Maxwellian spectrum of the form $f(\mathcal{E}) \propto \exp(-\mathcal{E}/T)$. Notice that energy units are used for T .

provides a first rough estimate of the energy gain. Larger energy values may be achieved in the course of the expansion of the sheath plasma, where ultimately electrons and ions will reach the same drift velocity. In metallic targets, protons are ordinarily present as surface impurities and are thus located near the peak of the sheath field; such localization, combined with the high charge-to-mass ratio, favors their acceleration with respect to heavier ions.

Typical proton spectra produced via TNSA are exponential-like up to a cut-off energy \mathcal{E}_{co} . Much of the experimental effort has been concentrated towards achieving higher values of \mathcal{E}_{co} , with particular regard to the range $\simeq 150\text{--}250\,\text{MeV}$ required for hadrontherapy of deep-seated tumors. Figure 10.2 (Left) reports a survey of values of \mathcal{E}_{co} observed in different laboratories, as a function of irradiance and pulse duration. The initial record of $\mathcal{E}_{co} \simeq 58\,\text{MeV}$ obtained with the petawatt laser at LLNL [3] has not been overcome for more than a decade, until $\mathcal{E}_{co} \simeq 67\,\text{MeV}$ was obtained with the Trident laser at LANL using 80 J pulse energy and special “microcone” targets to increase absorption [22].

Scaling studies [23, 24] have shown a slow growth of \mathcal{E}_{co} with the laser intensity (e.g. $\mathcal{E}_{co} \sim I^\alpha$ with $1/3 \leq \alpha \leq 1/2$), although a faster, near linear scaling has been observed over limited intensity ranges employing ultrashort pulses (see e.g. [19, 25]). In general, at the same value of the intensity higher energies are generally obtained with more energetic pulses of $\sim\text{ps}$ duration rather than with lower energy pulses having duration of tens of fs, which may be produced with “table-top”

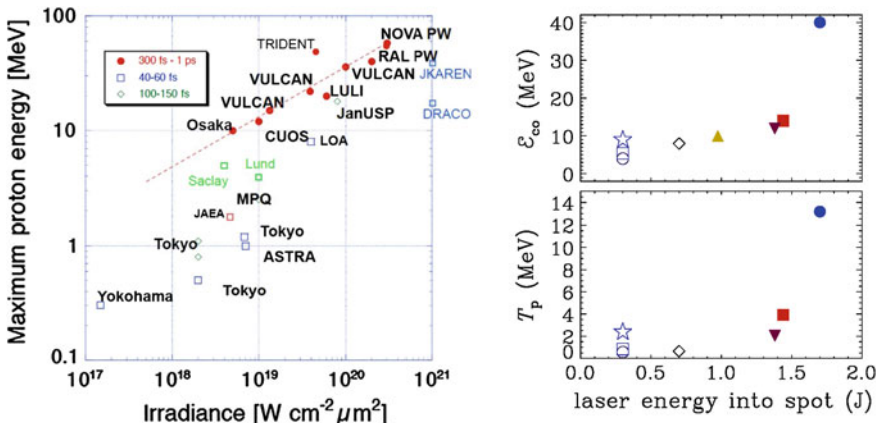


Fig. 10.2 Left proton cut-off energy \mathcal{E}_{co} observed in TNSA experiments for different laboratories (labels), as a function of irradiance and pulse duration. See [4, 157, 158] for full references to data point. Reprinted from [158] with permission. Right \mathcal{E}_{co} and spectrum “temperature” T_p (for spectra well approximated by simple exponential distributions) observed in a series of experiments with femtosecond laser pulses (duration 25–40 fs) having few joule energy (less than 2 J on target). Empty and filled symbols correspond to intensity ranges $I = (1 - 5) \times 10^{19}\,\text{W cm}^{-2}$ and $I = (0.8 - 2) \times 10^{21}\,\text{W cm}^{-2}$ respectively; all data are for simple plane targets except the data marked with the star symbol which has been obtained with a structured target [29] (see [19] for references to data sources). Reprinted from [19] with permission

systems. Table-top lasers, typically having a few joule energy, presently allow to reach up to a few tens of MeV at best as shown in Fig. 10.2 (right), with a $\mathcal{E}_{co} \simeq 40$ MeV record [26] which however appears to be out of scale with other work. However, there is great interest in the proton beam parameters obtained with such compact lasers because of lower cost and possible high repetition rate operation. Recently, the use of targets with limited mass [27, 28] or surface structuring [29, 30] has allowed, in proof-of-principle experiments, a significant cut-off increase compared to flat foil targets. Surface structuring has also been shown to lead to more homogeneous proton beams [31]. Key to the exploitation of structured targets to increase absorption is the use of laser pulses with ultrahigh contrast [32, 33], clean from “prepulses” able to cause early target damage. It is expected that fs laser systems with petawatt power will allow to further increase the proton energy; first experiments approaching such conditions (where a transition from TNSA to other mechanisms may be expected) have reported cut-offs of 30 MeV using the ASTRA-GEMINI laser at RAL/CLF (UK) [34] and 45 MeV using the PULSER I laser at GIST/APRI (Korea) [35].

Targets with special microstructuring and/or shaping of the rear side have been also used for spectral and spatial manipulation of the proton beam. For example, target shaping has been used for beam focusing [36–40] and the highly transient nature of the TNSA field has been used for dynamic focusing with chromatic capability using a two-beam configuration [41].

Localization of the accelerated ion species in a thin layer at the rear side of the foil was shown to be promising in order to obtain narrow spectra of both protons and carbon beams [42, 43] but this approach has not been further developed to the extent one would have expected. Recently, cryogenically freezing of heavy water on the rear surface of a foil target has allowed TNSA of a Deuterium ion beam with high purity and conversion efficiency (close to 10 %) [44]. It has also been shown that the deposition of a thin layer of material with high Z , *larger* than the atomic number of the target substrate (i.e. oppositely to the above mentioned examples where substrate ions are heavier than those in the thin layer) allows efficient acceleration of heavy (Fe), highly stripped ions [45]. Heavy ion acceleration may find application in laser-controlled nuclear physics, e.g. for production of rare isotopes.

10.2.2 Radiation Pressure Acceleration

10.2.2.1 Hole Boring Regime

Radiation pressure is ubiquitous in laser-matter interaction as it corresponds to the absorption of EM momentum by the target, yielding a pressure at a plane surface (for normal incidence)

$$P_{\text{rad}} = (1 + R - T) \frac{I}{c} = (2R + A) \frac{I}{c}, \quad (10.5)$$

where R, T and A are the reflection, transmission and absorption coefficients, respectively ($R + T = 1 - A$); for total reflection, $P_{\text{rad}} = 2I/c$. In the interaction with a dense plasma, the strong radiation pressure associated with ultraintense pulses pushes like a piston the interaction surface causing its recession and the steepening of the density profile. The recession velocity is known as the “hole boring” (HB) velocity u_{hb} (since roughly speaking the piston action drills a hole in the plasma density) and may be obtained from momentum balance as $u_{\text{hb}} = (I/\rho c)^{1/2}$ (for non-relativistic values and assuming $R = 1$ and $T = 0$), where ρ is the mass density. The momentum balance shows that there must exist a flow of ions “reflected” from the recession front at twice u_{hb} , resulting in a ion population with energy per nucleon

$$\mathcal{E}_{\text{hb}} = \frac{m_p}{2} (2u_{\text{hb}})^2 = \frac{2m_p I}{\rho c} = 2m_e c^2 \frac{Zn_c}{An_e} a_0^2, \quad (10.6)$$

where we used $\rho \simeq Am_p n_i = (A/Z)m_p n_e$. This formula is valid for a totally reflecting plasma with negligible temperature. Hot electron generation will reduce the HB efficiency by both causing a significant absorption and producing a strong kinetic pressure which counteracts the radiation pressure. However, the effect of radiation pressure can be maximized using circularly polarized pulses at normal incidence, because hot electron generation is strongly quenched in such conditions [46]. This also leads to a reduction of hard X-ray and γ -ray emission, as recently experimentally observed [47] which could be beneficial for applications.

In solid targets, typically \mathcal{E}_{hb} is much smaller than the energy obtained via TNSA, despite the favorable scaling with the laser intensity. Higher energies may be obtained via HB acceleration if the target density is reduced down to values slightly exceeding the cut-off density n_c . (Lower density values are not suitable since the laser pulse would be transmitted through the target without any “piston” action).

A proof-of-principle of HB acceleration has been given in an experiment using a CO₂ infrared laser ($\lambda \simeq 10 \mu\text{m}$), for which $n_c \simeq 10^{19} \text{ cm}^{-3}$, and a hydrogen jet target so that the density can be adjusted to approach n_c . Using circularly polarized pulses at intensities up to $10^{16} \text{ W cm}^{-2}$ narrow proton spectra with peak energy $\mathcal{E} \simeq 1 \text{ MeV}$ have been obtained [48]. These preliminary data confirm the theoretical expectation that with respect to other mechanisms at play in similar conditions such as shock acceleration (see Sect. 10.2.3) HB possibly leads to lower energies for the same laser intensity but also to higher number of accelerated particles, since HB is a “bulk” acceleration mechanism. This is a potentially interesting feature for applications requiring large ion currents at modest energies.

A foreseen advantage of using CO₂ lasers for HB acceleration is their suitability for high repetition rate operation, which is combined with the additional advantage

of using a flowing target that does not need a mechanical displacement. In addition, the scaling of a_0 with wavelength suggest the possibility to reach high values of a_0 at relatively low values of the laser intensity. However, the latter has to increase by at least two orders of magnitude in order to allow the production of ion energies useful for medical applications, which requires (and stimulates) substantial advances in CO₂ laser technology. Progress towards multi-TW CO₂ lasers is described e.g. in [49, 50].

At present, optical lasers ($\lambda \simeq 1 \mu\text{m}$) allow much higher values of a_0 . Key to the testing of HB with optical lasers is the development of targets with suitable density values (the challenge being to attain density values intermediate between those of gaseous and solid materials) and profiles. Strategies under investigations include, e.g., the engineering of high density gas jets [51] and the production of low-density foams [52]. On the other hand, the presence of a low-density plasma produced by the laser prepulse in front of solid targets may also favor HB acceleration. Evidence for dominant radiation pressure effects has been found from the observation of collimated, long-lasting plasma jets in petawatt interactions with few-micron thick targets [53, 54]. Figure 10.3 shows transverse interferograms of the plasma at 600 ps from the interaction in experiments using the VULCAN petawatt laser (intensity $I = 3 \times 10^{20} \text{ W cm}^{-2}$, duration $\tau_p = 0.7 - 0.9 \text{ ps}$) and 1 – 5 μm thick Cu targets. The inferred longitudinal velocity of the jet fairly agrees with the value obtained from (10.6) for the energy of bulk Cu ions. The comparison between interferograms obtained for linear and circular polarization suggests that in the latter case a more uniform jet is produced, as expected due to the quenching of hot electron generation and related instabilities.

Simulation studies have suggested that ion bunches with energies exceeding 100 MeV and narrow spectral features may be generated by sub-10 fs pulses having intensities exceeding $10^{22} \text{ W cm}^{-2}$ [55–57]. Laser systems delivering such “extreme” pulses at high repetition rate might be available in the near future.

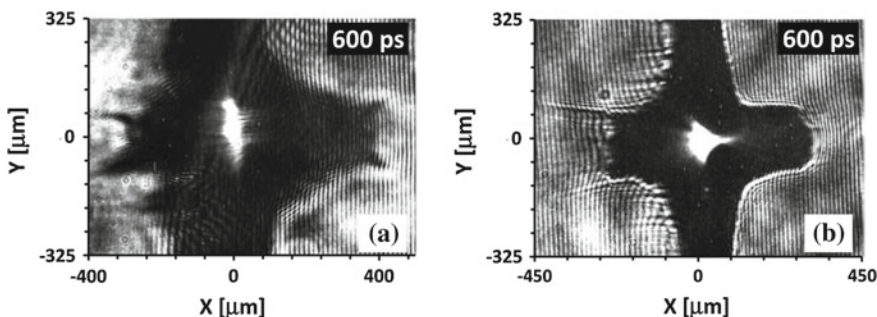


Fig. 10.3 Transverse interferogram of plasma densities [54] obtained after the interaction of a petawatt pulse with few- μm thick targets and showing the formation of collimated plasma jets. Frames **a** and **b** refer to the cases of linear and circular polarization of the laser pulse, respectively. Reprinted from [54] with permission

10.2.2.2 Light Sail Regime

If the target is thin enough, in the course of the HB process the pulse front reaches the rear side well before the end of the laser pulse and the central part of the target is accelerated as a whole. For very thin targets of thickness $\ell \ll u_{\text{hb}}\tau_p$, with τ_p the pulse duration, one may consider the whole mass of the target as being pushed by radiation pressure during the whole acceleration stage: this is the “light sail” (LS) regime. The simplest 1D model for LS is that of a plane mirror of finite surface mass boosted by a plane wave. This model allows to obtain a scaling of the peak energy

$$\mathcal{E}_{\text{ls}} = m_p c^2 \frac{\mathcal{F}^2}{2(1 + \mathcal{F})}, \quad \mathcal{F} = \frac{2I\tau_p}{\rho \ell c^2} = 2 \frac{Z n_c m_e \tau_p c}{A n_e m_p} \frac{a_0^2}{\ell}. \quad (10.7)$$

The scaling with the pulse energy per unit surface ($I\tau_p$) is very fast in the non-relativistic regime ($\mathcal{E}_{\text{ls}} \propto \mathcal{F}^2$ for $\mathcal{F} \ll 1$). The energy can be also increased by reducing the target thickness ℓ , but this approach is limited to the onset of pulse transmission through the target. If transmission occurs due to relativistic transparency, the pulse intensity has to be limited according to

$$a_0 \leq \zeta \equiv \pi \frac{n_e \ell}{n_c \lambda}. \quad (10.8)$$

Inserting the optimal condition $a_0 = \zeta$ in (10.7) leads to an effective scaling (for non-relativistic ions)

$$\mathcal{E}_{\text{ls}}^{(\text{opt})} = 2\pi^2 m_p c^2 \left(\frac{Z m_e c \tau_p}{A m_p \lambda} a_0 \right)^2 = 2\pi^2 m_e c^2 \left(\frac{m_e}{m_p} \right) \left(\frac{Z c \tau_p}{A \lambda} a_0 \right)^2. \quad (10.9)$$

For currently reachable laser intensities, the optimal thickness condition $a_0 = \zeta$ requires $\ell \lesssim 10^{-2} \lambda$, which corresponds to few tens of nm for solid densities. Foils with nm-thickness are technologically feasible, e.g. using diamond-like carbon foil technology [58], but clearly the use of such targets also requires ultrahigh pulse contrast.

The favorable scaling with laser parameters and the promise of monoenergetic spectra (as all ions in the target should move coherently along the axis at the same velocity) have stimulated the interest in studying LS acceleration experimentally. In principle, (10.9) predicts that energies exceeding 100 MeV are within reach with current laser and target technology. For example, using a Ti:Sa laser ($\lambda = 0.8 \mu\text{m}$) delivering 40 fs pulses ($c\tau_p/\lambda = 15$) at an intensity of $10^{21} \text{ W cm}^{-2}$ ($a_0 = 22$) we would obtain $\mathcal{E}_{\text{ls}}^{(\text{opt})} \simeq 150 \text{ MeV}$. However, first experimental investigations [54, 59–64] showed some promising results but also a number of optimization and stability issues which need to be addressed by further research.

As an example of experimental investigations of RPA-LS regime, Fig. 10.4 reports results obtained using the VULCAN petawatt laser ($I = 0.5 - 3 \times 10^{20} \text{ W cm}^{-2}$,

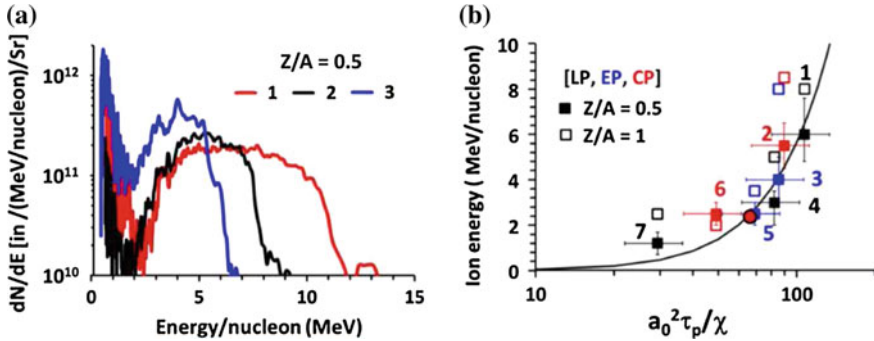


Fig. 10.4 Ion acceleration from petawatt laser interaction with sub-micrometric targets [61]. **a** Narrow band spectra from Cu targets for species with $Z/A = 1/2$. The laser amplitude $a_0 = 15.5, 10$, and 13.8 for spectra 1, 2 and 3, respectively, and the target thickness $\ell = 0.1 \mu\text{m}$ for 1 and 3 and $0.05 \mu\text{m}$ for 2. **b** Scaling of peak energies with the parameter $a_0^2 \tau_p / \chi \propto I \tau_p / \rho$. The line gives the theoretical scaling from the light sail model. Numbers refer to different target thickness and materials and colors to different polarizations (Linear, Elliptical, Circular). See [61] for details

$\tau_p = 0.7 - 0.9 \text{ ps}$ and thin metallic targets ($\ell = 0.1 - 0.8 \mu\text{m}$) containing carbon and hydrogen impurities [61]. Narrow-band spectra (with energy spread $\sim 20\%$) were observed centered at energies per nucleon approaching 10 MeV , displaying a scaling with $I \tau_p / \rho$ broadly consistent with the LS model prediction (10.7). The weak dependence on polarization is probably due to the relatively long laser pulse which leads to strong deformation of the target so that the incidence is not strictly normal anymore.

Recently, in order to investigate RPA-LS with extremely intense and sharp rising fs pulses, thin foil targets covered by a few-micron Carbon nanotube foam (CNF) on the interaction side have been used in order to generate self-focusing and self-steepening of the laser pulse in a plasma of density close to n_c . Using such technique on the GEMINI laser delivering 50 fs pulses at $I = 2 \times 10^{20} \text{ W cm}^{-2}$, enhanced acceleration of carbon ions (up to $\sim 20 \text{ MeV}$ energy per nucleon) with RPA features has been observed [65].

10.2.3 Collisionless Shock Acceleration

Under optimal conditions, high intensity laser-plasma interactions lead to the generation of collisionless shock waves, i.e. sharp fronts of density and electric field which propagate in the plasma with supersonic velocity $V_s = M c_s$, where the Mach number $M > 1$ and $c_s = (Z T_e / A m_p)^{1/2}$ is the “speed of sound” (velocity of ion-acoustic waves) in a plasma. The term “collisionless” originates from the fact that, contrary to standard hydrodynamics, collisional and viscosity effects are not needed for the formation of the shock front, which is sustained by charge separation

effects. The shock waves may be generated either due to the piston action of the laser in a hot plasma (so that the density perturbation produced by radiation pressure detaches from the interaction surface and propagates in the plasma) or by instabilities driven by the hot electrons.

Since the shock waves may be sustained by the hot electron population, in the expression for V_s we may replace T_e with T_h resulting in very high shock velocities. The electric field front may act as a potential barrier for ions in the plasma, accelerating some ions “by reflection” up to velocities $2V_s$, resulting in an energy per nucleon \mathcal{E}_{SA} given by

$$\mathcal{E}_{SA} = \frac{m_p}{2} (2V_s)^2 = 2 \frac{Z}{A} M^2 T_h. \quad (10.10)$$

As far as the shock front propagates at constant velocity, the reflected ions are monoenergetic.

Collisionless shock acceleration (CSA) has been invoked as the mechanism leading to the generation of highly monoenergetic proton spectra (up to ~ 20 MeV energy) in the interaction of CO₂ laser pulses with gaseous hydrogen jet targets [66]. The laser pulse was a sequence of 3 ps pulses with peak intensity $I \simeq 6 \times 10^{16} \text{ W cm}^{-2}$. The energy spread of less than 1 % is the narrowest one observed in laser-plasma acceleration experiments. However, the number of accelerated protons is very low, apparently about three orders of magnitude lower than produced via HB acceleration in similar laser and target conditions [48].

Recently, it has been shown that tailoring of the density profile using a low intensity prepulse may be effective to control and optimize the energy spectrum. Using this approach, quasi-monoenergetic proton spectra with peak energy ~ 1.2 MeV have been obtained with CO₂ pulses at $I = 2.5 \times 10^{16} \text{ W cm}^{-2}$ [67, 68].

Simulations [66] suggest that CSA could scale with laser intensity in order to produce >100 MeV protons, although this will require at least substantial upgrades in the laser system to allow an increase by two orders of magnitude in intensity. Demonstrating CSA with optical lasers requires the development of target media with suitable density profiles. The advantages and requirements are common to HB acceleration as already discussed in Sect. 10.2.2. However, although often confused in the literature, HB and CSA are different processes, the latter being effective in the presence of hot electrons. As stated above, a very relevant difference is the number of ions accelerated per shot. In CSA, such number must be low in order to preserve a monoenergetic spectrum; the reflection of too many ions from the shock front may lead to loading of the shock wave, which in turn may lose energy and slow down, causing a spectral chirp of the reflected ions, and eventually collapse. This limitation, although compensated by high repetition rate operation, has to be taken into account when considering the suitability of CSA for applications.

10.2.4 Acceleration in Underdense and Relativistically Transparent Plasmas

A few experiments have investigated ion acceleration during the interaction with underdense gas jet targets, which would be suited to high repetition rate operation. In these experiments, ion acceleration typically occurs in the radial direction with respect to the laser propagation axis, as the result of the drilling of a low-density channel (see e.g. [69, 70] and references therein); such uncollimated ion emission has low brilliance and is not ideal for applications.

Collimated, longitudinal ion emission from gas jets has been observed by using both a petawatt-class lasers ($6 \times 10^{20} \text{ W cm}^{-2}$ intensity, 1 ps duration) producing 40 MeV He ions [71], and a short terawatt pulse ($7 \times 10^{17} \text{ W cm}^{-2}$ intensity, 40 fs duration) achieving a surprising cut-off of 20 MeV [72]. An enhanced electric field, associated to electron vortices in a quasistatic magnetic field arising at the interface between gas and vacuum, has been proposed as having a role in both these experiments (see e.g. [73]). In the experiment of [72], it is also claimed that an important role is played by the formation of clusters in the gas jet. In general, laser-cluster interaction allows to generate MeV ions also with low-energy laser pulses of sub-relativistic intensity. This effect has been exploited for table-top nuclear fusion [74] and more recently to provide an ion source for high resolution ionography [75]. A limitation of these sources is the almost isotropic distribution of the accelerated ions.

Next generation lasers might allow a regime of efficient acceleration in underdense plasmas which has been foreseen theoretically [76]. Since the electrons in a propagating laser wave acquire the energy $\mathcal{E}_e = m_e c^2 a_0^2 / 2$, for $a_0 > m_p/m_e \simeq 43$ (i.e. for irradiances $I\lambda^2 > 2.6 \times 10^{21} \text{ W cm}^{-2}$) the effective mass of electrons becomes equal to the rest mass of protons, so that the latter stick to electrons and are accelerated in a “snow-plow” mode with high efficiency. The regime has features somewhat similar to RPA but does not require high-density targets. The simulations of [76] show that hundreds of MeV ions, collimated by self-generated magnetic fields, may be generated.

The interaction with so-called near-critical plasmas, with $n_e \simeq n_c$, has also attracted interest because of the high degrees of absorption and hot electron generation correlated with the transition from opacity to (relativistic) transparency. A way to produce a near-critical plasma is to use a special material as a foam; preliminary investigations in various regimes have been reported [77, 78].

An alternative strategy is to use a thin target with a thickness matched to the laser pulse in order for the target to become transparent during the interaction. This regime is often referred to as the breakout afterburner (BOA), particularly in relation to a series of experiments with the Trident laser at the Los Alamos National Laboratory (mostly oriented to the use of ions in fusion research [79]). Key to this regime is the onset of relativistic transparency near the peak of the laser pulse, which leads to strong electron heating and enhanced coupling to ions. Both protons and bulk ions a, (e.g. Carbon in [80]) can be efficiently accelerated employing

sub-ps pulses, typically with enhanced energies with respect to TNSA acceleration from thicker target under comparable laser conditions [80–82]. Other reported features are a different directionality compared to TNSA, leading to the observation of distinct beam components which can be associated to the different mechanisms [83, 84] and the observation of off-axis energy maxima, typically along annuli surrounding the laser axis [85].

For laser intensities above the transparency threshold for ultrathin targets, it is also possible to remove target electrons completely in a region with a size of the order of the focal radius. In such conditions, ions undergo a “Coulomb explosion”, i.e. they are accelerated by the electrostatic field generated by themselves which is the highest field attainable for a given target size. With respect to the same process undergoing in sub-wavelength clusters [86], Coulomb explosion in thin foils is “directed”, i.e. it accelerates ions in a preferential direction [87]. Recently a similar effect has been invoked to explain a transition in the proton energy scaling with laser intensity [35] and efficient acceleration of heavy Au ions from thin targets [88].

10.3 Perspectives for Biomedical Applications

10.3.1 Oncological Ion Beam Therapy

It was soon after the experimental observations in the year 2000 that several authors [8, 10, 89, 90] proposed LIA as an alternative to standard accelerators for oncological ion beam therapy (IBT). Originally proposed nearly 70 years ago by Wilson [91] and first demonstrated a decade later by Lawrence [92], IBT is the radiotherapy technique that uses protons or heavier ions to irradiate tumors. IBT exploits the highly localized energy deposition properties of ions, which deliver most of their energy at the end of their path, i.e. at the so-called Bragg peak. This property allows to minimize the irradiation of healthy tissues surrounding the tumor, and to increase the dose delivered near the stopping point. IBT thus offers a clear advantage with respect to radiotherapy with X-rays, γ -rays and electrons since all these particles have a smooth, continuous profile of energy deposition in matter. Such property, however, also demands a tight control of the beam deposition, resulting in the higher complexity of IBT with respect to other radiotherapy techniques. Since its proposal IBT has required major advances and developments in accelerator technology as well as in beam delivery techniques and clinical diagnostics to become suitable for clinical treatment.

Overviews of the status of IBT with conventional accelerators (synchrotron, cyclotron or linac) can be found in several review papers (see e.g. [93–96]) and reports [97]. Presently, about 50 IBT facilities operate worldwide, with several more becoming operative in a few years from now. Most of the IBT facilities use protons, with a minor number using carbon ions which are more effective for radioresistant and hypoxic tumors [96, 98]. While early application of IBT were

restricted to rare diseases not allowing standard treatments, presently IBT is applied to the treatment of a vast number of tumors and more than one hundred thousand patients have been treated. However, the high costs and large size of facilities are still a limiting factor for IBT, and the question of whether the cost to benefit ratio is justified and sustainable is the subject of long-lasting analysis and debate (see e.g. [99–101] and references therein). The cost would be lowered with the development of cheaper accelerators, although these are not the only items leading to large size and costs. For example, cumbersome and costly magnetic steering systems (Gantries) must be employed for multi-directional irradiation of patients. The weight of a Gantry exceeds 100 t when operating with protons, and 500 t with carbon ions [102].

LIA has often been cited as a possible option to reduce the cost and size of a IBT facility. However, ion beam parameters are still far from the IBT requirements and several hurdles and challenges are apparent. Besides the need to demonstrate ion acceleration up to the required energy range (150–300 MeV/nucleon for treating deep-seated tumors), major progress is needed for LIA in terms of transport and dose delivery capabilities, shielding from secondary radiation, as well as in source control and reproducibility [103].

Studies of how laser-driven beams can be used in therapy have already been initiated. For example, [104] identifies possible ad hoc treatment planning methods, based on axial and longitudinal clustering, which, with a broad proton spectrum containing $\sim 10^8$ particles and 10 Hz repetition, can provide in a few minutes a clinically relevant dose distribution. Future scenarios in which laser-driven beams could be used therapeutically are therefore conceivable, particularly considering on-going efforts to develop high-repetition laser drivers at high average power, and high-repetition targetry.

In any case it is clear that the possible application of LIA to IBT is still far away and that a long term research and development effort is needed to evaluate its real potential. To this aim, several projects either have been or are currently active worldwide (see e.g. [105–109] and [110] for a review). Unconventional and innovative solutions may be required at each stage of the design of a future LIA-IBT facility, including beam manipulation and transport [111–114], radiation shielding [115], gantry design [108], and treatment planning [104].

Currently IBT operation is performed with beams having a relative energy spread $\Delta \mathcal{E}/\mathcal{E} \simeq 10^{-2}$ which is typically from one to two orders of magnitude narrower than what is presently obtained with LIA. However, strict monoenergeticity is not required a priori for IBT since the energy spectrum must be modulated in order to obtain the optimal “spread-out Bragg peak” distribution required for optimal dose delivery over the tumor region. Methods to obtain directly such distribution from the native spectrum of laser-accelerated ions have been investigated [116–120].

The possible success of LIA as an option for IBT also relies on exploiting the peculiar properties of laser-driven ion beams. One of the main advantages would be the option of optical transport to the treatment rooms rather than transporting and

steering high energy ion beams with large magnets, so that all costs related to ion beam transport and radiation shielding on the way to the treatment room are removed. Such scenario would benefit further from the development of a compact beam handling system in replacement of the massive and costly gantries used in existing hadrontherapy facilities. Optical control combined with the dose concentration in small-duration bunches may have potential for the irradiation of moving targets [114], which is a major challenge for the IBT of specific organs.

10.3.2 Radiobiology Studies

A very peculiar characteristics of laser-driven beams is the possibility of achieving exceptionally high dose rates on an irradiated sample. This feature has stimulated several dedicated radiobiological studies, which has also required developments in dosimetric techniques [121–123]. In a typical arrangement, doses of up to a few Gys can be delivered to the cells in short bursts of \sim ns duration. In some experiments [124, 125] the dose is fractionated and the average dose rate is comparable to the one used in irradiations with conventional accelerators (~ 0.1 Gy s $^{-1}$). In single-shot irradiations, on-cell dose rates of the order of 10 9 Gy s $^{-1}$ have been estimated [122, 126, 127]. Such values are some nine orders of magnitude higher than normally used. It is therefore important to assess the biological effect of laser-driven ions with respect to conventional ion beams used in IBT and to other sources of radiation. To this aim, the Relative Biological Effectiveness (RBE), defined as the ratio D_x/D_p where D_x is a reference dose of a standard radiation source (usually X-rays) and D_p is the laser-accelerated proton dose producing the same biological effect, has been measured in several experiments. First cell irradiation experiments [125, 128] using ~ 2 MeV laser-accelerated protons obtained a RBE value of 1.2 ± 0.1 , comparable to that of protons from conventional accelerators having a similar value of Linear Energy Transfer (LET) $d\mathcal{E}/d(\rho x)$ [129]. In another experiment at ultra-high dose rate [126] a RBE of 1.4 ± 0.2 was measured (Fig. 10.5), also in line with expectations for the LET of the particles employed.

In addition, to address the effects of pulsed dose delivery which would be characteristic of laser-driven sources, comparative studies employing conventional proton accelerators in pulsed mode (with ns duration) and continuous mode (ms duration) have been carried out on cells [130], and in vivo mice on which human tumors were transplanted [131]. So far, none of these studies has revealed significant differences in the RBE associated to highly pulsed irradiation.

For a detailed discussion of the radiobiology experiments carried out so far, we refer the reader to [132]. However, while broadly relevant to possible future treatment modalities, experiments so far may not have yet reached conditions in which differences in the biological response are likely to emerge. For example, collective non-linear effects on the stopping power and the LET are predicted to take place when there is spatio-temporal overlap of the tracks formed by single

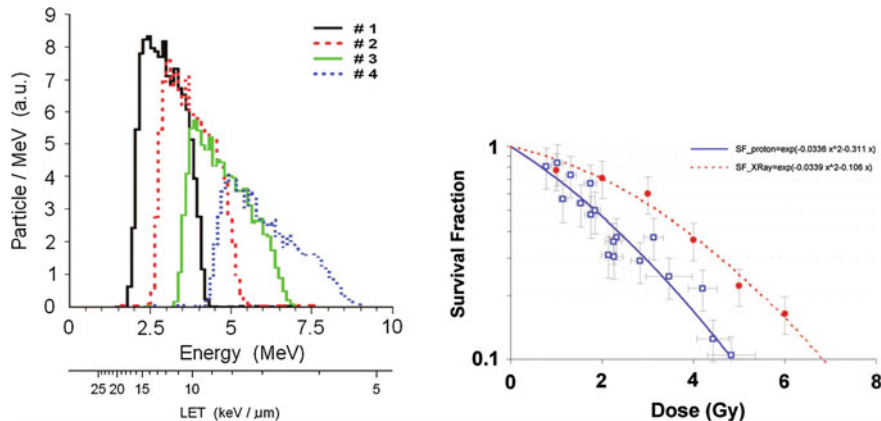


Fig. 10.5 Example of V79 Chinese Hamster cell irradiation experiment with laser-accelerated proton beams [126]. *Left frame* energy spectra delivered to four cell spots, with the corresponding entrance LET values. *Right frame* survival curve obtained with protons in the 1–5 MeV energy range (thick curve), compared to X-ray irradiation on the same cell (dashed). Reprinted from [126] with permission

particles in the irradiated biological sample [133]. These conditions may emerge in dedicated experiments employing higher doses and dose rates. Additionally, it is predicted that indirect effects, which involve the ionization of water and damage to the DNA via chemical processes involving free radicals, can be drastically modified at extreme dose rates, particularly under conditions of limited oxygen supply to the cells (*hypoxia*), mimicking the conditions tumor cells may encounter in the human body [134].

10.3.3 Production of Short-Lived Isotopes and Neutrons

Short-lived isotope production by proton-induced nuclear reactions has been used as a diagnostic for LIA experiments [11] and soon proposed as a way to produce radionuclides and positron emitters for medical diagnostics [12, 13]. Short-lived positron emitters are of great interest for Positron Emission tomography (PET) and are commonly produced using ~20 MeV protons or deuterons from cyclotrons, i.e. in an energy range currently well accessible with LIA. Reported values of the integrated activity produced using “table-top” femtosecond lasers typically operating at 10 Hz are some two orders of magnitude lower than required for use in PET [14, 135]. Higher activities and a large number of emitters were produced with larger lasers [136], but it is apparent that the low repetition rate of these system makes them unsuitable for application in PET [137]. On the basis of the extrapolation of present results and additional theoretical and simulation work [138, 139], the activity values required for PET may be reached with table-top lasers (typically

delivering 1 J, 30 fs pulses tightly focused to achieve intensities of $\sim 10^{20} \text{ W cm}^{-2}$) working at kHz rate. Recent work aimed at optimizing laser-driven deuteron beams for isotope production has been reported [140].

Nuclear reactions driven by proton or deuteron beams are also of interest for production of neutrons, which has been observed either from direct laser interaction with the bulk of deuterated targets [141–145] or by directing the ion beam on a secondary target, i.e. in a “pitcher-catcher” configuration [146–152]. A comparative study between the two approaches was reported in [153]. Reference [152] also reports a neutron radiograph obtained with deuterons accelerated in the BOA regime. Laser-driven neutron sources have potential advantages over traditional sources in term of cost, compactness, brightness and duration for applications such as fast neutron radiography [154] and studies of impulsive damage of matter [155]. In the biomedical context, neutrons may be used for hadrontherapy and for boron neutron capture therapy of cancer, although the potential of laser-driven sources in these areas is still unclear at the moment.

10.4 Concluding Remarks

Since the early observations of multi-MeV protons from solid targets in the year 2000, laser-driven ion acceleration has attracted a very large amount of effort, greatly stimulated by potential biomedical applications. Preliminary radiobiological studies have been also reported and many related projects are running. A main aim of current research is to demonstrate beam properties suitable for application in cancer therapy. In this context, an enhancement of energy per nucleon up to therapeutic window for deep-seated tumours (150–250 MeV) has been considered as a primary goal and would naturally represent a major milestone.

On this issue it might be argued that the progress since the $\simeq 58 \text{ MeV}$ energy cut-off observed with the NOVA Petawatt at LLNL [3] has been slow, the only published data with a higher energy being those obtained with TRIDENT at LANL in 2011 [22]. However, one should also notice that in absolute terms, the maximum laser power and energy available to experimenters have not been increased substantially since the NOVA measurements. On the other hand, significant progress has been achieved with ultrashort Ti:Sa systems, as the development of PW-class systems now allow accelerating protons to the 30–40 MeV range with laser pulses of tens of fs duration [26, 34, 35].

For TNSA, the observed scalings and trends with the laser parameters suggest that next generation facilities delivering unprecedented values of laser pulse energy and power [156] will be required for a significant enhancement of the accelerated ion energies. Transparency regimes offering enhanced coupling of the laser energy into electrons may lead to a reduction of these laser requirements, although the dynamics of this coupling are complex and still subject of investigation [84]. Amongst alternative acceleration mechanisms, RPA has a more promising theoretical scaling but its experimental investigation is still at a very preliminary stage.

Other alternative concepts such as CSA will also require major developments in the laser systems in order to fulfill theoretical expectations in experiments.

We should note that the experimental assessment of the efficiency of the different acceleration mechanisms at current intensities has been somehow distorted over the past few years by unpublished reports of the observation of very high proton energies, which are often taken at face value by part of the scientific community and even used to benchmark progress in the field although they have never passed a review process, and their validity is therefore unconfirmed.

These cases highlight a more general problem in the ion acceleration community, i.e. the need to establish agreed and recognised standards and procedures for experimental diagnosis, data analysis and reporting results. As a clear and important example, the maximum ion energy in a spectrum, which is normally taken as the key parameter for deriving scaling laws and comparing acceleration performance in different experiments or facilities, is a parameter which is intrinsically ill-defined (particularly for exponential-like spectral tails as observed in the majority of experiments). The maximum energies detectable are in most cases determined by diagnostic factors (such as the sensitivity of the diagnostics or the level of background noise) rather than by a clear, physical cut-off. The emergence from the community of agreed criteria, e.g. on how to discriminate signal from noise, or how a significant maximum energy should be defined, and their consistent application throughout the field would be highly beneficial to the progress of laser-driven ion acceleration.

While upcoming laser systems with multi-PW power are likely to provide access to the energy range of relevance to cancer therapy, over the past few years of research significant progress has been made in the understanding of ion acceleration mechanisms, and in the development of immediate applications (e.g. proton radiography or isochoric heating of warm dense matter) which do not require very high energies but exploit unique properties of laser-accelerated ion beams, such as high particle density and ultrashort burst duration. These achievements give us confidence towards further successful investigations and development in the next years.

Acknowledgements Funding from EPSRC (UK), grant : EP/K022415/1, and MIUR (Italy), FIR project “SULDIS” is acknowledged.

References

1. E.L. Clark, K. Krushelnick, J.R. Davies, M. Zepf, M. Tatarakis, F.N. Beg, A. Machacek, P. A. Norreys, M.I.K. Santala, I. Watts, A.E. Dangor, Phys. Rev. Lett. **84**, 670 (2000). doi:[10.1103/PhysRevLett.84.670](https://doi.org/10.1103/PhysRevLett.84.670)
2. A. Maksimchuk, S. Gu, K. Flippo, D. Umstadter, V.Y. Bychenkov, Phys. Rev. Lett. **84**, 4108 (2000). doi:[10.1103/PhysRevLett.84.4108](https://doi.org/10.1103/PhysRevLett.84.4108)
3. R.A. Snavely, M.H. Key, S.P. Hatchett, T.E. Cowan, M. Roth, T.W. Phillips, M.A. Stoyer, E.A. Henry, T.C. Sangster, M.S. Singh, S.C. Wilks, A. MacKinnon, A. Offenberger, D.M.

- Pennington, K. Yasuike, A.B. Langdon, B.F. Lasinski, J. Johnson, M.D. Perry, E.M. Campbell, Phys. Rev. Lett. **85**, 2945 (2000). doi:[10.1103/PhysRevLett.85.2945](https://doi.org/10.1103/PhysRevLett.85.2945)
4. A. Macchi, M. Borghesi, M. Passoni, Rev. Mod. Phys. **85**, 751 (2013). doi:[10.1103/RevModPhys.85.751](https://doi.org/10.1103/RevModPhys.85.751)
5. M. Borghesi, A.J. Mackinnon, D.H. Campbell, D.G. Hicks, S. Kar, P.K. Patel, D. Price, L. Romagnani, A. Schiavi, O. Willi, Phys. Rev. Lett. **92**, 055003 (2004). doi:[10.1103/PhysRevLett.92.055003](https://doi.org/10.1103/PhysRevLett.92.055003)
6. F. Nuernberg, M. Schollmeier, E. Brambrink, A. Blažević, D.C. Carroll, K. Flippo, D.C. Gautier, M. Geissel, K. Harres, B.M. Hegelich, O. Lundh, K. Markey, P. McKenna, D. Neely, J. Schreiber, M. Roth, Rev. Sci. Instrum. **80**, 033301 (2009). doi:[10.1063/1.3086424](https://doi.org/10.1063/1.3086424)
7. J. Fernández, B. Albright, F. Beg, M. Foord, B. Hegelich, J. Honrubia, M. Roth, R. Stephens, L. Yin, Nucl. Fusion **54**, 054006 (2014). doi:[10.1088/0029-5515/49/6/065004](https://doi.org/10.1088/0029-5515/49/6/065004)
8. S. Bulanov, T. Esirkepov, V. Khoroshkov, A. Kuznetsov, F. Pegoraro, Phys. Lett. A **299**, 240 (2002). doi:[10.1016/S0375-9601\(02\)00521-2](https://doi.org/10.1016/S0375-9601(02)00521-2)
9. E. Fourkal, B. Shahine, M. Ding, J.S. Li, T. Tajima, C.M. Ma, Med. Phys. **29**, 2788 (2002). doi:[10.1118/1.1521122](https://doi.org/10.1118/1.1521122)
10. V. Malka, S. Fritzler, E. Lefebvre, E. d'Humières, R. Ferrand, G. Grillon, C. Albaret, S. Meyroneinc, J.P. Chambaret, A. Antonetti, D. Hulin, Med. Phys. **31**, 1587 (2004). doi:[10.1118/1.1747751](https://doi.org/10.1118/1.1747751)
11. K. Nemoto, A. Maksimchuk, S. Banerjee, K. Flippo, G. Mourou, D. Umstadter, V.Y. Bychenkov, Appl. Phys. Lett. **78**, 595 (2001). doi:[10.1063/1.1343845](https://doi.org/10.1063/1.1343845)
12. M.I.K. Santala, M. Zepf, F.N. Beg, E.L. Clark, A.E. Dangor, K. Krushelnick, M. Tatarakis, I. Watts, K.W.D. Ledingham, T. McCanny, I. Spencer, A.C. Machacek, R. Allott, R.J. Clarke, P.A. Norreys, Appl. Phys. Lett. **78**, 19 (2001). doi:[10.1063/1.1335849](https://doi.org/10.1063/1.1335849)
13. I. Spencer, K.W.D. Ledingham, R.P. Singhal, T. McCanny, P. McKenna, E.L. Clark, K. Krushelnick, M. Zepf, F.N. Beg, M. Tatarakis, A.E. Dangor, P.A. Norreys, R.J. Clarke, R.M. Allott, I.N. Ross, Nucl. Inst. Meth. Phys. Res. B **183**, 449 (2001). doi:[10.1016/S0168-583X\(01\)00771-6](https://doi.org/10.1016/S0168-583X(01)00771-6)
14. S. Fritzler, V. Malka, G. Grillon, J.P. Rousseau, F. Burgy, E. Lefebvre, E. d'Humières, P. McKenna, K.W.D. Ledingham, Appl. Phys. Lett. **83**, 3039 (2003). doi:[10.1063/1.1616661](https://doi.org/10.1063/1.1616661)
15. K.W.D. Ledingham, P. McKenna, R.P. Singhal, Science **300**, 1107 (2003). doi:[10.1126/science.1080552](https://doi.org/10.1126/science.1080552)
16. Y. Salamin, Z. Harman, C. Keitel, Phys. Rev. Lett. **100**, 155004 (2008). doi:[10.1103/PhysRevLett.100.155004](https://doi.org/10.1103/PhysRevLett.100.155004)
17. B.J. Galow, Z. Harman, C.H. Keitel, Opt. Express **18**, 25950 (2010). doi:[10.1364/OE.18.025950](https://doi.org/10.1364/OE.18.025950)
18. H. Daido, M. Nishiuchi, A.S. Pirozhkov, Rep. Prog. Phys. **75**, 056401 (2012). doi:[10.1088/0034-4885/75/5/056401](https://doi.org/10.1088/0034-4885/75/5/056401)
19. A. Macchi, A. Sgattoni, S. Sinigardi, M. Borghesi, M. Passoni, Plasma Phys. Contr. Fusion **55**, 124020 (2013). doi:[10.1088/0741-3335/55/12/124020](https://doi.org/10.1088/0741-3335/55/12/124020)
20. P. Gibbon, *Short Pulse Laser Interaction with Matter* (Imperial College Press, 2005)
21. A. Macchi, *A Superintense Laser-Plasma Interaction Theory Primer*. SpringerBriefs in Physics (Springer, 2013). doi:[10.1007/978-94-007-6125-4](https://doi.org/10.1007/978-94-007-6125-4)
22. S.A. Gaillard, T. Kluge, K.A. Flippo, M. Bussmann, B. Gall, T. Lockard, M. Geissel, D.T. Offermann, M. Schollmeier, Y. Sentoku, T.E. Cowan, Phys. Plasmas **18**, 056710 (2011). doi:[10.1063/1.3575624](https://doi.org/10.1063/1.3575624)
23. J. Fuchs, P. Antici, E. d'Humières, E. Lefebvre, M. Borghesi, E. Brambrink, C.A. Cecchetti, M. Kaluza, V. Malka, M. Mancossi, S. Meyroneinc, P. Mora, J. Schreiber, T. Toncian, H. Pepin, P. Audebert, Nat. Phys. **2**, 48 (2006). doi:[10.1038/nphys199](https://doi.org/10.1038/nphys199)
24. L. Robson, P.T. Simpson, R.J. Clarke, K.W.D. Ledingham, F. Lindau, O. Lundh, T. McCanny, P. Mora, D. Neely, C.G. Wahlstrom, M. Zepf, P. McKenna, Nat. Phys. **3**, 58 (2007). doi:[10.1038/nphys476](https://doi.org/10.1038/nphys476)

25. K. Zeil, S.D. Kraft, S. Bock, M. Bussmann, T.E. Cowan, T. Kluge, J. Metzkes, T. Richter, R. Sauerbrey, U. Schramm, *New J. Phys.* **12**, 045015 (2010). doi:[10.1088/1367-2630/12/4/045015](https://doi.org/10.1088/1367-2630/12/4/045015)
26. K. Ogura, M. Nishiuchi, A.S. Pirozhkov, T. Tanimoto, A. Sagisaka, T.Z. Esirkepov, M. Kando, T. Shizuma, T. Hayakawa, H. Kiriyama, T. Shimomura, S. Kondo, S. Kanazawa, Y. Nakai, H. Sasao, F. Sasao, Y. Fukuda, H. Sakaki, M. Kanasaki, A. Yogo, S.V. Bulanov, P.R. Bolton, K. Kondo, *Opt. Lett.* **37**, 2868 (2012). doi:[10.1364/OL.37.002868](https://doi.org/10.1364/OL.37.002868)
27. S. Buffeouchoux, J. Psikal, M. Nakatsutsumi, L. Romagnani, A. Andreev, K. Zeil, M. Amin, P. Antici, T. Burris-Mog, A. Compart-La-Fontaine, E. d'Humières, S. Fourmaux, S. Gaillard, F. Gobet, F. Hannachi, S. Kraft, A. Mancic, C. Plaisir, G. Sarri, M. Tarisien, T. Toncian, U. Schramm, M. Tampo, P. Audebert, O. Willi, T.E. Cowan, H. Pépin, V. Tikhonchuk, M. Borghesi, J. Fuchs, *Phys. Rev. Lett.* **105**, 015005 (2010). doi:[10.1103/PhysRevLett.105.015005](https://doi.org/10.1103/PhysRevLett.105.015005)
28. K. Zeil, J. Metzkes, T. Kluge, M. Bussmann, T.E. Cowan, S.D. Kraft, R. Sauerbrey, B. Schmidt, M. Zier, U. Schramm, *Plasma Phys. Control. Fusion* **56**, 084004 (2014). doi:[10.1088/0741-3335/56/8/084004](https://doi.org/10.1088/0741-3335/56/8/084004)
29. D. Margarone, O. Klimo, I.J. Kim, J. Prokùpek, J. Limpouch, T.M. Jeong, T. Mocek, J. Pšíkal, H.T. Kim, J. Proška, K.H. Nam, L.S. Štolcová, I.W. Choi, S.K. Lee, J.H. Sung, T. J. Yu, G. Korn, *Phys. Rev. Lett.* **109**, 234801 (2012). doi:[10.1103/PhysRevLett.109.234801](https://doi.org/10.1103/PhysRevLett.109.234801)
30. T. Ceccotti, V. Floquet, A. Sgattoni, A. Bigongiari, O. Klimo, M. Raynaud, C. Riconda, A. Heron, F. Baffigi, L. Labate, L.A. Gízzi, L. Vassura, J. Fuchs, M. Passoni, M. Kvétová, F. Novotny, M. Possolt, J. Prokùpek, J. Proška, J. Pšíkal, L. S. Štolcová, A. Velyhan, M. Bougeard, P. D’Oliveira, O. Tcherbakoff, F. Réau, P. Martin, A. Macchi, *Phys. Rev. Lett.* **111**, 185001 (2013). doi:[10.1103/PhysRevLett.111.185001](https://doi.org/10.1103/PhysRevLett.111.185001)
31. D. Margarone, I.J. Kim, J. Psikal, J. Kaufman, T. Mocek, I.W. Choi, L. Stolcova, J. Proska, A. Choukourov, I. Melnichuk, O. Klimo, J. Limpouch, J.H. Sung, S.K. Lee, G. Korn, T.M. Jeong, *Phys. Rev. ST Accel. Beams* **18**, 071304 (2015). doi:[10.1103/PhysRevSTAB.18.071304](https://doi.org/10.1103/PhysRevSTAB.18.071304)
32. B. Dromey, S. Kar, M. Zepf, P. Foster, *Rev. Sci. Instrum.* **75**, 645 (2004). doi:[10.1063/1.1646737](https://doi.org/10.1063/1.1646737)
33. C. Thaury, F. Quere, J.P. Geindre, A. Levy, T. Ceccotti, P. Monot, M. Bougeard, F. Reau, P. d’Oliveira, P. Audebert, R. Marjoribanks, P. Martin, *Nat. Phys.* **3**, 424 (2007). doi:[10.1038/nphys595](https://doi.org/10.1038/nphys595)
34. J.S. Green, A.P.L. Robinson, N. Booth, D.C. Carroll, R.J. Dance, R.J. Gray, D.A. MacLellan, P. McKenna, C.D. Murphy, D. Rusby, L. Wilson, *Appl. Phys. Lett.* **104**, 214101 (2014). doi:[10.1063/1.4879641](https://doi.org/10.1063/1.4879641)
35. I.J. Kim, K.H. Pae, C.M. Kim, H.T. Kim, J.H. Sung, S.K. Lee, T.J. Yu, I.W. Choi, C.L. Lee, K.H. Nam, P.V. Nickles, T.M. Jeong, J. Lee, *Phys. Rev. Lett.* **111**, 165003 (2013). doi:[10.1103/PhysRevLett.111.165003](https://doi.org/10.1103/PhysRevLett.111.165003)
36. P.K. Patel, A.J. Mackinnon, M.H. Key, T.E. Cowan, M.E. Foord, M. Allen, D.F. Price, H. Ruhl, P.T. Springer, R. Stephens, *Phys. Rev. Lett.* **91**, 125004 (2003). doi:[10.1103/PhysRevLett.91.125004](https://doi.org/10.1103/PhysRevLett.91.125004)
37. S. Kar, K. Markey, P.T. Simpson, C. Bellei, J.S. Green, S.R. Nagel, S. Kneip, D.C. Carroll, B. Dromey, L. Willingale, E.L. Clark, P. McKenna, Z. Najmudin, K. Krushelnick, P. Norreys, R.J. Clarke, D. Neely, M. Borghesi, M. Zepf, *Phys. Rev. Lett.* **100**, 105004 (2008). doi:[10.1103/PhysRevLett.100.105004](https://doi.org/10.1103/PhysRevLett.100.105004)
38. S. Kar, K. Markey, M. Borghesi, D.C. Carroll, P. McKenna, D. Neely, M.N. Quinn, M. Zepf, *Phys. Rev. Lett.* **106**, 225003 (2011). doi:[10.1103/PhysRevLett.106.225003](https://doi.org/10.1103/PhysRevLett.106.225003)
39. T. Bartal, M.E. Foord, C. Bellei, M.H. Key, K.A. Flippo, S.A. Gaillard, D.T. Offermann, P. K. Patel, L.C. Jarrott, D.P. Higginson, M. Roth, A. Otten, D. Kraus, R.B. Stephens, H.S. McLean, E.M. Giraldez, M.S. Wei, D.C. Gautier, F.N. Beg, *Nature Phys.* **8**, 139 (2012). doi:[10.1038/nphys2153](https://doi.org/10.1038/nphys2153)

40. S.N. Chen, E. d'Humières, E. Lefebvre, L. Romagnani, T. Toncian, P. Antici, P. Audebert, E. Brambrink, C.A. Cecchetti, T. Kudyakov, A. Pipahl, Y. Sentoku, M. Borghesi, O. Willi, J. Fuchs, Phys. Rev. Lett. **108**, 055001 (2012). doi:[10.1103/PhysRevLett.108.055001](https://doi.org/10.1103/PhysRevLett.108.055001)
41. T. Toncian, M. Borghesi, J. Fuchs, E. d'Humières, P. Antici, P. Audebert, E. Brambrink, C. A. Cecchetti, A. Pipahl, L. Romagnani, O. Willi, Science **312**, 410 (2006). doi:[10.1126/science.1124412](https://doi.org/10.1126/science.1124412)
42. H. Schwoerer, S. Pfotenhauer, O. Jaeckel, K.U. Amthor, B. Liesfeld, W. Ziegler, R. Sauerbrey, K.W.D. Ledingham, T. Esirkepov, Nature **439**, 445 (2006). doi:[10.1038/nature04492](https://doi.org/10.1038/nature04492)
43. B.M. Hegelich, B.J. Albright, J. Cobble, K. Flippo, S. Letring, M. Paffett, H. Ruhl, J. Schreiber, R.K. Schulze, J.C. Fernandez, Nature **439**, 441 (2006). doi:[10.1038/nature04400](https://doi.org/10.1038/nature04400)
44. A.G. Krygier, J.T. Morrison, S. Kar, H. Ahmed, A. Alejo, R. Clarke, J. Fuchs, A. Green, D. Jung, A. Kleinschmidt, Z. Najmudin, H. Nakamura, P. Norreys, M. Notley, M. Oliver, M. Roth, L. Vassura, M. Zepf, M. Borghesi, R.R. Freeman, Phys. Plasmas **22**, 053102 (2015). doi:[10.1063/1.4919618](https://doi.org/10.1063/1.4919618)
45. M. Nishiuchi, H. Sakaki, T.Z. Esirkepov, K. Nishio, T.A. Pikuz, A.Y. Faenov, I.Y. Skobelev, R. Orlandi, H. Sako, A.S. Pirozhkov, K. Matsukawa, A. Sagisaka, K. Ogura, M. Kanasaki, H. Kiriyama, Y. Fukuda, H. Koura, M. Kando, T. Yamauchi, Y. Watanabe, S.V. Bulanov, K. Kondo, K. Imai, S. Nagamiya, Phys. Plasmas **22**, 033107 (2015). doi:[10.1063/1.4913434](https://doi.org/10.1063/1.4913434)
46. A. Macchi, F. Cattani, T.V. Liseykina, F. Cornolti, Phys. Rev. Lett. **94**, 165003 (2005). doi:[10.1103/PhysRevLett.94.165003](https://doi.org/10.1103/PhysRevLett.94.165003)
47. B. Aurand, S. Kuschel, C. Rdel, O. Jckel, J. Polz, B. Elkin, H. Zhao, A. Karmakar, P. Gibbon, M. Kaluza, T. Kuehl, Appl. Phys. B: Lasers Opt. **118**, 247 (2015). doi:[10.1007/s00340-014-5979-7](https://doi.org/10.1007/s00340-014-5979-7)
48. C.A.J. Palmer, N.P. Dover, I. Pogorelsky, M. Babzien, G.I. Dudnikova, M. Ispiriyany, M.N. Polyanskiy, J. Schreiber, P. Shkolnikov, V. Yakimenko, Z. Najmudin, Phys. Rev. Lett. **106**, 014801 (2011). doi:[10.1103/PhysRevLett.106.014801](https://doi.org/10.1103/PhysRevLett.106.014801)
49. D. Haberberger, S. Tochitsky, C. Joshi, Opt. Express **18**, 17865 (2010). doi:[10.1364/OE.18.017865](https://doi.org/10.1364/OE.18.017865)
50. B.G. Bravy, Y.A. Chernyshev, V.M. Gordienko, E.F. Makarov, V.Y. Panchenko, V.T. Platonenko, G.K. Vasil'ev, Opt. Express **20**, 25536 (2012). doi:[10.1364/OE.20.025536](https://doi.org/10.1364/OE.20.025536)
51. F. Sylla, M. Veltcheva, S. Kahaly, A. Flacco, V. Malka, Rev. Sci. Instrum. **83**, 033507 (2012). doi:[10.1063/1.3697859](https://doi.org/10.1063/1.3697859)
52. A. Zani, D. Dellasega, V. Russo, M. Passoni, Carbon **56**, 358 (2013). doi:[10.1016/j.carbon.2013.01.029](https://doi.org/10.1016/j.carbon.2013.01.029)
53. S. Kar, M. Borghesi, S.V. Bulanov, M.H. Key, T.V. Liseykina, A. Macchi, A.J. Mackinnon, P.K. Patel, L. Romagnani, A. Schiavi, O. Willi, Phys. Rev. Lett. **100**, 225004 (2008). doi:[10.1103/PhysRevLett.100.225004](https://doi.org/10.1103/PhysRevLett.100.225004)
54. S. Kar, K.F. Kakolee, M. Cerchez, D. Doria, A. Macchi, P. McKenna, D. Neely, J. Osterholz, K. Quinn, B. Ramakrishna, G. Sarri, O. Willi, X.H. Yuan, M. Zepf, M. Borghesi, Plasma Phys. Controlled Fusion **55**, 124030 (2013). doi:[10.1088/0741-3335/55/12/124030](https://doi.org/10.1088/0741-3335/55/12/124030)
55. A. Macchi, C. Benedetti, Nucl. Inst. Meth. Phys. Res. A **620**, 41 (2010). doi:[10.1016/j.nima.2010.01.057](https://doi.org/10.1016/j.nima.2010.01.057)
56. A.P.L. Robinson, Phys. Plasmas **18**, 056701 (2011). doi:[10.1063/1.3562551](https://doi.org/10.1063/1.3562551)
57. A.P.L. Robinson, R.M.G.M. Trines, N.P. Dover, Z. Najmudin, Plasma Phys. Control. Fusion **54**, 115001 (2012). doi:[10.1088/0741-3335/54/11/115001](https://doi.org/10.1088/0741-3335/54/11/115001)
58. W. Ma, V. Liechtenstein, J. Szerypo, D. Jung, P. Hilz, B. Hegelich, H. Maier, J. Schreiber, D. Habs, Nucl. Inst. Meth. Phys. Res. A **655**, 53 (2011). doi:[10.1016/j.nima.2011.06.019](https://doi.org/10.1016/j.nima.2011.06.019)
59. A. Henig, D. Kiefer, K. Markey, D.C. Gautier, K.A. Flippo, S. Letzring, R.P. Johnson, T. Shimada, L. Yin, B.J. Albright, K.J. Bowers, J.C. Fernández, S.G. Rykovanov, H.C. Wu, M. Zepf, D. Jung, V.K. Liechtenstein, J. Schreiber, D. Habs, B.M. Hegelich, Phys. Rev. Lett. **103**, 045002 (2009). doi:[10.1103/PhysRevLett.103.045002](https://doi.org/10.1103/PhysRevLett.103.045002)

60. C.A.J. Palmer, J. Schreiber, S.R. Nagel, N.P. Dover, C. Bellei, F.N. Beg, S. Bott, R.J. Clarke, A.E. Dangor, S.M. Hassan, P. Hilz, D. Jung, S. Kneip, S.P.D. Mangles, K.L. Lancaster, A. Rehman, A.P.L. Robinson, C. Spindloe, J. Szerypo, M. Tatarakis, M. Yeung, M. Zepf, Z. Najmudin, Phys. Rev. Lett. **108**, 225002 (2012). doi:[10.1103/PhysRevLett.108.225002](https://doi.org/10.1103/PhysRevLett.108.225002)
61. S. Kar, K.F. Kakolee, B. Qiao, A. Macchi, M. Cerchez, D. Doria, M. Geissler, P. McKenna, D. Neely, J. Osterholz, R. Prasad, K. Quinn, B. Ramakrishna, G. Sarri, O. Willi, X.Y. Yuan, M. Zepf, M. Borghesi, Phys. Rev. Lett. **109**, 185006 (2012). doi:[10.1103/PhysRevLett.109.185006](https://doi.org/10.1103/PhysRevLett.109.185006)
62. F. Dollar, C. Zulick, A.G.R. Thomas, V. Chvykov, J. Davis, G. Kalinchenko, T. Matsuoka, C. McGuffey, G.M. Petrov, L. Willingale, V. Yanovsky, A. Maksimchuk, K. Krushelnick, Phys. Rev. Lett. **108**, 175005 (2012). doi:[10.1103/PhysRevLett.108.175005](https://doi.org/10.1103/PhysRevLett.108.175005)
63. B. Aurand, S. Kuschel, O. Jaeckel, C. Roedel, H. Zhao, S. Herzer, A.E. Paz, J. Bierbach, J. Polz, B. Elkin, G.G. Paulus, A. Karmakar, P. Gibbon, T. Kuehl, M.C. Kaluza, New J. Phys. **15**, 033031 (2013). doi:[10.1088/1367-2630/15/3/033031](https://doi.org/10.1088/1367-2630/15/3/033031)
64. S. Steinke, P. Hilz, M. Schnürer, G. Priebe, J. Bränzel, F. Abicht, D. Kiefer, C. Kreuzer, T. Ostermayr, J. Schreiber, A.A. Andreev, T.P. Yu, A. Pukhov, W. Sandner, Phys. Rev. ST Accel. Beams **16**, 011303 (2013). doi:[10.1103/PhysRevSTAB.16.011303](https://doi.org/10.1103/PhysRevSTAB.16.011303)
65. J.H. Bin, W.J. Ma, H.Y. Wang, M.J.V. Streeter, C. Kreuzer, D. Kiefer, M. Yeung, S. Cousens, P.S. Foster, B. Dromey, X.Q. Yan, R. Ramis, J. Meyer-ter Vehn, M. Zepf, J. Schreiber, Phys. Rev. Lett. **115**, 064801 (2015). doi:[10.1103/PhysRevLett.115.064801](https://doi.org/10.1103/PhysRevLett.115.064801)
66. D. Haberberger, S. Tochitsky, F. Fiuzza, C. Gong, R.A. Fonseca, L.O. Silva, W.B. Mori, C. Joshi, Nat. Phys. **8**, 95 (2012). doi:[10.1038/nphys2130](https://doi.org/10.1038/nphys2130)
67. Y.H. Chen, M.H. Helle, A. Ting, D.F. Gordon, M.N. Polyanskiy, I. Pogorelsky, M. Babzien, Z. Najmudin, Proc. SPIE **9514**, 95140C (2015). doi:[10.1117/12.2182094](https://doi.org/10.1117/12.2182094)
68. O. Tresca, N.P. Dover, N. Cook, C. Maharjan, M.N. Polyanskiy, Z. Najmudin, P. Shkolnikov, I. Pogorelsky, Phys. Rev. Lett. **115**, 094802 (2015). doi:[10.1103/PhysRevLett.115.094802](https://doi.org/10.1103/PhysRevLett.115.094802)
69. A. Macchi, F. Ceccherini, F. Cornolti, S. Kar, M. Borghesi, Plasma Phys. Control. Fusion **51**, 024005 (2009). doi:[10.1088/0741-3335/51/2/024005](https://doi.org/10.1088/0741-3335/51/2/024005)
70. A. Lifschitz, F. Sylla, S. Kahaly, A. Flacco, M. Veltcheva, G. Sanchez-Arriaga, E. Lefebvre, V. Malka, New J. Phys. **16**, 033031 (2014). doi:[10.1088/1367-2630/16/3/033031](https://doi.org/10.1088/1367-2630/16/3/033031)
71. L. Willingale, S.P.D. Mangles, P.M. Nilson, R.J. Clarke, A.E. Dangor, M.C. Kaluza, S. Karsch, K.L. Lancaster, W.B. Mori, Z. Najmudin, J. Schreiber, A.G.R. Thomas, M.S. Wei, K. Krushelnick, Phys. Rev. Lett. **96**, 245002 (2006). doi:[10.1103/PhysRevLett.96.245002](https://doi.org/10.1103/PhysRevLett.96.245002)
72. Y. Fukuda, A.Y. Faenov, M. Tampo, T.A. Pikuz, T. Nakamura, M. Kando, Y. Hayashi, A. Yogo, H. Sakaki, T. Kameshima, A.S. Pirozhkov, K. Ogura, M. Mori, T.Z. Esirkepov, J. Koga, A.S. Boldarev, V.A. Gasilov, A.I. Magunov, T. Yamauchi, R. Kodama, P.R. Bolton, Y. Kato, T. Tajima, H. Daido, S.V. Bulanov, Phys. Rev. Lett. **103**, 165002 (2009). doi:[10.1103/PhysRevLett.103.165002](https://doi.org/10.1103/PhysRevLett.103.165002)
73. S.V. Bulanov, T.Z. Esirkepov, Phys. Rev. Lett. **98**, 049503 (2007). doi:[10.1103/PhysRevLett.98.049503](https://doi.org/10.1103/PhysRevLett.98.049503)
74. T. Ditmire, J. Zweibaum, V.P. Yanovsky, T.E. Cowan, G. Hays, K.B. Wharton, Nature **398**, 489 (1999). doi:[10.1038/19037](https://doi.org/10.1038/19037)
75. A.Y. Faenov, T.A. Pikuz, Y. Fukuda, M. Kando, H. Kotaki, T. Homma, K. Kawase, T. Kameshima, A. Pirozhkov, A. Yogo, M. Tampo, M. Mori, H. Sakaki, Y. Hayashi, T. Nakamura, S.A. Pikuz, I.Y. Skobelev, S.V. Gasilov, A. Giulietti, C.A. Cecchetti, A.S. Boldarev, V.A. Gasilov, A. Magunov, S. Kar, M. Borghesi, P. Bolton, H. Daido, T. Tajima, Y. Kato, S.V. Bulanov, Appl. Phys. Lett. **95**, 101107 (2009). doi:[10.1063/1.3210785](https://doi.org/10.1063/1.3210785)
76. T. Esirkepov, Y. Sentoku, K. Mima, K. Nishihara, F. Califano, F. Pegoraro, N. Naumova, S. Bulanov, Y. Ueshima, T. Liseikina, V. Vshivkov, Y. Kato, JETP Lett. **70**, 82 (1999). doi:[10.1134/1.568134](https://doi.org/10.1134/1.568134)

77. L. Willingale, S.R. Nagel, A.G.R. Thomas, C. Bellei, R.J. Clarke, A.E. Dangor, R. Heathcote, M.C. Kaluza, C. Kamperidis, S. Kneip, K. Krushelnick, N. Lopes, S.P.D. Mangles, W. Nazarov, P.M. Nilson, Z. Najmudin, Phys. Rev. Lett. **102**, 125002 (2009). doi:[10.1103/PhysRevLett.102.125002](https://doi.org/10.1103/PhysRevLett.102.125002)
78. M. Passoni, A. Zani, A. Sgattoni, D. Dellasega, A. Macchi, I. Prencipe, V. Floquet, P. Martin, T.V. Liseykina, T. Ceccotti, Plasma Phys. Control. Fusion **56**, 045001 (2014). doi:[10.1088/0741-3335/56/4/045001](https://doi.org/10.1088/0741-3335/56/4/045001)
79. B. Hegelich, D. Jung, B. Albright, J. Fernandez, D. Gautier, C. Huang, T. Kwan, S. Letzring, S. Palaniyappan, R. Shah, H.C. Wu, L. Yin, A. Henig, R. Hrlein, D. Kiefer, J. Schreiber, X. Yan, T. Tajima, D. Habs, B. Dromey, J. Honrubia, Nucl. Fusion **51**, 083011 (2011). doi:[10.1088/0029-5515/51/8/083011](https://doi.org/10.1088/0029-5515/51/8/083011)
80. D. Jung, L. Yin, B.J. Albright, D.C. Gautier, S. Letzring, B. Dromey, M. Yeung, R. Hrlein, R. Shah, S. Palaniyappan, K. Allinger, J. Schreiber, K.J. Bowers, H.C. Wu, J.C. Fernández, D. Habs, B.M. Hegelich, New J. Phys. **15**, 023007 (2013). doi:[10.1088/1367-2630/15/2/023007](https://doi.org/10.1088/1367-2630/15/2/023007)
81. P. Antici, J. Fuchs, E. d'Humières, E. Lefebvre, M. Borghesi, E. Brambrink, C.A. Cecchetti, S. Gaillard, L. Romagnani, Y. Sentoku, T. Toncian, O. Willi, P. Audebert, H. Pépin, Physics of Plasmas. **14**, 030701 (2007). doi:[10.1063/1.2480610](https://doi.org/10.1063/1.2480610)
82. B.M. Hegelich, I. Pomerantz, L. Yin, H.C. Wu, D. Jung, B.J. Albright, D.C. Gautier, S. Letzring, S. Palaniyappan, R. Shah, K. Allinger, R. Hrlein, J. Schreiber, D. Habs, J. Blakeney, G. Dyer, L. Fuller, E. Gaul, E. McCary, A.R. Meadows, C. Wang, T. Ditmire, J. C. Fernández, New J. Phys. **15**, 085015 (2013). doi:[10.1088/1367-2630/15/8/085015](https://doi.org/10.1088/1367-2630/15/8/085015)
83. F. Wagner, S. Bedacht, V. Bagnoud, O. Deppert, S. Geschwind, R. Jaeger, A. Ortner, A. Tebartz, B. Zielbauer, D.H.H. Hoffmann, M. Roth, Phys. Plasmas **22**, 063110 (2015). doi:[10.1063/1.4922661](https://doi.org/10.1063/1.4922661)
84. H.W. Powell, M. King, R.J. Gray, D.A. MacLellan, B. Gonzalez-Izquierdo, L.C. Stockhausen, G. Hicks, N.P. Dover, D.R. Rusby, D.C. Carroll, H. Padda, R. Torres, S. Kar, R.J. Clarke, I.O. Musgrave, Z. Najmudin, M. Borghesi, D. Neely, P. McKenna, New J. Phys. **17**, 103033 (2015). doi:[10.1088/1367-2630/17/10/103033](https://doi.org/10.1088/1367-2630/17/10/103033)
85. D. Jung, B.J. Albright, L. Yin, D.C. Gautier, R. Shah, S. Palaniyappan, S. Letzring, B. Dromey, H.C. Wu, T. Shimada, R.P. Johnson, M. Roth, J.C. Fernández, D. Habs, B.M. Hegelich, New J. Phys. **15**, 123035 (2013). doi:[10.1088/1367-2630/15/12/123035](https://doi.org/10.1088/1367-2630/15/12/123035)
86. T. Ditmire, J.W.G. Tisch, E. Springate, M.B. Mason, N. Hay, R.A. Smith, J. Marangos, M.H. R. Hutchinson, Nature **386**, 54 (1997). doi:[10.1038/386054a0](https://doi.org/10.1038/386054a0)
87. S.S. Bulanov, A. Brantov, V.Y. Bychenkov, V. Chvykov, G. Kalinchenko, T. Matsuoka, P. Rousseau, S. Reed, V. Yanovsky, D.W. Litzenberg, K. Krushelnick, A. Maksimchuk, Phys. Rev. E **78**, 026412 (2008). doi:[10.1103/PhysRevE.78.026412](https://doi.org/10.1103/PhysRevE.78.026412)
88. J. Braenzel, A.A. Andreev, K. Platonov, M. Klingsporn, L. Ehrentraut, W. Sandner, M. Schnürer, Phys. Rev. Lett. **114**, 124801 (2015). doi:[10.1103/PhysRevLett.114.124801](https://doi.org/10.1103/PhysRevLett.114.124801)
89. S.V. Bulanov, V. Khoroshkov, Plasma Phys. Rep. **28**, 453 (2002). doi:[10.1134/1.1478534](https://doi.org/10.1134/1.1478534)
90. E. Fourkal, J.S. Li, W. Xiong, A. Nahum, C.M. Ma, Phys. Med. Biol. **48**, 3977 (2003). doi:[10.1088/0031-9155/48/24/001](https://doi.org/10.1088/0031-9155/48/24/001)
91. R.R. Wilson, Radiology **47**, 487 (1946). doi:[10.1148/47.5.487](https://doi.org/10.1148/47.5.487)
92. J. Lawrence, Cancer **10**, 795 (1957). doi:[10.1002/1097-0142\(195707/08\)10:4<795::AID-CNCR2820100426>3.0.CO;2-B](https://doi.org/10.1002/1097-0142(195707/08)10:4<795::AID-CNCR2820100426>3.0.CO;2-B)
93. U. Amaldi, G. Kraft, Rep. Prog. Phys. **68**, 1861 (2005). doi:[10.1088/0034-4885/68/8/R04](https://doi.org/10.1088/0034-4885/68/8/R04)
94. A.R. Smith, Med. Phys. **36**, 556 (2009). doi:[10.1118/1.3058485](https://doi.org/10.1118/1.3058485)
95. G. Kraft, S.D. Kraft, New J. Phys. **11**, 025001 (2009). doi:[10.1088/1367-2630/11/2/025001](https://doi.org/10.1088/1367-2630/11/2/025001)
96. D. Schardt, T. Elsässer, D. Schulz-Ertner, Rev. Mod. Phys. **82**, 383 (2010). doi:[10.1103/RevModPhys.82.383](https://doi.org/10.1103/RevModPhys.82.383)
97. Nuclear Physics European Collaboration Committee (NuPECC), Nuclear physics for medicine. Tech. rep., European Science Foundation (2014)
98. D. Schardt, Nucl. Phys. A **787**, 633 (2007). doi:[10.1016/j.nuclphysa.2006.12.097](https://doi.org/10.1016/j.nuclphysa.2006.12.097)

99. M. Durante, J.S. Loeffler, *Nat. Rev. Clin. Oncol.* **7**, 37 (2010). doi:[10.1038/nrclinonc.2009.183](https://doi.org/10.1038/nrclinonc.2009.183)
100. J. van Loon, J. Grutters, F. Macbeth, *Lancet Oncol.* **13**, e169 (2012). doi:[10.1016/S1470-2045\(11\)70379-5](https://doi.org/10.1016/S1470-2045(11)70379-5)
101. Y. Lievens, M. Pijls-Johannesma, *Semin. Radiat. Oncol.* **23**, 134 (2013). doi:[10.1016/j.semradonc.2012.11.005](https://doi.org/10.1016/j.semradonc.2012.11.005)
102. W. Enghardt, M. Bussmann, T. Cowan, F. Fiedler, M. Kaluza, J. Pawelke, U. Schramm, R. Sauerbrey, A. Tünnermann, M. Baumann, *Proc. SPIE* **8079**, 80791F (2011). doi:[10.1117/12.886861](https://doi.org/10.1117/12.886861)
103. U. Linz, J. Alonso, *Phys. Rev. ST Accel. Beams* **10**, 094801 (2007). doi:[10.1103/PhysRevSTAB.10.094801](https://doi.org/10.1103/PhysRevSTAB.10.094801)
104. S. Schell, J.J. Wilkens, *Med. Phys.* **37**, 5330 (2010). doi:[10.1118/1.3491406](https://doi.org/10.1118/1.3491406)
105. P. Bolton, T. Hori, H. Kiriyama, M. Mori, H. Sakaki, K. Sutherland, M. Suzuki, J. Wu, A. Yogo, *Nucl. Inst. Meth. Phys. Res. A* **620**, 71 (2010). doi:[10.1016/j.nima.2010.01.063](https://doi.org/10.1016/j.nima.2010.01.063)
106. M. Borghesi, S. Kar, R. Prasad, F.K. Kakolee, K. Quinn, H. Ahmed, G. Sarri, B. Ramakrishna, B. Qiao, M. Geissler, S. Ter-Avetisyan, M. Zepf, G. Schettino, B. Stevens, M. Tolley, A. Ward, J. Green, P.S. Foster, C. Spindloe, P. Gallegos, A.L. Robinson, D. Neely, D.C. Carroll, O. Tresca, X. Yuan, M. Quinn, P. McKenna, N. Dover, C. Palmer, J. Schreiber, Z. Najmudin, I. Sari, M. Kraft, M. Merchant, J.C. Jeynes, K. Kirkby, F. Fiorini, D. Kirby, S. Green, *Proc. SPIE* **8079**, 80791E (2011). doi:[10.1117/12.888262](https://doi.org/10.1117/12.888262)
107. F. Schillaci, A. Anzalone, G.A.P. Cirrone, M. Carpinelli, G. Cuttone, M. Cutroneo, C.D. Martinis, D. Giove, G. Korn, M. Maggiore, L. Manti, D. Margarone, A. Musumarra, F.M. Perozziello, I. Petrovic, P. Pisciotta, M. Renis, A. Ristic-Fira, F. Romano, F.P. Romano, G. Schettino, V. Scuderi, L. Torrisi, A. Tramontana, S. Tudisco, *J. Phys: Conf. Ser.* **508**, 012010 (2014). doi:[10.1088/1742-6596/508/1/012010](https://doi.org/10.1088/1742-6596/508/1/012010)
108. U. Masood, M. Bussmann, T. Cowan, W. Enghardt, L. Karsch, F. Kroll, U. Schramm, J. Pawelke, *Appl. Phys. B* **117**, 41 (2014). doi:[10.1007/s00340-014-5796-z](https://doi.org/10.1007/s00340-014-5796-z)
109. URL <http://www.qub.ac.uk/A-SAIL>. A-SAIL project
110. K.W.D. Ledingham, P.R. Bolton, N. Shikazono, C.M.C. Ma, *Appl. Sci.* **4**, 402 (2014). doi:[10.3390/app4030402](https://doi.org/10.3390/app4030402)
111. E. Fourkal, J.S. Li, M. Ding, T. Tajima, C.M. Ma, *Med. Phys.* **30**, 1660 (2003). doi:[10.1118/1.1586268](https://doi.org/10.1118/1.1586268)
112. M. Nishiuchi, H. Sakaki, T. Hori, K. Ogura, A. Yogo, A.S. Pirozhkov, A. Sagisaka, S. Orimo, M. Mori, H. Sugiyama, H. Kiriyama, M. Tambo, I. Daito, H. Okada, S. Kanazawa, M. Tanoue, T. Shimomura, Y. Nakai, H. Sasao, D. Wakai, F. Sasao, P.R. Bolton, H. Daido, S. Kawanishi, Y. Iseki, T. Nagafuchi, K. Maeda, K. Hanawa, T. Yoshiyuki, H. Souda, A. Noda, *J. Phys: Conf. Ser.* **244**, 022051 (2010). doi:[10.1088/1742-6596/244/2/022051](https://doi.org/10.1088/1742-6596/244/2/022051)
113. I. Hofmann, J. Meyer-ter Vehn, X. Yan, A. Orzhevskovskaya, S. Yaramyshev, *Phys. Rev. ST Accel. Beams* **14**, 031304 (2011). doi:[10.1103/PhysRevSTAB.14.031304](https://doi.org/10.1103/PhysRevSTAB.14.031304)
114. K.M. Hofmann, S. Schell, J.J. Wilkens, *J. Biophotonics* **5**, 903 (2012). doi:[10.1002/jbio.201200078](https://doi.org/10.1002/jbio.201200078)
115. S. Faby, J.J. Wilkens, *Zeitschrift fr Medizinische Physik* **25**, 112 (2015). doi:[10.1016/j.zmed.2014.09.002](https://doi.org/10.1016/j.zmed.2014.09.002)
116. E. Fourkal, I. Velchev, J. Fan, W. Luo, C.M. Ma, *Med. Phys.* **34**, 577 (2007). doi:[10.1118/1.2431424](https://doi.org/10.1118/1.2431424)
117. W. Luo, J. Li, E. Fourkal, J. Fan, X. Xu, Z. Chen, L. Jin, R. Price, C.M. Ma, *Phys. Med. Biol.* **53**, 7151 (2008). doi:[10.1088/0031-9155/53/24/010](https://doi.org/10.1088/0031-9155/53/24/010)
118. S. Schell, J.J. Wilkens, *Phys. Med. Biol.* **54**, N459 (2009). doi:[10.1088/0031-9155/54/19/N04](https://doi.org/10.1088/0031-9155/54/19/N04)
119. D.H. Kim, T.S. Suh, Y. Kang, S. Yoo, K.H. Pae, D. Shin, S. Lee, *J. Korean Phys. Soc.* **62**, 59 (2013). doi:[10.3938/jkps.62.59](https://doi.org/10.3938/jkps.62.59)
120. S. Yoo, I. Cho, S. Cho, Y. Song, W.G. Jung, D.H. Kim, D. Shin, S. Lee, K.H. Pae, S. Park, *Australas. Phys. Eng. Sci. Med.* **37**, 635 (2014). doi:[10.1007/s13246-014-0292-7](https://doi.org/10.1007/s13246-014-0292-7)

121. C. Richter, L. Karsch, Y. Dammene, S.D. Kraft, J. Metzkes, U. Schramm, M. Schrer, M. Sobiella, A. Weber, K. Zeil, J. Pawelke, *Phys. Med. Biol.* **56**, 1529 (2011). doi:[10.1088/0031-9155/56/6/002](https://doi.org/10.1088/0031-9155/56/6/002)
122. F. Fiorini, D. Kirby, M. Borghesi, D. Doria, J.C.G. Jeynes, K.F. Kakolee, S. Kar, S. Kaur, K. J. Kirby, M.J. Merchant, S. Green, *Phys. Med. Biol.* **56**, 6969 (2011). doi:[10.1088/0031-9155/56/21/013](https://doi.org/10.1088/0031-9155/56/21/013)
123. K. Zeil, M. Baumann, E. Beyreuther, T. Burris-Mog, T. Cowan, W. Enghardt, L. Karsch, S. Kraft, L. Laschinsky, J. Metzkes, D. Naumburger, M. Oppelt, C. Richter, R. Sauerbrey, M. Schrer, U. Schramm, J. Pawelke, *Appl. Phys. B* **110**, 437 (2013). doi:[10.1007/s00340-012-5275-3](https://doi.org/10.1007/s00340-012-5275-3)
124. S.D. Kraft, C. Richter, K. Zeil, M. Baumann, E. Beyreuther, S. Bock, M. Bussmann, T.E. Cowan, Y. Dammene, W. Enghardt, U. Helbig, L. Karsch, T. Kluge, L. Laschinsky, E. Lessmann, J. Metzkes, D. Naumburger, R. Sauerbrey, M. Schrer, M. Sobiella, J. Woithe, U. Schramm, J. Pawelke, *New J. Phys.* **12**, 085003 (2010). doi:[10.1088/1367-2630/12/8/085003](https://doi.org/10.1088/1367-2630/12/8/085003)
125. A. Yogo, T. Maeda, T. Hori, H. Sakaki, K. Ogura, M. Nishiuchi, A. Sagisaka, H. Kiriyama, H. Okada, S. Kanazawa, T. Shimomura, Y. Nakai, M. Tanoue, F. Sasao, P.R. Bolton, M. Murakami, T. Nomura, S. Kawanishi, K. Kondo, *Appl. Phys. Lett.* **98**, 053701 (2011). doi:[10.1063/1.3551623](https://doi.org/10.1063/1.3551623)
126. D. Doria, K.F. Kakolee, S. Kar, S.K. Litt, F. Fiorini, H. Ahmed, S. Green, J.C.G. Jeynes, J. Kavanagh, D. Kirby, K.J. Kirkby, C.L. Lewis, M.J. Merchant, G. Nersisyan, R. Prasad, K. M. Prise, G. Schettino, M. Zepf, M. Borghesi, *AIP Adv.* **2**, 011209 (2012). doi:[10.1063/1.3699063](https://doi.org/10.1063/1.3699063)
127. J. Bin, K. Allinger, W. Assmann, G. Dollinger, G.A. Drexler, A.A. Friedl, D. Habs, P. Hilz, R. Hoerlein, N. Humble, S. Karsch, K. Khrennikov, D. Kiefer, F. Krausz, W. Ma, D. Michalski, M. Molls, S. Raith, S. Reinhardt, B. Rper, T.E. Schmid, T. Tajima, J. Wenz, O. Zlobinskaya, J. Schreiber, J.J. Wilkens, *Appl. Phys. Lett.* **101**, 243701 (2012). doi:[10.1063/1.4769372](https://doi.org/10.1063/1.4769372)
128. A. Yogo, K. Sato, M. Nishikino, M. Mori, T. Teshima, H. Numasaki, M. Murakami, Y. Demizu, S. Akagi, S. Nagayama, K. Ogura, A. Sagisaka, S. Orimo, M. Nishiuchi, A.S. Pirozhkov, M. Ikegami, M. Tampo, H. Sakaki, M. Suzuki, I. Daito, Y. Oishi, H. Sugiyama, H. Kiriyama, H. Okada, S. Kanazawa, S. Kondo, T. Shimomura, Y. Nakai, M. Tanoue, H. Sasao, D. Wakai, P.R. Bolton, H. Daido, *Appl. Phys. Lett.* **94**, 181502 (2009). doi:[10.1063/1.3126452](https://doi.org/10.1063/1.3126452)
129. M. Folkard, *Int. J. Rad. Biol.* **69**, 729 (1996). doi:[10.1080/095530096145472](https://doi.org/10.1080/095530096145472)
130. S. Auer, V. Hable, C. Greubel, G. Drexler, T. Schmid, C. Belka, G. Dollinger, A. Friedl, *Radiat. Oncol.* **6**, 139 (2011). doi:[10.1186/1748-717X-6-139](https://doi.org/10.1186/1748-717X-6-139)
131. O. Zlobinskaya, C. Siebenwirth, C. Greubel, V. Hable, R. Hertenberger, N. Humble, S. Reinhardt, D. Michalski, B. Röper, G. Multhoff, G. Dollinger, J.J. Wilkens, T.E. Schmid, *Radiat. Res.* **181**, 177 (2014). doi:[10.1667/RR13464.1](https://doi.org/10.1667/RR13464.1)
132. A. Yogo, Biological responses triggered by laser-driven ion beams. This volume
133. E. Fourkal, I. Velchev, C.M. Ma, J. Fan, *Phys. Med. Biol.* **56**, 3123 (2011). doi:[10.1088/0031-9155/56/10/015](https://doi.org/10.1088/0031-9155/56/10/015)
134. P. Wilson, B. Jones, T. Yokoi, M. Hill, B. Vojnovic, *Brit. J. Radiology* **85**, e933 (2012). doi:[10.1259/bjr/17827549](https://doi.org/10.1259/bjr/17827549)
135. M. Fujimoto, K. Matsukado, H. Takahashi, Y. Kawada, S. Ohsuka, S.I. Aoshima, *Rev. Sci. Instrum.* **80**, 113301 (2009). doi:[10.1063/1.3256113](https://doi.org/10.1063/1.3256113)
136. K.W.D. Ledingham, P. McKenna, T. McCanny, S. Shimizu, J.M. Yang, L. Robson, J. Zweit, J.M. Gillies, J. Bailey, G.N. Chimon, R.J. Clarke, D. Neely, P.A. Norreys, J.L. Collier, R. P. Singhal, M.S. Wei, S.P.D. Mangles, P. Nilson, K. Krushelnick, M. Zepf, *J. Phys. D Appl. Phys.* **37**, 2341 (2004). doi:[10.1088/0022-3727/37/16/019](https://doi.org/10.1088/0022-3727/37/16/019)
137. U. Linz, *J. Phys. D Appl. Phys.* **38**, 4256 (2005). doi:[10.1088/0022-3727/38/23/N01](https://doi.org/10.1088/0022-3727/38/23/N01)
138. E. Lefebvre, E. d'Humières, S. Fritzler, V. Malka, *J. Appl. Phys.* **100**, 113308 (2006). doi:[10.1063/1.2362908](https://doi.org/10.1063/1.2362908)

139. S. Kimura, A. Bonasera, Nucl. Inst. Meth. Phys. Res. A **637**, 164 (2011). doi:[10.1016/j.nima.2011.02.043](https://doi.org/10.1016/j.nima.2011.02.043)
140. A. Maksimchuk, A. Raymond, F. Yu, G.M. Petrov, F. Dollar, L. Willingale, C. Zulick, J. Davis, K. Krushelnick, Appl. Phys. Lett. **102**, 191117 (2013). doi:[10.1063/1.4807143](https://doi.org/10.1063/1.4807143)
141. P.A. Norreys, A.P. Fews, F.N. Beg, A.R. Bell, A.E. Dangor, P. Lee, M.B. Nelson, H. Schmidt, M. Tatarakis, M.D. Cable, Plasma Phys. Contr. Fusion **40**, 175 (1998). doi:[10.1088/0741-3335/40/2/001](https://doi.org/10.1088/0741-3335/40/2/001)
142. L. Disdier, J.-P. Garçonnet, G. Malka, J.L. Miquel, Phys. Rev. Lett. **82**, 1454 (1999). doi:[10.1103/PhysRevLett.82.1454](https://doi.org/10.1103/PhysRevLett.82.1454)
143. H. Habara, R. Kodama, Y. Sentoku, N. Izumi, Y. Kitagawa, K.A. Tanaka, K. Mima, T. Yamanaka, Phys. Plasmas **10**, 3712 (2003). doi:[10.1063/1.1593650](https://doi.org/10.1063/1.1593650)
144. H. Habara, K.L. Lancaster, S. Karsch, C.D. Murphy, P.A. Norreys, R.G. Evans, M. Borghesi, L. Romagnani, M. Zepf, T. Norimatsu, Y. Toyama, R. Kodama, J.A. King, R. Snavely, K. Akli, B. Zhang, R. Freeman, S. Hatchett, A.J. MacKinnon, P. Patel, M.H. Key, C. Stoeckl, R. B. Stephens, R.A. Fonseca, L.O. Silva, Phys. Rev. E **70**, 046414 (2004). doi:[10.1103/PhysRevE.70.046414](https://doi.org/10.1103/PhysRevE.70.046414)
145. C. Zulick, F. Dollar, V. Chvykov, J. Davis, G. Kalinchenko, A. Maksimchuk, G.M. Petrov, A. Raymond, A.G.R. Thomas, L. Willingale, V. Yanovsky, K. Krushelnick, Appl. Phys. Lett. **102**, 124101 (2013). doi:[10.1063/1.4795723](https://doi.org/10.1063/1.4795723)
146. S. Fritzler, Z. Najmudin, V. Malka, K. Krushelnick, C. Marle, B. Walton, M.S. Wei, R. J. Clarke, A.E. Dangor, Phys. Rev. Lett. **89**, 165004 (2002). doi:[10.1103/PhysRevLett.89.165004](https://doi.org/10.1103/PhysRevLett.89.165004)
147. S. Karsch, S. Düsterer, H. Schwoerer, F. Ewald, D. Habs, M. Hegelich, G. Pretzler, A. Pukhov, K. Witte, R. Sauerbrey, Phys. Rev. Lett. **91**, 015001 (2003). doi:[10.1103/PhysRevLett.91.015001](https://doi.org/10.1103/PhysRevLett.91.015001)
148. J.M. Yang, P. McKenna, K.W.D. Ledingham, T. McCanny, L. Robson, S. Shimizu, R. P. Singhal, M.S. Wei, K. Krushelnick, R.J. Clarke, D. Neely, P.A. Norreys, J. Appl. Phys. **96**, 6912 (2004). doi:[10.1063/1.1814421](https://doi.org/10.1063/1.1814421)
149. A. Youssef, R. Kodama, M. Tampo, Phys. Plasmas **13**, 030702 (2006). doi:[10.1063/1.2183707](https://doi.org/10.1063/1.2183707)
150. D. Jung, K. Falk, N. Guler, O. Deppert, M. Devlin, A. Favalli, J.C. Fernández, D.C. Gautier, M. Geissel, R. Haight, C.E. Hamilton, B.M. Hegelich, R.P. Johnson, F. Merrill, G. Schaumann, K. Schoenberg, M. Schollmeier, T. Shimada, T. Taddeucci, J.L. Tybo, S.A. Wender, C.H. Wilde, G.A. Wurden, M. Roth, Phys. Plasmas **20**, 056706 (2013). doi:[10.1063/1.4804640](https://doi.org/10.1063/1.4804640)
151. M. Storm, S. Jiang, D. Wertepny, C. Orban, J. Morrison, C. Willis, E. McCary, P. Belancourt, J. Snyder, E. Chowdhury, W. Bang, E. Gaul, G. Dyer, T. Ditmire, R.R. Freeman, K. Akli, Phys. Plasmas **20**, 053106 (2013). doi:[10.1063/1.4803648](https://doi.org/10.1063/1.4803648)
152. M. Roth, D. Jung, K. Falk, N. Guler, O. Deppert, M. Devlin, A. Favalli, J. Fernandez, D. Gautier, M. Geissel, R. Haight, C.E. Hamilton, B.M. Hegelich, R.P. Johnson, F. Merrill, G. Schaumann, K. Schoenberg, M. Schollmeier, T. Shimada, T. Taddeucci, J.L. Tybo, F. Wagner, S.A. Wender, C.H. Wilde, G.A. Wurden, Phys. Rev. Lett. **110**, 044802 (2013). doi:[10.1103/PhysRevLett.110.044802](https://doi.org/10.1103/PhysRevLett.110.044802)
153. L. Willingale, G.M. Petrov, A. Maksimchuk, J. Davis, R.R. Freeman, A.S. Joglekar, T. Matsuoka, C.D. Murphy, V.M. Ovchinnikov, A.G.R. Thomas, L.V. Woerkom, K. Krushelnick, Phys. Plasmas **18**, 083106 (2011). doi:[10.1063/1.3624769](https://doi.org/10.1063/1.3624769)
154. K.L. Lancaster, S. Karsch, H. Habara, F.N. Beg, E.L. Clark, R. Freeman, M.H. Key, J.A. King, R. Kodama, K. Krushelnick, K.W.D. Ledingham, P. McKenna, C.D. Murphy, P.A. Norreys, R. Stephens, C. Stoeckl, Y. Toyama, M.S. Wei, M. Zepf, Phys. Plasmas **11**, 3404 (2004). doi:[10.1063/1.1756911](https://doi.org/10.1063/1.1756911)

155. L. Perkins, B. Logan, M. Rosen, M. Perry, T.D. de la Rubia, N. Ghoniem, T. Ditmire, P. Springer, S. Wilks, Nucl. Fusion **40**, 1 (2000). doi:[10.1088/0029-5515/40/1/301](https://doi.org/10.1088/0029-5515/40/1/301)
156. C. Danson, D. Hillier, N. Hopps, D. Neely, High Power Laser Sci. Eng **3**, e3 (2015). doi:[10.1017/hpl.2014.52](https://doi.org/10.1017/hpl.2014.52)
157. M. Borghesi, A. Bigongiari, S. Kar, A. Macchi, L. Romagnani, P. Audebert, J. Fuchs, T. Toncian, O. Willi, S.V. Bulanov, A.J. Mackinnon, J.C. Gauthier, Plasma Phys. Contr. Fusion **50**, 124040 (2008). doi:[10.1088/0741-3335/50/12/124040](https://doi.org/10.1088/0741-3335/50/12/124040)
158. M. Borghesi, Nucl. Inst. Meth. Phys. Res. A **740**, 6 (2014). doi:[10.1016/j.nima.2013.11.098](https://doi.org/10.1016/j.nima.2013.11.098)

Chapter 11

Biological Responses Triggered by Laser-Driven Ion Beams

Akifumi Yogo

Abstract Laser-induced ion acceleration has potential advantages in terms of compactness and cost, compared with conventional ion accelerators. This feature can lead to future applications in hadron cancer therapy. The other feature of the laser-driven source is the extremely high peak current due mostly to the short duration of a single proton bunch. Typically, single high-intensity laser pulses can produce $10^8 - 10^{11}$ protons per bunch, corresponding to 1–1000 A peak ion currents 1-mm from the target. Recently, some pioneering works have experimentally investigated biological effects of such high-current, short-bunch laser-driven ion beams. In this chapter, we review the latest developments of laser-driven radiation beamlines for biomedical studies and discuss the biological effects triggered by high-current, short-bunch radiation beams.

11.1 Introduction

It has been widely recognized that the use of ion beams in cancer radiotherapy has the physical advantage of delivering longitudinally a more localized dose deposition associated with the well-known Bragg peak phenomenon. Further benefit of the ion beam therapy (IBT) is based on the increased relative biological effectiveness within the Bragg peak region. However, the high capital cost of IBT facilities remains a primary hurdle to a more widespread access to this treatment modality.

Recently, ion acceleration by high-intensity laser has been suggested as a potential, cost-saving alternative technology [1] to conventional ion accelerators for radiotherapy. Comprehensive description on the physics of laser-driven ion acceleration and its clinical application can be found in a recent review article [2]. When a laser pulse of intensity well above 10^{18} W/cm^2 interacts with a thin foil target, a laser-field-driven force accelerates a large number of electrons to relativistic

A. Yogo (✉)

Institute of Laser Engineering, Osaka University, 2-6 Yamadaoka,
Suita, Osaka, Japan
e-mail: yogo-a@ile.osaka-u.ac.jp

velocity. Some of these electrons pass through the thin target and generate a strong electrostatic accelerating field exceeding $1 \text{ MV}/\mu\text{m}$, higher than the acceleration field in conventional accelerators by as much as six orders of magnitude. This mechanism is well known as Target Normal Sheath Acceleration (TNSA) [3–6], which explains several experimental results achieving proton kinetic energies as high as 50 MeV. Nowadays, increasing attention is also devoted to a different mechanism: radiation pressure acceleration (RPA) or Light Sail (LS) scheme [7], where the whole laser-irradiated volume is pushed forward by the radiation pressure of the light. Whatever the acceleration regime, a fundamental question rises, “How does the biological effect of laser-accelerated ions compare to that of ions generated by conventional facilities?” The question is crucial when medical perspectives are considered [8].

The answer is not trivial because some characteristics of a laser-driven ion beams significantly differ from those delivered by conventional accelerators. For example, a unique feature of a laser-driven proton source is to provide extremely high current in a single ion bunches by virtue of both high bunch charge and short duration. The laser-accelerated ions therefore can deliver high single bunch doses. Cowan et al. [9] have shown that irradiation of a target with $\sim 10^{11}$ protons ($>10 \text{ nC}$) produced by a single 30-J laser pulse. The peak proton current reached ~ 10 amperes, assuming that the time duration of the proton bunch was $\sim 1 \text{ ns}$ at 100 mm from the source (i.e. from the laser irradiation spot at the target). Single bunch current can be further increased by using petawatt (PW) laser facilities, including LFEX [10] PW laser on ILE, Osaka University.

It has to be mentioned that investigation on biological effect induced by high intensity radiation was started using electrons; in one of the earliest works, bacterial cells were irradiated with 4×10^{12} rads/s electrons [11], when any laser-driven radiation source had not emerged yet. Nowadays, several investigations have been performed with laser-accelerated electrons [12, 13] and X-rays [14–16]. Recently, triggered by the first attempt to investigate the radiobiological effects for laser-accelerated ions [17] by JAEA (Japan Atomic Energy Agency), this novel field of radiobiology have involved several research groups of Dresden [18–21], Belfast [22, 23], Muenich [24], Extreme Light Infrastructure (ELI) [25, 26] and so on.

One of the most interesting topics is the high dose-rate effect on biological processes. Here, the dose rate indicates the energy deposited by ions in a unit of mass per a unit of time. On the way to the clinical use of laser-accelerated ions, it is inevitably required to determine whether ions irradiated with extremely high dose rate make biological effects different from those induced by low dose-rate ions usually used in the therapy with conventional accelerators. In fact, high dose-rate irradiation with laser-accelerated ion beams could induce *nonlinear* effects.

In this chapter, we discuss the radiobiological effects induced by high-current and short-duration bunch beam of protons accelerated by laser. In the next section, we give a brief overview of IBT from the perspective of physics. In Sect. 11.3, we focus on the experimental investigations performed by JAEA [17, 27, 28] and other facilities using *in vitro* cell samples of human cancer. In Sect. 11.4, we discuss the

criteria to evaluate the possible occurrence of a nonlinear regime affecting the biological processes from the viewpoint of ion-track structure of incident ions. The final section is devoted to conclusions.

11.2 Overview of IBT from a Perspective of Physics

In IBT, the ion (protons and carbon nuclei) beams of 100–300 mega electron volts per nucleon (MeV/u) are sent from outside into the patient's body to reach the cancer affected volume. In this case, the incident ions proceed and release most of their energy at a certain fixed depth in accordance with the ion species and energy. The dose distribution in the body shows a characteristic shape, such as been shown in Fig. 11.1a. Peak in the vicinity of the ion stop end is termed as Bragg peak, which it is possible to match with depth of the cancerous tissues, and greatly reduce the dose delivered to healthy tissues. For example, protons with kinetic energy of 150 MeV/u before the incidence will be decelerated to a few tens of MeV/u in the vicinity of Bragg peak after propagating for about 15 cm inside the body. Figure 11.1b shows the linear energy transfer (LET) of protons and carbons in water, which indicates the energy loss of the ions due to electronic collisions while traversing a unit distance. One can see that the energy of the incident ions decreases from 150 to 15 MeV/u, while the LET increases nearly 10-fold. As a result, Bragg peak is located in the deepest reachable layer. This feature is particularly important. Ion energy of the order of 150 MeV/u is not necessary when reproducing the reaction between ion beam and cancer cells at the Bragg peak; in other words, ions having energy of a few tens of MeV/u or less are suitable for the cell sample

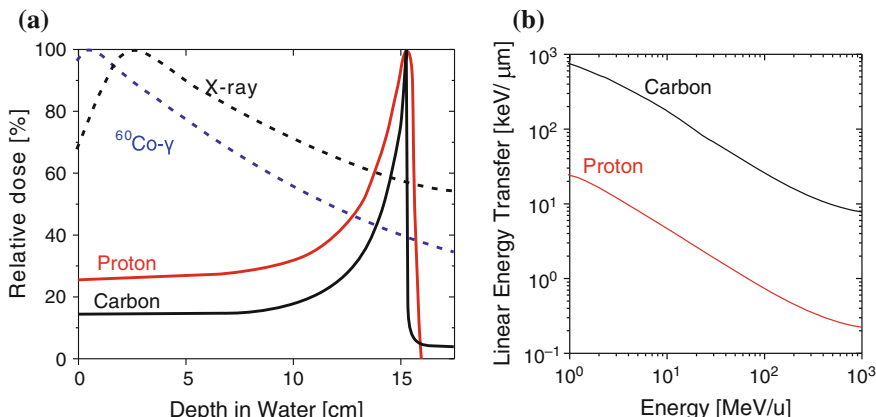


Fig. 11.1 **a** Depth distributions of relative absorption dose calculated for proton, carbon, X-ray and $^{60}\text{Co}-\gamma$ in water. **b** Linear energy transfer (LET) of proton and carbon in water as a function of the kinetic energies in unit of MeV/u

experiment, where ions are directly injected on the cells, without passing through a human body. In recent years, proton of a few tens MeV are obtained stably in many facilities. However, when performing the actual cell-irradiation experiments, there are other problems to be solved also more challenging than the energy of the beam. While introducing the researches at JAEA in the next section, we'll discuss such problems.

11.3 Experimental Investigations

In performing biological studies with laser-driven proton beam, the following points summarizes the main conditions required for a proton beam irradiation apparatus.

1. Laser-driven proton beams generated via TNSA mechanism have a Boltzmann-like continuous energy distribution. Hence, it is necessary to select the energy of the protons arriving at the cell sample. In addition, background radiations (X-ray and electrons) generated from the laser plasma simultaneously with the protons have to be removed from the beam.
2. It is possible to irradiate samples with a given number of protons having a stable energy spectrum over several laser shots, provided energy distribution, number of particles (charge) and the time duration of the proton bunch is evaluated shot by shot.
3. Needless to say, samples cells are alive, and they have to be placed in a medium (culture solution) during the irradiation not to weaken the cells. It is necessary to stop the irradiation before the cells start to repair their DNA damages but, in that time, the dose irradiated must produce measurable biological effects.
4. Considering the usual sample size, the particle beam has to be uniform, in terms of areal density and energy, in an irradiation field of, at least, 5-mm in diameter.
5. If attention is paid to the high dose-rate effects, several protons (two at least, 10 or more, if possible) have to reach the same cell nuclei simultaneously during a single irradiation. Since the typical size of the cancer cell nucleus is about 10–20 μm , an areal proton density of about 10^4 mm^{-2} is necessary.

Among the items above, 1 and 2 are physical conditions, and 3 and 4 are the requirements for a biological experiments. The item 5 is the specific requirements in laser-driven ion irradiation.

In the followings, we describe a laser-driven ion irradiation apparatus for biological studies developed by JAEA in 2008, which resulted in the first demonstration [17] of DNA double-strand breaks of *in vitro* human cancer cells and discuss the potential of the laser-driven ion beam as a short-pulse excitation source for biochemical reactions.

The experiment was performed using the J-KAREN [29] Ti:sapphire laser system at JAEA. The laser pulses of 0.6 J energy and 35 fs duration are focused to reach a peak intensity of $5 \times 10^{19} \text{ W/cm}^2$ onto a thin foil target, which is

continuously fed by a servomotor, providing a ‘fresh’ target surface for each laser shot. The laser pulses are delivered at a repetition rate of 1 Hz. As illustrated in Fig. 11.2a, such intense laser irradiation generates energetic protons that diverge from the rear side of the target with a half-cone angle of $\sim 10^\circ$ with respect to the normal of the foil rear surface. The proton beam has a continuous distribution of the energy up to 2.5 MeV, as illustrated in Fig. 11.3a with a gray line.

Accompanying proton emission, electrons and X-rays are generated simultaneously from the laser-induced plasma. In order to remove electrons and X-rays, a pair of dipole magnets with magnetic fields of 0.04 T oriented antiparallel to each other are used, as shown in Fig. 11.2a. Protons, electrons and X-rays enter the first magnetic field through a 1-mm-wide one-dimensional aperture made on a lead shield. Protons are steered in the opposite direction to that of the electrons, while X-rays propagate straight through along the target normal axis. In this experiment, electron energies are observed to be lower than 2 MeV, corresponding to a Larmor

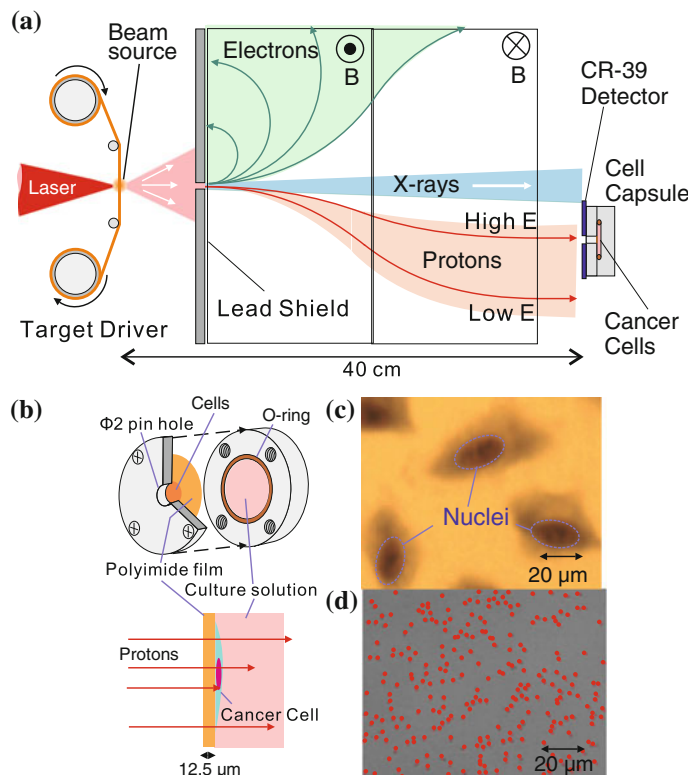


Fig. 11.2 A schematic drawing of the experimental setup [17] (a) and cell capsule (b). **c** An image of cancer cells taken by a microscope. **d** Spatial distribution of protons detected by CR-39 in a single laser shot. Each red point represents a single proton bombardment. The screen size is set to be same as that in the frame **c**

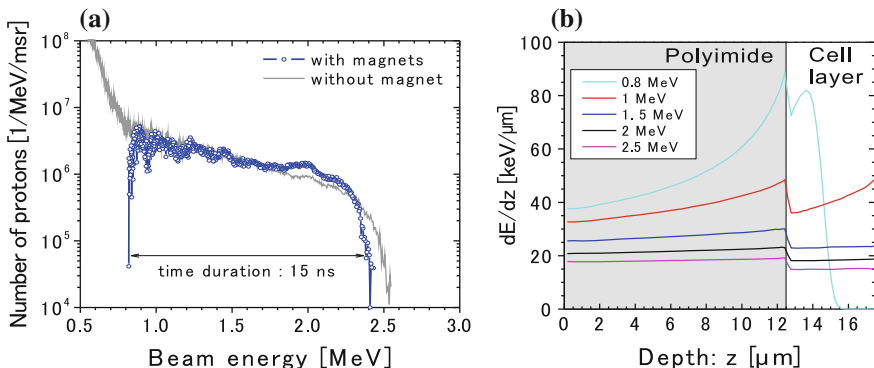


Fig. 11.3 **a** Typical energy spectra of proton beams obtained with the magnetic fields (blue line) and without the magnetic fields (gray line). Each spectrum shows the number of protons obtained in a single laser shot. **b** The results of 3D Monte-Carlo simulations: Distributions of electronic energy loss $d\mathcal{E}/dz$ as a function of the depth z

radius of about 20 cm; meaning that they are completely swept away from the proton beam. On the other hand, the proton trajectory is steered slightly by the first magnetic field, and again by the second one, such that transmitted proton trajectories are laterally displaced from the target normal axis by an energy-dependent distance.

The experimental setup as shown in Fig. 11.2a is placed in a vacuum chamber; and the cancer cell culture to be irradiated is enclosed in a specially designed capsule placed in vacuum with an interface window. As shown in Fig. 11.2b, the capsule consists of a vessel for culture solution and a 12.5- μm -thick polyimide foil window for protons. The foil window and the vessel are sealed by a silicon rubber o-ring that is fixed by screws with a lid having a pin-hole of 2 mm in diameter on its center. The cell sample used is human lung cancer cells: A549 pulmonary adenocarcinoma, the microscopic image of which is shown in Fig. 11.2c. The average cell nucleus size is $\sim 20 \mu m$ and thickness $\sim 5 \mu m$, as determined by a laser-probe microscope (Keyence VK-9700 Generation II). The in vitro A549 cells are cultured directly on the surface of the polyimide foil. Protons irradiate the cells after penetrating the polyimide film. The polyimide foil is strong enough to sustain 1 atmosphere pressure difference across it (the culture solution is in air at 1 atm). During the proton irradiation, the capsule are placed at the exit of the magnet pair, shifting the capsule window by 5 mm from the center axis of the magnets. Consequently only higher-energy protons enter the capsule window and irradiate the cells, as shown in Fig. 11.2b. X-rays emitted from the target emerging around the center axis are cut off by the lead shields. They do not radiate the cell samples.

The energy and number of protons are determined by a time-of-flight (TOF) spectrometer [30] located downstream of the magnets, with the capsule temporarily removed and a different 2-mm-wide aperture placed at the same position as the capsule window. A typical incident energy spectrum obtained at this location

is shown as a blue line in Fig. 11.3a. The figure clearly shows that the energy spectrum loses its lowest-energy components (<0.8 MeV, visible in the gray line spectrum) when the magnets are used. The proton bunch duration at the capsule position is about 15 ns. Protons with the energies above 0.8 MeV can penetrate the polyimide window to irradiate cancer cells. The measured number of protons per bunch varies by less than 20 % (bunch-to-bunch) at the 1 Hz repetitive rate.

The number of protons was corroborated during cell irradiation by an ion-track detector (CR-39), which is covered with another 12.5- μm -thick polyimide foil and placed beside the capsule window. Protons penetrating the foil window impinge on the CR-39, as shown in Fig. 11.2d. Each red point in the image represents the bombardment of one proton, which is visualized with software postprocessing. The screen size ($80 \mu\text{m} \times 110 \mu\text{m}$) is set to be same as that in Fig. 11.1c. The average number of protons per bunch irradiating the cells is measured to be $2.5 \pm 0.5 \times 10^4$ with the energy spread from 0.8 to 2.4 MeV. Then, we are in a high-dose rate regime.

The proton dose is estimated from the measured proton number and energy spectrum per bunch using a Monte-Carlo simulation with the TRIM code [31]. TRIM is a group of programs which calculate the stopping power and range of ions (10 eV–2 GeV/u) in matter using a quantum mechanical treatment of ion-atom collisions. Note that the TRIM code accurately calculates the range and energy loss of ions having lower energies below the region where Bethe-Bloch equation is adopted. The stopping power table used in this work was SRIM2008. Sufficient statistics was achieved by repeating the calculation with 10,000-times injections of protons for each beam energy. The energy loss of the protons are calculated in a 3-dimensional (3D) target consisting of the layers of 12.5- μm -thick polyimide and 5- μm -thick liquid water, which is assumed to be equivalent to the layer of the cancer cells planted on the polyimide-foil window.

Figure 11.3b shows the calculated z dependent proton energy loss distribution $d\mathcal{E}/dz$ (to the target electrons) for several beam energies in the range $\mathcal{E} = 0.8$ to 2.5 MeV. Here, the depth of $z = 0 \mu\text{m}$ represents the entrance (upstream) surface of the polyimide window. Note that protons with energies of $\mathcal{E} = 0.8$ and 2.5 MeV leave the bottom of the polyimide window with energies of 0.16 and 2.17 MeV, respectively, and encounter the cancer cells. For $\mathcal{E} \geq 1.5$ MeV, the electronic energy loss $d\mathcal{E}/dz$ is about 20 keV/ μm in the cell layer ($12.5 \leq z \leq 17.5 \mu\text{m}$). At lower incident energy ($\mathcal{E} = 0.8$ MeV), protons have the highest $d\mathcal{E}/dz$ value and are stopped in the cell layer. The $d\mathcal{E}/dz$ used in this work is equivalent to the linear energy transfer (LET), which is one of the most important and useful parameters to evaluate the dependence on the radiation dose in radiobiological studies. As illustrated in Fig. 11.2a, more than 85 % of the protons have energy above 1 MeV level. Belli et al. [32] has reported that RBE exhibits a strong dependency on the LET of the primary ions: For protons, the RBE takes a maximum with the LET range of 20–30 keV/ μm . Hence, in the present experiment, the cancer cells are irradiated predominantly with protons of energy near the RBE maximum.

The energy E_d deposited on the cell layer is determined by integrating the stopping power according to: $E_d(\mathcal{E}) = \int_{z1}^{z2} (d\mathcal{E}/dz) dz$. Here, $d\mathcal{E}/dz$ is in units of

keV/ μm for each incident beam energy \mathcal{E} and integrated over the cell layer from $z_1 = 12.5 \mu\text{m}$ to $z_2 = 17.5 \mu\text{m}$. Therefore absorbed dose D of a single proton bunch is estimated (in Gy units) by the following relation: $D = \int d\mathcal{E}[E_d(\mathcal{E}) \cdot N(\mathcal{E})]/[(z_2 - z_1) \cdot Q] 1.602 \times 10^{-7}$, where $N(\mathcal{E})$ is the proton fluence distribution at the capsule entrance (in units of $\text{mm}^{-2} \text{ MeV}^{-1}$), and Q is the mass density of liquid water in g/cm^3 . The absorbed dose of protons is determined to be $D \simeq 0.1 \pm 0.02$ in a single laser shot.

DNA double-strand breaks (DSB) induced on A549 are investigated by using phosphorylated histone H2AX immunostaining method. In general, when ionizing radiation induces DNA damage on a cell, histon H2AX, which is one of the histon H2A variants, is phosphorylated by DNA-damage-sensor proteins such as ATM. Subsequently, the proteins involved in the DNA-damage response accumulate on this damage site in order to perform cell-cycle arrest, chromatin remodeling, and DNA repair. In the present work, the cells were incubated at 37°C for 30 min. with CO_2 incubator after the cell irradiation. The cells were subsequently fixed with 95 % methanol for 10 min, rinsed three times with phosphate buffer saline, and blocked with 20 % bovine serum albumin. For immunofluorescence staining of γ -H2AX and nuclear staining, Alexa Fluor 488 conjugated anti- γ -H2AX antibody (#9719, Cell Signaling Technology, MA, Denver) and DAPI (4', 6-diamino-2-phenylindole, Fluka) were used, respectively.

It has been recognized [33] that the H2AX phosphorylation along the DNA strand corresponds only with the site of DSB. Therefore, the remark of phosphorylated H2AX in the nuclei (termed as γ -H2AX focus formation) can be used as a criterion for DNA DSB. Figure 11.4a illustrates the results of γ -H2AX immunofluorescence staining obtained for the proton irradiation with 20 Gy. The proton dose was accumulated with 200 laser shots at a repetition rate of 1 Hz. Here, nuclei and γ -H2AX foci are stained with blue and green, respectively. One can easily find that γ -H2AX focus formation is detected in the nuclei. Moreover, the

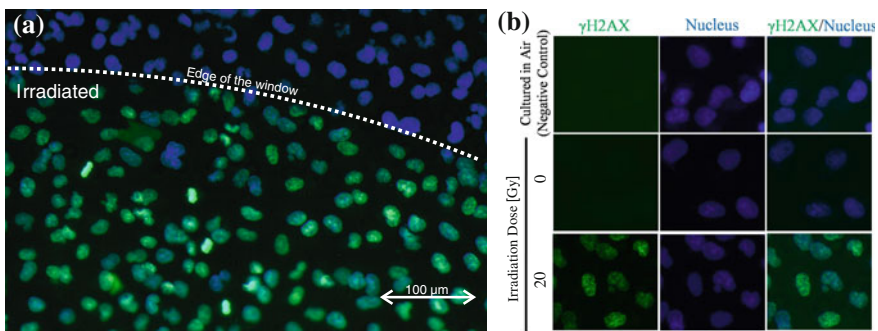


Fig. 11.4 **a** γ -H2AX foci induced by irradiation of laser-accelerated protons with 20 Gy [17]. γ -H2AX and nuclei are stained with anti- γ -H2AX antibody (green) and DAPI (blue). **b** The upper panels show the cells cultured in air. The middle and lower panels show that cells irradiated with 0 and 20 Gy, respectively

region of γ -H2AX positive exhibits a clear boundary along the edge of the capsule window; indicating that γ -H2AX foci are generated only in the nuclei that were irradiated with the protons. Note that γ -H2AX foci are generated independently of the culture condition in the following method: In Fig. 11.4b, the upper panels show the cells cultured in air, where no γ -H2AX focus is observed because the cells have not undergone DNA double-strand breaks. The middle and lower panels show the cells irradiated with 0 and approximately 20 Gy, respectively. Note that in the 0-Gy case the capsule was kept in vacuum for 10 min, which is the time taken for all procedures of the 20-Gy irradiation. One can easily find that γ -H2AX focus formation is detected in the nuclei only for the 20-Gy irradiation. Therefore, we conclude that DNA DSB were induced by the irradiation of the laser-accelerated protons.

Above results are of great significance since they show the laser-generated plasma is positioned as a new acceleration technology in addition to the conventional accelerator to investigate biological responses triggered by fast ion irradiation. However, in these studies, the energy distribution of the proton beam is definitely broad, although the low energy component was removed with the magnetic system. The energy spread of the protons used here leads to a large spread of LET that ranges from 15 to 80 keV/ μm , as shown in Fig. 11.3b. In order to quantitatively evaluate the biological response triggered by laser-driven ions, it is necessary to reduce the energy spread of the beams such an extent that the outcome results can be compared with those obtained with conventional accelerators, which deliver mono-energetic ion beams. Indeed, using the apparatus mentioned above, JAEA group measured the DSB yield for a high flux ($\sim 10^{15} \text{ cm}^{-2}$) single bunch irradiation of laser-accelerated protons [27], shown in Fig. 11.5; however, their discussion remained qualitative because of the energy spread of the beam.

In order to improve the energy resolution of the protons and solve the problem mentioned above, JAEA group drastically rearranged the design of the energy-selection magnets in 2010. The reconstructed setup of the energy-selection system (ESS) [28] for laser-driven ion beams is shown in Fig. 11.6. Laser pulses of 1 J energy and 45 fs duration from the J-KAREN are focused to an intensity of $\sim 5 \times 10^{19}$ onto a polyimide target foil of 7.5- μm -thickness. Compatible with the 1 Hz laser repetition-rate a new target area is provided for each pulse by advancing the foil tape with a servomotor. At the foil source the initial proton spectrum is continuous with a 4 MeV maximum kinetic energy.

The proton beam line consists of four dipole magnets, described by Luo et al. [34] in their design of therapy machine. Each dipole magnet consists of a pair of rectangular permanent magnets, generating a central magnetic field of 0.78 T. The second and third magnetic fields are parallel with each other and oriented antiparallel to the first and fourth ones. Protons are collimated by an entrance pinhole and laterally displaced from the target normal axis in the midplane (midway between the second and third magnets) by the first two magnets. Proton energy and energy spread is set by a movable 5 mm diameter pinhole that is located in this midplane. The final two magnets steer protons back to the target normal axis. The transverse beam

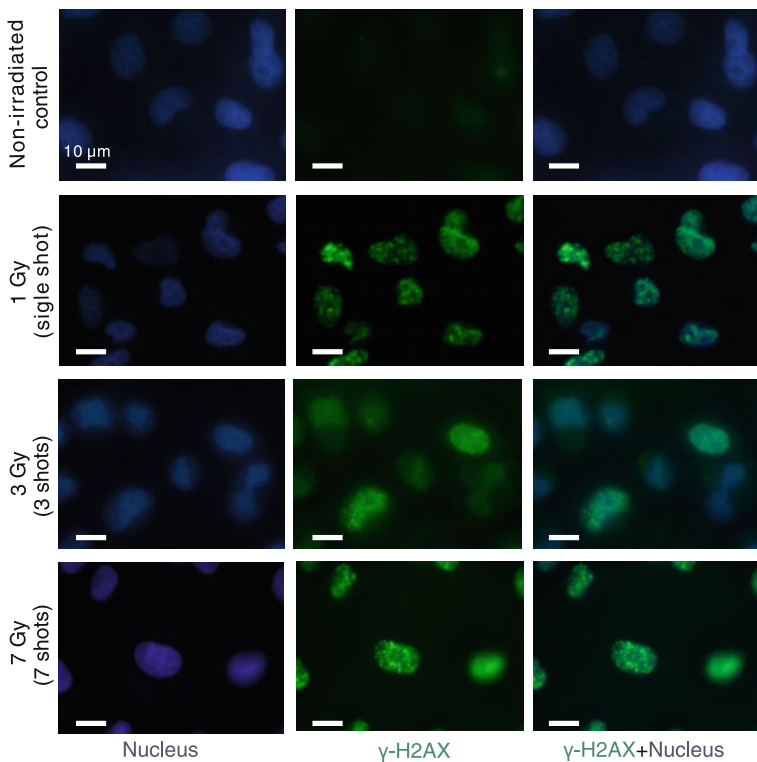


Fig. 11.5 Results of γ -H2AX immunofluorescence microscopy obtained in [27] for the laser-accelerated proton irradiations of 1, 3, and 7 Gy. Bar size: 10 μm

profile is adjusted by a pinhole. The obtained quasi-monochromatic proton spectra are shown in Fig. 11.7 and discussed below. Protons are finally extracted from vacuum into air through a thin polyimide window of 7.5- μm -thickness and 10 mm diameter.

As seen in Fig. 11.6, the capsule of cell samples is located close to the vacuum window. Cell samples are cultured on a polyimide cell dish of 7.5- μm thickness at the bottom of the capsule. To irradiate these cells protons must pass through the first 7.5- μm -thick polyimide vacuum window, 3-mm of laboratory air and the 7.5- μm -thick cell dish, keeping their kinetic energy to be high enough to penetrate the cell monolayer.

Cultured cancer cells from the human salivary gland (HSG cells) were used for all cell experiments. HSG cells are purchased from Human Science Research Resource Bank (HSGc-C5, JCRB 1070). Cells were maintained in Minimum Essential Medium Eagle (SIGMA M4655) supplemented with 10 % fetal calf serum (FCS). Cells were cultured and then harvested with 0.25 % trypsin [Trypsin-EDTA(1X), GI-BACO, 25200] in PBS. They were then seeded in the central part (5 mm in diameter) of the polyimide cell dish at a density of 2×10^5 cells in 50 μl of medium.

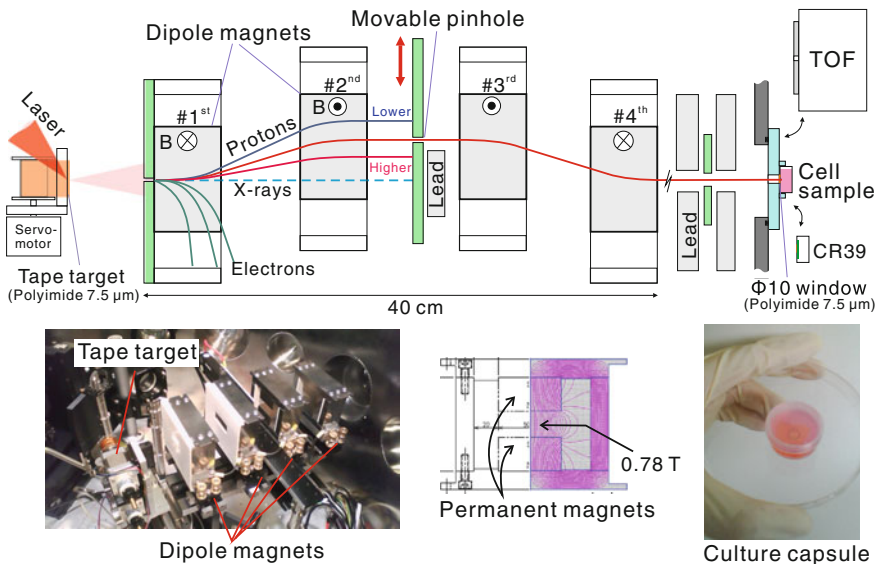


Fig. 11.6 Experimental setup of the laser-driven *quasi-monoenergetic* proton beamline [28] equipped with Energy-Selection System (ESS)

The dishes were cultured for about 1 day at 37 °C in a 5 % CO₂ incubator, and excess medium (5 ml/dish) was added. Consequently cells were cultured only in the central 5-mm region of the dish. After another day of incubation, cell dishes were placed on the bottom of our capsules and new medium was added into the capsules prior to the proton and reference x-ray exposure. The cell capsules used during the irradiation were specially designed for our experiments. The capsule (30 mm in diameter) consisted of a vessel and a lid made of heat-resistant plastic, which were sterilized with an autoclave. Beam irradiation enters through the 7 mm diameter aperture on the bottom, where the polyimide disc is fixed.

The proton energy spectrum transported through the beam line is measured with online single bunch Time-of-Flight (TOF) spectrometry. The TOF detector is equipped with an upstream 5-mm diameter collimator to duplicate the cell capsule aperture. Figure 11.7a shows the tunable quasi-monoenergetic proton spectra transported through the beam line. The central energy could be tuned from 1.5 to 3 MeV by moving the midplane pinhole position laterally between 22 and 10 mm from the target normal axis. 2.25-MeV protons were used for cell irradiation.

To assess the shot-to-shot fluctuation, TOF spectra are recorded for 20 successive laser shots before and after cell irradiation on a single day as seen in Fig. 11.7b and c, respectively (single-shot spectra are superimposed in gray and the averaged spectrum is displayed in black). The shot-to-shot reproducibility of spectral shape is reasonable at 1 Hz. The energy spread of the averaged spectrum is 0.66 MeV (full width at half maximum, FWHM). The variation (standard deviation, σ_{fluc}) of proton number over 20 shots is 12.9 and 12.3 % in Fig. 11.7b and c respectively. This is

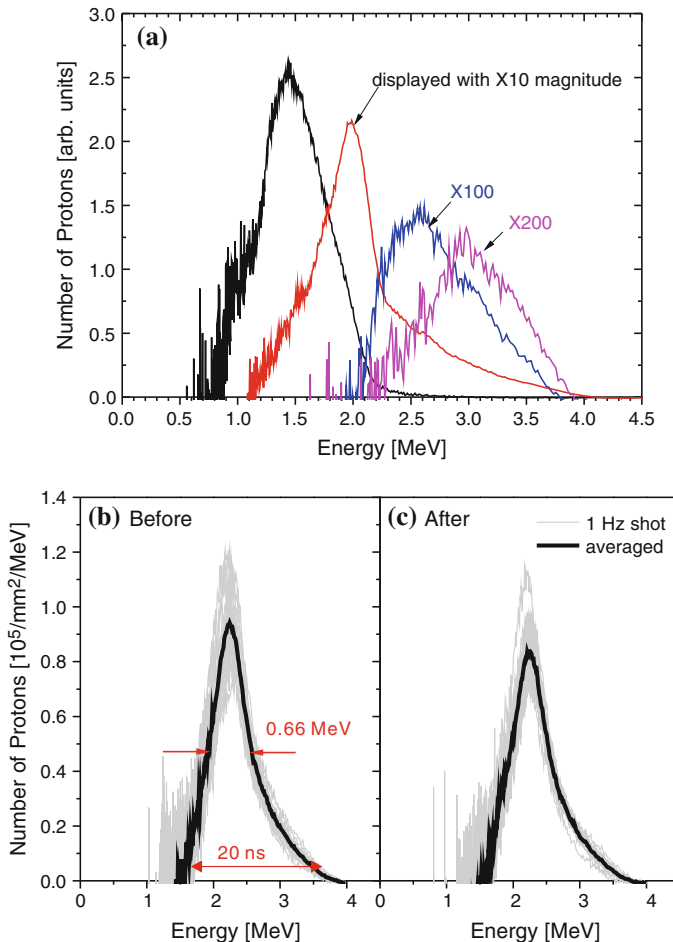


Fig. 11.7 **a** Results of beam-energy selection [28] by the four dipole magnets observed with a TOF spectrometer for different energy tunes. **b, c** Energy spectra of protons monitored before and after cell irradiation

attributed to the short-term variation of the laser intensity. Over the duration of one measurement cycle (that included irradiation of 14 samples and CR-39 measurements) the proton number of the averaged spectra of Fig. 11.7b and c reveal a longer term drift of 10.5 %.

The areal distribution of protons was observed before and after cell irradiation with CR-39 track detector film alternatively placed at the cell sample position. Figure 11.8a displays a CR-39 image (after KOH chemical etching) indicating the proton distribution. The large circular white region, whose diameter matches that of the cell capsule aperture, is induced by proton bombardment of boundary. Cancer cells were located on the center of this proton irradiation field as indicated by the

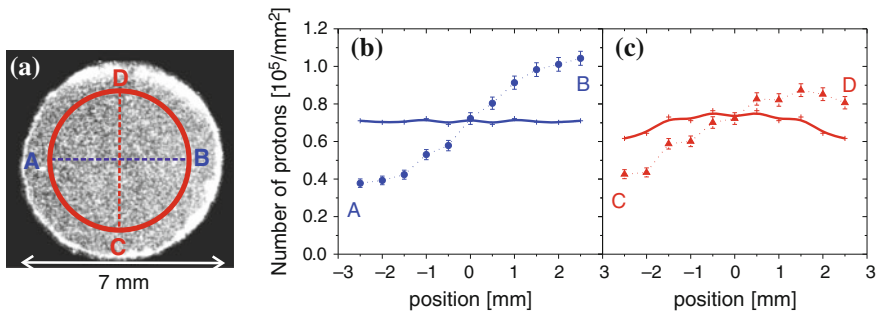


Fig. 11.8 **a** A beam-spot image near the cell sample position (red circle) measured with CR-39. **b, c** The proton areal densities along the axes, A–B and C–D respectively of **a**. The proton distributions used for the cell irradiation using the 180° cell rotation are shown with solid lines

red circle (5 mm in diameter) in the figure. The areal distribution profile is determined by counting the number of proton-induced etch-pits (tracks) with a microscope along the horizontal (A–B) and vertical (C–D) lines of Fig. 11.8a. The distribution of proton areal density is displayed as dots in Fig. 11.8b and c in units of 10⁵/mm² for the A–B and C–D lines respectively. The nonuniform areal proton density distribution is observed as a consequence of tilt. After the first ten of twenty shots the cell capsule was therefore rotated by 180° to reduce this nonuniformity. A more uniform density distribution ($\sigma_{area} = 8.0\%$) was achieved by the rotation as seen in the solid lines of Fig. 11.8b, c for the A–B and C–D lines respectively.

The absorbed dose D integrated over n bunches is determined by the following equation:

$$D[\text{Gy}] = n \int_{\mathcal{E}_0} d\mathcal{E}_0 \cdot \frac{C \cdot N(\mathcal{E}_0) \cdot E_d(\mathcal{E}_0)}{Q\Delta x} \cdot 1.602 \times 10^{-7}. \quad (11.1)$$

Here, $C = 7.20 \times 10^4 \text{ mm}^{-2}$: the averaged density of proton number cross-checked by TOF and CR-39 detectors, $Q = 1 \text{ g/cm}^3$: the mass density of liquid water and $\Delta x = 5 \mu\text{m}$: the thickness of the cell monolayer. \mathcal{E}_0 is the proton energy in vacuum (i.e. before entering the thin-foil window) and $N(\mathcal{E}_0)$ is the normalized energy distribution of protons satisfying $\int N(\mathcal{E}_0) d\mathcal{E}_0 = 1$. We can determine $N(\mathcal{E}_0)$ from the averaged TOF spectrum seen in Fig. 11.7b, c. $E_d(\mathcal{E}_0)$ is the energy that is deposited in the cell layer (in keV units) by protons with energy \mathcal{E}_0 . The dynamics of energy deposition are simulated with the TRIM code [31]. The energy loss of protons are calculated in a multilayer target consisting of the 7.5- μm -thick polyimide window, 3-mm of air, the 7.5- μm -thick polyimide cell dish and 5- μm of liquid water (assumed to be equivalent to the cell monolayer). Typically, protons of $\mathcal{E}_0 = 2.25 \text{ MeV}$ are decelerated down to 1.9 MeV at the entrance of cell layer. From (11.1), the single bunch dose is estimated to be 0.2 Gy corresponding to a single bunch dose rate of 10⁷ Gy/s. At the 1 Hz repetition-rate this amounts to

a duty factor of 2×10^{-8} with an average dose rate of 0.2 Gy/s. We estimate the statistical error of the integrated proton dose (n shots) to be:

$$\Delta D = D \sqrt{(\sigma_{fluc}^2 + \delta^2)/n + \sigma_{area}^2} \quad (11.2)$$

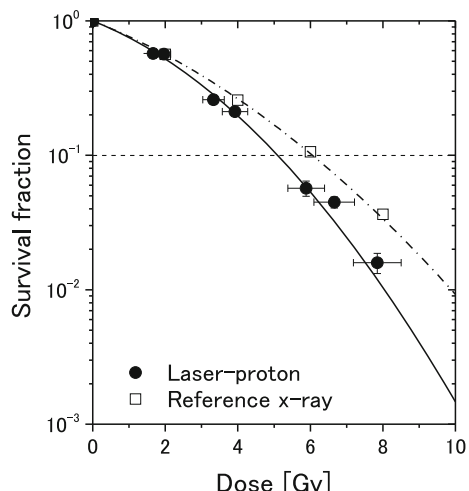
where the first standard deviation, σ_{fluc} (12.9 %) is the shot-to-shot fluctuation of proton number, the second one, δ (10.5 %) is its long term drift and the third one, σ_{area} (8.0 %) is the areal proton density fluctuation.

The proton LET in the cell monolayer is evaluated also with the TRIM. A volume-averaged LET is $\int_{\mathcal{E}_0} d\mathcal{E}_0 N(\mathcal{E}_0) \cdot E_d(\mathcal{E}_0)/\Delta x$. Taking into account the proton energy spread of 0.66 MeV (FWHM), the LET is determined to be $17.1 \pm 2.8 \text{ keV}/\mu\text{m}$.

In order to quantitatively evaluate the radiobiological response triggered by the laser-driven protons, measurements on relative biological effectiveness (RBE) were performed. The RBE, which is one of the most important index of radiobiological response, is the ratio of biological effectiveness of one kind of ionizing radiation relative to another standard radiation, given the same amount of absorbed energy. The RBE value were determined for cell inactivation by laser-accelerated ions, using a colony formation assay: irradiated cells were immediately trypsinized, harvested, counted, and diluted to plate onto triplicate 60-mm-diameter plastic dishes aiming for 50–100 colonies per dish for cell-survival assays. After a 13 days incubation, colonies were fixed by 10 % formalin solution and stained by 1 % methylene blue solution. Any colony consisting of more than 50 cells was counted as a surviving colony. The number of colonies at each dose point was decided as an average of triplicate plates.

Figure 11.9 shows the fraction of surviving cells [28] after the irradiation with the laser-accelerated protons (closed symbols) and a reference x-ray (open symbols)

Fig. 11.9 The fraction of surviving cells after the irradiation with the laser-accelerated protons (closed symbols) and a reference x-ray (open symbols) as a function of dose [28]. For the proton data, the statistical error ΔD is indicated by horizontal bars

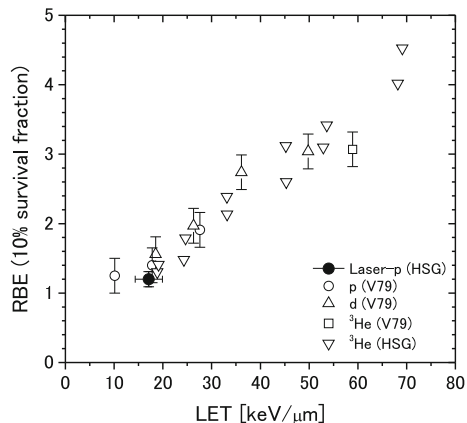


as a function of dose D up to 8 Gy. A 4-MV clinical linac at HIBMC provided the x-ray irradiation [35]. The data obtained are analyzed according to linear-quadratic model [36], where the surviving fraction (SF) is described by the equation, $SF = \exp(-\alpha D - \beta D^2)$. By the curve fits with least-squares method, we determine the parameter values of $\alpha = 0.243 \pm 0.027$ and $\beta = 0.0409 \pm 0.0091$ for the proton data and $\alpha = 0.244 \pm 0.006$ and $\beta = 0.0224 \pm 0.0017$ for the reference X-ray data. In Fig. 11.9, the fit curves are shown with solid (proton) and dotted (X-ray) lines. RBE is evaluated from the dose at the 10 % surviving fraction, $D_{10}(p) = 5.06$ Gy for protons and $D_{10}(x) = 6.06$ Gy for X-rays. Including errors on the proton dose, we determine the RBE value to be $RBE = D_{10}(x)/D_{10}(p) = 1.20 \pm 0.11$ for the laser-accelerated protons with a volume-averaged LET of 17.1 ± 2.8 keV/ μm , mentioned above. It should be emphasized that the RBE value obtained is the first result evaluating the biological response of human cancer cells to the laser-accelerated proton beams.

In Fig. 11.10, we compare the RBE value obtained with the laser-accelerated protons with those obtained using conventional ion accelerators. Folkard et al. [37] obtained an RBE value of 1.4 ± 0.2 for hamster cells (V79) irradiated by protons and deuterons having the LET around 20 keV/ μm . Furusawa et al. [38] obtained, for V79 and HSG cells irradiated with ${}^3\text{He}$ ions, an RBE which is the same as with the laser case. Although it is important to consider the difference between the cell lines, one can find that there is no significant difference between the RBE for V79 and HSG in the results by Furusawa et al. [38]. Therefore, we conclude that there is no evidence of “nonlinear” effect that drastically changes the value of RBE for laser-accelerated 2.15-MeV protons in the region up to $3.6 \times 10^{12} \text{ mm}^{-2} \text{ s}^{-1}$ in beam flux, 1×10^7 Gy/s in dose rate.

In the following section, we discuss the reason why the laser-driven proton beam did not induce nonlinear effects, by considering the interactions between incident MeV ions and DNA molecules in terms of interaction area and time.

Fig. 11.10 The RBE value obtained for cell inactivation by laser-accelerated protons [28] compared with those obtained using conventional ion accelerators [37, 38]



11.4 Discussion: Dose Rate that Can Induce Nonlinear Effect on the Biological Response

In general, MeV ions ionizes and excites electrons while traveling through the material ballistically; they also induces a region of high-excitation along their trajectory. This region is referred to as “ion track”, a central portion of which is ionized or excited by the incident ions directly (track core). The electrons having an excess kinetic energy (secondary electrons) generate an ionized region (penumbra) surrounding the track core.

Figure 11.11 shows a schematic diagrams of ion-cell interactions as a function of time [39]. In radiation chemistry, it is recognized [39, 40] that the chemical transformation induced by the energetic ions continues over a wide time scale ranging from 10^{-13} to 10^{-6} s, when DNAs consisting of biological molecules suffer a several kinds of damages including single- and double-strand breaking, and base-pair damage. In the RBE studies of JAEA [28], $\sim 7.2 \times 10^4$ laser-driven protons irradiate a 1 mm^2 cell-layer, which corresponds to $1 \times 10^7 \text{ Gy/s}$ in dose rate at peak, within a time interval of only 20 ns. In a typical operation of IBT, tumors are irradiated with the beam with flux of $\sim 10^{-4} \text{ mm}^{-2} \text{ ns}^{-1}$ and a proton bunch duration of 0.5 s. The dynamics differ by seven orders of magnitude for these cases, as shown in Fig. 11.11. Therefore, the laser-driven source delivers protons with a proton number comparable to that delivered with 0.5-s-duration pulse in the IBT operation only within 20 ns, which overlaps with the time region in which DNA molecules are damaged by incident ions.

In addition to the discussion on the time scale, we should consider the relationship between the spatial size and number density of ion tracks. According to conventional theoretical models, the radius of track core and penumbra in water, which is a main component of the cell damaging, is expressed in $R_c = 0.67\sqrt{E/A} [\text{nm}]$ [40] and $R_p = 0.0616(E/A)^{1.7} [\mu\text{m}]$ [41], respectively. Here, $E/A [\text{MeV/u}]$ is the kinetic energy of ions per nucleon. In the case of protons of 2 MeV, we obtain $R_c = 0.9 \text{ nm}$, and $R_p = 0.2 \mu\text{m}$. Again considering the number density of incident protons $7.2 \times 10^4 \text{ mm}^{-2}$, we can estimate the average distance between incident protons to be $\sim 2 \mu\text{m}$, which is definitely larger than the outer radius of ion track $R_p = 0.2 \mu\text{m}$. Hence, the ion track of the laser-driven protons are generated simultaneously in the

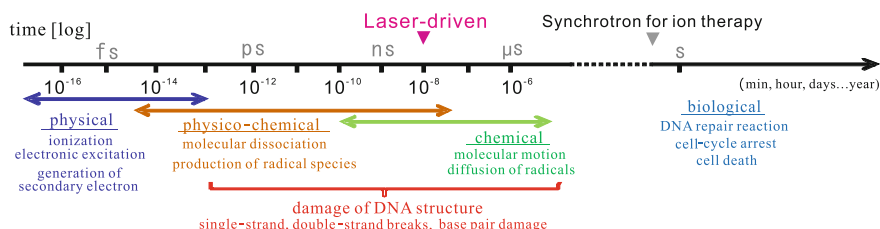


Fig. 11.11 Schematic diagram of ion-matter interactions as a function of time [39]

time scale of chemical reactions, but never overlap spatially each other. Since no nonlinear effects were observed in this condition, we can reach the following criterion: even if more than two ions impinge within a time as short enough as the typical time of DNA damaging, nonlinear biological effects do not occur if the average distance between the ions is larger than the ion track radius.

On the other hand, the group of Belfast [22, 23] investigated the effect of proton irradiation on V79 cells at dose rates exceeding 10^9 Gy/s in a single exposure. As a result, they obtained RBE at 10 % survival of 1.4 ± 0.2 , which is in line with previously published results [37]. The track-core and penumbra radii of their proton beams (5–20 MeV) are estimated to be $R_c = 3$ nm and $R_p = 10$ μm at maximum, respectively, while their proton areal density of 10^6 mm^{-2} corresponds to the average distance between protons of $0.3 \sim 1$ μm . This finding leads to the further conclusion that nonlinear effects are neither induced when the average distance between the ions is smaller than the radius of penumbra. We recall that in the region of penumbra, DNA structures are damaged by the chemical reaction of moving active molecules, such as OH radicals and not damaged directly by the incident ions. Generally, the density of active molecules are considered to decrease as the distance from the ion trajectory increases. It is reasonable that the effective region where DNA damages are frequently generated is narrower than the penumbra region. Recently, Moribayashi [42] theoretically found that the secondary electrons are drawn back by the electric field of the ion track itself. As a result, the penumbra region can be narrower than that assumed in the conventional model [41]. In the author's opinion, still many points remain to be investigated for the ion-track region where DNA damage is predominantly induced. Fourkal et al. [43] theoretically predicted that when the average distance between protons in a cluster is less than or equal to their velocity divided by the characteristic frequency of the collective excitations supported by the medium, the linear stopping power increases and the elevated radiobiological effectiveness may take place. To realize this condition, the proton flux should be 10^{24} $\text{mm}^{-2} \text{s}^{-1}$, an extremely high value which cannot be achieved with the present laser-driven ion sources.

From the experimental results discussed above, we conclude that no nonlinear biological effect can be induced by the protons having a beam flux lower than 10^{15} $\text{mm}^{-2} \text{s}^{-1}$. However there is a general expectation that the rapid progress of the laser-driven particle sources will provide a powerful, novel research tool, allowing in particular to open a novel field of research on radiation biology in the high dose-rate regime.

11.5 Conclusion and Future Prospect

Nonlinear effects on the radiobiological response triggered by laser-accelerated ion beams having a flux lower than 10^{15} $\text{mm}^{-2} \text{s}^{-1}$ were not observed experimentally so far. This limit beam flux corresponds to the dose of about 10 Gy per pulse,

which is nevertheless higher value than dose usually applied to the cancerous organ of patients in IBT, where ions are irradiate tumors for several days with a total amount 20 Gy dose. Thus, one can say that laser-driven proton beams have an equivalent therapeutic effect as the accelerator beam without inducing any nonlinear effect, which might be unfavorable from the perspective of advanced therapy but assures anyway the effectiveness of laser techniques. Recently, several new attempts have been performed toward the realization of cancer therapy by laser-driven beams. Dresden group [44, 45] has performed in vivo studies of laser-driven electron irradiation onto the tumour cells injected in the ear of mice. Design of laser-driven IBT beamlines [34, 44, 45] including radiation safety [46] has been started by several groups. Because IBT machines are required extremely high accuracy on the control of particle energy and irradiation dose, it will be difficult even in future that the therapy device is composed only of laser-driven ion source, without a beamline including energy-selection magnets and radiation shieldings. Anyway, further studies are necessary to demonstrate the feasibility of the cancer therapy with laser-driven ion sources.

References

1. S.V. Bulanov, T. Zh Esirkepov, V.S. Khoroshkov, A.V. Kuznetsov, F. Pegoraro, Oncological hadrontherapy with laser ion accelerators. *Phys. Lett., Sect. A: Gen. Atomic Solid State Phys.* **299**(2–3):240–247 (2002)
2. S.V. Bulanov, J.J. Wilkens, T.Z. Esirkepov, G. Korn, G. Kraft, S.D. Kraft, M. Molls, V.S. Khoroshkov, Laser ion acceleration for hadron therapy. *Phys. Usp.* **57**(12), 1149–1179 (2014)
3. A. Macchi, M. Borghesi, M. Passoni, Ion acceleration by superintense laser-plasma interaction. *Rev. Mod. Phys.* **85**(2), 751–793 (2013)
4. H. Daido, M. Nishiuchi, Alexander S Pirozhkov. Review of laser-driven ion sources and their applications. *Rep Prog Phys.* **75**(5), 056401 (2012)
5. M. Borghesi, M. Roth, Fast ion generation by high intensity laser-irradiation of solid targets and applications. *Fusion Sci. Technol.* **49**, 412–439 (2006)
6. J. Fuchs, P. Antici, E. D’Humières, E. Lefebvre, M. Borghesi, E. Brambrink, C. A. Cecchetti, M. Kaluza, V. Malka, M. Mancossi, S. Meyroneinc, P. Mora, J. Schreiber, T. Toncian, H. Pépin, P. Audebert, Laser-driven proton scaling laws and new paths towards energy increase. *Nat. Phys.* **2**(1), 48–54 (2006)
7. T. Esirkepov, M. Borghesi, S.V. Bulanov, G. Mourou, T. Tajima, Highly efficient relativistic-ion generation in the laser-piston regime. *Phys. Rev. Lett.* **92**(17), 175003 (2004)
8. U. Linz, J. Alonso, What will it take for laser driven proton accelerators to be applied to tumor therapy? *Phys. Rev Spec Top—Accelerators Beams* **10**(9), 094801 (2007)
9. T.E. Cowan, J. Fuchs, H. Ruhl, A. Kemp, P. Audebert, M. Roth, R. Stephens, I. Barton, A. Blazevic, E. Brambrink, J. Cobble, J. Fernández, J.C. Gauthier, M. Geissel, M. Hegelich, J. Kaae, S. Karsch, G.P. Le Sage, S. Letzring, M. Mancossi, S. Meyroneinc, A. Newkirk, H. Pépin, N. Renard-LeGalloudec, Ultralow emittance, multi-MeV proton beams from a laser virtual-cathode plasma accelerator. *Phys. Rev. Lett.* **92**(20), 204801 (2004)
10. J. Kawanaka, N. Miyanaga, H. Azechi, T. Kanabe, T. Jitsuno, K. Kondo, Y. Fujimoto, N. Morio, S. Matsuo, Y. Kawakami, R. Mizoguchi, K. Tauchi, M. Yano, S. Kudo, Y. Ogura, 3.1-kJ chirped-pulse power amplification in the LFEX laser. *J. Phys: Conf. Ser.* **112**(3), 032006 (2008)

11. E.R. Epp, Herbert Weiss, Ann Santomasso, The oxygen effect in bacterial cells irradiated with high-intensity pulsed electrons. *Radiat. Res.* **34**(2), 320–325 (1968)
12. E. Beyreuther, W. Enghardt, M. Kaluza, L. Karsch, L. Laschinsky, E. Lessmann, M. Nicolai, J. Pawelke, C. Richter, R. Sauerbrey, H.P. Schlenvoigt, M. Baumann, Establishment of technical prerequisites for cell irradiation experiments with laser-accelerated electrons. *Med. Phys.* **37**(4), 1392–1400 (2010)
13. L. Laschinsky, M. Baumann, E. Beyreuther, W. Enghardt, M. Kaluza, L. Karsch, E. Lessmann, D. Naumburger, M. Nicolai, C. Richter, R. Sauerbrey, H.-P. Schlenvoigt, J. Pawelke, Radiobiological effectiveness of laser accelerated electrons in comparison to electron beams from a conventional linear accelerator. *J Radiat. Res.* **53**(3), 395–403 (2012)
14. C Tillman, G Grafström, A.C. Jonsson, B.A. Jönsson, I. Mercer, S. Mattsson, S.E. Strand, S. Svanberg, Survival of mammalian cells exposed to ultrahigh dose rates from a laser-produced plasma x-ray source. *Radiology*, **213**(3), 860–865 (1999)
15. K. Shinohara, H. Nakano, N. Miyazaki, M. Tago, R. Kodama, Effects of single-pulse (\leq or ps) X-rays from laser-produced plasmas on mammalian cells. *J. Radiat. Res.* **45**(4), 509–514 (2004)
16. K. Sato, M. Nishikino, Y. Okano, S. Ohshima, N. Hasegawa, M. Ishino, T. Kawachi, H. Numasaki, T. Teshima, H. Nishimura, g-H2AX and phosphorylated ATM focus formation in cancer cells after laser plasma X irradiation. *Radiat. Res.* **174**(4), 436–445 (2010)
17. A. Yogo, K. Sato, M. Nishikino, M. Mori, T. Teshima, H. Numasaki, M. Murakami, Y. Demizu, S. Akagi, S. Nagayama, K. Ogura, A. Sagisaka, S. Orimo, M. Nishiuchi, a. S. Pirozhkov, M. Ikegami, M. Tampo, H. Sakaki, M. Suzuki, I. Daito, Y. Oishi, H. Sugiyama, H. Kiriyama, H. Okada, S. Kanazawa, S. Kondo, T. Shimomura, Y. Nakai, M. Tanoue, H. Sasao, D. Wakai, P. R. Bolton, H. Daido, Application of laser-accelerated protons to the demonstration of DNA double-strand breaks in human cancer cells. *Appl. Phys. Lett.* **94**(18), 181502 (2009)
18. S.D. Kraft, C. Richter, K. Zeil, M. Baumann, E. Beyreuther, S. Bock, M. Bussmann, T.E. Cowan, Y. Dammene, W. Enghardt, U. Helbig, L. Karsch, T. Kluge, L. Laschinsky, E. Lessmann, J. Metzkes, D. Naumburger, R. Sauerbrey, M. Schüller, M. Sobiella, J. Woithe, U. Schramm, J. Pawelke, Dose-dependent biological damage of tumour cells by laser-accelerated proton beams. *New J. Phys.* **12**(8), 085003 (2010)
19. C. Richter, L. Karsch, Y. Dammene, S.D. Kraft, J. Metzkes, U. Schramm, M. Schüller, M. Sobiella, A. Weber, K. Zeil, J. Pawelke, A dosimetric system for quantitative cell irradiation experiments with laser-accelerated protons. *Phys Med. Biol.* **56**(6), 1529–1543 (2011)
20. K. Zeil, M. Baumann, E. Beyreuther, T. Burris-Mog, T.E. Cowan, W. Enghardt, L. Karsch, S. D. Kraft, L. Laschinsky, J. Metzkes, D. Naumburger, M. Oppelt, C. Richter, R. Sauerbrey, M. Schüller, U. Schramm, J. Pawelke, Dose-controlled irradiation of cancer cells with laser-accelerated proton pulses. *Appl. Phys. B: Lasers Opt.* **110**, 437–444 (2013)
21. J. Metzkes, L. Karsch, S.D. Kraft, J. Pawelke, C. Richter, M. Schüller, M. Sobiella, N. Stiller, K. Zeil, U. Schramm, A scintillator-based online detector for the angularly resolved measurement of laser-accelerated proton spectra. *Rev. Sci. Instrum.* **83**(12), 123301 (2012)
22. D. Doria, K.F. Kakolee, S. Kar, S.K. Litt, F. Fiorini, H. Ahmed, S. Green, J.C.G. Jeynes, J. Kavanagh, D. Kirby, K.J. Kirkby, C.L. Lewis, M.J. Merchant, G. Nersisyan, R. Prasad, K. M. Prise, G. Schettino, M. Zepf, M. Borghesi, Biological effectiveness on live cells of laser driven protons at dose rates exceeding 109 Gy/s. *AIP Adv.* **2**(1), 011209 (2012)
23. F. Fiorini, D. Kirby, M. Borghesi, D. Doria, J.C. Jeynes, K. Kakolee, S. Kar, S. Kaur, K. J. Kirby, M.J. Merchant, Dosimetry and spectral analysis of a radiobiological experiment using laser-driven proton beams. *Phys. Med. Biol.* **56**, 6969–6982 (2011)
24. J. Bin, K. Allinger, W. Assmann, G. Dollinger, G.A. Drexl, A.A. Friedl, D. Habs, P. Hilz, R. Hoerlein, N. Humble, S. Karsch, K. Khrennikov, D. Kiefer, F. Krausz, W. Ma, D. Michalski, M. Molls, S. Raith, S. Reinhardt, B. Röper, T.E. Schmid, T. Tajima, J. Wenz, O. Zlobinskaya, J. Schreiber, J.J. Wilkens, A laser-driven nanosecond proton source for radiobiological studies. *Appl. Phys. Lett.* **101**(24), 243701 (2012)

25. V. Scuderi, S. Bijan Jia, M. Carpinelli, G.A. P. Cirrone, G. Cuttone, G. Korn, T. Licciardello, M. Maggiore, D. Margarone, P. Pisciotta, F. Romano, F. Schillaci, C. Stancampiano, A. Tramontana, Development of an energy selector system for laser-driven proton beam applications. *Nucl. Instrum. Meth. Phys. Res. Sect. A: Accelerators, Spectrometers, Detectors and Associated Equipment*, **740**, 87–93 (2014)
26. G.A.P. Cirrone, M. Carpinelli, G. Cuttone, S. Gammino, S. Bijan Jia, G. Korn, M. Maggiore, L. Manti, D. Margarone, J. Prokupek, M. Renis, F. Romano, F. Schillaci, B. Tomasello, L. Torrisi, A. Tramontana, A. Velyhan, ELIMED, future hadrontherapy applications of laser-accelerated beams. *Nucl. Instr. Meth. Phys. Res. Sect. A: Accelerators, Spectrometers, Detectors and Associated Equipment*, **730**, 174–177 (2013)
27. A. Yogo, K. Sato, M. Nishikino, T. Maeda, H. Sakaki, T. Hori, K. Ogura, M. Nishiuchi, T. Teshima, H. Nishimura, K. Kondo, P.R. Bolton, S. Kawanishi. Measurement of DNA double-strand break yield in human cancer cells by high-current, short-duration bunches of laser-accelerated protons. *Japanese J. Appl. Phys.* **50**(10 PART 1), 106401 (2011)
28. A. Yogo, T. Maeda, T. Hori, H. Sakaki, K. Ogura, M. Nishiuchi, A. Sagisaka, H. Kiriyama, H. Okada, S. Kanazawa, T. Shimomura, Y. Nakai, M. Tanoue, F. Sasao, P.R. Bolton, M. Murakami, T. Nomura, S. Kawanishi, K. Kondo, Measurement of relative biological effectiveness of protons in human cancer cells using a laser-driven quasimonoenergetic proton beamline. *Appl. Phys. Lett.* **98**(5), 053701 (2011)
29. H. Kiriyama, M. Mori, Y. Nakai, T. Shimomura, H. Sasao, M. Tanoue, S. Kanazawa, D. Wakai, F. Sasao, H. Okada, I. Daito, M. Suzuki, S. Kondo, K. Kondo, A. Sugiyama, P.R. Bolton, A. Yokoyama, H. Daido, S. Kawanishi, T. Kimura, T. Tajima. High temporal and spatial quality petawatt-class Ti:sapphire chirped-pulse amplification laser system. *Opt. Lett.* **35**(10), 1497–1499 (2010)
30. A. Yogo, H. Daido, A. Fukumi, Z. Li, K. Ogura, A. Sagisaka, A.S. Pirozhkov, S. Nakamura, Y. Iwashita, T. Shirai, A. Noda, Y. Oishi, T. Nayuki, T. Fujii, K. Nemoto, I.W. Choi, JHee Sung, D.K. Kyeong Ko, J. Lee, M. Kaneda, A. Itoh. Laser prepulse dependency of proton-energy distributions in ultraintense laser-foil interactions with an online time-of-flight technique. *Phys. Plasmas*, **14**(4), 043104 (2007)
31. J.F. Ziegler, J.P. Biersack, M.D. Ziegler. *SRIM, The Stopping and Range of ions in Matter*. SRIM Company, 2008
32. M. Belli, R. Cherubini, S. Finotto, G. Moschini, O. Sapora, G. Simone, M.A. Tabocchini. RBE-LET relationship for the survival of V79 cells irradiated with low energy protons. *Int. J. Radiat. Biol.* **55**(1), 93–104 (1989)
33. J.A. Downs, Michel C Nussenzweig, and André Nussenzweig. Chromatin dynamics and the preservation of genetic information. *Nature*, **447**(7147):951–958 (2007)
34. W. Luo, E. Fourkal, J. Li, C.-M. Ma, Particle selection and beam collimation system for laser-accelerated proton beam therapy. *Med. Phys.* **32**(3), 794–806 (2005)
35. K. Kagawa, M. Murakami, Y. Hishikawa, M. Abe, T. Akagi, T. Yanou, G. Kagiya, Y. Furusawa, K. Ando, K. Nojima, M. Aoki, T. Kanai, Preclinical biological assessment of proton and carbon ion beams at Hyogo Ion Beam Medical Center. *Int. J. Radiat. Oncol. Biol. Phys.* **54**(3), 928–938 (2002)
36. B.G. Douglas, J.F. Fowler, The effect of multiple small doses of x rays on skin reactions in the mouse and a basic interpretation. *Radiat. Res.* **66**(2), 401–426 (1976)
37. M. Folkard, K.M. Prise, B. Vojnovic, H.C. Newman, M.J. Roper, B.D. Michael, Inactivation of V79 cells by low-energy protons, deuterons and helium-3 ions. *Int. J. Radiat. Biol.* **69**(6), 729–738 (1996)
38. Y. Furusawa, K. Fukutsu, M. Aoki, H. Itsukaichi, K. Eguchi-Kasai, H. Ohara, F. Yatagai, T. Kanai, K. Ando, Inactivation of aerobic and hypoxic cells from three different cell lines by accelerated (3)He-, (12)C- and (20)Ne-ion beams. *Radiat. Res.* **154**(5), 485–496 (2000)
39. M. Burton, J.L. Magee. (eds.), *Advances in radiation chemistry*. vol 1, (1969)
40. R D Cooper and R W Wood. Physical mechanisms in radiation biology. Technical Report CONF 721001 (1974)

41. J. Kiefer, H. Straaten, A model of ion track structure based on classical collision dynamics. *Phys. Med. Biol.* **31**(11), 1201–1209 (1986)
42. K. Moribayashi, Incorporation of the effect of the composite electric fields of molecular ions as a simulation tool for biological damage due to heavy ion irradiation II. *AIP Conf. Proc.* **1465**, 241–245 (2012)
43. E. Fourkal, I. Velchev, C.-M. Ma, J. Fan, Linear energy transfer of proton clusters. *Phys. Med. Biol.* **56**(10), 3123–3136 (2011)
44. U. Masood, M. Bussmann, T.E. Cowan, W. Enghardt, L. Karsch, F. Kroll, U. Schramm, J. Pawelke. A compact solution for ion beam therapy with laser accelerated protons. *Appl. Phys. B.* 41–52 (2014)
45. K.M. Hofmann, S. Schell, J.J. Wilkens, Laser-driven beam lines for delivering intensity modulated radiation therapy with particle beams. *AIP Conf. Proc.* **1546**(11), 81–83 (2013)
46. Sebastian Faby, Jan J. Wilkens, Assessment of secondary radiation and radiation protection in laser-driven proton therapy. *Zeitschrift für Medizinische Physik* **25**(2), 112–122 (2015)

Chapter 12

High Resolution Ion and Electron Beam Radiography with Laser-Driven Clustered Sources

Anatoly Faenov, Tatiana Pikuz and Ryosuke Kodama

Abstract The unique properties of protons, multicharged ions and electron beams generated by high-intensity laser-matter interactions, especially in terms of spatial quality and temporal duration, have opened up a totally new area of radiography applications. We present and discuss here methods and recent results obtained with laser-driven protons, multicharged ions and electrons. In particular, high resolution radiography with multicharged ions and electron beams using a femtosecond laser-driven-cluster-based source will be discussed. This novel techniques are suitable for a wide range of applications including biomedical ones.

12.1 Introduction

It is well known that a beam of X-rays could penetrate matter and produce radiography that reveals the core of objects. Today, X-radiography is an indispensable tool for medicine, industry, and science. Also proton and electron beams have been widely used for effective radiography of some specific objects. The use of ion beams, and especially proton beams, for radiographic applications as a counterweight or in addition to the X-ray, was first proposed in the 1960s. Indeed, positively charged constituents of atomic nuclei are able to penetrate thick materials more effectively

A. Faenov (✉) · R. Kodama

Institute for Academic Initiatives, Osaka University, Suita, Osaka 565-0871, Japan
e-mail: anatolyf@hotmail.com

R. Kodama

e-mail: kodama@eei.eng.osaka-u.ac.jp

A. Faenov · T. Pikuz

Joint Institute for High Temperatures, RAS, Moscow 125412, Russia

T. Pikuz

Graduate School of Engineering, Osaka University, 2-1, Yamadaoka, Suita,
Osaka 565-0871, Japan

R. Kodama

PPC and GSE Osaka University, 2-1, Yamadaoka, Suita, Osaka 565-0871, Japan

than X-rays. Quasi-monochromatic beams of ions from conventional accelerators have been successfully used for detecting areal density variations in samples, with spatial resolution. However, the cost of conventional accelerators is rather high. Additionally, there are sometimes problems with using externally-produced high energy particle beams for radiography of various objects. In particular, this is the case of time-resolved radiography of mega bar shocks generated by laser interaction with matter. Another serious disadvantage of conventional proton accelerators is the relatively long duration of ion pulses, which has limited the application of such diagnostic techniques. The unique properties of protons produced by high-intensity lasers, especially in terms of spatial quality and temporal duration, have opened up a totally new area of proton/multicharged ions radiography applications (see, for example, [1–3]).

In this Chapter, the main results of laser-driven proton and electron radiography for different applications will be briefly reviewed. In particular, results of high resolution multicharged ions and electron beams radiography using femtosecond laser-driven-cluster-based plasma sources will be presented.

12.2 Laser-Accelerated Proton/Ion Beams Applied to Radiography of Solids and Plasmas

The high quality of proton radiography with laser techniques was achieved by exploiting the energy deposition properties of the particles in matter through a number of different methods: differential stopping radiography; marginal range radiography, which is based on the enhanced sensitivity of ions to areal density variations toward the end of their range; and scattering radiography, which exploits the intensity pattern created via scattering in the ion beam intensity cross section for samples with thickness smaller than the stopping range. One of such promising imaging methods is the point projection technique using protons or multicharged ions produced by short, intense laser pulse irradiation of solid targets [4–19] and below some important results, using this radiography technique, will be discussed.

Applying point projection proton radiography technique allowed already to demonstrate the possibility of obtaining high contrast images with spatial resolution 2–3 μm [4]. It provides a new diagnostic capability to study inertial-confinement-fusion (ICF) and high-energy-density (HED) plasmas. For example, proton point projection radiography of laser-driven implosion was successfully used to characterize the density gradients at different times through the implosion, and to demonstrate asymmetries of implosion both during the early and stagnation stages of implosion [7]. Some very important physical features for understanding the target normal sheath acceleration (TNSA) mechanism of proton acceleration under irradiation of solid targets by short relativistic intensities laser pulses have been discovered with this method [8]. In such experiments, the structure of the electric field driving the expansion of the proton beam has been resolved by proton radiography with high spatial and temporal resolution. It allowed to provide the

experimental evidence of an initial intense sheath field and a late time field peaking at the beam front, and, to show that experimental data are consistent with the results from particle-in-cell and fluid simulations of thin plasma expansion in vacuum.

Further examples of important, ICF related, studies are presented in [9, 10]. They include time-resolved measurements of the mass distribution and electromagnetic field structures using target normal sheath acceleration (TNSA) for a proton backscatterer. It was experimentally demonstrated the appearance of Rayleigh-Taylor-induced magnetic fields due to the Biermann battery effect. Proton radiography experiments [11] clarified the physics behind the gas filling effect of capsules for indirect-drive implosions. They demonstrated the roles of spontaneously generated electric and magnetic fields in hohlraum dynamics and capsule implosions. Additionally, proton radiography shows the spatial structure and temporal evolution of plasma blowing off from a hohlraum wall. It revealed how the filling gas counteracts the wall blow-off, inhibits plasma jet formation, and impedes plasma stagnation in the hohlraum. Such important effects as inhibition of the heat transfer from the gas region in the laser beam paths to the surrounding cold gas, resulting in a local plasma temperature increase, were demonstrated. The experiments additionally show that interpenetration and mixing of the two materials (gas and wall) occur due to the classical Rayleigh–Taylor instability as the lighter, decelerating ionized fill gas pushes against the heavier, expanding gold wall blow-off.

Another important application of point projection proton radiography is investigation of the magnetic field dynamics of a solid target irradiated with a relativistic intensity picosecond laser pulses [12]. The spatial and temporal resolution of proton radiography permitted to show that toroidal magnetic field with amplitude of tens megagauss generated at both sides of a laser irradiated foil. It was demonstrated that such magnetic fields are strong enough to effectively confine the radial expansion of the plasma region where they are generated. Since such a self-confining effect qualitatively resembles the collimation of astrophysical jets, it was proposed to investigate similar mechanisms in down-scaled laboratory experiments. The actual experiment [13] performed temporally and spatially resolved measurements of the precursory stages that lead to the formation of an unmagnetized, supercritical collisionless shock in a laser-produced laboratory plasma. It was found that the measured evolution of the electrostatic potential associated with the shock unveils the transition from a current free double layer into a symmetric shock structure, stabilized by ion reflection at the shock front, which is analogous to ion reflection at supercritical collisionless shocks in supernova remnants.

Observation of side-view time sequence of proton radiographic images [14] enables showing of a unique phenomenon—the evolution of self-organized electromagnetic field structures in counter-streaming plasmas. These structures persist for thousands of ion- and tens of thousands of electron-kinetic timescales. Relation between electric and magnetic field structures and their proton radiography images was considered in detail in [15] and permitted a more clear understanding of the formation of proton images in the limits of weak and strong intensity variations; caustic formation and structure; image inversion to obtain line-integrated field characteristics; direct relations between images and electric or magnetic field

structures in a plasma; imaging of sharp features such as Debye sheaths and shocks, limitations on spatial and temporal resolution and similarities with optical shadowgraphy.

Another aim, which is very important currently for the material science, medicine and nano-industry studies is the development of methods and tools for radiography and diagnosis of low-contrast, ultra-thin objects with submicron resolution. Probing fluxes of energetic photons (X-ray radiography), as well as of massive particles (ionography), are usually used for such imaging. In the stopping radiography mode, the best contrast and spatial resolution will be provided if the stopping range of the probing particles slightly exceeds the thickness of the sample, and the latter is placed in contact with the detector. The particles need enough energy to penetrate through the sample and reach the detector, which means that for several micron-thick samples, the energy of the probe particles should be in the range of hundreds of eV for X-ray photons and sub-MeV for ions. Until recently, X-ray and proton/ion radiography of micro and nano-objects, required large and expensive facilities such as synchrotrons or heavy proton or ion accelerators. Now, they can be successfully replaced by compact femtosecond laser facilities.

12.3 Features of Laser-Cluster Compared with Laser-Solid and Laser-Gas Interactions

One of the most promising approaches for production of multicharged ions with some hundreds keV energies is the utilization of femtosecond laser pulses coupled with gas-cluster targets [20–39]. Indeed, the interaction of short intense laser pulses with clusters enhances absorption of the incident laser light compared with solid targets (see Fig. 12.1).

Due to the increased absorption, these targets are heated significantly, leading to enhanced emission of X-rays, generation of fast electrons, and multiply-charged ions with kinetic energies from tens of KeV to tens of MeV (see also Fig. 12.2).

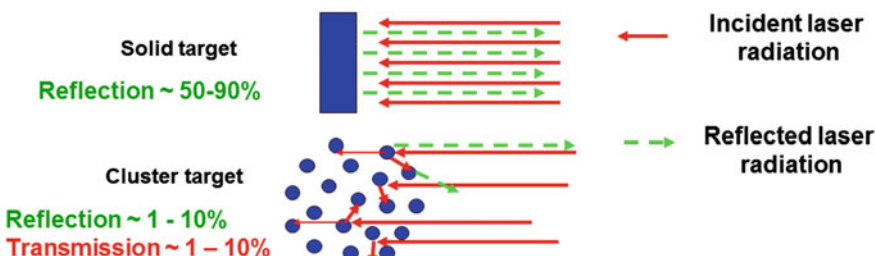


Fig. 12.1 The main feature of laser-cluster interaction, compared with laser-solid or laser-cluster interaction is higher absorption, i.e. more energy delivered to each atom or molecule

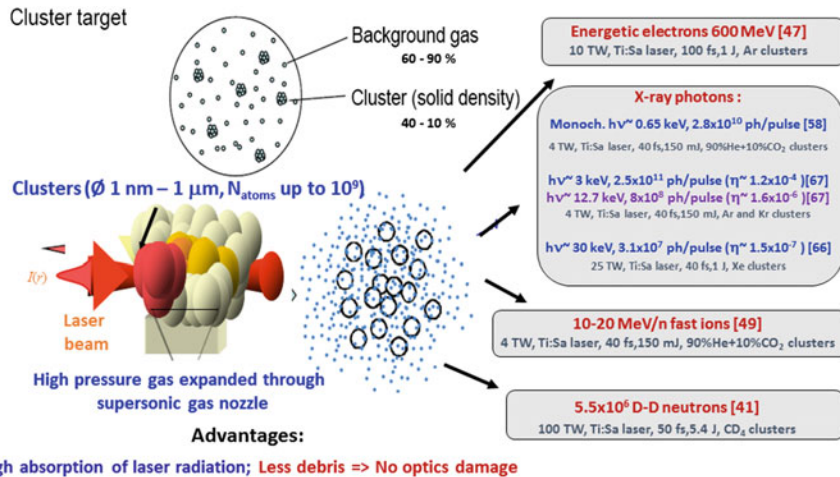


Fig. 12.2 The main advantages of laser-cluster interaction, which make clusterized media promising for many practical applications

This allows for the use of new approaches for solving a number of applied problems, such as the initiation of nuclear reactions [40–46], the acceleration of electrons and heavy particles [22, 23, 39, 47–57], and the creation of a bright X-ray emission source for medical, biological, and lithographic studies [58–70].

For effective laser-cluster interaction it is necessary to use significantly large clusters, because the ultrashort laser pulse is always accompanied by prepulses, which usually have complex temporal structures. The contrast of the laser pulse, i.e., the ratio of the peak power of the main laser pulse to the power of the prepulses is usually of the order of 10^4 – 10^6 (to get better contrast special devices are needed). This means that, if the main pulse is fairly intense (experiments are usually performed at the intensities of $I_{\text{las}} > 10^{17}$ – 10^{20} W/cm^2), the intensity of the prepulse is not lower than 10^{13} – 10^{14} W/cm^2 and is sufficient to destroy the clusters, even before the arrival of the main pulse. It is obvious, that one of the solutions to such a problem is enhancing the laser contrast up to the level of 10^{10} – 10^{12} (see for example [71]). But even in this case, the level of the laser prepulse in the picosecond scale remains $<10^6$ which means that a cluster can be still partially or completely destroyed [72, 73].

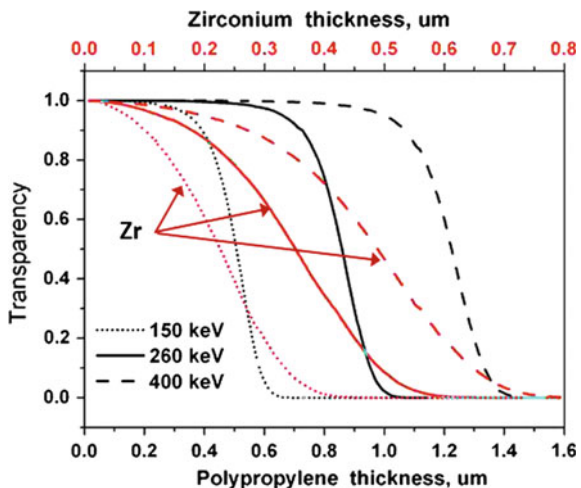
Another possibility for effective matching of femtosecond laser pulses with a cluster is to use large-sized clusters. Using specially designed nozzles, the diameter of clusters from different gases could reach 0.2–1.5 μm [74–77]. On the other side, laser pulses with high contrast (10^8 – 10^{10}) provide highly efficient laser-cluster interaction and allow for the creation of bright sources of various quantum beams: soft and hard X-rays, fast electron and ion beams [55].

12.4 High-Resolution Radiography Using a Femtosecond Laser-Driven-Cluster Based Source of Multicharged Ions

As it was mentioned above, proton and multicharged ion radiography with spatial resolution below 10 microns have been successfully demonstrated in the case of using plasma source produced by femto/picosecond laser interaction with solid targets [4, 78–81]. Here, we present a review of experimental results [82–84], in which femtosecond-laser-driven-cluster-based plasma has been used as a source of multicharged ions with about 1 MeV energies for contact radiography with sub-micron spatial resolution of low contrast ultrathin foils and biological samples. It is necessary to underline that the best contrast of proton or ion images could be provided if the stopping range of probing particles slightly exceeds the expected thickness of the sample. For the multicharged ion radiography of ultrathin objects it means that the energy of particles should be in the range of some hundreds KeV for obtaining good spatially resolved images with high contrast. Plots of Fig. 12.3, show the transmission polypropylene (black solid and dashed lines) and Zr (red ones) foils of increasing thickness for different initial energy of Oxygen ions, as simulated by SRIM code [85]. Notice that the slope of the curves defines the sensitivity of ionography method to the thickness of imaged objects. Also, the plots show the useful range of thickness for different ion energies. Due to the fact that fast ion absorption efficiency is inverses to the square of the ion charge, highly charged ions are suitable at imaging different objects with high contrast. Furthermore, if we compare photons and ions of the same energy in terms of radiography, photons are more suitable for thick samples while ions fit thin foils.

It is well known, that changing laser intensity on the target simply allows optimizing the energy of produced protons or ions. This is a unique advantage of

Fig. 12.3 SRIM code [85] simulation showing transmission of Zr (*red lines* and values) and polypropylene (*black lines* and values) foils of increasing thickness, irradiated by Oxygen ions of three different initial energies [82]



laser driven protons and ions. Protons or multicharged ions with the energy until MeV's were observed in nano- and pico-second laser interactions with plasmas from solid targets at intensities in the range 10^{14} – 10^{16} W/cm². When the intensity of laser radiation on the target reaches the value of 10^{18} W/cm², the conditions for proton and ion generation, with energy of tens MeV, can be created. So, a large variety of materials can be analyzed using particles from plasma sources created at various laser intensities. As could be seen from Fig. 12.3, in the case of ultrathin structures optimum imaging can be achieved with multicharged ions of energies in the range of 100–500 keV. Using a compact femtosecond laser facility with power of several TW, it is relatively easy to produce multicharged ions with such energies and obtain high-contrast images of extremely thin objects like membranes, nanostructures and biological cells.

As it was stressed above, the most effective approach for the production of multicharged ions with energy of hundreds keV, is the utilization of femtosecond laser pulses coupled with gas cluster targets. This combination provides higher absorption of the laser energy by the target, compared with solid or gas targets, and allows to significantly reduce the requirements on the performance of laser facilities needed for multicharged ion acceleration. As it was previously shown [39], additional cuts of the needed laser intensity can be applied if self-focusing the laser pulse in cluster target occurs. Such a feature creates easier requirements for multicharged ions acceleration of up to several MeV by using moderate intensity of femtosecond laser pulses. Another important advantage of femtosecond-laser-driven-cluster-based source is the fact that the main mechanism of multicharged ions acceleration is Coulomb explosion makes ions expanding isotropically from the source. Indeed, it allows to obtain high quality images with a large field of view, which is the key difficulty for a number of precise methods of imaging and microscopy.

Radiography experiments were carried out at Kansai Photon Science Institute JAEA (Japan) on the JLITE-X facility where the Ti:Sapphire laser pulse with the duration of 36 fs and energy of 120 mJ was focused by parabolic mirror to the spot with 50 μm diameter that provided the intensity in the focal spot of 4×10^{17} W/cm². The target consisted of the gas clusters, delivered by a custom-designed super-sonic nozzle. A mix of 90 % He + 10 % CO₂ at a pressure of 60 bar was used to obtain 0.2–0.5 μm size CO₂-clusters [74–77]. The laser pulses were focused on the jet axis at the distance of 1.5 mm from the nozzle output (see Fig. 12.4a). Parameters of the plasma produced by femtosecond laser pulses and energy distributions of the fast ions were measured by FSSR X-ray spectrometers [27, 86].

FSSR Spectrometers, based on spherically bent mica crystals, allow high spectral and spatial resolution. Typical spectra, obtained with spatial resolution in the direction along and perpendicular to the laser beam propagation are presented in Fig. 12.4b. Strong Doppler broadening of spectral lines due to the multicharged ions motion is clearly seen. Plasma parameter diagnostics were carried out using comparison of relative intensities and shapes of X-ray spectral lines with theoretical modeling [29], which allowed to estimate the following plasma parameters: the electron temperature t_e , the electron density n_e , and the ion charge population. Some

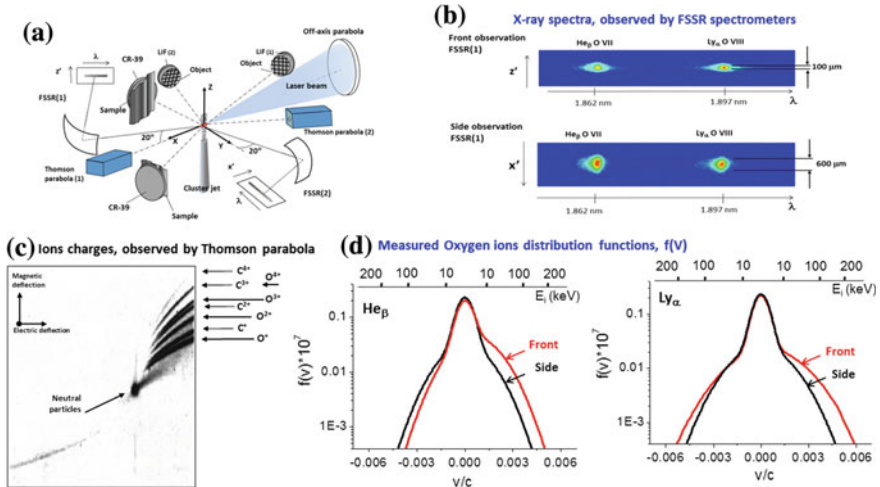


Fig. 12.4 Basics from radiography experiments performed at JAEA [74–77, 82–84]. **a** Experimental set up. X-ray spectra were measured from front and back sides of laser beam propagation by FSSR spectrometers with spatial resolution. **b** Spatially resolved spectra of He-like and H-like ions of oxygen in the spectral range of 1.85–1.92 Å. **c** Ions charges of carbon and oxygen measured by Thomson parabola [53]. **d** One-dimensional velocity distribution function extracted from experimental spectra of He_β and Ly_α lines of Oxygen ions

parameters of laser-produced cluster plasma measured by comparison of modeled and experimental intensities of Oxygen spectra are presented in Fig. 12.4d.

As it was previously demonstrated [29, 39], the energy distribution of fast ions could be determined from the analysis of spectral line profiles. As a result, the energy distributions of multicharged Oxygen ions for two orthogonal observation directions (along and across the laser beam axis) were obtained (see Fig. 12.4d). The positive and negative velocities of ions represent the motion of ions towards the spectrometer, or from it. Black and red solid lines are linked to the motion of ions, along or perpendicular to the laser beam propagation, respectively. X-ray spectroscopy demonstrates that in the femtosecond laser cluster plasma the fluxes of H- and He-like oxygen O (VII, VIII) ions were accelerated to the energy about 100–300 keV rather isotropically, which is in accordance with current models of Coulomb explosion of clusters. Different multicharged ions of Oxygen and Carbon accelerated up to MeV energies were also observed simultaneously by two Thomson parabolas [53] and can be seen in Fig. 12.4c.

Samples to be imaged by fast ions were situated at a distance of 140 and 160 mm from the ion source respectively, both perpendicular to the laser beam axis as shown in Fig. 12.4a. Ions transmitted through the sample reached the dosimetry polymer film CR-39, in contact with the sample back surface. After chemical etching of the CR-39 film, the latent track of every absorbed fast particle appeared as a channel with the cross section of $\sim 0.2 \mu\text{m}$ and longitudinal size of $\sim 1 \mu\text{m}$, depending on the particle energy. After etching, the images were observed by

optical microscope. As a result, every single track on the surface of the film was imaged as single or double concentric diffraction fringes with dimensions similar to illuminating wavelength of $\sim 0.6\text{--}0.9 \mu\text{m}$ (see Figs. 12.5 and 12.6a) This value defines a spatial resolution limit of this method.

The achieved submicron spatial resolution in a wide field of view, the isotropy of the ion flux, the sensitivity of the method to thickness and density, allow to systematically investigate a wide variety of samples [82–84]. For the analysis of the ion flux isotropy, images of polypropylene film of $1 \mu\text{m}$ thickness were obtained at two different positions of the object to the plasma ion source (with orthogonal observation directions to each other), as it is shown in Fig. 12.4a. As it is clearly seen in Fig. 12.5, both CR-39(1) and CR-39(2) images have uniform background across the entire $35 \times 38 \text{ mm}^2$ area. This means that the cluster-based laser plasma source produces isotropic homogeneous ion flux in an entirely solid angle. The linear elongated structures, visible on images of Fig. 12.5, represent the “waves” wrinkles of the foil, formed during the fixation on the film holder. The possible geometry of the waves allows to conclude that the effective thickness of the film along the probe ion propagation may change between $1.0 \pm 0.1 \mu\text{m}$. Based on that, it was concluded that the proposed ionography method possesses the sensitivity to the target thickness in the order of 100 nm even for objects consisting of light chemical elements (C, H). Furthermore, as it can be seen from Fig. 12.5, single inclusions and the areas of density, or thickness inhomogeneities with typical dimension from 1 to 10 microns, have been resolved. Due to an almost equal number of ions measured in different positions of the detector, the total number of fast ions was estimated to be about 10^8 ions per laser shot in 4π solid angle. It is necessary to underline that, simultaneously, in some experiments, Thomson parabolas [53] placing in the same distances and directions as CR-39 film detectors have been used. They showed that Carbon and Oxygen ions with charges from +1 to +4 and energies up to 4 MeV were generated in

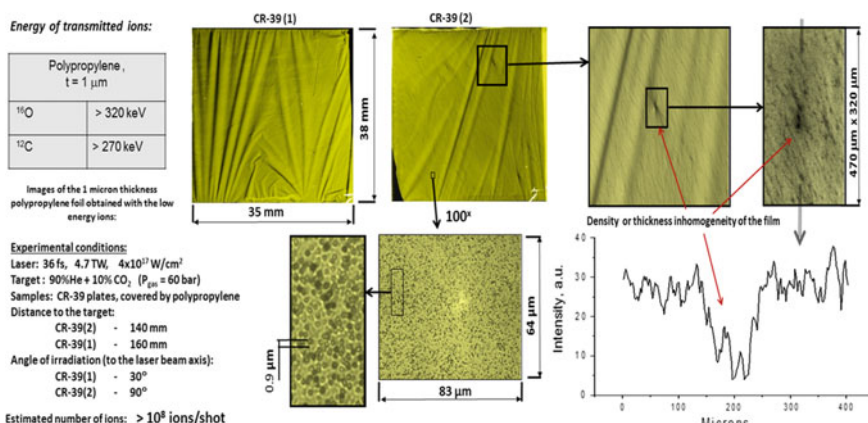


Fig. 12.5 Ion imaging of 1 micron thickness polypropylene foils, which demonstrated ion tracks in the scale of $0.6\text{--}0.9 \mu\text{m}$ and distribution of ion flux quasi-isotropic [82–84]. Features and local defects of micron and submicron sizes are clear seen

these laser-cluster driven experiments. At the same time no evidence of protons or He ions have been observed. In control experiments, when pure He was used as a gas expanding in the nozzle, no images on CR-39 films have been observed. It was concluded from these experimental results that images received on CR-39 films have been produced by Oxygen and Carbon fast ions. Provided in [82–84] modeling using SRIM [85] code allows to estimate that in order to pass through polypropylene foil with 1 μm thickness the energy of such ions should be more than 250–300 keV.

To measure the actual spatial resolution of this radiography, the image of high-contrast test object with known geometry (two-dimensional 2000 lpi mesh made of Cu wires) was produced (see Fig. 12.6a). The thickness of mesh wires is 5 μm , and the open square of mesh is 7.7 $\mu\text{m} \times$ 7.7 μm . Observation of the image under an optical microscope with magnification of 100 \times allows to resolve separated granules on the CR-39 film surface, representing etching latent tracks of fast ions. According to this image, the \sim 600 nm limit on spatial resolution is achieved for high contrast objects. That also corresponds to diffraction limit of the optical microscope which provided the image read-out from detector. Intensity profile of the row with several periods of mesh (see plot in Fig. 12.6b) also demonstrates perfect contrast, homogeneous background value, and the spatial resolution at the rate of about 600 nm. Taking into account that the probing ion flux possesses uniform intensity in an area of tens mm size, we can conclude that this unique ion source is able to image microscopic objects with field-of-view/spatial resolution ratio in order of 10⁵.

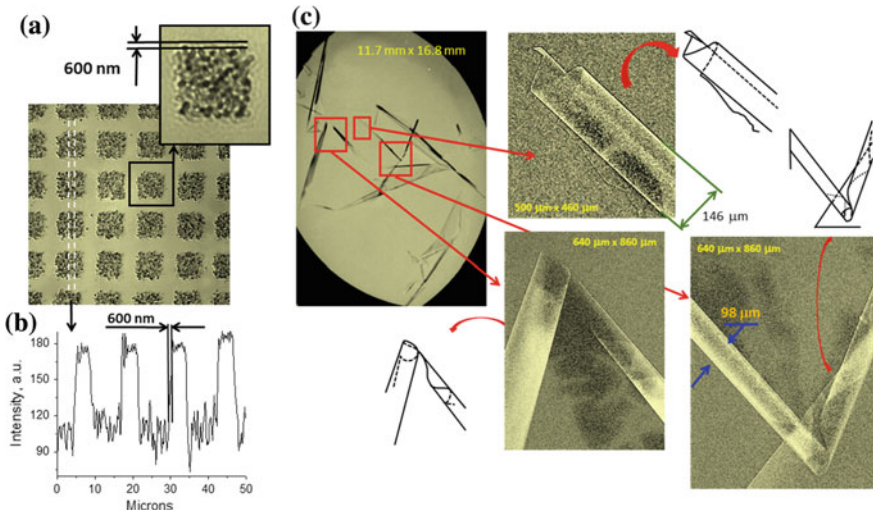


Fig. 12.6 **a** Image of 2000 lpi mesh, showing separate latent tracks produced by ions penetrated through the object and recorded in Cr-39 film. **b** Trace of the image, which clearly demonstrated a spatial resolution \sim 600 nm in a wide field of view. **c** Images of the damaged 100 nm thick Zr foil self-shaped into swirls and tubes. Multiple \approx 100-nm thick structures of Zr foils are clearly resolved [82–84]

This ions source, based on a clusterized gas-jet irradiated by ultraintense fs laser pulses, has been used in [82–84] for ionography of nanoscale thickness foils and thin biological objects. The image of 100 nm thick Zirconium foils is shown in Fig. 12.6c as an example. Actually, that is the image of the damaged Zr filter (Lebow company production), which curl up into tubes and swirls. Images of the tiny pieces of foil, which consist of several layers of 100 nm foil, and their schematic reconstruction are shown in the detail sections of Fig. 12.6c. The nanometric surfaces formed by single, twice, triple, or multiple layers can be easily resolved.

The simulations of ion imaging for the 1 μm polypropylene foil waves (see also Fig. 12.5) and 100 nm Zr foil cylindrical tube (see also Fig. 12.6c), are presented in Fig. 12.7a, b, respectively. Modeling [82–84] was carried out employing MPRM code [87] based on SRIM Monte-Carlo simulation package [85]. In the case of 1 μm polypropylene foil, waves were simulated as change of foil thickness between 100 and 150 nm, irradiated with parallel beam of carbon ions with energy 250 keV. In the case of the Zr tube, a 2D cross-section was modeled in the same way as the plastic micro balloon [88]. The detector plane was positioned at a nominal distance of 10 micron from the tube. A parallel monoenergetic (320 keV) beam of Oxygen was used, as the particle probe and particle number density across the detector was constructed. For both modeling cases a close qualitative match with

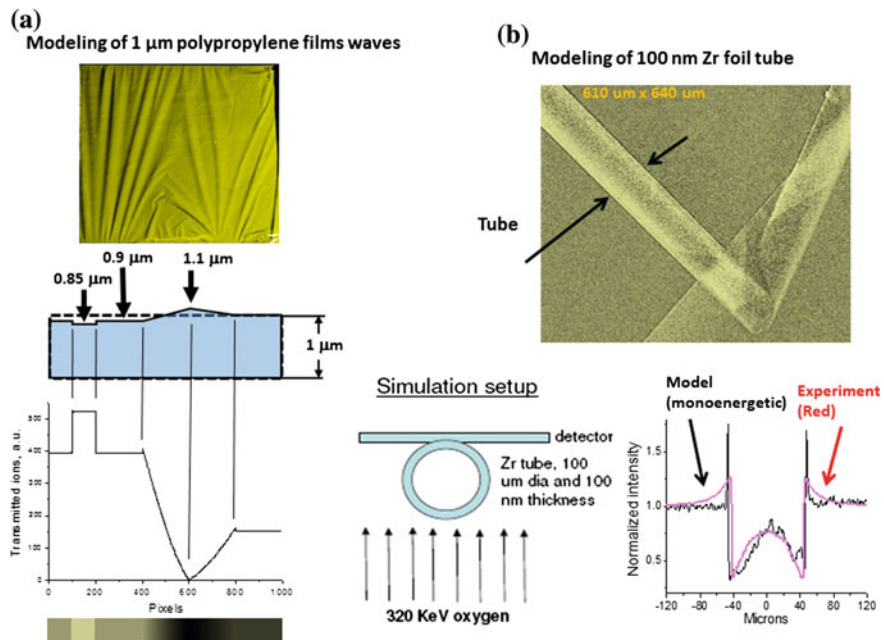


Fig. 12.7 The simulations (bottom) for the case a of 1 μm polypropylene foil waves was performed with 250 keV carbon ions [82–84]. Clear steps on the image correspond to variations of polypropylene thickness of 100–150 nm; for the case b of 100 nm Zr foil tube simulation was performed with 320 keV oxygen ions

the experimental images was obtained (see Fig. 12.7a, b). Furthermore, as it is seen from lineouts in Fig. 12.7b, a solid quantitative agreement is obtained by the simulation for a Zr tube of 90 micron diameter and 100 nm thicknesses. So it is possible to conclude that, this method of ionography is suitable for nanostructure diagnostics and measurements of foils thinner than 100 nm. It is necessary to note that, by decreasing the energy of ions, their collision frequency with the atoms of the target is sufficiently increases. Due to the close collisions, the incident ions can deflect on wide angles, which leads to spatial divergence of the ion flux passed through the imaging object. This effect results in some reduction of spatial resolution of the imaging, and also explains the appearance of single particles in the detector region, closed by the objects with large thickness (see, the single inclusions, shown in Fig. 12.6a). In order to lower the negative effect of ion fluxes' divergence on the image quality, the detector has to be placed in contact with the back surface of the sample.

An impressive confirmation of high quality ionography with submicron spatial resolution using multicharged ions, produced with the method described above, was achieved [82–84], with images of low-contrast biological microscopic samples. Ionography produced images of a dragonfly and a spider web, with various insects fixed in it, as presented in Fig. 12.8a, b. The image of the dragonfly shows not only unique field of view $\sim 35 \text{ cm}^2$ but also demonstrate high contrast and high spatial resolution. Meanwhile the magnified area of the spider net image allows to distinguishing the details and to measure the thickness of the web fiber, drops of biological glue on it, and also investigate the insect's structure. As evident from the upper right fragment (see Fig. 12.8b), the seta on one of the insect extremity are perfectly resolved, the thickness of which does not exceed 1 μm .

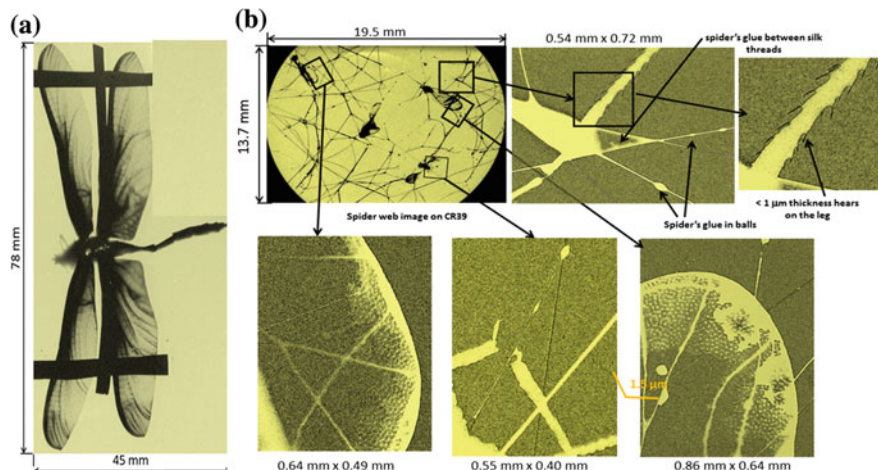


Fig. 12.8 **a** Full scale ($\sim 3500 \text{ mm}^2$) dragonfly's image on the CR-39 ion detector. **b** Ionography images of spider web with insects caught on it. Structures of size less than 1 μm are clearly observed

To conclude this Section we recall that:

1. The femtosecond laser plasma of gas cluster targets can provide an almost isotropic, homogeneous source of fast multicharged ions with energies of >300 keV and with flux exceeding 10^8 ions/per shot, which is suitable for ionography with large field of view;
2. Using such a source for ionography, images with spatial resolution around 600 nm have been obtained, which correspond to the unique field-of-view/resolution ratio $>10^5$; the sensitivity of the method to sample thickness is of about 100 nm, even for objects consisted of light chemical elements (C, H);
3. It is possible to use this method for imaging of low-contrast biological specimens, nanostructures, and density modulations of thin films.

In the future, optimization of laser parameters, cluster target, distances from ion source to the object and detectors, will allow obtaining images in 1–10 laser shots. The results based on the femtosecond laser plasma ion source and ways of obtaining ionography images will provide the complex diagnostic tool for precise measurements of thickness, density and structure of low-contrast nanosized objects.

12.5 Using Laser-Accelerated Electron Beams for High Resolution Radiography

The development of various reliable nondestructive techniques to identify the presence of defects in dense structures, ranging from turbine blades to nuclear reactor vessels, is at state-of-the art for the modern-day physics and industrial applications. Portable electron radiography system will be very attractive for these applications. A conventional portable 30 MeV electron source and radiography system has been designed and built recently for such purposes in Los Alamos National Laboratory [89] and demonstrated the possibility to reach submillimeter spatial resolution in the case of density measurements for static and dynamic objects with $0.01\text{--}1.0 \text{ g/cm}^2$ area densities. Typical drawbacks of such devices are rather long pulse duration of electron beam and difficulties of synchronization in the case of dynamic object investigations. It means that the elaboration of portable laser-driven electron source is very attractive because it gives a possibility to obtain electron beams with ultra-short pulses and synchronize them with various dynamic processes under investigation.

Main requirements to future laser-driven electron source are: (i) The source must be based on energetic electron beams in order to achieve the desired level of penetration in dense material. (ii) The radiation should be produced in a well-collimated beam to permit transport over large distances without loss of brightness. (iii) The intrinsic size of the source should be on the order of microns for confident spatial resolution of microstructures on the image. (iv) The laser-driven electron source should be compact and cost effective to be competitive

with conventional electron sources. (v) A source allowing raster scanning is highly desirable in order to make possible irradiation of large size objects, which could be also located relatively far from the electron beam source.

There have been intensive investigations during the past decade which led to the achievements of all the goals mentioned above. For example, there has been demonstration of acceleration of bright, monoenergetic electron beams with energies 0.1–4.2 GeV by using laser—wakefield acceleration through the interaction of 0.05–1 PW, 30-fs scale laser pulses with a supersonic gas jets, capillary discharges, or gas-filled cells [90–99]. High bunch charge up to 500 pC, low divergence in the scale of some mrad, and micrometric source size, make these sources ideal for high-resolution radiographic studies of cracks or voids embedded in dense materials, also when placed at some distance from the source. Ti:Sa laser systems, used for such investigations, are already sufficiently portable and work with repetition rate 1–10 Hz. All of these attributes make it worthwhile to consider the application of the laser-driven energetic electron beams for nondestructive radiography.

The first practical demonstration of laser-driven electron beam radiography was provided recently [100]. A bright, monoenergetic electron beam (with energy >100 MeV) was generated by the laser-wakefield acceleration through the interaction of 50-TW, 30-fs laser pulses with a supersonic helium jet. In order to measure the resolving power of the electron beam a stainless steel block of thickness 5 cm and width 5 cm, with submillimeter gaps of width 250, 500 and 750 μm , embedded within it, was used. The object consisted of 2.5-cm long voids that were embedded within a 5-cm thick stainless steel block placed 2-m from the supersonic jet. Three different void thicknesses were imaged, with widths of 250, 500, and 750 μm . Ten electron beam shots, each with electron energy 150 ± 20 MeV and an angular divergence of 4.7 ± 0.5 mrad, were used to acquire the radiograph measurements. An image plate placed behind the steel block was used for radiography. The 250 μm gap was clearly resolved and was used for determination of the resolving power of the source. Using Fourier filtering technique for improving signal-to-noise ratio allowed finally to reach the submillimeter spatial resolution.

One of the very important applications of laser-driven electron radiography could be using it for investigations of several dynamical processes in matter. An example of such unique application was recently demonstrated in [101]. Using electron bunches, generated by laser wakefield acceleration as a probe, the temporal evolution of magnetic fields generated by a $4 \times 10^{19} \text{ W/cm}^2$ ultrashort (30 fs) laser pulse focused on solid density targets studied experimentally. Magnetic field strengths of order $B_0 \sim 10^4 \text{ T}$ were observed expanding at close to the speed of light from the interaction point of a high-contrast laser pulse with a 10 μm —thick aluminum foil to a maximum diameter of ~ 1 mm. This experiment demonstrated that laser-driven electron beams are tunable in energy, have ultrashort duration, and are easily synchronized. Despite the fact that in those experiments, the electron spectrum was very broad, which led to some loss of spatial resolution, important results about magnetic field generation and relativistic laser-plasma interactions were achieved.

Another very important possible application of laser-driven electron sources is using it for ultrafast electron diffraction. The first experimental demonstration of longitudinal compression of laser-accelerated electron pulses associated with an experiment of ultrafast electron diffraction was done in [102]. Accelerated by a femtosecond laser pulse with an intensity of 10^{18} W/cm², an electron beam, with an energy of around 350 keV and a relative momentum spread of about 10^{-2} , was compressed to a 500-fs pulse at a distance of about 50 cm from the electron source by using a magnetic pulse compressor. This pulse was used to generate a clear electron diffraction pattern of a gold crystal in a single shot. Such result demonstrated that femtosecond laser plasma can serve as a high-brightness electron source providing a self-compressed femtosecond electron pulse with energy of hundreds of kilo electronvolts. This technique has great potential for the generation of extremely high-charge femtosecond pulses in the mid-energy range, because the space-charge effect does not limit the charge in a pulse. A relevant feature is that, since the compression system does not produce time jitter between the electron pulse and the laser pulse, it will be possible to obtain high temporal resolution in pump and-probe experiments that can be utilized for any application that needs femtosecond probing or driving.

12.6 High Resolution Electron Radiography Using a Laser-Driven-Cluster-Based Source

According to early study [103] arguments already mentioned in Section III of this Chapter, cluster medium has a higher absorption of femtosecond laser energy, allowing a more efficient generation of quantum beams (see also, [55]). It was already demonstrated electron acceleration by laser from cluster targets up to tens of MeV energies [104] and even higher energies up to 600 MeV in recent investigations [50]. Additionally, a very high charge of about 3 nC could be obtained in the direction perpendicular to the laser propagation in the case of irradiation of Ar clusters by 1 J Ti:Sa laser with pulse duration of 100 fs [50]. Even higher values of electron bunch charge, up to 12 nC for ~ 2 MeV electron beam was observed [56, 57]. In this latter case, a low energy (only 80 mJ) Ti:Sa laser pulse with duration 40 fs but with higher laser contrast was focused with the laser intensity $\sim 1.7 \times 10^{18}$ W/cm² onto the Ar cluster jet. As for the higher electron energies (>20 MeV), it was shown that the total accelerated electron charge in the case of clustering gas target could reach ~ 170 pC [105]. Such performances of femtosecond laser-driven cluster-based electron sources allowed recently to get first radiography measurements [56, 57].

Electron radiography based on femtosecond-laser-driven cluster-based electron source was carried out at the Intense Laser Irradiation Laboratory of the CNR in Pisa. The interaction of a high-contrast 80 mJ, 40 fs duration, 2 TW laser pulses focused with intensity 1.7×10^{18} W/cm² an Argon cluster target was performed to

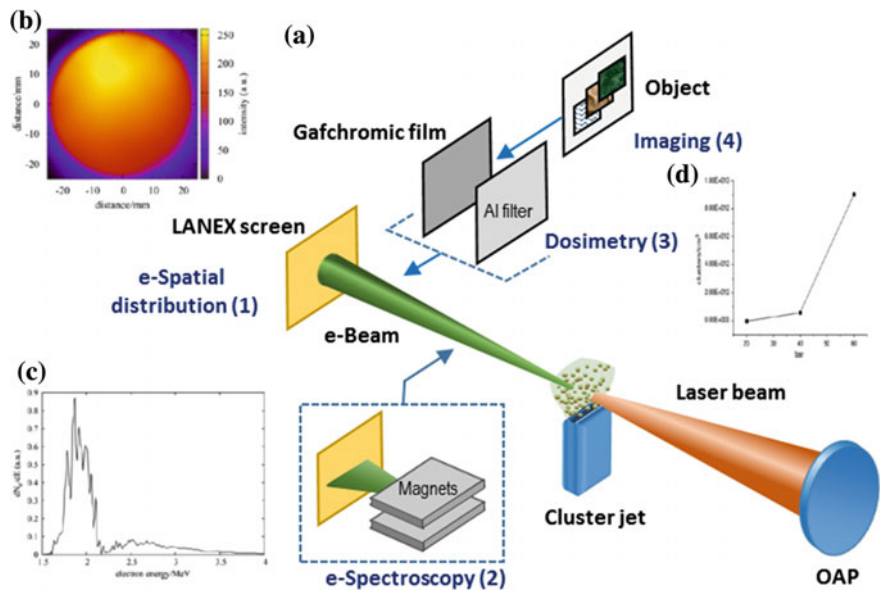


Fig. 12.9 **a** Experimental set up for electron radiography [57]. **b** Typical spatial distribution of the accelerated electron beam as detected by the scintillating screen at a distance of 15 cm from the gas-jet nozzle. **c** Typical energy distribution of the electron beam obtained for the laser-cluster interaction parameters like in **(b)**. **d** Theoretical modeling of cluster density as a function of Ar gas backing pressure

generate MeV electrons with a high charge. As it follows from set up presented in Fig. 12.9a the following elements were applied: (1) Lanex screen was used for e-spatial distribution measurements; (2) Electron spectrometer was used for measurements of electron spectra distribution; (3) Gafchromic film was used for electron beam charge measurements; (4) Complex objects were placed in contact with the radiochromic film detector. To produce Ar clusters the supersonic gas-jet a nozzle 4 mm long and 1.2 mm wide was used. The laser propagated parallel to the shorter edge of the nozzle and was focused nearby to the edge of the gas-jet closest to the focusing optics, at a vertical distance of 0.5 mm from the nozzle exit plane. Optimized cluster formation in gas jet targets occurred at pressures between 40 and 50 bar (see Fig. 12.9d) with a maximum of cluster size and cluster concentration. In this condition the atomic density of gas in the laser interaction region is around $4 \times 10^{19} \text{ cm}^{-3}$. Stable operation of efficient electron production was found at 46 bar, and under these conditions the clusters size was 35 nm in radius with 5.5×10^6 atoms per cluster and 12 % of clusterized fraction (dryness of the medium was about 88 %). A Kodak Lanex Regular scintillating screen (marked as (1) in Fig. 12.9a) was mounted at a distance of about 15 cm from the gas-jet nozzle for the characterization of the spatial profile of the electron beam. The spatial distribution of the electron beam obtained from the interaction of a single laser pulse with an Ar-cluster target at a backing pressure of 46 bar is displayed in Fig. 12.9b. The

electron beam demonstrates a very homogeneous spatial distribution over a wide region, well beyond the region imaged by the scintillating screen. Over the whole diameter of the scintillating screen of 5 cm the signal changes by less than a factor of two. The energy distribution of the electron beam above the lower spectral limit of spectrometer (1.5 MeV) is shown in Fig. 12.9c for the electron beam generated in the Ar-cluster target when the backing pressure was 46 bar. The spectrum shows a bright peak at about 1.9 MeV with a low-intensity tail at higher energies. The sharp cut toward lower energies is due to the spectral limit of a spectrometer used in such experiments. The charge of the electron bunch obtained in such conditions was 12 ± 6 nC in the case of Ar cluster targets, which was more than one order of magnitude higher than in the case of the He target (results to be of the order of 300 pC). It is necessary also to underline the high shot-to-shot reproducibility of electron source parameters which reached \sim of 77 % [57].

Such good production quality of an electron beam allowed to provide high resolution electron radiography of centimeter-sized samples placed at contact with the radiochromic film detector (see Figs. 12.10 and 12.11) at the distance of 10 cm from the electron-source. At this distance the electron beam had a transverse extent of more than 5 cm and its intensity on the detector allowed to obtain an image with a good signal-to-noise (S/N) ratio using accumulation of 30 consecutive laser shots. In order to test the radiographic system parameters, including resolution and sensitivity

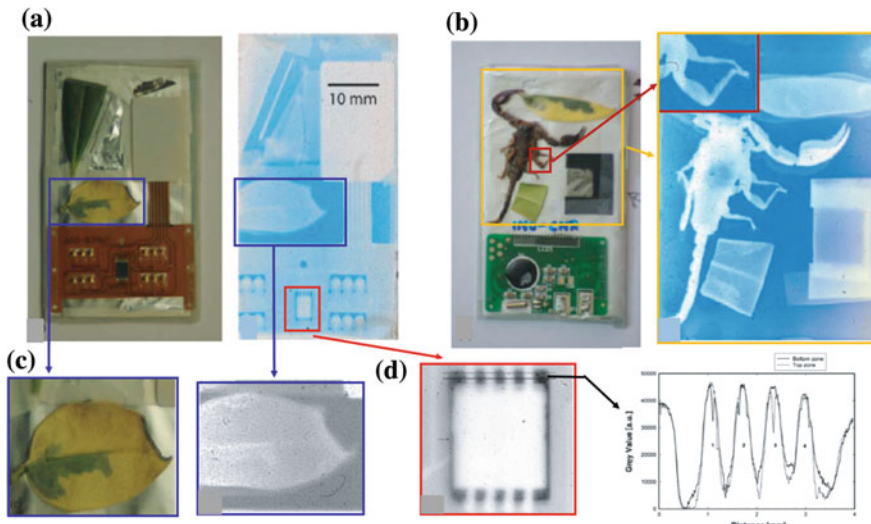


Fig. 12.10 Femtosecond laser-driven cluster-based 2 MeV electron radiography of two samples with sizes $34\text{ mm} \times 63\text{ mm}$ (a) and $35\text{ mm} \times 48\text{ mm}$ (b) (left panels are photo of samples, right panels are electron radiography images) placed at the distance 10 cm from the electron beam source [56, 57]. c Magnified images (left photo, right electron radiography) of a two-colored leaf with clearly resolved structure of its pigmentation. d $6\text{ mm} \times 7\text{ mm}$ electron radiography of a chip. Lineouts taken along the lines marked in the radiography image, which demonstrated spatial resolution $\sim 150\text{ }\mu\text{m}$

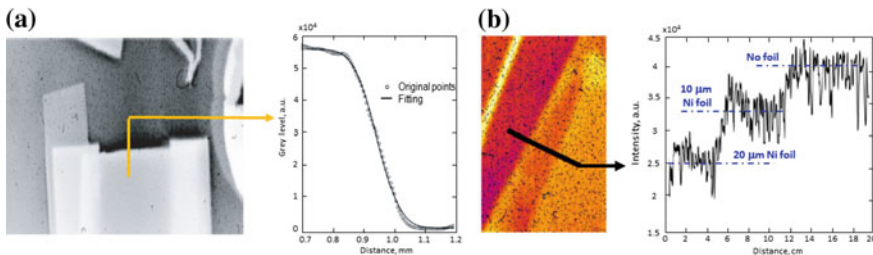


Fig. 12.11 Femtosecond laser-driven cluster based 2 MeV electron radiography of **a** the 5 micron tantalum foil with the sizes 13 mm x 29 mm and lineout at their edge [56]. Fitting of the experimental data gave a spatial resolution of 60 μm (RMS width obtained from the error function); **b** image of two layers of a 10 μm thick Ni foil and its lineout [57]. The difference in absorption of 20 μm of Ni, 10 μm of Ni, and no Ni foil is clear resolved, though the total stopping range of 1 MeV electrons in Ni is about 680 μm

to the areal density distribution, two samples with known different material compositions, thicknesses and spatial details were carefully prepared using both organic and inorganic objects to be imaged by laser–driven electron beam. The first sample (see Fig. 12.10a) consisted of an electronic component (integrated circuit), two leaves, three Al foils of 13 μm thickness and a glass fiber. The second sample (see Fig. 12.10b) included a scorpion, two leaves, an electronic integrated circuit, a tantalum thin foil (5 μm in thickness) and two tungsten fine wires of 20 μm diameter.

A detailed description of the radiographic results can be found in [56, 57]. Here the main features of such electron radiography are discussed. The scans of the entire radiographic images corresponding to both samples are shown in Fig. 12.10a, b. Under these conditions the estimated absorbed dose for each shot is of the order of 0.5 Gy. All objects, which were illuminated by electron beam are clearly visible, including the three low-absorbing Al foils (13 μm in thickness) in the upper left part of Fig. 12.10a. Figure 12.10c shows details of a leaf sample, where some local structures and its changes in pigmentation can be clearly seen. Indeed, a small green chlorophyll-rich area is still visible in an otherwise dried, yellow tissue. A comparison of the electron radiograph image with the original leaf photo shows that the green region has a higher absorption than the surrounding yellow region. This difference is likely to be due to the presence of water in the green region, which increases the areal density compared with the dried yellow region. These results visibly indicated sensitivity of electron imaging to the chemical or structural differences in leaf sample qualitatively similar to that obtained by using soft x-ray radiography. These results clearly demonstrate that, as it could be seen from upper left corner of the image in Fig. 12.10b, high quality imaging of rather thick biological objects could be obtained. In Fig. 12.10a, d the image of a small electronic integrated circuit demonstrated the possibility to reach spatial resolution $\sim 150 \mu\text{m}$ for thick- enough samples. Higher spatial resolution was obtained from the radiographic image of a sharp edge of 5 μm thick Ta foil (see Fig. 12.11a). Assuming a Gaussian point-spread-function, the RMS spot size was found to be 60 μm , which is the highest spatial resolution published so far for laser-driven electron source

radiography. It is also necessary to stress that not only high spatial resolution could be obtained using femtosecond laser-driven cluster-based electron radiography, but also the high sensitivity for low absorbing materials is possible. Indeed, as can be seen from Fig. 12.11b Ni foils with a step thickness of only 10 μm could be clearly resolved despite of the fact that the total stopping range of 1 MeV electrons in Ni is about 680 μm .

To conclude this part we should mention that:

1. The ultrashort pulse Ti:Sa lasers even with relatively small energies could be used to drive electrons in a plasma up to the multi MeV energies with a $\approx n\text{C}$ charge. Such approach is particularly attractive and promises to overcome some limitations of existing conventional electron guns at high beam energies especially for ultrafast applications.
2. Laser-electron guns can be successfully applied to transmission electron radiography of thin and thick, cm-scale samples and, with the use of suitable detectors. This approach can be extended to even larger field of view and higher electron energy with as expected spatial resolution in the scale of μm level.

12.7 Conclusions and Perspectives

Protons, multicharged ions and electrons generated by irradiating suitable targets with a high-intensity laser have shown to possess interesting characteristics in terms of energy, emittance, current, and pulse duration. Therefore, in the near future, they might become competitive with respect to conventional sources. Recent theoretical, numerical, and experimental studies have already demonstrated the advantages of laser-driven particle beams radiography. Particular attention has been devoted to femtosecond laser-driven cluster-based radiography due to its proved capability to reach submicron spatial resolution with multicharged ions and tens of micron resolution with electrons. We would like to stress that contemporary existing table-top lasers of moderate intensity (10–100 TW), could be already relatively easily introduced and managed in applicative context for biology, medicine and industry as it is shown in this chapter. Further progress on source performance can be achieved by in-depth studies of laser interaction with a variety of targets, foremost the clusterized gases.

We also believe that developing petawatt-class lasers, particular with a high repetition rate and femtosecond pulse duration, opens a new era for different applications of laser-driven quantum beams and particularly for high-performance radiography.

Acknowledgements This work was supported from the MEXT by X-ray Free Electron Laser Priority Strategy Program (contract 12005014) and by Russian Basic Research Funds via grants 14-22-02089, 15-32-21121.

References

1. R.P. Drake, *High-Energy-Density Physics: Fundamentals, Inertial Fusion, and Experimental Astrophysics*, 1st ed. (Springer, 2006). ISBN-13: 978-3540293149
2. B. Remington, R. Drake, D. Ryutov, Rev. Mod. Phys. **78**, 755 (2006)
3. V.E. Fortov, *Extreme States of Matter on Earth and in the Cosmos* (Springer, 2011). ISBN 978-3-319-18952-9
4. J.A. Cobble, R.P. Jonson, T.E. Cowan, N. Renard-Le Galoudec, M. Allen, J. Appl. Phys. **92**, 1775 (2002)
5. M. Roth, A. Blazevich, M. Geissel, T. Schlegel, T.E. Cowan, M. Allen, J.-C. Gauthier, P. Audebert, J. Fuchs, J. Meyer-ter-Vehn, M. Hegelich, S. Karsch, A. Pukhov, Phys. Rev. ST Accel. Beams **5**, 061002 (2002)
6. M. Borghesi, D.H. Campbell, A. Schiavi, M.G. Haines, O. Willi, A.J. MacKinnon, P. Patel, L.A. Gizzi, M. Galimberti, R.J. Clarke, F. Pegoraro, H. Ruhl, S. Bulanov, Phys. Plasmas **9**, 2214 (2002)
7. A.J. Mackinnon, P.K. Patel, M. Borghesi, R.C. Clarke, R.R. Freeman, H. Habara, S. P. Hatchett, D. Hey, D.G. Hicks, S. Kar, M.H. Key, J.A. King, K. Lancaster, D. Neely, A. Nikkro, P.A. Norreys, M.M. Notley, T.W. Phillips, L. Romagnani, R.A. Snavely, R.B. Stephens, R.P.J. Town, Phys. Rev. Lett. **97**, 045001 (2006)
8. L. Romagnani, J. Fuchs, M. Borghesi, P. Antici, P. Audebert, F. Ceccherini, T. Cowan, T. Grismayer, S. Kar, A. Macchi, P. Mora, G. Pretzler, A. Schiavi, T. Toncian, O. Willi, Phys. Rev. Lett. **95**, 195001 (2005)
9. A.B. Zylstra, C.K. Li, H.G. Rinderknecht, F.H. Séguin, R.D. Petrasso, C. Stoeck, D.D. Meyerhofer, P. Nilson, T.C. Sangster, S. Le Pape, A. Mackinnon, P. Patel, Rev. Sci. Instrum. **83**, 013511 (2012)
10. M.J.-E. Manuel, C.K. Li, F.H. Seguin, J. Frenje, D.T. Casey, R.D. Petrasso, S.X. Hu, R. Betti, J.D. Hager, D.D. Meyerhofer, V.A. Smalyuk, Phys. Rev. Lett. **108**, 255006 (2012)
11. C.K. Li, F.H. Seguin, J.A. Frenje, N. Sinenian, M.J. Rosenberg, M.J.-E. Manuel, H.G. Rinderknecht, A.B. Zylstra, R.D. Petrasso, P.A. Amendt, O.L. Landen, A.J. Mackinnon, R.P. J. Town, S.C. Wilks, R. Betti, D.D. Meyerhofer, J.M. Soures, J. Hund, J.D. Kilkenny, A. Nikroo, Nucl. Fusion **53**, 073022 (2013)
12. G. Sarri, A. Macchi, C.A. Cecchetti, S. Kar, T.V. Liseykina, X.H. Yang, M.E. Dieckmann, J. Fuchs, M. Galimberti, L.A. Gizzi, R. Jung, I. Kourakis, J. Osterholz, F. Pegoraro, A.P.L. Robinson, L. Romagnani, O. Willi, M. Borghesi, Phys. Rev. Lett. **109**, 205002 (2012)
13. H. Ahmed, M.E. Dieckmann, L. Romagnani, D. Doria, G. Sarri, M. Cerchez, E. Ianni, I. Kourakis, A.L. Giesecke, M. Notley, R. Prasad, K. Quinn, O. Willi, M. Borghesi, Phys. Rev. Lett. **110**, 205001 (2013)
14. N.L. Kugland, D.D. Ryutov, P.-Y. Chang, R.P. Drake, G. Fiksel, D.H. Froula, S.H. Glenzer, G. Gregori, M. Grosskopf, M. Koenig, Y. Kuramitsu, C. Kuranz, M.C. Levy, E. Liang, J. Meinecke, F. Miniati, T. Morita, A. Pelka, C. Plechaty, R. Presura, A. Ravasio, B.A. Remington, B. Reville, J.S. Ross, Y. Sakawa, A. Spitkovsky, H. Takabe, H.-S. Park, Nat. Phys. **8**, 809 (2012)
15. N.L. Kugland, D.D. Ryutov, C. Plechaty, J.S. Ross, H.-S. Park, Rev. Sci. Instrum. **83**, 101301 (2012)
16. S. Kar, M. Borghesi, P. Audebert, A. Benuzzi-Mounaix, T. Boehly, D. Hicks, M. Koenig, K. Lancaster, S. Lepape, A. Mackinnon, P. Norreys, P. Patel, L. Romagnani, High Energy Density Phys. **4**, 26 (2008)
17. L. Volpe, R. Jafer, B. Vauzour, Ph Nicolai, J.J. Santos, F. Dorches, C. Fourment, S. Hulin, C. Regan, F. Perez, S. Baton, K. Lancaster, M. Galimberti, R. Heathcote, M. Tolley, Ch. Spindloe, W. Nazarov, P. Koester, L. Labate, L.A. fOliveiraGizzi, C. Benedetti, A. Sgattoni,

- M. Richetta, J. Pasley, F.N. Beg, S. Chawla, D.P. Higginson, A.G. MacPhee, D. Batani, *Plasma Phys. Control Fusion* **53**, 032003 (2011)
18. H. Daido, M. Nishiuchi, A.S. Pirozhkov, *Rep. Prog. Phys.* **75**, 056401 (2012)
19. M. Nishiuchi, I.W. Choi, H. Daido, T. Nakamura, A.S. Pirozhkov, A. Yogo, K. Ogura, A. Sagisaka, S. Orimo, I. Daito, S.V. Bulanov, J.H. Sung, S.K. Lee, T.J. Yu, T.M. Jeong, I. J. Kim, C.M. Kim, S.W. Kang, K.H. Pae, Y. Oishi, J. Lee, *Plasma Phys. Control Fusion* **57**, 025001 (2015)
20. T. Ditmire et al., *Phys. Rev. Lett.* **78**, 2732 (1997)
21. M. Lezius, S. Dobosz, D. Normand, M. Schmidt, *Phys. Rev. Lett.* **80**, 261 (1998)
22. S. Dobosz, M. Schmidt, M. Pedrix, P. Meynadier, O. Gobert, D. Normand, A.Y. Faenov, A.I. Magunov, T.A. Pikuz, I.Y. Skobelev, N.E. Andreev, *JETP Lett.* **68**, 454–459 (1998)
23. S. Dobosz, M. Schmidt, M. Pedrix, P. Meynadier, O. Gobert, D. Normand, K. Ellert, T. Blenski, A.Y. Faenov, T.A. Pikuz, I. Yu. Skobelev, A.I. Magunov, N.E. Andreev, *JETP*, **88**, 1122–1129 (1999)
24. C. Stenz, V. Bagnoud, F. Blasco, J.R. Roche, F. Salin, A.Ya. Faenov, A.I. Magunov, T.A. Pikuz, I.Y. Skobelev, *Quantum Electron.* **30**, 721–725 (2000)
25. J. Abdallah Jr., A.Y. Faenov, I.Y. Skobelev, A.I. Magunov, T.A. Pikuz, T. Auguste, P. D’Oliveira, S. Hulin, P. Monot, *Phys. Rev. A* **63**, 032706 (2001)
26. I.Y. Skobelev, A.Y. Faenov, A.I. Magunov, T.A. Pikuz, A. Boldarev, V.A. Gasilov, J. Abdallah, Jr., G.C. Junkel-Vives, T. Auguste, S. Dobosz, P. Monot, P. D’Oliveira, S. Hulin, F. Blasco, F. Dorchies, T. Caillaud, K. Bonte, C. Stenz, F. Salin, B.Y. Sharkov, *JETP* **94**, 73 (2002)
27. F. Blasco, C. Stenz, F. Salin, A.Y. Faenov, A.I. Magunov, T.A. Pikuz, I.Y. Skobelev, *Rev. Sci. Instrum.* **72**, 1956 (2001)
28. G.C. Junkel-Vives, J. Abdallah Jr., F. Blasco, C. Stenz, F. Salin, A.Y. Faenov, A.I. Magunov, T.A. Pikuz, I.Y. Skobelev, *Phys. Rev. A* **64**, 021201(R) (2001)
29. A.I. Magunov, A.Y. Faenov, I.Y. Skobelev, T.A. Pikuz, S. Dobosz, M. Schmidt, M. Perdrix, P. Meynadier, O. Gobert, D. Normand, C. Stenz, V. Bagnoud, F. Blasco, J.R. Roche, F. Salin, B.Y. Sharkov, *Laser Part. Beams* **21**, 73 (2003)
30. G.C. Junkel-Vives, J. Abdallah Jr., T. Auguste, P. D’Oliveira, S. Hulin, P. Monot, S. Dobosz, A.Y. Faenov, A.I. Magunov, T.A. Pikuz, I.Y. Skobelev, A.S. Boldarev, V.A. Gasilov, *Phys. Rev. E* **65**, 036410 (2002)
31. G.C. Junkel-Vives, J. Abdallah Jr., F. Blasco, F. Dorchies, T. Caillaud, C. Bonte, C. Stenz, F. Salin, A.Y. Faenov, A.I. Magunov, T.A. Pikuz, I.Y. Skobelev, *Phys. Rev. A* **66**, 033204 (2002)
32. A.I. Magunov, T.A. Pikuz, I.Y. Skobelev, A.Y. Faenov, F. Blasco, F. Dorchies, T. Caillaud, K. Bonte, C. Stenz, F. Salin, P.A. Loboda, I.A. Litvinenko, V.V. Popova, G.V. Bairdin, J. Abdallah, Jr., G. C. Junkel-Vives, *JETP Letters*, **74**, 375–379 (2001)
33. I.Y. Skobelev, A.Y. Faenov, A.I. Magunov, T.A. Pikuz, A.S. Boldarev, V.A. Gasilov, J. Abdallah, Jr., G.C. Junkel-Vives, T. Auguste, S. Dobosz, P. D’Oliveira, S. Hulin, P. Monot, F. Blasco, F. Dorchies, T. Caillaud, C. Bonte, C. Stenz, F. Salin, P.A. Loboda, I.A. Litvinenko, V.V. Popova, G.V. Bairdin, B.Y. Sharkov, *JETP* **94**, 966–976 (2002)
34. J. Abdallah Jr., G. Csanak, Y. Fukuda, Y. Akahane, M. Aoyama, N. Inoue, H. Ueda, K. Yamakawa, A.Y. Faenov, A.I. Magunov, T.A. Pikuz, I.Y. Skobelev, *Phys. Rev. A* **68**, 063201 (2003)
35. M.B. Smirnov, I.Yu. Skobelev, A.I. Magunov, A.Y. Faenov, T.A. Pikuz, Y. Fukuda, K. Yamakawa, Y. Akahane, M. Aoyama, N. Inoue, H. Ueda, *JETP*, **98**, 1123 (2004)
36. V.P. Gavrilenko, A.Y. Faenov, A.I. Magunov, I.Y. Skobelev, T.A. Pikuz, K.Y. Kim, H.M. Milchberg, *Phys. Rev. A* **73**, 013203 (2006)
37. M.E. Sherrill, J. Abdallah Jr., G. Csanak, E.S. Dodd, Y. Fukuda, Y. Akahane, M. Aoyama, N. Inoue, H. Ueda, K. Yamakawa, A.Y. Faenov, A.I. Magnov, T.A. Pikuz, I.Y. Skobelev, *Phys. Rev. E* **73**, 066404 (2006)
38. M. Kanasaki, S. Jinno, H. Sakaki et al., *Radiat. Meas.* **83**, 12 (2015)

39. K.Y. Kim, V. Kumarappan, H. Milchberg, A.Y. Faenov, A.I. Magunov, T.A. Pikuz, I.Y. Skobelev, Phys. Rev. E **78**, 066463 (2006)
40. T. Ditmire et al., Nature **398**, 489 (1999)
41. Y. Kishimoto, T. Masaki, T. Tajima, Phys. Plasmas **9**, 589 (2002)
42. G. Grillon et al., Phys. Rev. Lett. **89**, 064004 (2002)
43. F. Buersgens et al., Phys. Rev. E **74**, 016403 (2006)
44. H.Y. Lu et al., Phys. Rev. A **80**, 051201(R) (2009)
45. A.P. Higginbotham et al., Rev. Sci. Instrum. **80**, 063503 (2009)
46. I. Last, S. Ron, J. Jortner, Phys. Rev. A **83**, 043202 (2011)
47. T. Ditmire et al., Nature **386**, 54 (1997)
48. T. Tajima, Y. Kishimoto, M.C. Downer, Phys. Plasmas **6**, 3759 (1999)
49. S. Sakabe et al., Phys. Rev. A **69**, 023203 (2004)
50. Lu Zhang et al., Appl. Phys. Lett. **100**, 014104 (2012)
51. T. Nakamura, Y. Fukuda, A. Yogo, M. Tampo, M. Kando, Y. Hayashi, T. Kameshima, A.S. Pirozhkov, T.Z. Esirkepov, T.A. Pikuz, A.Y. Faenov, H. Daido, S.V. Bulanov, Phys. Lett. A. **373**, 2584–2587 (2009)
52. Y. Fukuda, A.Y. Faenov, M. Tampo, T.A. Pikuz, T. Nakamura, M. Kando, Y. Hayashi, A. Yogo, H. Sakaki, T. Kameshima, A.S. Pirozhkov, K. Ogura, M. Mori, T. Esirkepov, J. Koga, A.S. Boldarev, V.A. Gasilov, A.I. Magunov, P. Kodama, P. Bolton, Y. Kato, T. Tajima, H. Daido, S.V. Bulanov, Phys. Rev. Lett. **103**, 165002 (2009)
53. T. Nakamura, Y. Fukuda, A. Yogo, M. Tampo, M. Kando, Y. Hayashi, T. Kameshima, A.S. Pirozhkov, T.Z. Esirkepov, T.A. Pikuz, A.Y. Faenov, H. Daido, S.V. Bulanov, Phys. Plasmas **16**, 113106 (2009)
54. Y. Fukuda, H. Sakaki, M. Kanasaki, A. Yogo, S. Jinno, M. Tampo, A.Y. Faenov, T.A. Pikuz, Y. Hayashi, M. Kando, A.S. Pirozhkov, T. Shimomura, H. Kiriyama, S. Kurashima, T. Kamiya, K. Oda, T. Yamauchi, K. Kondo, S.V. Bulanov, Radiat. Meas. **50**, 92–96 (2013)
55. A.Ya. Faenov, T.A. Pikuz, Y. Fukuda, I.Y. Skobelev, T. Nakamura, S.V. Bulanov, Y. Hayashi, H. Kotaki, A.S. Pirozhkov, T. Kawachi, L.M. Chen, L. Zhang, W.C. Yan, D.W. Yuan, J.Y. Mao, Z.H. Wang, V.E. Fortov, Y. Kato, M. Kando, Contrib. Plasma Phys. **53**, 148–160 (2013)
56. G.C. Bussolino, A. Faenov, A. Giulietti, D. Giulietti, P. Koester, L. Labate, T. Levato, T. Pikuz, L.A. Gizzi, J. Phys. D Appl. Phys. **46**, 245501 (2013)
57. P. Koester, G.C. Bussolino, G. Cristoforetti, A. Giulietti, A. Faenov, T. Pikuz, D. Giulietti, T. Levato, L. Labate, L.A. Gizzi, Laser Part. Beams **33**, 331–338 (2015)
58. A. McPherson et al., Nat. (Lond.) **370**, 631 (1994)
59. T.D. Donnelly et al., Phys. Rev. Lett. **76**, 2472 (1996)
60. H.-H. Chu et al., Phys. Rev. A **71**, 061804(R) (2005)
61. Y. Fukuda A.Ya. Faenov, T. Pikuz, M. Kando, H. Kotaki, I. Daito, J. Ma, L.M. Chen, T. Homma, K. Kawase, T. Kameshima, T. Kawachi, H. Daido, T. Kimura, T. Tajima, Y. Kato, S.V. Bulanov, Appl. Phys. Lett. **92**, 121110 (2008)
62. N.L. Kugland et al., Rev. Sci. Insturm. **79**, 10E917 (2008)
63. N.L. Kugland et al., Appl. Phys. Lett. **92**, 241504 (2008)
64. T.A. Pikuz, A.Ya. Faenov, S.V. Gasilov, I.Y. Skobelev, Y. Fukuda, M. Kando, H. Kotaki, T. Homma, K. Kawase, Y. Hayashi, T. Kawachi, H. Daido, Y. Kato, S. Bulanov, Appl. Opt. **48**, 6271–6276 (2009)
65. S.V. Gasilov, A.Ya. Faenov, T.A. Pikuz, Y. Fukuda, M. Kando, T. Kawachi, I.Y. Skobelev, H. Daido, Y. Kato, S.V. Bulanov, Opt. Lett. **34**, 3268–3270 (2009)
66. A. Faenov, T. Pikuz, Y. Fukuda, M. Kando, H. Kotaki, T. Homma, K. Kawase, I. Skobelev, S. Gasilov, T. Kawachi, H. Daido, T. Tajima, Y. Kato, S. Bulanov, Japan. J. Appl. Phys. **49**, 06GK03 (2010)
67. L.M. Chen et al., Phys. Rev. Lett. **104**, 215004 (2010)
68. Y. Hayashi, Y. Fukuda, A.Y. Faenov, M. Kando, K. Kawase, T.A. Pikuz, T. Homma, H. Daido, S.V. Bulanov, Japan. J. Appl. Phys. **49**, 126401 (2010)
69. Y. Hayashi et al., Opt. Lett. **36**, 1614 (2011)

70. L. Zhang et al., Opt. Express **19**, 25812 (2011)
71. H. Kiriyama, M. Mori, Nakai et al., Opt. Lett. **35**, 1497 (2010)
72. A.Ya. Faenov, I.Y. Skobelev, T.A. Pikuz, V.E. Fortov, A.S. Boldarev, V.A. Gasilov, L.M. Chen, L. Zhang, W.C. Yan, D.W. Yaun, J.Y. Mao, Z.H. Wang, JETP Lett. **94**, 187–193 (2011)
73. A.Ya. Faenov, I.Y. Skobelev, T.A. Pikuz, S.A. Pikuz, V.E. Fortov, Y. Fukuda, Y. Hayashi, A. Pirozhkov, H. Kotaki, T. Shimomura, H. Kiriyama, S. Kanazawa, Y. Kato, J. Colgan, J. Abdallah and M. Kando, Laser Part. Beams **30**, 481–488 (2012)
74. A.S. Boldarev, V.A. Gasilov, A.Ya. Faenov, J. Tech. Phys. **49**, 388–395 (2004)
75. A.S. Boldarev, V.A. Gasilov, A.Ya. Faenov, Y. Fukuda, K. Yamakawa, Rev. Sci. Instrum. **77**, 083112 (2006)
76. S. Jinno, Y. Fukuda, H. Sakaki, A. Yogo, M. Kanasaki, K. Kondo, A. Ya. Faenov, I.Y. Skobelev, T. A. Pikuz, A.S. Boldarev, V.A. Gasilov, Appl. Phys. Lett. **102**, 164103 (2013)
77. S. Jinno, Y. Fukuda, H. Sakaki, A. Yogo, M. Kanasaki, K. Kondo, A. Ya. Faenov, I.Y. Skobelev, T.A. Pikuz, A.S. Boldarev, and V.A. Gasilov, Opt. Expr. **21**, 20656–20674 (2013)
78. M. Borghesi, A. Schiavi, D.H. Campbell, M.G. Haines, O. Willi, A.J. Mackinnon, P. Patel, M. Galimberti, L.A. Gizzi, Rev. Sci. Instrum. **74**, 1688 (2003)
79. T. Repsilber, M. Borghesi, J.-C. Gauthier, K. Lowenbruck, A. Mackinnon, V. Malka, P. Patel, G. Pretzler, L. Romagnani, T. Toncian, and O. Willi, Appl. Phys. B, **80**, 905 (2005)
80. S. Orimo, M. Nishiuchi, H. Daido, A. Yogo, K. Ogura, A. Sagisaka, Z. Li, A. Pirozhkov, M. Mori, H. Kiriyama, S. Kanazawa, S. Kondo, Y. Yamamoto, T. Shimomura, M. Tanoue, Y. Nakai, A. Akutsu, S. Nakamura, T. Shirai, Y. Iwashita, A. Noda, Y. Oishi, K. Nemoto, I. W. Choi, T. J.Y. J. H. Sung, T. M. Jeong, H.T. Kim, K.-H. Hong, Y.-C. Noh, D.-K. Ko, J. Lee, Japan. J. Appl. Phys. **46**, 5853 (2007)
81. A.A. Andreev, V.A. Komarov, K.Y. Platonov, A.V. Charukhchev, Tech. Phys. Lett. **33**, 239 (2007)
82. A.Ya. Faenov, T.A. Pikuz, Y. Fukuda et al., Appl. Phys. Lett. **95**, 101107 (2009)
83. A.Ya. Faenov, T.A. Pikuz, Y. Fukuda et al., JETP Lett. **89**, 485–491 (2009)
84. A.Y. Faenov, T.A. Pikuz, S.A. Pikuz Jr. et al., Contrib. Plasma Phys. J. **49**, 507–516 (2009)
85. <http://www.srim.org/#SRIM>
86. A.Ya Faenov, S.A. Pikuz, A.I. Erko et al., Physica Scripta **50**, 333–338 (1994)
87. S. Kar, M. Borghesi, P. Audebert, A. Benuzzi-Mounaix, T. Boehly, D. Hicks, M. Koenig, K. Lancaster, S. Lepape, A. Mackinnon, P. Norreys, P. Patel, L. Romagnani, High Energy Density Phys. **4**, 26 (2008)
88. A.J. Mackinnon, P.K. Patel, M. Borghesi, R.C. Clarke, R.R. Freeman, H. Habara, S. P. Hatchett, D. Hey, D.G. Hicks, S. Kar, M.H. Key, J.A. King, K. Lancaster, D. Neely, A. Nikkro, P.A. Norreys, M.M. Notley, T.W. Phillips, L. Romagnani, R.A. Snavely, R.B. Stephens, R.P.J. Town, Phys. Rev. Lett. **97**, 0450001 (2006)
89. F.E. Merrill, C.L. Morris, K. Folkman, F. Harmon, A. Hunt, B King, in *Proceedings of 2005 Particle Accelerator Conference*, Knoxville, Tennessee, IEEE Catalog Number 05CH37623C (2005). ISBN 0-7803-8860-7
90. V. Malka, J. Faure, Y.A. Gaudel, E. Lefebvre, A. Rousse, K.A. Phuoc, Nat. Phys. **4**, 447 (2008)
91. S. Fritzler, E. Lefebvre, V. Malka, F. Burgy, A.E. Dangor, K. Krushelnick, S.P.D. Mangles, Z. Najmudin, J.-P. Rousseau, B. Walton, Phys. Rev. Lett. **92**, 165006 (2004)
92. J. Faure, Y. Glinec, A. Pukhov, S. Kiselev, S. Gordienko, E. Lefebvre, J.-P. Rousseau, F. Burgy, V. Malka, Nature **431**, 541 (2004)
93. C.G.R. Geddes, C. Toth, J. van Tilborg, E. Esarey, C.B. Schroeder, D. Bruhwiler, C. Nieter, J. Cary, W.P. Leemans, Nature **431**, 538 (2004)
94. S.P.D. Mangles, C.D. Murphy, Z. Najmudin, A.G.R. Thomas, J.L. Collier, A.E. Dangor, E. J. Divall, P.S. Foster, J.G. Gallacher, C.J. Hooker, D.A. Jaroszynski, A.J. Langley, W.B. Mori, P.A. Norreys, F.S. Tsung, R. Viskup, B.R. Walton, K. Krushelnick, Nature **431**, 535 (2004)

95. W.P. Leemans et al., Nat. Phys. **2**, 696 (2006)
96. X. Wang et al., Nat. Commun. **4**, 1988 (2013)
97. H.T. Kim et al., Phys. Rev. Lett. **111**, 165002 (2013)
98. P.E. Masson-Laborde, M.Z. Mo, A. Ali, S. Fourmaux, P. Lassonde, J.C. Kieffer, W. Rozmus, D. Teychenné, R. Fedosejevs, Phys. Plasmas **21**, 123113 (2014)
99. W.P. Leemans et al., Phys. Rev. Lett. **113**, 245002 (2014)
100. V. Ramanathan, S. Banerjee, N. Powers, N. Cunningham, N.A. Chandler-Smith, K. Zhao, K. Brown, D. Umstadter, Phys. Rev. Spec. Topics Accelerators Beams **13**, 104701 (2010)
101. W. Schumaker, N. Nakanii, C. McGuffey, C. Zulick, V. Chyvkov, F. Dollar, H. Habara, G. Kalintchenko, A. Maksimchuk, K.A. Tanaka, A.G.R. Thomas, V. Yanovsky, K. Krushelnick, Phys. Rev. Lett. **110**, 015002 (2013)
102. S. Tokita, M. Hashida, S. Inoue, T. Nishioji, K. Otani, S. Sakabe, Phys. Rev. Lett. **105**, 215004 (2010)
103. Y. Kishimoto, L. Hillman, T. Tajima, *High Field Science* (Kluwer- Plenum, NewYork, 2000), p. 85
104. Y. Fukuda et al., Phys. Lett. A **363**, 130 (2007)
105. L.M. Chen, W.C. Yan, D.Z. Li, Z.D. Hu, L. Zhang, W.M. Wang, N. Hafz, J.Y. Mao, K. Huang, Y. Ma, J.R. Zhao, J.L. Ma, Y.T. Li, X. Lu, Z.M. Sheng, Z.Y. Wei, J. Gao, J. Zhang, Sci. Rep. **3**, 1912 (2012)

Chapter 13

Recent Progress in Laser Ion Acceleration

Toshiki Tajima

Abstract The first laser ion acceleration experiments have begun with a method based on the TNSA (target normal sheath acceleration) that did not have an adiabatic process of the accelerating structure created by laser. A great deal of efforts have been dedicated to ever increase the adiabatic process of the accelerating structure with the ions since then. This acquiring of adiabaticity may be done by reducing the group velocity of the laser significantly to match that of ions, or to increase the ion velocity as fast as possible in order to match the fast accelerating structure created by laser. The methods of RPA (radiation pressure acceleration) and CAIL (coherent acceleration of ions by laser) belong to the latter. Finally, the recent entry of the single-cycle laser pulse acceleration (SCPA) marks another notch in the progress to make ion acceleration condition even more accessible and the acceleration results far more attractive by eradicating the oscillatory interference effects.

13.1 Introduction

Veksler [1] introduced the concept of collective acceleration in 1956. His vision is consisted of two elements. The first element is the introduction of plasma as the accelerating medium. In the conventional acceleration method when we increase the accelerating electric field in a vacuum surrounded by a metallic tube, the electric field on the surface of the metallic wall increases and eventually the surface begins to spark, yielding electron breakdown of the metal. As is necessary in most accelerator structure, waveguide comes with a slow wave structure. Such a structure is accompanied by a protruded surface metallic structure, which makes the local electric field even greater. In addition most materials contain impurities within its material structure, such as f-centers. These in combination make the metallic breakdown field far greater than the typical gradient that shifts the electronic

T. Tajima (✉)

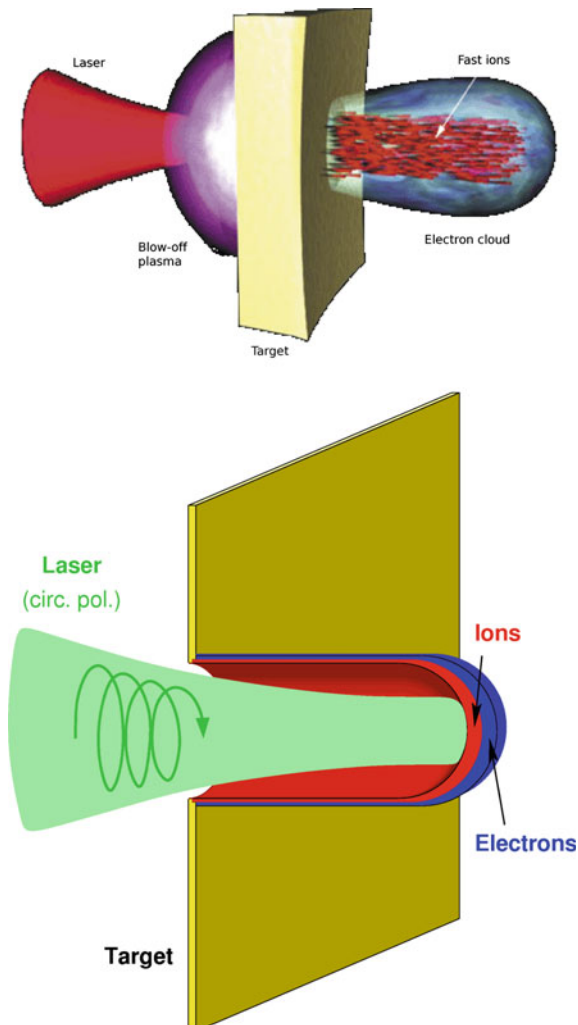
Department of Physics and Astronomy, University of California at Irvine, Irvine, CA, USA
e-mail: ttajima@uci.edu

wavefunction by an eV over an Angstrom, i.e. electric field of 10^8 eV/cm down to typically MeV/cm (or even less). In order to overcome this difficulty Veksler suggested to use the already broken down material of plasma to begin with. His second element is to resort to the collective field as opposed to collective force. As is known, the fields in plasma permeate in such a way that a charge feels nearly all charges through the Coulombic interaction. If we further marshal the plasma to form a collection of charges made up with Ne (with N charges), the interaction force is proportional to $(Ne)^2$, indicating that the collective force is proportional to N^2 , as opposed to the conventional linear force proportional to N . (If N is 10^6 , the collective force is 10^6 times greater than its linear counter part).

Lured by this concept, a large body of investigations ensued [2–5]. Norman Rostoker's program was one of them: some of these efforts are reviewed in the Proceedings of the Norman Rostoker Memorial Symposium [6]. For example, in one of these attempts [7] an electron beam is injected into a plasma to cause a large amplitude plasma wave by the beam-plasma interaction (a collective interaction). It was suggested that such large amplitude wave would trap ions and accelerate them to the similar speed of the electron beam. If ions were to be trapped by speeding electron cloud or beam with energy ε_e , the ions would be accelerated to the energy of $\varepsilon_i = (M/m)\varepsilon_e$, where M and m are masses of ions and electrons, respectively, because they would speed with the same velocity. Since the mass ratio M/m of ions to electrons is nearly 2000 for protons and greater for other ions, the collective acceleration of ions would gain a large energy boost. None of the collective acceleration experiments in those days, however, found energy enhancement of this magnitude mentioned above. The primary reason for this was attributed to the sluggishness (inertia) of ions and the electrons being pulled back to ions, instead of the other way around, too fast 'reflexing (return flow) of electrons' as described in [7]. The ion acceleration takes place only over the sheath of electrons (of the beam injected) that are ahead of ions, while the sheath is tied to the beam injection aperture (an immovable metallic boundary in that experiment). As we see in more detail, Mako and Tajima theoretically found that the ion energy may be enhanced only by a factor of $2\alpha + 1$ (which is about 6 or 7 for typical experimental situations and α will be defined later in Sect. 12.2) over the electron energy, instead of by a factor of nearly 2000, due to the electron reflexing and no co-propagation of the electron beam and the ions, while the formed sheath is stagnant where it was formed. (For example, Tajima and Mako [8] suggested to reduce the culpable electron reflexion by providing a concave geometry. Similar geometrical attempt to facilitate the laser-driven ion acceleration would appear also later in 2000s–2010s.) In year 2000 the first experiments [9–11] to collectively accelerate ions by laser irradiation were reported. In these experiments a thin foil of metallic (or other solid) materials was irradiated by an intense laser pulse, which produced a hot stream of electrons from the front surface that faced the laser pulse, propagating through the thin foil emerging from the back surface of the metal foil. Now this physical situation of what is happening at the rear surface of the foil is nearly equivalent to what the group of Rostoker had done in 1970s and 80s in terms of the dynamics of electrons emanating from the metallic boundary and its associated ion response.

The superheated electrons by the laser caused the acceleration of ions in the sheath which was stuck stationary on the rear surface of the target, but not beyond. Such acceleration was then called the Target Normal Sheath Acceleration (TNSA) [9–12]. (The words “target normal” were attached, though in some of the experiments the laser incidence was away from the normal direction of the surface. Yet, the accelerated ions were in the normal direction of the rear surface. This shows that the ion momentum was not a direct transfer of that of laser photon momentum, but an indirect one via the conversion through the electron heating. The more direct momentum conversion remained a task for the future.) Since then, a large amount of efforts have been steadily dedicated to this subject following different schemes. Figure 13.1 compares qualitatively TNSA and CAIL schemes. We revisit some of

Fig. 13.1 Comparison of the TNSA laser-target interaction and the CAIL one. In the TNSA (*top*), the target remains unmoved, behind which a sheath is formed and ion acceleration is limited over this sheath. When the target is sufficiently thin (*bottom*), some portion of the target may commove with the ponderomotively accelerated electron layer. This achieves partial coherence of ion motion behind the electron sheet (CAIL) (from [22])



these electron dynamics in some detail and analyze subsequent ion dynamics under these electron dynamics. Since much of the similarities of the physics at the sheath and somewhat lost knowledge of the earlier (1970s and 1980s) research, it may not be without merit to revisit of this analysis below. From such a discussion we hope in this paper that we can connect the research of the earlier collective acceleration and the contemporary laser ion acceleration and learn the lesson from the former for the latter.

Because of the advantage in accelerating limited mass by laser to cope with the mismatch between the electron and ion dynamics as discussed above, experiments producing high-energy ions from sub-micrometer to nanometer targets (much thinner than ones in early experiments) driven by ultrahigh contrast (UHC) short-pulse lasers [13–17] have attracted a recent strong interest. Of particular focus is how much the ion energy enhancement is observed in the experiments and simulations in these thin targets and how it scales with the laser intensity.

The experiments and simulations show that the proton energy increases as the target thickness decreases for a given laser intensity, and that there is an optimal thickness of the target (at several nm) at which the maximum proton energy peaks and below which the proton energy decreases. This optimal target thickness for the peak proton energy is consistent with the thickness dictated by the relation $a_0 \sim \sigma = \frac{n_0 d}{n_c \lambda}$, where σ is the (dimensionless) normalized electron areal density, a_0 , d are the (dimensionless) normalized amplitude of electric field of laser and target thickness [18–20]. Here we introduce the dimensionless parameter of the ratio of the normalized areal density to the normalized laser amplitude $\xi = \sigma/a_0$. This optimal condition is understood as arising from the condition that the radiation force pushes out electrons from the foil layer if $\sigma \leq a_0$ or $\xi \leq 1$, while with $\sigma \geq a_0$ or $\xi \geq 1$ the laser pulse does not have a sufficient power to cause maximal polarization to all electrons. Note that this optimal thickness for typically available laser intensity is way smaller than for cases with previously attempted target thicknesses (for ion acceleration). See Fig. 13.2 for increased degrees of adiabaticity of ion acceleration. In the case (a) of Fig. 13.2, laser generates energetic electrons on the front surface of the thick target. Electrons travel through the target to emerge from the rear side with a broad energy spread. These electrons exit into vacuum and pull ions. However, most electrons are pulled back to the immobile target before ions gain much energy. Electrons at the margin of the electron cloud are ejected out by the electron space charge. In the case of Fig. 13.2b electrons with a Delta-function energy spectrum enter from the metallic immobile (real) surface. Electrons rush out in vacuum to pull ions. However, most electrons are pulled back to the immobile boundary before ions gain large energy. Some electrons are ejected forward. The electron dynamics has much in common with case (a), although the electron spectrum is broad and has a tail in (a). Considering the case Fig. 13.2c, one significant difference of (c) from (a) is that the electron energy is directly determined by the laser and its ponderomotive potential beyond the rear surface of that target. Thus the energy of ions is expected to have a narrow distribution and a higher peak than in (a). When the target is sufficiently thin (Fig. 13.2d) the rear

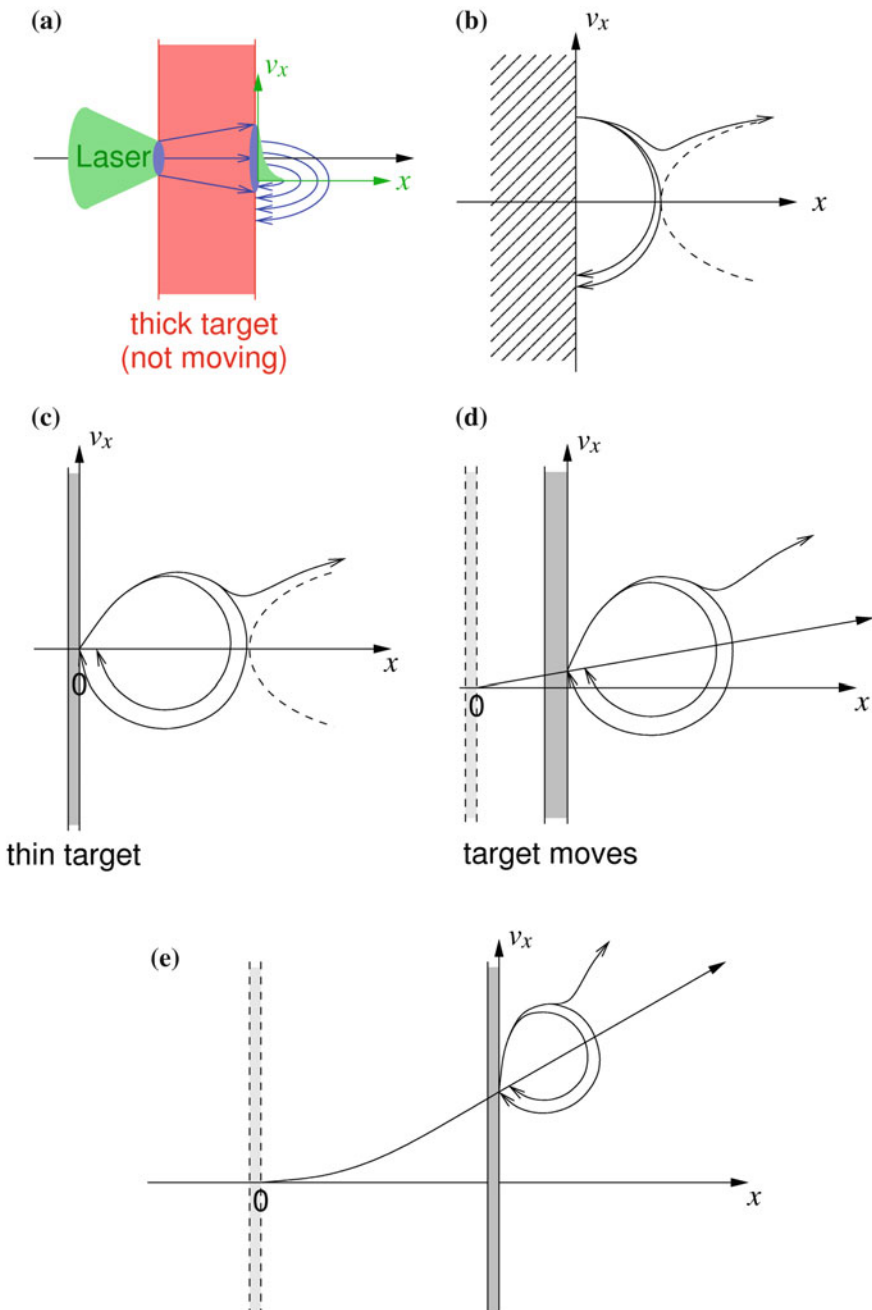


Fig. 13.2 Various degrees of target motions from TNSA (a) to totally commoving case (e). **a** A TNSA. **b** The Mako-Tajima scenario. **c** A case study with an ultra thin target that is immobile. **d** When the target is sufficiently thin. **e** When the target is pushed with the laser ponderomotive force (such as the circularly polarized laser pulse) without too much heating of electrons (from [22])

surface of the target (and some times entire target) begins to move, while the laser pushes the target. When the target is pushed with the laser ponderomotive force (such as with circularly polarized laser pulse) without too much heating of electrons (Fig. 13.2e), ions in the target as a whole are trapped in an accelerating bucket with tight phase space circles. If and when the laser leaks through and electrons are ejected forward, the bucket may begin to collapse. Cases (c)–(e) belong to the regime of CAIL, while (e) is in particular in the RPA conditions.

Thus we attribute the enhanced value of the maximum proton energy observed in the experiment [21] to the ability at identifying and providing prepared thin targets on the order of nm to reach this optimal condition. This experiment has been analyzed closely [22, 23]. In reality at this target thickness the laser field teeters over partial penetration through the target, rendering the realization of optimum rather sensitive. Under this condition, electron motions maintain primarily those organized characteristics directly influenced by the laser field, rather than chaotic and thermal motions of electrons resulting from laser heating. In 1D Particle-In-Cell (PIC) simulation we observe that momenta of electrons show in fact coherent patterns directing either to the ponderomotive potential direction, the backward electrostatic pull direction, or the wave trapping motion direction, in a stark contrast to broad momenta of thermal electrons. In another word, through a very thin target the partially penetrated laser fields enable the electrons to execute dynamic motions still directly tied with the laser rather than thermal motions. We note that the ponderomotive force due to this trapped radiation contributes to the acceleration of electrons in this sheet and thus retards these electrons from being decelerated by the electrostatic force emanated from the diamond foil. In a typical sheath acceleration scheme the termination of ion acceleration commences due to this electron reflexing by the electrostatic field.

On the other hand, most of the theories have been based on the so-called Plasma Expansion Model (PEM) [12], which is motivated by much thicker and massive target. In this regime electrons are first accelerated by the impinging relativistic laser pulse and penetrate the target driven by ponderomotive force. Leaving the target at the rear side, electrons set up an electrostatic field that is pointed normal to the target rear surface, which is the so-called TNSA (Target Normal Sheath Acceleration) acceleration. Most electrons are forced to turn around and build up a quasistationary electron layer. These fast electrons are assumed to follow thermal or Boltzmann distribution in theoretical studies of the conventional TNSA mechanism for thicker targets [12, 14, 24, 25], where the acceleration field is estimated by the exponential potential dependency in the Poisson equation. Though this mechanism is widely used in the interpretation of the experimental results, it does not apply to the ultrathin nanometer scale targets, because the direct laser field and attenuated partially transmitted laser pulse play an important role in electron dynamics and the energetic electrons oscillate coherently, instead of chaotic thermal motions. Based on a self-consistent solution of the Poisson equation and TNSA model, Andreev et al. [14] had proposed an analytical model for thin foils and predicted the optimum target thickness is about 100 nm. It obviously does not explain the experimental results [21, 26].

13.2 Self-consistent Electrostatic Sheath Dynamics

We consider the electrostatic sheath that is created behind the ponderomotive drive of the laser pulse and its dynamics in a self-consistent treatment to evaluate the maximal ion energies in the laser driven foil interaction in which the foil dynamics also counts when the foil is sufficiently thin. When the foil is thick with $\xi \gg 1$, the foil is not moving and this is the in the regime of TNSA. (When the foil is thick and the laser pulse is completely reflected, the ion acceleration may be described by the plasma expansion model for thicker targets [24].) On the contrary, in case of $\xi \ll 1$, the transmission is dominant and the laser passes without too much interaction with the target (see Fig. 13.3). However, we will note that there is a regime ($\xi \gg 1$) with thickness still much smaller than that for TNSA for thicker targets. The optimum ion acceleration condition is, as discussed, in the range of $\xi \sim 1$ ($0.1 < \xi < 10$). There appears a partially transmitted laser pulse and behind the target energetic electrons still execute the collective motions in the laser field. Electrons quiver with the laser field and are also pushed forward by the ponderomotive force. In the region ahead of the exploding thin target, there are three components of characteristics orbits: a set of orbits in forward direction (with angle 0°), the second backward (with 180°), and the third with loci with curved loops [23]. The first two are characteristics observed even in a simple sheath, but also present in the current case, where perhaps the forward is as vigorous or more so as the backward one. The third category belongs to the orbits of trapped particles in the laser field or the ponderomotive potential. For a reflexing electron cloud the distribution shows only two components, the forward one and the backward one.

In an ultra-thin target, the laser electromagnetic fields largely sustain coherent motions of electrons. As partially penetrated laser fields in addition to the laser fields in the target, the electron motion under laser fields is intact and is characterized by the transverse field. The electron energy consists of two contributions,

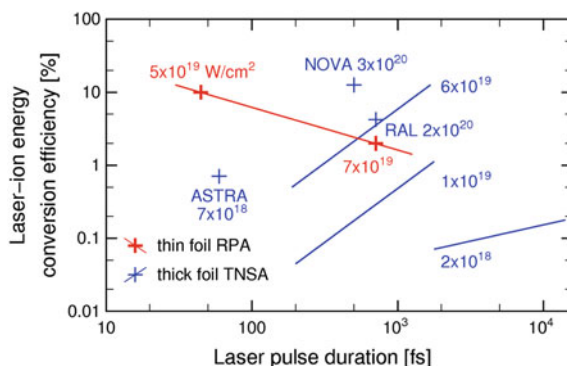


Fig. 13.3 Comparison of the conversion efficiency of laser energy to ion energy from thick targets (TNSA mechanism, blue crosses and lines) with ultrathin targets (CAIL, red crosses and line). For the TNSA mechanism smooth curves from the fluid model by Fuchs [13] are shown together with some experimental points: ASTRA [48], NOVA [9], RAL [49] (from [22])

the kinetic energy of (organized) electrons under laser and the ponderomotive potential of the partially penetrated laser fields that help sustain the electron forward momentum. Following the analysis of Mako and Tajima [8], the plasma density can be determined by:

$$n_e = 2 \int_0^{V_{\max}} g(V_x) dV_x, \quad (13.1)$$

$$V_{\max} = c \sqrt{1 - m_e^2 c^4 / (E_0 + m_e c^2)^2}, \quad (13.2)$$

where g is the electron distribution function and E_0 is the maximum electron energy in this theoretical distribution and we call this the characteristic electron energy hereon.

The forward current density of electrons J and electron density n_e are related through

$$J(v) = -e \int_0^{V_{\max}} V_x g dV_x, \quad (13.3)$$

$$n_e = \frac{2}{e} \int_0^{V_{\max}} \frac{dJ/dv}{v} dv. \quad (13.4)$$

At a given position in the reflexing electron cloud where the potential is ϕ , the total particle energy (disregarding the rest mass energy) is given by

$$E = (\gamma - 1)m_e c^2 - e\phi. \quad (13.5)$$

Current density can be determined from the 1D simulations results.

In the regime between the TNSA and the RPA [27] and its sisters [28–31] sits a regime in which ion acceleration is more coherent with the electron dynamics than the TNSA but it is not totally synchronous as in the RPA. In this regime the acceleration of charged particles of ions produces a propensity to gain energies more than thermal effects would, as is the case for TNSA (and thus entailing the exponential energy spectrum) with heavier relative weight in the greater energy range in its energy spectrum characteristics. The power spectrum is one such example. On the other hand, in this regime the ponderomotive force and its induced electrostatic bucket behind it are not strong enough to trap ions, in contrast to the relativistic RPA where the laser's ponderomotive drive, following electrostatic bucket, ions trapped in it are moving in tandem along the laser. In the RPA the train of bow shock of electrons preceding the laser pulse and the following electrostatic bucket that can be stably trap ions is stably formed. This structure is not so unlike the wave train of laser wakefield acceleration (LWFA) [32]. In LWFA since particles to be accelerated are electrons, it is when the

amplitude of the laser becomes relativistic (i.e. $a_0 = eE_l/m\omega_0c \sim O(1)$, about 10^{18} W/cm²), the electron dynamics sufficiently relativistic so that trapping of electrons with the phase velocity c is possible and a process of coherent electron acceleration and thus a peaked energy spectrum is possible. For the ion acceleration for RPA wave structure that is speeding at nearly $\sim c$ to trap ions in the electrostatic bucket, it takes for ions to become nearly relativistic, i.e. $a_0 \sim O(M/m)$, or $\sim 10^{23}$ W/cm². Otherwise, the phase velocity of the accelerating structure for ions has to be adiabatically (i.e. gradually) increased from small value to nearly c . Only an additional slight difference is that the LWFA excites an eigen mode of plasma, which is the plasma oscillations as a wake of the electrostatic charge separation caused behind the laser pulse, while the electrostatic bucket for the ion acceleration is not exciting eigen modes of the plasma. Thus the more direct comparison of the RPA structure is the ponderomotive acceleration as discussed in [33]. In any case the spectrum of RPA can show (in its computer simulations such as in [27]) some isolated peak of the energy spectrum for the trapped ion bucket. Here we recall that in the experimental history of even in the LWFA till the so-called self-injection of electrons by the LWFA bucket's 3D structure was realized by short enough (and strong enough) laser pulse [34–36], the energy spectrum had not shown isolated peaked distribution.

In this section, we focus on the regime between the TNSA and RPA, having a power energy spectrum. In this sense the power law spectrum is a symbol for this regime between TNSA and RPA. Here, it is instructive to pose the power law dependence of the electron current as a function of the electron energy: the power-law dependence may be characterized by two parameters, the characteristic electron energy E_0 and the exponent of the power-law dependence on energy E .

$$J(E) = -J_0(1 - E/E_0)^\alpha. \quad (13.6)$$

The ‘coherence’ index α here designates the steepness of the energy dependence on electrons and is a measure of coherence of the electron motion. In other words the greater α is, the more electrons in coherent motion are contributing to the overall current of electrons. Thus we may call α the coherence parameter of electrons. Usually the most energetic electrons are lost from the system and have minor contribution to the ion acceleration [26]. The maximum electrostatic potential is smaller than the laser ponderomotive potential or the characteristic electron energy E_0 . In the high laser intensity case the relativistic electrons are dominant so that the integral is carried out with the relativistic kinematics as:

$$\begin{aligned} n_e &= \frac{2}{e} \int_0^{V_{\max}} \frac{dJ(v)/dv}{v} = \frac{2}{ec} \int_{-e\phi}^{E_0} \frac{dJ(E)}{dE} dE \\ &= \frac{2J_0}{ec} (1 + e\phi/E_0)^\alpha = n_0(1 + e\phi/E_0)^\alpha, \end{aligned} \quad (13.7)$$

where n_0 is the initial plasma density and $J_0 = en_0c/2$.

13.3 Self-similar Evolution of Ion Dynamics

The system's evolution needs to be tracked self-consistently with electrons, ions and the interacting electrostatic potential in time. These consist of a highly non-linear coupled system of equations. We treat electrons as discussed in section II, while we describe ions in non-relativistic nonlinear equations in this section.

The non-relativistic fluid equations are used to describe the response of the ions to the electrostatic field as follows:

$$\frac{\partial n_i}{\partial t} + \frac{\partial}{\partial x}(v_i n_i) = 0, \quad (13.8)$$

$$\frac{\partial v_i}{\partial t} + v_i \frac{\partial v_i}{\partial x}(v_i n_i) = \frac{Qe}{M} \frac{\partial \phi}{\partial x}. \quad (13.9)$$

where the laser ponderomotive force for ions is neglected.

In order to solve the equations self-consistently, the self-similar condition is invoked by using the fluid equations and electron distribution with the self-similar parameter

$$\zeta = x/(v_0 t), \quad (13.10)$$

$$v_0 = (Qe\phi_0/M)^{1/2}, \quad (13.11)$$

$$e\phi_0 = E_0, \quad (13.12)$$

which is the characteristic electron energy. We introduce the dimensionless parameters:

$$U = v_i/v_0, \quad \mathfrak{R} = n_i/n_0, \quad \psi = \phi/\phi_0 \quad (13.13)$$

Equations (13.8) and (13.9) now take the form:

$$\mathfrak{R}'(U - \zeta) + \mathfrak{R}U' = 0, \quad (13.14)$$

$$U'(U - \zeta) + \frac{d\psi}{d\mathfrak{R}} \mathfrak{R}' = 0, \quad (13.15)$$

$$\mathfrak{R} = (1 + \psi)^\alpha. \quad (13.16)$$

In deriving (13.16) the quasi-neutrality condition is imposed.

The conservation of energy is assessed with the boundary condition on the surface of the target:

$$U^2/2 + \psi = 0 \quad \text{at } \zeta = 0. \quad (13.17)$$

The solutions to the set of (13.14–13.16) are:

$$\Re = \left\{ \frac{\alpha}{(2\alpha+1)^2} (\zeta - \sqrt{2\alpha+1})^2 \right\}^\alpha, \quad (13.18)$$

$$U = \frac{2\alpha+2}{2\alpha+1} \zeta - \sqrt{\frac{2}{2\alpha+1}}, \quad (13.19)$$

$$\psi = \frac{\alpha}{(2\alpha+1)^2} (\zeta - \sqrt{2\alpha+1})^2 - 1. \quad (13.20)$$

Equations (13.18–13.20) also read in usual units as:

$$n_i = n_0 \left\{ \frac{\alpha}{(2\alpha+1)^2} \left(\zeta - \sqrt{2(2\alpha+1)} \right)^2 \right\}^\alpha, \quad (13.21)$$

$$v_i = \left(\frac{QE_0}{M} \right)^{1/2} \left(\frac{2\alpha+2}{2\alpha+1} \zeta - \sqrt{\frac{2}{2\alpha+1}} \right), \quad (13.22)$$

$$\phi = \phi_0 \frac{\alpha}{(2\alpha+1)^2} (\zeta - \sqrt{2\alpha+1})^2 - \phi_0. \quad (13.23)$$

The maximum energy is assessed when the ion density vanishes. This yields from (13.18–13.19):

$$\epsilon_{\max,i} = (2\alpha+1)QE_0. \quad (13.24)$$

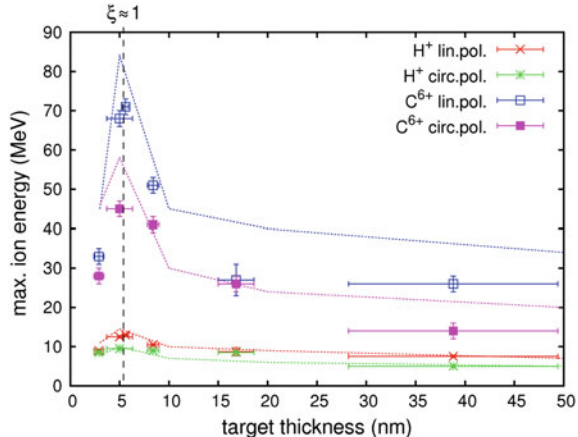
In (13.24) we see that the ion energy is greater if the coherence parameter of electrons is greater. Here E_0 takes the following form $E_0 = mc^2(\sqrt{(1+a_0^2)-1})$ [22].

A more general expression for the time-dependent maximum kinetic energy at the ion front from (13.22) is:

$$\epsilon_{\max,i}(t) = (2\alpha+1)QE_0 \left((1+\omega t)^{1/(2\alpha+1)} - 1 \right), \quad (t \leq 2\tau). \quad (13.25)$$

Here τ is the laser pulse duration and ω is the laser frequency. At the beginning the ion energy is $\epsilon_{\max,i}(0) = 0$ and the ion energy approaches infinity as long as the time $t \rightarrow \infty$. Normally as the maximum pulse duration of a CPA (Chirped Pulse

Fig. 13.4 Maximum ion cutoff energies as a function of target thickness in the regime of CAIL experiments [21]. Theoretical curves are from the CAIL theory [22, 23]. Observed values and theory (CAIL) are in good agreement over a broad parameter range (from [22])



Amplification) laser is less than picoseconds, the final ion energy from (13.25) is only about $\varepsilon_{\max,i}(t = 1 \text{ ps}) = 2(2\alpha + 1)QE_0$.

The above theory of CAIL has been developed to analyze the experiment [21]. Along with this theory computational simulation has been also carried out [22, 23]. These three are well agreeing with each other (see Fig. 13.4). It is further noted that while the linearly polarized (LP) laser irradiation process is well described, such as the maximum energies by the CAIL, when the polarization is switched to the circular polarization (CP), the energy spectrum of the accelerated ions show a quasi-monoenergy feature [21]. This latter tendency is interpreted as the CP's ability to accelerate electrons and thus ions more adiabatically [21]. This insight indicates a potentially very important path toward improving laser driven ion acceleration. The more recent experiment by a Korean group also shows similar tendency. They have adopted far higher intensity of laser (up to $6 \times 10^{20} \text{ W/cm}^2$) than in [21] and also obtained much higher energies of accelerated ions [37] than in [21]. More importantly, their results [37] show that the CP irradiation shows some preliminary evidence that its acceleration process is more adiabatic (accompanying a slightly isolated high energy population, which does now show up in the LP case. This tendency, though still very preliminary, is consistent with the earlier finding of [21]. We will continue this discussion in the next section.

13.4 Single-Cycled Pulse Acceleration (SCPA)

Before we discuss the SCPA here, let us briefly review the RPA [27]. With the intensity of a laser pulse ($I \sim 10^{23} \text{ W/cm}^2$) so that the ion dynamics becomes nearly relativistic, as we have mentioned above, the stably generated space charge separation (bucket) behind the ponderomotively accelerated electron layer driven by this

intense laser can manage to pick up ions to stably and adiabatically accelerate them in the bucket. Therefore, the energy spectrum shows a distinct (monoenergetic) peak, rather than monotonically decreasing spectra of TNSA (exponential) or CAIL (\sim power-law). Furthermore, the energy gain of an ion asymptotically becomes relativistic [27]:

$$\varepsilon_i(t) = \left[a_0^2 (\omega_0 / \omega_p)^2 (m/M) (ct/l) \right]^{1/3}, \quad (13.26)$$

where l is the ion layer thickness, m and M are the electron and ion masses. At this stage the system settles with a slow increase of ion energy in time (1/3-power of t). Including the saturation, we obtain:

$$N_i \varepsilon_i|_{\max} / 2\kappa \varepsilon_l \sim 2\kappa \varepsilon_l / [2\kappa \varepsilon_l + N_i M c^2], \quad (13.27)$$

where κ is the reflected fraction of the laser, N_i the ion number, and ε_l is the laser energy. Thus we see that RPA can be a very efficient acceleration method, if the laser energy is highly relativistic ($2\kappa \varepsilon_l > N_i M c^2$). This is because first the energy transfer from laser to electrons is nearly perfect, and secondly the electron energy is very effectively and adiabatically transferred to ions, as both electrons and ions are nearly synchronously moving at about the speed of light c , which in turn is the speed at which the laser is propagating. In this regime, as mentioned, the ion energy may become relativistic (>GeV). All the three entities: photons, electrons, and then ions, in this regime of RPA are synchronously behaving. These features are extremely attractive. Alas, the necessary laser intensity is very high. It would typically take 10 kJ compressed laser over 20–30 fs pulse. So far we have not realized this regime experimentally.

After the original laser ion acceleration experiments in 2000, laser-driven ion acceleration has been vigorously investigated both theoretically and experimentally in recent years (see reviews [38, 39]). The earliest and most discussed laser ion acceleration regime of the TNSA [9–12] has a large divergence of ion beam and almost 100 % energy spread. In TNSA the ion energy is tied to the energy of spreading electrons that are heated by the injected laser and thus the ion energy gain, broadly speaking, has a relatively weak laser intensity dependence (such as the power of intensity 1/3 to ½), although it depends on other conditions and parameters too. Here the laser intensity I is proportional to a_0^2 . In many modern laser ion acceleration experiments lasers are in the domain of $a_0 > 1$. Substantial efforts have been dedicated to decrease the energy spread of ions, such as to restrict ions in a small region where the sheath field could be treated as homogenous [29, 30, 40, 41]. Such a method relies on complicated target fabrication techniques and the conversion efficiency is still quite low. For a more sophisticated path of the RPA (radiation pressure acceleration) with a thin plane foil irradiated by an ultra intense laser pulse [20, 27, 28], the ion energy gain is greater than the TNSA and its intensity dependence is more favorable, proportional to the first (1) power of the laser intensity $a_0 \gg 1$, while the ion energy spectrum is much narrower than that of TNSA, though the required laser intensity is

huge (typically on the order of 10^{23} W/cm 2). The CAIL (coherent acceleration of ions by laser) regime, on the other hand, requires less laser power that is already currently available [21–23, 27] and has the ion energy dependent on the $\frac{1}{2}$ power of the intensity (for $a_0 \gg 1$, though again it depends on other parameters as well) with a quasi-monoenergetic ion spectrum. Thus CAIL sits mechanism-wise in between the TNSA and RPA. In many of ion acceleration experiments the laser contrast requirement remains a challenge for the state-of-art laser technology. In addition, because of the hole boring effects and transverse instabilities such as Rayleigh-Taylor instability, the acceleration would be soon terminated, which reduces the acceleration efficiency seriously [28, 29].

One way to improve this situation is to employ a circularly polarized laser. A marked reduction of laser intensity that Esirkepov et al. [27] required may be accomplished if the ponderomotive acceleration of electrons by the laser pulse is smoother and more adiabatic over a linearly polarized laser irradiation with otherwise like parameters of laser and target even if the laser intensity is far less than that of Esirkepov et al. [27]. This is because the ponderomotive acceleration of CP removes a component of electron acceleration at 2ω frequency, which is present in the LP pulse case. Recall that the longitudinal acceleration of electrons is exerted by the Lorentz term $v \times B$, in which v is proportional to E , the laser field. In these experiments some evidence of semi-isolated or quasi-monoenergetic energy spectrum begins to manifest. However, their spectrum remains to be improved to become a beam of isolated monoenergy. There is some circumstantial evidence of ions to be trapped behind the electron charge sheet. To increase the adiabaticity of ion acceleration, additional possibilities include to make the group velocity of the laser to increase from the small (near zero) at the beginning to gradually increase to a high value. This may be done by setting the plasma density at the entrance at the critical density and to reducing it gradually so that the group velocity of the laser tends to increase [40, 41]. Here we reminisce an earlier proposal by Rau and Tajima [42] to make an adiabatic acceleration by changing the group velocity of electromagnetic pulse in the increasing magnetic field (or equivalently decreasing the plasma density) in a magnetized plasma in such a way to increase the Alfvén velocity.

An alternative approach to this is to remove the multiple oscillations of the ponderomotive force by eliminating the multiple oscillations of the laser pulse itself. An earliest such a suggestion was made by Rau et al. [43] by the subcycle laser pulse acceleration. In their computer simulation it was known that a coherent monoenergetic electron pulse may be produced that could trigger a coherent ions acceleration. However, even though a subcyclic pulse (in purely 1D) is a solution of Maxwell's equation, a realization in 3D geometry is not easy.

In 2014 a new method of compression of a contemporary ultrashort (typically ~ 30 fs) laser pulse further into a single-cycle pulse has been invented [44]. This method is expected to be highly efficient (on the order of 90 % conversion). Thus if we have a typical 1PW laser [45] at 30 fs, this thin film compression technique would reduce the laser pulse into a single cycle with ~ 10 PW at 3 fs. It has been recently suggested to employ such a single-cycle laser pulse to drive ion

acceleration [46]. This idea provides a new highly efficient and instability-free ion acceleration mechanism using contemporary available lasers on the PW class. This regime of acceleration is different and far more efficient with a far sharper monoenergetic spectrum of ions unlike the classical TNSA and CAIL. Further, this regime takes far smaller laser energy than that required in the known regimes of RPA. When a single cycle Gaussian pulse with intensity 10^{23} W/cm² incides on a 50 nm planar CH foil, the single-cycle pulse pushes forward through the ponderomotive force an isolated relativistic electron bunch and in turn protons can be accelerated in the longitudinal electrostatic field. With a thin target this mechanism can accelerate ions in quite a long distance stably without suffering from the transverse instabilities. Under this quite stable acceleration structure a highly monoenergetic ultrashort (\sim fs) proton bunch should be obtained.

First, a computational comparison between different laser pulses by varying laser amplitude a_0 and pulse duration τ under the same total energy E , where $E \propto a_0^2\tau$ is being made. It is found that with different pulse durations the acceleration efficiency of ions sharply varies. For example, a scan has been done of the normalized laser vector potential $a_0 = 50, 100, 200$ and correspondingly the of pulse duration $\tau = 16T, 4T, 1T$, respectively, where T is the laser oscillation period. With the higher laser amplitude and shorter pulse duration (in particular with the single-cycle pulse) the cutoff energy of ions is increased by a large amount. Another important new point [46] is that under the single-cycle pulse condition the ratio ξ between the electron areal density and normalized laser amplitude is about 0.1 and is much smaller than the optimal value of this ratio in the traditional RPA acceleration ($\xi_{opt} \sim 0.4 + 3/a_0$) [18].

The single pulse acceleration is investigated in detail by two-dimensional particle-in-cell (2D-PIC) simulations [46]. The best result arises when the ratio between electron areal density and normalized laser intensity in our single-cycled laser case is $\xi = 0.12$. When the intense laser pulse incides on the nanometer foil, a compressed electron slice is pushed forward by the pulse and go ahead together with the pulse wavefront along the longitudinal direction. Different from the traditional RPA, the SCPA results show that the acceleration structure is quite stable and do not suffer from the transverse instability. Here, protons are accelerated at a certain distance behind electrons, rather than nearly in the same longitudinal position as in RPA. By a later stage, a thin proton slice is formed behind electron layer. And with the Gaussian pulse and simple plane foil the acceleration time is much longer than that in the traditional RPA reported. In such a dynamics the density of relativistic compressed electron bunch can stay above the critical density. A stable longitudinal electrostatic field may be formed, which accelerates the isolated proton slice at a distance behind the electrons.

Finally, in Zhou et al. [46] it is observed that a cutoff energy scan of the single laser pulse with ultra thin plane foil acceleration regime from $a_0 = 20$ to $a_0 = 400$ has a scaling law about $E \propto a_0^{1.67}$. This exponent 1.67 (under the domain of $a_0 \gg 1$) is greater than those found in the cases of TNSA and CAIL and rivals that of RPA (for $a_0 \gg 1$). This is another indication that the SCPA is highly efficient and efficacious.

In conclusion in SCPA the ratio ξ between electron areal density and normalized laser amplitude is much smaller compared to the optimal value in the traditional RPA. After the electron bunch is pushed forward by the laser ponderomotive force, ions are effectively accelerated in the stable longitudinal electrostatic field over a long distance. Thus the SCPA is simple and robust, yielding high quality, ultra-short and high energy proton bunches in a very compact fashion. This way a compressed ultra-short proton bunch (femtosecond) may be achieved from a standard PW class laser compressed by the thin foil compression technique [44]. If one combines the CAN laser [47] with the present new technique, we may be also able to access highly repetitive ultra-short proton bunches. Such proton bunches should have broad and revolutionary applications, including extremely compact injectors, medicine (such as proton oncology), high energy physics, and high fluence neutron (such as for the driver of subcritical reactors ADR) and muon beams. Because of the fs time resolution, time sensitive measurements and triggers may become available for the first time.

13.5 Conclusions

We are exploring how best we improve the physics of TNSA. We connected the earlier collective accelerator research in which a similar physics of sheath acceleration was discussed and try to learn lessons from them. The analysis of Mako-Tajima [8] as applied to the CAIL regime of laser ion acceleration showed that the laser-driven electron sheath that was generated ahead of the thin target is stuck to the target material. In the extreme limit of TNSA, the target is not moving at all. Thus the sheath is also stuck there, for the accelerating structure unable to acquire any phase velocity at all. The accelerating length is limited to the sheath thickness. When the target thickness (and/or mass) of the target is reduced to a nanometric size, the target too begins to move upon an intense laser pulse irradiation. Under such a condition the regime of CAIL may appear, which shows a greater accelerating length and thus energy of ions and also often a more collimated longitudinal energy spectrum. This is because the thinner target allows target acceleration that in turn allows more coherent acceleration of ions over a longer length of distance without the sheath stuck in a stationary position as in TNSA. In the other hand, when we increase the laser intensity to make the ion dynamics become (close to) relativistic, as is the case in the RPA [27], ion acceleration becomes coherent over a long distance, as the speed of the electrons that are accelerated by the strong ponderomotive potential by the intense laser pulse is capable of pulling ions instantaneously toward the electron bunch. If the ion velocity approaches quickly to the speed of light, the ion dynamics coheres with the laser pulse. In this regime, all the dynamics become synchronized with the laser pulse and thus the acceleration becomes relativistic (and the relativistic coherence manifests). The ions acceleration length is lengthened and therefore the energy

spectrum of ions becomes sharper. The drawback of such RPA regime is its requirement of very high intensity laser (in the neighborhood of 10^{23} W/cm²). Such high intensities are not easy (nor cheap) to realize in the lab for current 20–30 fs pulse duration.

The incentive of SCPA is to remedy this drawback by introducing a method (at slightly lower intensity and much lower laser energy per pulse) to accelerate ions coherently over a long distance. By reducing the pulse from tens of fs to a few fs we eliminate the oscillatory interferences of acceleration in the ponderomotive acceleration of electrons and thus making the sheath acceleration of ions to become more effective and efficient. This way, we are increasing the intensity of the pulse in inversely proportional to the pulse length in comparison with CAIL, i.e. $I \sim 1/\tau$, while the laser energy is decreasing from RPA as $\varepsilon \sim \tau$. The reduction of the pulse length τ over CAIL and RPA is about an order of magnitude in SCPA. Thus SCPA (along with RPA) achieves the relativistic acceleration of ions in coherence, i.e. it achieves the condition of the phase velocity of the accelerating structure in SCPA nearly equal to c and coherently. This mechanism of ponderomotive acceleration of electrons followed by the electrostatic wave structure (or sheath) is analogous to the laser wakefield acceleration [32]. In fact LWFA was invented to overcome the difficulty of the early collective acceleration deficiencies as discussed above, i.e. the lack of the coherency of the accelerating structure with the particles (ions) to be accelerated. The only difference between SCPA and LWFA is that while the former does not excite the eigen mode of the plasma, the latter does excite the eigen mode of plasma oscillations.

The invention of the thin film compression into single-cycle laser pulse [44] allows us now to access the SCPA regime as a near-term reality. If such a technique is established, a few 10s Joule class laser with a few 10 fs pulse length (nowadays commercially available) may be compressed into a single-cycle pulse. Such a pulse is in fact what we anticipate in the above application. The employment of such a laser and compression should lead to a variety of very exciting ion accelerator schemes. These include a very compact and relatively inexpensive laser ion accelerator toward proton beam therapy. Because ions are already coherent, the reach to relativistic energies is not difficult. Thus a variety of applications of laser ion accelerators will become possible in relativistic energies such as to the ADS (accelerator driven system) and to other nuclear beams (such as neutron, muon, and neutrino) as well as isotope generations.

Acknowledgments The work has been supported by the Norman Rostoker Fund. I thank Dr. A. Giulietti's encouragement throughout this work. Collaboration and discussions with Drs. M. Zhou, X.Q. Yan, G. Mourou, J. Wheeler and I.J. Kim are deeply appreciated. I dedicate this paper to the memory of the late Professor Norman Rostoker, who made education of me and remained a source of inspiration. In the final stage of the preparation of this paper (in fact the last weeks) I learned the passing of Professor Wolfgang Sandner, who was serving as Co-Chair of ICUIL (International Committee for Ultrahigh Intensity Lasers) among other leadership roles (while I serve as Chair of ICUIL). I am dedicating this paper also to the memory of Dr. Sandner.

References

1. V.I. Veksler, *CERN Symposium on High Energy Accelerators and Pion Physics* (CERN, Geneva, 1956), p. 80
2. S.E. Graybill, J.R. Uglum, *J. Appl. Phys.* **41**, 236 (1970)
3. J.W. Poukey, N. Rostoker, *Plasma Phys.* **13**, 897 (1971)
4. N. Rostoker, M. Reiser, *Collective Methods of Acceleration* (Harwood, London, 1979)
5. D.D. Ryutov, G.V. Stupakov, *Soviet J. Plasma Phys.* **2**, 309 (1976)
6. F. Mako, in the Proceedings of Norman Rostoker Memorial Symposium, eds. by T. Tajima, M. Binderbauer (in publication, AIP, New York, 2016)
7. F. Mako, A. Fisher, N. Rostoker, D. Tzach, C.W. Roberson, *I.E.E.E. Trans, Nucl. Sci.* **26**, 4199 (1979)
8. F. Mako, T. Tajima, *Phys. Fluids* **27**, 1815 (1984). See also T. Tajima, F. Mako, *Phys. Fluids* **21**, 1459 (1978)
9. R.A. Snavely, M.H. Key, S.P. Hatchett, T.E. Cowan, M. Roth, T.W. Phillips, M.A. Stoyer, E. A. Henry, T.C. Sangster, M.S. Singh, S.C. Wilks, A. MacKinnon, A. Offenberger, D.M. Pennington, K. Yasuike, A.B. Langdon, B.F. Lasinski, J. Johnson, M.D. Perry, E.M. Campbell, *Phys. Rev. Lett.* **85**, 2945 (2000)
10. E.L. Clark, K. Krushelnick, J.R. Davies, M. Zepf, M. Tatarakis, F.N. Beg, A. Machacek, P.A. Norreys, M.I.K. Santala, I. Watts, A.E. Dangor, *Phys. Rev. Lett.* **84**, 670 (2000)
11. A. Maksimchuk, S. Gu, K. Flippo, D. Umstadter, V.Yu. Bychenkov, *Phys. Rev. Lett.* **84**, 4108 (2000)
12. P. Mora, *Phys. Rev. Lett.* **90**, 185002 (2003)
13. J. Fuchs, P. Antici, E. D'humières, E. Lefebvre, M. Borghesi, E. Brambrink, C.A. Cecchetti, M. Kaluza, V. Malka, M. Mancossi, S. Meyroneinc, P. Mora, J. Schreiber, T. Toncian, H. Pépin, P. Audebert, *Nat. Phys.* **2**, 48 (2006)
14. A. Andreev, A. Levy, T. Ceccotti, C. Thaury, K. Platonov, R.A. Loch, P. Martin, *Phys. Rev. Lett.* **101**, 155002 (2008)
15. A.A. Andreev, S. Steinke, T. Sokollik, M. Schnürer, S. Ter Avetsyan, K.Y. Platonov, P.V. Nickles, *Phys. Plasmas* **16**, 013103 (2009)
16. D. Neely, P. Foster, A. Robinson, F. Lindau, O. Lundh, A. Persson, C.-G. Wahlström, P. McKenna, *Appl. Phys. Lett.* **89**, 021502 (2006)
17. T. Ceccotti, A. Lévy, H. Popescu, F. Réau, P. D'Oliveira, P. Monot, J.P. Geindre, E. Lefebvre, Ph. Martin, *Phys. Rev. Lett.* **99**, 185002 (2007)
18. T. Esirkepov, M. Yamagawa, T. Tajima, *Phys. Rev. Lett.* **96**, 105001 (2006)
19. K. Matsukado, T. Esirkepov, K. Kinoshita, H. Daido, T. Utsumi, Z. Li, A. Fukumi, Y. Hayashi, S. Orimo, M. Nishiuchi, S.V. Bulanov, T. Tajima, A. Noda, Y. Iwashita, T. Shirai, T. Takeuchi, S. Nakamura, A. Yamazaki, M. Ikegami, T. Mihara, A. Morita, M. Uesaka, K. Yoshii, T. Watanabe, T. Hosokai, A. Zhidkov, A. Ogata, Y. Wada, T. Kubota, *Phys. Rev. Lett.* **91**, 215001 (2003)
20. X.Q. Yan, C. Lin, Z.M. Sheng, Z.Y. Guo, B.C. Liu, Y.R. Lu, J.X. Fang, J.E. Chen, *Phys. Rev. Lett.* **100**, 135003 (2008)
21. A. Henig, S. Steinke, M. Schnürer, T. Sokollik, R. Hoerlein, D. Kiefer, D. Jung, J. Schreiber, B.M. Hegelich, X.Q. Yan, J. Meyer-ter-Vehn, T. Tajima, P.V. Nickles, W. Sandner, D. Habs, *Phys. Rev. Lett.* **103**, 245003 (2009)
22. T. Tajima, D. Habs, X.Q. Yan, *Rev. Accel. Sci. Tech.* **2**, 201 (2009)
23. X.Q. Yan, T. Tajima, B.M. Hegelich, L. Yin, D. Habs, *Appl. Phys. B* **98**, 711 (2009)
24. M. Passoni, V.T. Tikhonchuk, M. Lontano, V.Yu. Bychenkov, *Phys. Rev. E* **69**, 026411 (2004)
25. J. Schreiber, F. Bell, F. Grüner, U. Schramm, M. Geissler, M. Schnürer, S. Ter-Avetisyan, B.M. Hegelich, J. Cobble, E. Brambrink, J. Fuchs, P. Audebert, D. Habs, *Phys. Rev. Lett.* **97**, 045005 (2006)

26. S. Steinke, A. Henig, M. Schnürer, T. Sokollik, P.V. Nickles, D. Jung, D. Kiefer, T. Tajima, X.Q. Yan, J. Meyer-ter-Vehn, W. Sandner, D. Habs, *Laser Part. Beams* **28**, 215 (2010)
27. T. Esirkepov, M. Borghesi, S.V. Bulanov, G. Mourou, T. Tajima, *Phys. Rev. Lett.* **92**, 175003 (2004)
28. A. Macchi, F. Cattani, T.V. Liseykina, F. Cornolti, *Phys. Rev. Lett.* **94**, 165003 (2005)
29. A.P.L. Robinson et al., *New J. Phys.* **10**, 013021 (2008)
30. B.M. Hegelich et al., *Nature (London)* **439**, 441–444 (2006)
31. H. Schwoerer et al., *Nature (London)* **439**, 445–448 (2006)
32. T. Tajima, J.M. Dawson, *Phys. Rev. Lett.* **43**, 267 (1979)
33. C. Lau, P.C. Yeh, O. Luk, J. McClenaghan, T. Ebisuzaki, T. Tajima, *Phys. Rev. STAB* **18**, 024401 (2015)
34. J. Faure, Y. Glinec, A. Pukhov, S. Kiselev, S. Gordienko, E. Lefebvre, J.-P. Rousseau, F. Burgy, V. Malka, *Nature* **431**, 541 (2004)
35. C.G.R. Geddes, C. Toth, J. van Tilborg, E. Esarey, C.B. Schroeder, D. Bruhwiler, C. Nieter, J. Cary, W.P. Leemans, *Nature* **431**, 538 (2004)
36. S.P.D. Mangles et al., *Nature* **431**, 535 (2004)
37. I Jong Kim et al., in *Radiation Pressure Acceleration of Protons with Femtosecond Petawatt Laser Pulses*, International Conference on Ultra-High Intensity Lasers—ICUIL 2014 (Goa, India). Available at www.icuil.org/downloads/category/37.html
38. H. Daido, M. Nishiuchi, A.S. Pirozhkov, *Rep. Prog. Phys.* **75**, 309 (2012)
39. A. Macchi, M. Borghesi, M. Passoni, *Rev. Mod. Phys.* **85**, 751 (2013)
40. X.Q. Yan, H.C. Wu, Z.M. Sheng, J.E. Chen, J. Meyer-ter-Vehn, *Phys. Rev. Lett.* **103**, 135001 (2009)
41. Hu Ronghao, Bin Liu, Lu Haiyang, Meilin Zhou, Chen Lin, Zhengming Sheng, Chia-erh Chen, Xiantu He, Xueqing Yan, *Sci. Rep.* **5**, 1549 (2015)
42. B. Rau, T. Tajima, *Phys. Plasmas* **5**, 3575 (1998)
43. B. Rau, T. Tajima, H. Hojo, *Phys. Rev. Lett.* **78**, 3310 (1997)
44. G. Mourou, S. Mironov, E. Khazanov, A. Sergeev, *Euro Phys. J. Spec. Topics* **223**, 1181 (2014)
45. M. Guillaume et al., CLEO 2013 CTh5C.5 (2013). doi:[10.1364/CLEO_SI.2013.CTh5C.5](https://doi.org/10.1364/CLEO_SI.2013.CTh5C.5)
46. M.L. Zhou, X.Q. Yan, J.A. Wheeler, T. Tajima, G. Mourou, Presentation at IZEST Conference on *Outlook on Wake Field Acceleration: the Next Frontier—CERN—Geneva—Switzerland* (2015). Available at <http://www.izest.polytechnique.edu/izest-home/izest-events/102015-outlook-on-wake-field-acceleration-the-next-frontier/outlook-on-wake-field-acceleration-the-next-frontier-cern-geneva-switzerland-322660.kjsp>
47. G. Mourou, B. Brocklesby, T. Tajima, J. Limpert, *Nat. Photonics* **7**, 258 (2013)
48. L. Spencer et al., *Phys. Rev. E* **67**, 046402 (2003)
49. P. McKenna et al., *Phys. Rev. E* **70**, 034405 (2004)
50. TZh Esirkepov, S.V. Bulanov, K. Nishihara, T. Tajima, F. Pegoraro, V.S. Khoroshkov, K. Mima, H. Daido, Y. Kato, Y. Kitagawa, K. Nagai, S. Sakabe, *Phys. Rev. Lett.* **89**, 175003 (2002)
51. T. Tajima, *Proc. Jpn. Acad. Ser. B* **86**, 147 (2010)

Index

A

Absolute dosimetry of laser-driven beams, 205
Absorbed dose, 256
Absorbed flux, 124
Activated air, 123, 128
Activation, 99
 issues, 119
Activator protein 1 (AP-1), 79
Activity, assessment, 106
Adaptative responses, 41
Adiabaticity, 308
All-optical sources, 183
Amplified spontaneous emission (ASE), 7
Apoptosis, 73
Areal density distribution, 288
Areal distribution of protons, 260
Assessment of activity, 106
Autophagy, 76
Average density of proton, 261
Average population, 107

B

Backscattering, 195
Beam loading effect, 144
Beatwave pattern, 26
Beta decay, 121
Beta particles, 122
Betatron emission, 191
Betatron radiation, 153, 155
Bethe-Bloch formula, 113
Bethe formula, 113
Biodosimetry, 33
Biological effect of laser-accelerated, 250
Biological studies, 252
Biological target, 35
Biomarkers, 70, 87
Biomolecular damage, 35
Biomolecule (BM) damage, 31
Biomolecules, 33

Brachytherapy, 1

Bragg peak, 68, 221
Break-out afterburner (BOA), 118, 232
Bremsstrahlung, 184
Bremsstrahlung radiation, 214
Broadband spectrum, 191
Bunch, 195

C

Coherent acceleration of ions by laser (CAIL), 295
Cancer radiotherapy, 39
Cancer therapy, 34, 43
Cases of cancer, 1
cDNA microarray, 82
Cell cycle, 69
Cell damages, 69
Cell death, 72
Cell inactivation, 262
Cell-irradiation experiments, 252
Cell network, 79
Channel guiding, 146
Channels, 109, 111
Chemical reaction of moving active molecules, 265
Chirped pulse amplification (CPA), 183
Chromatin packaging, 77
Circularly polarized laser, 308
Clonogenic survival, 73
Coherence index, 303
Coherent diffraction imaging (CDI), 158
Collection aperture, 195
Colliding pulse, ionization injection, 164
Collisionless shock acceleration, 231
Collisionless shocks, 222
Collisionless shock waves, 230
Colony formation assay, 262
Compton scattering, 192
Contact radiography, 276

- Continuous spectrum, 196
 Contrast, 184
 Contrast of the laser pulse, 275
 Control of risks, 105
 Conventional ion accelerators, 263
 Conversion efficiency, 301
 Coulomb explosion, 233, 277
 CPA laser technology, 2
 Cross section, 107, 109, 110
 Cut-off energy, 225
 CyberKnife®, 52
 and brain lesions, 53
 and liver lesions, 57
 and lung lesions, 56
 and prostate lesions, 60
 and reirradiation, 60
 and spine lesions, 54
 Cytokines, 87
 Cytokine secretion, 89
 Cytokine signature analysis, 90
- D**
 Decay, 125
 of population, 109
 Deep tumors, 34
 Defocused laser generated proton fields, 129
 Delocalised electrons, 21, 29
 Dephasing length, 142, 185
 Depletion length, 143
 Development of Ionization Injection, 178
 Diffraction, 141
 Discharge of activated gases, 128
 Discipline, 105
 DNA damage, 37, 38, 252
 DNA damage response (DDR), 72
 DNA-damage-sensor proteins, 256
 DNA double-strand breaks (DSB), 256
 DNA methylation, 77
 DNA repair mechanisms, 71
 Doppler shift, 194
 Dose, 124, 125
 calculation, 120, 122
 Dose delivered to healthy tissues, 251
 Dose delivery, 34
 Dose rate, 153
 Dosimetric simulations with Monte Carlo methods, 214
 Dosimetric techniques, 235
 Dosimetry, 12
 Dosimetry polymer film CR-39, 278
 Double strand breaks (DSBs), 71
 Downramps, 199
 1D simulator, 118
 1D solver, 120
- 3D Monte-Carlo simulations, 254
 Dynamics of energy deposition, 261
- E**
 Early genes, 79
 Effectiveness of laser techniques, 266
 Electric fields, 25
 Electrodynamics process, 193
 Electron acceleration, 136
 Electron kinetic energy, 2
 Electron radiation therapy, 152
 Electron radiography, 153
 Electrostatic bucket, 302
 Elimination, reduction, isolation, control, protection and discipline (ERICPD), 104, 105
 Energy distribution, 187
 Energy resolution of the protons, 257
 Energy-selection system (ESS), 259
 Energy spectra of proton beams, 254
 Energy spread of ions, 307
 Energy spread of the beam, 257
 Enhancement of laser-plasma coupling, 189
 Entrance pinhole, 257
 Environment, discharges to, 129
 Epigenetic changes, 77
 Equivalent therapeutic effect, 266
- F**
 Faraday cup, 212
 Fast electrons, 187
 Femtochemistry, 31
 Femtolysis, 28, 30
 Femtolysis experiments, 32
 Field-of-view/resolution ratio, 283
 Filling factor, 196
 FISPACT, 126
 FISPACT II, 126
 Fluid environment, 127
 Flux function, 107
 Focal spot, 198
 Focused laser generated proton fields, 129
 Fourier transform (FT) holographic imaging, 158
 Fraction of surviving cells, 262
 FSSR spectrometer, 277
 Functional proteins, 87
- G**
 Gafchromic XR-CT2 films, 207
 Gafchromic XR-M2 films, 207
 Gamma dose, 124
 γ -H2AX foci, 72, 256
 γ -ray source, 190

- Gas cell, 146
Gaseous discharges, 129
Gaseous isotopes, 130
Gas-filled capillary discharge waveguide, 148
Gas-jet, 185
Geant4, 127
GEANT4 toolkit, 215
Gene expression profile (GEP), 78
Genetic alterations, 84
Genetic variability, 83
Genome-wide analysis, 84
Giant Dipole Resonance, 10
Grey, 120
Group structure, 112
Growth of hadrotherapy, 4
- H**
- H2AX phosphorylation, 256
Hadrontherapy, 225
Hadrotherapy, 1
Harmonics, 196
Hazards, 99
Hazards, radiological, 102
Head-on collision, 196
Heavy ion acceleration, 226
High-contrast, 280
High dose rate, 28
High dose-rate effect, 250
High efficiency, 9
High-energy photons, 154
High energy radiation femtochemistry (HERF), 19, 20, 23, 28
High harmonics, 155
High-LET, 6
High peak power lasers, 5
High resolution electron radiography, 287
High resolution radiography, 283
Hohlraum dynamics, 273
Hole boring, 227
Homologous recombination (HR), 71
Hot electrons, 224
Hydronium ion (H_3O^+), 22
Hypofractionated scheme, 56
Hypoxia-inducible factor 1 α (HIF-1 α), 79
- I**
- Imaging of low-contrast biological specimens, 283
Immune system, 87
Immunofluorescence microscopy, 258
Immunological molecules, 87
Immunomodulatory cytokines, 89
Infrastructures, 184
Injector, 150
- Injector-accelerator scheme, 151
Instability-free ion acceleration, 309
Instantaneous dose rate, 10
Integrated tiger series (ITS), 127
Intensity-modulated radiation therapy (IMRT), 153
Interaction area and time, 263
Interface window, 254
Interferon (IFN)-related genes, 81
Intracellular signalling, 82
Intraoperative electron radiation therapy (IOERT), 72, 75, 204
Intra-operative radiation therapy (IORT), 1, 9
Inverse compton scattering, 156
Ion beam therapy, 233, 249
Ion beam transport, 235
Ion cutoff energies, 306
Ionisation clusters, 29
Ionization chamber, 209
Ionization channels, 21
Ionization injection, 163, 187
 1D injection theory, 166
 injection theory, 167
 low energy spread, 167
 principle, 164
 wakefield acceleration, 164, 165
Ion-matter interactions, 264
Ionography, 281
Ion producing laser-targets, 116
Ion stopping, 114
Ion track, 264
Ion track radius, 265
IR bystander effects, 78
Isolation of risks, 104
Isotopes, 192
- L**
- Larmor formula, 193
Larmor radius, 254
Laser-accelerated proton beams, 221
Laser-cluster interaction, 275
Laser-driven cluster-based electron sources, 285
Laser-driven electron beam radiography, 284
Laser-driven electron source, 283
Laser-driven ion acceleration, 222, 249
Laser-driven neutron sources, 237
Laser-driven particle beams radiography, 289
Laser-driven proton and electron radiography, 272
Laser-driven proton source, 250
Laser-electron guns, 289
Laser pulse contrast, 7
Laser shot, 103

- Laser-solid interactions, 221
 Laser techniques, 19
 Laser wake-field acceleration (LWFA), 2, 136
 Lawson-Woodward theorem, 137
 Light sail, 229
 Linear absorption coefficient, 121
 Linear energy transfer (LET), 8, 235, 251
 Linear-quadratic model, 263
 Linear Thomson scattering, 195
 Lorentz-boosted frame, 149
 Lorentz factor, 138
 Lorentz force, 137
 Low energy radiation femtochemistry (LERF), 19, 20
 Low energy spread, two stage, 167
 Low-LET, 6
- M**
 Magnetic field dynamics, 273
 Magnetic fields, 257
 Management strategies, 100
 for radiological facilities, 101
 Mass absorption coefficients, 114, 121
 Mass attenuation coefficients, 115
 Matched condition, 186
 MCNP, 126
 Mitigation strategy, 100
 Mitogen-activated protein kinase (MAPK), 81
 Mitotic catastrophe (MC), 76
 Modified error function, 130
 Mono-energetic ion beams, 257
 Mono-energeticity, 141
 Monoenergetic particle, 34
 Monte Carlo codes, 196
 Monte Carlo simulations, 116, 214
 MS-based studies, 85
 Multicharged Ions, 276
 Multi electron beam, 163, 168
 Multi electron beam, comblike energy spectrum, 170
 Multi-fraction doses (MFD) of IR, 81
 Multi-GeV electron beams, 11
 Multiple laser-plasma acceleration stages, 150
- N**
 Nanobiodosimetry, 42
 Nanodosimetry, 19
 Nanometer targets, 298
 Nanometric tracks, 24
 Nanostructure diagnostics, 282
 Near-critical plasmas, 232
 Necrosis, 74
 Neutron spectrum, 118
 Neutron transport, 115
- Nonadiabatic transitions, 24
 Nondestructive radiography, 284
 Non destructive testing, 190
 Non-linear effects, 6, 263
 Non mass spectrometry (MS)-based studies, 85
 Non-targeted effects, 78
 Normalized amplitude, 195
 Normalized vector potential, 138
 Norman Rostoker's program, 296
 Nuclear Factor kappa B (NF- κ B), 79
 Number density of ion tracks, 264
- O**
 OH radicals, 265
 OMICS approach, 70
 Optical scattering pulse, 199
 Optimal target thickness, 298
 Orion facility, 119
 Outer shells, 188
- P**
 p53 factor, 73
 Particle bunches, 28
 Peak brilliance, 199
 Percentage depth dose (PDD) curve, 206
 Personalized radiogenomic research, 85
 Petawatt (PW) laser pulses, 136
 Petawatt laser, 229
 Phase mixing, 180
 Photon counting, 197
 Photon fields, 114
 Plasma, 26
 Plasma bubble, 26
 Plasma bubble acceleration, 136
 Plasma expansion model (PEM), 300
 Plasma frequency, 138
 Plasma-mirror, 8
 Plasma tailoring, 186
 Plasma wake-field acceleration (PWFA), 136
 Plasma wave, 138
 Plasma waveguide acceleration, 136
 Plasma wavelength, 140
 Point projection technique, 272
 Polyacrylamide gel electrophoresis (2D-PAGE), 85
 Ponderomotive drive, 302
 Ponderomotive force, 184, 222
 Ponderomotive injection, 187
 Population, 107
 Positron emission tomography, 236
 P-polarized radiation, 188
 Prehydrated electron, 22
 Prepulse, 7
 Prethermal process, 32

- Prethermal radical process, 33
Prethermal regime, 31, 41, 42
Projection proton radiography, 272
Protection, 102, 105
Protein expression, 86
Proteogenomics, 70
Proteomic science, 85
Proton bunch duration, 255
Proton radiography, 272
Proton spectral envelope, 117
Ps-pedestal, 8
Pulsed radiotherapy, 43
Pump and-probe experiments, 285
- Q**
Quasi-monoenergetic electrons, 26
- R**
Radiated power, 190
Radiation, 120
Radiation damage, 21
Radiation pressure, 223, 226
Radiation reaction, 197
Radiation therapies, 1
Radiobiological studies, 235
Radiobiology, 68
Radiochromic films, 207
Radiogenetics, 83
Radiogenomic research, 85
Radio-isotopes, 10
Radiological assessment, 130
Radiological safe, 12
Radioresistant cell fractions (RCF), 90
Rayleigh range, 141
Rayleigh–Taylor instability, 273
Reactions, 110
Reactive oxygen species (ROS), 69
Reduction of risks, 104
Relative biological effectiveness (RBE), 8, 42, 68, 235, 262
Relative dosimetry of laser-driven, 205
Relativistic particle, 24
Relativistic self-focusing effect, 142
Relativistic transparency, 223, 229
Resonance absorption, 187
Resonant excitation, 189
RF-based devices, 3
Risks
 control of, 105
 isolation of, 104
 radiological, 102
 reduction, 104
Radiation pressure acceleration (RPA), 295
- S**
Safety, 12, 99
Scattered energy, 199
Secondary sources, 11
Self-focusing, 277
Self-guiding, 145
Self-injection, 186
Self-phase modulation, 190
Self-similar evolution, 304
Self-truncated ionization injection, 168
 beam quality, 164
Senescence, 75
Senescent associated secretory phenotype (SASP), 75
Senescent phenotype, 90
Sensitivity of electron imaging to the chemical or structural differences, 288
Sheath, 185
Sheath acceleration, 222
SHEEBA radiochromic film stack device, 9
Shock acceleration, 227
Short-lived isotope production, 236
Signalling pathways, 79
Signal transducers and activators of transcription members (STATs), 79
Simulation, 125
Single-cycle laser, 7
Single-cycle laser pulse acceleration (SCPA), 295
Single dose (SD) of IR, 81
Single fraction, 57
Single irradiation shot, 36
Single-nucleotide polymorphisms (SNPs), 83
Single pulse ionization injection, 176
Single strand breaks (SSBs), 71
Skin of test person, 124
SNP profiles, 84
Soft-X-ray pulses, 154
Soluble factors, 78
Spatial resolution, 280
Spatio-temporal radiation biomedicine, 34
Spectral function, 108
Spectral line profiles, 278
Splitting, 198
S-polarized radiation, 188
Spot size, 141
Spread-out Bragg peak, 234
SRIM program, 111
Steel, 109
Stereotactic radiotherapy (SRT), 51
Stereotactic re-irradiation, 61
Stopping powers, 114, 255
Strategy, three tier strategy, 103

- Structured targets, 226
 Subcycle laser pulse acceleration, 308
 Submersion dose, 123
 Sub-MeV electron bunches, 10
 Submicron spatial resolution, 276
 Supersonic jet, 9
 Supersonic nozzle, 146
 Surface, radiation from, 122
- T**
 Table-top lasers, 226
 Target normal sheath acceleration (TNSA), 223, 295
 Target thickness, 111
 Temporal overlap, 198
 TGF β , 80
 Therapy protocols, 39
 Thin foil compression technique, 310
 Thin targets, 300
 Thomson/Compton scattering, 184
 Thomson cross section, 194
 Thomson parabola, 279
 Time-of-flight (TOF) spectrometer, 254
 TNSA target, 116
 Transcriptional regulation, 82
 Transcription factors (TFs), 79
 Transport, 112
 Transverse emittance, ionization injection, 163, 173, 176
 Trapped radiation, 300
 Treatment planning, 40
 TRIM, 255
 Tumor cell lines, 89
- Tunable electron source, 40
 Tuneability, 199
 Two-color ionization injection, 163, 170, 178
 Two-color ionization injection, emittance, 170
 Two-color laser, 163, 167, 179
 Types of cancer, 68
- U**
 Ultrafast electron diffraction, 285
 Ultrahigh contrast (UHC), 298
 Ultraintense lasers, 183
 Ultrashort duration, 6
 Ultrashort radiation, 35
 Ultra-thin objects, 274
 Ultra-thin target, 301
 Underdense gas jet targets, 232
 Undulator radiation, 154
- V**
 VHEE electrons, 41
 sources, 40
 Vimentin, 86
- W**
 Wakefield, 25
 Water molecules, 21
 Wave breaking, 140, 186
 Well-tolerated radiation technique, 62
 Wiggler, 155
- X**
 X-ray phase contrast imaging (XPCI), 157